

PAUL SCHERRER INSTITUT



SwissFEL Conceptual Design Report



PSI Bericht Nr. 10-04
April 2012

Cover figure description

SwissFEL Building front view: With a total length of 719 m, the accelerator and undulators are located in the ground floor of a two-storey building. Most of the building will be underground, but the upper floor (technical buildings) will only be semi-covered with soil, to ensure good maintenance access. The experimental area building is a single-storey building which is naturally covered by the surrounding land, and the main entrance to this area is clearly visible on the figure.

Editor

Romain Ganter

Editorial Board

Rafael Abela

Hans Heinrich Braun

Terry Garvey

Bruce Patterson

Marco Pedrozzi

Luc Patthey

Sven Reiche

With contributions from:

Executive Summary

Keil B.
Braun H.H. Kuenzi R.
Ganter R. Pedrozzi M.
Patterson B. Raguin J.-Y.

Design Strategy and Parameters Choice

Sanfilippo S.
Schilcher T.
Schlott V.
Adelmann A. Schmidt T.
Beutner B. Schulz L.
Falone A. Trisorio A.
Kim Y. Vermeulen D.
Milas N. Wiegand P.
Prat E. Zennaro R.
Reiche S. Zimoch E.

Electron Components

Alex J.
Aiba M.
Arsov V.
Calvi M.
Citterio A.
Egli S.
Gough C.
Hauri C.
Hunziker S.
Ischebeck R.
Joehri H.

Photon Components

Flechsigg U.
Juranic P.
Patthey L.
Patterson B.
Pedrini B.
Oberta P.
Vicario C.

Assembly and Commissioning

Alex J.
Aiba M.
Dreyer K.
Keil B.
Kobler R.
Kuenzi R.
Luethy M.
Schietinger T.
Wickstroem J.

Building and Infrastructure

Baechli A.
Fuchs A.
Ganter R.
Hohmann E.
Janzi G.
Kiselev D.
Loertscher Y.
Luescher R.
Ming P.
Roser W.
Teichmann S.

Acknowledgements

The author list of this report is limited to the people who have actually written text or supplied figures or tables appearing in the CDR. Many more people from PSI and abroad have contributed to SwissFEL and indirectly to the content of the CDR. The authors of this CDR recognize in particular that the concept for SwissFEL emerged from the “LEG/FEL” R&D activity which was launched at PSI under the leadership of Prof. Albin Wulich in 2003 [1,2]. Many contributions to the concept as well as to technical solutions which appear in this conceptual design report can be traced back to the work of this R&D activity, although it was not always possible to put references to this work.

Furthermore we profited from the advice and collaboration with many experts from other laboratories. In particular we would like to thank our colleagues from CANDLE, CERN, DESY, ELETTRA, EMPA, HZB, INFN-LNF, INAP, SLAC and SPRING8.

Last, not least we acknowledge the enormous help and constructive criticism we got from the SwissFEL machine advisory committee FLAC chaired by Prof. Jörg Rossbach.

Table of contents

1	Executive Summary	4
1.1	SwissFEL project goals and CDR objectives	4
1.2	SwissFEL design rationale	4
1.3	SwissFEL building	8
1.4	Key parameters and operational modes	12
1.5	SwissFEL project schedule	14
1.6	Overview of SwissFEL Science Case	16
2	Design strategy and parameter choice	18
2.1	Overview and design parameters	18
2.2	Simulation tools	20
2.3	Accelerator simulation	21
2.4	Undulator line parameters and simulations	37
3	Electron beam components	46
3.1	Laser system	46
3.2	RF systems	50
3.3	Timing and synchronization	67
3.4	Magnets	76
3.5	Undulators	91
3.6	Electron beam diagnostics concept	103
3.7	Vacuum concept	114
3.8	Mechanical support systems	118
3.9	Control system	124
4	Photon beam components	128
4.1	Front end enclosure layout (Athos and Aramis)	129
4.2	Photon beam diagnostics	131
4.3	Photon switchyard (Athos, Aramis)	135
4.4	Experimental hall	144
4.5	Experiment hall special components	149
5	Assembly and commissioning	152
5.1	Machine installation	152
5.2	Components to infrastructure interface	159
5.3	Machine commissioning plan	159
5.4	Feedback systems and electron beam-based alignment	162
6	Building and infrastructure	168
6.1	Building layout	168
6.2	Safety issues	180
6.3	Supply installations (Status as of October 2011)	193
6.4	Appendix A: Drawing SwissFEL Building	202
6.5	Appendix B: Version modifications SwissFEL CDR	208
7	References	210

1 Executive Summary

1.1 SwissFEL project goals and CDR objectives

The goal of SwissFEL is to provide a source of extremely bright and short X-ray pulses enabling scientific discoveries in a wide range of disciplines, from fundamental research to applied science. The eminent scientific need for such a source is well documented in the SwissFEL Science Case Report [3].

The technical design of SwissFEL has to keep a delicate balance between the demand from experimentalists for breathtaking performance in terms of photon beam properties, on the one hand, and essential requirements for a user facility, such as confidence in technical feasibility, reliable and stable functioning, and economy of installation and operation, on the other hand. A baseline design has therefore been defined which relies entirely on state-of-the-art technologies without fundamental feasibility issues. This SwissFEL Conceptual Design Report (CDR) describes the technical concepts and parameters used for this baseline design, as of the end of 2011. The objective of the CDR is to provide a reference for the machine design, thus ensuring that the various teams working on SwissFEL use consistent planning assumptions. A positive side-effect of the considerable work which went into this CDR is the identification and correction of several design inconsistencies. Given that the design is still evolving, all relevant modifications relative to the CDR have to be documented in an unambiguous manner accessible to all personnel involved in SwissFEL. The design with all accumulated modifications and more detailed technical component

descriptions and specifications will have to be compiled again in the technical design report (TDR), which will then be the technical reference for project execution.

R&D on various advanced options beyond the baseline design choices is being pursued at PSI, namely on field-emitter arrays, pulsed-diode electron guns and advanced FEL seeding schemes. Although not all these options are included in the CDR, they can still be integrated into SwissFEL, either during the project preparation phase or as a later upgrade if technical maturity and superior performance compared to the baseline design are demonstrated. The same is of course true for relevant advancements on FEL technology elsewhere.

1.2 SwissFEL design rational

1.2.1 Introduction

In a free-electron laser, the active medium is a beam of relativistic electrons. This beam moves in vacuum through a periodic magnet array, called an undulator, forcing the electrons to follow a wiggling orbit centered on a straight line. The wiggling orbit introduces a transverse velocity component, which allows the electrons to exchange energy with a light wave which is co-linear with the electron beam. The electrons become accelerated or decelerated, depending on the phase of the transverse electric field of the light wave. For a particular wavelength of the light beam, this exchange becomes resonant for

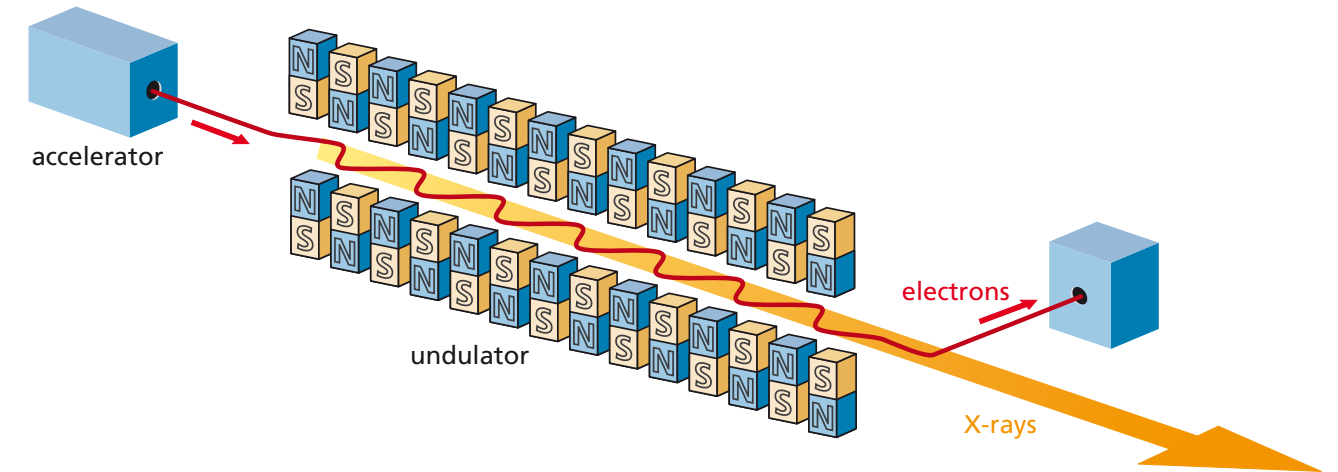


Fig.1.2.1: e-beam in undulator with lightwave.

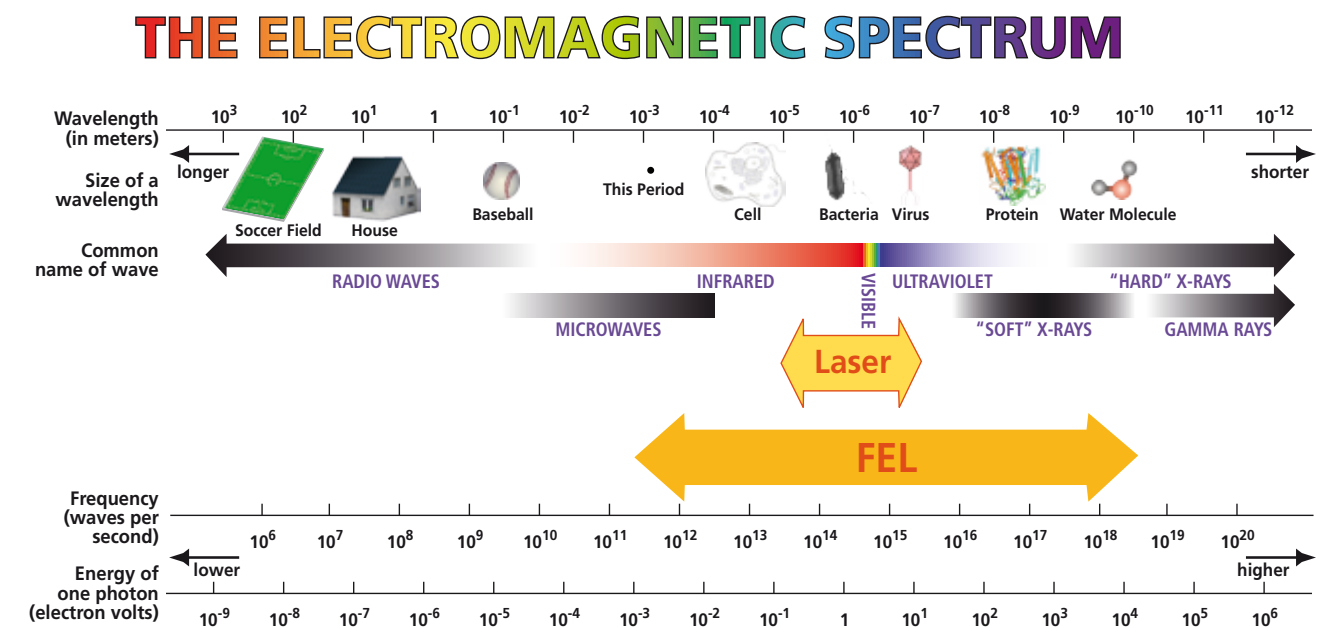


Fig. 1.2.2: Wavelength range of the FEL vs. a quantum laser.

a single electron, leading to a continuous transfer of energy from the electron to the light wave. The resonant wavelength is given by

$$\lambda = \frac{\lambda_U}{2\gamma^2} \left(1 + \frac{K^2}{2} \right)$$

where λ_U is the period length of a planar undulator and K is the undulator parameter, defined by

$$K = \frac{1}{2\pi} \frac{e}{mc} B_U \lambda_U$$

with B_U the peak magnetic field of the undulator on the axis. Since the path length of the electrons depends on the electron energy, the energy modulation induced by

the radiation field is converted to a bunching of the electrons with the periodicity of the light wave. Thus the electrons are concentrated at the phase of the light wave where efficient energy transfer occurs and the light wave becomes coherently amplified. As a result, the entire system acts analogously to a light amplifier in the well-known optical quantum laser. However, the FEL has the fundamental advantage that its operation does not depend on quantum transitions in a specific laser medium. Therefore, the FEL scheme can be applied over a much wider photon wavelength range than the quantum laser principle, as shown in Figure 1.2.2.

The FEL principle is the only proven method for providing coherent light pulses reaching the hard X-ray wavelength regime. However, the FEL scheme is also faced with severe difficulties at these wavelengths. No mirrors with sufficient reflectivity and bandwidth exist; therefore, the FEL cannot be built in an oscillator configuration but has rather to operate in a single-pass mode, lining up a large number of undulator magnets to drive the lasing process into saturation. Furthermore, no seeding source is readily available for these wavelengths. This latter problem is overcome by using the broadband signal from the shot noise spectrum of the electron beam and using it to start the amplification process. This type of FEL operation is called self-amplified spontaneous emission (SASE) and has recently been demonstrated to work for wavelengths as short as 1.5 Å [4]. There is worldwide research on alternative seeding methods at X-ray wavelengths, with the hope of obtaining even better X-ray FEL performance. PSI is participating in this research, but SASE is presently the only proven method, and other approaches become increasingly difficult as the wavelength is made shorter.

Another challenge comes from the requirement to maintain a good overlap between the electron beam and the light beam. Since the divergence of the light beam decreases proportional to λ , the demands on electron beam quality become more stringent at shorter wavelengths. The figure of merit for electron beam quality is the normalized emittance, which is given by the “surface” occupied by the beam particles in a plane spanned by the deviation in the transverse position from the nominal orbit. The normalized emittance is conserved under beam acceleration and therefore depends mainly on the performance of the electron injector. This makes the design of the injector a particular challenging task for X-ray FELs. Optimum matching of the electron beam to the light beam can be achieved if the condition

$$\varepsilon_N \leq \gamma \frac{\lambda}{4\pi}$$

is met, where ε_N is the normalized emittance, γ is the relativistic factor, proportional to the electron’s energy, and λ is the lasing wavelength. Present injector technology requires acceleration of electrons to very high energy in order to operate a FEL in the X-ray regime. However, it has been demonstrated that FELs can operate with reduced efficiency even if the normalized emittance exceeds this optimum condition by a factor four to five. Despite this, progress in injector performance is very desirable until the emittance condition is met. An introduction to the theory of FELs can be found in [5].

The SwissFEL baseline design aims to produce FEL pulses covering the wavelength range 1 Å to 70 Å, with a compact and economic design which is affordable on the scale of a national laboratory. The overall cost of a linear accelerator is almost proportional to the final beam energy. Therefore, a key design goal is to minimize the required electron beam energy for a given radiation wavelength. The dependence of photon beam wavelength on electron beam energy and undulator wavelength, as discussed in the last Section, implies the use of undulators with short period length and rather low K -value. The emittance achievable with the injector puts another lower limit on the beam energy. Both constraints are most stringent for the shortest lasing wavelength.

Table 1.2.1:

Parameters for lasing at 1 Å	
Beam energy	5.8 GeV
λ_U	15 mm
K	1.2

Based on these factors, and considering the best performance achievable with leading edge undulator and electron injector technology, the parameters of table 1.2.1 were chosen to achieve lasing with the SwissFEL at 1 Å wavelength.

1.2.2 Technical highlights of SwissFEL

In order to meet both the performance requirements and the cost constraints, substantial technical developments for some key components are underway to push their performance beyond the present state of the art. For these developments, SwissFEL profits not only from the excellent R&D performed at PSI since 2003, but also from the vast experience and progress achieved at other laboratories active in electron linac and FEL design. In particular, active collaboration and information exchange with SLAC, DESY, SPRING8, KEK, BESSY, CERN, LNF, ELETTRA and LAL has inspired the design concepts described here. Introduction of key technologies makes the SwissFEL accelerator unique. These innovations can be listed as follows:

- A newly developed 2.6 cell RF gun which combines the advantages of two existing electron guns, namely the PHIN gun from LAL and the LCLS gun at SLAC.
- A wavelength-tunable gun laser system, in order to minimize the intrinsic emittance (the ultimate theoretical limit to high beam brightness). This laser has

already been used and its beneficial effects on intrinsic emittance have been experimentally demonstrated at PSI.

- SwissFEL will utilise solid-state power modulators on a large scale for the linac RF sources. PSI is pioneering, with this technology, an approach which promises superior RF stability and a more compact construction compared to existing linear accelerators.
- The main linac uses C-band RF technology, which has been developed in Japan during recent years. SwissFEL will use this technology for the first time for a large-scale accelerator project outside Japan. The RF parameters chosen for SwissFEL are the result of new overall system optimization performed at PSI to minimize electricity consumption and overall system cost.
- The hard X-ray line (the first of the two SwissFEL FEL lines to be built) is based on in-vacuum undulator technology with an unprecedented short magnet period for this kind of applications. This requires pushing the limits of undulator technology in terms of magnetic materials and mechanical precision. Here, the extensive experience of PSI with a similar state-of-the-art undulator built at the SLS, as well as a very fruitful collaboration with SPRING8, is a major advantage.
- The soft X-ray line (the second of the two SwissFEL FEL lines to be built) is based on APPLE II undulator technology, with the capability of full polarization control. These objects are very demanding in terms of magnetic and mechanical engineering. SwissFEL profits from the experience gathered with the APPLE II undulators built by PSI in collaboration with BESSY for SLS.

1.2.3 The injector

The baseline technology for the SwissFEL electron injector relies on the RF gun photo-injector concept. A photocathode placed in a high-field RF cavity is illuminated with a short-pulse laser. The timing of the laser pulses is synchronized to the RF, so that electrons are emitted when the accelerating RF field on the cathode reaches an optimum value. For the past two decades, RF gun technology has been the subject of intense R&D activities at various leading accelerator laboratories worldwide, and remarkable progress has been achieved. The present state of the art allows the production of electron pulses of 200 pC with normalized emittances below 0.4 μm . This is sufficient to operate the SwissFEL at nominal

wavelength and beam energy. However, to reach these parameters, the pulses produced from the gun have to be much longer (typically several ps) than the final pulse of a few fs required in the FEL. Therefore, the pulse has to be longitudinally compressed in the linear accelerator, downstream from the injector.

Demonstration of intrinsic emittance reduction by tuning the gun laser wavelength has been performed at the LEG test-facility [6]. The SwissFEL photo-injector laser system was developed with the novel feature of a large tunable wavelength capability, to allow thermal emittance reduction.

1.2.4 The accelerator

The SwissFEL linear accelerator (linac) must fulfil two functions:

- acceleration of the electron pulse from the injector to the nominal energy of the FEL
- time compression of the electron pulse from 5 ps rms to 25 fs rms.

The demands for compactness and economy suggest the use of a normal-conducting, pulsed RF system for acceleration, with rather high accelerating fields. A key design parameter for such a linac is the total RF energy supplied per pulse by the RF transmitters to the accelerating cavities. This parameter strongly influences the investment cost and electric power consumption of the overall facility, and can be minimized either by reducing the local accelerating field or by increasing the RF frequency. Since reducing the field increases the overall facility length, an increase of the RF frequency is the more promising approach. However, such an increase goes together with a decrease of the size of the accelerator components, thus leading to even tighter mechanical and electrical tolerances. While most normal-conducting electron linear accelerators nowadays operate at an RF frequency of 3 GHz, the SwissFEL foresees the use of a 5.7 GHz C-band RF system, and will be the first large-scale linac of this type in Europe.

For temporal pulse compression, two magnetic chicanes are placed in the linac at 355 MeV and 2.0 GeV. The electron pulse is accelerated in the linac slightly off the crest of the RF wave. This introduces a time/energy chirp along the electron pulse. The energy dependence of the electron path length in the magnetic chicane leads to

a time compression, as depicted in Figure 1.2.3. Two 12 GHz RF structures are used to linearize this dependence before entering in the magnetic chicane.

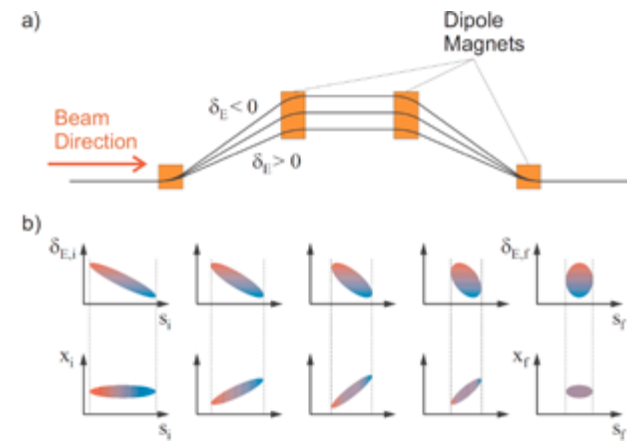


Fig. 1.2.3: The rotation of electrons in the energy–time plane by a magnetic chicane. $\delta_{E,i}$ represents the relative energy spread over the bunch, s_i is the longitudinal coordinate along the bunch and X_i is the transverse beam size (Figure courtesy of A. Bolzmann [7]).

1.2.5 The FELs

Two SASE FEL lines will be driven by the linac – a hard X-ray FEL named Aramis and a soft X-ray line named Athos. Aramis covers the wavelength range 1–7 Å, and Athos the wavelength range 7–70 Å.

For Aramis, a planar undulator with a novel type of permanent magnet (dysprosium-enriched NdFeB) is planned. The magnet array is mounted inside the vacuum tank. To reach the required parameters, the inter-magnet gap which is available for the beam is as small as 4.5 mm. The use of dysprosium-enriched NdFeB magnets allows these undulators to be operated at room temperature, thus avoiding a costly liquid nitrogen cooling system, as is normally required for undulators with comparable parameters. A total of 12 undulators of this type, each 4 m long, have to be aligned in a row within tight tolerances to ensure that the Aramis FEL can reach the SASE saturation regime.

For the Athos FEL, the undulator period length is more relaxed, and the permanent magnet arrays can therefore be situated outside the vacuum chamber. These undulators are built in the so-called APPLE II configuration, which allows full control of the FEL polarization and wavelength by adjusting the mechanical position of the magnet arrays with high precision. Movements of the

magnet arrays with submicron accuracy have to be performed in the presence of very strong magnetic forces, making the mechanical design of the mover systems particularly challenging. The feature of polarization control will be particularly advantageous for magnetization dynamics experiments.

Furthermore, it is foreseen that the Athos FEL be operated either with seeding by an optical laser system or with self seeding. Such seeding schemes allows the spectral width of the FEL radiation to be narrowed by an order of magnitude with full longitudinal coherence. However, despite its obvious attractiveness, FEL seeding at these short wavelengths is an as-yet unproven technology, and considerable R&D, with uncertain outcome, is required in order to apply it for the SwissFEL. The subject of FEL seeding is a strong focus of R&D worldwide, with PSI playing a strong role in the theoretical modelling of the process and in technical developments. Nevertheless, without experimental proof of feasibility, the SwissFEL baseline design has to rely on SASE operation for both FEL lines.

1.3 SwissFEL building

1.3.1 Building overview

As well as for the machine design, the building concept should meet both the cost constraints and the safety requirements. The overall length of the facility is about 720 m, with a width varying between 6 and 40 m. The building is 10 m high where two levels are foreseen. The building will be located in the direct vicinity of PSI. A drawing of the facility is shown in Figure 1.3.1.1.

The electron accelerator (gun to Linac 3) is built on two levels (see Figure 1.3.1.2), with the electron beam tunnel below ground, to minimize the radiation protection requirements (concrete wall thickness). This also has the advantages of better temperature and mechanical stability, and the overall visual impact on the landscape is minimized. On the top floor of the electron accelerator section, a series of infrastructure buildings will host all the necessary RF power stations, control units, water cooling system, electrical power supply and air conditioning system. These infrastructure buildings are separated from the electron beam tunnel by a thick concrete floor,

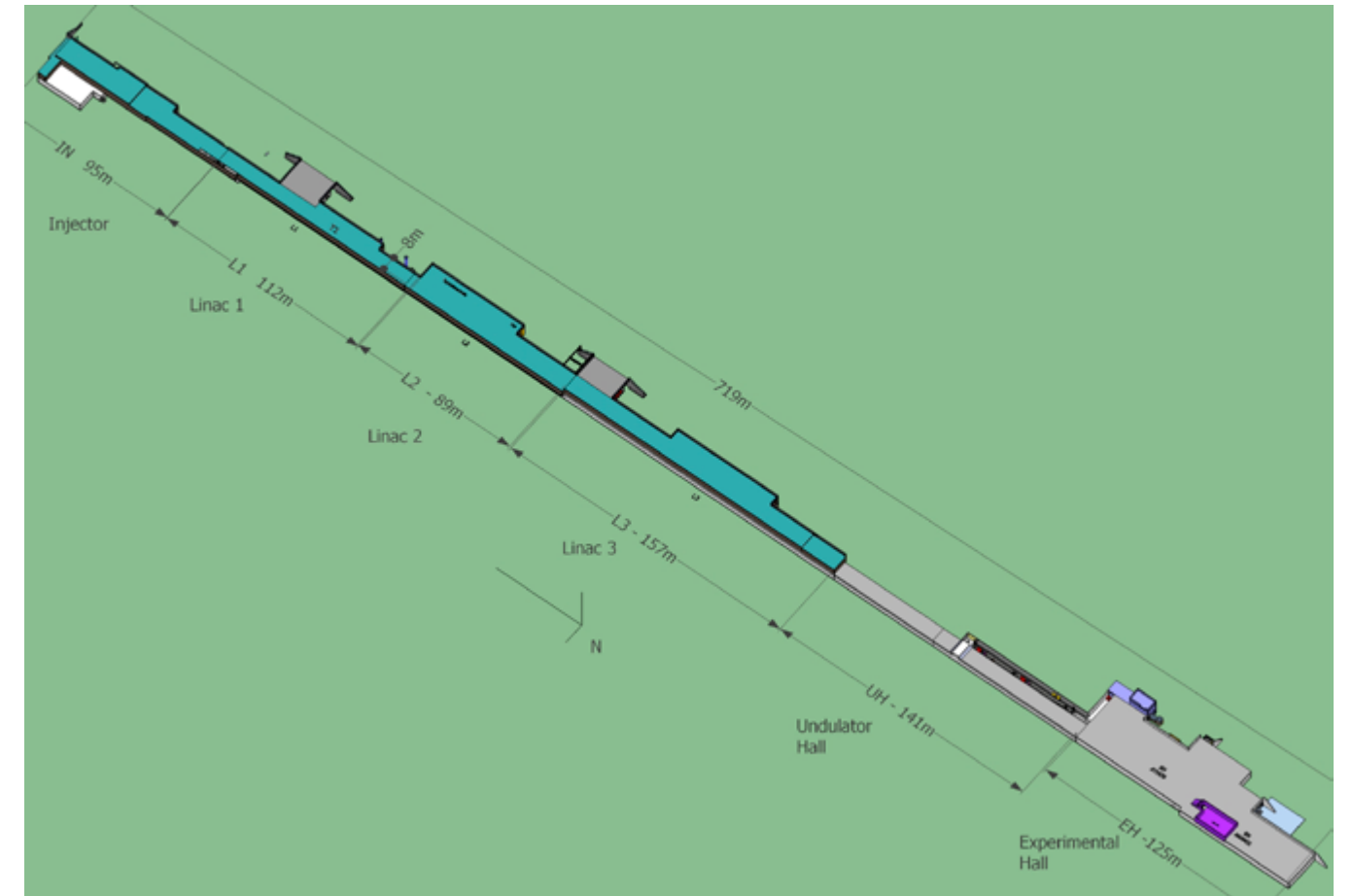


Fig. 1.3.1.1: SwissFEL Facility overview from the electron gun (at the left end) to the Aramis experimental hall (on the right). Surrounding ground is not represented.

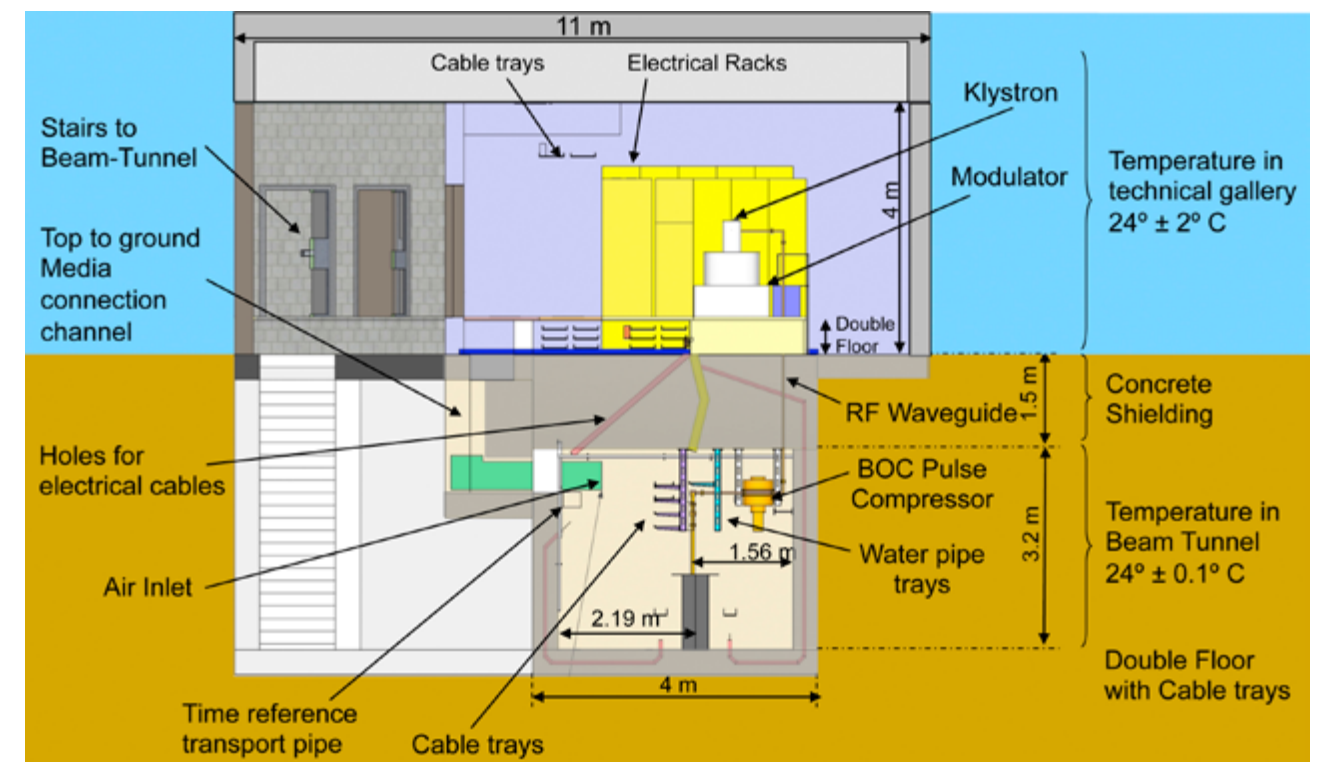


Fig. 1.3.1.2: Sectional view of the SwissFEL Electron Accelerator Facility ($z=150$ m, Linac 1), showing the electron beam axis in the underground tunnel and the technical building on the upper level.

for radiation shielding. This allows easy access during facility operation for maintenance of all technical installations.

The undulator hall (100 m long) is mainly underground, and a dedicated area near the experimental hall is foreseen for the preparation and measurements of the undulator modules. The undulator hall is then followed by a drift section of ~ 120 m, dedicated to X ray diagnostics, before it enters the experimental stations. The Aramis experimental hall is divided into 3 separated experimental 'hutches' to ensure full-time use of the FEL light: one experimental station is in operation, while the other two are preparing their experiments.

1.3.2 SwissFEL facility site

The location of the 700m-long SwissFEL facility and the auxiliary buildings for the SwissFEL project is shown on Figure 1.3.2.1. The site has been chosen because of almost ideal conditions for stability and the availability of ground water for an efficient cooling-water supply at low and constant incoming temperature.

All the activities related to the preparation of SwissFEL are located within one kilometre of the installation site. The C-band RF test stand has entered into operation in 2011 and will be able to test a full RF module with 4 C-band structures of 2 m in length each. The SwissFEL Injector Test Facility is currently in used for SwissFEL R&D program (2011) and will be moved to the SwissFEL site in 2015.

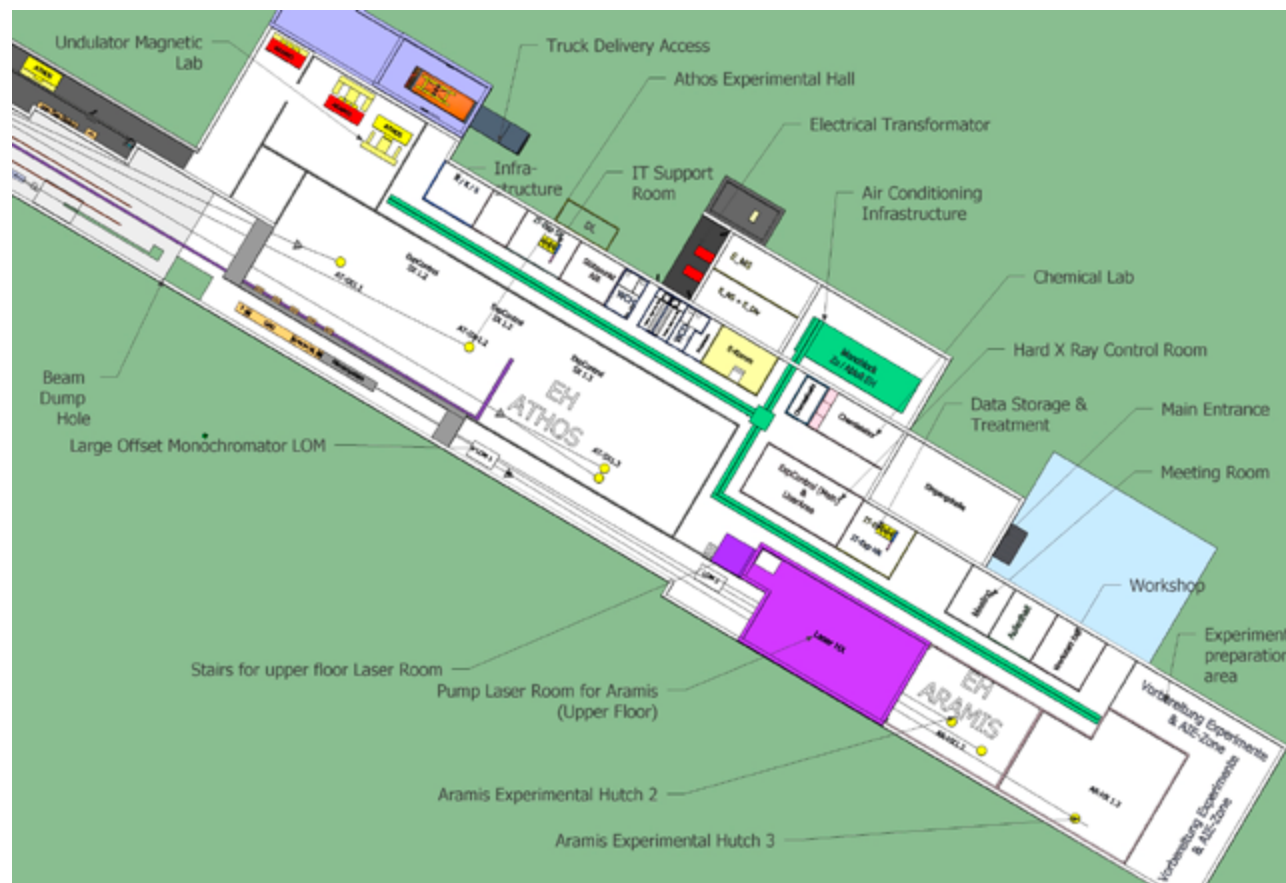


Fig. 1.3.1.3: Inside view of the experimental halls (underground). There are three experimental hutches with shielding for experiments with hard X rays to Aramis. The Athos experiment hall has space for three experiments in one single housing.



Fig. 1.3.2.1: The locations of the SwissFEL facility and auxiliary buildings.

1.4 Key parameters and operational modes

SwissFEL key parameters

Some key parameters and features of SwissFEL are summarized in Table 1.4.1 below.

Table 1.4.1

Key parameters and features of SwissFEL	
Overall length (incl. experimental hall)	720 m
Total electrical power consumption	5.2 MW
Maximum electron beam energy	5.8 GeV
Height of beamline above tunnel floor	1.2 m
Electron gun	3 GHz RF gun with 2.5 cells
Cathode type	Cu photocathode driven by a frequency-tripled TiSa laser
Injector booster	Normal-conducting travelling wave structures (copper) with $\nu = 3$ GHz
RF source main linac	Klystron with solid-state modulator and RF pulse compression
Accelerating structures, main linac	Normal conducting travelling wave structures (copper) with $\nu = 5.7$ GHz and $G = 26 - 28$ MV/m
Linac repetition rate	100 Hz
Bunch compression	Two 4-magnet chicane bunch compressors at 0.35 GeV and 2.0 GeV. With X-band harmonic cavity at 1 st bunch compressor
Number of FEL lines	2 (Aramis and Athos)
Undulator type, Aramis	In-vacuum permanent magnet with $\lambda_U = 15$ mm
Wavelength range, Aramis FEL	1 Å – 7 Å (SASE)
Polarization, Aramis	Linear
Undulator type, Athos	Apple II permanent magnet with $\lambda_U = 40$ mm
Wavelength range, Athos FEL	7 Å – 70 Å; seeded and SASE
Polarization, Athos	Variable (circular, elliptical and linear)

The SwissFEL injector and accelerator permit a wide range of electron beam parameters that are described in Section 2. Two basic modes – “long pulse” and “short pulse” – are defined as the standard operation modes. The beam parameters for these modes, and the corre-

sponding performance of the Aramis FEL, are summarized in Table 1.4.2.

Table 1.4.2 Expected Performance of Linac, Aramis and Athos lines. Performances for different operation regimes are detailed in Chapter 2.

Design parameters for the electron beam	Operation Mode	
	Long Pulses	Short Pulses
Charge per bunch (pC)	200	10
Core slice emittance (mm.mrad)	0.43	0.18
Projected emittance (mm.mrad)	0.65	0.25
Slice energy spread (keV, rms)	350	250
Relative energy spread (%)	0.006	0.004
Peak current at undulator (kA)	2.7	0.7
Bunch length (fs, rms)	25	6
Bunch compression factor	125	240

Performance of Aramis for 5.8 GeV electron energy and 1 Å lasing wavelength	Long Pulses	Short Pulses
Maximum saturation length (m)	47	50
Saturation pulse energy (μJ)	150(*)	3
Effective saturation power (GW)	2.8	0.6
Photon pulse length at 1 Å (fs, rms)	21	2.1
Number of photons at 1 Å ($\times 10^9$)	73	1.7
Bandwidth, rms (%)	0.05	0.04
Peak brightness (# photons. $\text{mm}^{-2} \cdot \text{mrad}^{-2} \cdot \text{s}^{-1} / 0.1\%$ bandwidth)	7.10^{32}	1.10^{32}
Average Brightness (# photons. $\text{mm}^{-2} \cdot \text{mrad}^{-2} \cdot \text{s}^{-1} / 0.1\%$ bandwidth)	$2,3 \cdot 10^{21}$	$5,7 \cdot 10^{18}$

(*) 150 μJ is based on a designed slice emittance of 0.43 mm.mrad but up to 1 mJ has been obtained with start to end simulation (see section 2).

Performance of Athos (SASE) For example at 3.4 GeV electron energy and 2.8 nm lasing wavelength	Long Pulses
Maximum saturation length (m)	22 m
Saturation pulse energy (μJ)	360
Effective saturation power (GW)	11.2
Photon pulse length at 1 Å (fs, rms)	13
Number of photons at 1 Å ($\times 10^9$)	5000
Bandwidth (%)	0.19
Peak brightness (# photons. $\text{mm}^{-2} \cdot \text{mrad}^{-2} \cdot \text{s}^{-1} / 0.1\%$ bandwidth)	6.10^{35}
Average Brightness (# photons. $\text{mm}^{-2} \cdot \text{mrad}^{-2} \cdot \text{s}^{-1} / 0.1\%$ bandwidth)	8.10^{23}

The SwissFEL linac operates with a repetition rate of 100 Hz. At each linac pulse, two microbunches are accelerated with a spacing of 28 ns. While the first pulse goes straight to the Aramis FEL line, the second is deviated to the Athos FEL by a fast kicker in the switchyard between Linac 2 and Linac 3 at 3.0 GeV. This timing scheme allows both FEL lines to be operated simultaneously at 100 Hz, thus doubling the number of photon pulses sent to the experiments. An additional small linac in the Athos line insures the independence of the two FEL line wavelength tuning. Indeed the energy in the Athos line can be varied from 2.6 to 3.4 GeV. The main characteristic of Athos is that it will be a seeded FEL light, improving the longitudinal coherence.

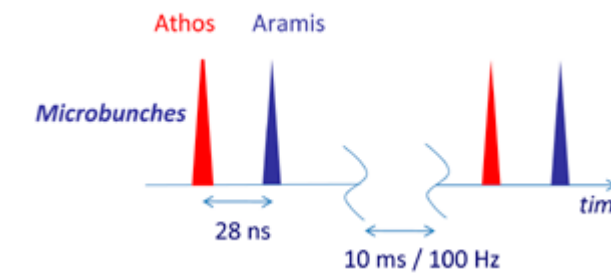


Figure 1.4.1: Time structure of linac beam.

SwissFEL operations scenario

SwissFEL plans to operate continuously 24 h a day and 7 days a week. A maintenance break of 12 hours from 6:00–19:00, is planned during one of the working day of each week. The following shift of this shutdown day, will be dedicated to beam development and beam set-up from 19:00–7:00.

Experiments get beam time in 12 h portions with a first shift 7:00–19:00 and the next shift 19:00–7:00 (except for shift before maintenance day which finishes at 6:00). Both FEL lines are served simultaneously at 100 Hz with charges of 10–200 pC in each FEL, but charges, pulse length and repetition rate are similar for both lines. Both X-ray beams can be switched off and on independently. Both electron bunches can also be switched off and on independently. However, switching off ARAMIS electron bunch may require some readjustment of ATHOS beam. Photon beam repetition rate can be reduced independently for both lines.

Before tunnel access after high repetition rate running, cool down period of about 1 h is foreseen.

On each FEL line one experiment will run, one will be ready for taking data (in case of sudden and unexpected

beam availability), one experiment will in preparation. It is also possible to split the x-ray pulse into two experiments simultaneously. Ready for taking data implies availability of user and instrument within less than 1 h.

Repetition rate beam (Hz)	Application	Comments
1 or single shot	Beam set-up with increased risk of losses (i.e. recovery after machine triggered beam interlock because of losses)	
10	Beam set-up and commissioning	Maybe some burst timing configuration with mean 10Hz repetition rate will be required
50	Fall back in case of time slot separation problems	Synchro with selectable mains raising/falling edge
100	Normal running condition	

Repetition rate of RF needs adjustment independent of beam (i.e. gun laser), such that usually $f_{\text{beam}} \leq f_{\text{RF}}$. This is required to keep RF in thermal equilibrium.

In case of beam loss, the machine protection system (MPS) shall, depending on loss level, reduce repetition rate or stop beam (RF will however not be stopped to avoid thermal transients). MPS shall stop LLRF (Low Level RF) in case of exceeding dark current beam loss.

MPS interlocks in injector, linac 1 and linac 2 will stop both beams. MPS interlocks in linac 3 will stop only the ARAMIS beam. RF interlocks in ATHOS will only stop ATHOS beam.

In ARAMIS, the hutch running with beam is closed, while the others are accessible. In ATHOS, all experimental areas are always accessible. During commissioning period July 2016 – July 2017, frequent access periods of tunnel of variable length will most probably be required. Accesses happen frequently on short notice. During ATHOS installation 2018 – 2019 two installation periods (shutdown) of about 5 month will be required.

Each year, one long shut down period of 4 – 6 weeks for component maintenance and installation is foreseen. In addition, about 3 short down periods of one week will be planned during the year.

1.5 SwissFEL project schedule

1.5.1 Overview of SwissFEL construction phases

The present planning for SwissFEL is summarized in Figure 1.5.1. Presently, the R&D for key components, such as linac RF systems and undulators, is already in progress, together with the definition of the buildings and the procedures for building permits. Thus, civil construction can start end 2012, if a positive funding decision is taken in 2012. The construction of the SwissFEL tunnel and buildings, including experimental halls and the technical infrastructure, will be in 2013 and 2014, while the installation of the accelerator in the tunnel will start at the beginning of 2015, after civil engineering and technical infrastructure installation has been completed. The preparation and storage of accelerator components before installation in the SwissFEL

complex will be carried out in an assembly building temporarily leased by PSI. This building will be ready for use before the end of 2012. While the SwissFEL Injector Test Facility in WLHA is the test bed for most beam related components, the prototype of the main linac C-band accelerator module is tested in an RF high-power test stand, which is installed in the existing OBLA building on the PSI East site from the end of 2010 onwards. In 2015, the complete injector will be moved from the WLHA test hall to the SwissFEL tunnel. Thereafter, WLHA can be used for development, assembly and storage of SwissFEL components and the leased building will no longer be required. An overview of the building locations is given in Figure 1.3.2.1.

By the mid of 2016, installation of the injector, the linac and the Aramis line will be completed, and commissioning of SwissFEL will start in fall 2016, with hardware commissioning in general and RF conditioning in particular. Some initial tests, yet to be defined, will be

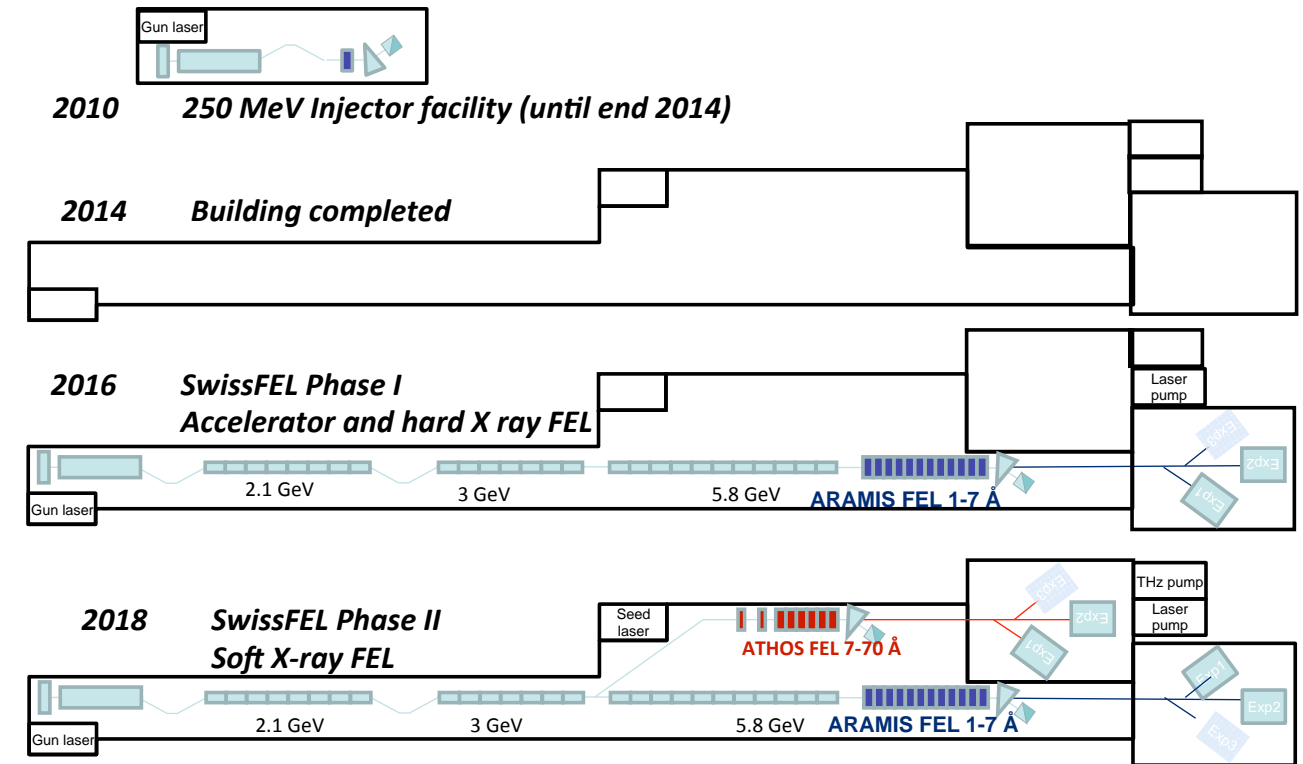


Fig. 1.5.2: Schematic of the Assembly sequence (see Chapter 6 for exact and latest building drawing).

SwissFEL Schedule December 2011

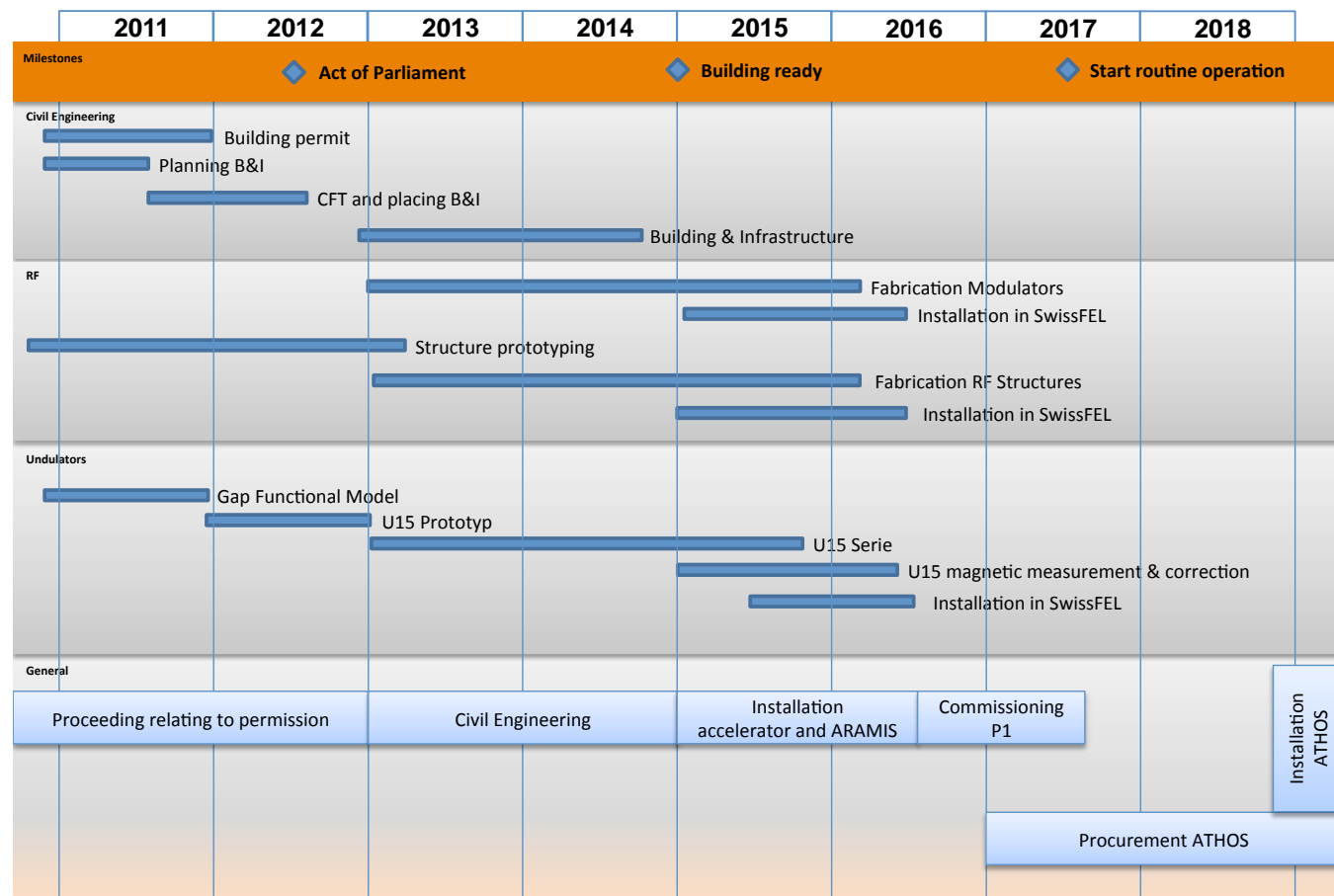


Fig.1.5.1. Schedule for SwissFEL construction.

performed beforehand, during the course of 2016, to allow debugging and improvement of critical systems before main machine commissioning. First beam tests will start in fall 2016, with the goal of having first FEL lasing of Aramis by spring 2017 and regular user operation by the mid of 2017.

The Athos undulator line will be installed during a shutdown period in 2018 and subsequently commissioned. With this commissioning period, the SwissFEL construction project will be completed by the end of 2018 and SwissFEL will be operated as one of PSI's large user facilities thereafter. A schematic sequence of the construction steps is shown in Figure 1.5.1.

1.5.2 Future extensions

SwissFEL will be initially built with two FEL undulator lines, each with its own experimental hall. The photon

beam from each FEL line can be switched to three different experiment hutches in each hall. The baseline operation mode foresees the provision of X-ray pulses at 100 Hz repetition rate simultaneously for both undulator lines. An obvious extension of the facility's capabilities is an increase of the electron beam energy from 5.8 GeV to 6.5 GeV, extending the Aramis wavelength range from 1 Å to 0.8 Å. Such an upgrade is essential for studying resonant Mössbauer absorption, as described in the Science Case Report [3], p.14. This new upgrade can be achieved by adding two C-band RF stations, and space reservation for such an upgrade is part of the baseline design.

At present, there are no comprehensive plans for future extensions and upgrades, but provisions are being made in the civil engineering and site selection to allow buildings to be added for another hard X-ray FEL line and another soft X-ray FEL line, with their respective experimental halls. Both additional FELs could be driven by the existing linac.

1.6 Overview of SwissFEL Science Case

This Section gives a short overview of the experiments planned at SwissFEL and the expected scientific progress. A much more detailed description can be found in the SwissFEL Science Case Report [3].

Three dominant trends in today's science and technology are 'smaller', 'faster' and 'more complex'. Nanotechnology entails the measurement and manipulation of matter on the molecular scale. The relevant time-scale for dynamic processes is then the 'ultrafast' domain, defined by the femto-second vibration of an atom in a chemical bond. Complexity, which may manifest itself as chemical diversity, lack of crystalline order and/or non-equilibrium states, holds the promise of advanced materials with enhanced functionality. The predominant tool for investigating matter is light; the SwissFEL X-ray laser will be a unique light source, which will expand the frontiers of knowledge: at the nanoscale, of ultrafast phenomena and in complex materials.

In close consultation with experts representing a wide range of scientific research, a selection was made of particularly relevant areas of application for the SwissFEL. The SwissFEL Science Case emphasizes dynamical investigations of condensed matter and imaging of nanostructure objects. Further possible applications include time-resolved spectroscopy of plasmas and molecular gases, the study of sub-femto-second electron dynamics, the generation with intense X-ray pulses of new states of matter, and probing fundamental interactions. The SwissFEL has been conceived to address pressing scientific challenges of importance to society, in which it will doubtless make ground-breaking contributions.

The important generic types of experiment to be performed on condensed matter with the SwissFEL are:

- “pump-probe” measurements of irreversible dynamics
- “probe-probe” (split-and-delay) double-pulse measurements of equilibrium fluctuations
- lensless “flash imaging” of nanostructure objects.

The d'Artagnan undulator, used for seeding Athos, also produces soft X-rays. In the “water window”, water is transparent, but organic matter absorbs. A future upgrade of the SwissFEL will extend the Aramis spectrum from 12.4 to approximately 15 keV (violet segment). The

dots indicate resonant elemental absorption features (red: K; blue: L₃; green: M₃).

An overview of the photon energy range accessible with the SwissFEL undulator beamlines and the fields of investigation are shown in Figure 1.6.1. The principal areas of application are the following.

1.6.1 Nanoscale magnetization dynamics

A wide variety of magnetic effects operate on the SwissFEL time and length scales, and the availability of circularly-polarized pulses of radiation at approximately 1 nm wavelength and a synchronized THz pump source make the planned facility an ideal instrument for the study of magnetization dynamics. Research goals include the development of high-performance devices for information storage and spintronics computing, as well as the fundamental understanding of magnetism in two-, one- and zero-dimension systems.

1.6.2 Solution chemistry and surface catalysis

Controlled catalytic reactions are the key to the efficient use of resources, the production of clean energy and the elimination of environmental pollution. Using a laser or THz trigger, followed by the scattering or absorption of SwissFEL X-ray pulses, it will be possible to produce molecular movies of fast chemical reactions, allowing detailed study of the vitally important short-lived intermediate states.

1.6.3 Coherent diffraction by nanostructures

Besides being very bright and of very short duration, the SwissFEL X-ray pulses will, in addition, have a high transverse coherence. Coupled with modern computational techniques, this opens the intriguing possibility of forming high-resolution images without the use of lenses. Radiation damage of the sample is elegantly avoided by the ultrashort pulses: the necessary information is gathered before destruction of the sample occurs. The biggest achievement will be the ability to image in-

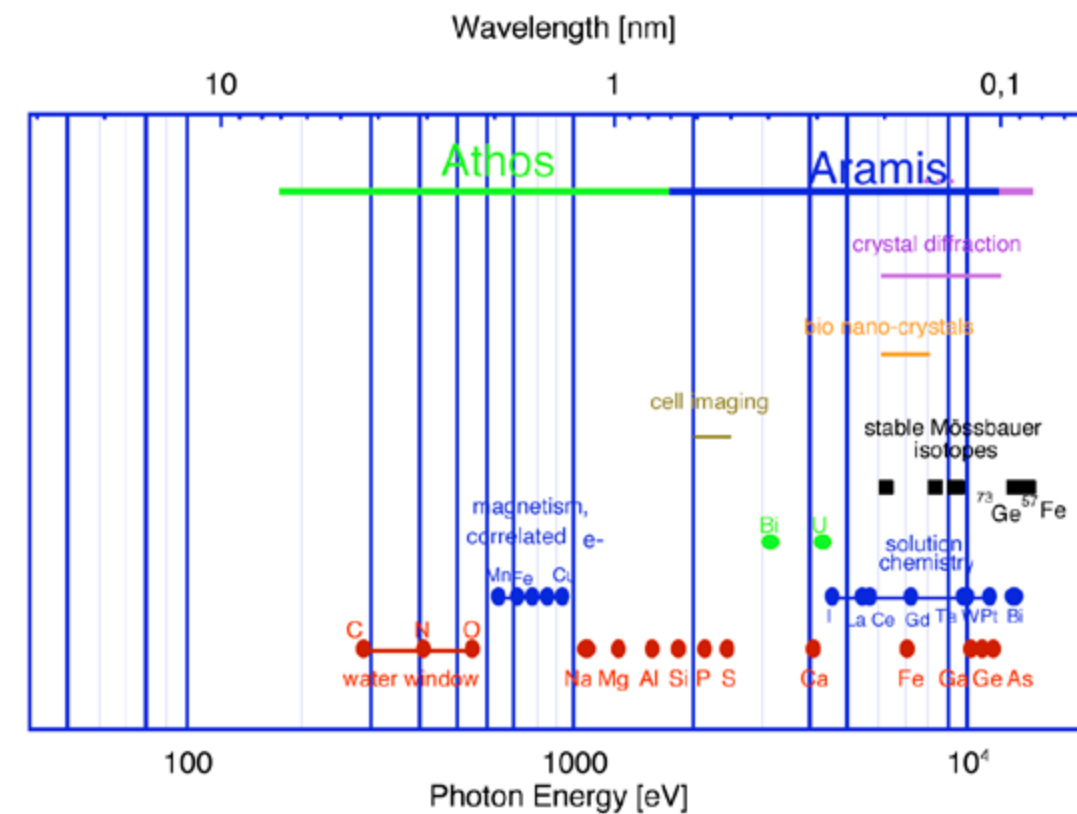


Fig. 1.6.1: An overview of photon energies accessible with the SwissFEL beamlines, and the corresponding areas of application.

dividual biomolecules, thus avoiding the necessity of purifying and crystallizing large amounts of scarce material.

1.6.4 Ultrafast biochemistry

Just as a rolling ball minimizes its energy by seeking the lowest point in a bowl, biochemical reactions, which are the molecular basis of living matter, can be thought of in terms of trajectories on higher-dimensional energy surfaces. Examples are the ultrafast sequence of conformations experienced by the rhodopsin molecule upon excitation by light in the photoreceptors of the eye, and the pathways by which initially unfolded protein molecules achieve their preferred configurations. Study with the SwissFEL X-ray pulses of the detailed energy landscapes experienced by such biomolecules has great potential for the intelligent design of next-generation pharmaceuticals.

1.6.5 Time-resolved spectroscopy of correlated electron materials

After more than 20 years of intense effort, a theoretical explanation for the most prominent discovery in modern solid-state physics, that of high-temperature superconductivity, is still lacking. These oxide materials are examples of the larger class of correlated electron systems, which are distinguished by intimate interactions between the behaviour of the electronic charges, the electronic spins, the atomic orbitals and the crystal lattice. By directing the energy of a pump laser into one of these entities, and using the SwissFEL X-ray pulses to register the reaction of another one, the complex network of interactions in these materials can be untangled, paving the way for the development of novel material applications in, for example, thermoelectric devices, ultra-sensitive magnetic reading heads, spintronics and quantum computing.

2 Design strategy and parameter choice

2.1 Overview and design parameters

The design parameters are defined so that they correspond to the specifications required to fulfil the experimental programme of the SwissFEL Science Case Report [3]. The start-to-end simulations presented in this chapter provide a more precise set of beam and machine parameters which meet the design parameters. More specific details on the SwissFEL layout and optics can be found in a PSI report [8].

The design parameters of the machine for the shortest wavelength operation (1 Å) are summarized in Tables 2.1.1 (electron beam output parameters) and 2.1.2 (photon beam output parameters). There are two nominal operation modes at 200 pC and 10 pC. Two additional special operation modes are also foreseen: one which offers a large bandwidth photon spectrum and another which will produce ultra-short photon pulses (attoseconds). The wavelength of Aramis can be tuned from 0.1 nm to 0.7 nm by adjusting the energy of the electron beam in Linacs 2 and 3 (Figure 2.1.1).

Table 2.1.1: Design parameters of the electron beam output parameters for 1 Å radiation.

Electron Beam Design Parameters	Nominal Operation Mode		Special Operation Mode	
	Long Pulses	Short Pulses	Large Bandwidth	Ultra-Short Pulses
Charge per bunch (pC)	200	10	200	10
Beam energy for 1 Å (GeV)	5.8	5.8	5.8	5.8
Core slice emittance (mm.mrad)	0.43	0.18	0.43	0.25
Projected emittance (mm.mrad)	0.65	0.25		0.45
Energy spread (keV, rms)	350	250	25000	1000
Relative energy spread (% , rms)	0.006	0.004	0.3	0.02
Peak current at undulator (kA)	2.7	1.6	3	15
Bunch length (fs, rms)	25	2	22	0.3
Bunch compression factor	125	533	136	5000
Repetition rate (Hz)	100	100	100	100
Number of bunches / RF pulse	2	2	2	2
Bunch spacing (ns)	28	28	28	28

Table 2.1.2: Design parameters of the photon pulses at 1 Å (Aramis) required for the SwissFEL science programme.

FEL Beam Design Parameters	Nominal Operation Mode		Special Operation Mode	
	Long Pulses	Short Pulses	Large Bandwidth	Ultra-Short Pulses
Undulator period (mm)	15	15	15	15
Undulator parameter	1.2	1.2	1.2	1.2
Energy spread (keV)	350	250	17000 (FW)	1000
Saturation length (m)	47	50	50	50
Saturation pulse energy (μJ)	150	3	100	15
Effective saturation power (GW)	2.8	0.6	2	50
Photon pulse length (fs, rms)	21	2.1	15	0.06
Beam radius (μm)	26.1	17	26	17
Divergence (μrad)	1.9	2	2	2.5
Number of photons (×10 ⁹)	73	1.7	50	7.5
Special bandwidth, rms (%)	0.05	0.04	3.5 (FW)	0.05
Peak brightness (# photon/mm ² . mrad ² . s ⁻¹ .0.1% bandwidth)	7.10 ³²	1.10 ³²	8.10 ³⁰	1,3.10 ³³
Average brightness (# photon/mm ² . mrad ² . s ⁻¹ .0.1% bandwidth)	2,3.10 ²¹	5,7.10 ¹⁸	3.10 ¹⁹	7,5.10 ¹⁸

Table 2.1.3: Design parameters of the photon pulses from the Athos beamline (corresponding electron beam parameters are the same as in Table 2.1.1).

Expected Parameters	Large Gap	Small Gap	Large Gap	Small Gap
	High Energy	High Energy	Small Energy	Low Energy
Electron beam energy (GeV)	3.4	3.4	2.1	2.1
Undulator period (mm)	40	40	40	40
Undulator parameter K	1.0	3.2	1	3.2
Undulator module length (m)	4.0	4.0	4.0	4.0
Undulator section length (m)	4.75	4.75	4.75	4.75
Average b-function (m)	10	10	10	10
FEL wavelength (nm)	0.7	2.8	1.8	7
Saturation length (m)	41.6 (*)	22.3	29.7	16.1
Saturation pulse energy (mJ)	0.12	0.36	0.10	0.18
Effective saturation power (GW)	4.4	11.2	3.2	6.5
Number of photons at saturation	4.2·10 ¹¹	5.0·10 ¹²	8.7·10 ¹¹	6.5·10 ¹²
Bandwidth (% , rms)	0.15	0.19	0.17	0.25
Pulse length (fs, rms)	11.1	12.9	12.0	11.0
Beam radius (μm, rms)	33.4	40.1	45.9	56.1
Beam divergence (μrad, rms)	4.1	15.0	8.3	30.9

(*): The Athos beamline has a total length of 30 m, based on seeding operation. The value shown in the Table (41.6 m) indicates the total length required for SASE operation (§ 2.4).

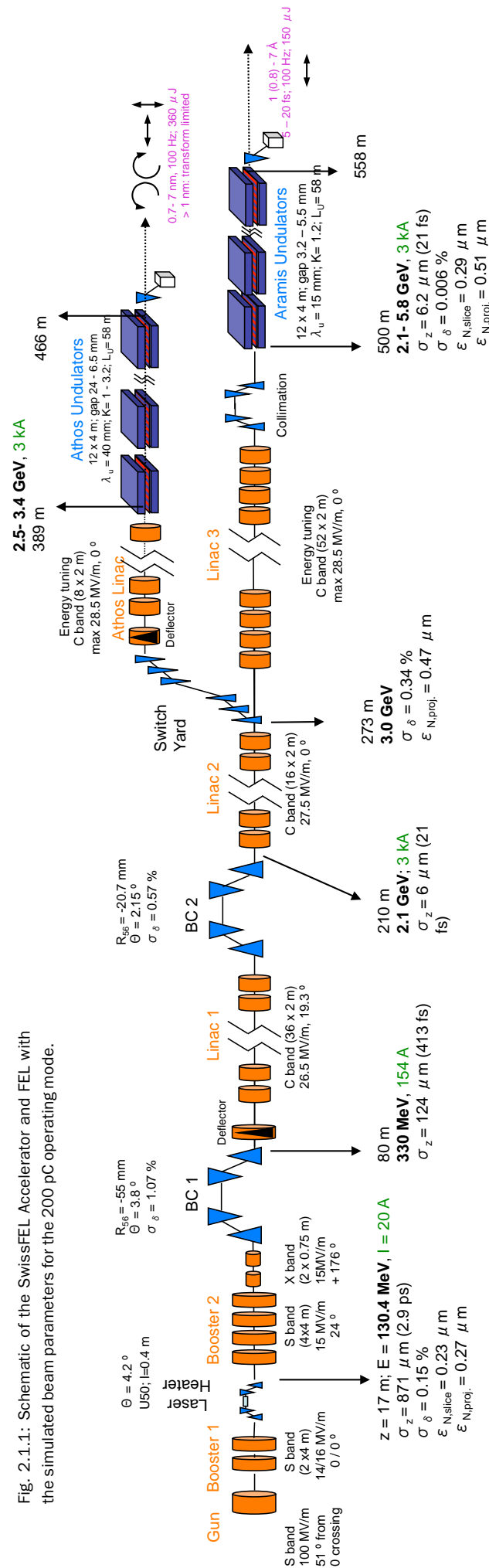


Fig. 2.1.1: Schematic of the SwissFEL Accelerator and FEL with the simulated beam parameters for the 200 pC operating mode.

The design parameters of the soft X-ray beamline Athos are shown in Table 2.1.3 for the long-pulse operation mode. The electron beam parameters required to achieve these FEL performances are the same as those in Table 2.1.1, except for the beam energy. In this beamline, the wavelength tuning from 0.7 nm to 7 nm is carried out by continuous variation of the electron beam energies in the Athos Linac from 2.5 GeV to 3.4 GeV and by varying the undulator gap.

With a total length of about 550 m (from gun to undulator end), the SwissFEL facility can be divided into sections, as follows:

- Gun, Booster 1 and 2 (§ 2.3.1)
- Bunch Compressors 1 and 2 (§ 2.3.2)
- Linacs 1, 2 and 3 (§ 2.3.3)
- Switchyard and collimator (§ 2.3.4)
- Aramis Undulator line (§ 2.4)
- Athos Undulator line (with Athos Linac) (§ 2.4)

Results from simulations of each of these sections will be presented in the following Sections. As discussed in Chapter 1, it is planned to operate SwissFEL (up to the switch-yard) with two electron bunches per RF macropulse. The simulated parameters presented here are also valid for the second electron bunch, assuming that inter-bunch wake-field effects are negligible.

A schematic overview of the accelerator is displayed in Figure 2.1.1.

2.2 Simulation tools

To model the SwissFEL facility, a suite of different computer codes has been utilized. These range from simple, fast codes to perform coarse but rapid optimization of the beam line, to highly detailed particle tracking codes to investigate subtle effects of the beam dynamics.

For the dynamics in the gun and the first accelerating structure, the particle tracking code ASTRA [9] is used, based on the detailed field maps of the RF cavities and solenoids. Faster but coarser estimates can be obtained with HOMDYN [10] and BET [2].

Tracking through the main linac is done with the code ELEGANT [11], after matching the transverse optics with MADX [12] and optimizing the longitudinal dynamics with

LITRACK [13]. For the case of bunch compression, the results of ELEGANT, which uses a 1D CSR model, has been cross-checked with CSRTRACK [7].

The FEL performance is simulated with GENESIS 1.3 [14], after coarse optimization using the fast and efficient Ming Xie model [15] in MATLAB.

Once the layout is sufficiently defined, highly detailed start-to-end simulations are carried out, tracking the electron bunch from the cathode to the exit of the undulator. In order to do this, particle distributions are exchanged between ASTRA, ELEGANT and GENESIS. OPAL (Object Oriented Parallel Accelerator Library) [16,17], will be used for precise beam dynamics simulations.

2.3 Accelerator simulation

2.3.1 Gun and Booster section

This section describes the design considerations for the electron gun and first booster section (Booster 1) of SwissFEL (see Figure 2.1.1). It contains the electron source, a short diagnostics section, and two S-band accelerator modules, providing an energy of ~ 130 MeV. The main requirement for the gun and Booster 1 is to provide a low projected emittance, below 0.4 mm.mrad, as well as a slice emittance below 0.3 mm.mrad at a peak current above 20 A.

A laser heater follows Booster 1 and is described in paragraph 2.3.1.4 (Figure 2.1.1). Since Booster 2 plays a role in the overall bunch compression scheme, it will be detailed in the next paragraph, 2.3.2.

2.3.1.1 Gun and Booster 1 layout

The electron source for SwissFEL will be a conventional RF gun, similar to the one installed at LCLS [18][1]. PSI plans to build a 2.5 cell normal-conducting gun in-house, based on the LCLS [19] and PHIN [20] designs, which are scaled to the RF frequency of 2998.8 MHz. The features of the gun can be summarized as follows:

- A peak accelerating gradient of 100 MV/m in the cavity, in order to minimize the effects of space charge during the first centimetres of acceleration, which is beneficial for reaching low slice emittance.

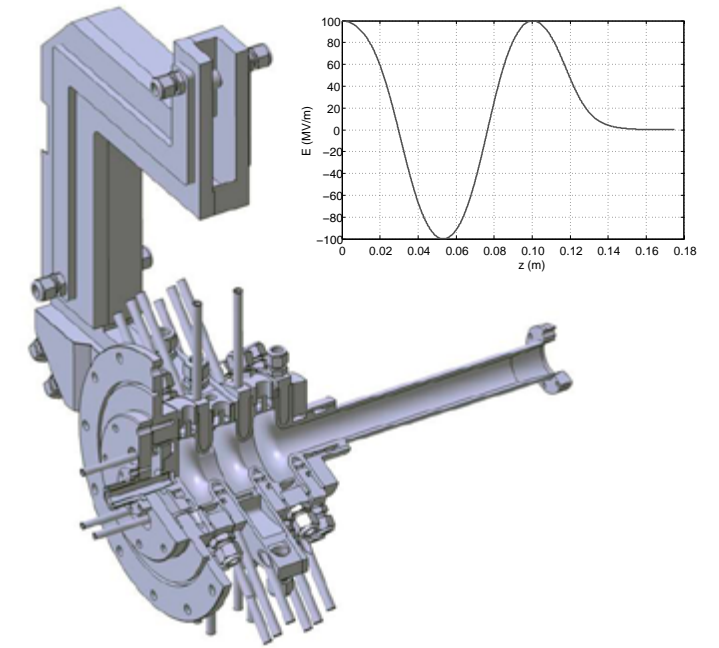


Fig. 2.3.1.1: Current design and on-axis field distribution of the SwissFEL gun.

- The frequency separation between the π and $\pi/2$ mode is about 16 MHz. This is achieved by using a large iris diameter.
- The second cell (coupler cell) is coupled to two symmetric rectangular waveguides to suppress the dipole kick. A racetrack shape of the coupler cell has also been adopted to minimize the quadrupole field on the beam axis.
- In order to reduce dark current as much as possible, the back wall of the gun is used as the cathode surface (i.e. no cathode loading hole is foreseen).

Figure 2.3.1.1 shows a drawing of the latest design of the SwissFEL gun. Directly after the electron gun, centered at $z = 0.3$ m from the cathode position ($z = 0$ m), there is a solenoid for emittance compensation. The subsequent diagnostics section incorporates current monitors, screens, slits for emittance measurements. A dipole deflects the beam into a dispersive section for momentum and momentum spread measurements.

The first booster (Booster 1) starts at $z = 2.95$ m and consists of two 4.15 m-long S-band structures operated on-crest. Envelope matching is applied at the booster entrance with the help of the gun solenoid, in order to apply the emittance compensation principle [21,22] and to obtain the lowest possible emittance at the end of the Booster 1 section (at 12.6 m from the cathode, at electron beam energies of ~ 130 MeV).

2.3.1.2 Gun and Booster 1 parameters

Beam dynamics simulations of the injector, up to 130 MeV, have been carried out using the particle code ASTRA [9]. The main concept is to use the emittance compensation principle [21,22], in which the booster entrance position and gun solenoid field are adjusted such that the electrons are accelerated on the invariant envelope. This basically freezes the low emittance obtained in the gun during the booster acceleration.

Astra and Opal simulations of the gun have been carried out (FEL-FA84-006-01) [23]. The following table summarizes the main parameters.

Table 2.3.1.1: Gun and booster 1 parameters (ASTRA) for the two operation modes at 130 MeV.

Bunch charge	200 pC	10 pC
Gun gradient	100 MV/m	100 MV/m
Beam current	20 A	3 A
Laser spot transverse size (rms)	215 μm	101 μm
Laser pulse length (Full Width)	9.9 ps	3.7 ps
Intrinsic (Thermal) emittance	0.195 μm	0.092 μm
Projected normalized emittance at 130 MeV	0.275 μm	0.114 μm
Slice normalized emittance at 130 MeV	0.230 μm	0.092 μm

Figure 2.3.1.2 shows the layout of the gun and Booster 1 section, together with the main simulation parameters for the standard case (100 MV/m, 200 pC; Table 2.3.1.1). All the following figures also refer to this case.

Intrinsic emittance: It is necessary to comment on the intrinsic emittance values and model used in the ASTRA simulations. ASTRA applies the three-step model in which the emitted electrons leave the cathode with an average kinetic energy E_k , defined as:

$$E_k = \frac{h\nu - \Phi_{\text{eff}}}{2} \quad (1)$$

where $h\nu$ is the laser photon energy and Φ_{eff} is the effective work function (taking into account the barrier reduction due to the applied electric field).

The intrinsic emittance is then expressed as follows, where σ_{laser} is the rms laser spot size:

$$\epsilon_{th} = \sigma_{\text{laser}} \sqrt{\frac{2E_k}{3mc^2}} \quad (2)$$

For the intrinsic emittance value used in the simulations (also quoted in the upper Table), a fixed value of $\epsilon_{th} = \sigma_{\text{laser}} * 0.91 \text{ mm.mrad/mm}$ was used, according to measurements at LCLS (at a gradient of 115 MV/m) [24]. This corresponds to an average kinetic energy of 0.63 eV in the ASTRA model and was used independently of the gun gradient (100 MV/m or 120 MV/m), thus slightly overestimating the intrinsic emittance in the 100 MV/m case. Recent measurements at the SwissFEL gun test-stand [6,25,26] have demonstrated an intrinsic emittance as low as 0.41 mm.mrad/mm laser spot size, using 282 nm laser wavelength on a copper cathode for 1 pC charge.

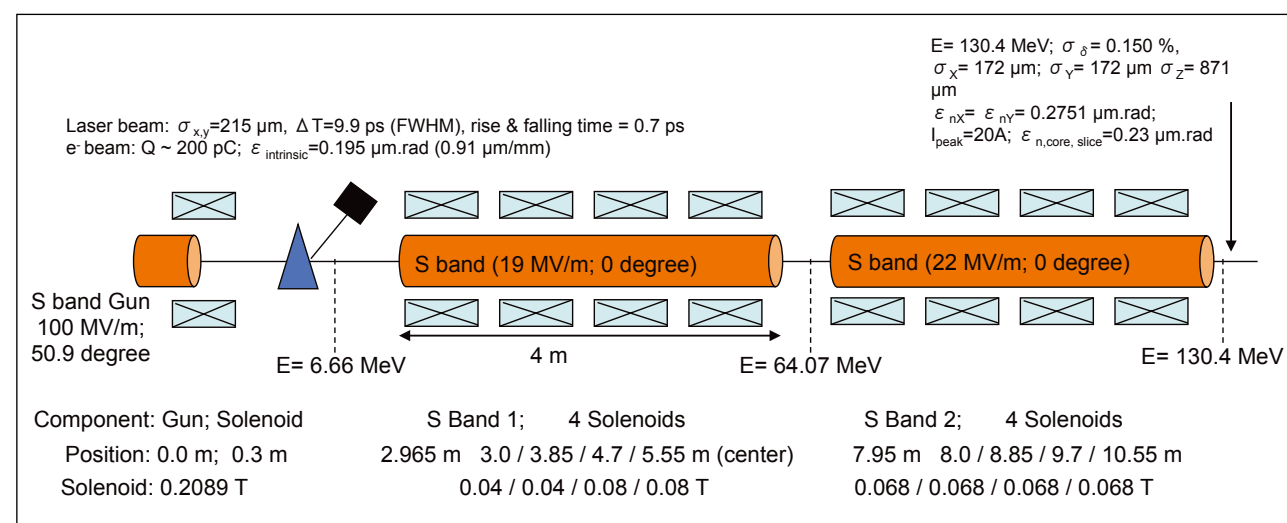


Fig. 2.3.1.2: Layout of gun and Booster 1 section with some of the simulated parameters.

2.3.1.3 Gun and Booster 1 simulation results

The following graphs in Figure 2.3.1.3 represent the ASTRA simulation results for the standard case (100 MV/m, 200 pC, and 20 A). Simulations for a higher gun gradient and lower charges have been presented elsewhere [18,23,27].

As can be seen from the transverse emittance curve (Figure 2.3.1.3), the invariant envelope matching results in a continuous decrease of the projected emittance during the booster acceleration. Solenoid compensation around the two S-band structures maintains the beam size below 0.3 mm rms along Booster 1. The beta-

function directly after the gun (i.e. in the gun solenoid) is relatively large, resulting in a potentially higher chromatic effect. The slice emittance along the bunch (at $z = 13 \text{ m}$) is displayed and reaches values as low as 0.23 mm.mrad at the centre of the bunch. The Twiss matching parameter at the end of the section ($z = 13 \text{ m}$) is almost flat, which means the mismatch over the central 80% of the bunch corresponds to a value of $\xi \leq 1.1$ for the mis-match parameter. This is also shown with the slice phase space ellipses.

The following graphs in Figure 2.3.1.4 shows a comparison between the ASTRA and OPAL simulation for the standard case (100 MV/m, 200 pC).

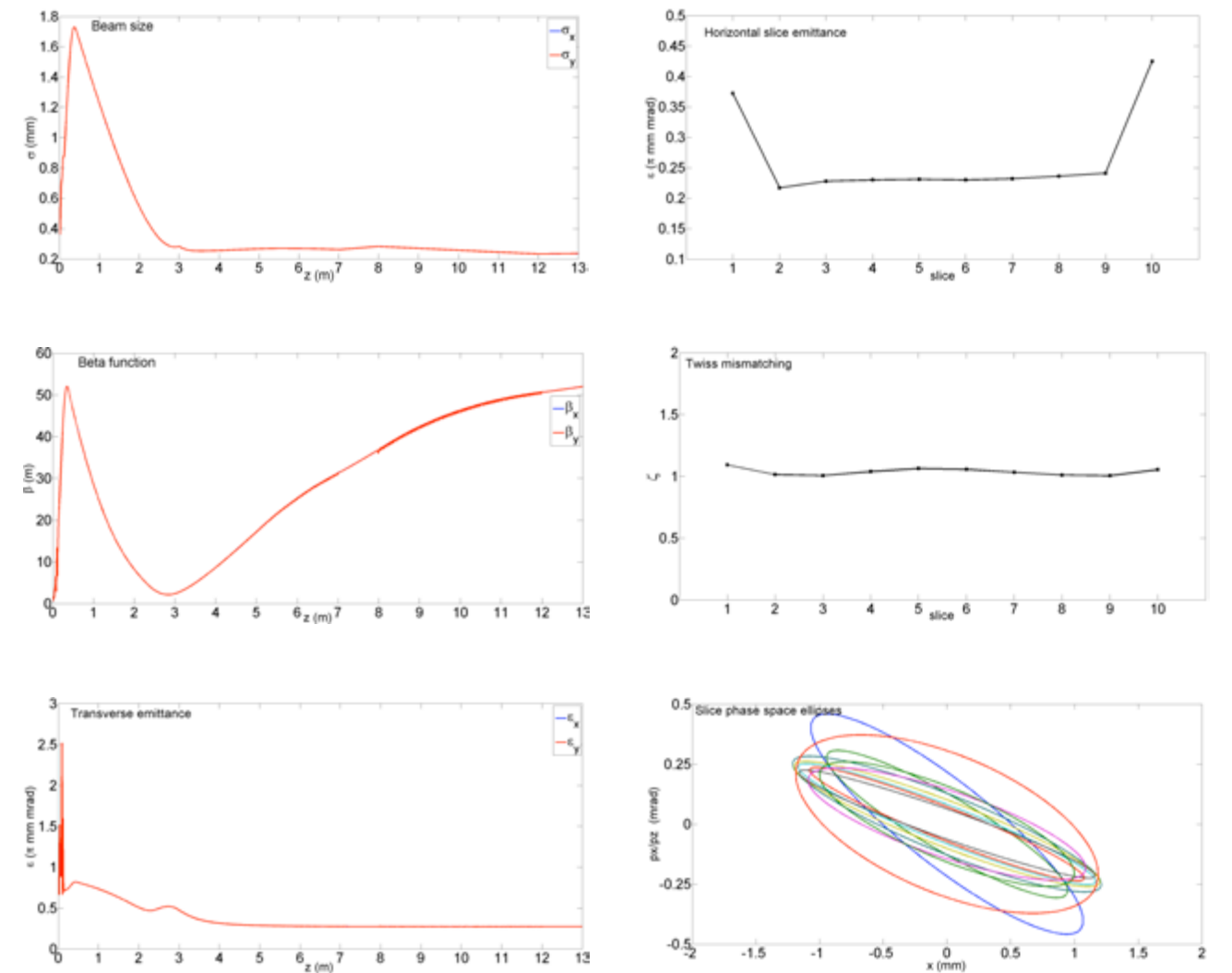


Fig. 2.3.1.3: Simulation results for the standard case (100 MV/m, 200 pC); On the left-hand side, from top to bottom: rms transverse beam size, beta-function and projected emittance development along the first 13 m of the accelerator; On the right, from top to bottom: slice emittance along the bunch; Twiss mis match parameter along the bunch and slice phase space ellipses at $z=13 \text{ m}$.

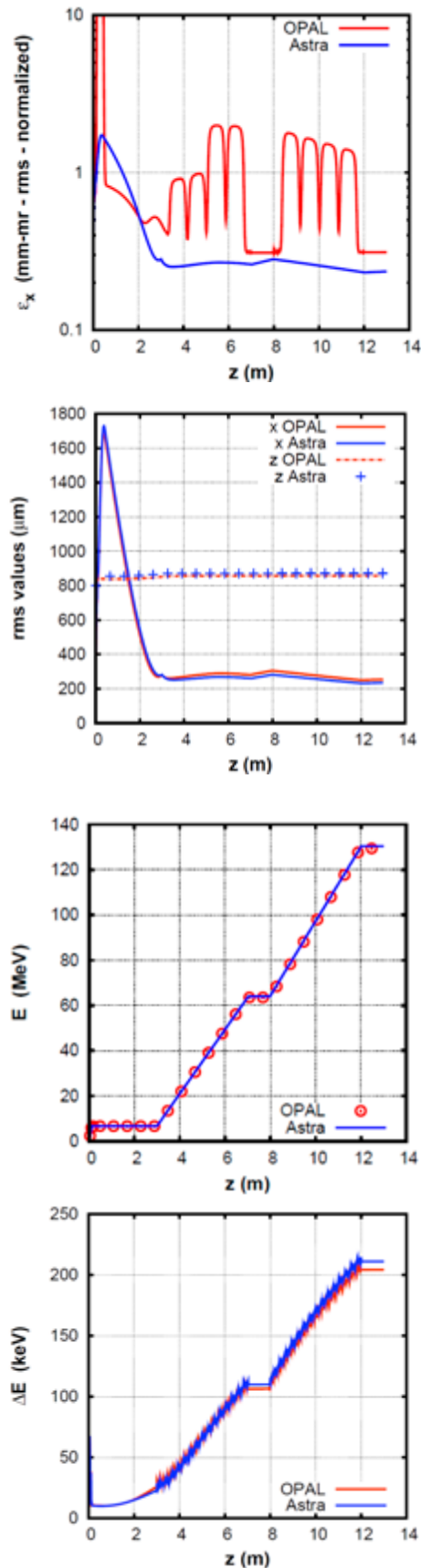


Fig. 2.3.1.4: Astra and OPAL simulation results for the standard case (100 MV/m, 200 pC). From top to bottom: normalized transverse emittance, transverse and longitudinal beam size. Energy, energy spread.

2.3.1.4 Laser heater

Based on experience at LCLS, a laser heater is foreseen after Booster 1 (at $z = 13$ m), to suppress the microbunch instability. For the simulations presented in this report, only a 2.5 m drift space is reserved for a laser heater, but no explicit design has been done. If the laser heater significantly improves the simulated FEL performance, it will be installed in the beam line. A first estimate of the laser heater parameters indicate that it would be similar to the LCLS laser heater design (Table 2.3.1.2).

Table 2.3.1.2: Main parameters of the SwissFEL laser heater.

Beam Energy at Entrance	131 MeV
Undulator length L_u	40 cm
Period length λ_u	5 cm
Undulator parameter K	1.24
Resonant wavelength λ_r	800 nm
Dipole length L_b	10 cm
Bending angle	3.82°
Drift L_{D1}	20 cm
Drift L_{D2}	110 cm

2.3.2 Bunch compression scheme (from Booster 2 to BC2)

The overall SwissFEL design parameters are motivated by the goal of 200 pC bunch charge, accelerated to 5.8 GeV and compressed to a peak current of more than 2.7 kA. Ultimately, the goal is to increase the FEL photon power and this requires basically a flat top longitudinal current profile at 5.8 GeV so that a maximum number of electrons contribute to the FEL lasing.

A two-stage bunch compression system is used to achieve this goal. The whole bunch compression system consists, apart from the two magnetic chicanes, of two linac sections (Booster 2 and Linac 1) to imprint the energy chirp on the beam, and an X-band section to linearise the energy – time correlation along the bunch (see Figure 2.3.2.1). After the compression, the energy chirp is reduced by virtue of the longitudinal wakefields in Linacs 2 and 3.

The overall compression scheme for each operation regime can be summarized as follow:

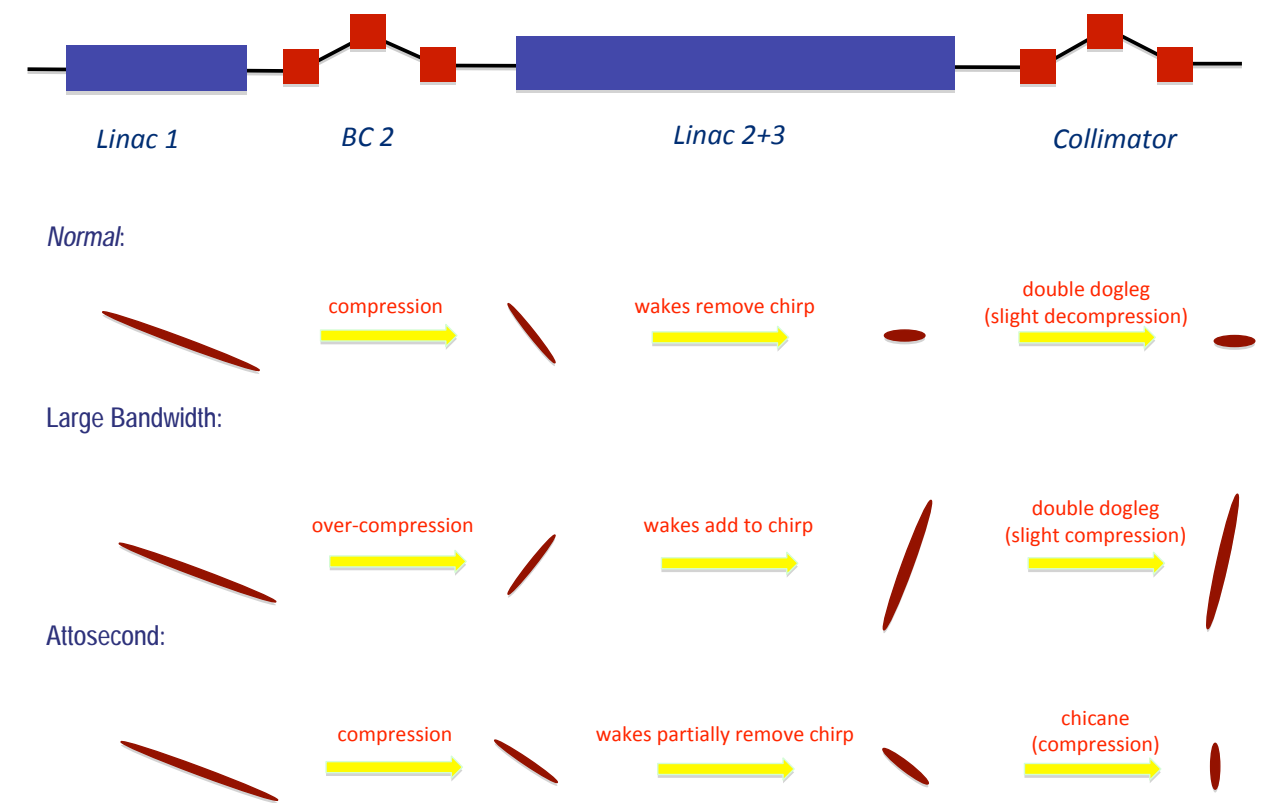


Fig. 2.3.2.1: Schematic of the different compression schemes: from Linac 1 to Aramis Collimator.

Normal 200 pC mode: Chirp in Booster 2 – BC1 compression – chirp control in Linac 1 – BC2 compression – wakefields remove chirp in Linacs 2/3 – slight decompression in Aramis collimator

Normal 10 pC mode: Chirp in Booster 2 – BC1 compression – chirp control in Linac 1 – BC2 compression – wakefields partially remove the chirp

Large Bandwidth 200 pC mode: Chirp in Booster 2 – BC1 compression – chirp control in Linac 1 – BC2 over compression – wakefields increase chirp in Linacs 2+3 – Aramis Collimator slightly compresses.

Attosecond 10 pC mode: Chirp in Booster 2 – BC1 compression – chirp control in Linac 1 – BC2 compression – wakefields partially remove the chirp in Linacs 2+3 – Aramis collimator compression.

A semi-analytical model has been used [28] to find out the theoretical optimum operation parameters (compression factor of each bunch compressor chicane, gradient and phases of the different accelerating sections). That is to say, the operating parameters leading to a flat top current profile before entering the undulators. Those theoretical parameters are then used in a start-to-end simulation to simulate the final current bunch profile. If the simulated bunch profile still differs from what is

expected (flat top), then the difference between the theoretical and simulated beam parameters are fed in the analytical formulas to obtain a correction of the operation parameters. Those parameters are again simulated until after several iterations the quasi flat top bunch profile is obtained from the start-to-end simulation.

This optimisation method is fast (minutes) and can be used for each mode of operation (200 pC, 10 pC, ...) planned at SwissFEL.

The RF gun and Booster 1 have been described previously, in Section 2.3.1. The second part of the booster, Booster 2 (consisting of 4 S-band cells), generates the necessary longitudinal chirp, through off-crest operation, for the bunch compression. Its parameters are summarised in Table 2.3.2.1. The transverse beam optics is controlled by a quadrupole doublet downstream of each S-band structure. The simulation results presented below are obtained assuming an input peak current of 22 A for 200 pC instead of the optimized value of 20 A found in section 2.3.1. This does not change the tolerances and general bunching concept. Parameters such as RF gradient, RF phase or bending angle are slightly changing depending on the operation mode.

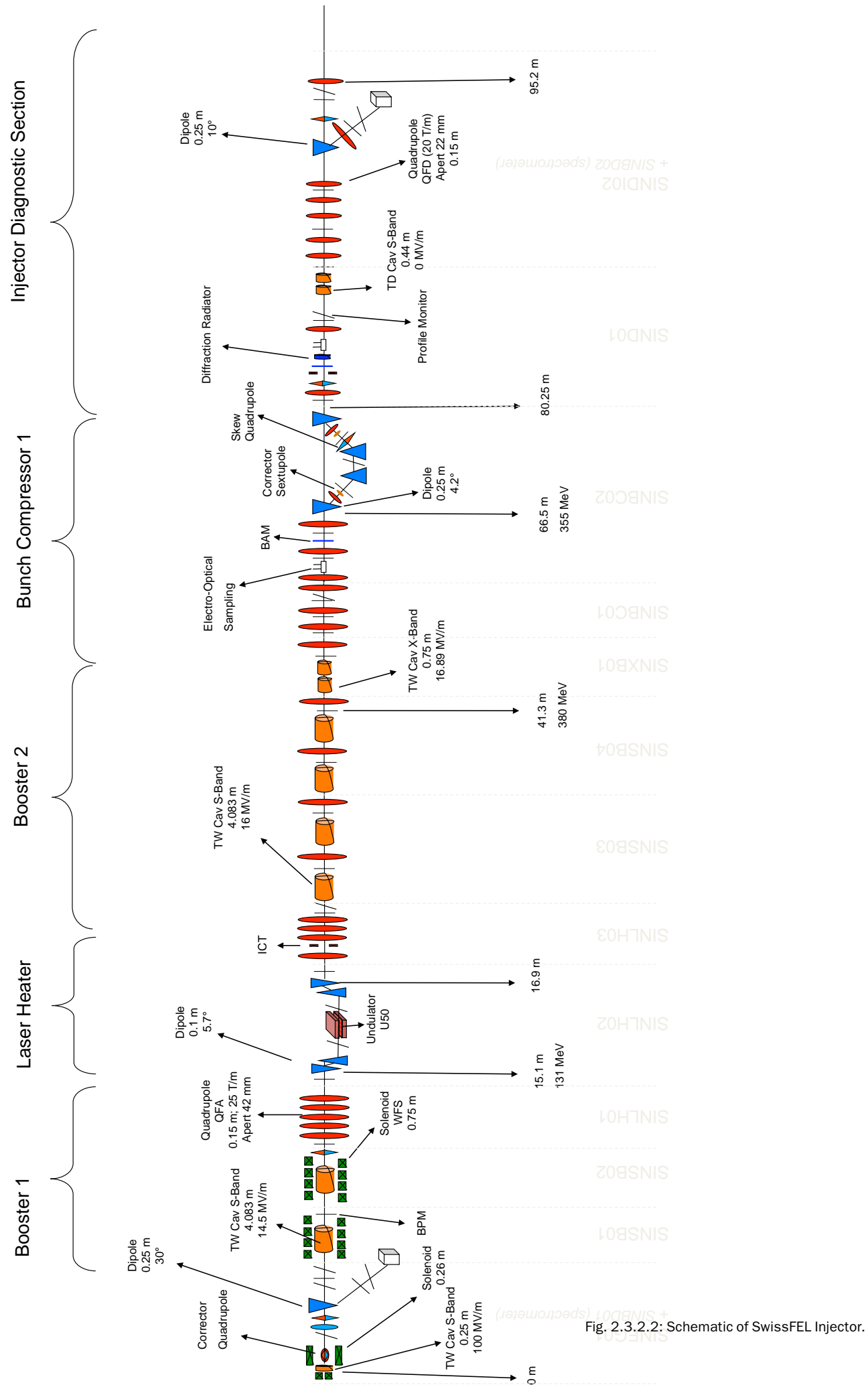


Fig. 2.3.2.2: Schematic of SwissFEL Injector.

Table 2.3.2.1: Summary of Booster 2 parameters.

Cell layout	Quadrupole Doublet Lattice			
Cell length	5.9 m			
Number of cells	4			
S-band cavities per cell	1			
S-band cavity length, L_c	4.15 m (reserved) / 4.07 m (effective)			
Booster 2 Cell length	5.5 m			
Quadrupole length, L_Q	15 cm			
Quadrupole Strength Typical	0.57 m ² (at 200 pC)			
Operation mode	200 pC Normal	10 pC Normal	200 pC (BW)	10 pc (as)
S-band cavity gradient	14.88 MV/m	14.61 MV/m	15.22 MV/m	14.61 MV/m
S-band cavity phase	23.66°	25.57°	27.05°	25.57°

Table 2.3.2.2: Summary of X-band parameters.

Cavity length	0.965 m (reserved) / 0.750 m (effective)			
Beam Energy at X band entrance	353 MeV			
Separation of cavities	60 cm			
Number of cavities	2			
Operation mode	200 pC Normal	10 pC Normal	200 pC (BW)	10 pc (as)
X-band cavity gradient	15.50 MV/m	20.37 MV/m	15.07 MV/m	20.37 MV/m
X-band cavity phase	-176.05°	-167.74°	-165.98°	-167.74°

Longitudinal phase space (energy – time correlation) linearization is completed with an X-band cavity, operated at the 4th harmonic of the 2.9988GHz; that is to say, at 11.9952 GHz. The parameters of the X band structures are depicted in Table 2.3.2.2 for the two operation modes 10 and 200 pC.

Two magnetic chicanes, BC1 and BC2 (with four dipoles arranged in D-shape), are used to generate a non-zero momentum compaction factor, R56. A schematic layout and parameter summary are given in Figure 2.3.2.3 and Table 2.3.2.3. Coherent Synchrotron Radiation (CSR) effects, especially on the slice emittance, can be mitigated when the horizontal beam size has a waist in the fourth dipole of the chicane. We have chosen beta functions below 7 m and 5 m in BC1 and BC2, respectively, while the vertical parameters are not subject to tight constraints.

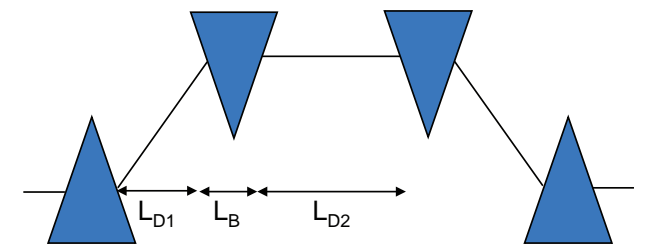


Fig. 2.3.2.3: Schematic layout of the bunch compressors BC 1 and BC 2.

Table 2.3.2.3: Summary of bunch compressor BC1 and BC2 parameters for the 200 pC and 10 pC operation modes.

BC 1				
Bending magnet length, L_B	0.25 m			
Drift, L_{D1}	6.0 m			
Drift, L_{D2}	1 m			
Beam energy	330 MeV			
Matching condition at last bend	$\beta_x < 5$ m, $\alpha_x = 0$, $\beta_y < 40$ m			
Operation mode	200 pC Normal	10 pC Normal	200 pC (BW)	10 pC (as)
Bending angle	3.82°	3.82°	3.82°	3.82°
R_{56}	55.1 mm	55.1 mm	55.1 mm	55.1 mm
Peak current at last bend	233 A	14 A	220 A	15 A
Slice norm. emittance last bend	0.3 mm.mrad	0.11 mm.mrad	0.3 mm.mrad	
Bunch length, rms σ_z	87.1 μ m	66.8 μ m	87 μ m	
Compression factor	10	5	10	5
BC 2				
Bending magnet length, L_B	0.5 m			
Drift, L_{D1}	7.0 m			
Drift, L_{D2}	1 m			
Beam energy	2100 MeV			
Matching condition at last bend	$\beta_x < 3$ m, $\alpha_x = 0$, $\beta_y < 40$ m			
Operation mode	200 pC Normal	10 pC Normal	200 pC (BW)	10 pC (as)
Bending angle	2.15°	2.15°	2.15°	2.15°
R_{56}	-20.7 mm	-20.7 mm	-20.7 mm	-20.7 mm
Peak current at last bend	3000 A	830 A	3970 A	15000 A
Slice norm. emittance last bend	0.3 mm.mrad	0.13 mm.mrad	0.34 mm.mrad	
Bunch length, rms σ_z	5.1 μ m	1 μ m	4.8 μ m	0.2 μ m
Compression factor	14	30	18	

Chirp adjustments between the compressor chicanes are carried out on the C-band (5.712 GHz) structures of Linac 1. The main purpose here is to control the compression factor in BC2 independently of BC1. Linac 1 parameters are summarised in Table 2.3.2.4.

The electron bunch profile (energy spread, current and emittance) directly after the second bunch compressor BC2 are shown on Fig 2.3.2.4 for the two main operation modes at 10 and 200 pC as well as for the special mode 200 pC large bandwidth.

Table 2.3.2.4: Summary of Linac 1 parameters.

Linac 1				
Beam Energy at Entrance	330 MeV			
Number of cavities	36			
Length of cavity, L_c	2.05 m (reserved) / 1.978 (effective)			
Cavity frequency	C-Band			
Beam Energy at Exit	2100 MeV			
Operation mode	200 pC Normal	10 pC Normal	200 pC (BW)	10 pC (as)
Cavity gradient	26.45 MV/m	26.38 MV/m	26.92 MV/m	26.38 MV/m
Cavity phase	19.31°	19.41°	22.01°	19.41°

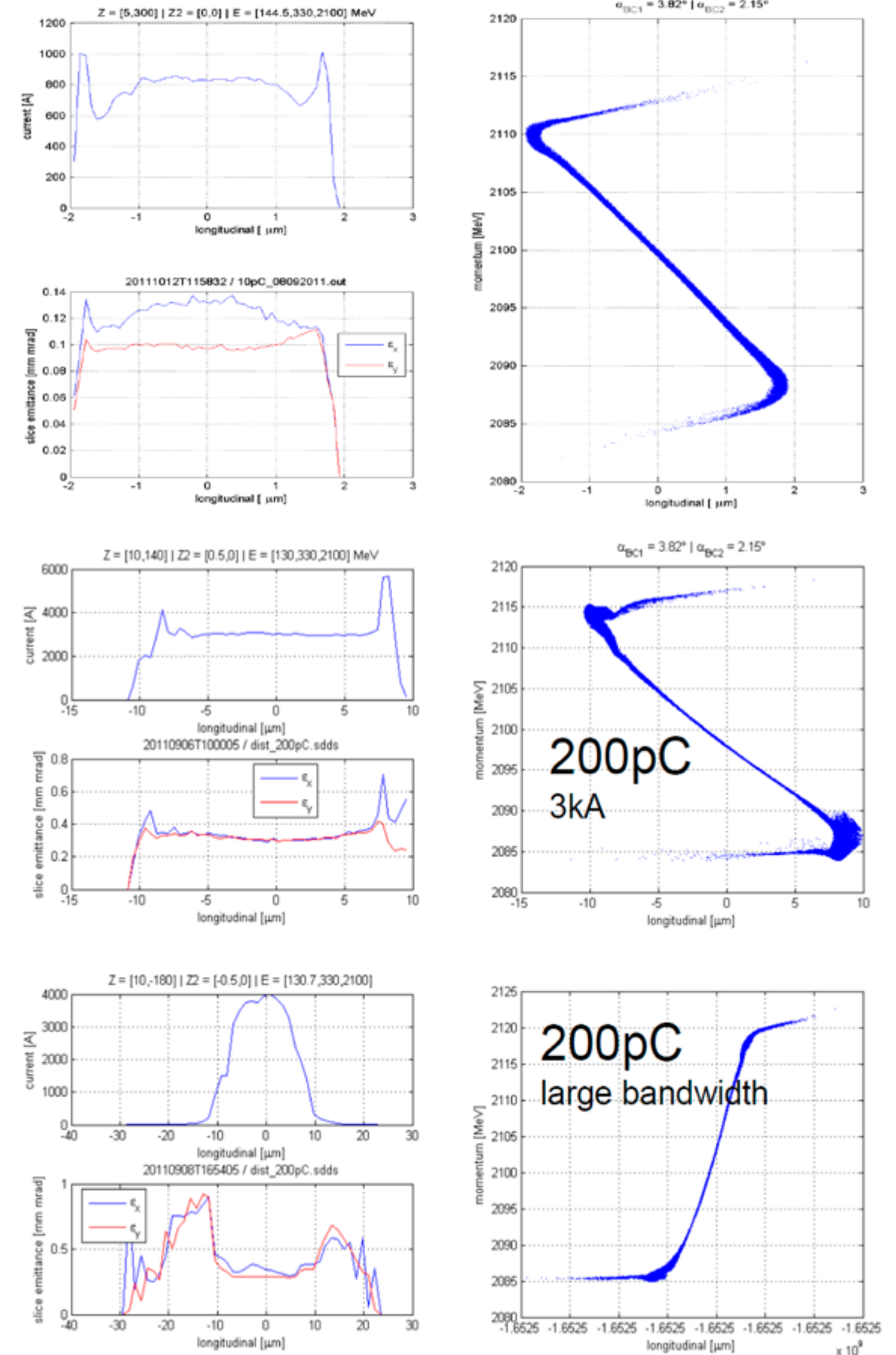


Fig. 2.3.2.4: Bunch profiles from Elegant simulations after the last dipole of BC2 ($z = 203$ m) for the normal mode with 10 pC charge (top figures) and with 200 pC charge normal mode (middle) and the 200 pC large bandwidth mode (bottom).

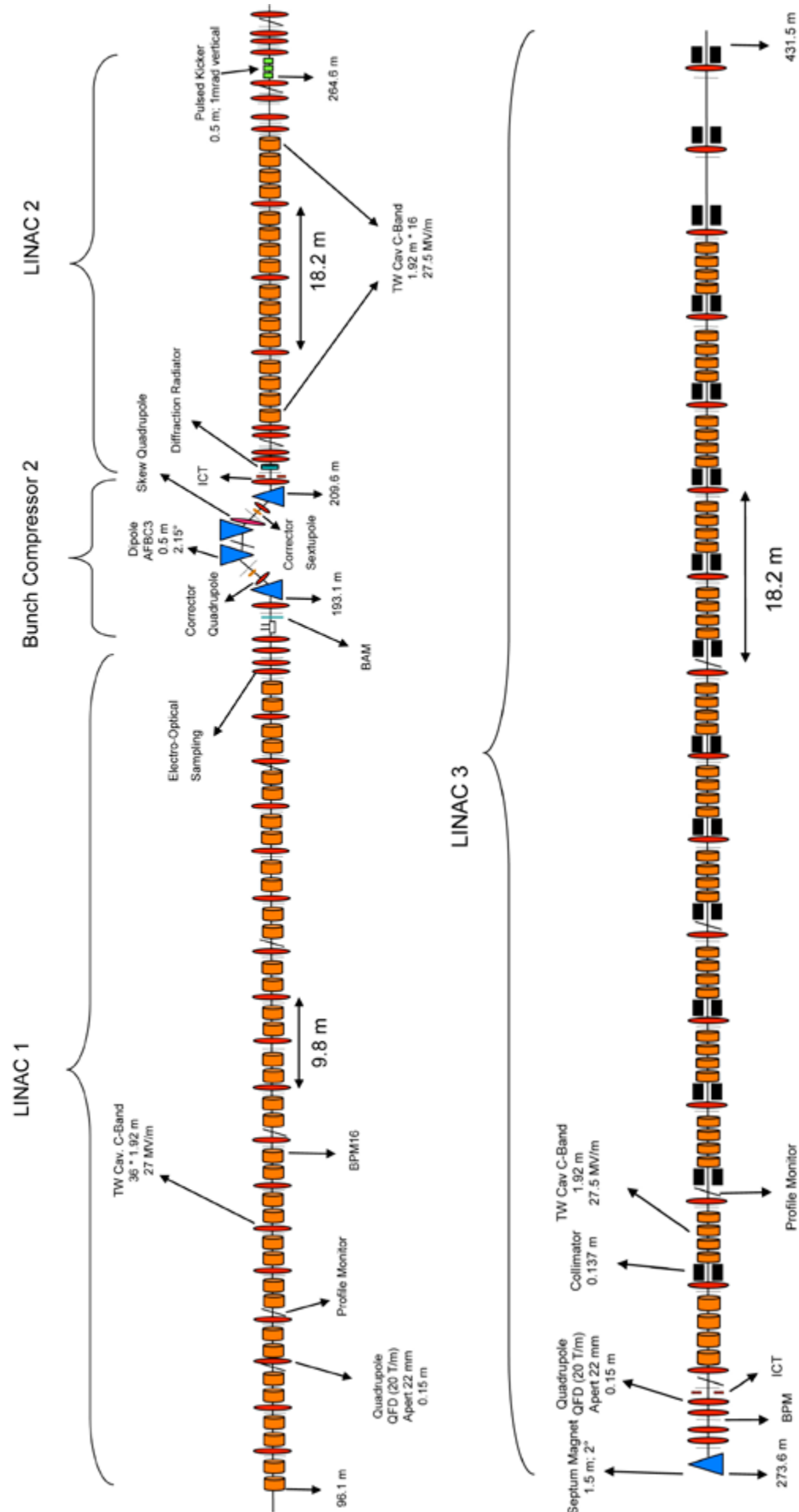


Fig. 2.3.2.5: Linac 1 to Linac 3 Layout.

In the nominal operation mode of 200 pC, the bunch is compressed from initially $\sigma_z = 871 \mu\text{m}$, rms (or 2.9 ps, rms) to $\sigma_z = 124 \mu\text{m}$ (413 fs) after the first chicane, and to $\sigma_z = 5.7 \mu\text{m}$ (19 fs rms) final bunch length, with a peak current of 3.0 kA at 200 pC.

2.3.3 Linac layout (Linac 2 and Linac 3)

The main bunch acceleration is driven by three C-band linacs (Fig. 2.3.2.5). The first of these (Linac 1) is located between the bunch compressors and has already been described in Section 2.3.2. Downstream of the second bunch compressor, Linac 2 defines the energy at the switchyard, with the extraction point to the seeded long-wavelength FEL beamline (Athos). Final acceleration to the short wavelength FEL line (Aramis) is achieved in Linac 3. The parameters of the three main linac sections are summarised in Table 2.3.3.1.

As mentioned in Chapter 3, the frequency for SwissFEL Linacs 1, 2 and 3 is 5.712 GHz, in contrast to the S-band (2.998 GHz) of the Booster.

Apart from considerations for the RF electrical consumption, C-band frequency also presents some advantages for the beam dynamics, in comparison to an S-band linac. At higher frequencies, a higher effective gradient is possible, allowing a shorter linac length. The lower iris diameter of C-band structures compared to S-band results in stronger wakefields. While wakefield effects on the transverse emittance are tolerable, the longitudinal component helps in the reduction of the energy chirp generated for the compressors, resulting in FEL bandwidth reduction. Removal of chirp in Linacs 2 and 3 would not be possible if the frequency would be S-band.

The phases in Linac 1 are optimized for maximum compression and for a flat top current profile with peak current above 3 kA. The phases in Linacs 2 and 3 are chosen to be on crest for maximum acceleration. Note that the choice of the phases takes into account longitudinal wakefields.

To reach 5.8 GeV, Linac 3 requires fewer RF stations than the number for which space is available in the lattice. This extra space is reserved for future energy upgrades.

Table 2.3.3.1: Parameters of the main linac sections (Linacs 1, 2 and 3).

	Linac 1	Linac 2	Linac 3
Cell layout	FODO		
Phase advance	70°		
Cell length	9.8 m	18.2 m	18.2 m
Number of cells	9	2	6.5
Cavities per half-cell	2	4	4
Length of cavity L_C	2.05 m (reserved)/1.983 (effective)		
Cavity frequency	C-band		
Cavity gradient	26.8 MV/m (*)	27.5 MV/m (**)	28.5 MV/m
Cavity phase	19.31°	0°	0°
Drift, L_{D1} (bellows)	10 cm		
Drift, L_{D2}	5 cm		
Drift, L_{D3} (bellows)	5 cm		
Quadrupole length, L_Q	25 cm (reserved)/15 cm (effective)		
Drift, L_{D4} (BPM & Gate Valve)	35 cm		

(*) for 200 pC, refer to Table 2.3.2.4 for the other operation modes; (**) Linac 2 has a lower gradient than Linac 3 since it is applied to two bunches.

The matching condition for the FODO lattice is 70° phase advance per cell, which is not a strong condition. It can be adjusted to different values if needed, to ease the matching from or to other sections. Only a few profile monitors are foreseen per linac to measure the optical functions. For the best resolution, the monitors are separated by 1.5 linac cells, corresponding to 105° betatron phase advance. The measurement is completed by the orbit response function, measured with the BPMs along the entire linac. However for a more reliable measurement of the optical function in the lattice, three profile monitors per linacs are highly desirable. The layout of the half FODO cells of Linacs 1, 2, 3 and Athos Linac are shown in Figure 2.3.3.1.

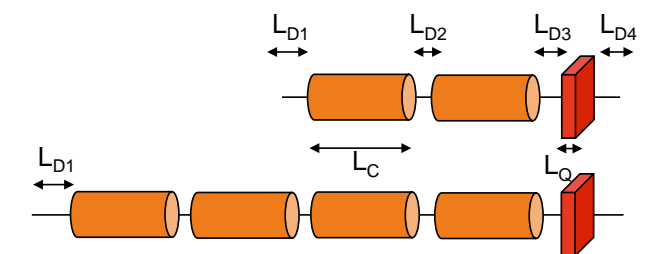


Fig. 2.3.3.1: Half-cell layout for Linac 1 and Athos Linac (top) and Linacs 2 & 3 (bottom).

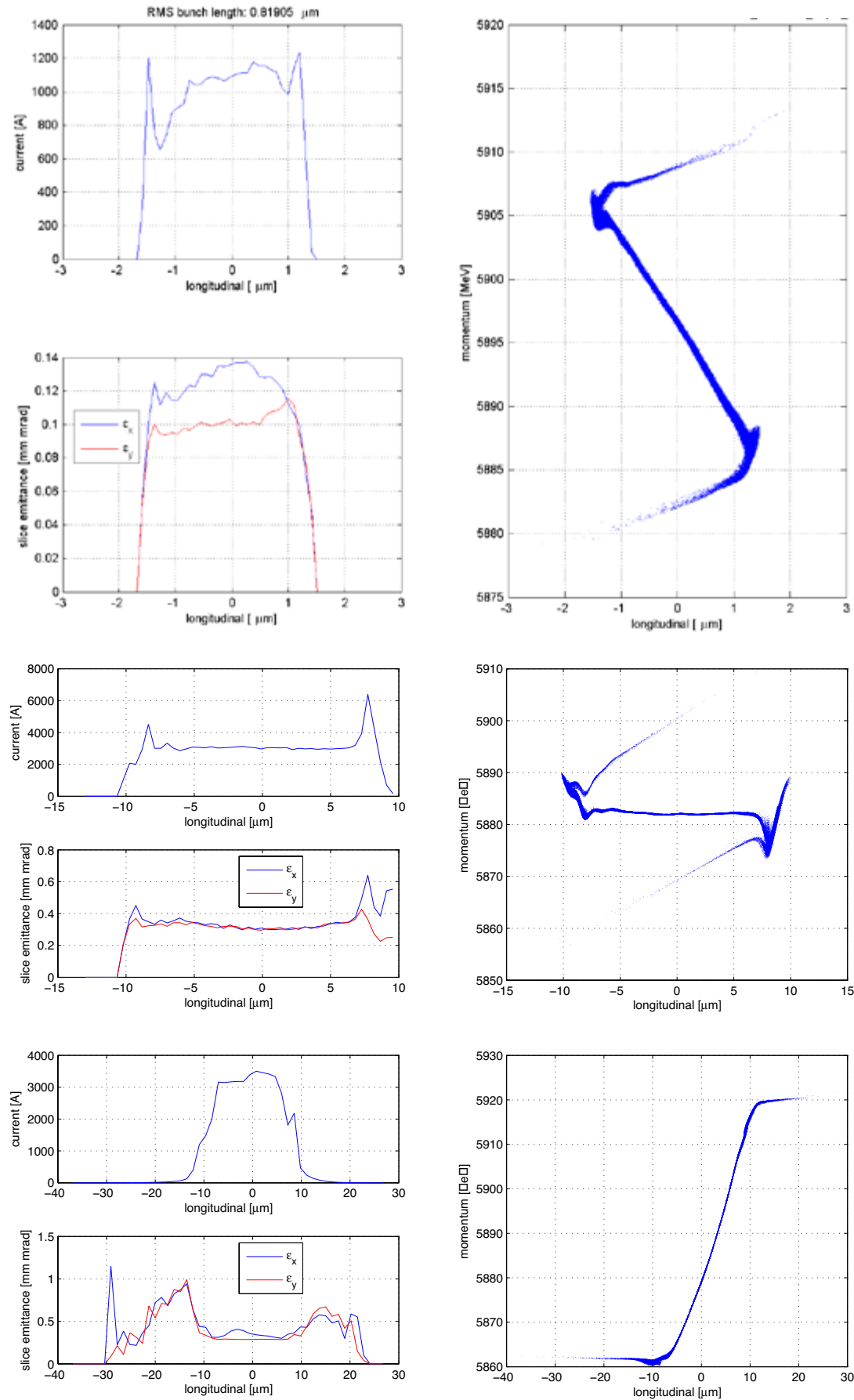


Fig. 2.3.3.2: Bunch profiles from Elegant simulations before the Aramis undulator ($z = 490$ m) for the normal mode with 10 pC charge (top figures) and with 200 pC charge normal mode (middle) and the 200 pC large bandwidth mode (bottom).

During the transport from BC2 to the Aramis undulator line, the linac 3 wakefields and the Aramis collimator chicane parameters are used to give the final shape of the current profile for optimum FEL lasing. In Fig. 2.3.3.2, the final longitudinal bunch current profile before Aramis undulator is presented, they all present a quasi-flat top profile together with small slice emittance. The particular case of the attosecond bunch profile is shown in Fig. 2.3.3.3.

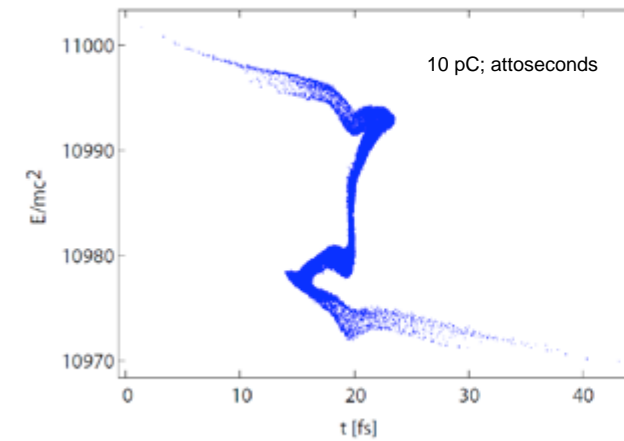


Fig. 2.3.3.3: Electron bunch phase space at Aramis Undulator entrance for the 4 modes of operation.

Beam optics consists of the FODO channels in each linac section, in the undulators, and in a diagnostic line downstream of BC1. Assembly of five quadrupoles between these sections enables beam matching during

transition to another section and to special elements such as the chicanes or the switchyard. The overall beam optics of the full linac layout is shown in Figure 2.3.3.4.

2.3.4 Switchyard and collimators

2.3.4.1 Switchyard layout

The switchyard for SwissFEL diverts the beam coming from Linac 2, with an energy of 3.0 GeV, to the long wavelength undulator (Athos beamline). At the switchyard entrance a fast kicker followed by a Lambertson magnet (Section 3.4.6) will deviate the second of the two bunches accelerated in the Linac. This second bunch will then be further deviated towards the Athos beamline while the first bunch continues straight towards Aramis. In the Athos line two different types of operation modes are envisioned, SASE and ECHO enabled seeding. For the former case the nominal bunch length is desirable however for the latter case the beam goes through a series of chicanes that compresses the beam and CSR effects spoil the beam quality so that a slightly longer bunch is preferable. In view of these requirements, and to allow some flexibility for this beamline it is possible to set up the switchyard for a range of values of R_{56} .

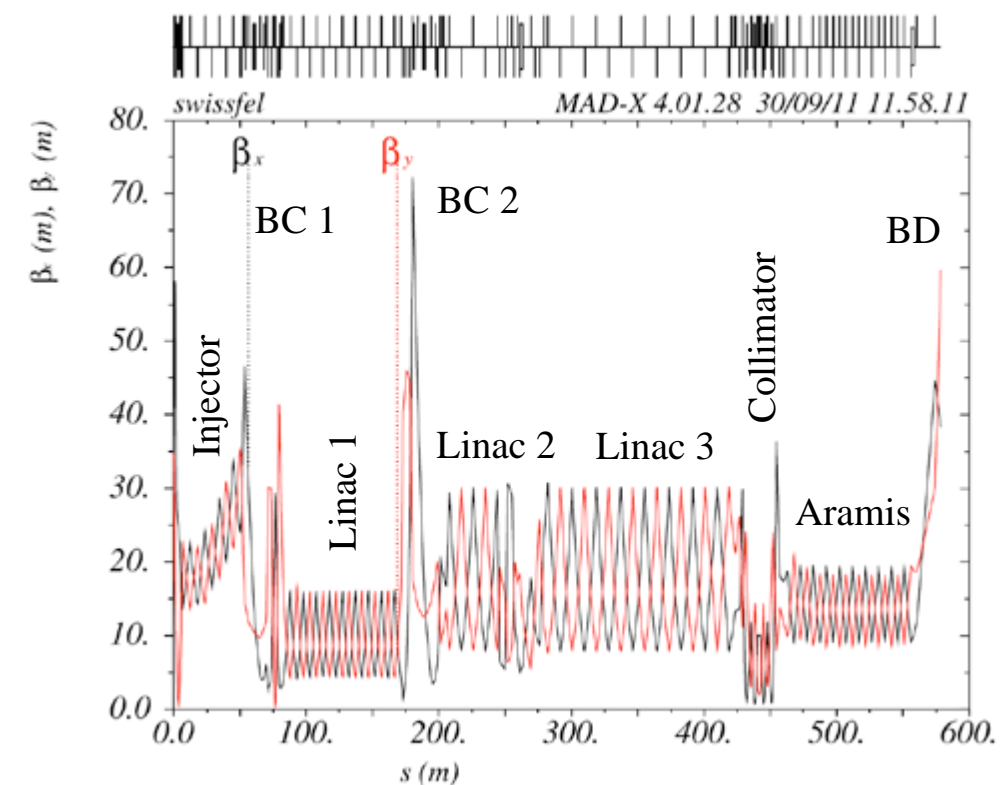


Fig. 2.3.3.4: Beam optics along SwissFEL.

Table 2.3.4.1: Electron beam parameters at Switchyard entrance.

Matching Position	Kicker Magnet Entrance
β_x	5.0 m
α_x	0.0
β_y	18 m
α_y	1.5

In the nominal set-up of the switchyard, its total length is 65 m and the separation between the Athos and Aramis beamlines is 3.75 m, with a net bending angle equal to zero, making the two beamlines parallel to each other, as shown in Figure 2.3.4.1. This design has one triple-bend (TBA) and one double-bend (DBA) achromat section; each section has a total bending angle of 5°. The switchyard was divided in sectors, each sector having a specific function:

- The central dipole in the triple bend is weaker and is situated in a high dispersive area. By changing the dispersion function in this magnet we can choose the value of R_{56} , making the sector go from isochronous (no variation on the bunch length) to a value of $R_{56} = 6$ mm (corresponding to a bunch lengthening factor of 1.9).
- Since the kickers deviate the beam vertically (Section 3.4.6) it is also required that in the switchyard the beam is brought back to nominal vertical position with respect to the rest of the machine and that the vertical dispersion is closed. This is performed by a set of 2 dipoles immediately after the triple-bend;
- The phase advance between the two sets of bends (TBA and DBA) is adjustable by changing the settings of the quadrupoles in the transport line (Fig. 2.3.4.1, 5 quadrupoles after the second vertical dipole). The lattice functions of the dipoles of the switchyard are set to the minimum value possible so that kicks due to coherent synchrotron radiation (CSR) are minimized. By adjusting the phase advance between them, we can compensate for the emittance dilution caused by CSR.
- Finally, the second bend set is set up in order to accommodate the energy collimators.

In order to evaluate emittances and beam size changes throughout the switchyard, we have performed simulations with an electron distribution at the entrance of the Lambertson magnet, which was obtained from a field map output from an ELEGANT simulation for the 200 pC case. For the simulations, the PTC module embedded in the latest MADX version was used. CSR effects are not taken into account, but are evaluated separately using ELEGANT (in 1D only). The initial beam conditions are shown in Table 2.3.4.1 and have an initial normalized emittance of $\epsilon_x = 0.47$ mm.mrad and $\epsilon_y = 0.35$ mm.mrad (according to simulations for the 200 pC case); and a bunch length of 8.6 μ m.

The non-linear effects observed in the switchyard are mainly due to chromatic aberrations coming from the quadrupoles and in order to correct it, 2 sets of sextupoles were placed in the bending sections (maximum dispersion, Figure 2.3.4.2 right). The corrections are localized (closing dispersion and minimizing the beta-beat) at the end of each bending section so as to minimize the sextupole strengths. In Figure 2.3.4.3 we show an example of the effects of the sextupoles for the setup with $R_{56} = 4$ mm. In this case the offsets are almost completely cancelled and there is just a small mismatch at the end of the beamline for particles with an energy offset of 1%. This is not as good for all values of R_{56} , and we observed that the residual offset can account for a projected emittance blow-up of 1.5% in the nominal operation mode and up to 8% in the broad-band mode (considering a rms energy dispersion in the bunch of 1%).

In Figures 2.3.4.4 and 2.3.4.5 it is possible to see the distortions in longitudinal phase space and current distribution caused by CSR for three different values of R_{56} . The total effect of CSR on the emittance is not negligible, however the amount of projected emittance growth can be minimized by changing the phase advance between the two bending sets. Although the projected emittance is very sensitive to the phase advances, the sliced emittance is conserved along the whole switchyard, as shown in Figure 2.3.4.6.

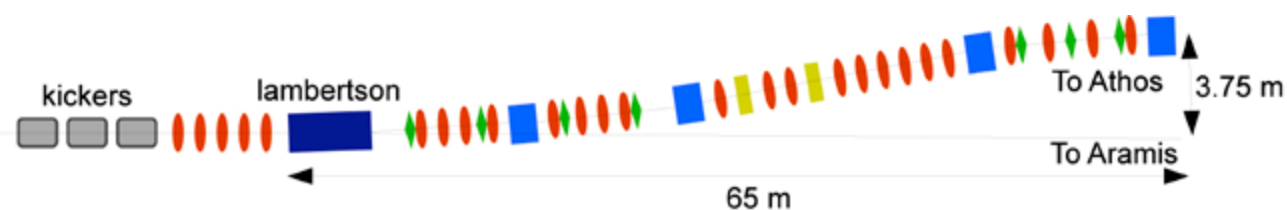


Fig. 2.3.4.1: Schematic layout of the switchyard (elements not to scale). The blue elements are horizontal dipoles, yellow elements are vertical dipoles, red elements quadrupoles and green elements are sextupoles. The switchyard is composed of a TBA, a DBA and a transport line. With the TBA we can tailor the value of R_{56} and in the DBA section we introduced the energy collimators for Athos.

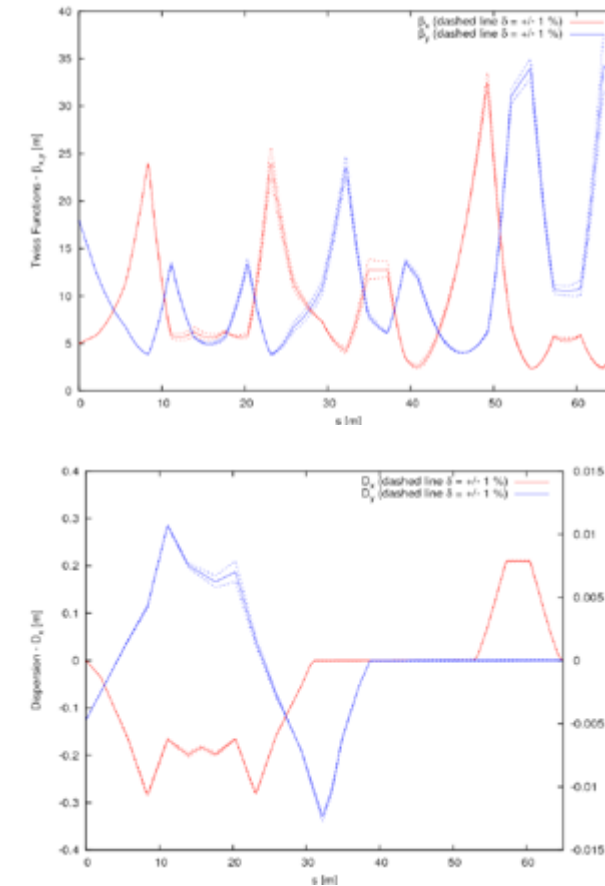


Fig. 2.3.4.2: Lattice function for the switchyard for a value of $R_{56} = 4$ (top) and horizontal and vertical dispersion (bottom). The dashed lines shown the off energy lattice function for particles with $\pm 1\%$ energy deviation.

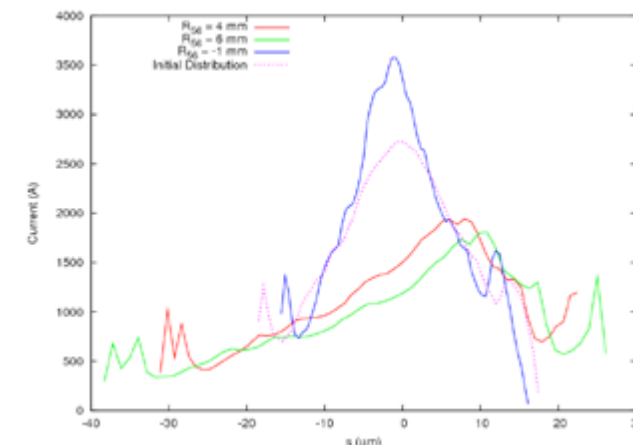


Fig. 2.3.4.4: Longitudinal current profile at the beginning (dashed line) and at the end of the switchyard (full lines) for three different values of R_{56} .

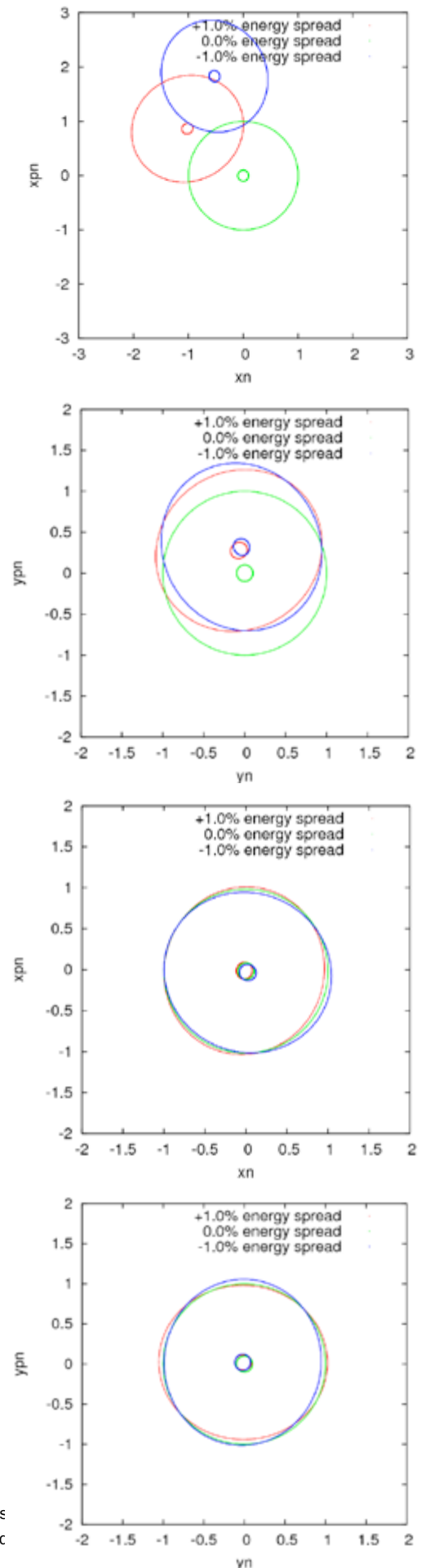


Fig. 2.3.4.3: Normalized transverse phase-space ellipses for $\delta=0$ and $\pm 1\%$ energy deviation and radius of 0.1σ and 1σ . (top) sextupoles off and (bottom) sextupoles on.

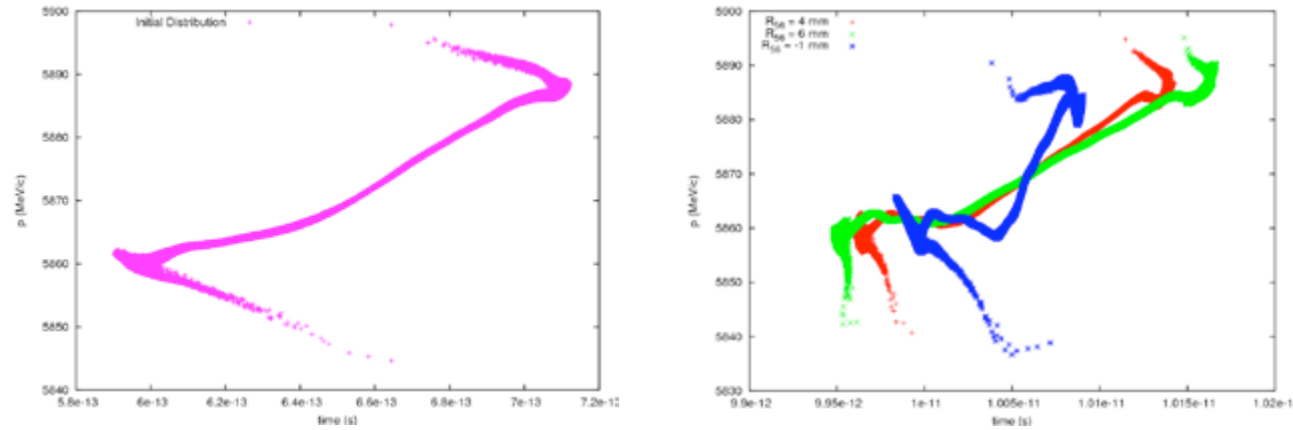


Fig. 2.3.4.5: Longitudinal phase-space. (left) entrance of the switchyard and (right) at the end of the switchyard for three different values of R_{56} .

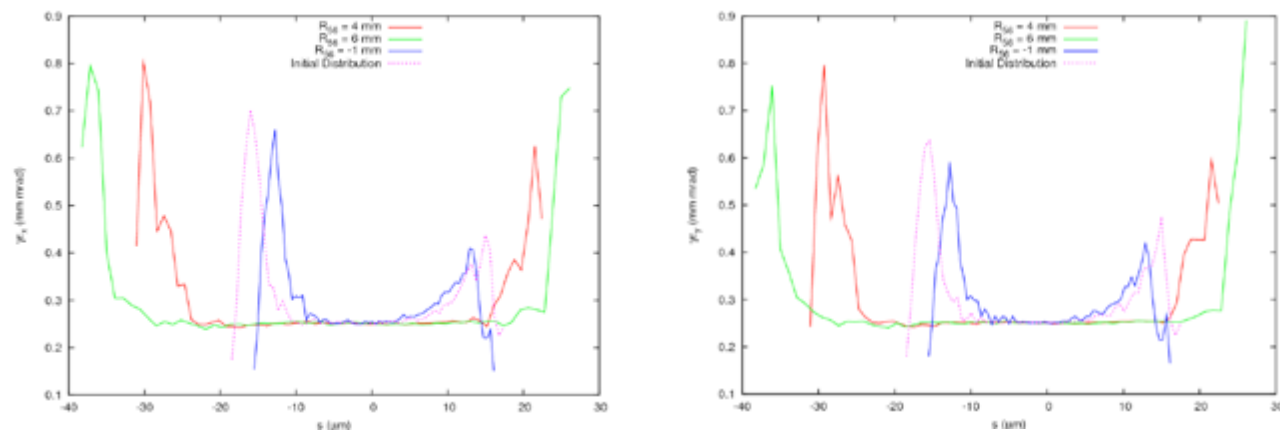


Fig. 2.3.4.6: Vertical (right) and horizontal (left) normalized slice emittance at the end of the switchyard for three different values of R_{56} .

The misalignments of quadrupole magnets have no large impact on emittance. For a Gaussian distribution of transverse misalignments, with a width of $50 \mu\text{m}$ the maximum projected emittance growth observed in simulations was smaller than 1% (Figure 2.3.4.7). Although the projected emittance does not change much, misalignments can excite betatron oscillations, which can spoil the performance of the undulators. For the misalignment distributions studied, the average rms spread of offsets at the end of the switchyard is $400 \mu\text{m}$ and $1000 \mu\text{m}$ for misalignments of $50 \mu\text{m}$ in horizontal and vertical plane respectively. These offsets can be corrected by the use of beam-based-alignment and an orbit feedback system (see Section 3.1.1). Effects from multipole errors and fringe fields have not yet been addressed.

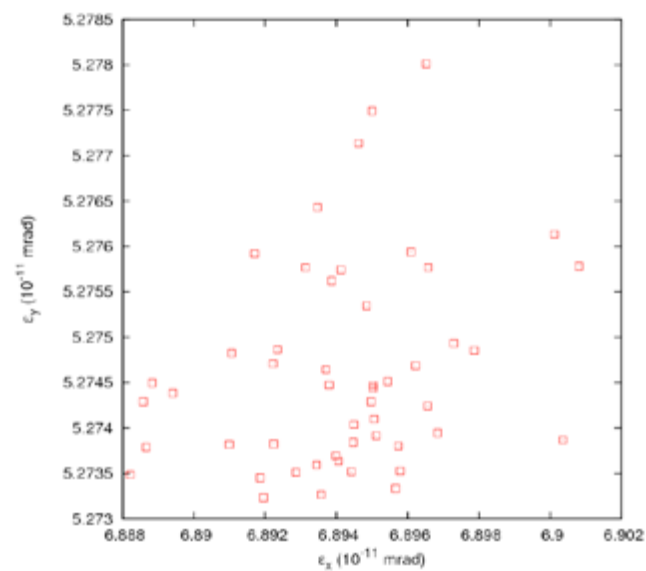


Fig. 2.3.4.7: Fluctuation of the projected emittance for transverse misalignments with a Gaussian distribution with a width of $50 \mu\text{m}$. In this case $R_{56} = 4 \text{ mm}$.

2.3.4.2 Athos collimator design

The electron bunch deviated towards Athos will first pass through a collimator to prevent damage to the Athos undulators. The initial design for the collimator at the Athos beamline foresees a set of transverse collimators at a FODO type lattice after the switchyard and a dispersive energy collimator is located in the second set of bends in the switchyard.

2.3.4.3 Aramis collimator design

The electron bunch heading straight towards the Aramis undulator will also pass through a collimator to prevent damage to the Aramis undulators. The initial design for the collimator at the Aramis beamline foresees a transverse collimator where the beam drifts through a waist and a dispersive energy collimator in form of a magnetic chicane. Sufficient quadrupoles have been added to let the magnetic chicane acts as two “dog-legs”. For the 200 pC, large bandwidth mode of operation, the collimator should be set to operate as two dog-legs keeping the energy chirp. For the ultra-short, low charge bunch mode the collimator is set such that it acts like a compression chicane. All other modes can be operated with both configurations. It remains to be studied, which is the best approach in terms of emittance preservation.

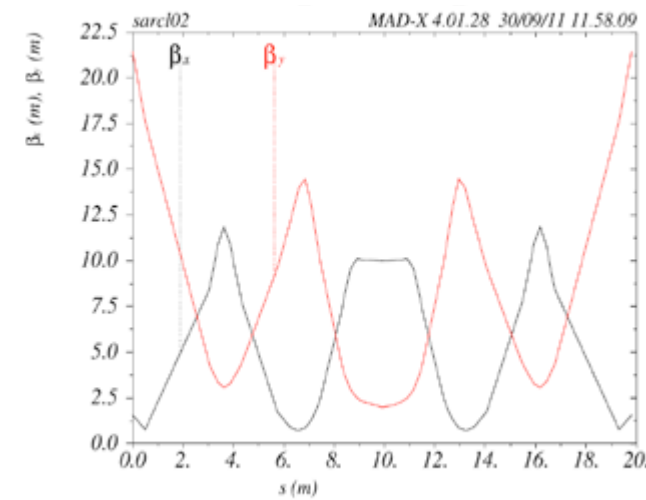


Fig. 2.3.4.8: Beta function at the Aramis collimator chicane, the origin ($s=0 \text{ m}$) on the graph corresponds to $z = 444 \text{ m}$.

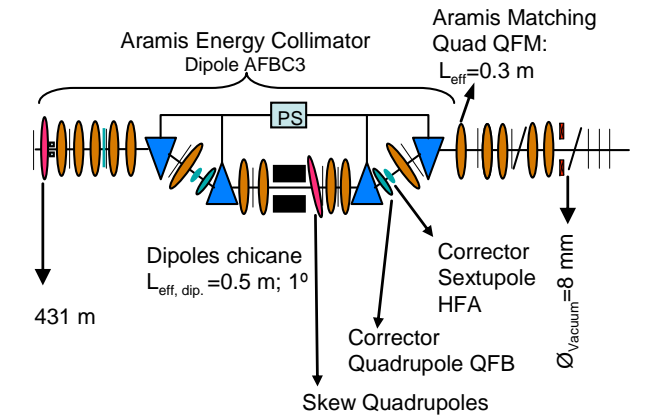


Fig. 2.3.4.9: Aramis Collimator Design.

Table 2.3.4.2: Aramis collimator design parameters.

Length of Collimator Block	1 m
Bend Magnet Length L_B	0.5 m
Bending Angle	1°
Length of Longitudinal Collimator Section L_{CE}	20 m
Chicane Matching Condition (Center of E-Col.)	$\beta_x = 10 \text{ m}, \beta_y = 2 \text{ m}, \alpha_{x,y} = 0$
Length of Horizontal collimator Block	0.8 m
Drift L_{D2}	110 cm

2.4 Undulator line parameters and simulations

The SwissFEL goal is to provide FEL radiation which spans the wavelength range from 1 \AA to 7 nm , with a compact design. A natural cut in the wavelength is at around 7 \AA , because the optics to transport the radiation differs significantly for longer or shorter wavelengths. Thus the hard X-ray beamline Aramis covers the wavelength range from 1 to 7 \AA . Operation at the shortest wavelength also defines the overall compactness of the facility, because it requires the highest beam energy and has typically the longest gain length, and thus the longest undulator beamline. For the soft X-ray beamline Athos, a tuning range from 0.7 to $>7 \text{ nm}$ is ensured by varying the electron beam energy with the Athos Linac from 2.6 GeV to 3.4 GeV . The beam energy at the switchyard kicker magnet is fixed at 3 GeV and the Athos Linac is used to accelerate to 3.4 GeV or decelerate to 2.6 GeV .

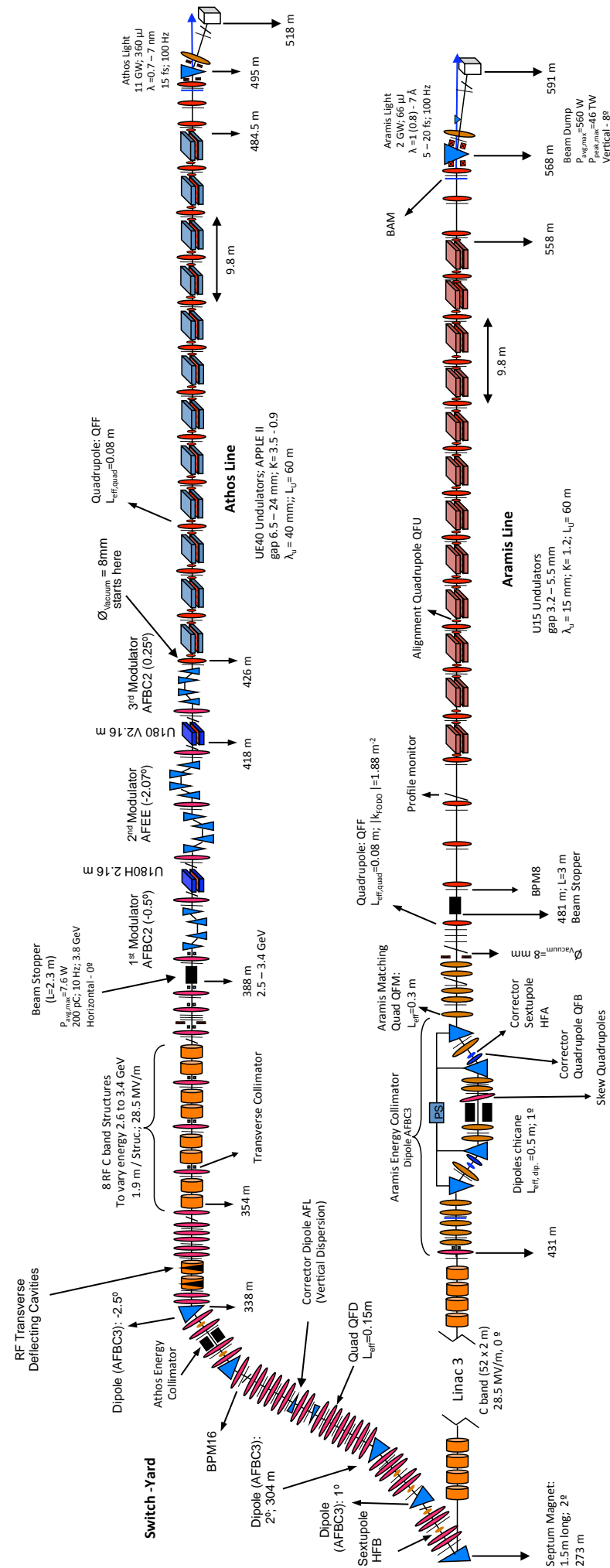


Fig. 2.4.1.1 Schematic of the SwissFEL Switch-Yard and FEL lines Aramis (0.1 – 0.7 nm) and Athos (0.7 to 30 nm)

2.4.1 Aramis

To achieve the shortest facility length, the Aramis undulator is designed to provide the shortest undulator period with a reasonable value for the undulator parameter K above 1. The tuning is primarily done by the electron beam energy. However, this implies the possibility of only a single hard X-ray beamline in any future extension of the facility, due to the coupling of the FELs through the electron beam energy.

The undulator is split up into 12 modules, each of 4 m length (see Fig. 2.4.1.1). All modules have an undulator period of 15 mm and a nominal undulator parameter K of 1.2. The gap of the in-vacuum undulator is between 4 and 5 mm, to achieve the required field strength for the K parameter. The resulting wakefields for a 5 mm gap and a 2.7 kA current profile, obtained with start-to-end simulations, are shown in Figure 2.4.1.2 for aluminum and copper [29]. The expected wakefield gradient is about 50 keV/m at the core of the electron beam, which, firstly, lies within the acceptance bandwidth of the FEL at 1 Å, and secondly, can be efficiently compensated by a small taper along the undulator. The difference between the wakefields for aluminium and copper is negligible.

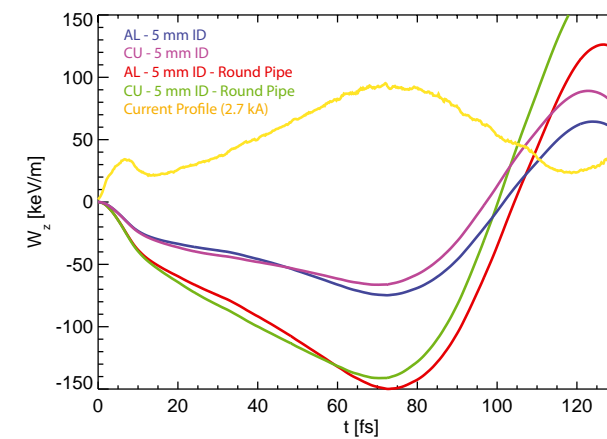


Fig. 2.4.1.1: Wake potential in the Aramis beamline for different vacuum chamber cross-sections and materials-

The FEL performance of Aramis for the nominal design parameters is listed in Table 2.4.1.1, assuming a flat current profile. In comparison, start-end simulations show a much better slice emittance (about 0.3 mm mrad) and thus show a better FEL performance (higher pulse energy, shorter saturation length) as seen in figure 2.4.1.2 and 2.4.1.3. The expected output energy is up to 600 μJ. However, the beam divergence and the bandwidth is larger in the start-end results than in the design case. The former comes from the mismatch of the beam slices along the bunch, which couples to a higher mode. The

latter arises from the fact that the longitudinal chirp is not completely removed by the wakes in the linac. To achieve that a more careful study of all wakefield sources (e.g. bellows, valves, collimator) needs to be done. Nevertheless it can be expected that a small residual chirp can be removed with off-crest acceleration in the linac 3, in particular when the longitudinal phase distribution can be measured directly with a transverse deflector and a dispersive region in front of the undulator.

Table 2.4.1.1: Performance of the Aramis hard X-ray beamline.

Beam energy	5.8 GeV	2.2 GeV
Peak current	2.7 kA	2.7 kA
Charge	200 pC	200 pC
Central Slice Energy spread	350 keV	350 keV
Central Slice Emittance	0.43 mm.mrad	0.43 mm.mrad
Undulator period	15 mm	15 mm
Undulator parameter	1.2	1.2
Undulator module length	4.00 m	4.00 m
Undulator section length	4.9 m	4.9 m
Average β -function	15 m	15 m
Wavelength	1 Å	7 Å
Saturation length	48 m	33 m
Saturation pulse energy	0.15 mJ (*)	0.20 mJ
Effective saturation power	2.8 GW	5.5 GW
Photons at saturation	$7.3 \cdot 10^{10}$	$9.84 \cdot 10^{11}$
Bandwidth (rms)	0.05 %	0.2 %
Pulse length (rms)	21 fs	20 fs
Beam radius	26.1 μm	77.9 μm
Beam divergence	1.9 μrad	7.4 μrad

(*) Simulated values obtained with Gaussian approximation but up to 1 mJ has been reached after simulation optimisation.

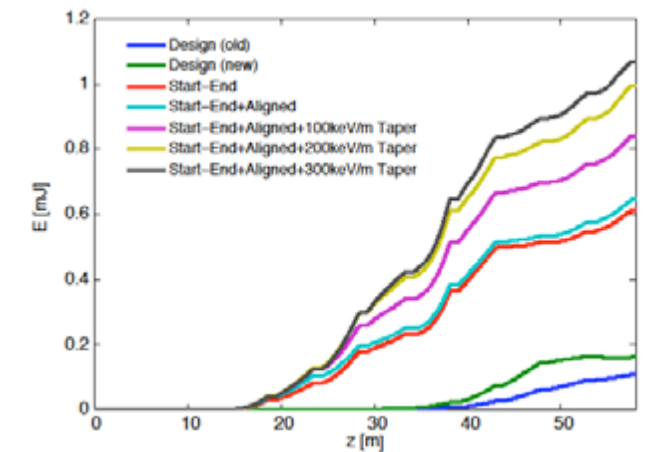


Fig. 2.4.1.2: Growth in the FEL pulse energy at 1 Å for the Aramis beamline. The “old” design (in blue) corresponds to a Gaussian current profile. All the curves above the red one are results of the start to end simulation (current profile from Elegant simulation and optimized to have a flat top distribution).

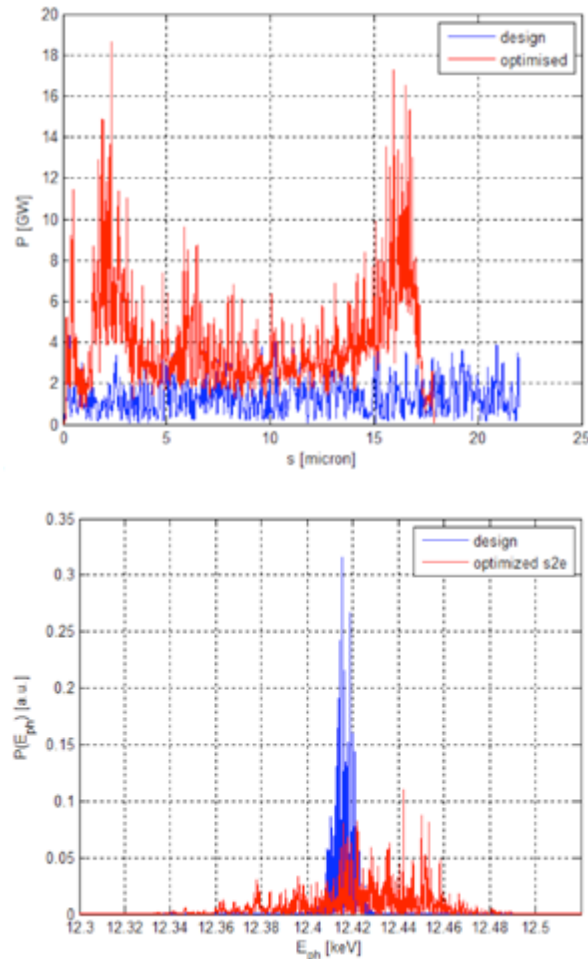


Fig. 2.4.1.3: Radiation profile and spectrum at saturation for the Aramis beamline, tuned to 1 Å. The design parameters (in blue) correspond to the design current profile. In red is represented the results of a start to end simulation where the current profile was optimized for more FEL power. Note that the larger bandwidth in the spectrum arises from a residual energy chirp in the start-end simulation.

2.4.2 Athos

The soft X-ray beamline Athos (see Fig. 2.4.1.1) is tuned independently of the Aramis line by varying the beam energy of the Athos Linac and / or by changing the undulator gap and thus the K-parameter.

Therefore, Athos is operated with beam energies from 2.6 GeV to 3.4 GeV, and a reduced tuning range of K between 1 and 3.2. In an APPLE II-type configuration with a period length of 4 cm, the minimum undulator gap is larger than 5 mm and thus sufficiently large to reduce the impact of wakefields. The corner stones for the tuning range are given by a maximum energy of 3.4 GeV and a K-value of 1 for a wavelength of 0.7 nm and by the minimum energy of 2.5 GeV and a K-value of 3.2 for

a wavelength of 7 nm. In the intermediate range the parameter choice is not necessarily unique though the preference is to maximize the beam energy for the highest possible photon flux.

Table 2.4.2.1: Performance of the Athos soft X-ray beamline in SASE Operation.

Beam energy	3.4 GeV	2.5 GeV
Peak current	2.7 kA	2.7 kA
Charge	200 pC	200 pC
Energy spread	350 keV	350 keV
Emittance	0.43 mm.mrad	0.43 mm.mrad
Undulator period	40 mm	40 mm
Undulator parameter	1.0	3.2
Undulator module length	4.0 m	4.0 m
Undulator section length	4.9 m	4.9 m
Average β -function	15 m	15 m
Average β -function	10 m	10 m
Wavelength	0.7 nm	7 nm
Saturation length	45 m	19 m
Saturation pulse energy	0.4 mJ	1.1 mJ
Effective saturation power	7.7 GW	21 GW
Bandwidth (rms)	0.05 %	0.2 %
Photons at saturation	$1.4 \cdot 10^{12}$	$3.8 \cdot 10^{13}$
Bandwidth	0.15 %	0.56 %
Pulse length	20. fs	20 fs
Beam radius	39.1 μ m	86 μ m
Beam divergence	3.9 μ rad	25.0 μ rad

2.4.3 Seeding: HHG; ECHO and self seeding schemes

Seeding is foreseen for the soft X-ray beamline of SwissFEL down to a wavelength of 1 nm. In comparison to SASE, seeding increases the longitudinal coherence and improves the pulse to pulse stability. The Echo-Enabled Harmonic Generation (EEHG) scheme [30] has been successfully tested for wavelengths of one hundred nanometers [31] [32] and can potentially produce high bunching directly at 1 nm, hence it is presently considered as the first choice for seeding at SwissFEL. However, EEHG is highly demanding and complex at 1 nm, therefore other strategies like High-Harmonic Generation (HHG) [33] and self-seeding [34] are also under consideration, while High-Gain Harmonic Generation (HG) [35] is not considered because of the higher sensitivity

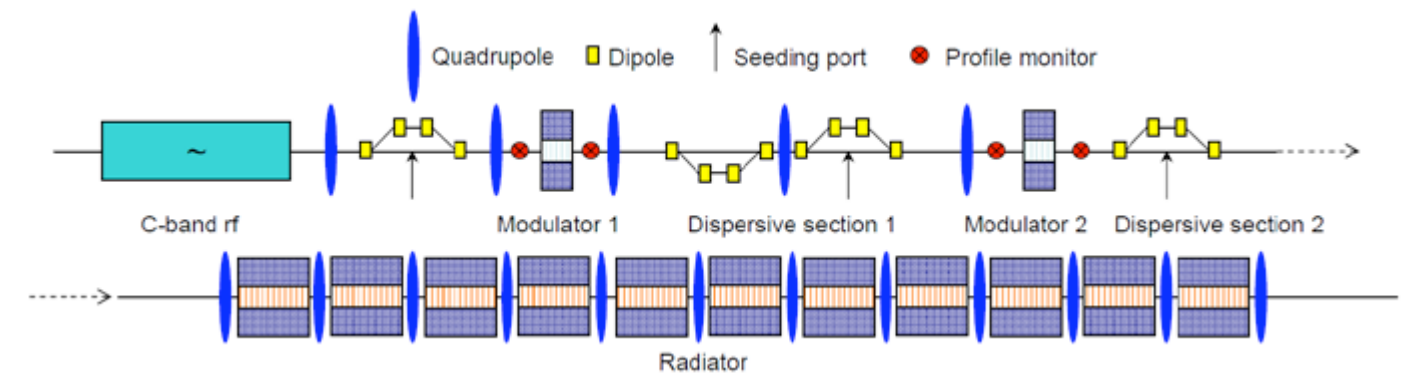


Fig. 2.4.3.1: EEHG layout for the soft X-ray beamline of SwissFEL (not drawn to scale).

to beam fluctuations and the energy spread increase in a “non-fresh” bunch approach [36].

EEHG uses two modulators and two dispersive sections to generate high harmonic density modulation. In the first modulator a laser with a wavelength λ_0 is used to modulate the energy of the electron beam. After that the beam is overcompressed in the first dispersive section. Then a laser with a wavelength $\lambda_1 = \lambda_0/K$ is used to do the second modulation, K being the ratio of the wavelengths of the two lasers (in our case we presently assume $K = 1$). The electrons then propagate through a second dispersive section with a small strength to generate the bunching at λ_0/h , where h is the harmonic number. The beam is finally sent through the radiator which is tuned to the wavelength λ_0/h . Assuming an initial seed signal with $\lambda_0 = 250$ nm, our final goal is to directly produce EEHG bunching at 1 nm with a harmonic conversion $h = 250$.

Figure 2.4.3.1 shows a sketch of the EEHG layout of the soft X-ray beamline of SwissFEL. The space required for the seeding is about 30 m (excluding the radiator). The dispersive section and undulator parameters are indicated in Table 2.4.3.1 and Table 2.4.3.2.

Table 2.4.3.1: Configuration of the EE-HG seeding beamline D’Artagnan, when operated at 5 nm and 3.4 GeV.

	Dispersive section 1	Dispersive section 2
Dipole length	1 m	0.25 m
Distance between dipoles	1 m	0.5 m
Maximum angle	2.2 deg.	1.2 deg.
Maximum R56	~10 mm	~1 mm

Table 2.4.3.2. Undulator parameters.

	Modulators	Radiator
Period length	36 cm	4 cm
# Periods per unit	6	100
Unit length	2.16 m	4 m
Units	2	11

The EEHG design strategy is to find a compromise between generating high modulation amplitudes, which require high laser powers and induces a large energy spread, and high dispersion strengths, which impose a limitation due to ISR/CSR effects. To find the optimum EEHG parameters we first use analytical expressions and do 1D simulations. Later we perform *Genesis* simulations, which take into account the beam-laser interaction in the modulators and the transverse effects, to finally tune the EEHG configuration.

We presently consider a beam energy of 3 GeV. This value is large enough so that the relative energy spread of the beam is sufficiently small for the FEL process, and is sufficiently small such as to not exceed the limit set by ISR and CSR effects. Based on start-to-end simulations results, we assume that the beam has an initial uncorrelated energy spread of 350 keV (rms), a

normalized emittance of $0.4 \mu\text{m}$, a peak current of 2.7 kA , and a beam charge of 200 pC . In our present design the modulation amplitudes in both modulators are 5 times the initial uncorrelated energy spread of the beam (i.e. 1.5 MeV rms), which corresponds to a modulator laser power of about 1.1 GW per modulator. The dispersion strengths are $R_{56}^1 = -8.7 \text{ mm}$ and $R_{56}^2 = -70 \mu\text{m}$.

Figure 2.4.3.2 shows the longitudinal phase-space at the radiator entrance. Bunching at 1 nm is about 4% . Figure 2.4.3.3 shows the radiation power at 1 nm and the electron beam energy spread along the radiator. FEL saturation can be achieved in about 20 m (6 radiator segments) and the saturation power is close to 3 GW . Table 2.4.3.3 shows the EEHG parameters and performance.

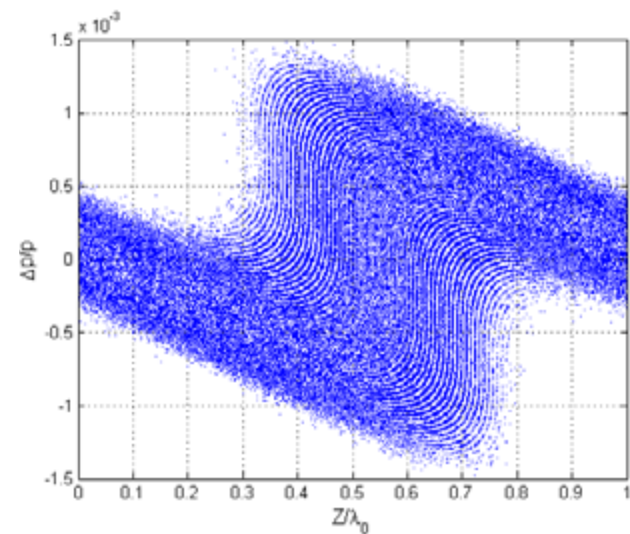


Fig. 2.4.3.2: Longitudinal phase-space at the radiator entrance. Bunching at the 250th harmonic (1 nm) is about 4% .

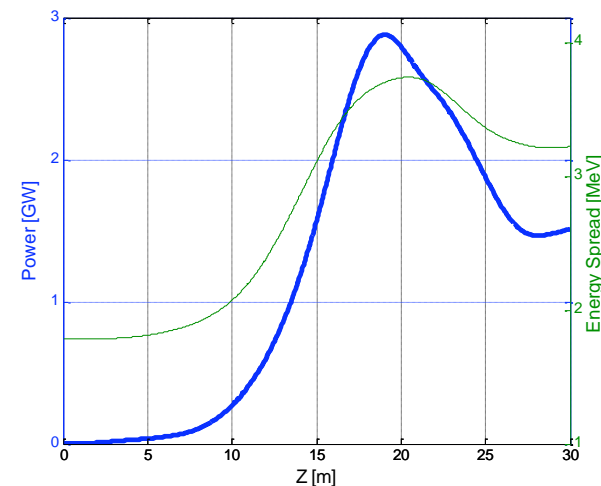


Fig. 2.4.3.3: Radiation power at 1 nm and beam energy spread along the radiator.

Table 2.4.3.3: EEHG parameters and performance.

Energy modulation in modulator 1 (rms)	1.5 MeV
Laser power in modulator 1	1.1 GW
First dispersion strength (R_{56}^1)	-8.7 mm
Energy modulation in modulator 2 (rms)	1.5 MeV
Laser power in modulator 2	1.07 GW
Second dispersion strength (R_{56}^2)	-0.07 mm
Bunching at 1 nm	$\sim 4\%$
Undulator length to achieve saturation	$\sim 20 \text{ m}$
Radiation power at 1 nm	$\sim 3 \text{ GW}$

A laser beam waist of $500 \mu\text{m}$ is assumed in the modulators, sufficiently larger than the electron beam size (well below $50 \mu\text{m}$) to avoid a bunching degradation due to transverse effects. Other issues which can smear the density modulation are ISR and CSR effects, especially in the first dispersive section (due to its large strength). First calculations performed with *Elegant* show a reduction of the bunching due to ISR/CSR of about $30\text{--}40\%$. Despite this bunching degradation, the EEHG seeding would still work (i.e. GW of power would be produced in the radiator at 1 nm). Other effects which can degrade the bunching such as intra-beam scattering need to be studied. Moreover, full 6D start-to-end simulations need to be done to study properties like the radiation spectrum and to investigate effects such as the initial energy chirp of the beam.

More information about the present status of the EEHG seeding design for SwissFEL can be found in [37].

2.4.4 Sensitivity and tolerance study for the bunch compression layout

An important factor for user facilities is the stability of the photon pulses leaving the undulator toward the user stations. Shot-to-shot jitter, as well as long-term drifts of machine parameters, such as RF phases and amplitudes, will affect the overall FEL performance. The main properties for the FEL process which need to be stabilized are the electron **beam energy**, the **arrival time** and the **peak current**.

Long-term drifts induced by temperature changes can be compensated for by slow feedback systems. The main concerns regarding performance are shot-to-shot fluctuations of various sub-systems.

The downstream performance depends on the stability of certain sub-systems. This dependence or **sensitivity** can be fitted with a first-order approximation. The sensitivities give a measure of bunch parameter variations, such as peak current, when changes occur in an upstream machine parameter. More details on the beam tolerances can be found in [38]. The sensitivities are obtained by a series of tracking runs from the electron gun to the undulator entrance. A set of parameters such as the magnet strength in BC 1 or the RF phase offsets are varied in a certain interval around the nominal settings. The resulting beam parameters at the undulator are then evaluated as a function of the individual varied parameter. The linear terms of polynomial fits to these dependencies are used as the sensitivities. Since the tightest tolerances are expected for the hard X-ray line, only the performance goals of the Aramis undulator have been studied in detail.

The **stability goals** (Table 2.4.4.1) of the machine can be divided by the corresponding sensitivity to obtain the allowed deviation from the design parameter (**jitter budget or tolerance**), assuming this is the only deviating property. Since some components are driven by uncorrelated jitter sources, such as for the linac RF stations, one can take the square root of the number of independent sources (4 klystrons for the S-band linac, 8 klystrons for the C-band linac 1, and 18 sources for C-band linac 2).

The stability goals at the undulator entrance are determined from the SASE dynamics. Intrinsic fluctuations of the FEL process can be used to define the tightest tolerances. It will not improve machine performance to stabilize the beam on a level below these intrinsic fluctuations. This defines the level of allowed peak current fluctuations, which is the result of a series of Genesis runs. Beam arrival time jitter is assumed to be on the order of the photon pulse length. A jitter of 0.05% in the mean energy would keep the resonant condition within the FEL bandwidth. Figures 2.4.4.1 and 2.4.4.2 give a summary of these tolerances for the different operation regime of SwissFEL. FEL light users might accept a larger FEL jitter, which would relax the given beam tolerances by the same factor.

In order to evaluate if those stability goals can be met, we used expected jitter values (table 2.4.4.2) for all critical accelerator components and multiplied them by the corresponding sensitivities. The final bunch stability (blue bar in Fig. 2.4.4.1) is then the quadratic sum of all independent jitter sources (red bars in Fig. 2.4.4.1)

divided by the number of jittering parameters. The obtained electron bunch parameter (peak current; arrival time, energy spread) fluctuations at the undulator entrance are shown in Fig. 2.4.4.1 for the standard 200 pC and 10 pC mode.

Table 2.4.4.1: Stability goal assumed to calculate the tolerance budget.

Main Beam Parameters for FEL process	Stability Goal at Aramis Entrance	
	200 pC	10 pC
Peak Current Fluctuations (%)	5	15
Beam Arrival Time Jitter (fs)	20	5
Beam Energy Jitter (%)	0.05	

Table 2.4.4.2: Expected RMS stability performance of SwissFEL subsystems. Those tolerances are assumed to simulate the beam performance stability presented in Fig. 2.4.4.1 and Fig. 2.4.4.2.

S-Band Phase stability (SBP) [deg]	0.018
S-Band Voltage stability (SBA) [%]	0.018
X-Band Phase stability (XBP) [deg]	0.072
X-Band Voltage stability (XBA) [%]	0.018
Linac 1 Phase stability (L1P) [deg]	0.036
Linac 1 Voltage stability (L1A) [%]	0.018
Linac 2 Phase stability (L2P) [deg]	0.036
Linac 2 Voltage stability (L2A) [%]	0.018
Linac 3 Phase stability (L3P) [deg]	0.036
Linac 3 Voltage stability (L3A) [%]	0.018
Charge stability (LHQ) [pC]	1%
Initial arrival time jitter (LHt) [fs]	30
Initial Energy stability (LHE) [%]	0.01
BC1 angle jitter [%]	0.005
BC2 angle jitter [%]	0.005

The assumed tolerances for the S band phase and amplitude stability in Table 2.4.4.2 are obtained from measurements at the SwissFEL Injector Test Facility. The values for the other RF systems are assumed to be a multiples of this.

From the numbers presented in Figures 2.4.4.1 and 2.4.4.2, the most critical components in terms of stability requirements can be identified. In this design, it is obvious that the RF phase offsets in the S- and X-band systems upstream of the first bunch compressor chicane are the critical parts.

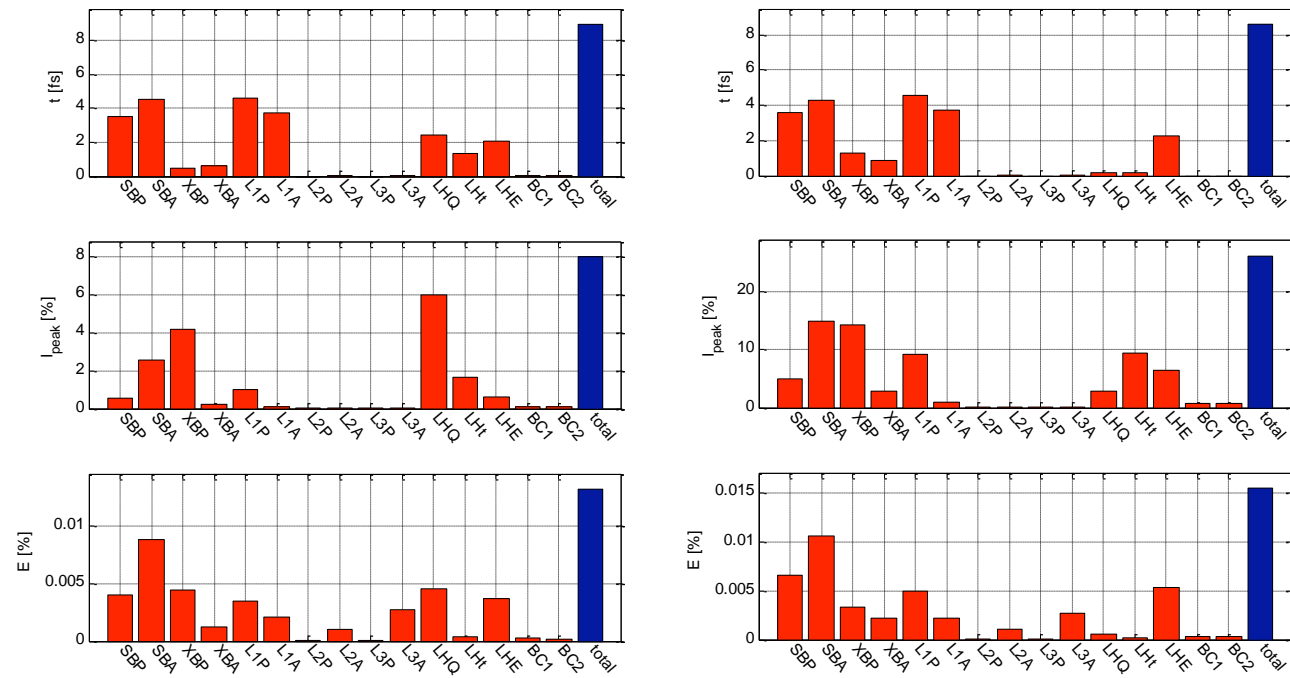


Fig. 2.4.4.1: Expected beam performances of the standard operation modes 10 and 200 pC. The red bars indicate independent RMS jitter sources, their total is given by the blue bar. The arrival time (top), peak current (middle), and energy jitter (bottom) are given for the 200 pC (left) and 10 pC mode (right). The jitter denomination (SBP; SBA ...) is explained in Table 2.4.4.2.

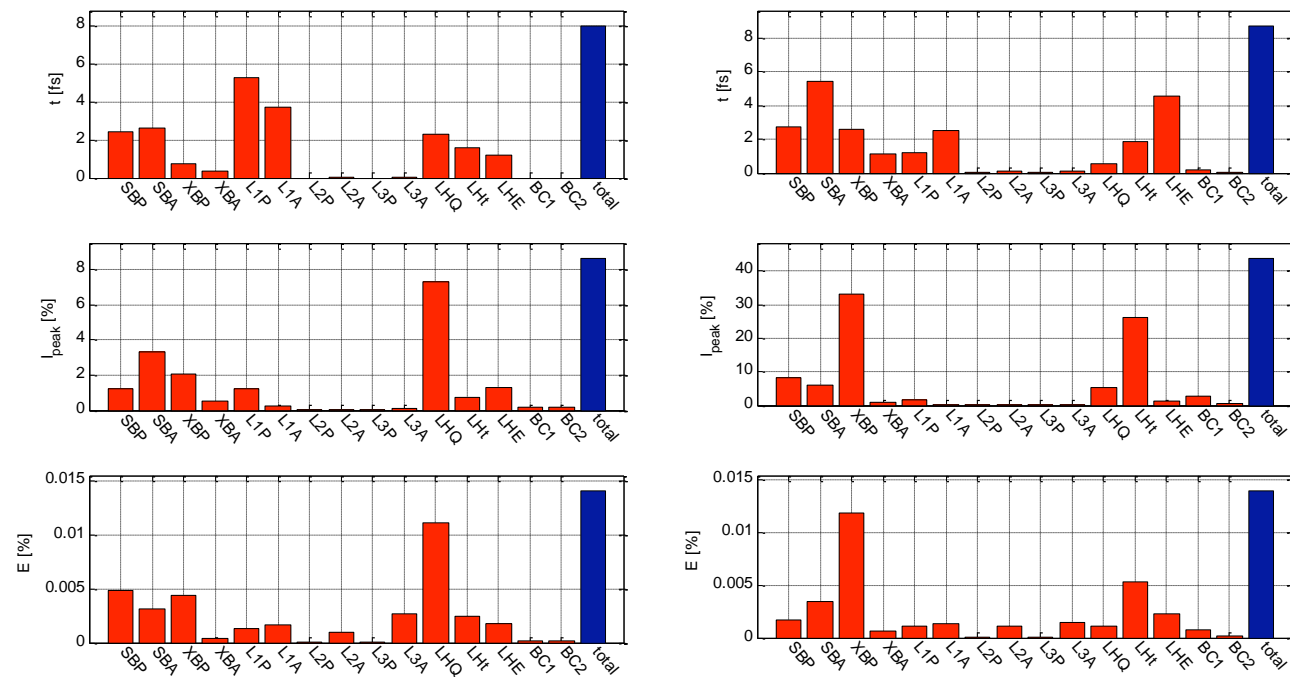


Fig. 2.4.4.2: As for Fig. 2.4.4.1 but for the the 200 pC large bandwidth mode (left) and 10 pC attosecond mode (right).

2.4.5 Sensitivity of the FEL performance

Any disruption of the FEL process may be a combination of two effects: reduction in the transverse overlap and longitudinal synchronization between the electron beam and radiation field. These are caused by multiple error sources, such as quadrupole misalignments, detuning of undulator modules or injection errors. The hard X-ray beam Aramis at 1 Å requires the best alignment of the system, and is the point of operation which defines the sensitivity/tolerances of the SwissFEL. At longer wavelengths, in the soft X-ray beamline Athos, the sensitivity is reduced and the tolerances are more relaxed. The results of the sensitivity study are listed Table 2.4.5.1.

Table 2.4.5.1: Sensitivities of the Aramis beamline at 1 Å leading to 40 % FEL pulse energy drop.

Error source	RMS Sensitivity
Undulator module K detuning	0.073 %
Undulator vertical misalignment	83 μm
Quadrupole (between undulators) field errors	21 %
Quadrupole (between undulators) transverse misalignment	4.6 μm
Injection offset between electron beam and undulator axis	11.7 μm
Injection angle between electron beam and undulator axis	0.78 μrad
Mismatch β/β_0	1.42

Note that the sensitivity corresponds to a drop by $\sim 40\%$ in the FEL pulse energy at the point of saturation for the undisturbed FEL performance. The tolerance budget is the combined effect of weighted sensitivities to limit the increase in the saturation length by less than 2 m. In addition, some of the sensitivities, such as mismatch or injection errors, are the results of the combined errors in the injector and linac itself.

For the seeding option of the Athos beamline, additional sensitivities are apparent; mainly the arrival time jitter and the energy jitter of the electron beam. However, the explicit seeding scheme has not yet been fully designed and optimized.

3 Electron beam components

3.1 Laser system

3.1.1 Gun laser system

A copper photo-cathode is presently the base-line electron source candidate fulfilling the SwissFEL injector requirements in terms of beam brightness. For the operation of SwissFEL, a laser system capable of generating 200 pC of photo-electrons is required. A minimum energy per pulse of 100 μ J at 266 nm is required to produce 200 pC of photoelectrons from a copper surface, assuming a QE of 10^{-5} . Such pulse energies can easily be achieved with current Ti:Sa amplifier systems. In addition, Ti:Sa laser systems provide pulses as short as 50 fs, so that it becomes possible to generate a uniform longitudinal profile (square profile) with a rise time of a few 100 fs by frequency-domain pulse shaping.

Ti:Sapphire systems are commercially available and have reached high technological maturity, due to their widespread use in research laboratories throughout the world. In addition, many diagnostic tools and pulse-shaping techniques are available for the near-IR/visible spectral region, and frequency-tripling of the fundamental laser wavelength allows easy access to the UV.

Table 3.1.1: Gun laser characteristics for SwissFEL.

Laser specifications	
Maximum pulse energy on cathode	60 μ J
Central wavelength	250–300 nm
Bandwidth (FWHM)	1–2 nm
Pulse repetition rate	100 Hz
Double-pulse operation	yes
Delay between double pulses	28 ns
Laser spot size on cathode (rms) (10 pC / 200 pC)	0.1 / 0.27 mm
Minimum pulse rise-time	<0.7 ps
Pulse duration (FWHM)	3–10 ps
Longitudinal intensity profile	various
Transverse intensity profile	Uniform
Laser-to-RF phase jitter on cathode (rms)	<100 fs
UV pulse energy fluctuation	<0.5% rms
Pointing stability on cathode (relative to laser diameter)	<1% ptp

Conventional Ti:sapphire amplifiers, however, suffer from spectral narrowing due to the limited gain bandwidth, yielding spectra of 30–40 nm (FWHM) at the mJ level and making wavelength tuning impossible. The scheme presented here overcomes this limitation and furthermore offers enhanced pulse energy stability and direct UV pulse shaping. This should help to produce electron bunches with low emittance at the gun.

3.1.2 General layout

The laser system consists of 4 subsequent amplifier stages. As seed laser, a Rainbow oscillator (Femtolaser, Inc.) delivering 380 mW is used. This seed is an ultra-broadband source needed for further amplification while maintaining short pulses.

The pre-amplified (10 μ J) and temporally stretched (\approx 500 ps) pulse seeds the regenerative amplifier, which is followed by sequential multi-pass amplifiers. An acousto-optic programmable gain-control filter (Mazzler, Fastlite Inc. [39]) situated in the regenerative cavity is used as an adaptive spectral filter, providing broad spectra with up to 120 nm (FW). Wavelength selection is performed by a Dazzler. The current amplifier scheme allows continuous variation of the central wavelength within a range of 755 to 845 nm, with a spectral width of 30 nm. The compressed pulses (20 fs, up to 21 mJ) are frequency-converted from the near-IR to the UV by second-harmonic generation (SHG) and subsequent sum-frequency generation (SFG) in β -barium borate (BBO) crystals. The expected wavelength tunability covers 260–280 nm, with pulse energies up to 1 mJ.

The large number of six identical diode pump lasers helps to increase stability, since pump-laser induced energy fluctuations can be significantly reduced by mixing different pump sources.

3.1.3 UV temporal and spatial pulse shaping

The spatial and temporal shape of the amplified laser pulse is nominally Gaussian. Electron beam dynamics simulations indicate that a flat-top-like pulse shape helps to generate uniform temporal and spatial electron distribution, resulting in lower transverse emittance at the gun. Since other simulations show that a Gaussian-like electron distribution is less sensitive to timing jitter in the undulator, it is more likely that an intermediate pulse shape will be optimal for best FEL performance[40]. Our approach for achieving high-quality shaped UV pulses is based on direct UV pulse stretching and shaping. A UV stretcher based on highly efficient transmissive UV gratings (Ibsen Photonics Inc.) allows the stretching of Gaussian pulses (see Fig. 3.1.2). This setup is very compact and gives the possibility of temporal shaping by using spectral filtering in the Fourier domain of the stretcher. The pulse length can be continuously varied

from 2 to 10 ps FWHM by changing the distance between the two gratings.

An alternative technique that is considered for producing ps flat-top-like pulses is the so called “pulse stacking technique”. α -cut β -barium borate (BBO) crystals of length L are used to generate replicas of the initial pulse. Each crystal generates two orthogonally polarized replicas separated in time by a delay $t = \frac{L}{c}(n_o - n_e)$ as can be seen in Fig. 3.1.3. The use of several crystals of adequate lengths allows the generation of flat-top-like ps pulses with an efficiency of 70% (or 30% energy loss). Temporal pulse characterization will be performed by cross-correlation with the fundamental laser pulse.

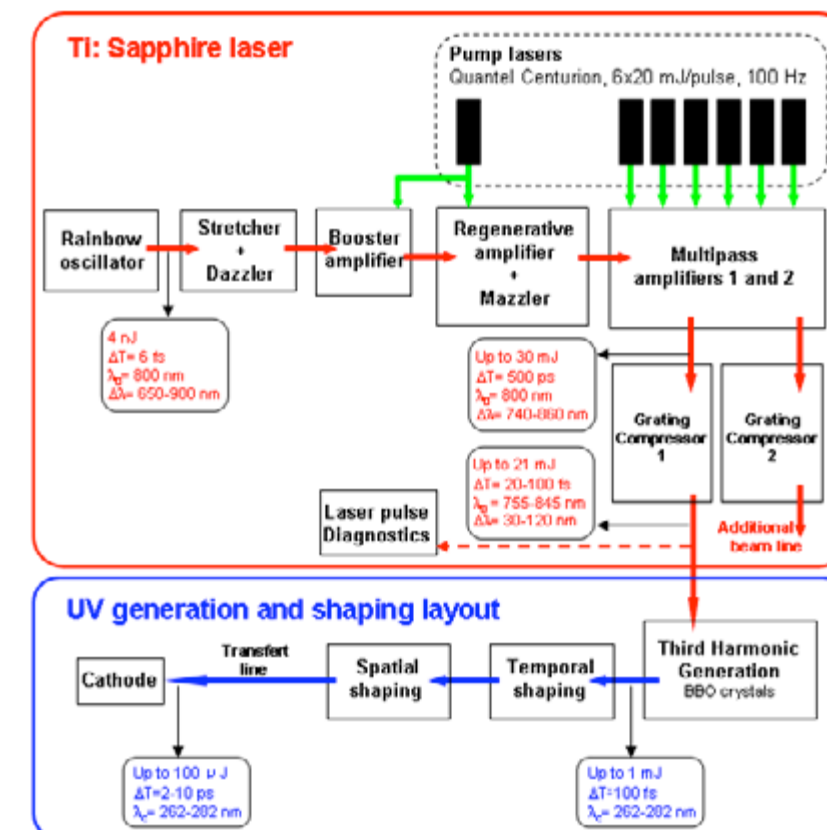


Fig. 3.1.1: Schematic drawing of Ti:Sapphire gun laser.

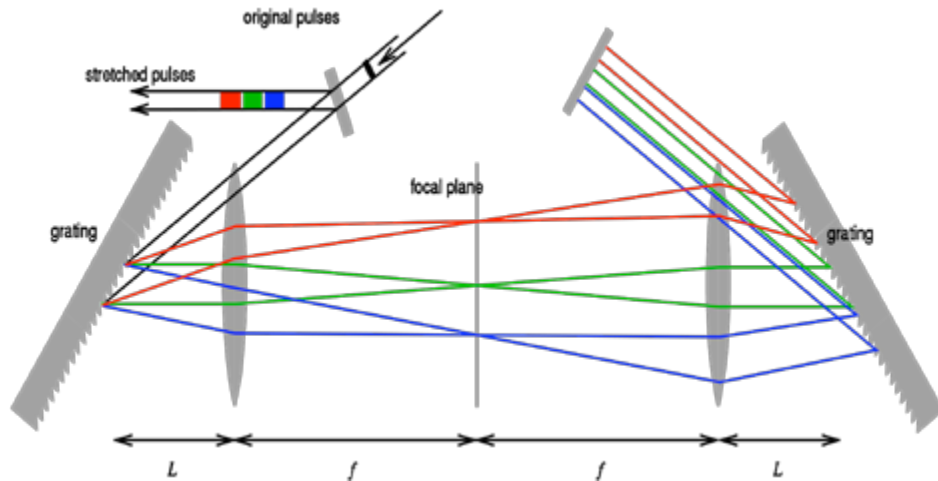


Fig. 3.1.2: UV pulse stretcher based on UV transmissive gratings.

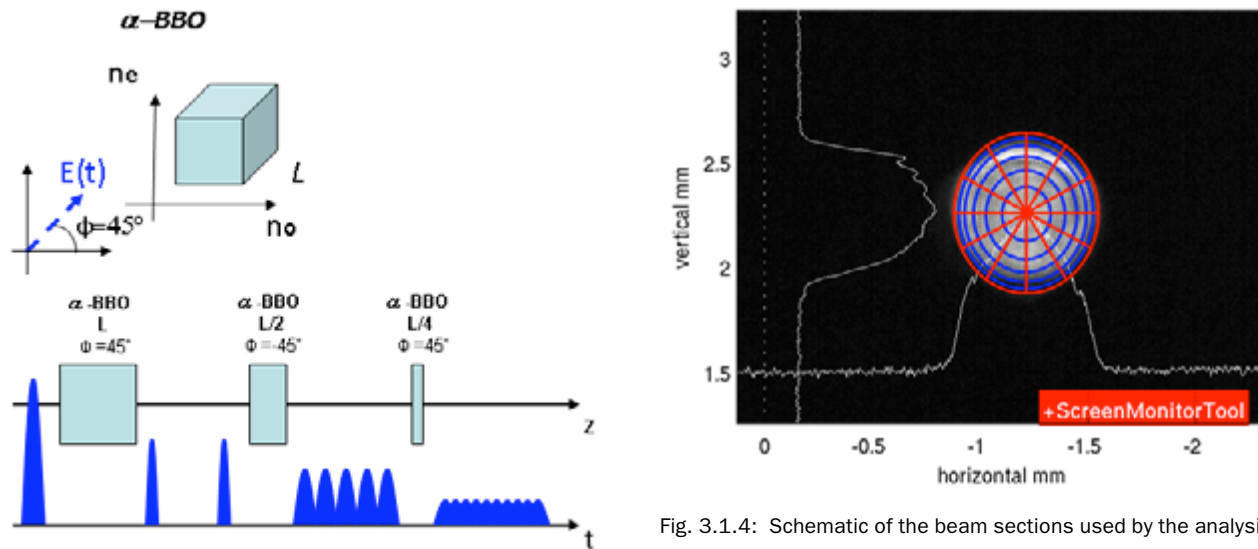


Fig. 3.1.3: Left: glass capillary for beam homogenization; right: set of apertures for transverse flat-top beam generation.

In order to produce a homogeneous flat-top electron beam profile (transversally) on the cathode surface, the laser intensity profile must also be flat-top. Laser transverse homogenization techniques are described below. In order to quantify the quality of the laser intensity transverse profile we defined some key parameters and developed an analysis tool. The tool computes the beam ellipticity as well as the beam transverse and radial uniformity:

- the ellipticity is computed showing the ratio of the beam diameter measured over two orthogonal axis.
- the beam transverse and radial uniformity calculations are based on the following method: the beam is divided in transverse (Fig. 3.1.4 in blue) and radial (Fig. 3.1.4 in red) sections, each section having the same area. Then, the normalized average intensity in each

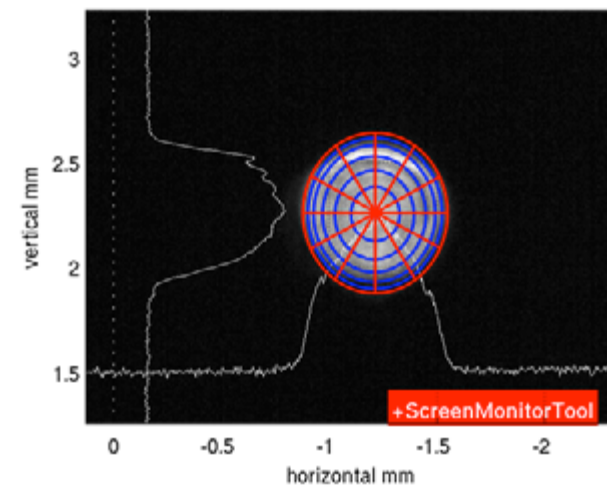


Fig. 3.1.4: Schematic of the beam sections used by the analysis tool. The blue concentric circles are used for transverse beam homogeneity calculations while the red 'pizza portions' are used for radial intensity homogeneity.

section is estimated. Finally, the RMS and standard deviation for transverse and angular uniformity is computed.

The optical technique for transverse beam shaping consists of selecting the core part of the intensity profile by a spatial mask, which is relay-imaged onto the cathode surface. Prior to this, the UV beam passes through a beam homogenizer for reduction of intensity hot spots arising during third-harmonic generation process. The beam homogenizer consists of a 15–30 cm-long glass waveguide with a 400 μm air-filled core. For appropriate beam parameters, the waveguide acts as a low-pass filter, since strong coupling is only achieved for the fundamental HE_{11} mode.

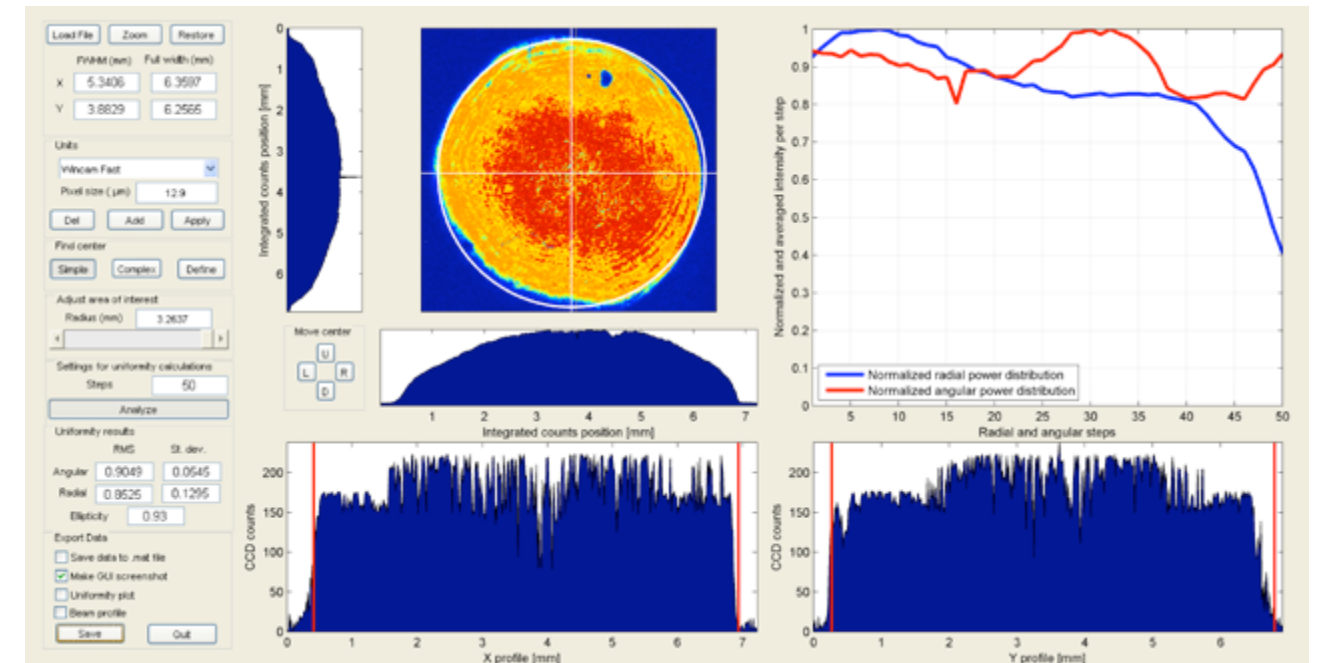


Fig. 3.1.5 shows a screenshot of the analysis tool. As can be seen, other interesting parameters like the integrated beam profiles over x and y axis, as well as the plot of transverse and radial average intensity versus beam section are displayed.

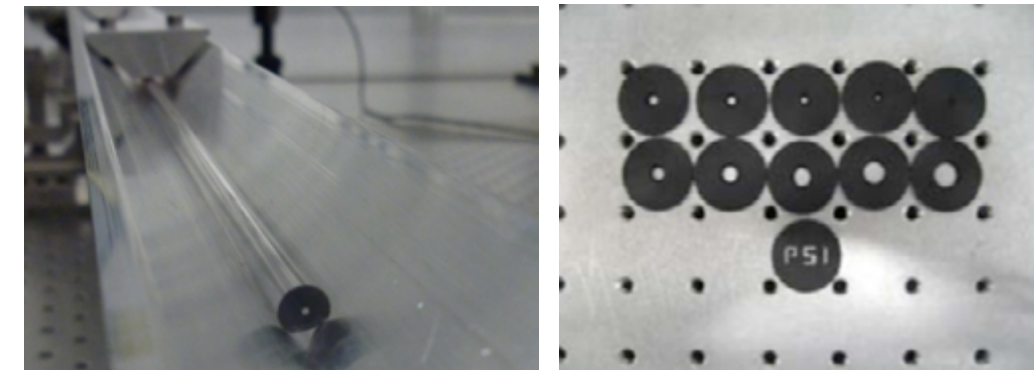


Fig. 3.1.6: Left: glass capillary for beam homogenization; right: set of apertures for transverse flat-top beam generation.

3.1.4 Laser room for the SwissFEL injector

The amplitude stability of laser systems is highly dependent on environmental conditions (temperature, air turbulence, humidity). In order to provide the best environmental quality for the laser system, the SwissFEL injector will include a temperature and humidity controlled clean room. The room provides a Class 10000 environment with a temperature stability of $\pm 0.1^\circ\text{C}$. The humidity is limited to a maximum of 45%, in order to avoid condensation on optical components.

The analogue and optical Master Oscillator also requires a stable environment. For this reason, both will be hosted in the laser room.

3.1.5 HHG-based seeding laser system

A promising approach for seeding a FEL is based on high-order harmonic generation (HHG) in gases by an intense femtosecond laser system. HHG yields fully coherent XUV radiation in very short pulses, ranging from femtoseconds to attoseconds. It is planned to seed the soft X-ray beamline of the SwissFEL with both a 12 nm and a 5 nm seeding source. While HHG at 12 nm is feasible with a state-of-the-art Ti:Sapphire laser system ($\lambda_{\text{laser}} = 800 \text{ nm}$), the generation of 5 nm coherent radiation by HHG requires the development of a powerful mid-IR driver (e.g. ($\lambda_{\text{laser}} = 3000 \text{ nm}$)).

Table 3.1.2: Parameters of the laser for High Harmonic Generation (HHG) seeding.

Seed laser	Unit	
Harmonic wavelength	nm	12 (5)
Driving laser wavelength	mm	0.8 (3)
Laser energy	mJ	20 (10)
Conversion efficiency		$1 \cdot 10^{-6}$ ($1 \cdot 10^{-6}$)
Photon energy	eV	103.3 (248)
Minimal average power	kW	50 (100)
Pulse duration, rms (s)	fs	<35
FEL gain bandwidth, Dw/w		0.003 (0.001)
Temporal pulse form		train
Size of e beam, rms (s)	mm	25
Mode size, rms HHG	mm	>25
Loss beam transport	%	50
Loss in HHG-FEL coupling	%	90

3.1.6 Laser system for laser heater

An electron beam with a small energy spread may introduce micro-bunching instabilities in the electron beam and subsequent problems for electron beam diagnostics equipment, due to coherent synchrotron radiation.

Table 3.1.3: Parameters of the laser heater laser.

Laser heater	Unit	
Pointing stability, rms	μm	<20
Laser energy	μJ	10...100
Laser spot-size, rms (s)	μm	300
Transverse profile		Gaussian
Laser peak power	MW	10...20
Laser wavelength	nm	800
Rayleigh range	m	0.5
Pulse duration	ps	10...100
Longitudinal profile		Gaussian
Pulse energy stability, rms	%	<2
Repetition rate	Hz	100

To avoid this, the uncorrelated energy spread of the electron beam needs to be increased. This can be done with the help of a powerful infra-red laser beam, which is overlapped with the electron bunch in an undulator situated in a chicane. The laser heater beam is a split from the gun laser system, since this system provides enough power to drive the gun and the heater synchronously. The transport from the laser hutch to the laser

heater will be performed in vacuum tubes, to provide the required beam pointing stability at the laser heater. The required laser parameters are listed above.

3.2 RF systems

3.2.1 Main parameters of different SwissFEL RF structures

See Table 3.2.1.1 on the right.

3.2.2 RF photogun design

The RF gun for Swiss FEL consists of $2\frac{1}{2}$ cells operating in the π mode. The final RF frequency choice for all S-band cavities and accelerating structures of the injector will be 2998.8 MHz to have a common sub-harmonic ($f_b=142.8$ MHz) with the American C-band linac (the C-band linac frequency is 5712 MHz) (see Table 3.2.1.1). The second cell is coupled to two waveguides symmetrically arranged to cancel the dipolar component of the field. It also has a racetrack profile to minimize the quadrupolar field component. To reduce the thermal stress and to decrease the pulsed surface heating, the coupling between the waveguides and the second cell is optimized by adopting coupling all along the length of the second cell (z-coupling) and by increasing the radius on the inside surface of the coupling aperture. The dimensions of the coupling iris have also been optimized so that the coupling factor β is equal to 2. This allows faster filling of the cavity. The frequency separation between the operating mode and the next lower mode ($\pi/2$ mode) is more than 16 MHz. This feature, achieved by increasing the radius of the irises between the cells, is expected to minimize the impact of the neighbouring modes on potential emittance degradation.

For two-bunch operation, flat-topping of the accelerating field can be obtained with an amplitude modulation of the klystron input power. To achieve a flat-top accelerating field of 100 MV/m for 150 ns (Figure 3.2.2.2) with an RF pulse length of $1\mu\text{s}$, the input power from the klystron has to be set to about 19 MW for 850 ns, and then, decreased to about 13 MW for 150 ns. In addition, care has to be taken to adjust the phase of the accelerating field.

Table 3.2.1.1: Summary of the key parameters of the different accelerating structures of SwissFEL.

	Unit	S-band photogun	S-band cavities (injector)	X-band cavities (injector)	C-band cavities (Linacs 1)	C-band cavities (Linacs 2)	C-band cavities (Linacs 3)	C-band cavities (Athos linac)
Frequency (MHz) – $f_b=142.8$ MHz		2998.8 ($21 \times f_b$)	2998.8 ($21 \times f_b$)	11995.2 ($84 \times f_b$)	5712 ($40 \times f_b$)			
Phase Advance		π	$2\pi/3$	$5\pi/6$	$2\pi/3$			
Active Length	mm	162	4070	750	1978			
Total Length	mm		4150	965	2050			
Number of Cells		2.5	122	72	113			
Operating Temperature	$^{\circ}\text{C}$	40	40	31	40			
Maximum Gradient	MV/m	120	25	34	28	28	30	30
Operating Gradient	MV/m	100	14.8	25	27	27.5	28.5	28.5
Required Input Peak Power per structure		19 MW for 100 MV/m	24 MW for 16 MV/m	7 MW for 20 MV/m	27.2 MW for 27.5 MV/m			
Klystron maximum performance		35 MW – $4.5 \mu\text{s}$	45 MW – $4.5 \mu\text{s}$	50 MW – $1.5 \mu\text{s}$	50 MW – $2.5 \mu\text{s}$ 40 MW – $3 \mu\text{s}$			
Filling Time	ns	490	1000	105	322			
Number of structures		1	6	2	36	16	52	8
Number of structures per klystron		1	1 or 2	2	4			

Optimizing the radius of each cell allows field balance to be obtained (Figure 3.2.2.1).

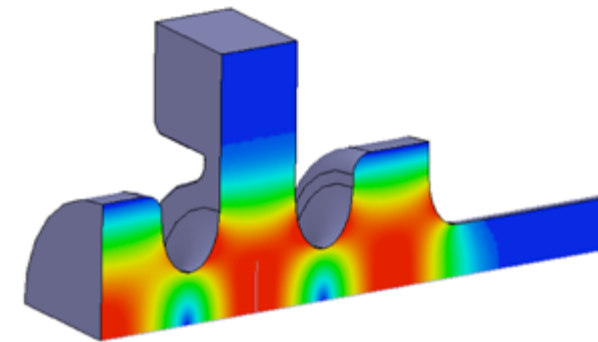


Fig. 3.2.2.1: 3D field map of the complex amplitude of the accelerating electric field.

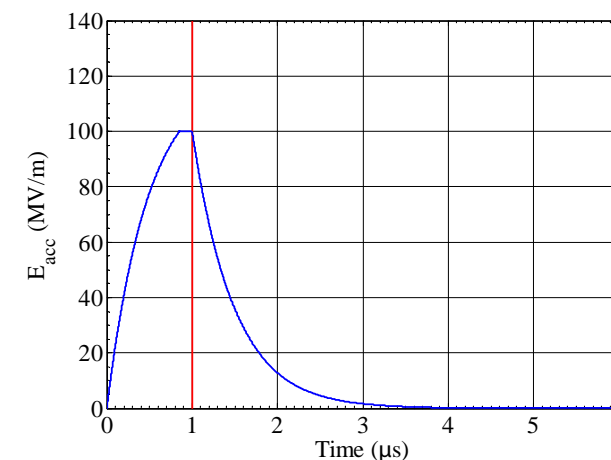


Fig. 3.2.2.2: Peak on-axis accelerating electric field vs. time.

Operating with a pulse length as small as $1 \mu\text{s}$ in the amplitude modulation mode substantially decreases the average power of the RF gun and, therefore, reduces the thermal stress. For an accelerating field of 100 MV/m, a repetition rate of 100 Hz and a pulse length of $1 \mu\text{s}$, the dissipated average power is as low as 0.9 kW (Figure 3.2.2.3). The maximum temperature rise due to pulsed surface heating, located at the coupling irises, is as low as 17°C – well below the 50°C considered acceptable.

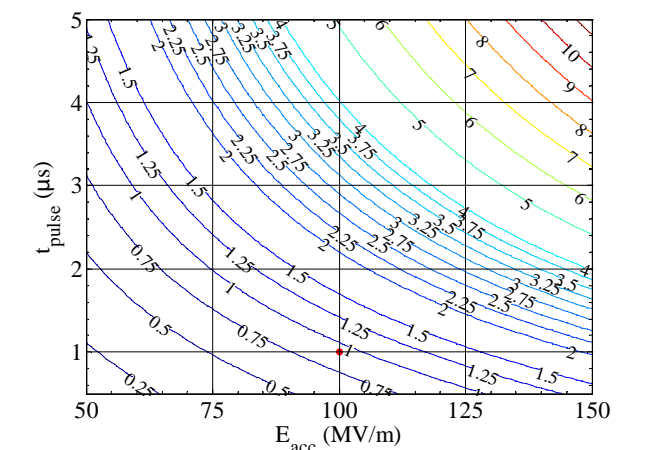


Fig. 3.2.2.3: Contour plot of dissipated average power (kW) vs. accelerating field and pulse length for a repetition rate of 100 Hz.

Three RF pick-ups, one per cell, are foreseen to monitor and control the RF field in the gun during operation. The operating temperature will be 40°C . Dimple holes on each cell are also foreseen to allow tuning for reaching

the required frequency during cold measurements. The back plane of the $\frac{1}{2}$ cell, which is used as cathode plate, is also longitudinally adjustable, giving another degree of freedom for the tuning of the gun.

3.2.2 RF systems of the SwissFEL injector

The general layout of the RF system for the SwissFEL Injector is shown in Figure 3.2.3.1.

The accelerator starts with the S-band RF-photoinjector described in Section 3.2.2. A booster linac composed of 6 S-band structures, 4 m long, provides the required acceleration and energy chirp for the magnetic compression. Two 12 GHz cavities are located in front of the compression chicane for linearization of the longitudinal phase space. Two S-band deflecting cavities will be installed for diagnostics purposes to characterize the longitudinal phase space and slice parameters of the beam. This choice will allow fine control of the RF focusing (gradient optimization) for optimal invariant envelope matching, avoiding any cross-talk between cavities. SLED compressors have not been considered for the initial phase to suppress any additional complication. The modulator and the klystron run in a short-pulse mode for maximum gradient tests (25 MV/m) and in the long-pulse mode (45 MW) to later allow RF compression tests.

The RF systems already installed at the SwissFEL Injector Test Facility, which has two S-band structures less and one X-band structure less, will be moved to the

SwissFEL building in 2015. The SwissFEL Injector Test Facility is currently operated at the European frequency (S-band: 2997.912 MHz; X-band: 11991.648 MHz) but soon tests at the SwissFEL design frequencies (Table 3.2.1.1) will be performed.

3.2.3.1 S-band structures

Booster linac

As mentioned above, the actual SwissFEL booster linac consists of six constant-gradient $2\pi/3$ travelling-wave accelerating structures separated by short drifts, where corrector, BPM and screen monitor are located. For small correction of the transverse focusing, each cavity is surrounded by four solenoid magnets, each 70 cm long (operated with peak magnetic field between 40 and 80 mT (cf. Section 3.4.1)).

The actual structure RF design derives from the Linac II DESY structures and was optimized to decrease the power requirement. The final structure consists of 122 cells, including the coupler cells. The iris profile has an elliptical shape at its tip to reduce the maximum surface electric field (Figure 3.2.3.1.1). The iris aperture ranges linearly from 12.695 mm upstream to 9.31 mm downstream and the iris thickness is 5 mm for all cells. The input and output coupler cells have been symmetrized with dual feed and racetrack geometry. A 3D model of the waveguide system at the input/output coupler is shown in Figure 3.2.3.1.1. The variations of the iris radius and cell radius along the structure are shown in

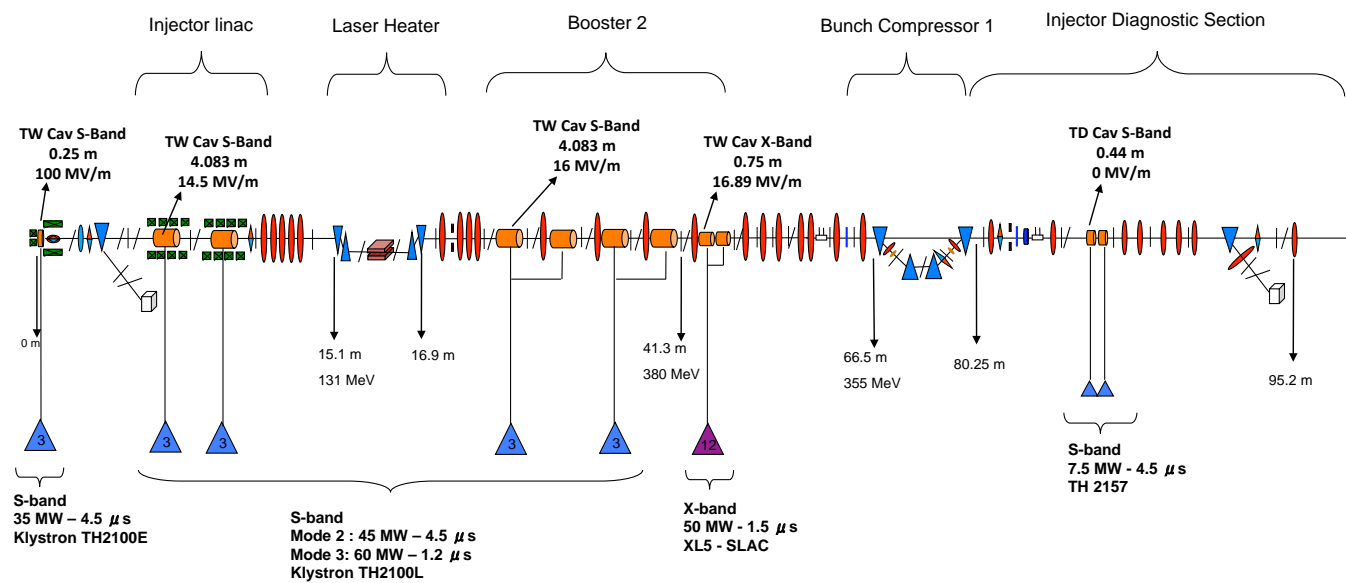


Fig. 3.2.3.1: General layout of the RF systems for the SwissFEL Injector.

Figure 3.2.3.1.2. Figure 3.2.3.1.3 shows the group velocities and the r/Q along the structure and Figure 3.2.3.1.4 the quality factor Q . The accelerating gradient and the maximum surface electric field along the structure are shown in Figure 3.2.3.1.5.

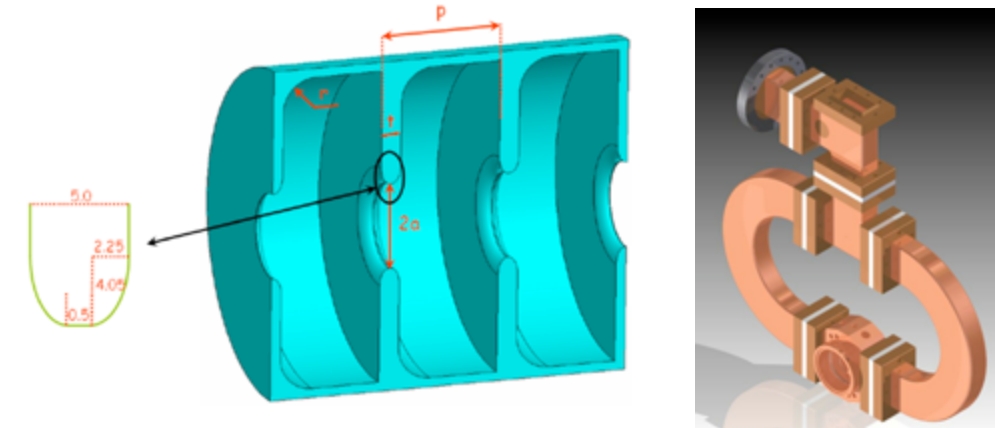


Fig. 3.2.3.1.1: Cell geometry and detail of the iris design for the S-band structures ($r = 10$ mm, $t = 5$ mm, $p = 33.324$ mm) and 3D model of the waveguide system at the input/output coupler (only the coupler cell is shown here).

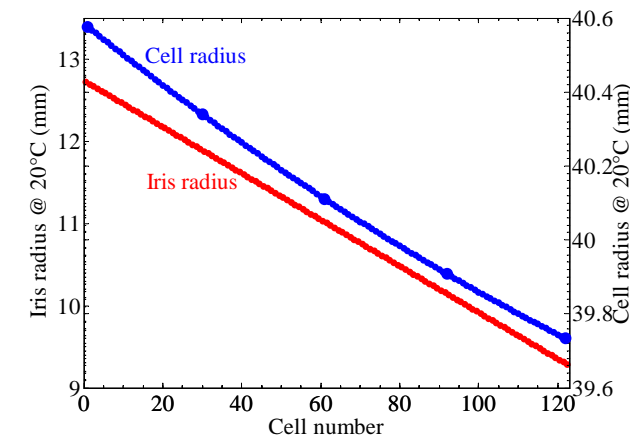


Fig. 3.2.3.1.2: Variation of iris and cell radii vs. cell number.

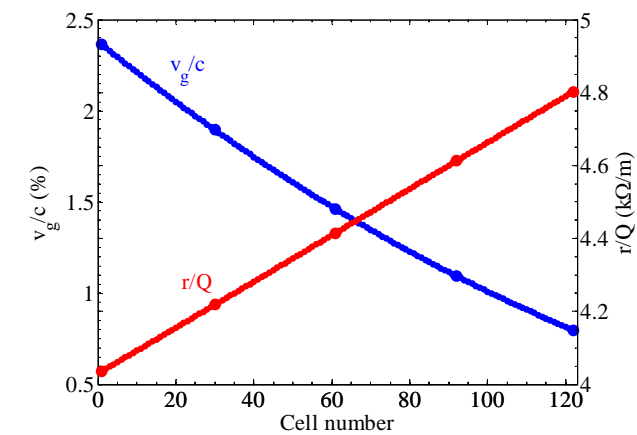


Fig. 3.2.3.1.3: Variation of v_g/c and r/Q vs. cell number.

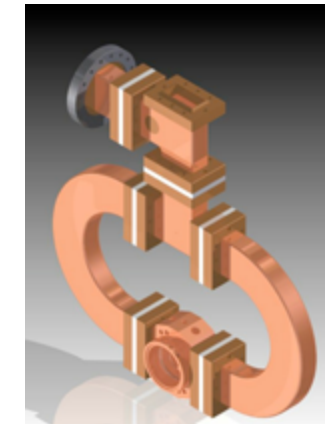


Fig. 3.2.3.1.4: Variation of quality factor Q vs. cell number.

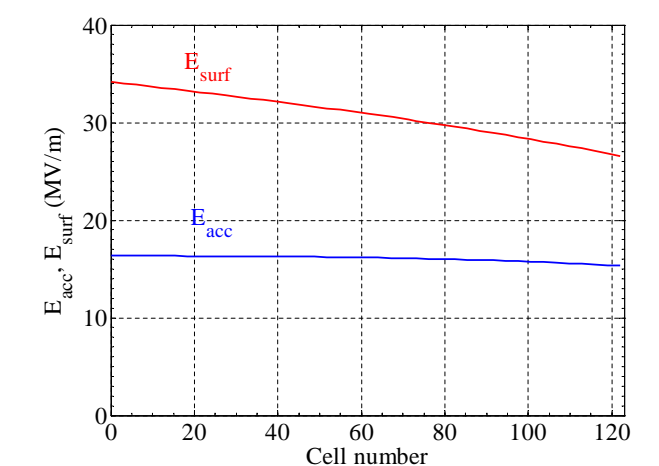


Fig. 3.2.3.1.5: Accelerating gradient and maximum surface electric field along the S-band accelerating structure.

The main parameters of the S-band accelerating structures are summarized below in Table 3.2.3.1.1.

Table 3.2.3.1.1: Main parameters for the S-band structures,

Operating frequency	2998.8 MHz
Operating temperature	40 °C ± 0.1 °C
Phase advance	$2\pi/3$
Flange-to-flange total length	4150 mm
Number of cells (including coupler cells)	122
Cell length at operating temperature	33.324 mm
Iris thickness at 20 °C	5 mm
Iris radius at 20 °C	12.695 mm ... 9.310 mm
Cell radius at 20 °C	40.553 mm ... 39.725 mm
Input coupler	Double-feed type, racetrack geometry
Output coupler	Double-feed type, racetrack geometry
Accelerating gradient	16 MV/m
Maximum accelerating gradient	25 MV/m
Shunt impedance per unit length	56.5 M Ω /m
Peak power – accelerating gradient of 16 MV/m	24 MW
Filling time	1000 ns
RF pulse length (60 MW)	1.2 μ s
Optional RF pulse length (45 MW)	4.5 μ s
Maximum pulse repetition rate	100 Hz
Material of the cavity	Cu-OFE
Material of the flanges, supports and cooling connectors	316LN
Concentricity tolerance	± 150 μ m
Maximum pressure drop of the cooling channels	4 bar

3.2.3.2 X-band structures

The X-band harmonic structure is a modification of the SLAC H75 structure. This structure (Figure 3.2.3.2.1) is being developed in collaboration with CERN where it will be tested for high-gradient applications within the CLIC high-gradient R&D program.

Two structures have been manufactured for PSI in the frame of a CERN, PSI, ELETTRA collaboration. The oper

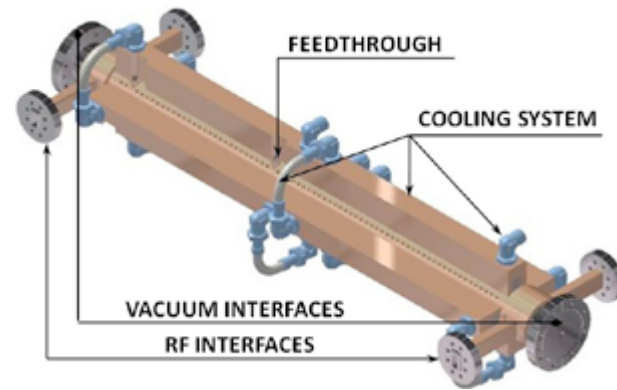


Fig. 3.2.3.2.1: General view of the X-band cavity.

ating frequency for the SwissFEL Injector is 11995.2 MHz (see Table 3.2.1.1) with a temperature around 31 °C. The SwissFEL Injector test facility will, however, initially operate the two X-band structures at 11991.648 MHz and 49 °C. This travelling-wave structure is of the constant-gradient type with a $5\pi/6$ phase advance and 72 cells, including the matching cells [41]. The active length is about 750 mm.

The iris aperture varies linearly from 4.991 mm upstream to 4.106 mm downstream (see Figure 3.2.3.2.2). The iris thickness ranges, also linearly, from 3.300 mm to 3.586 mm. With such a small iris aperture, this structure will dominate the impedance budget of the entire injector. Misalignments larger than 10 μ m can generate large transverse kicks with catastrophic consequences on the final emittance. For this reason, cell numbers 36 and 63 have been radially coupled to four wave guide systems (Figure 3.2.3.2.5) to extract dipole mode signals which will give an indication about the cavity misalignment.

The variation of the cell radius along the structure is shown in Figure 3.2.3.2.2. Figure 3.2.3.2.3 shows the group velocities and of the r/Q along the structure and Figure 3.2.3.2.4 the quality factor Q .

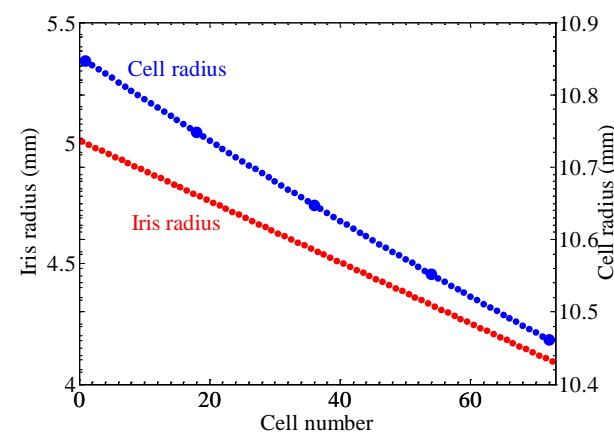


Fig. 3.2.3.2.2: Variation of iris and cell radii vs. cell number.

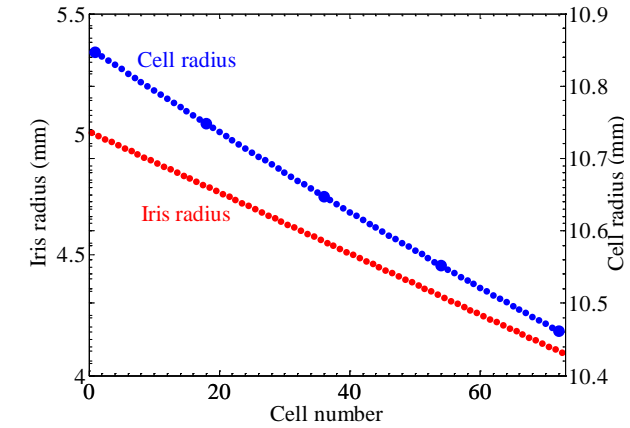


Fig. 3.2.3.2.3: Variation of v_g/c and r/Q vs. cell number.

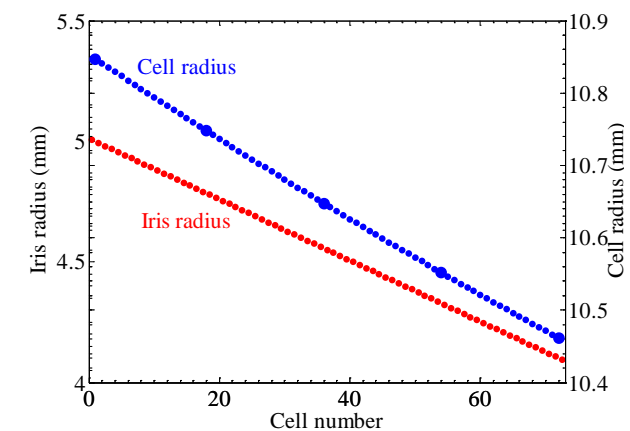


Fig. 3.2.3.2.4: Variation of quality factor Q vs. cell number.

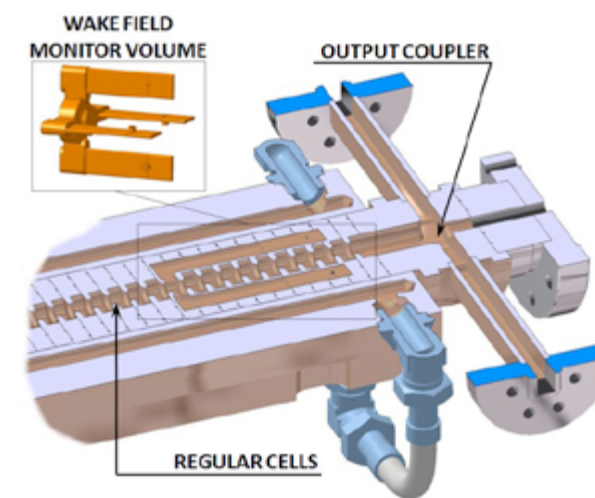


Fig. 3.2.3.2.5: Special cell design with output port for dipole mode monitoring.

Mode launchers are used to feed the RF power into the structure and to couple out the residual power (Figure 3.2.3.2.6).

The manufacturing process will require a machining precision better than 2 μ m. According to the experience

accumulated at CERN and SLAC in this field, such a specification can be reached with modern temperature- and vibration-stabilized micro-machining tools (diamond turning).

Table 3.2.3.2.1 shows the main parameters for the two X-band structures.

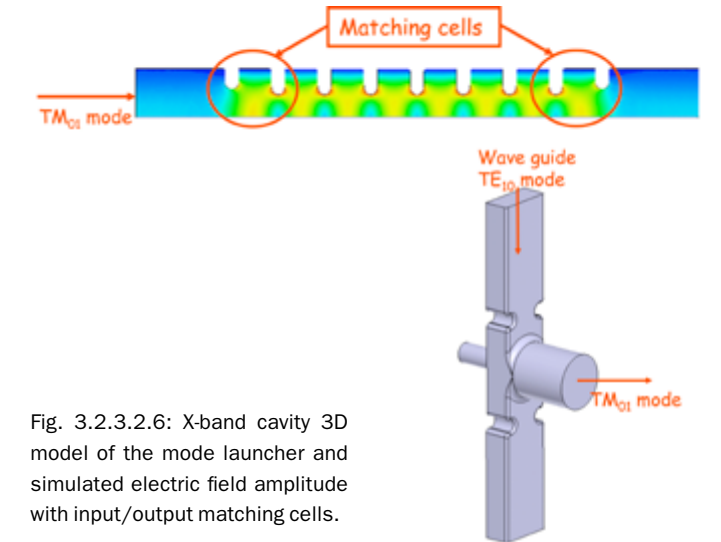


Fig. 3.2.3.2.6: X-band cavity 3D model of the mode launcher and simulated electric field amplitude with input/output matching cells.

Table 3.2.3.2.1: Main parameters for the X-band structures.

Operating frequency	11995.2 MHz
Operating temperature	31 °C ± 0.1 °C
Phase advance	$5\pi/6$
Flange-to-flange total length	965 mm
Number of cells (including matching cells)	72
Cell length at operating temperature	10.414 mm
Iris thickness at 20 °C	3.300 mm ... 3.586 mm
Iris radius at 20 °C	4.991 mm ... 4.106 mm
Cell radius at 20 °C	10.837 mm ... 10.462 mm
Input coupler	Mode launcher type
Output coupler	Mode launcher type
Maximum average decelerating gradient	34 MV/m
Operating average decelerating gradient	17 MV/m
Shunt impedance per unit length	60.2 M Ω /m
Peak power – decelerating gradient of 20 MV/m	7 MW
Filling time	105 ns
Maximum pulse repetition rate	100 Hz
Material of the cavity	Cu-OFE
Material of the flanges, supports and cooling connectors	316LN

3.2.3.3 Deflecting structures

There are two RF deflecting structures (built by INFN – LNF) located between BC1 and the Linac 1 at 355 MeV. The injector deflector is scaled from the structure developed for the SPARC project. The cavity is a 5-cell standing-wave structure (see Fig 3.2.3.3.2). The operating mode is the π -like TM_{110} hybrid mode. The RF parameters of this structure are summarized in Table 3.2.3.3.2.

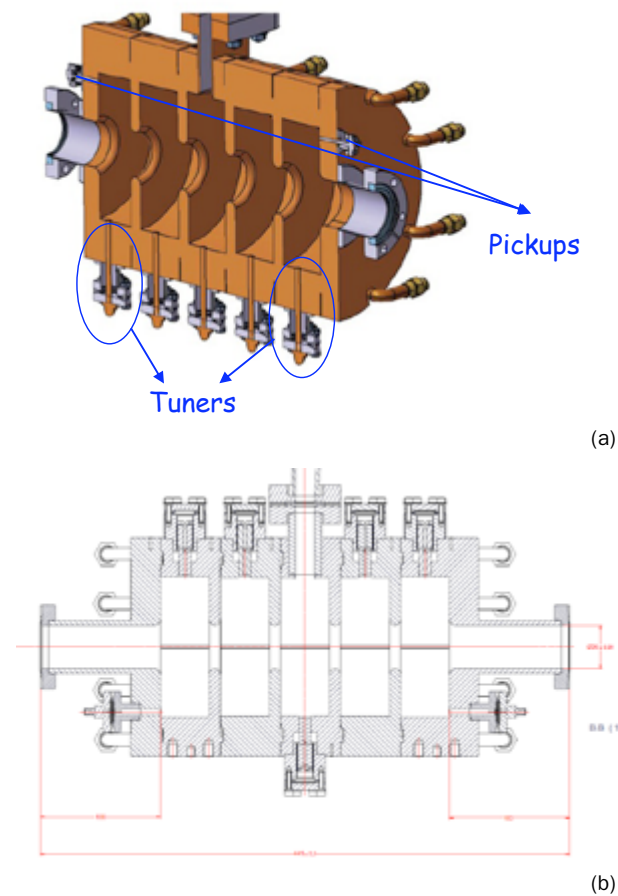


Fig. 3.2.3.3.2: 3D model of the deflecting cavity designed by INFN for the FERMI project (a) and the PSI version with the tuners displaced on the upper side (b).

Another set of two RF deflecting structures are foreseen after the second bunch compressor (BC2) at 3 GeV (in the Athos branch). Due to the higher beam energy, C band RF deflecting structure will be used. The design of the C band deflector should be very similar if not identical to the C band deflecting structures used in the Japanese FEL SACLA [42]. Table 3.2.3.3.3 summarizes the main parameters foreseen for the deflecting system at 3 GeV.

Table 3.2.3.3.2: Specification for the 5-cell RF deflector (2 structures to be installed at 355 MeV).

No. of Cells	5
Frequency (MHz)	2998.8
Nominal/Maximum deflecting voltage (MV)	4.5 / 4.9
Nominal/Maximum input power (MW)	4.2 / 5
Operating mode	π
Repetition rate (Hz)	100
Filling time (μ s)	~ 0.8
Nearest mode – different polarity (MHz)	50
Length flange to flange (m)	0.5
Quality factor – Q0	~ 15000
Aperture Beam pipe – diameter (mm)	38
Working temperature	40°
Temperature range (°C)	35 – 50
No. Pickups	2

Table 3.2.3.3.3: Specification for C band RF deflector (2 structures to be installed at 3 GeV).

Length of deflecting structure (m)	1.706
Frequency (MHz)	5712
Maximum deflecting voltage per structure (MV)	96 MV
Input power per structure in 1 μ s (MW)	50 MW
Operating mode	$5\pi/6$
Repetition rate (Hz)	100
Filling time (μ s)	~ 0.5
Length middle deflector to screen (m)	9.5
Theoretical resolution (fs/mm)	27
Operating beam energy (GeV)	3
Number of structures	2

3.2.4 RF systems of the SwissFEL linacs 1, 2 and 3

3.2.4.1 C-band module overview

The Swiss FEL linac consists of 112 two-metre long accelerating structures to boost the beam energy from 350 MeV at the injector to the final energy of 5.8 GeV (Aramis beamline). The accelerating structures are grouped into 28 so-called RF modules, each module being composed of four accelerating structures, one pulse compressor, one 50 MW klystron and one solid-state modulator (Figure 3.2.4.1). The 28 modules are distributed over three Linacs: Linac1 composed of

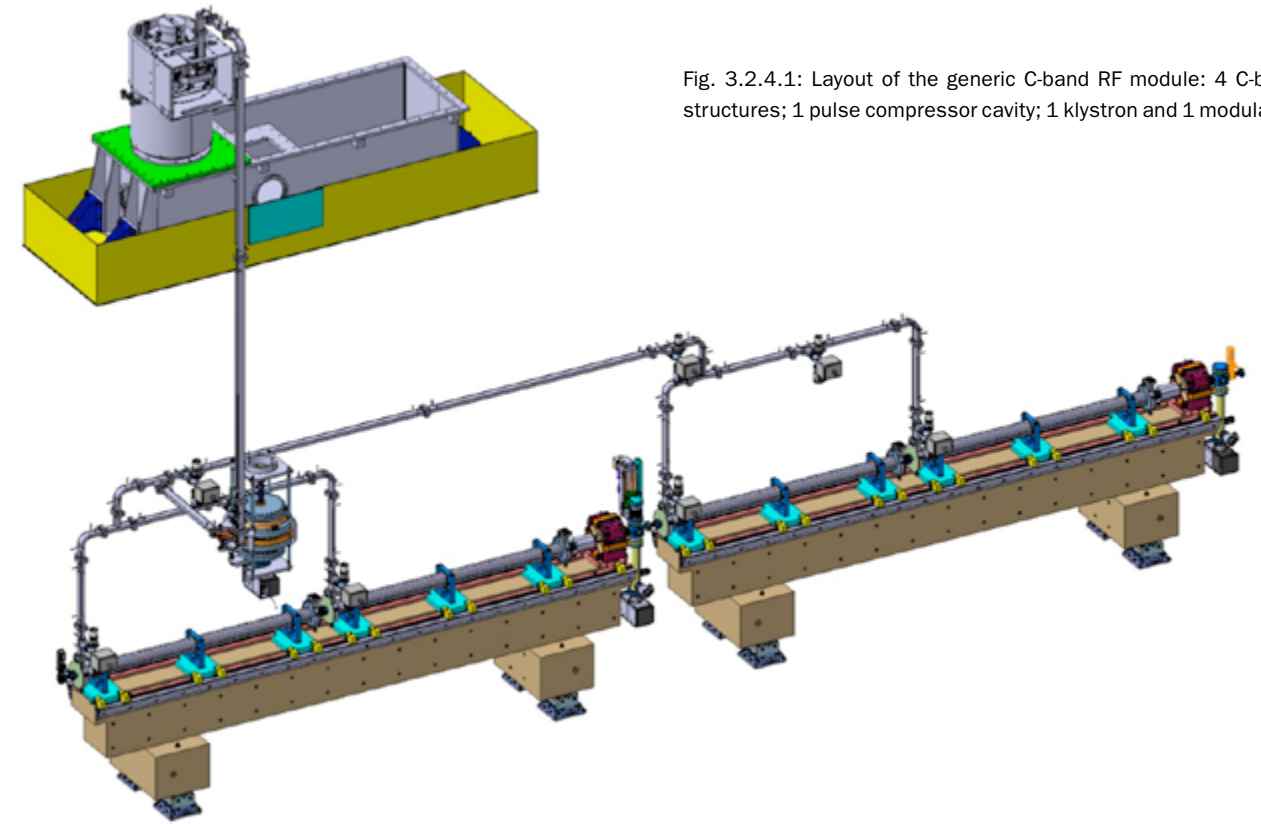


Fig. 3.2.4.1: Layout of the generic C-band RF module: 4 C-band structures; 1 pulse compressor cavity; 1 klystron and 1 modulator.

9 modules and inserted between the two bunch compressors, Linac2 composed of 4 modules, between the second bunch compressor and the switchyard, and Linac3 composed of 13 modules after the switchyard and delivering the beam to the Aramis beamline. There are two additional modules between the switchyard and the Athos beamline. The design frequency of these C-band structures is 5712 MHz as in the linac of the SACLA project [43].

The maximum peak power of the klystron is 50 MW with a 3 μ s pulse length. The power requirements are determined by the required average gradient (27.5 MV/m), the accelerating structure design, the energy multiplication factor of the pulse compressor (see Figure 3.2.4.12) and the overall losses in the waveguide network. Single-bunch operation requires 28 MW at the accelerating cavity input. The waveguide network is based on an asymmetric design to take into account both phase synchronism and group delay for an optimum operation with the pulse compressor. The average RF path length from the klystron output to the accelerating structure input is roughly 10 metres which ideally corresponds to 7% losses. Taking into account the pulse compressor and all the flanges, a conservative value of 20% has been assumed for the losses.

In the case of two-bunch operation mode with a bunch spacing of 28 ns, the required power is below 40 MW.

3.2.4.2 C-band Accelerating Structure

The C-band accelerating structure has 113 cells, including two coupler cells of the J-type (see Figure 3.2.4.2), and operates with a $2\pi/3$ phase advance. The length of each cell is 17.495 mm and the active length of each structure is 1.978 m. Each cell has rounded walls to increase the quality factor (Figure 3.2.4.3). Note that a disk-loaded structure and a structure with cup-like cells have also been considered. However, having a lower quality factor, they require slightly more input power to achieve the same accelerating gradient. All along the structure the iris tips are elliptically shaped and are optimized to ensure minimum peak surface electric field, the iris thickness being constant at 2.5 mm – a good compromise between high shunt impedance and mechanical rigidity.

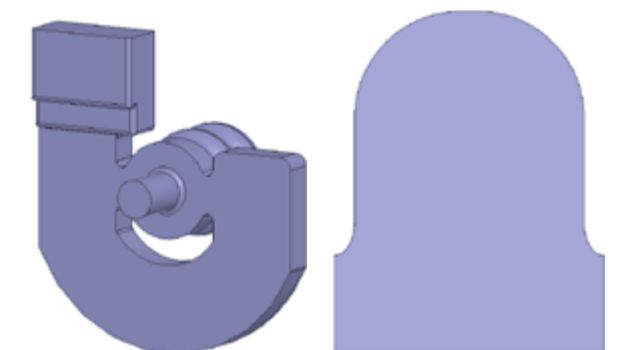


Fig. 3.2.4.2 (left): J-type coupler for the C-band accelerating structure. Fig. 3.2.4.3 (right): Cell topology of the C-band accelerating structure.

The iris and cell radius dimensions for each cell have been determined so that the structure is of the constant-gradient type and has an average iris radius of about 6.437 mm at the operating temperature, this later choice being dictated by longitudinal short-range wakefields issues and beam-dynamics requirements. In this design, the iris radius is chosen to vary linearly along the structure. The variations of the iris radius and cell radius along the structure are shown in Figure 3.2.4.4. Figure 3.2.4.5 shows the group velocities v_g/c and of the r/Q along the structure and Figure 3.2.4.6 the quality factor Q .

The required RF power to achieve an accelerating gradient of 27.5 MV/m without pulse compressor is about 27.2 MW.

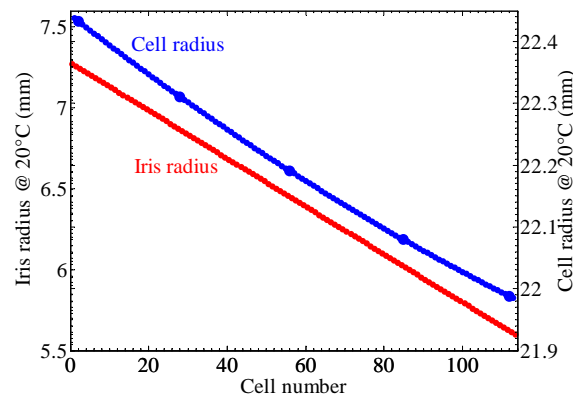


Fig. 3.2.4.4: Variation of iris and cell radii vs. cell number.

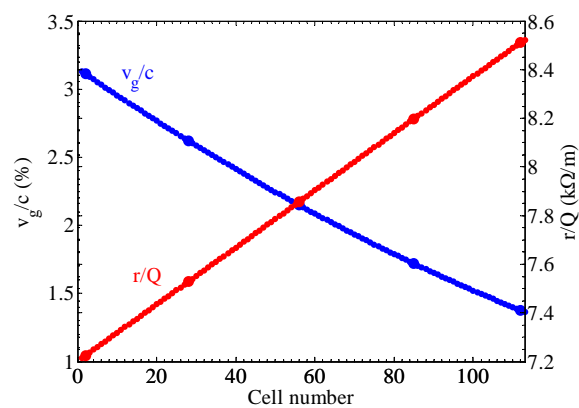


Fig. 3.2.4.5: Variation of v_g/c and r/Q vs. cell number.

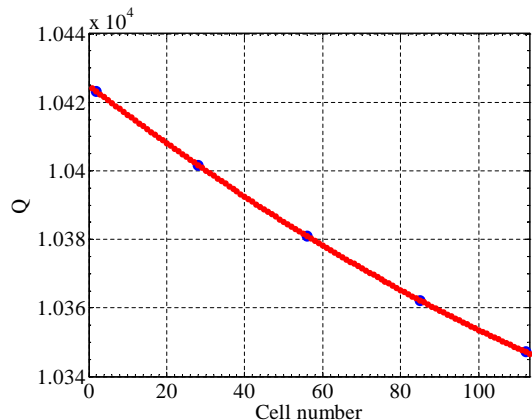


Fig. 3.2.4.6: Variation of quality factor Q vs. cell number.

Table 3.2.4.1 shows the main parameters of the synthesized C-band structure.

Table 3.2.4.1: Main parameters for the C-band structures.

Operating frequency	5712.0 MHz
Operating temperature	40 °C ± 0.1 °C
Phase advance	$2\pi/3$
Flange-to-flange total length	2050 mm
Number of cells	113
Cell length at operating temperature	17.495 mm
Iris thickness at 20 °C	2.5 mm
Iris radius at 20 °C	7.257 mm ... 5.612 mm
Cell radius at 20 °C	22.432 mm ... 21.988 mm
Input coupler	J type
Output coupler	J type
Average (over Linacs) accelerating gradient	27.5 MV/m
Shunt impedance per unit length	81.7 MΩ/m
Peak power – accelerating gradient of 27.5 MV/m – no SLED	27.2 MW
Filling time	322 ns
Maximum pulse repetition rate	100 Hz
Material of the cavity	Cu-OFE
Material of the flanges, supports and cooling connectors	316LN
Concentricity tolerance	± 25 μm
Maximum pressure drop across the cooling channels	4 bar

3.2.4.3 Wakefield effects in the C-band structure

Long range wakefields, both longitudinal and transverse, can affect the multibunch operation causing degenerative effects on the quality of the second bunch (emittance dilution). The wakefield analysis takes into account the regular cells of one single C-band accelerating structure by neglecting the effect of the input and output J-type couplers. The approximated geometry causes an over-estimation of the wake envelope, trapping the wakes inside the structure instead of flowing through the couplers. This conservative approach in the evaluation of the wake envelope is also applied to the RF losses which are not considered. The time decay of the wakes is then determined only by the synchronous frequency distributions.

The most relevant HOM (Higher Order Mode) passbands are obtained by performing at first frequency domain

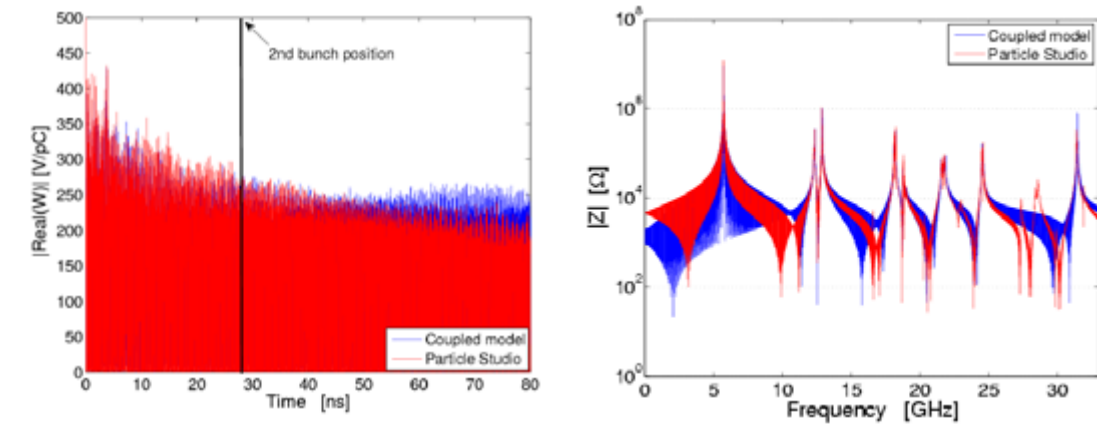


Fig. 3.2.4.7: Left: Time behaviour of the long range longitudinal wakefields for fundamental mode plus HOMs (for a 2 m structure) computed by fitting dispersion curve method (blue line) and Particle Studio (red line). Right: Impedance spectrum of the long range longitudinal wakefields.

simulations for five accelerating cell geometries. The synchronous frequencies of their dispersion curves are used to get the synchronous kicks and phase advances. With the synchronous frequency and the kick distributions the wake envelope is computed following a quasi-coupled approximation. The obtained results (Figures 3.2.4.7 and 3.2.4.8), referring to a point-like beam size, agree well with the time-domain simulations of Particle Studio where their spectra are normalized to the frequency dependent form factor in a post-processed step.

The pulse to pulse amplitude stability requirement for the 200 pC operation regime of the first C-band Linac (Linac1) is one of the most critical tolerances and is $\Delta V/V = 6 \cdot 10^{-5}$. Such an amplitude variation corresponds to a pulse to pulse charge fluctuation as high as 5.3 %, which is much higher than the specification of pulse-to-pulse charge stability ($\leq 1\%$).

The long range transverse wakefields have six relevant bands filling the frequency spectrum up to 25 GHz (Figure 3.2.4.9). To keep a conservative approach to the wake envelope, at 28 ns a trailing charge experiences a transverse wake of 5 V/pC/mm.

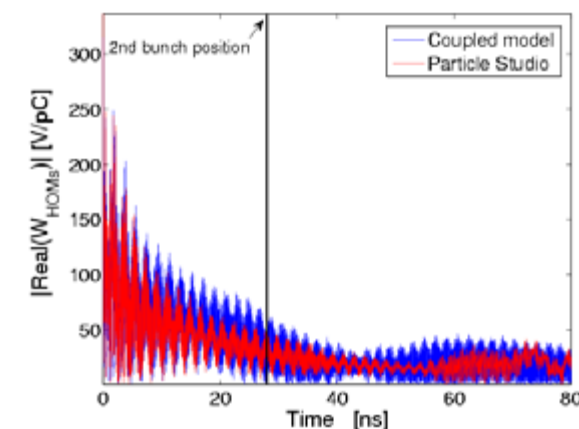


Fig. 3.2.4.8: HOM contribution to the long range longitudinal wakefields.

Assuming a transverse wake of 5 V/pC/mm at 28 ns, the leading and the trailing bunches were tracked in MADX simulating a random displacement of 100 μm rms of the C-band structures (Figure 3.2.4.10). At the switchyard the collected statistics of the position of the second bunch relative to the first one shows a distribution with $\sigma = 6 \mu\text{m}$. This result follows the static approach where the charge of the bunch doesn't change. If 1% of charge fluctuation is taken into account, the beam jitter obtained is 60 nm, largely within the tolerances.

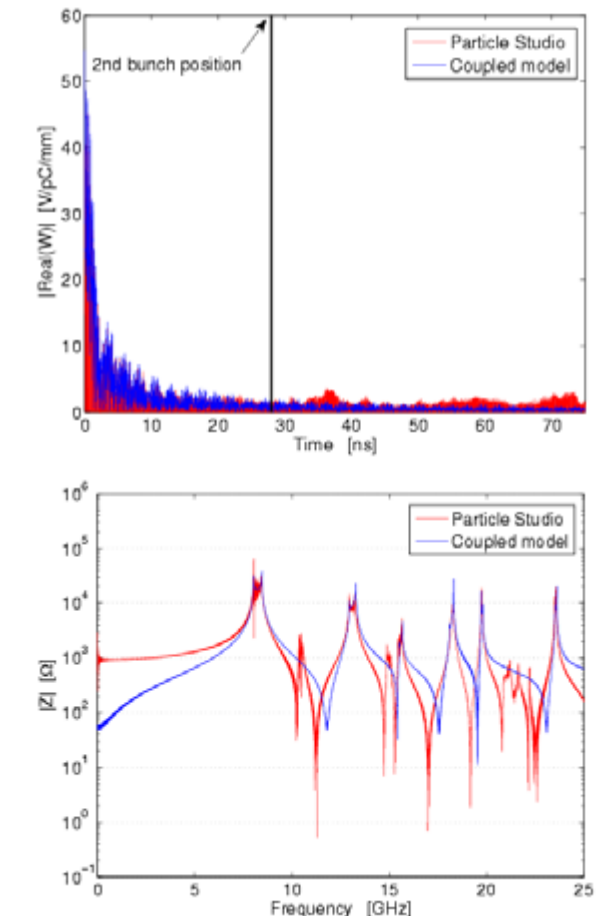


Fig. 3.2.4.9: Time behaviour (top) and impedance spectrum (bottom) of the long range transverse wakefields.

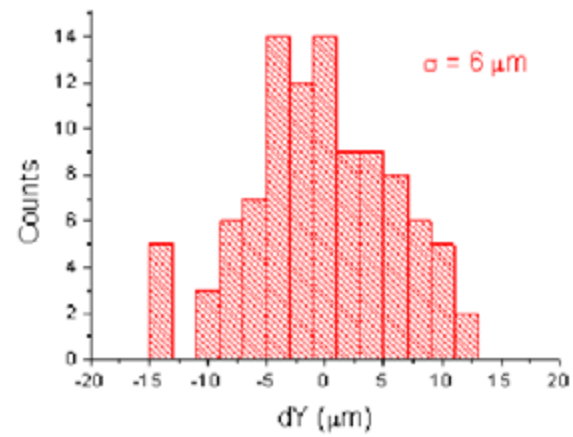


Fig.3.2.4.10: Relative position of the trailing bunch under the effect of a 5 V/pC/mm transverse wakefields.

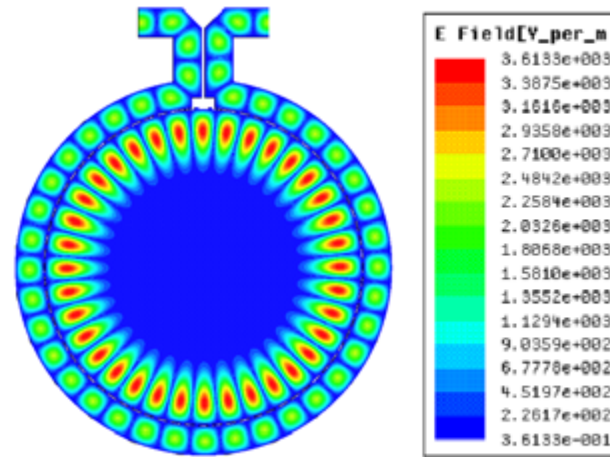


Fig. 3.2.4.12: Electric field amplitude at a given time of the BOC in its symmetry plane.

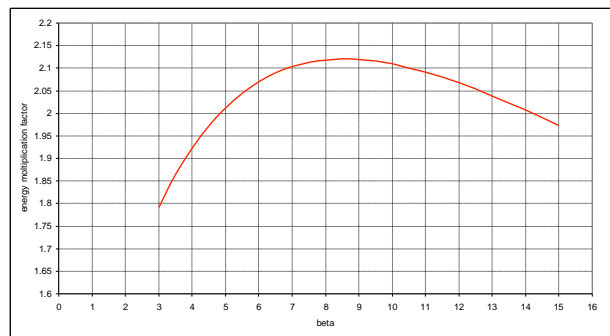


Fig. 3.2.4.13: Energy gain multiplication factor for BOC vs. coupling factor.

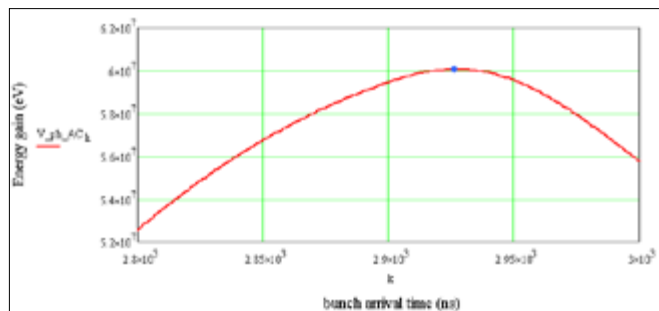


Fig. 3.2.4.14: Energy gain per accelerating structure vs. bunch arrival time; single-bunch operation assuming 40 MW 3 μs klystron output power, 100 ns for the phase jump, 20 % losses in waveguide, acceleration on crest.

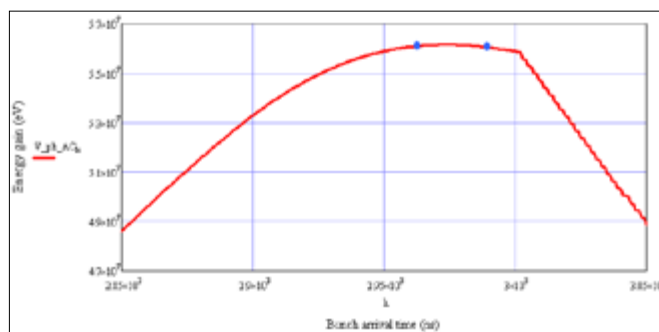


Figure 3.2.4.15 Energy gain per accelerating structure vs. bunch arrival time; double-bunch operation assuming 40 MW 3 μs klystron output power, 100 ns for the phase jump, 20 % losses in waveguide, +347 kHz BOC detuning, acceleration on crest.



Fig. 3.2.4.11: 3 GHz BOC used at the CLIC Test Facility (CERN).

3.2.4.4 RF C-band pulse compressor

The key device of the RF power distribution is the pulse compressor. The preferred solution is a C-band version of the Barrel-Open Cavity (BOC) developed at CERN by Igor Syrathev (Figure 3.2.4.11).

The BOC for the SwissFEL is a new design using the whispering-gallery mode TE_{18,1,1} and providing very large Q (~190,000), as well as being compact (single cavity; diameter around 500mm). The electric field configuration of this BOC is shown in Figure 3.2.4.12 in the symmetry plane.

The RF efficiency of an accelerating module is determined by the quality factor and by the coupling factor β of the pulse compressor. Figure 3.2.4.13 shows the beam energy multiplication factor for an expected Q of 190,000.

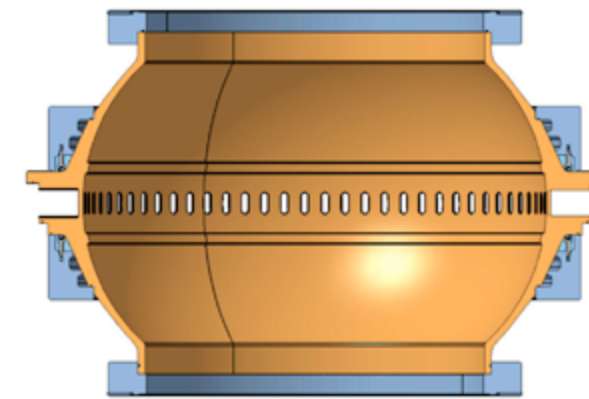


Fig. 3.2.4.16: Views of the BOC cavity.

The design value of the coupling coefficient β is 9 to maximize the efficiency (see Figure 3.2.4.13). For single-bunch operation an energy gain per structure up to 60 MeV is achievable (Figure 3.2.4.14) with a klystron output power of 40 MW.

For two-bunch operation and a 28 ns bunch spacing, the favoured option is an almost flat plateau in the curve of energy gain per accelerating structure vs. bunch arrival time. This can be achieved by performing a phase modulation on the klystron drive signal and by slightly detuning the BOC by adjusting the cooling temperature (Figure 3.2.4.15). This operating technique easily provides the required 54 MeV energy gain per structure, with equivalent energy gain for the two bunches and also an equivalent integrated voltage slope. This is especially important in Linac 1, before the bunch compressor.

The mechanical design of the BOC is based on four brazed rings. The inner one fully defines the body of the resonant cavities and the 70 (real) +2 (fake) coupling slots. The outer one composes part of the waveguide coupled to the inner cavity; two stainless steel rings provide the cooling and make the body stiffer (Figure 3.2.4.16). The 2.2 kW heat load requires a water flow of 0.5 l/s to provide 1°C ΔT of the water.

The tuning is provided by machining two tuning rings after the final brazing for a total tuning range of ± 8 MHz.

One advantage of the BOC is the very small impedance for vacuum; one pump is directly connected to the bottom of the cavity which is vertically connected to the ceiling of the tunnel; see Figure 3.2.4.1. The device

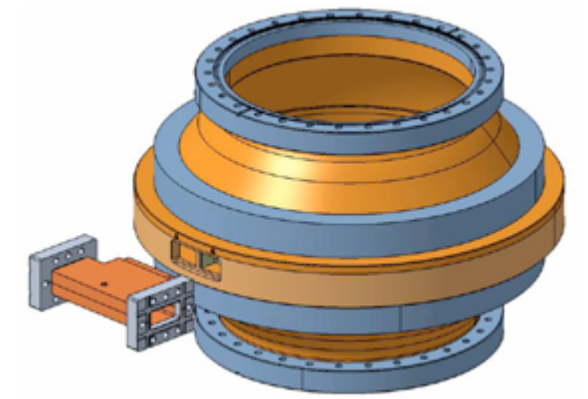


Fig. 3.2.4.17: Views of the fully assembled BOC.

includes also an on/off remotely controlled mechanism that provides operation without pulse compression by detuning of the BOC (Figure 3.2.4.17).

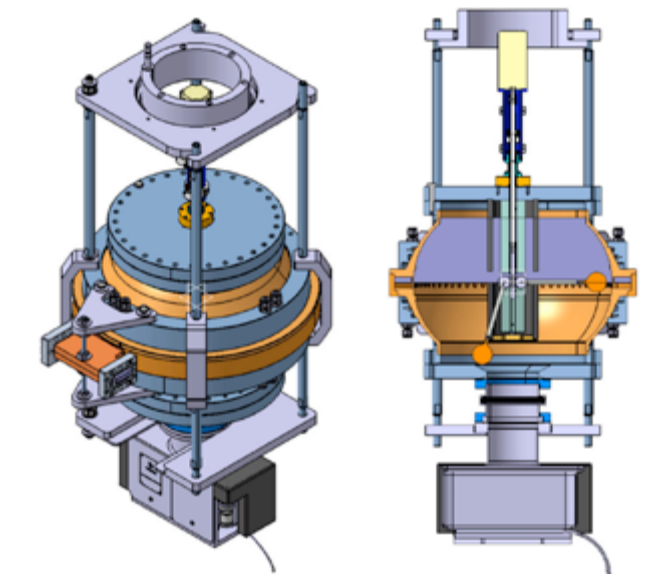


Fig. 3.2.4.17: Views of the fully assembled BOC.

3.2.5 RF Power systems for SwissFEL injector

The power modulators provide the high-voltage pulsed power for the klystron amplifiers. These different sources are characterized by their peak power, pulse width, high voltage and current capabilities. The klystrons will be powered by solid-state modulators, as in the existing SwissFEL Injector Test Facility. The maximum electrical parameters of the modulator power sources installed at

Table 3.2.5.1: Modulator operational parameters of the klystron amplifiers at the SwissFEL Injector Test Facility (European frequencies).

	3 GHz RF gun K2-1L	3 GHz Linac – mode 1 to 3 K2-2S			12 GHz K2-3X	3 GHz TDC K1-2S	Unit
RF peak power	30	30	45	60	50	7.5	MW
RF average power	15	4.5	22.5	9	5	3.75	kW
Peak power klystron	71.4	69.7	104	146	107	15.7	MW
Average power klystron	53.1	19.6	65.2	42.5	26.5	10.2	kW
Klystron voltage range	266	261	307	351	410	148	kV
Klystron current range	268	267	340	416	262	106	A
Pulse length (top)	5	1.5	5	1.5	1	5	μ s
Max pulse length (at 76%)	7.4	3.9	7.4	3.9	3.4	7.4	μ s
Repetition rate adjustable	1–100	1–100			1–100	1–100	Hz
Flat-top flatness (dV)	< ± 0.2	< ± 0.2			< ± 0.2	< ± 0.2	%
Rise rate (at 50% voltage)	170/270	250–360			300–420	148	kV/ μ s
Fall rate (at 50% voltage)	170/270	250–360			300–420	70–148	kV/ μ s
HV Amplitude stability (rms)	< 0.004*	< 0.006*			< 0.02	< 0.02	%
Pulse-to-pulse jitter (rms)	< 5	< 5			< 5	< 5	ns
Pulse length jitter (rms)	< ± 10	< ± 10			< ± 10	< ± 10	ns

(*) measured klystron output amplitude stability pulse to pulse.

the SwissFEL Injector Test Facility are given as an example in Table 3.2.5.1.

Modulators that provide this high power are connected to the klystron loads with low leakage inductance and low stray capacitance high-voltage step-up pulse transformers. The flat top of the voltage pulses produced is approximately equal to the RF pulse width of the klystron. The modulator energy efficiency is mainly determined by the rise and fall times of the voltage pulses, which will be approximately 1 μ s and 2 μ s (10 to 90%), respectively.

The primary energy storage in each modulator can be either a pulse-forming network (PFN) or a capacitor. The PFN line-type modulator method (Figures 3.2.5.1 and 3.2.5.2) provides a fixed pulse width voltage pulse having a source impedance that is matched to the klystron impedance. The stored energy in the PFN is made just sufficient to satisfy the klystron load requirements. In this case, the high-voltage switch on the primary side of the pulse transformer needs to be only an ON device, such as a Thyatron or SCR assembly.

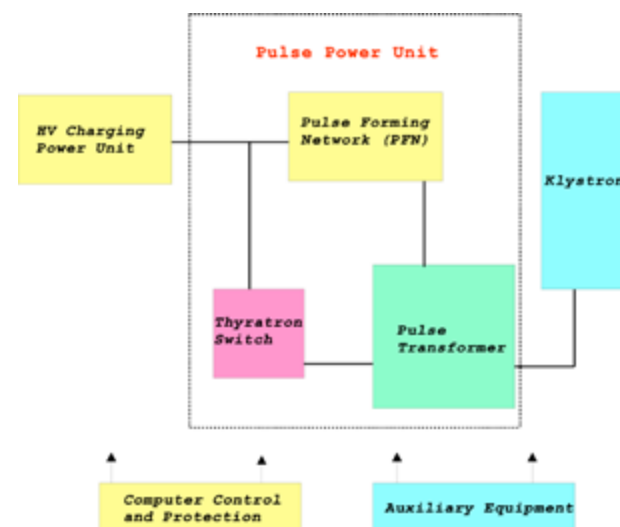


Fig. 3.2.5.1: Line-type modulator block diagram.

In the second method (see Figure 3.2.5.3), where a capacitor discharge source is used, the stored energy has to be much larger than that required by the klystron load, to ensure a flat-top voltage region with a small percentage voltage drop. Additional protection is needed in this case, to protect the klystron from receiving excessive energy from the storage capacitor in the case of a gun arc. This type of modulator mostly uses an IGBT

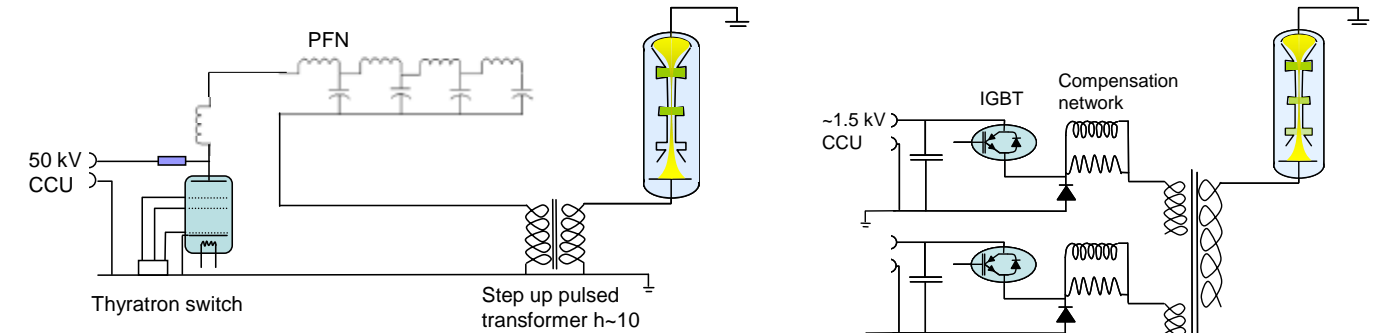
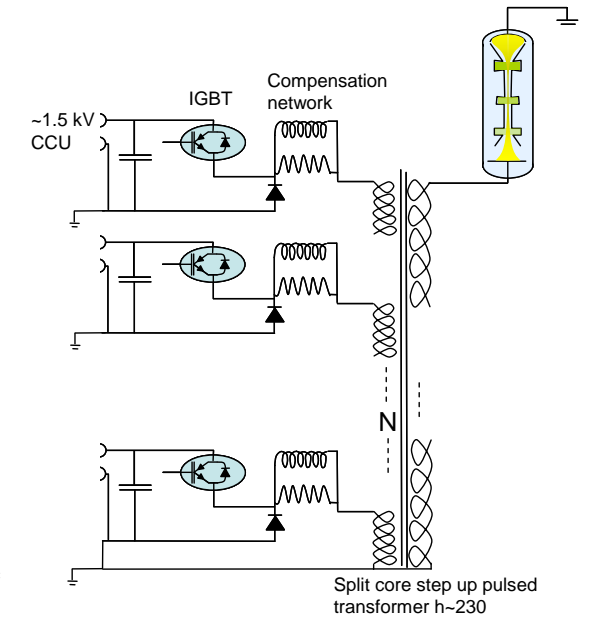


Fig. 3.2.5.2: Typical scheme of a PFN modulator.

Fig. 3.2.5.3: Electrical schematic of a solid-state modulator.



solid-state on-off switch to define the voltage pulse duration. Since these devices operate in a lower voltage region (3 to 6 kV), the step-up ratio of the pulse transformer needs to be a higher ratio than when a Thyatron switch is used (30 to 40 kV), and consequently requires special transformer technology to ensure that the rise and fall times mentioned above can be achieved.

Both these types of modulator have been investigated from the point of view of performance specification, reliability, maintainability and cost.

PFN modulators using conventional thyatron switch technology are already in operation at the SwissFEL Gun Test Facility (now decommissioned) and the SLS, with known reliability and running experience. The main weakness of this approach, especially at high repetition rates, is the relatively short lifetime of the thyatron switch (15,000 to 20,000 hours), which substantially contributes to the operational costs and reliability. The pulse behaviour is fixed by the number of cells in the PFN and can be modified only by changing the capacitor configuration inside the modulator rack. The size of the components and the mechanical assembly is adapted to the relatively high voltages of the PFN line, fixing a physical limit to the compactness of the HV cabinet.

A low-power solid-state modulator has been purchased for the SwissFEL Gun Test Facility (LEG), introducing a new technology to PSI. This very compact device has been tested, with extremely fast installation and com-

missioning times. The modulator is composed of a series of low voltage (~1 kV) switching modules connected in parallel to the step-up transformer (see Figure 3.2.5.3). Experience at PSI with the solid-state modulator has shown the following advantages:

1. Fast installation (only three main connections for electrical power, cooling and controls)
2. Modularity (the same switch modules can be stacked in different configurations, i.e. fewer spare components needed)
3. Reliability (70,000 hours without failures recorded by the suppliers; a few modules can fail without perturbing modulator operation)
4. Compactness
5. Adjustable pulse length
6. KHz repetition rate

At a comparable investment cost, and based on the experience obtained so far, PSI has decided to explore the solid-state option for the SwissFEL Injector Test Facility. The 3 GHz and 12 GHz klystron modulators will produce a much higher peak power, and the design needs a large amount of parallel-operating solid-state IGBT devices with a high-ratio step-up pulse transformer, in order to handle the same power as a PFN modulator with a single thyatron or SCR assembly could handle. The new modulators have been delivered as “single rack” amplifier units, integrating the tank, water distribution and power supplies for the klystron solenoids and heater (see Figure 3.2.5.4).

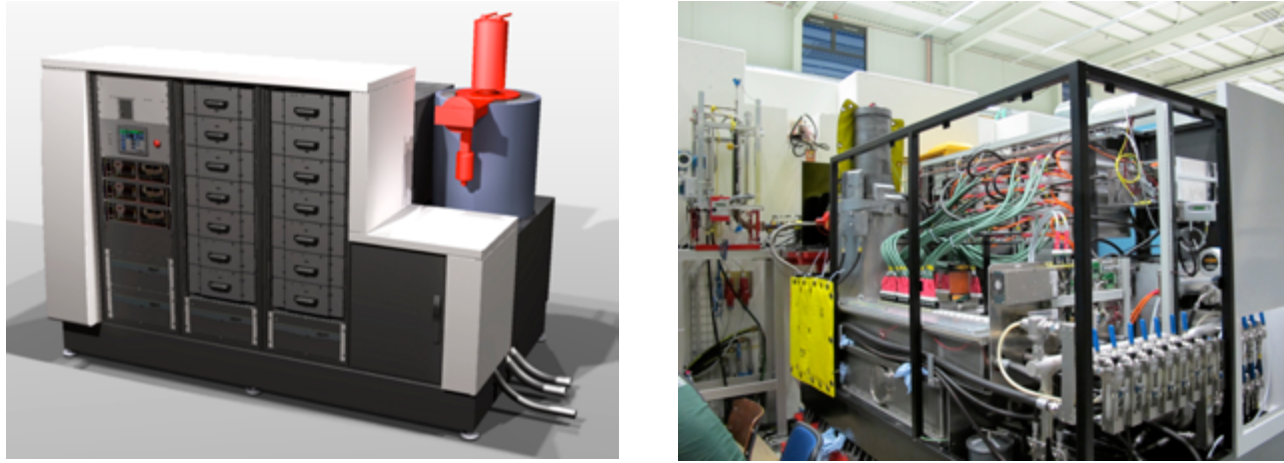


Fig. 3.2.5.4: Drawing of the high-power modulator K2 from the company SCANDINOVA (10–60 MW; 200–450 kV) (top), and photograph of the installed prototype at the SwissFEL Injector Test Facility (bottom).

The klystron loads for the modulators are high-gain RF power amplifiers that usually have a narrow bandwidth (10%) at the fundamental frequency. The Thales TH2100 klystron shown below (Figure 3.2.5.5) is a typical example.

The RF output pulses from each klystron are transmitted via an RF window that is conditioned to operate with an SF₆ gas pressure of about 2 bars. This electro-negative gas enhances the voltage hold-off capability in the presence of high forward and reflected power occurring in phase together at the window. If this should occur, the used gas is recovered in a closed-circuit system and the window volume is flushed with clean gas and re-filled.



Fig. 3.2.5.5: High-power klystron amplifier TH2100 (Thales).

As mentioned above, the shot-to-shot RF phase and amplitude stability are particularly critical, because they can potentially generate large FEL fluctuations (arrival time, power, wave length). Assuming a stable distribution network, the RF phase and amplitude are mainly driven by the modulator voltage stability. To meet the FEL specifications (~ 0.018 deg rf rms), the relative voltage stability must be of the order of 10^{-5} . This will require an effort to improve the capacitor charging scheme, which usually reaches values one order of magnitude larger than those specified. To overcome this problem, we are performing at the injector facility, and in collaboration with the modulator suppliers, an R&D programme to improve the performance of the commercially available hardware. Recent encouraging measurements of achievable phase stability have been carried out at the SwissFEL Injector Test Facility. The experimental data reproduced below in Figure 3.2.5.6 indicates that a solid-state-based S-band power plant is able to reach shot-to-shot phase stabilities below 0.02° . A slow feedback system is nevertheless needed to correct slow phase fluctuations which might be induced by thermal drifts of the power plant components.

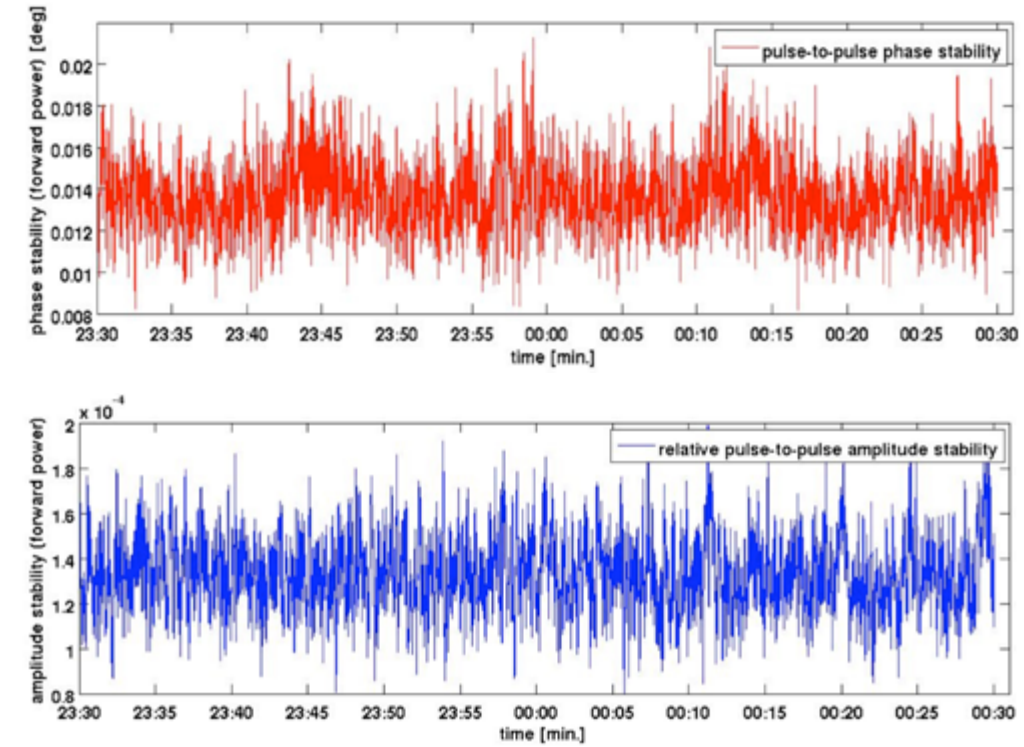


Fig. 3.2.5.6: Top: Pulse-to-pulse phase stability of the incident RF power as standard deviation over the last 40 pulses (repetition rate 10 Hz). At each pulse, the phase is averaged over 400 ns, the rms stability is 0.019° . Bottom: Pulse-to-pulse amplitude stability of the incident RF power as standard deviation over the last 40 pulses, measured at the S-band power plant of the SwissFEL Injector Test Facility, the amplitude stability is 6.10^{-5} rms.

3.2.6 Power systems for the SwissFEL linac

The basic idea for the linac RF power system is to keep it identical to the injector systems as far as possible.

3.2.6.1 C-Band klystron

Due to the frequency choice the available klystron types are limited. Toshiba has developed a new version adapted to 100 Hz repetition rate and $3 \mu\text{s}$ pulse length.



Fig. 3.2.6.1.1: Similar C-Band klystron (Toshiba E3748).

Table 3.2.6.1.1: Technical data of the C-Band klystron types.

	Existing Klystron E37202	Upgraded Version E37210	Unit
Nominal Frequency	5712	5712	MHz
RF peak power	50	50	MW
Peak Cathode Voltage	370	370	kV
Peak Klystron Current	344	344	A
High Voltage Pulse Width	6.2	6.2	μs
RF Pulse Width	2.5	3	μs
Average RF Power	7.2	15.6	kW
Average Collector Power Dissipation	35	78	kW
Pulse Repetition Rate	60	100	pps
RF Bandwidth @ -1.5 dB	± 5	± 5	MHz
Gain	50	50	dB

3.2.6.2 C-Band modulator

The modulator technical requirements are very close to the data of the S-Band systems. The modulator baseline design is an updated version of that system. Re-design of the modulator will be required in order to optimise the system for the linac operation. The modulators shall be built in a way to allow transportation in the technical building and installation with only a small local crane at the modulator final position. The modulator will have to be built with an integrated power factor compensation in order to limit the harmonic current and asymmetric phase currents on the mains.

Table 3.2.6.2.1: Target parameters for the C-Band modulator.

	Value	Unit
Peak Voltage	370	kV
Peak Current	344	A
Pulse Repetition Frequency	100	Hz
Pulse-to-pulse stability (Std. Deviation)	10^{-5}	pps
High Voltage Pulse Width @76%	< 6.2	μs
Flat-top Ripple (peak-peak)	< 0.4 %	
Mains Supply	400	V
Mains Power Factor	> 99 %	

The modulator will be separated in two or more mechanical units in order to allow transportation and installation inside the SwissFEL technical building. Figure 3.2.6.2.1 shows the reference design for the modulator mechanics. The tank with the transformer and the klystron socket will be a separate unit. The racks with the electronics and auxiliaries will be placed close to the modulator on a double floor.

3.2.7 Low-Level RF

The Low-Level RF (LLRF) system has to synchronize and control the RF fields in the accelerating structures to the tight tolerances specified in Section 2.3.5. In the SwissFEL injector, each RF structure, namely the 3 GHz RF gun and the S-band and X-band travelling wave structures, is fed by a separate klystron, in contrast to the main linac, where a single klystron and an RF pulse compressor delivers RF power to four C-band structures (see Section 3.2.3). A generic overview of one RF station in the main linac is given in Figure 3.2.7.1. The controller therefore has to regulate amplitude and phase of the vector sum of a string of four accelerating structures.

The LLRF system is based on modern FPGA technology and floating point processing platforms. Such a system allows the required flexibility for different RF stations, especially for the necessary phase switch for the RF pulse compression in the main linac. The RF signals from pick-ups and directional couplers are down-converted to common intermediate frequencies (f_b), which are digitized by high-resolution, low-noise analogue-to-digital converters (ADC). Thus, the digital signal processing hardware and main parts of the firm- and software are generically independent of the RF frequency (f_{RF}). Local phase-locked loops generate a phase-stable, low-noise RF signal, with the frequency which is required at each RF station to drive the vector modulator (see Section 3.3.1). The IF frequency has to be chosen so that it is a sub-harmonic of the RF frequency (f_{RF}), in order to alleviate the frequency generation. In addition, it has to be high enough to allow for a sufficient detection bandwidth of the RF signal, but finally also low enough to avoid performance degradation due to clock jitter of the successive ADCs. Today's state-of-the-art technology can provide 16 bit ADCs with sampling rates well beyond 100 MHz. The application of the non-IQ algorithm [44] for the I/Q detection in the LLRF digital signal processing part implies the use of IF frequencies of the order of a few 10's of MHz up to a maximum of 100 MHz.

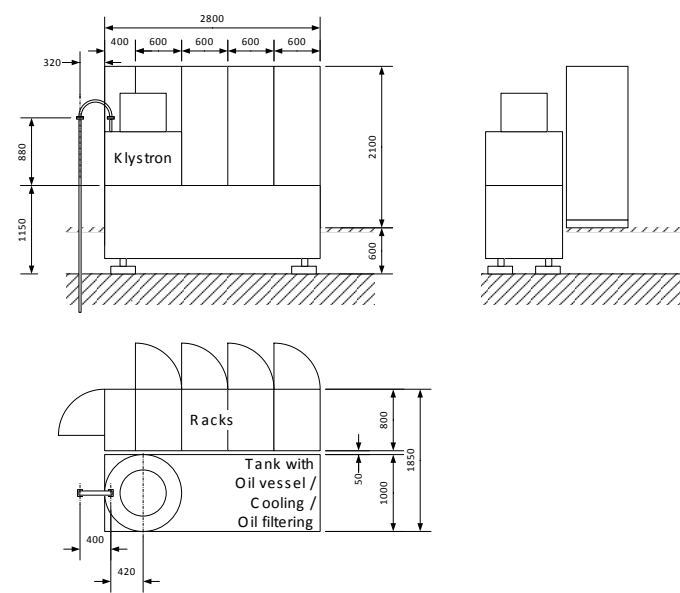


Fig. 3.2.6.2.1: Modulator Mechanics Reference Design.

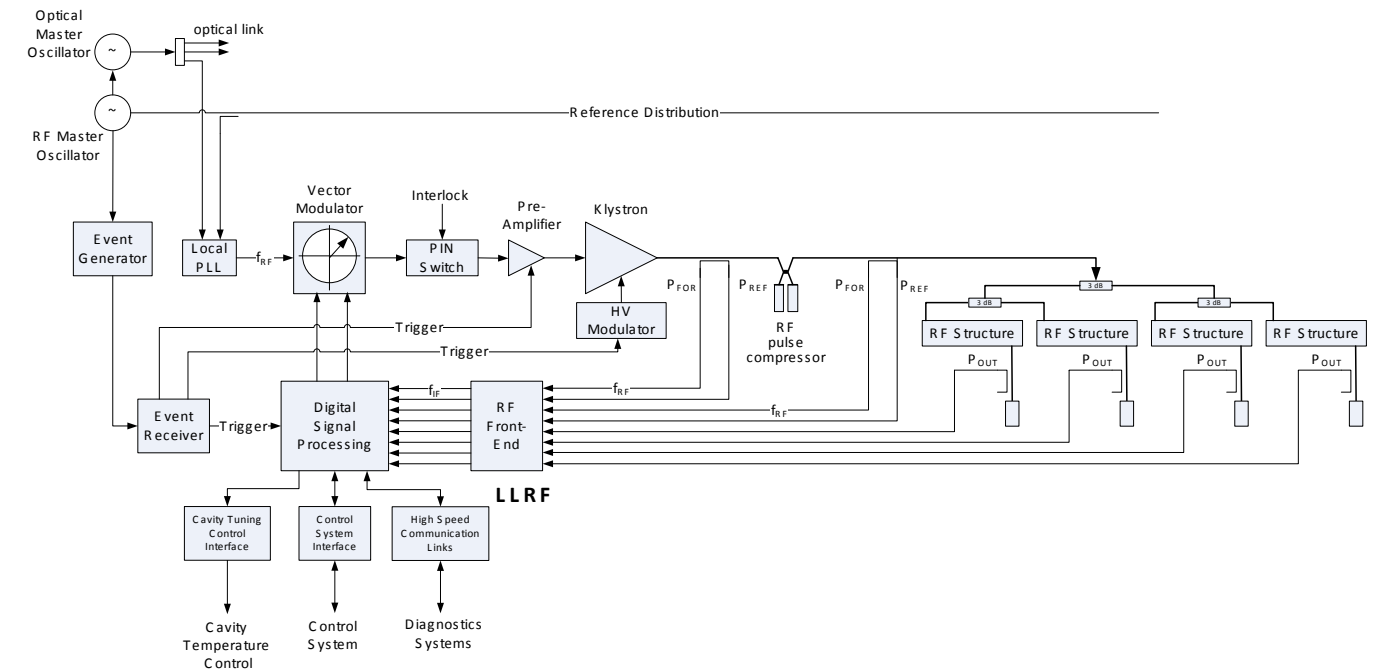


Fig. 3.2.7.1: RF system overview of one RF station in the main linac with RF pulse compression.

All frequencies of the LLRF system (ADC/DAC clocks, local oscillator frequencies for the RF front-ends) are derived from the reference distribution and thereby tightly locked to the master oscillator. The trigger signals for pre-amplifier, modulator and digital signal processing are generated by an event-receiving unit which is directly coupled to the global event generator. The RF pulse duration is of the order of a few μs , which is too short for efficient intra-RF pulse feedback, due to the inherent latency of the digital system. In case the high-voltage modulators or the pre-amplifiers do not provide the necessary short-term stability, which may result in pulse-to-pulse phase jitter, the implementation of fast analogue intra-pulse phase stabilization loops around the amplifier chain may be necessary. Pulse-to-pulse feedback corrects slow drifts in amplitude and phase, while adaptive feed-forward techniques provide the ability to reduce repetitive distortions. In order to compensate for drifts, it is therefore of utmost importance to minimize the drift of the components in the measurement path. To achieve this goal, all measurement cables from the directional couplers to the LLRF system, and the LLRF electronics itself, will be placed in a temperature-stabilized environment, with temperature variations not exceeding $\pm 0.1^\circ\text{C}$. During the R&D phase, the application of pulse-to-pulse calibration techniques will be explored, to minimize any remaining drifts and low-frequency jitter in the measurement of amplitudes and phases. In addition, the LLRF

electronics provides optical high-speed Gigabit communication links to other sub-systems, which allows the implementation of beam-based feedbacks, such as longitudinal feedback. Pulse-to-pulse stability is then solely determined by the stability of the actuator chain, which consists of the reference distribution, the local phase-locked loops, the vector modulator, the pre-amplifier and the high-voltage modulator, together with the klystron. Each of these components has to provide stability such that the required short-term amplitude and phase stability of a RF station (as given in Section 2.4.4) is reached.

3.3 Timing and synchronization

3.3.1 Reference distribution system

3.3.1.1 Purpose of the timing and synchronization system

In an accelerator (and particularly in a free electron laser (FEL)) the electron bunches to be accelerated and linearly compressed demand extremely stable field phases in the RF accelerating cavities (with respect to the time they have been emitted from the gun photocathode by

the gun laser). The SwissFEL RF structures, which will be operated at frequencies around 3, 6 and 12.0 GHz (S, C and X-band, respectively), need reference signals with the property that the temporal position of their zero-crossings, measured over a certain time (some ms) at different points in the machine, has to achieve a stability level below 10 fs. Moreover, the temporal stability and synchronization of laser systems at the experimental stations of the SwissFEL facility need to be kept within the lengths of the X-ray pulses over the duration of pump probe experiments (several minutes to hours). A number of diagnostics systems, such as, for example, beam arrival time monitors (BAM) and electro-optical bunch length monitors (EOM), will be able to measure the longitudinal properties of the electron bunches with reference to a temporally stable timing and synchronization system. Such beam-based information may be used to further improve the temporal stability of SwissFEL through longitudinal feedback systems. Although some other “clients”, such as the master event generator for the timing system and the beam position monitors (BPMs) for measuring transverse beam position, may not need such high timing stability, the SwissFEL timing and synchronization system will be designed to provide fs stability, during short time periods of some μ s up to some ms, to the majority of the “critical clients” along the accelerator and at the various experimental stations.

3.3.1.2 Concept of reference generation and distribution

The SwissFEL with its extreme jitter and stability demands (cf. Section 2.4.4) poses new challenges for the synchronization system, i.e. the reference signal generation as well as its distribution. Our concept is based on optimized microwave fiber-optic links, which is a well established, cost effective, low risk and reliable technology and also offers the best potential performance and flexibility. Systems with less critical jitter and drift requirements, as, for example, beam position monitors, will be synchronized with coaxial electrical links. Temperature-insensitive cables with drifts as low as a few fs/K/m will be used for short coaxial links. Uncritical systems can be fed with sub-distributions based on coaxial cable trunk lines with local phase-locked oscillators. The reference signal generation and most critical links of the reference distribution system will be optimized to achieve a benchmark jitter performance of around 10 fs, and a long-term (few hours) drift stability of a few 10's of fs in the most critical parts of the machine. Frequency stability will be $< 10^{-10}/\text{yr}$. Less than 10 fs in jitter and in long-term drift are being targeted with this fiber-optics-based system. Figure 3.3.1.1 shows a generic block diagram of the synchronization system. The RF frequencies to be distributed are derived from a common subharmonic, f_b . This subharmonic should be around

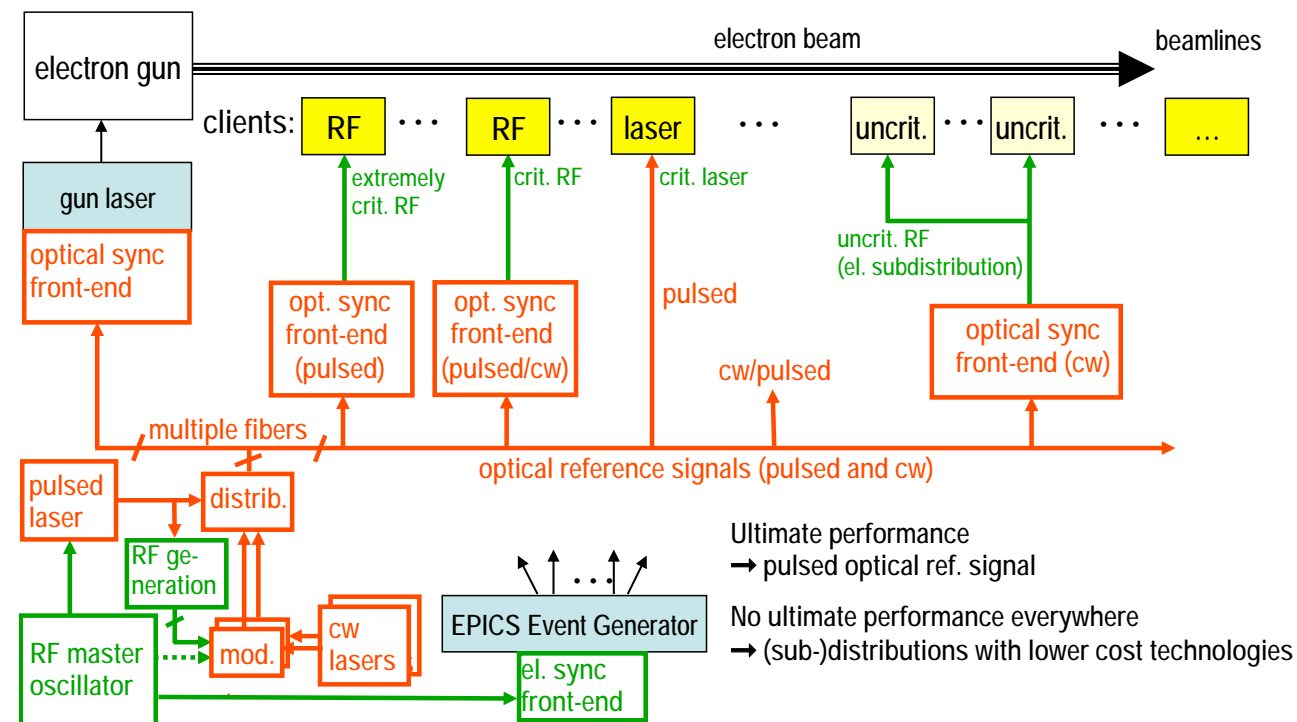


Fig. 3.3.1.1: Generic layout of the hybrid optical/electrical reference distribution system planned to be implemented in SwissFEL.

100 MHz, to enable optimum performance of the pulsed laser (optical master oscillator) and the pulsed optical receivers. The optical master oscillator laser's repetition rate is ideally chosen to be equal to this subharmonic frequency. Higher flexibility could be achieved if a single frequency standard (European only or US only) could be used for the RF systems in the machine. However, SwissFEL will mix two standards and has to find the minimum common sub-harmonic (see Section 3.3.5). A higher repetition-rate laser can be locked to this basic repetition rate, using optical cross-correlation.

3.3.1.3 Most critical jitter and drift requirements

The most critical clients with respect to jitter and drift are located in the injector, as well as in the experimental areas. In addition, BAMs located at various points in the machine and the seeding laser also require extremely stable reference signals. Table 3.3.1.1 summarizes the requirements and Table 3.3.1.2 shows the expected performance, using various principles.

Table 3.3.1.1: Most critical jitter and drift requirements (BAM: beam arrival time monitor).

Most critical parameters for sync system: Jitter (RMS, 10Hz..10MHz) and long-term drift (hours)	
<u>Gun laser:</u>	≈ 30 fs expected (goal: 10 fs), to be measured with BAM
<u>Most critical RF stations:</u>	goal is "0.02° phase jitter at 3GHz (18.5 fs)" for SwissFEL RF system contributes >10 fs (far out) intrinsic jitter, <5 fs (diff. mode) is the requirement for the sync system
<u>Experiment (pump-probe) lasers:</u>	<10 fs (optical sync combined w. BAM for sorting of jittery experimental data)
<u>Seeding laser:</u>	<10 fs (optical sync combined w. BAM for drift FB)
<u>E/O sampling lasers:</u>	<50 fs
<u>BAM (opt. sync only):</u>	approximately 6 fs timing resolution/stability (down to 10pC)
"Differential mode jitter" between stations is critical, "common mode jitter" (all clients jittering with ref.) is uncritical.	
Many drift/jitter specs for SwissFEL are not yet clear today → a flexible & future-proof ref. system is required!	
10 fs is equivalent to 3 μm in air!	

Table 3.3.1.2: Expected jitter and drift performance for different synchronization systems.

Link technology	Jitter ¹	Drift ²	Principle
RF/coax (temp. stab. ³)	some fs (potential)	\approx ps, ≈ 50 fs ³	RFMO, power amp., trunk, taps, (RF phase det., thermal phase control ³)
optical pulsed (≈ 200 fs)	<1 fs (potential)	<10 fs	OMO (RF sync), disp. compens., opt. x-corr.-based link stab.
optical cw (interferom. link stab.)	some fs (potential)	<20 fs	RFMO, ultra-stable cw laser, E/O modulator, lin. stage/vector mod.
optical cw (RF based link stab.)	<10 fs (potential)	\approx ps, ≈ 50 fs ³	telecom DFB laser, E/O modulator, RF phase det., lin. stage/vector mod.

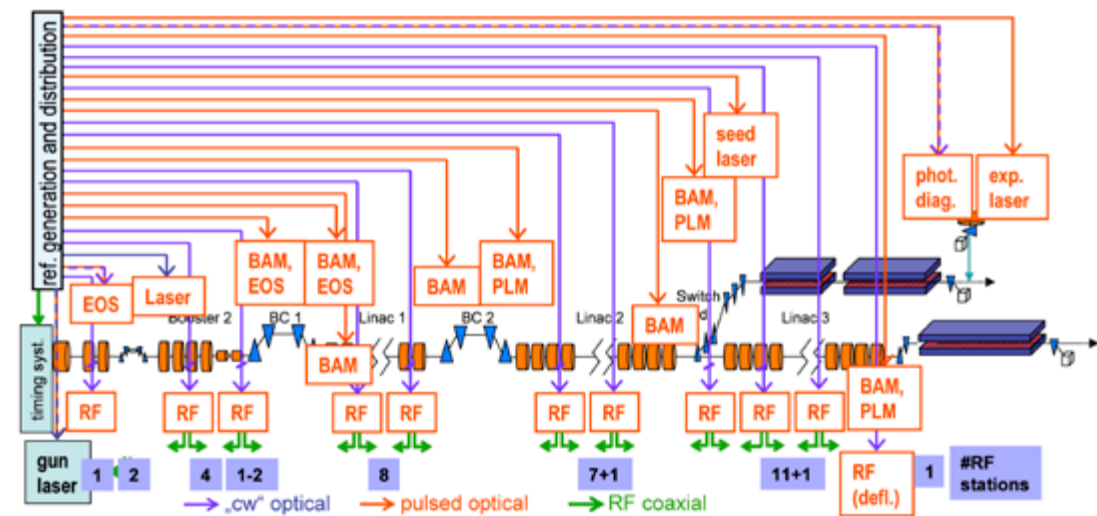
¹ 10 Hz – 10 MHz rms with respect to reference

² drift over some hours

³ with RF link stabilization

3.3.1.4 Reference distribution layout for SwissFEL

Ultimate performance, particularly drift stability, and evolutive design can only be achieved with optical technologies. These offer extremely low drift (the possibility of using sophisticated link stabilization techniques), easy configurability and flexibility, EMI immunity, and simple and cost-effective installation. A star distribution will give the highest flexibility and can easily be realized with optical fibers (Figure 3.3.1.2).



An RF station gets its reference signal over a dedicated optical link.
An "RF" block in the drawing represent the number of RF stations, each of which requires an individual stabilized optical link.

Fig. 3.3.1.2: Proposed layout of the SwissFEL synchronization system (a block "RF" represents a group of RF stations, each of which requires an individual stabilized optical link).

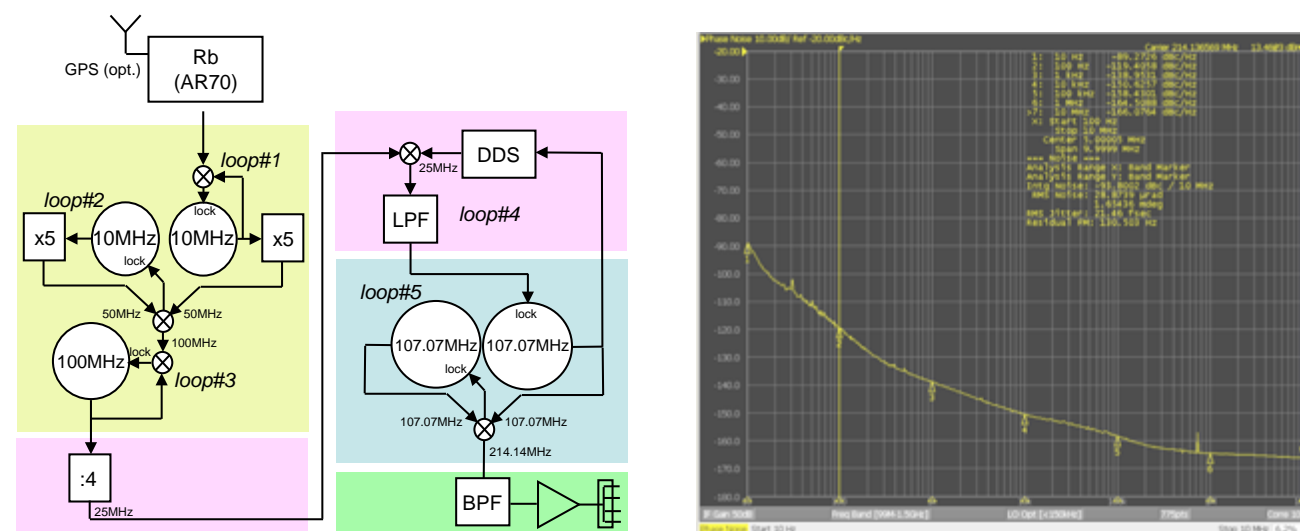


Fig. 3.3.1.3: SwissFEL Injector Test Facility RF master oscillator [45]. Block diagram (left), Phase noise spectrum (right).

3.3.1.5 RF master oscillator

A low phase noise RF master oscillator operating at a reference frequency of 214.1366 MHz (14th subharmonic of Eu S-band RF frequency) has already been implemented in the SwissFEL Injector Test Facility. The master oscillator consists of a cascade of mutually phase-locked, ultra-low, phase-noise oscillators, each optimizing a certain range of the phase-noise spectrum (Figure 3.3.1.3). Integrated absolute timing jitter between 100 Hz and 10 MHz is <21.5 fs. If phase-lock loops (electrical or optical) are locked to this oscillator, jitter contributions below the loop bandwidth (some 100 Hz up to ≈ 1 kHz) are "common mode" and therefore almost synchronous for all clients. This means that its integral influence on the electron bunch is strongly suppressed.

3.3.2 Optical synchronization system

3.3.2.1 Pulsed optical synchronization system

High-gain free-electron lasers are capable of generating UV and X-ray pulses in the fs range. To fully exploit the high temporal resolution offered, appropriate linac stability has to be achieved. In addition, user experiments have also to be synchronized to the machine with the corresponding accuracy. In order to secure long-term stability in the sub-10 fs range, an optical reference system is foreseen. Best performance can be achieved with such a system if pulsed links are used, similar to the ones developed at MIT [46, 47] and DESY [48, 49]. The reference pulses of a highly stable low phase-noise, mode-locked laser optical master oscillator (OMO) are distributed point-to-point (star configuration) to the remote client stations of the accelerator. The different stability requirements (from an ultra-low to a low-drift and ultra-low timing stability) over long distances and extended periods of time leads to a hybrid optical system with tailored performance, to optimize cost. This utilizes the advantages of both: the ultimate-performance pulsed links and the cost-effective "cw" links. There are several key components along the accelerator, in the diagnostics and in the experimental areas which are more naturally stabilized optically.

3.3.2.2 Critical components of the pulsed optical synchronization system

a. Laser master oscillator

One prerequisite for high-accuracy synchronization is a stable optical master oscillator. Its timing jitter in the high-frequency range should be in the fs range. This is necessary due to the limited bandwidth (<50 kHz) for locking of a mode-locked laser to an RF reference. Whereas the low-frequency noise is determined by the stability of the RF reference, the high-frequency part beyond the locking bandwidth follows that of a free-running mode-locked laser. In addition, stabilized fiber links have an intrinsic bandwidth limitation, determined by the round trip of the reference laser pulse. For a 1 km fiber, the round-trip travel time is ~ 10 ms. Any fluctuations in the pulse train faster than this can not be compensated. Low-jitter hybrid (Er-Yb fiber/solid state) lasers are already commercially available [50]. An integrated timing jitter in the range 1kHz–10MHz as low as 3.3 fs

(rms) has been measured on the 14th harmonic of the laser repetition rate of 214.1366 MHz [45], making the laser an ideal candidate for an optical master oscillator (Figure 3.3.2.1).

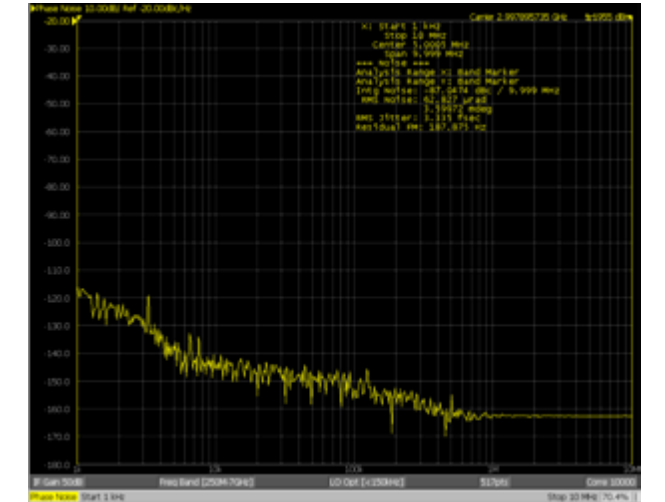


Fig. 3.3.2.1: Optical master oscillator laser jitter measurement (measured with harmonic extraction photodetector).

b. Optical cross-correlation for laser synchronization and group delay measurement

Balanced optical cross-correlation [51, 52] allows optical synchronization of a wide diversity of lasers – from mode-locked [48, 51] to Q-switched [53] – as well as group delay measurement for length stabilization of optical fiber links [47, 52, 54]. The principle is illustrated in Figure 3.3.2.2.

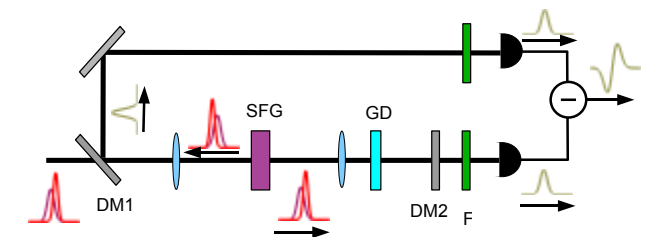


Fig. 3.3.2.2: Principle of balanced optical cross-correlation [52]. DM-dichroic mirror, SFG – nonlinear crystal for sum-frequency generation, F-filter, GD-group delay control.

In such a scheme, 4.4 fs jitter over 12 hours has been achieved [54]. When the wavelengths are different, a phase-matched BBO crystal with an appropriate cut angle can be used [48, 53]. Here the most efficient is the Type I interaction (parallel input polarizations), which is not background free, but nevertheless efficient when appropriate bandpass filters in front of the photodetectors are used. In this scheme, pulse swapping in the backward direction is achieved either by the group delay in the available optical elements (lenses, dichroic mir-

rors, etc) [48], or, if the bandwidths of the interacting optical pulses are orders of magnitude different, by a delay stage [53].

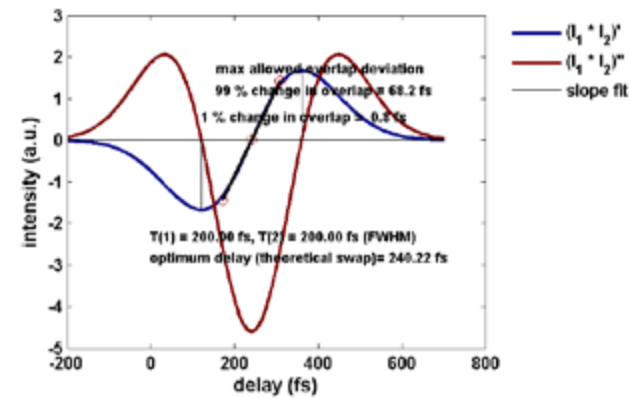


Fig. 3.3.2.3: Sensitivity of an optical cross-correlator to changes in signal overlap (blue curve). The delay between the incoming and back-reflected Gaussian pulses is chosen such that maximum sensitivity to overlap changes is achieved (red curve). The sensitivity of the scheme is theoretically sub-fs, as illustrated in Figure 3.3.2.3.

c. Length-stabilized fiber links for pulse transmission

A layout of an optical link, length-stabilization system for ultra-low drift transmission of the reference laser pulses is illustrated in Figure 3.3.2.4. The distribution after the master oscillator laser might be either free space or in fiber multiplexers. Acoustic noise and thermal fluctuations may cause variations of the optical path length in

the fiber, which leads to arrival time deviations in the transmitted reference laser pulses. Therefore, active stabilization of the link length through optical cross-correlation is necessary [47, 52, 54]. Part of the reference pulse is back reflected from the link end through a Faraday rotating mirror. The arrival time of this pulse in the link front-end is sensitive to changes in the link length. Through an appropriate phase-lock loop (PLL), the error signal, proportional to the overlap mismatch of the pulses in the balanced optical cross-correlator, can be used to compensate for the short-term (jitter) and long-term (drift) fibre length variation. The jitter is compensated with a fibre piezo-stretcher and the drift by a free-space optical delay.

Several effects have to be taken into consideration:

- Optical cross-correlation is sensitive to pulse length and polarization changes. Fibre chromatic dispersion is mitigated using dispersion compensating fibers (DCF), whereas polarization has to be controlled at the link input and output.
- Polarization mode dispersion (PMD) also leads to pulse broadening in long fibres. The effect can be minimized using low-PMD fibers [55] ($PMD \leq 40 \text{ fs}/\sqrt{\text{km}}$).
- In order to reduce undesirable non-linear effects in the link, the pulse energy has to be kept below 100 pJ. On the other hand, sufficient power should be secured for optical cross-correlators. Therefore, cascade pulse

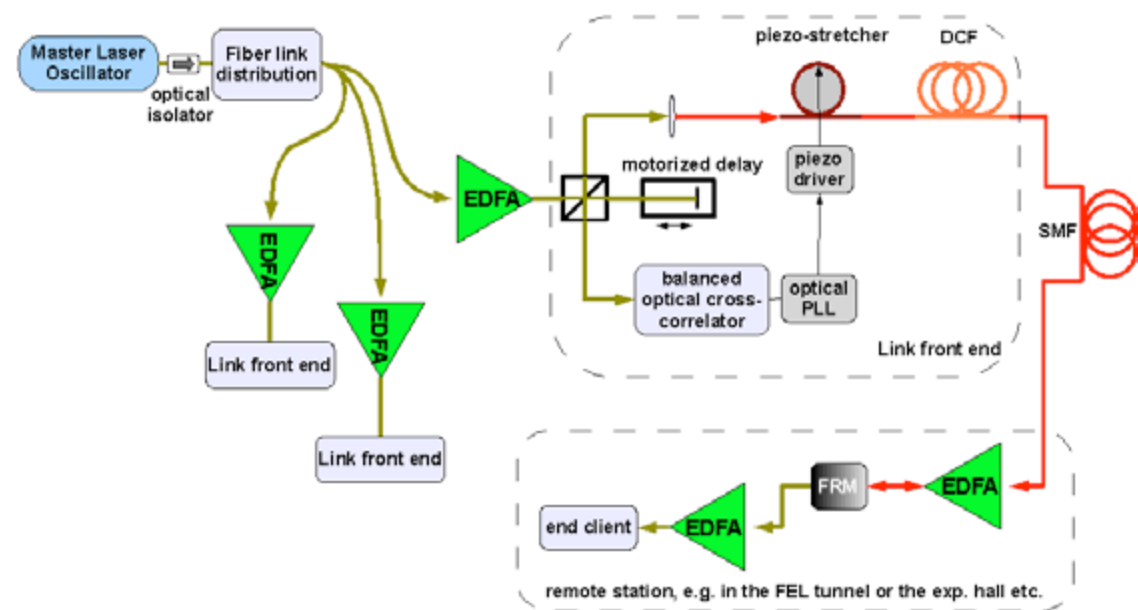


Fig. 3.3.2.4: Layout of the optical link length stabilization for drift-free distribution of the reference laser pulses: EDFA – Erbium-Doped Fiber Amplifier; PLL – Phase-Lock Loop; DCF – Dispersion Compensating Fiber; SMF – Single-Mode Fiber (standard single-mode fiber); FRM – Faraday Rotating Mirror.

amplification at both ends of the link is necessary, e.g. with Erbium-doped fibre amplifiers (EDFA), with carefully balanced seed and pump parameters to reduce the added integrated timing jitter [54].

- Radiation-hard (if required) as well as low temperature drift, non-actively stabilized fibres (for short links) are commercially available.

3.3.2.3 Alternative optical link concept: optical “cw” link

The pulsed optical links described above are those with the potentially best drift and jitter performance.

Besides “pulsed” links, another type of optical link will be used: the “continuous wave” (cw) optical link. Both technologies offer the possibility of implementing link group delay stabilization. Without this stabilization possibility, the required long-term phase/timing stability could not be achieved.

With optical “cw” links, very low jitter (<10 fs) and relatively low drift (some tens down to about 10 fs avg. p-p per day) can be achieved, whereas pulsed links offer ultimate (approx. 1 fs) jitter and drift performance (some fs avg. p-p per day). The simplicity, potentially lower cost and proven reliability of “cw” links makes them a candidate as workhorse in the optical reference distribution system (e.g. [56]). Interferometric or RF phase detection

can be used. In the former case, phase instead of group delay is stabilized, and therefore a correction has to be applied.

3.3.3 Stabilization of lasers

3.3.3.1 Ultimate stability: optical cross-correlation

There are several laser systems along the accelerator, which have to be synchronized to the master laser oscillator. Among them are: the gun laser (Ti:Sa at 800 nm or Nd:YLF at 1047 nm), the laser for longitudinal bunch electro-optical diagnostic (Yb- fiber at 1030 nm or Ti:Sa), the seed laser (typically Ti:Sa), the laser for pump-probe experiments (Ti:Sa), the laser heater (Ti:Sa) and, optionally, the laser for the optical replica (Ti:Sa). In addition, the arrival time of the photo-injector laser on the cathode can be stabilized via active stabilization of the optical transfer line (propagation in free air). For optical-to-optical synchronization, a balanced optical cross-correlator can be used, with which a 300 as rms jitter in the range 0.01 Hz-2.3 MHz has been demonstrated [51]. Because of the different wavelengths of the master laser oscillator (Er fiber laser @ 1560 nm) and the client (Ti:Sa or Yb fiber), a cost-effective, two-colour balanced optical cross-correlator, based on a single BBO crystal, can be used [48, 53]. The synchronization scheme is similar to

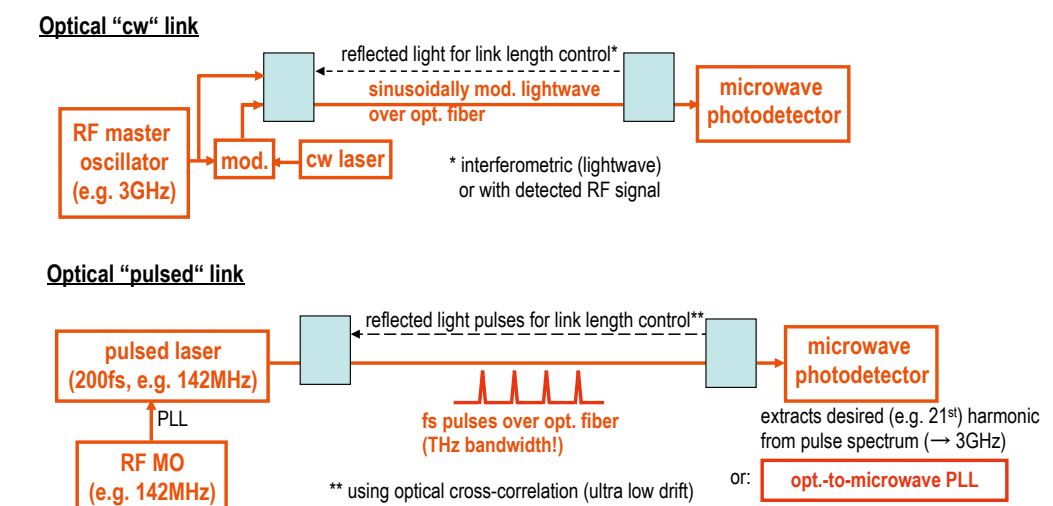


Fig. 3.3.2.5: Comparison of optical link types to be used in the SwissFEL synchronization system.

the one shown in Figure 3.3.2.2, with the exception that Type I interaction (parallel input polarizations) is used. The layout is illustrated in Figure 3.3.3.1. The laser which is to be stabilized optically has to be initially locked to the reference laser with an RF PLL. This secures initial temporal stability between the two optical pulses, necessary to achieve overlap in the balanced optical cross-correlator. After the sum frequency pulse, proportional to the overlap mismatch, has been achieved, the optical cross-correlator PLL may take over.

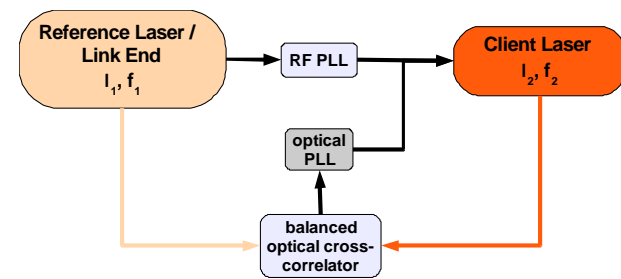


Fig. 3.3.3.1: Layout of direct optical-to-optical laser stabilization: PLL - Phase Lock Loop.

3.3.3.2 Laser synchronization with relaxed drift stability

Long-term fs stability can be achieved by means of two-wavelength optical cross-correlation alone. Long-term stability of the order of some 10 fs (for laser clients with somewhat relaxed requirements) and fs jitter is possible using optimized classical PLL techniques with harmonic extraction (see, for example, [57]).

3.3.4 RF generation

3.3.4.1 Balanced optical-to-microwave phase detector

Ultimate drift (a few fs) and jitter (a few fs) performance can potentially be achieved with a technique developed at MIT, the so called “balanced optical-to-microwave phase detector”-based PLL [47]. This method has been successfully demonstrated for RF frequencies above 10GHz. For lower RF frequencies, some problems still have to be solved [58]. A drawback of the method is its high cost.

3.3.4.2 Direct harmonic extraction photodetector

If excellent jitter, but not ultimate drift, performance is required, and cost has to be significantly minimized (e.g. synchronization of RF stations with a pulsed optical reference), the RF frequency can be directly extracted from the photo-electron current of a photodetector, illuminated with the reference pulses, which occur with a repetition rate that is a subharmonic of the RF frequencies (Figure 3.3.4.1). It has been demonstrated that jitter of some fs can be achieved with this scheme (Figure 3.3.2.4). Using optimized photodetectors and stabilization techniques, long-term drift stability of the order of 10 fs can be achieved [45, 58–60].

An advantage of direct harmonic extraction is the fact that jitter is (as opposed to PLL-based solutions) synchronous for all clients served by the same laser pulses (common-mode jitter only).

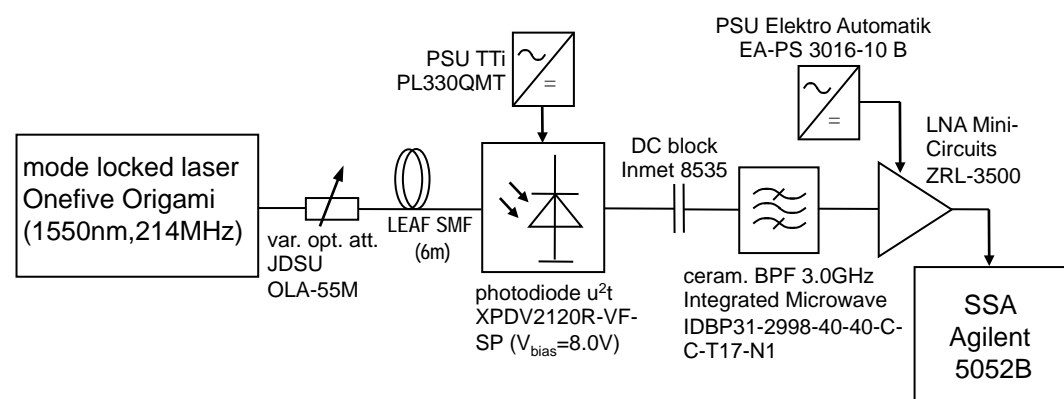


Fig. 3.3.4.1: Block diagram of a direct harmonic extraction receiver [45].

3.3.5 Synchronization system for mixed European/US RF frequencies

For cost reasons, RF systems operating at European and US frequencies will both be used simultaneously in

SwissFEL (European: S-band and X-band; US: C-band). This poses some restrictions on the synchronization system. A common subharmonic has to be found, from which both European and US frequencies can be derived:

$f_b = 142.8$ MHz (common subharmonic)			
C-band	5712 MHz	$=40 \times f_b$	American Frequency
S-band	2998.8 MHz	$=21 \times f_b$	detuning from 2997.912 MHz: + 0.888 MHz
X-band	11995.2 MHz	$=84 \times f_b$	detuning from 11991.648 MHz: + 3.552 MHz

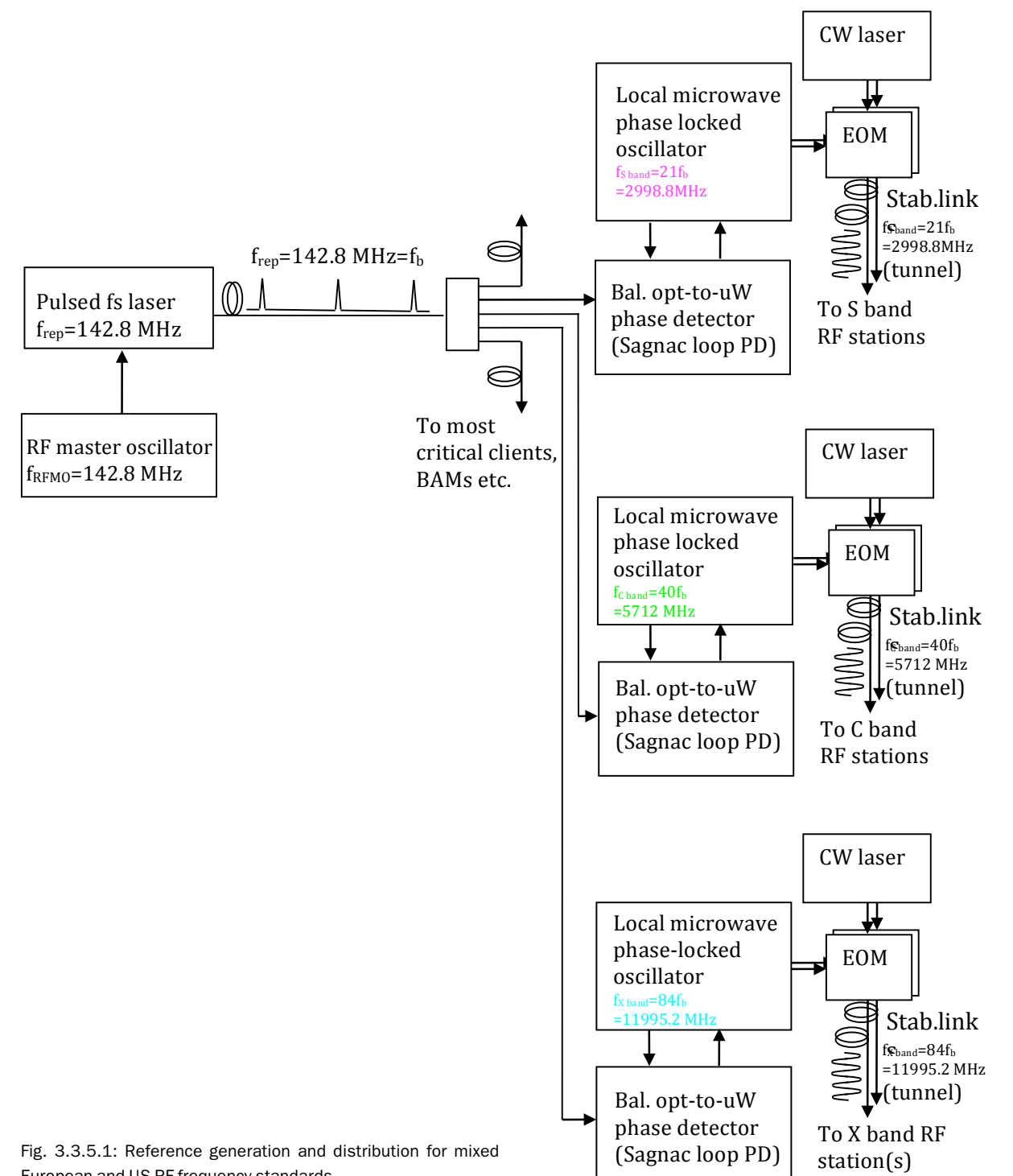


Fig. 3.3.5.1: Reference generation and distribution for mixed European and US RF frequency standards.

Figure 3.3.5.1 shows a block diagram of a possible synchronization system. The balanced optical-to-RF phase-detector-based PLLs are synchronized with the common (subharmonic = repetition rate) optical signal and guarantee extremely low drift (ultimately of the order of some fs) between the RF frequencies. The latter are then further distributed within the accelerator tunnel by means of cost-effective optical “cw” links.

3.4 Magnets

Beamline magnets (solenoids, bending dipoles, quadrupoles and correctors) will be used all along the accelerator, to focus (solenoids, quadrupoles) and longitudinally compress the beam (bending dipoles in chicanes) and to correct the field quality (correctors, quadrupoles). An overview of the accelerator layout with the foreseen magnets is presented in Chapter 2. For the Aramis project phase, there are 10 solenoids, 179 quadrupoles and 28 dipoles. For the Athos next phase of the project, an additional 23 quadrupoles and 16 dipoles will be required. Around 50 magnets (quadrupoles, solenoids, dipoles) already exist and are installed on the SwissFEL Injector Test Facility [61]. The same magnets will be used for SwissFEL. The characteristics of the magnets will now be reviewed, type by type.

Table 3.4.1.1: Parameters of gun solenoid system.

	Bucking Coil WFB	Quad. Correctors	Steerers SFB	Gun Solenoid WFG
Location	$z = -60$ mm	Concentric to WFG	On WFG faces	$Z = 0.3$ m
Aperture	220 mm	46 mm	80 mm	80 mm
Outer Diameter				385 mm
Strength	4.3 mT @ cathode	27 mT/m	0.25 mT	0.35 T
Mechanical Length		70 mm	10 mm	0.26 m
Calibration (Gauss/A)			0.25 G/A	17.59 G/A
$\int \Delta B/B.ds$				10^{-4}
Magnetic axis measured accuracy				0.1 mm
Maximum Current	10 A	10 A	20 A	220 A
Resistance at 50°C			2×60 mΩ	110 mΩ
Cooling	air	air	air	Water
Ref. PSI Drawing	1-50022.41.338		50021.41.101	0-50022.41.169
Magnet Interface Data				FEL-SS88-004-0
Reference name for Magnet Measurement Data	WFB	QFCOR	SFB	WFG

3.4.1 Solenoid magnets

In the SwissFEL Injector Test Facility, a gun solenoid right after the electron gun and 8 solenoids for the S-band accelerating structures have already been built and measured. The same magnets will be installed at the SwissFEL Injector. Below is the description of those injector magnets. More parameters (for example measurements reports) are available at PSI magnet group database (<http://magnet.web.psi.ch>).

3.4.1.1 Gun solenoid system:

The Gun Solenoid system consists of 4 magnet elements:

- the main Gun Solenoid ($z = 0.3$ m; WFG) which focuses the beam at gun exit.
- the bucking coil: (positioned at $z = -0.1$ m upstream of the cathode plane; WFB) to cancel the fringe magnetic field of gun solenoid at the cathode plane (no magnetic field should be present on photocathode surface).
- the quadrupoles and skew quadrupoles (1 layer loops around vacuum chamber; QFCOR) correctors to compensate imperfection in the gun solenoid.
- the corrector dipoles (on each end of solenoid’s iron yoke; SFB) to steer the beam horizontally and vertically.

The parameters of those magnets are summarized in the table 3.4.1.1 and Fig. 3.4.1.1 represents the gun solenoid.

The gun solenoid, positioned just after the RF gun, aims to focus the beam immediately downstream of the cathode. Indeed, the beam experiences strong RF and space charge defocusing forces that are radially symmetric. The focusing force must also be radially symmetric or the beam will not be optimally compensated. Therefore, a solenoid is required to contain the beam. The basic solenoid specifications are listed in the Table 3.4.1.1. The solenoid consists of two coils with 161 turns/coil (double solenoid) covered with an iron yoke. Each coil consists of 14 layers glued with glass-epoxy. The solenoid axial position must be correct to approximately 0.1 mm. Therefore, the measurement of the axis of the solenoids was accurately made with a Hall-probe, and the 0.1 mm accuracy was achieved. It was also desired that the solenoid field varies linearly with current, and the field must be radially symmetric and also axially symmetric to within 2 % about the centre of the magnet. Quadrupoles and skew quadrupoles are installed within the solenoid aperture to correct beam asymmetries.

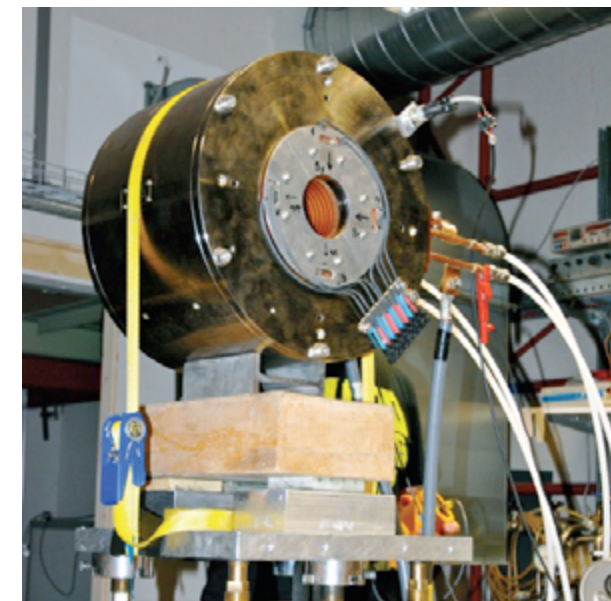


Fig. 3.4.1.1: Gun solenoid on his test bench (the steerers V and H are visible on front plane).

3.4.1.2 S-Band solenoids

The S-band solenoids (WFS) surround the S-band cavities along the injector. They will provide additional focusing, to reduce emittance enlargement due to space charge effects during booster 1 acceleration. Specifications are shown in Table 3.4.1.2. Accuracy on the knowledge of the magnetic axis was also 0.1 mm. The solenoid consists of two adjacent coils (150 turns/coil).

Table 3.4.1.2: Requirements for the solenoids installed in the SwissFEL Injector Test Facility.

	S-band Solenoid
Location	injector
Quantity	8
Aperture	220 mm
Outer Diameter	345 mm
Max. Strength	103.52 mT
Mechanical Length	750 mm
Calibration (Gauss/A)	0.518 mT/A
$\int \Delta B/B.ds$	10^{-4}
Magnetic axis measured accuracy	0.1 mm
Maximum Current	200 A
Resistance at 50 °C	141 mΩ
Cooling	Water: 4.1 l/min
Ref. PSI Drawing	1-50022.41.043
Reference Interface	FEL-GRO6-39_0
Reference name for Magnet Measurement Data	WFS

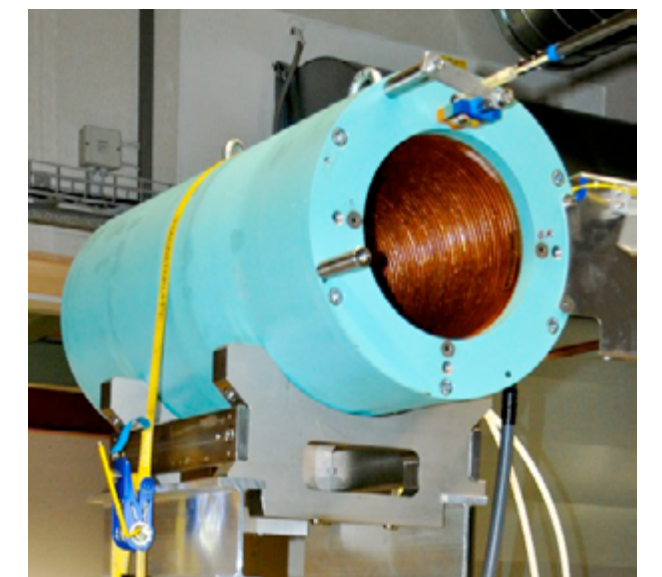


Fig. 3.4.1.2: S band solenoid on his test bench.

3.4.2.2 Quadrupoles in linac and undulator sections:

For SwissFEL, a total of 450 quadrupole magnets with apertures of 22 and 12 mm are planned. In order to avoid the plugging phenomena of the hollow magnet conductors by water corrosion and the effect of the cooling water on the magnet vibration, an air-cooled design is favoured. Table 3.4.2.3 shows the parameters of these quadrupoles.

The quadrupoles QFD and QFE will be installed in the SwissFEL linacs 1,2 and 3. They will include horizontal and vertical steering function.

The 22 mm-aperture quadrupoles will be used in the linac sections and beam matching sections. The shorter QFD quads (0.15 m) are foreseen for Linacs 1, 2 and 3. The longer QFM magnets (0.3 m) will be used in matching sections at higher beam energy where stronger focussing is required. For similar reasons to those mentioned above, the magnet cores of the quadrupoles

will be made of laminations. The gradient reproducibility from one quadrupole to another has to be kept within 10^{-3} . Pole profiles have to be optimized in order to minimize the 12-pole term below 10^{-3} times the quadrupole main field. The characterization of each magnet will consist of measuring the integral field strength versus current (magnetization curve, hysteresis cycle), the field quality (integral harmonics up to order $n=10$) and the magnetic axis. These measurements are planned to be carried out using a 19 mm-aperture rotating mole currently under design at CERN and a vibrating wire system. The accuracy of the field quality measurements remains a challenge in the case of such small-aperture magnets. The challenge here is represented by the limited size of the coil to maintain the needed mechanical stability. A design using 3 coils directly wound on the shaft body may be the solution, leading also to higher winding precision. A relative accuracy of 10^{-4} appears to be achievable.

The position of the magnetic axis with respect to external fiducials has to be known within 50–100 μm rms.

Measurements using a vibrating wire system will be systematically performed on all the quadrupoles. The precision of the vibrating wire technique together with the precision on mechanical reference positions (fiducials) leads to an overall accuracy of 50 μm rms in the magnetic axis position.

Table 3.4.2.4: Requirements for the quadrupoles used for the SwissFEL Aramis and Athos undulator beamlines.

Location / Project phase	QFF	
	Undulator Aramis	Undulator Athos (2018)
Number	19	14
Aperture	12 mm	
Gradient G	50 T/m	
Yoke length	0.08 m	
Gradient measurement accuracy	10^{-3}	
Multipole measurement accuracy at $r = 8$ mm	10^{-3}	
Max. Current	10 A	
Turns / coil	84	
Cooling	air	
Resistance at 50 °C	0.39 Ω	
Weight	32 kg	
Ref. Interface	FEL-SS88-008	
Power Supply Type	bipolar	
Ref. Drawing	50023.41.035	
Integrated Steering Dipoles	10 A	
Steering Dipoles maximum angle (5.8 GeV)	200 μrad	
Steerer max. field	500 G	

Table 3.4.2.3: Requirements for the quadrupoles used for the SwissFEL linac and in the Athos undulator beamline.

Location (Project Phase)	QFD		QFM	QFS (skew QFD)
	Aramis (2016)	Athos (2018)	Aramis (2016)	Aramis (2016)
Quantity	110	7	18	3
Aperture	22 mm		22 mm	22 mm
Gradient G	20 T/m		50 T/m	20 T/m
Yoke length	0.15 m		0.3 m	0.15 m
Gradient measurement accuracy	10^{-4}		10^{-4}	10^{-4}
Multipole measurement accuracy at $r \sim 19$ mm	10^{-3}		10^{-3}	10^{-3}
Max. Current	10 A		50 A	10 A
Accuracy in magnetic axis determination (rms)	50 μm		50 μm	50 μm
Turns / coil	104		48	104
Cooling	air		water	air
Resistance at 50 °C	0.5 Ω		0.4	0.5 Ω
Total Weight	80 kg			80 kg
Ref. Interface	FEL-SS88-007			FEL-SS88-007
Ref. Drawing	1.50023.41.001			1.50023.41.001
Power Supply Type	bipolar		bipolar	bipolar
Steering max. field (H and V)	30 mT		30 mT	30 mT
Steerer maximum current	2 x 10 A		2 x 10 A	2 x 10 A
Steerer Resistivity	2 x 0.15 Ω			2 x 0.15 Ω

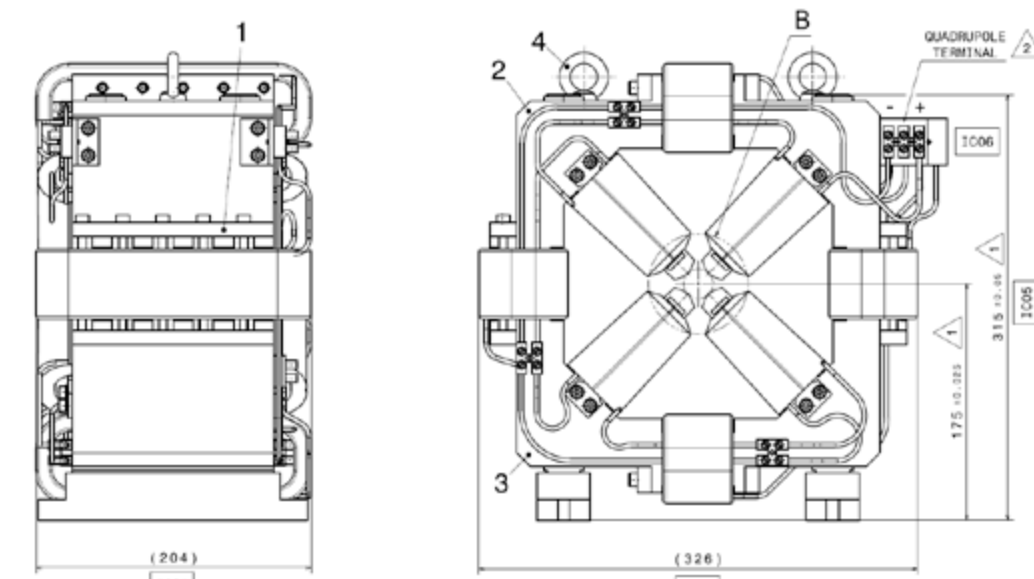
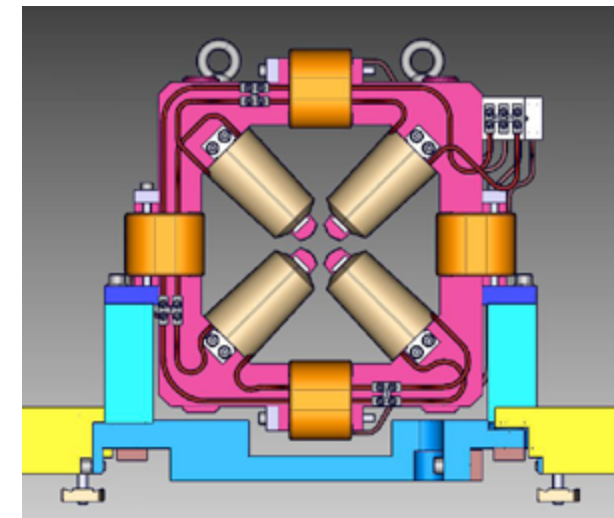


Fig. 3.4.2.3: Quadrupoles QFD drawing which include horizontal and vertical steering function. Four position references (fiducials) are on the top of the quadrupole yoke.

QFF quadrupoles (50 T/m, 12 mm apertures) will be placed in the undulator beamlines. The same measurement goals as for the linac quadrupoles are required and the tolerance on the field quality is at the level of one percent. The integrated field gradient and the field quality can be measured using a 10 mm-aperture rotating mole, that will be developed at CERN in 2012. The main difficulty will be the determination of the magnetic quadrupole axis in respect to fiducials reference sitting on the quadrupole frame. SwissFEL will use a beam-based alignment technique to align the quadrupoles to the needed accuracy (less than $1 \mu\text{m}$). However, an initial accuracy of the quadrupole alignment not worse than

$50 \mu\text{m}$ is required. In addition, each undulator frame will incorporate two small alignment quadrupoles (specifications are still to be defined) on the same girder support (see Section 3.5.3). The fiducialization of the undulator and quadrupole will be carried out using the vibrating wire technique. The impact of the thermal effects on the magnetic axis position has to be carefully measured. To save space, all quadrupoles (QFD, QFM and QFF) will contain integrated steering functions in the horizontal and vertical directions. These steerer dipoles are air cooled and designed for 10 A maximum current with a bandwidth.

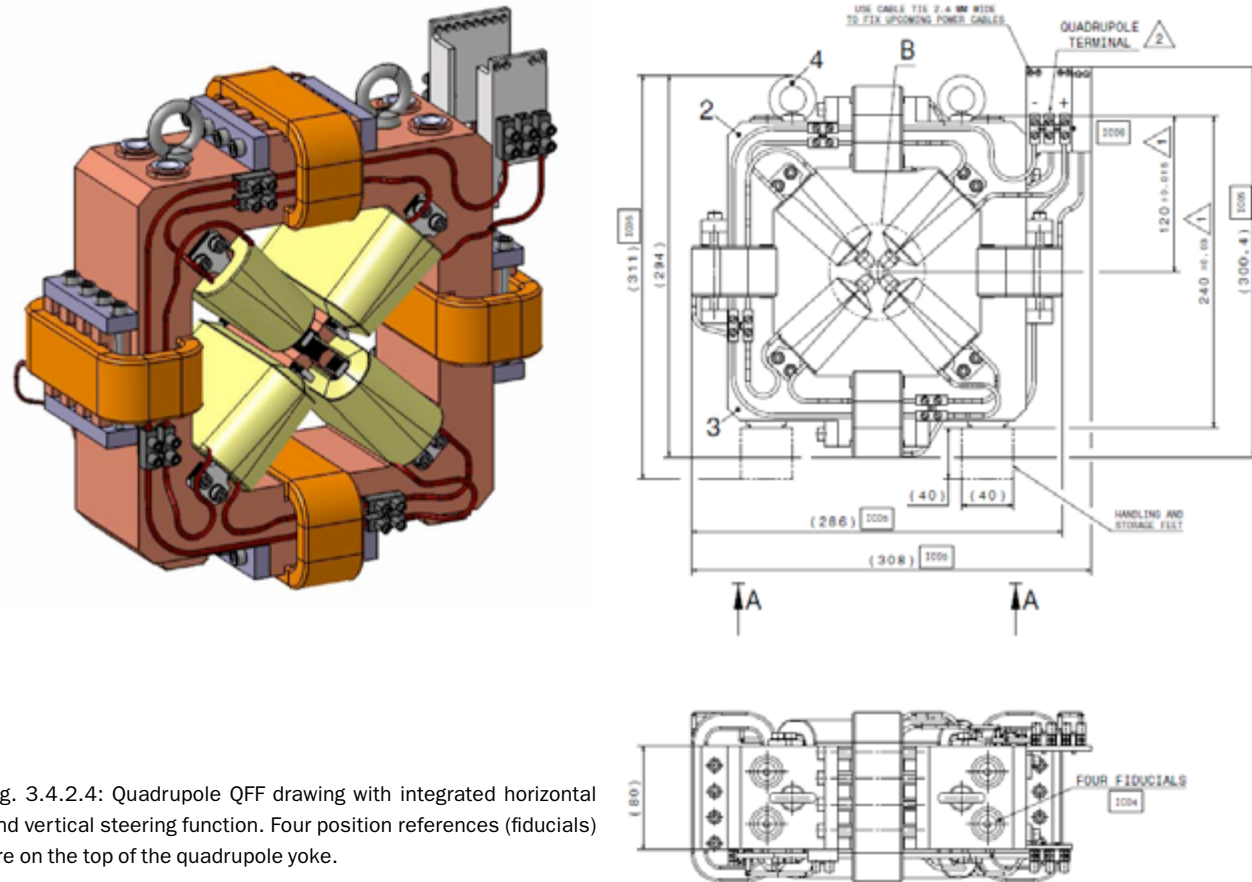


Fig. 3.4.2.4: Quadrupole QFF drawing with integrated horizontal and vertical steering function. Four position references (fiducials) are on the top of the quadrupole yoke.

3.4.3 Dipole magnets

Table 3.4.3.1: Summary of dipole magnets along SwissFEL. Corrector dipole magnets are not included.

Location (section)	Name	Number
Gun Spectrometer	SHA	1
Laser Heater Chicane	AFL	4
Bunch Compressor 1	AFBC2	4
Injector Spectrometer	AFBC3	1
Bunch Compressor 2	AFBC3	4
Switchyard Dipoles	AFBC3	4
Switchyard Dipoles Vertical	AFL	2
Aramis collimator	AFBC3	4
Aramis dump (+ safety permanent magnet)	AFD1	2
Athos Modulator Chicanes	AFBC2	8
Athos Modulator Dog Leg	AFEE	8
Athos dump (+ safety permanent magnet)	AFD2	2
Total		44

The different types of dipoles are summarized in Table 3.4.3.1. Two magnetic chicanes will be used for the two bunch compressors BC1 and BC2 to generate a non-zero momentum compaction factor R_{56} . A schematic layout and parameter summary is given in Chapter 2. The dipoles in the bunch compressor BC1 with a magnetic gap of 30 mm are installed on the SwissFEL Injector Test Facility. The uniformity of the dipole field ($\text{dB}/\text{B}(x)$) and the width over which this uniformity is kept is extremely important for compression of a low emittance beam [62]. A good field region of $\pm 35 \text{ mm}$ with a field uniformity of $\text{dB}/\text{B} < 0.01\%$ in the field integral has been measured [63]. Special attention was paid to the manufacturing tolerances to ensure a precise geometry. To build dipoles as similar as possible to each other, all dipole yokes will be cut and machined from one piece of iron so as to avoid differences in the material composition. The tolerance on the pole parallelism and flatness will be tightened to $10 \mu\text{m}$ and $5 \mu\text{m}$ respectively. Each dipole winding will integrate one additional loop separately powered, to correct possible differences between dipoles. Two dipoles for beam dump and diagnostics complete the bending magnets of the injector.

For bunch compressor 2, dipoles with the same accuracy goals will be built. For a bending angle of 2.15° at energy of 2032.9 MeV, the dipoles will have a magnetic length of 0.5 m and a magnetic field of 0.5 T. Additional dipoles for beam dump; switchyard section and diagnostic purposes are also planned. A total of 43 dipoles (Table 3.4.31) is planned. Corresponding specifications are preliminary defined in Table 3.4.3.2 to Table 3.4.3.3.

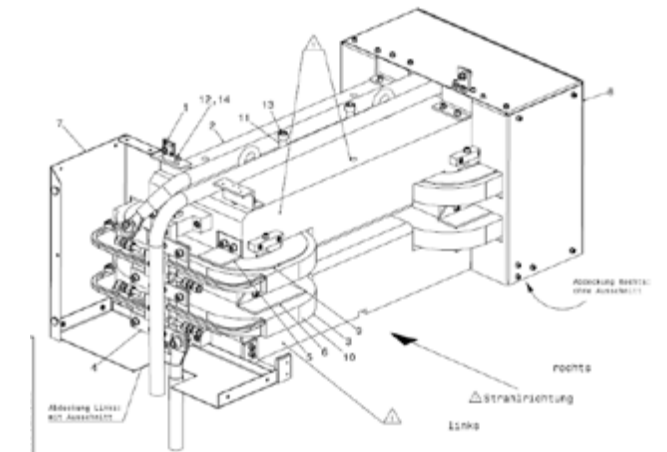


Fig. 3.4.2.4: Bunch compressor 1 dipole (AFBC2), magnetic length is 0.27 m and gap is 3 cm.

Table 3.4.2.3: Requirements for the quadrupoles used for the SwissFEL linac and in the Athos undulator beamline.

Location	Laser Heater	BC1	BC2	SPECTRO. GUN	Spectrometer Injector
Number of magnets	6	4	4	1	1
Max. Strength	0.3 T	0.4 T	0.5 T	0.2 T	
Effective Length	0.1 m	0.27 m	0.5 m	0.25 m	
Fig. Type	H – Magnet	H – Magnet	H – Magnet	Window Frame	
$\int \Delta B/B.ds$	10^{-4}	10^{-4}	10^{-4}	10^{-4}	
Transverse good field region	> 1 mm	150 mm	70 mm	60 mm	
Bending angle	3.82 deg (130 MeV)	4.2 deg (355.5 MeV)	2.15 deg (2100 MeV)	30 deg (30 MeV)	15 deg (355 MeV)
Full gap	30 mm	30 mm	20 mm	101.2 mm	30 mm
Pole width		280 mm	200 mm	108 mm	
Magnet Type name	AFL	AFBC2	AFBC3	SHA	
Calibration		2 mT/A		1.686 mT/A	
Maximum Current	150 A	200 A	150 A	50 A	
Turns per coil		2* 28 turns/ coil		2* 136 turns/ coil	
Cooling	water	water	Water	water	
Flow Rate		0.68 l/min.		1 l/min.	
Mass		500 kg			
Resistance		24 m Ω		256 m Ω	
Ref. Drawing		1-50022.41.223		1-00101.41.373	

Table 3.4.3.3: Requirements on the dipoles used for SwissFEL: Linac 2 to End.

Location	Switch-Yard	Switch Yard Vertical	Aramis Collimator chicane	ATHOS 1 ST MODULATOR & 3 RD MOD.	Athos 2 nd Modulator Dog-Leg
Number of magnets	4	2	4	8	8
Max. Strength	0.5 T	0.3 T	0.5 T	0.4 T	
Effective Length	0.5 m	0.1 m	0.5 m	0.27 m	1 m
Fig. Type	H – Magnet	H – Magnet	H – Magnet	H – Magnet	
$\int \Delta B/B.ds$	10^{-4}	10^{-4}	10^{-4}	10^{-4}	10^{-4}
Transverse good field region	70 mm	> 1 mm	70 mm	150 mm	
Bending angle	1 – 2.5 deg (3000 MeV)	0.12 deg (3000 MeV)	1 deg (5800 MeV)	0.5/0.25 deg (3383 MeV)	2.07 deg (3383 MeV)
Full gap	20 mm	30 mm	20 mm	30 mm	
Pole width	200 mm		200 mm	280 mm	
Magnet Type name	AFBC3	AFL	AFBC3	AFBC2	AFEE
Calibration				2 mT/A	
Maximum Current	150 A	150 A	150 A	150 A	150 A
Turns per coil				2*28 turns/coil	
Cooling	Water	water	Water	water	
Flow Rate				0.68 l/min.	
Mass				500 kg	
Resistance				24 m Ω	
Ref. Drawing				1-50022.41.223	

Table 3.4.3.4: Requirements on the dipoles used for SwissFEL Aramis and Athos Spectrometer (Beam Dumps).

Location	Aramis Spectrometer Dipole	Aramis Permanent Magnet Beam Dump	Athos Spectrometer Dipole	Aramis Permanent Magnet Beam Dump
Number of magnets	1	1	1	1
Max. Strength	1.34 T	1 T	1.04 T	0.88 T
Effective Length	2 m	0.8 m	1.5 m	0.5 m
Fig. Type	H – Magnet	permanent magnet	H – Magnet	permanent magnet
$\int \Delta B/B.ds$	10^{-4}	10^{-4}	10^{-4}	10^{-4}
Bending angle	8 deg (5800 MeV)	2 deg (5800 MeV)	8 deg (3382 MeV)	2 deg (3382 MeV)
Full gap	20 mm	20 mm	20 mm	20 mm
Magnet Type name	AFD1	AFP1	AFD2	AFP2
Maximum Current	200 A	N.A.	200 A	N.A.
Cooling	Water	air	Water	air

3.4.4 Corrector magnets

Twenty-six separated steering magnets for horizontal and vertical correction of the beam position have already been built and will be used for the injector part of the machine (< 450 MeV). They display “window frame” geometry with four iron yokes fitted with coils, two of which are connected in series to create a vertical and a horizontal dipole, with a deflection of 1 mrad. The yoke parts are completely machined out of ARMCO iron. They work at a nominal current of 10 A, producing a nominal field of 20 mT. The magnetic length is 0.05 m and the equivalent aperture is 80 mm.

The steering function for the new SwissFEL elements will be integrated in the quadrupole magnets by additional corrector coils driven by 10 A power supplies. A deflection angle of 0.3 mrad at maximum energy is specified for the QFD steerers and 0.2 mrad for the QFF steerers at 5.8 GeV.

3.4.5 DC magnet power supplies

The Power Supplies (PS) for the DC magnets mentioned above are designed and tested in-house and have a direct interface to the EPICS control system. As for any particle accelerator application, the PS for the SwissFEL must fulfil very high stability and precision requirements.

They will consist of switched-mode converters controlled by 2nd generation PSI-type Digital Power Electronics Controllers (DPC).

A simple buck converter structure is used for the unipolar PSs (1Q), whereas the bipolar PSs (4Q) are realized with H-bridges. Depending on the current and voltage ratings of the PS, IGBTs or MOSFETs are used as semiconductor switches. Simplified block diagrams of the two PS structures are shown in Figure 3.4.5.1. The DC source is either realized with a diode bridge or (for a low-power PS) with an off-the-shelf AC to DC converter. Several PS, will share a common DC source, to reduce costs. The switching frequency and the output filter cut-off frequency are chosen to be as high as possible, in order to obtain a high system bandwidth, which is essential for a high-precision PS. These types of converters have been used at the Swiss Light Source (SLS) for more than 10 years, and have proven to be very reliable.

For the SLS, a fully digital PS control system was developed 12 years ago [64], [65]. This controller has been adopted in several particle accelerators across the world, and several thousands are in service, to the complete satisfaction of their users [66]. Based on this good experience, a second generation of this PS control system, called DPC (digital power electronics controller), has been developed [67] and will be used for SwissFEL (refer to Figure 3.4.5.2). The DPC consists mainly of a controller board and a high-precision analogue to digital converter board. A backplane links the two boards and acts as the interface to the outside world. Compared to

the first generation, computing power has been improved remarkably, allowing faster control cycles and/or more complex control algorithms.

The new controller board contains also 12 ADC channels for protection functions. For PS with relaxed stability requirements the separate and expensive high-precision ADC can be omitted and a cheaper current measuring head can be used. The increased computing power of the controller board allows to control up to 3 independent PS with one single controller board. The current stability (noise 0.1...10 Hz, drift over 8 h, reproducibility)

will be less than 200 ppm peak to peak with omitted ADC board, which will be the standard case for most of the PSs. However, by adding the high precision ADC board and selecting a more precise measuring head the current stability can be lowered down to 50ppm peak to peak or even more. This will be necessary for sensitive magnets like the bunch compressor dipoles and some sensitive quadrupoles.

The current list of power supplies is summarized in Table 3.4.5.1. The table also shows the cooling type and the power rating per PS.

Table 3.4.5.1: Preliminary power supply list for SwissFEL.

PS type	Used in	Number	Cooling	Power	Remark
2*10A/10V/bipolar	Injector (11) Linac (5) Aramis (5) Athos (8)	29	air	0.2kW	1)
20A/10V/ bipolar	Injector (13)	13	air	0.2kW	1)
3*10A/12V/bipolar	Injector (9) Linac (57) Aramis (20) Athos (69)	155	air	0.36kW	
50+2*10A/24V/bipolar	Injector (20) Aramis (18) Athos (2)	40	air	1.7kW	
150A/40V/bipolar	Injector (3) Linac (1) Athos (8)	12	water	6.0kW	1) 2)
150A/110V/	Linac BC2 (1) Aramis (1)	2	water	16.5kW	1) 2)
200A/50V/bipolar	Injector BC1 (1)	1	water	10.0kW	1)
220A/40V/unipolar	Injector (5)	5	water	8.8 kW	1)
220A/100V/unipolar	Injector (2)	2	water	22.0kW	1)
220A/200V/unipolar	Aramis beam dump (1) Athos beam dump (1)	2	water	44.0kW	1) 2)

Remark 1) These PS are already built and in operation at the SwissFEL Injector Test facility and will be moved to the SwissFEL
 Remark 2) The specification of some of the magnets is not yet known. We plan to reuse the PS already built for the SwissFEL Injector Test facility and eventually adapt the output voltages.

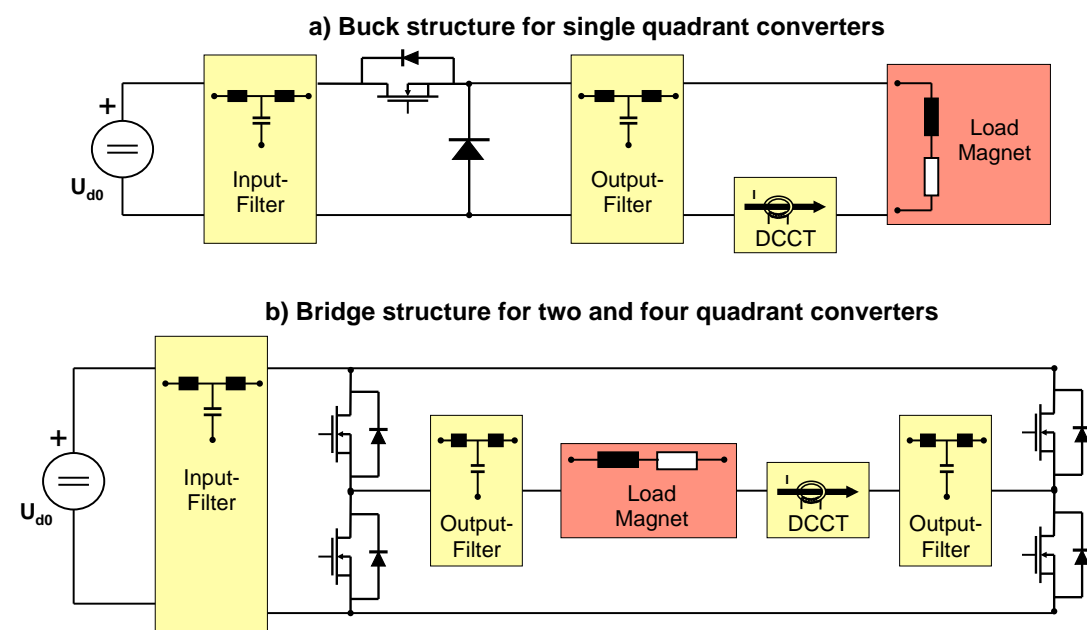


Fig. 3.4.5.1: Simplified Converter structure.

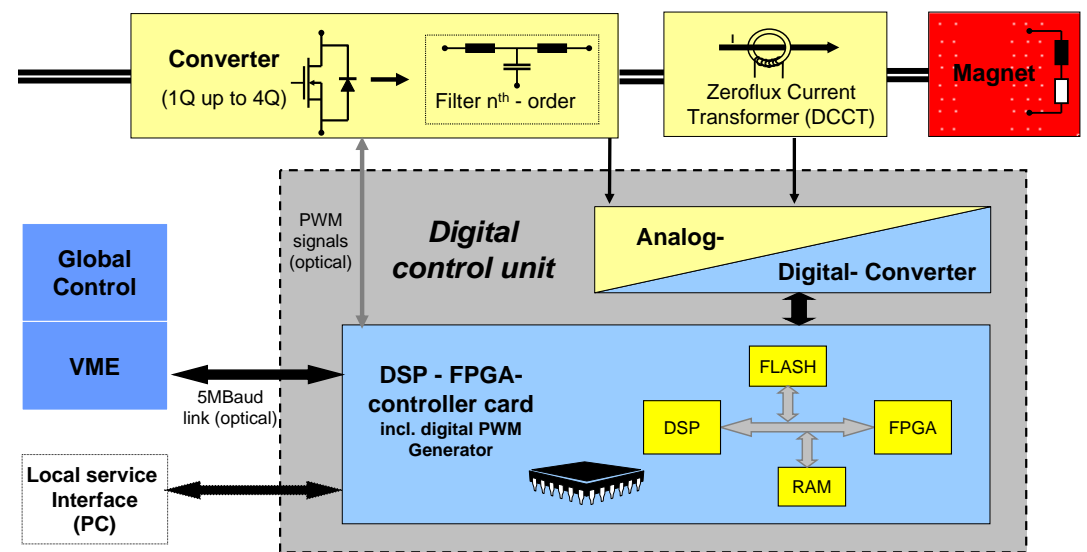


Fig 3.4.5.2: Digital Power Supply Control System (DPC).

The sextupole magnets, some quadrupole magnets and most of the corrector windings integrated in the dipole magnets are energized by 10A PSs according to fig. 3.4.5.3 and 20A PSs according to fig. 3.4.5.4. Each PS is installed in a 19' module and has its own AC/DC-converter. These PSs are already built and in operation at the SwissFEL Injector Test facility. Optionally the current feedback can be realized with a high-precision ADC, if the stability requirements are very high. One 20A- or two 10A-PS are controlled by one DPC controller with a serial optical link to the EPICS control system. Up to 7 such 19' modules are installed in a rack. For reliability reasons, fans are omitted wherever possible. The controllers as well as the DC/DC-converters are designed to operate with free convection cooling.

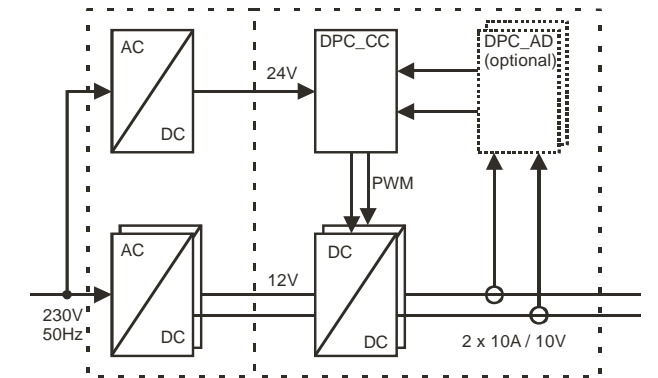


Fig. 3.4.5.3: Converter concept 2*10A.

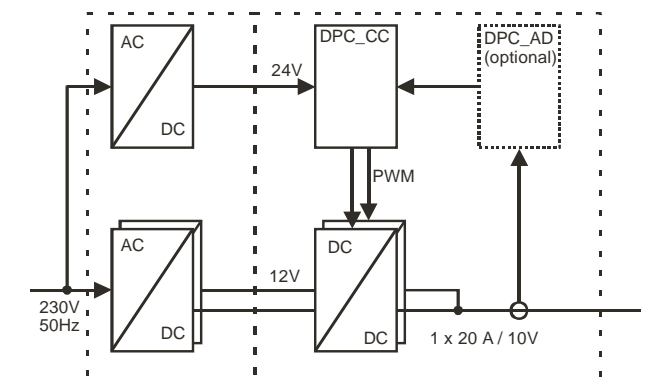


Fig. 3.4.5.4: Converter concept 20A.

Each of the quadrupole magnets QFD, QFF and QFM has three windings, one quadrupole- and two corrector-windings. The quadrupole windings are rated 10A for the QFD- and QFF-magnets and 50A for the QFM-magnet respectively. All corrector windings are rated 10A. These magnets are energized from 3*10A PS according to fig. 3.4.5.5 and 50A+2*10A PS according to fig. 3.4.5.6. Optionally one channel of the triple PS (usually the one connected to the quadrupole winding) can be equipped with a high-precision ADC, if the stability requirements are very high. The triple PS is controlled by one DPC controller with a serial optical link to the EPICS control system. Up to 7 PS 3*10A and up to 4 PS 50A+2*10A can be installed in a rack, which contains a common DC link for all the converters. The DC link voltage can be adjusted as required, allowing the DC/DC converters to operate with a reasonable modulation index. For reliability reasons, fans are omitted wherever possible. The controllers as well as the DC/DC-converters are designed to operate with free convection cooling.

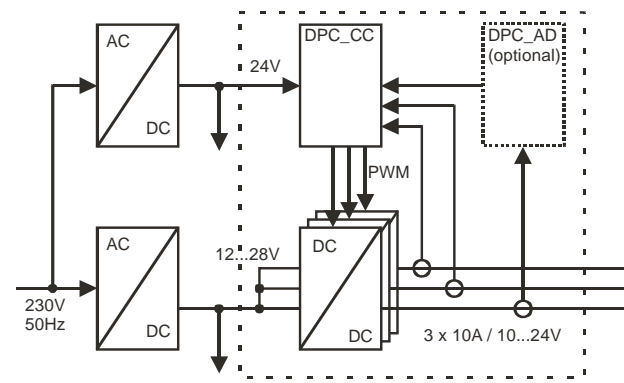


Fig. 3.4.5.5: Converter concept 3*10A.

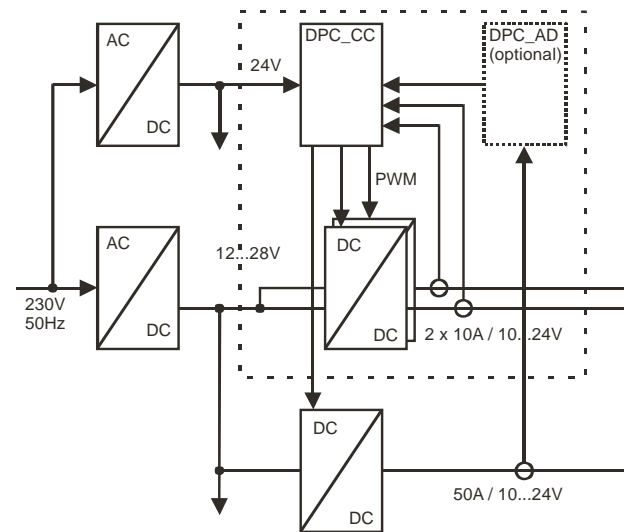


Fig. 3.4.5.6: Converter concept 20A.

The QFA magnets in the injector are built for a rated current of 150A. However, a maximum current of 50A is sufficient for the use in the SwissFEL. Therefore these 20 magnets are also energized from 50A+2*10A PS. The 10 A channels will be used to energize the neighbouring SFC magnets.

The PSs with higher current ratings are built according to fig. 3.4.5.7. They are already in service at the SwissFEL Injector Test facility and will be moved to the SwissFEL. Some dipole magnet specs are not yet known; eventually the maximum output voltage has to be adapted. Totally 6 different types are used in SwissFEL:

- PS 220A / 40V / unipolar 2 pc. per rack
- PS 220A / 100V / unipolar 1 pc. per rack
- PS 220A / 200V / unipolar 1 pc. per rack
- PS 200A / 50V / bipolar 1 pc. per rack
- PS 150A / 40V / bipolar 2 pc. per rack
- PS 150A / 110V / bipolar 1 pc. per rack

A 6-pulse diode rectifier, connected to the mains via a transformer, serves as source for the DC link. The DC/DC-converters are realized with hard switched IGBTs operating with a switching frequency of 25 kHz. Each PS is controlled by a dedicated DPC-controller and an associated high-precision DPC.

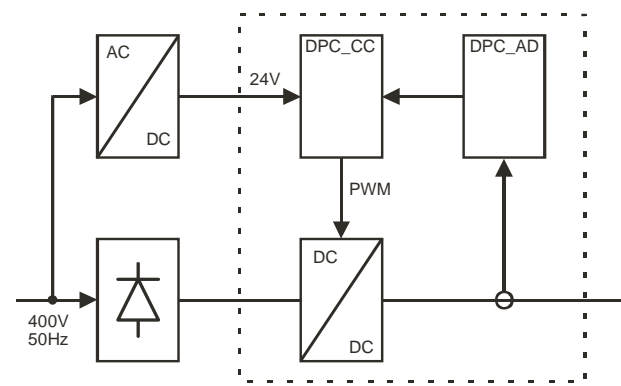


Fig. 3.4.5.7: Converter concept 150....220 A.

Figure 3.4.5.8 shows the allocation of the different PS to the magnets with rated currents of 50A and more

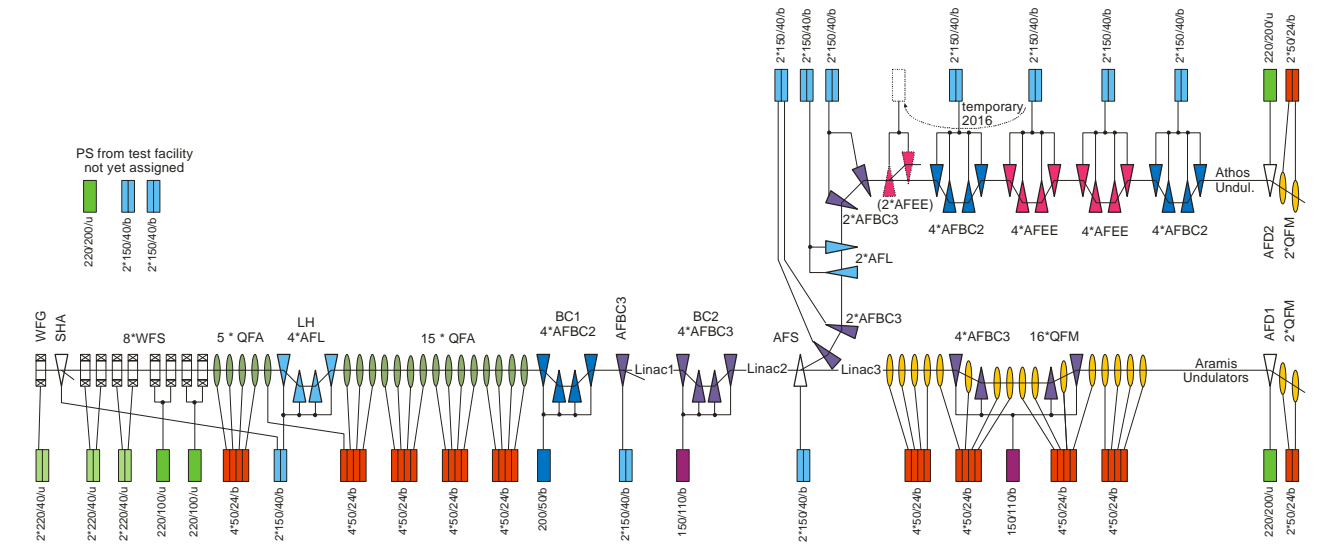


Figure 3.4.5.8: Schematic overview of SwissFEL magnets and power supplies with current ratings of 50A and more.

(large magnets) and visualizes series connections of magnets.

3.4.6 Kicker systems

SwissFEL operation is planned with two electron bunches per RF macro pulse, separated by 28 ns, at a repetition rate of 100 Hz. One electron bunch will continue through the ARAMIS undulator line, the other bunch will be deviated by the kicker system towards the ATHOS undulator line. The general approach is to use a kicker to give a small, fast deflection, then to follow with a septum magnet, which gives the large but stable angular change. From previous experience with septa at PSI, a beam separation at the septum entrance of 7mm is a good compromise.

Table 3.4.6.1: Starting parameters for system design.

Beam energy +10% system reserve	3.3 GeV
Rise time	28 ns to within system tolerance
Beam size	20 μm rms (H), 50 μm rms (V)
Deflection angle	2° (35mrad)
Deflection tolerance of system	< ±10 ppm (under discussion)
Available length	~ 8 m or ~14 m, depending on quadrupole placement

In Table 3.4.6.1, the deflection tolerance is extremely small and all possibilities will be explored to relax this. Using the principle of equipartition of errors, the toler-

ances are divided equally between amplitude and time jitter, and inversely proportional to the deflection angle; the results are shown in Table 3.4.6.2.

Table 3.4.6.2: Error Budget for Septum and Kicker.

Global Error	± 10 ppm peak-peak (under discussion)
Beam separation at septum entrance	7 mm
Approximate deflection for kickers	~7 mm / 7 m = 1 mrad
Deflection Ratio Septum: Kicker	~33 mrad / 1 mrad = 33
Septum Pulse shape	half sine or DC
Septum Amplitude Jitter, peak-peak	< ±2.5 ppm pk-pk
Septum Time Jitter, peak-peak	< ±2.5 ppm pk-pk (reserve for pulsed septum variant)
Kicker Pulse shape	sine wave
Kicker Amplitude Jitter, peak-peak	< 33 x ±2.5 ppm pk-pk < ±82.5 ppm pk-pk
Kicker Time Jitter, peak-peak	< 33 x ±2.5 ppm < ±2.9 ppt pk-pk of full cycle time < ±161 ps pk-pk at ~18MHz

With present technology (pulsers based on thyratrons or step recovery diodes), the rise time is difficult but possible to implement. However the amplitude and time jitter values are well beyond the typical values. Conse-

quently, the kicker will be implemented as a novel system using a high Q factor lumped-element resonator with a resonant frequency of ~18 MHz, phase locked to the linac RF and driven by high voltage MOSFETs. With the high Q resonator, the jitter specification should be achieved. The general parameters for the septum and kickers are found using the program MAGNET, and the results are given in Table 3.4.6.3–4. The septum can be either pulsed or DC and the final choice is dependent upon stability considerations. The septum gap is made arbitrarily small to give low current, magnetic forces and magnetostriction, with the aim of maximising mechanical stability.

Table 3.4.6.3: Septum parameters.

Parameter	Given	Derived
Maximum particle energy, E	3.3 GeV	
Magnet gap length, l	1.5 m	
Angle	35 mrad	
Bending radius		42.8 m
Field intensity		256.9 mT
Magnet gap width, w	50 mm	
Magnet gap height, g	6 mm	
Number of turns on magnet	1	
Magnet inductance		15.71 μ H
Peak current		1.23 kA-t
Energy in magnet		11.8 J

Table 3.4.6.4: Kicker parameters.

Parameter	Given	Derived
Maximum particle energy, E	3.3 GeV	
Magnet gap length, l	500 mm	
Angle	1 mrad	
Bending radius		500 m
Field intensity		22.0 mT
Magnet gap width, w	16 mm	
Magnet gap height, g	70 mm	
Number of turns on magnet	1	
Magnet inductance		157.0 nH
Peak current		1.32 kA
Energy in magnet		234 mJ
Pulse repetition rate	100 Hz	
Resonator power loss		~300 W
Resonator voltage		~20 kV

Using the estimated lengths in the septum and kicker tables above, a possible mechanical layout in the tunnel is shown in Figure 3.4.6.1.

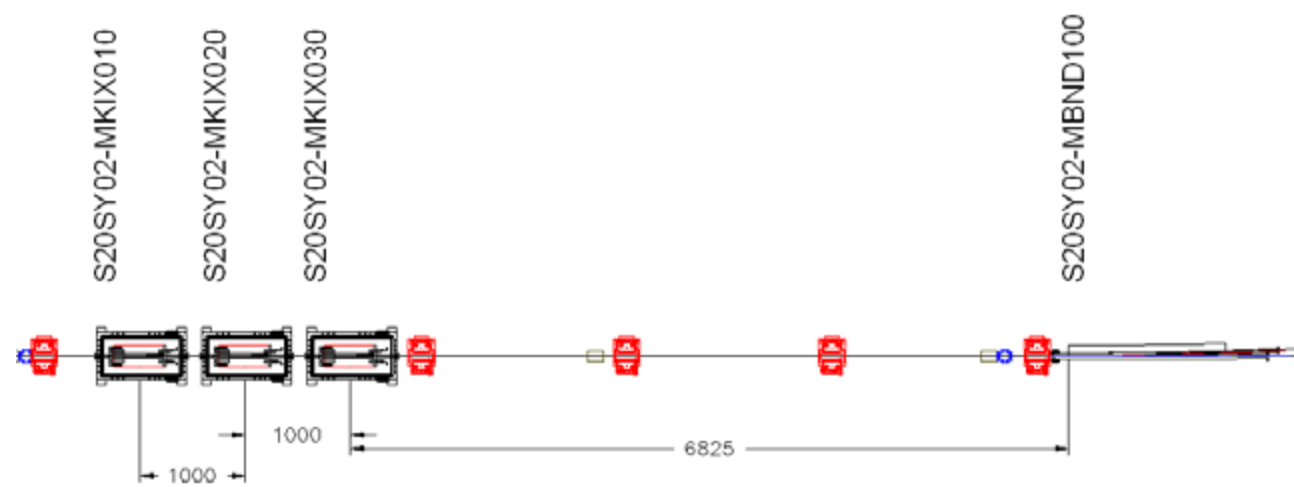


Fig. 3.4.6.1. Plan of kicker and septum layout, with intervening quadrupoles.

3.5 Undulators

The SwissFEL will have two undulator lines. The one for hard X-rays from, 7 Å (2 keV) to 1 Å (12.4 keV), with an electron energy of 5.8 GeV, is named Aramis. The second one, covering the entire soft X-ray range, from about 200 eV to 2 keV with full polarization control, is named Athos. The Athos line will be a seeded FEL line to improve spectral bandwidth, FEL power and synchronisation with external pump sources. There are two seeding schemes currently foreseen: Echo Enable Harmonic Generation (EEHG) and High Harmonic Generation (HHG) seeding schemes.

The undulator design for the Aramis line is based on PSI's experience with short-period, small-gap in-vacuum undulators, and experience with APPLE II type (**A**dvanced **P**lanar **P**olarized **L**ight **E**mitter) undulators for the Athos line.

The emitted photon wavelength is given by the following resonance condition for planer undulators:

$$\lambda = \frac{\lambda_U}{2\gamma^2} \left(1 + \frac{1}{2} K^2\right)$$

where electron energy $\gamma = E/E_0$, the period length of the undulator is λ_U and the magnetic field B . K is defined by: $K = 0.0934 \times B [\text{T}] \times \lambda_U [\text{mm}]$.

All undulators will be based on permanent magnet technology, with its well-established optimization concepts.

Electromagnetic alternatives do not deliver sufficient magnetic field strength and superconducting undulators do not yet deliver the required field quality.

3.5.1 Aramis undulator

In the hard X-ray beamlines, the photon wavelength is varied by increasing the electron energy from 2.1 GeV up to 5.8 GeV, the maximum value achievable with the present linac design. In order to produce photons with wavelengths as low as 0.1 nm at this electron energy, the undulator has a 15 mm period (U15) and a small K value of 1.2. This last choice only allows small tuning of the output wavelength, because K must be larger than 1 (for $K < 1$, there is a drop in the coupling between radiation and electron beam). However, this margin is large enough for tapering the undulator modules, to compensate for electron energy loss along the undulator, or to vary the photon energy around an absorption edge. This working point demands a magnetic field of about 0.85 T, requiring small gaps, because the field scales with the ratio of the period length and gap. To minimize the undulator length, in-vacuum undulator technology has been developed. In the vacuum chamber, a 100 μ m-thick copper-nickel coated foil covers the magnets, in order to provide good electrical boundaries, and hence low impedance. The minimum gap allowed is 3.2 mm, providing a maximum K of 1.8.

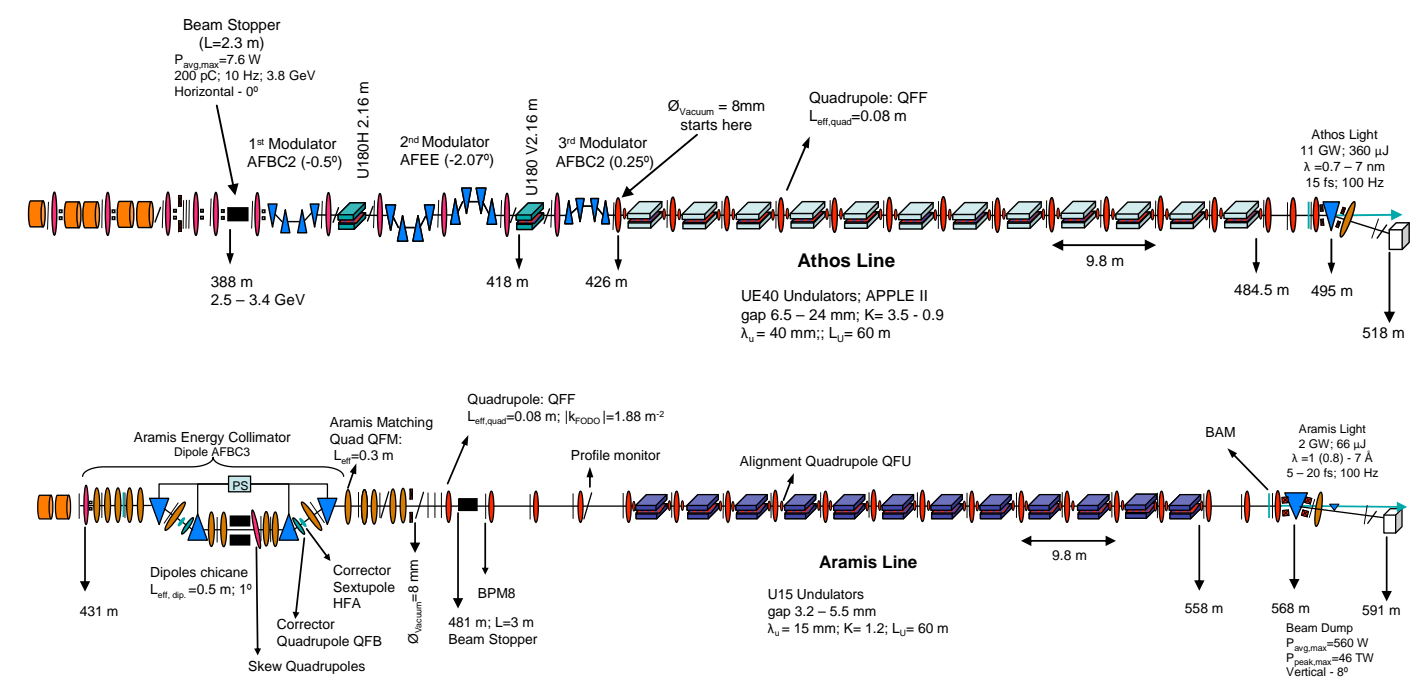


Fig. 3.5.1: Schematic layout of the undulators, Athos Line (top) and Aramis Line (Bottom).

Table 3.5.1: The main parameters of the Aramis undulators.

Requirements (Nominal Parameters for 200 pC)					Unit
Undulator Type	Hybrid – In Vacuum				
Undulator Magnetic Length	3990				mm
Number of Undulators	12				
Period λ_u	15				mm
Number of periods per segment (including ends)	266				
Nominal Undulator parameter K value	1.8	1.4	1.2	1.0	
Nominal Gap value g (*)	3.2	4.2	4.7	5.5	mm
Pole Magnetic Field B_z on axis	1.27	1	0.85	0.7	T
Magnetic Remanence B_r	1.25				T
Magnetic Coercivity H_{cJ}	>2400				kA/m
Maximum Gap	20				mm
Minimum Gap step	0.3				μm
Magnetic Material	NdFeB-Dy				
Individual Magnet thickness	4.1				mm
Pole Material	Permendur (CoFeVa)				
Thickness of Coating Foil Material Cu-Ni	100				μm
Operating Temperature (ambient)	24				deg
Weight	20000				kg
Dissipated Power (positioning motors)	0.4				kW
Electrical Interface:					
Motor Programmable Logic Control (PLC)	Beckhoff motion control				
Cooling					
	no				
Mechanical Interface					
Mechanical Drawings reference	50023.28.011				
Local magnetic field measurements method	Hall Probe				
Field integrals: Angle and Offset	Stretched single wire				
Segment Positioning method in Tunnel	Laser Tracker				
Transport Art after final alignment of magnet arrays	Air Cushion				
Vacuum					
Vacuum level	1.00E-07				mbar
Baking maximum temperature	No Baking				

* Minimum magnetic gap (Vacuum gap: 3 mm).

The magnet material has to provide a high flux density and high stability against radiation-induced demagnetization, expressed by the remanence B_r and coercivity H_{cJ} . The materials of choice are the rare-earth magnets $\text{Sm}_2\text{Co}_{17}$ and NdFeB. Samarium-cobalt is less strong, but of high stability, Neodymium-iron-boron is stronger, but generally less stable. Stability has been increased by replacing some Nd with Dy, but because the magnetic moment of Dy is opposite to Nd and Fe, remanence is lowered. One solution is to operate the undulator at cryogenic temperatures, because both parameters have

a negative temperature gradient. Recently, a new fabrication technique has been developed which provides improvements at room temperature. Dy is added at a later process step by diffusion along the grain boundaries, and it can stabilize the magnet without a negative effect on the strength. The remanence can be increased from 1.08 T, as used at the SLS undulators, up to 1.25 T (with diffused Dy) or to >1.5 T (with cryogenic undulator). For the SwissFEL U15, the material with $B_r = 1.25$ T at $H_{cJ} = 2400$ kA/m seems to be sufficient and avoids the additional complications due to the cryogenic components.

For the single-pass FEL, the good field region requirement around the beam axis is smaller than that for undulators used in storage rings. This allows narrower poles to be used, which concentrates the flux density in the centre and reduces the magnetic load by reducing the volume under the pole. With a chamfered pole, with 15 mm pole tip, and 30 mm-wide magnets, a maximum K value of about 1.4 is achievable at a gap of 4 mm, using diffused dysprosium-enriched NdFeB magnets at room temperature. The design K value of 1.2 will be reached with a gap of 4.7 mm. Using the cryogenic permanent magnet undulator (CPMU) technology, the maximum K could even be 1.75, and a K value of 1.2 could already be achieved with a 5.3 mm gap. Finally the good field region where $\Delta B/B < 10^{-4}$ is 2 mm full width in the horizontal direction and 60 μm in the vertical direction.

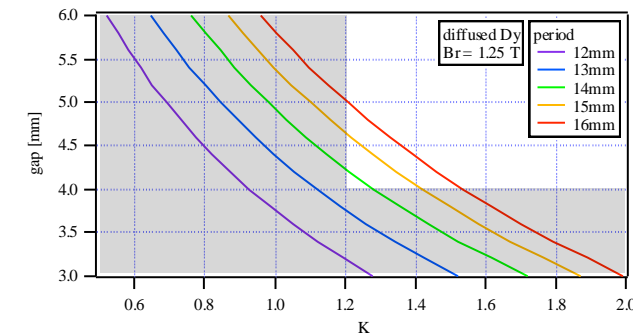


Fig 3.5.1.1: Gap versus K value for period length between 12 and 16 mm. It is planned to build a U15 with 15 mm period and recently developed NdFeB stabilized with diffused Dy. The white area is the working area: $K > 1.2$ with gap > 4 mm. A period of 16 mm conflicts with the demand of 1 Å with the maximum 5.8 GeV, and is given only for reference. A higher remanence would move the curves to the right, also allowing shorter periods.

• Aramis Undulator Matching Magnets (Ends Design):

The design of the magnet arrangement at the entrance and exit (the firsts and lasts few periods) of each undulator segment is very important since it enables the electrons to wiggle on the undulator axis without kick angle and offset. The end design of the undulator should also insure that the first and second field integrals stay at zero over the entire gap range.

The most simple design follows the scheme: $\frac{1}{2}; -1; 1; \dots$ ($\frac{1}{2}$ magnet thickness; 1 magnet thickness reverse polarity; 1 magnet thickness; ...) which results in an oscillation parallel to the axis but with an offset. The on axis wiggling can be achieved with an arrangement: $\frac{1}{4}; -\frac{3}{4}; 1; -1; \dots$ matching scheme (see Fig. 3.5.1.2). In our hybrid design this can be realized with a first magnet of half the nominal thickness.

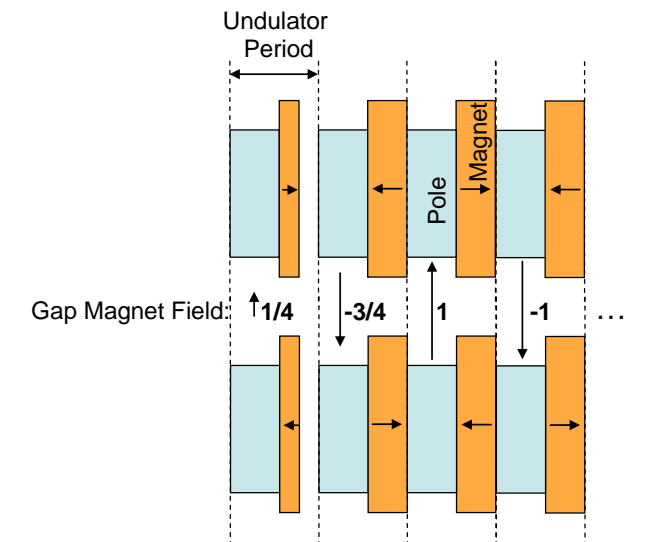


Fig 3.5.1.2: Conceptual magnet arrangement at the two extremities of each Aramis undulator to ensure that electrons wiggle around the undulator axis (no kick angle, no offset). Assuming that the field in the periodic part is driven by two magnets, the field under the first pole is about 1/4 and the field under the second pole 3/4.

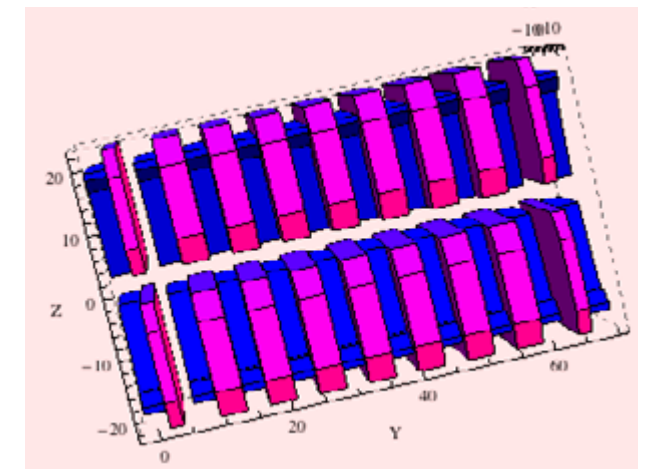


Fig 3.5.1.3: Undulator geometry with the end design foreseen for the U15 (only 9 periods are used in this simulation). The undulator starts and ends with a pole and the most outer magnets have about half the thicknesses.

Simulations of the magnetic field of the U15 undulator (using geometry of Fig. 3.5.1.3) have been performed for two different end magnet thicknesses (Fig. 3.5.1.4 and Fig. 3.5.1.5).

A thickness of half the nominal thickness results in a wiggling parallel but slightly off axis as shown in figure 3.5.1.4. Indeed, for the nominal gap of 4.7 mm, the expected axis offset after 4 m of undulator length is around 0.4 μm .

A slightly increased thickness of the end magnet (thickness $\times 0.55$) results in a wiggling more on axis, but the angle still has to be corrected (i.e. by adjusting gap of the end poles), Fig. 3.5.1.5.

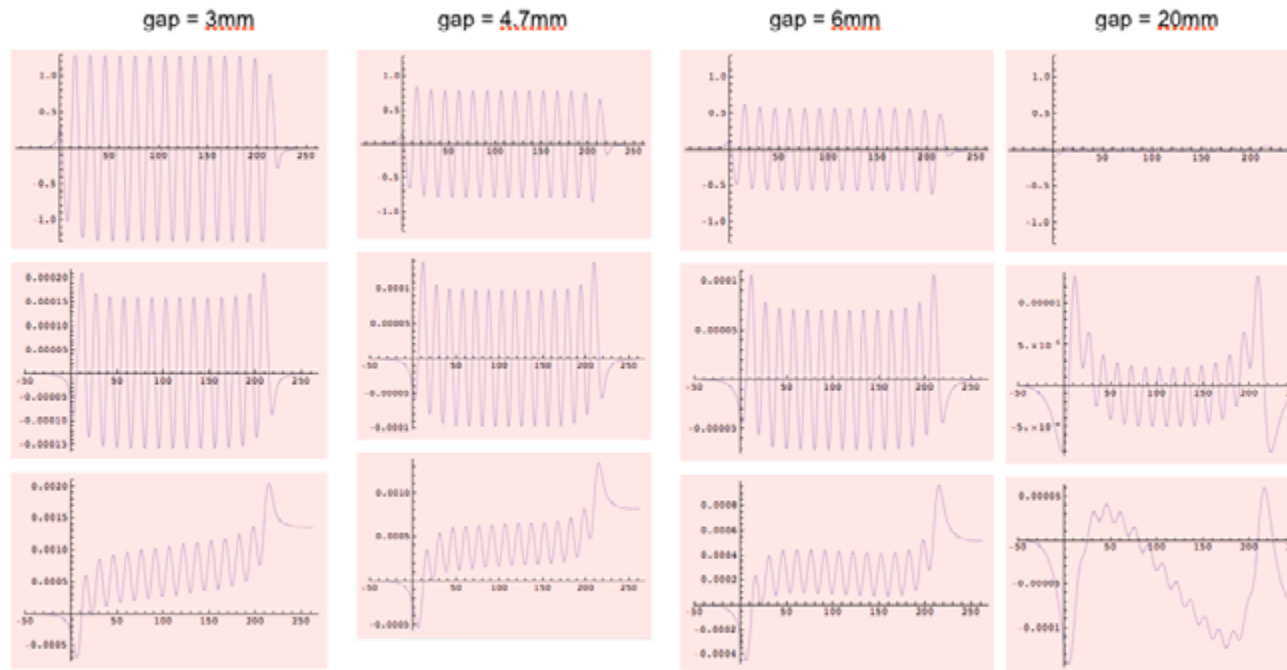


Fig. 3.5.1.4: Magnetic field (top graphs), angle (middle graphs) and trajectory (bottom graphs) calculation for the entire gap range from 3 to 20 mm. Field is given in T, angle in rad and trajectory in mm. The end magnets have a thickness of $0.5 \times 4.1 \text{ mm} = 2.05 \text{ mm}$. The calculations are done with only 14 periods instead of 264.

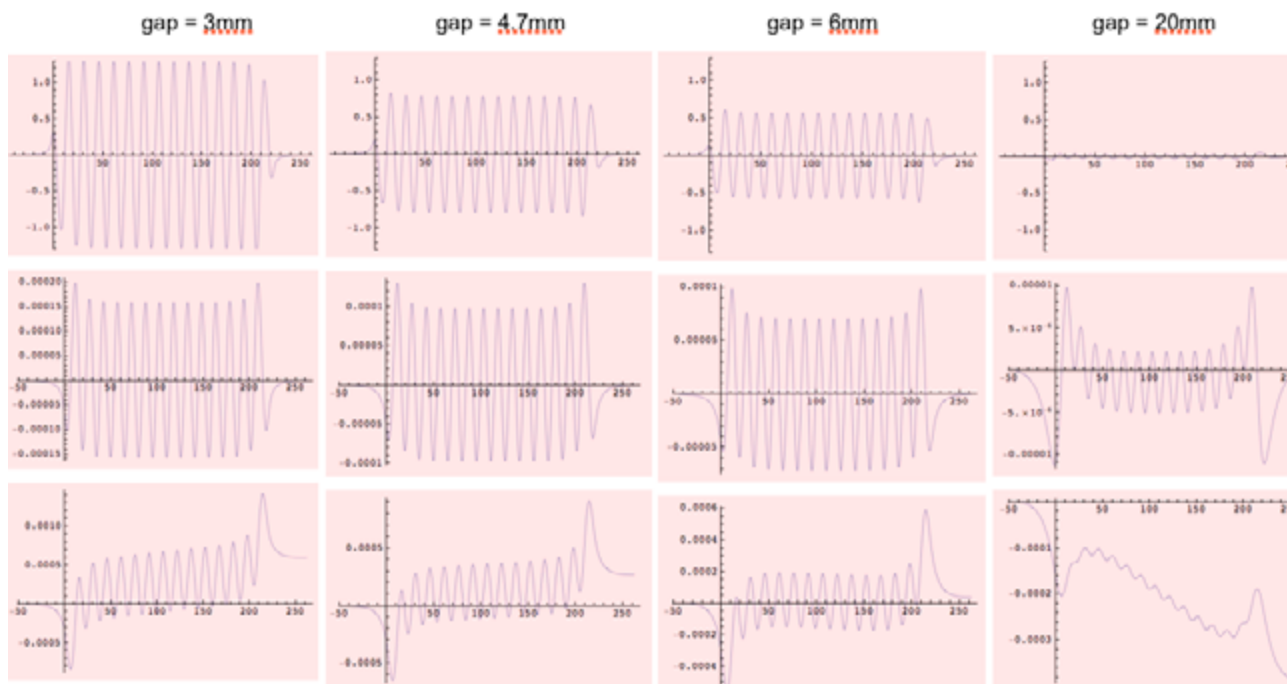


Fig. 3.5.1.5: Field, angle and trajectory calculation for the entire gap range from 3 to 20 mm. Field is given in T, angle in rad and trajectory in mm. The end magnets have a thickness of $0.55 \times 4.1 \text{ mm} = 2.255 \text{ mm}$.

3.5.2 Athos undulator

The basic concept in the layout of the soft X-ray beamline is to combine the tunability of the undulators with switchable extraction energy. An APPLE II type undulator with 40 mm period length (UE40), in combination with extraction energies of 2.1 and 3.4 GeV, is capable of covering the entire wavelength range from 200 eV to 2 keV on the fundamental harmonic, the first emission line of the undulator. The exact photon energy range depends on the maximum undulator parameter K in the various modes of operation: Linear polarization continuously changeable from $0-180^\circ$, as well as circular, which varies between 3.5 and 2.3. The extraction point is located at 3.4 GeV. For operation at 2.1 GeV, Linac 2 is not triggered and the beam is transported beyond 2.1 GeV through idle cavities up to the extraction point.

Operation of the APPLE II undulators is more challenging than with the in-vacuum undulators. Firstly, because of the different modes of operation, and secondly, the electron trajectory lies in the fringe field of the four magnet arrays. Although these pure permanent magnets have no iron poles, their magnets have a permeability which differs slightly from unity. This results in nonlinearities, which are the source of a variation in the field integrals when shifting the magnet arrays. Those nonlinearities also lead to distortions of the cosine behaviour of the magnetic field, which are responsible for small errors in the prediction of the energy and polarization. Samarium-cobalt (SmCo_5) shows significantly smaller nonlinearities. In addition, it shows a smaller temperature dependency, so that samarium-cobalt seems to be a serious candidate, although it is more delicate to handle because it is more brittle compared with neodymium-iron-boron.

Table 3.5.2: The main parameters of the Athos line undulators.

Name	U360V	U360H	UE40	Unit
Period	360	360	40	mm
Gap (magnetic)			[6.5 – 24]	mm
K	9.68	9.68	[3.5 – 0.9]	
Gap (vacuum)			$5 \cdot 10$	mm
Gap variation			32	mm
Open gap / $K\text{min}^2$			38.5 / 0.3	
Magnet size			$20 \cdot 20 \cdot 10$	
Pole size				
Remanence			1.08	
B_z / B_x			0.94 / 0.81	T
K_z / K_x			3.5 / 3.0	
Type			APPLE II	
Number of segments	1	1	12	
Segment length	2.16	2.16	4	m
Number of periods	6	6	98	

Table 3.5.3: Material parameter permanent magnets.

Material	SmCo	NdFeB		
Grade		27VH	diff. Dy	CPMU
Radiation hard	yes	yes	yes	yes
B_r [T]	0.95 – 1.1	1.08	1.25	1.5
dB/dT [%/K]	-0.035		-0.1	
Permeability	1.01/1.04		1.06/1.15	
Mech. prop.	brittle	ok	improved	improved
Suitable for	UE40	UE40	U15	U15

3.5.3 Undulator module

The expected saturation length of SwissFEL varies with the electron energy, but should not exceed 45 m. Including contingency, this means for Aramis a total length of 60 m is needed. Hence the undulator has to be segmented to allow space for focusing, beam diagnostic and electron beam corrections (see Figure 3.5.3). Undulator segments are inserted in a periodic FODO section where quadrupole magnets are separated by 4.9 m (FODO period = 9.8 m). This leaves 900 mm for the inter-undulator segment components.

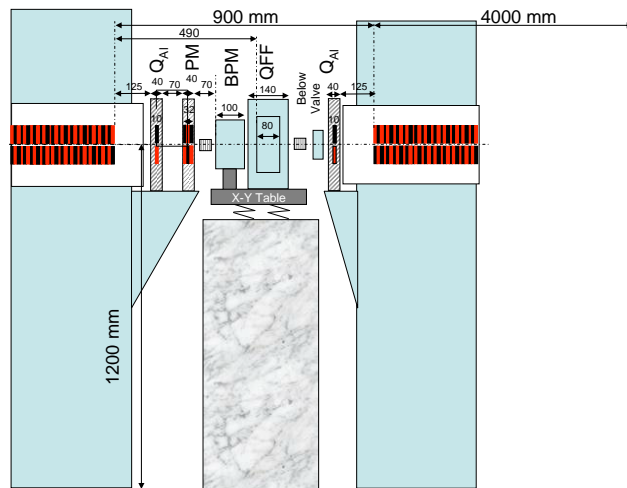


Fig. 3.5.3: Layout of the undulator module: 1 module is 4.9 m long, from left to right: alignment quadrupole (Qal), phase matching unit (PM), Beam Position Monitor (BPM); bellows; FODO Quadrupole Magnet QFF; bellows; alignment quadrupole (Qal).

An undulator module consists of a 4 m-long undulator, two 100 mm flexible taper sections, to guarantee a continuous change of the gap for the in-vacuum undulator, a phase-matching unit (PM), a cavity beam position monitor (BPM) and a quadrupole (QFF) with an integrated correction coil at the downstream side and two small quadrupoles (Qal) installed close to the undulator, one upstream and one downstream, used for undulator beam-based alignment and turned off during regular operation (or retracted in case of permanent magnet based alignment quadrupole).

The Qal are installed on the undulator frame and aligned with respect to the undulator axis in the magnetic measurement laboratory (MML). With different gaps, the axis of the Qal can move away from the undulator axis due to the changing forces on the common frame, hence the beam-based alignment should be performed with the same gap used for the magnetic alignment.

The module is completed by a bellows and a sector valve, for a total length of 4900 mm. For the in-vacuum undulator, pumping will take place along the magnet structure. For UE40, with a vacuum chamber having a tiny cross-section of $5 \times 10 \text{ mm}^2$, the flexible tapered sections can be replaced by a pumping port, so that the total length may be identical for both modules.

3.5.4 Mechanics

SwissFEL undulators are all equipped with the same frame, see Figure 3.5.5. This consists of four units, consisting of two identical pairs: the lower and the upper “base” and the two sides. This new approach increases the symmetry with respect to the classical C frame adopted for synchrotron light sources and allows for more compact solutions. The main disadvantage is decreased accessibility to the magnet region. The functionality of the frame is also changed, and it now plays a central role in the rigidity of final magnet configuration.

In this design, the frame transfers its stiffness to the I-beam through a wedge-based gap drive system. Because the I-beam is supported over about 70% of its total length, its height can be substantially reduced with respect to the C-frame solution.

An electron beam height of 1200 mm can be realized with this concept, allowing the hosting of the vacuum vessel of the in-vacuum undulator with all of its interior components, as well as the moveable magnet arrays of the APPLE undulator. The entire module can be aligned in 5 degrees of freedom by means of the SLAC camshaft movers, which have also been used for the SLS and LCLS.

Detailed studies carried out both in PSI and by industry have confirmed that the general concept of this new frame can be further improved by making use of mineral cast material, which has better internal damping than the more popular cast iron, is not magnetic and has a lower density.

The openings on the side of the frame allow access to the magnets and to the differential screws at the interface to the in-vacuum inner I-beam, essential for magnetic optimization.

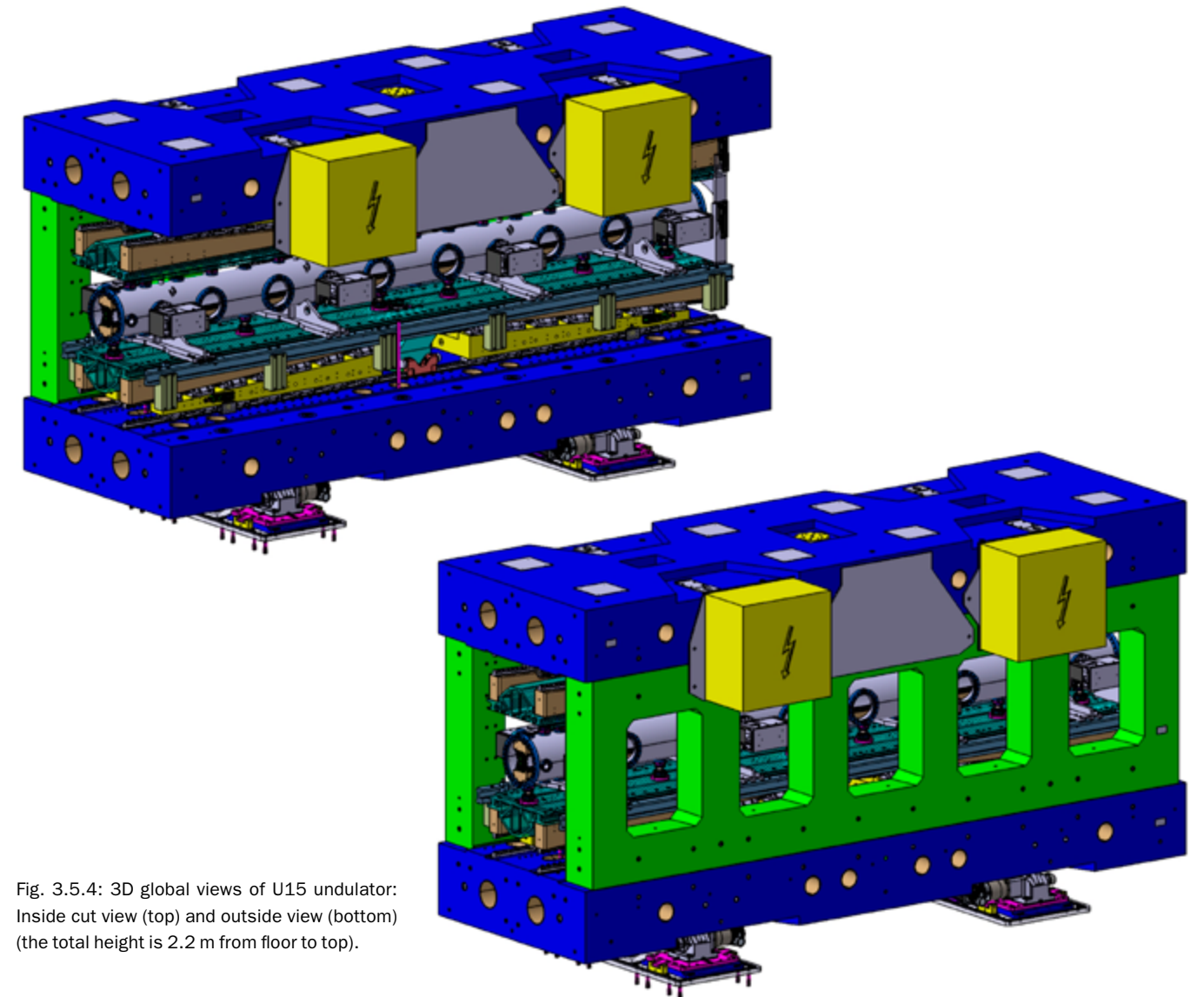


Fig. 3.5.4: 3D global views of U15 undulator: Inside cut view (top) and outside view (bottom) (the total height is 2.2 m from floor to top).

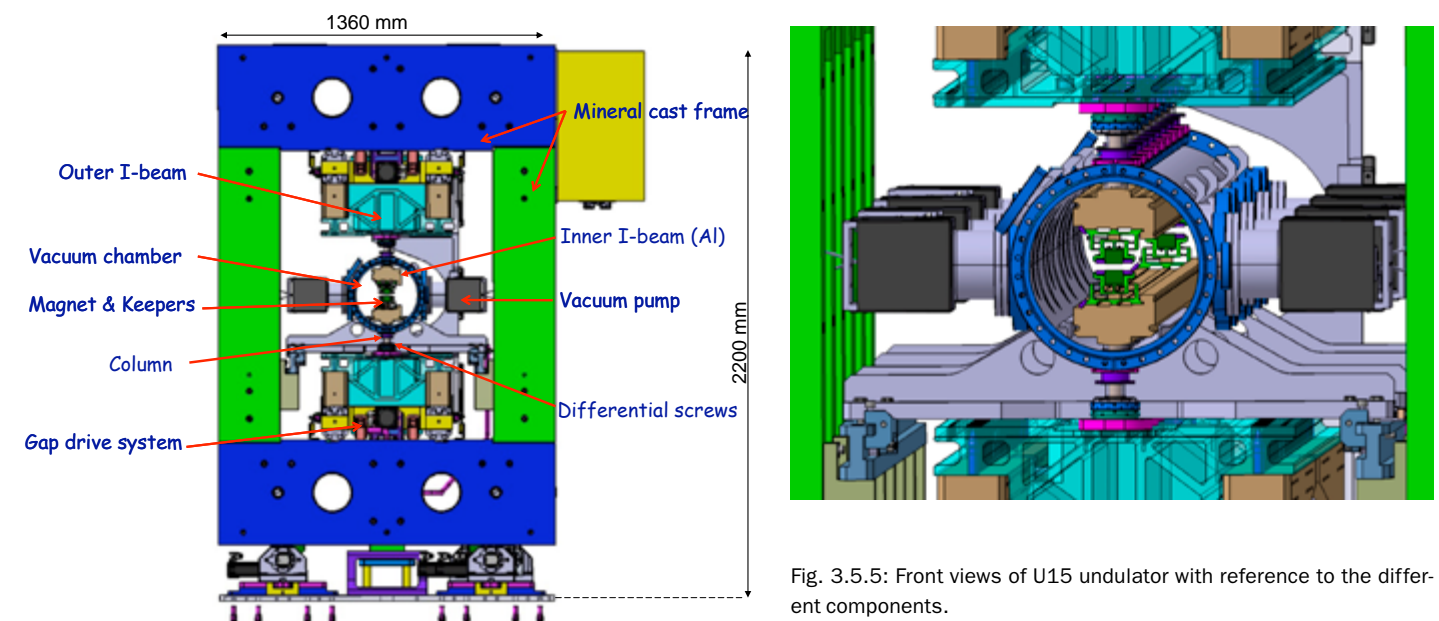


Fig. 3.5.5: Front views of U15 undulator with reference to the different components.

Besides the support structure, cost effective solutions for the keeper, which holds the permanent magnets, are also being studied. Designs of block-keeper for planar undulators based on extruded aluminum have been carried out and successfully tested. Those designs allow adjustment of magnet position with the help of a single screw to a precision of 20 μm and a similar design is being evaluated for APPLE II type undulators (see Figure 3.5.6).

In order to improve positioning precision (transversally), stiffness and cost, the 266 periods of one segment will be distributed over 12 block-keepers (Fig. 3.5.6). Each block is 33 cm long and carries 22 undulator periods. The block-keepers are made out of extruded aluminium and every magnet-pole pairs are bolted on the keeper but can still be adjusted vertically independently from neighbouring periods. The keeper is a flexor system and is preloaded by the wedge below the magnets. With the screw up to $\pm 30 \mu\text{m}$ can be continuously adjusted.

The magnets are held by the blue clamps. The poles are clamped by two screws from the left and the right which allows a horizontal adjustment and hence a correction of the horizontal field. First the vertical trajectory will be corrected and then horizontal trajectory and phase with the wedge.

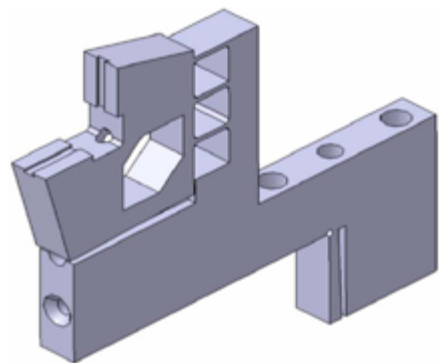


Fig. 3.5.7: Preliminary ideas for the keepers of the PM Apple II undulator Athos.

In figure 3.5.7 a preliminary design for a keeper of an APPLE II undulator is shown. This keeper is also adjustable in x and y.

3.5.5 Phase matching unit (phase shifters) design

In the drift, between the undulator modules, the electrons transverse velocities experience a phase shift in respect to the radiated electromagnetic wave. Such a phase mismatch causes the electrons to momentarily gain energy from the radiation field, interrupting the amplification process. The adjustable phase shifter corrects this difference before the next undulator unit.

The designs of the phase shifters for the SwissFEL hard and soft X ray beam lines are presented below, both the physical dimensions and material properties are specified together with a detail analysis of the performance. Fig. 3.5.5.1 shows the conceptual magnetic structure used for the Aramis line. It consists of five sections: 3 central magnets and 2 end cups at each extremity. The end cups thickness guarantees a zero first field integral and the trajectory is optimized with respect to a nominal GAP of 14 mm. The presence of end magnets helps to reduce the longitudinal stray field (see Fig. 3.5.5.4 Top) which could perturb the components sitting close to the phase shifter.

Both designs have been realized with Samarium Cobalt which has a residual magnetization of 1.1 T, and lower non-linearity in comparison to the NdFeB. It is also less

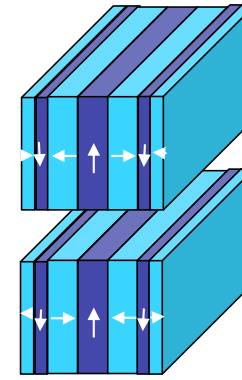


Fig. 3.5.5.1 Conceptual Phase Shifter magnetic structure chosen for both the hard and soft X-ray beam lines.

sensitive to temperature variations. The calculations have been made for the nominal K values of 1.2 and 3.5 for Aramis and Athos beam-line respectively.

• Aramis phase shifter design

Fig. 3.5.5.2 shows the 3D model of the Aramis (U15) phase shifter together with a parameter table. The overall length (along the beam line) of the device does not exceed 36.5 mm, compatible with the allocated space (about 100 mm, see Fig. 3.5.4). The central magnet blocks are 7.5 mm thick and are identical, in shape, to the U15 magnets. The same keeper can then be used.

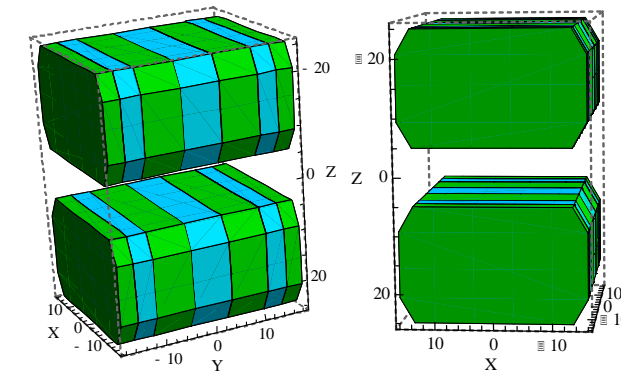


Figure 3.5.5.2: The Aramis (U15) phase shifter design, on the top the geometry of the 3D magnetic model (a) and on the bottom the summary table of the main parameters.

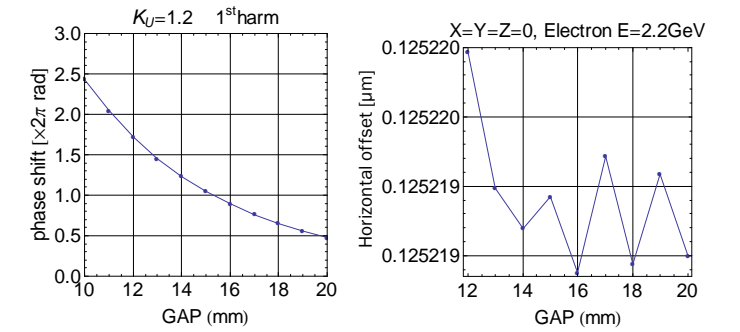


Fig. 3.5.5.3 On the left side the phase shift as a function of the GAP, on the right the horizontal offset as a function of the GAP at minimum energy. The design is optimized with respect to a GAP of 14 mm.

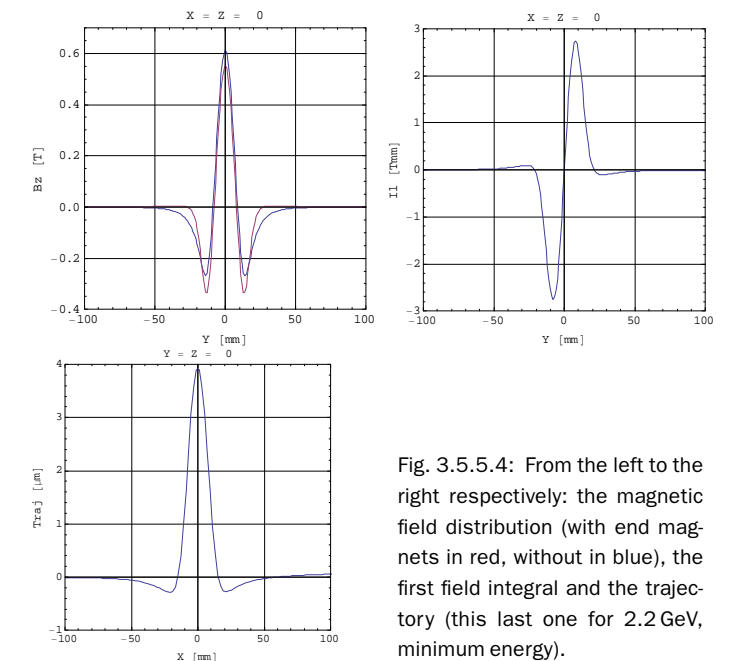


Fig. 3.5.5.4: From the left to the right respectively: the magnetic field distribution (with end magnets in red, without in blue), the first field integral and the trajectory (this last one for 2.2 GeV, minimum energy).

• Athos phase shifter design

Fig. 3.5.5.5 shows the 3D model of the Athos (UE40) shifter together with a parameter table. The overall length (along the beam line) of the device does not exceed 31.5 mm which is compatible with the allocated space (about 100 mm).

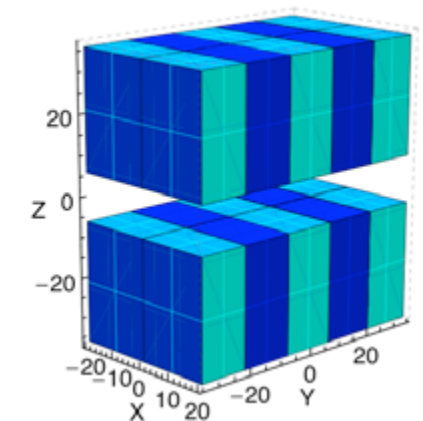
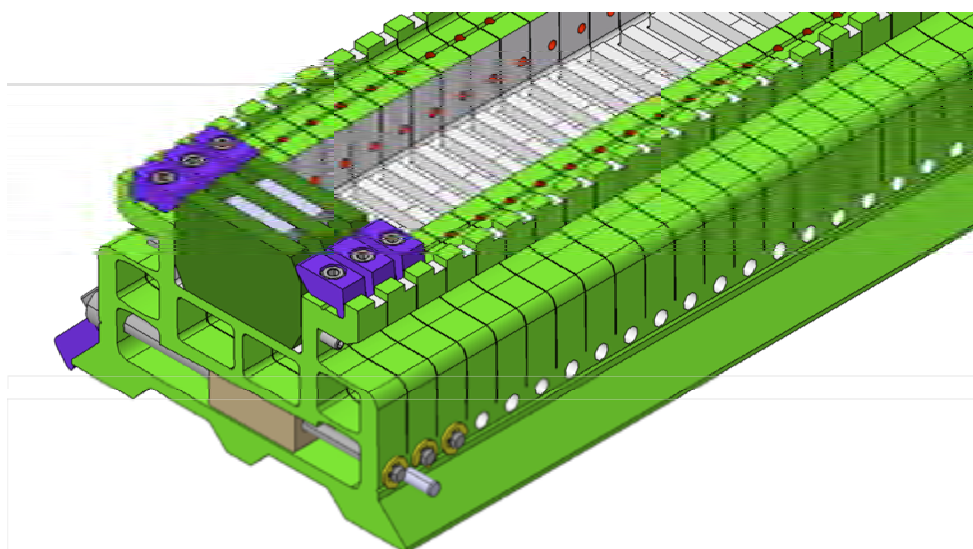


Fig. 3.5.6: 33 cm long block-keeper for 22 periods. The block is partially cut in slices (wire eroded) to allow vertical adjustment of individual pairs pole (blue)/magnet (dark green).



Parameter	Value	Unit
Pseudo-period	56	mm
Total length	< 69	mm
Magnet dimensions (TxWxH)	14 × 40 × 30	mm
Ends thickness	96.27	%
Magnetic material	SmCo	
Br	1.1	T
Non linearities	0.01 / 0.04	
Nominal gap	14	mm
Minimum gap	12	mm
Maximum gap	20	mm
d (gap) / d (phase)	8.7	μm/°

Fig. 3.5.5.5 The Athos (UE40) shifter design, on the left the geometry of the 3D magnetic model (a) and on the right the summary table of the main parameters.

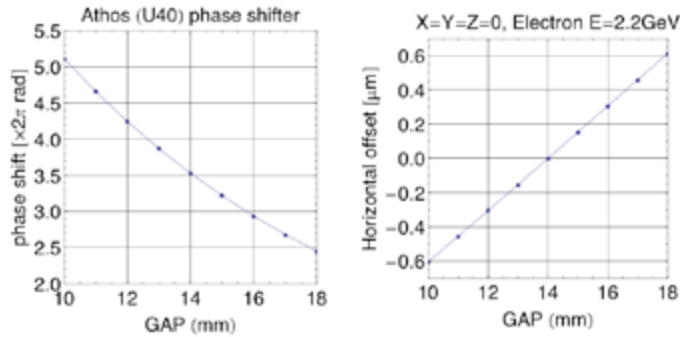


Fig. 3.5.5.6 Phase shift as a function of the GAP (left), horizontal offset as a function of the GAP at minimum energy (right). The design is optimized for a GAP of 14 mm.

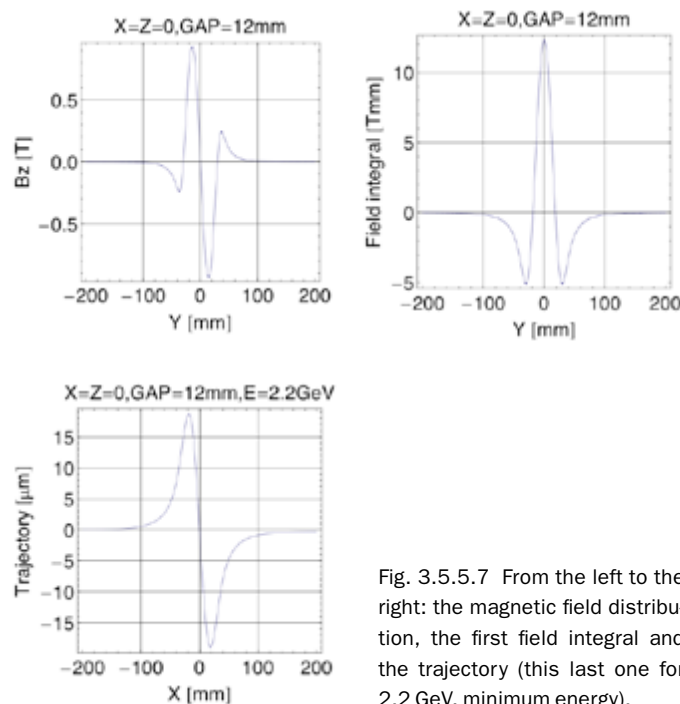


Fig. 3.5.5.7 From the left to the right: the magnetic field distribution, the first field integral and the trajectory (this last one for 2.2 GeV, minimum energy).

3.5.6 Undulator tolerances

3.5.6.1 Error sources in the undulator lines

The FEL process can be affected by two types of errors within the undulator beamline:

- mismatch in the transverse overlap between the gain – guided optical mode of the radiation field and the electron beam
- synchronization mismatch between the electron micro-bunching phase and the radiated field phase.

Table 3.5.4 summarized the calculated sensitivity of the output FEL energy on various parameters of the FEL line. Each error corresponds to a 40 % reduction in the FEL output energy and assumed that all other parameters are unperturbed (ideal).

Table 3.5.4: Sensitivity of FEL output energy on undulator parameters (Parameter fluctuations leading to 40 % FEL output energy reduction). Each tolerance assumed that other parameters are ideal (single error source) [FEL-RS06-005].

Parameters errors for 40 % FEL energy reduction (single error source):		
Undulator K detuning between 2 undulator segments (rms)	0.073	%
Undulator Vertical Misalignment between undulators (rms)	83	μm
Injection trajectory offset of electron beam in one segment / reference straight orbit (rms)	11.7	μm
Injection angle in 1 segment between electron beam / reference straight orbit (rms)	0.78	μrad
Quadrupole Misalignment / reference straight orbit (rms)	4.6	μm

The influence of the K fluctuation within one segment on the FEL pulse energy is illustrated by figure 3.5.6.1. The shorter is the period of fluctuations and the smaller is the FEL energy loss. For example, for a $\Delta K/K$ of 0.6 % with a modulation period of $Lu/2$, the FEL energy is two times higher than if the modulation period is $Lu/3$. Long modulation period means longer distances of non-overlapping beam/radiation which is detrimental to FEL process. For Aramis undulators, the local $\Delta K/K$ from magnet to magnet will be adjusted through the keeper and the long range variation ($< Lu/2$) can be adjusted with the I-beam columns support (also adjustable when the magnet array is installed in the vacuum vessel).

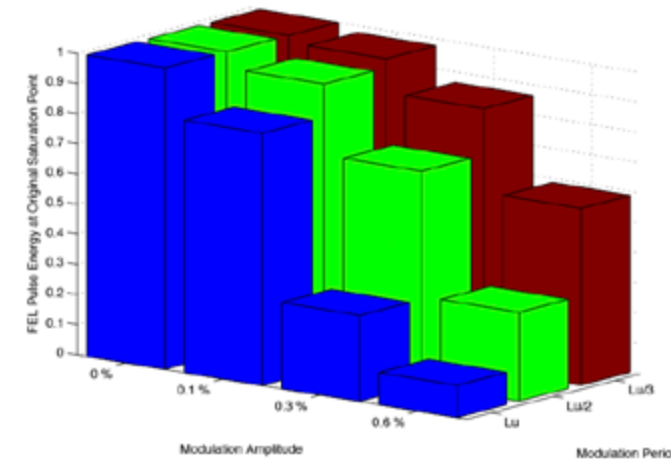


Fig. 3.5.6.1: Loss of FEL pulse energy in function of the $\Delta K/K$ amplitude and period over one segment of length Lu .

In order to approach the optimum FEL performances, the undulator beamline design should be better than the tolerances listed in Table 3.5.4 (single error sources). Table 3.5.5 summarized the expected stabilities and precisions for the current undulator design and environmental parameters.

The magnetic flux density is linked via the resonance condition to the photon wavelength, and for small K value variation we have:

$$\frac{\delta\lambda}{\lambda} \approx \frac{K^2}{1 + \frac{1}{2}K^2} \frac{\delta K}{K} = \alpha \frac{\delta K}{K}$$

($K = 1 \rightarrow \alpha = 0.67$, $K = 1.2 \rightarrow \alpha = 0.84$, $K = 1.4 \rightarrow \alpha = 0.99$).

Gap variation in U15: 1 μm gap change corresponds to a relative field variation of $2.5e-4$. If the gap can be controlled with 0.3 μm precision then the corresponding change in the FEL photon energy is 1.2 eV (for 12.4 keV photons).

Table 3.5.5: Expected stabilities and precision for undulators and environmental parameters.

Expected Stability and Precision:		
Residual field integral over one segment	40	μT.m
Sensitivity to temperature dB/dT	-0.1	%/K
Air Temperature stability over 24 h and over 5 m	0.1	K
Air Temperature stability over week and over 60 m	1	K
Uniformity of K value over 1 segment	10^{-4}	
Phase shake tolerance per segment	2.5	°/λr
Mechanical tolerances for magnets /pole dimensions	20	μm
Precision in magnetic remanence Br	1	%
Good field region width (where dB/B < 1e-4)	2	mm
Good field region height (where dB/B < 1e-4)	60	μm
Minimum Gap increment (1G)	0.3	μm
Magnetic Field Resolution	1	G
Straightness of inner I-beam undulator (over 4 m)	10	μm
Magnetic Field Measurement Art	Hall Probe	
Magnetic Axis Determination Technique	stretched wire	

Table 3.5.6: Aramis Undulator individual magnet dimensions with mechanical tolerances. 20 μm mechanical precision is consistent with magnetic remanence precision.

Magnet	Dimension [mm]	Tolerance [mm]
width	32	± 0.03
height	20	± 0.02
thickness	4.1	± 0.01

3.5.6.2 Measurements and alignment of undulator magnet arrays

The alignment of individual periods of one undulator segment will be performed in the magnetic laboratory of the SwissFEL building around 100 m away of the final position of the undulator. The ambient air in the magnet laboratory will be regulated like in the undulator hall to 24 degrees ± 0.1 degrees. An air cushion vehicle is

foreseen to carefully transport the undulators (after alignment) to their final place.

Two techniques are foreseen for the alignment and characterization of the undulator segment. With a Hall Probe, the $B(z)$ will be measured along the undulator segment. The trajectory angle ($\int B \cdot dz$) and offset ($\int \int B dz^2$) is then calculated locally (at every magnet period) and corrected by vertical adjustment of the incriminated keeper support and the horizontal adjustment of the pole. This adjustment insures a good transverse overlap of the electron beam and radiated field during the FEL process.

Equally important for the FEL process is the synchronization between the radiation and the electron bunch and this requires perfect periodicity of the magnetic field $B(z)$. In consequence, the local phase variation (or the difference in electron excursion time at each period) over the entire segment is also measured and corrected also by adjusting the gap height locally.

In complement to the Hall Probe measurements, stretched wire techniques are used to determine trajectory offset and angle after a full undulator segment.

The measurements and adjustment of the local magnetic field is illustrated in Fig. 3.5.6.1 and can be summarized as follow:

- 1) A pointing stabilized laser beam defines two parallel straight lines through the undulator pointing to a position sensitive photodiode [68].
- 2) A Hall probe sliding longitudinally will measure the magnetic field variation along this laser line ($B(z)$). The laser beams are partially blocked by pinholes, so that a transverse displacement can be detected and corrected in a closed loop. The position accuracy is below the resolution of the laser-tracker ($\pm 20 \mu\text{m}$). Measurements with an external laser interferometer are under preparation.
- 3) A control system will calculate the necessary height corrections to correct the transverse trajectory and phase error.
- 4) A screwing robot will act on the incriminated keepers to change locally the gap.

This method will be tested on a prototype undulator. The semi-automatized optimization should be very fast and can so result in optimum phase error and trajectory straightness.

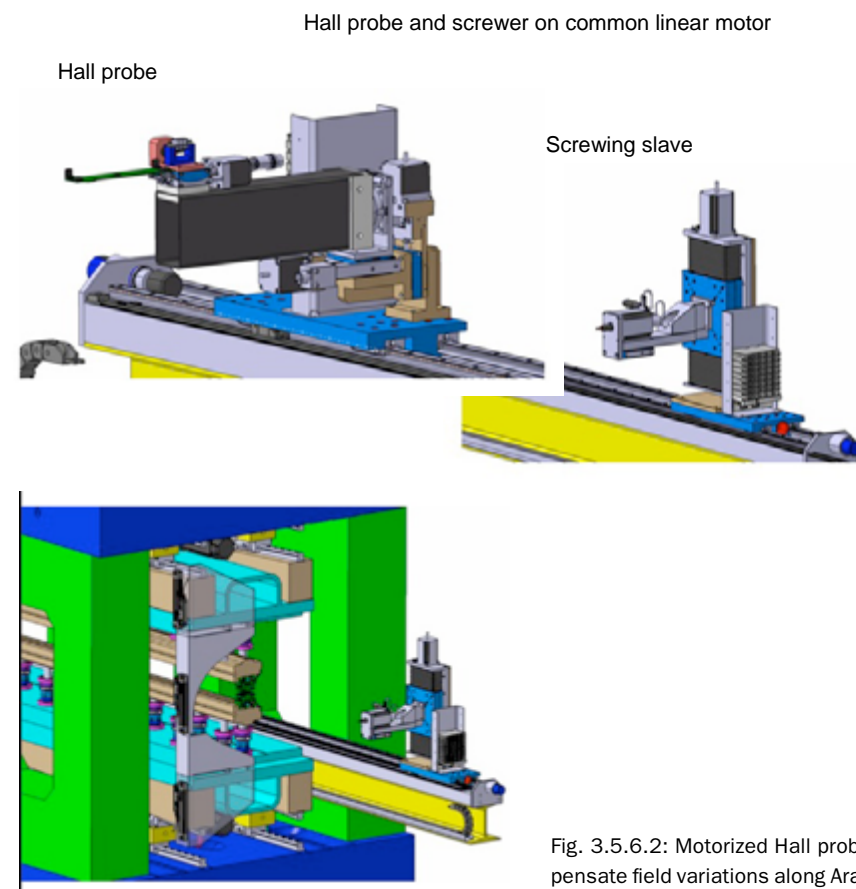


Fig. 3.5.6.2: Motorized Hall probe Measurement and adjustment of gap to compensate field variations along Aramis undulators.

3.6 Electron beam diagnostics concept

Electron beam diagnostics have to provide a full set of instrumentation for all SwissFEL operation modes, to accommodate three major tasks:

- Support accelerator commissioning and machine start-up (e.g. during SwissFEL commissioning, but also after shut-downs and future upgrades) by permitting the measurement and optimization of all electron beam parameters within an extended dynamic range.
- Provide, where possible, online information about all relevant beam parameters to the control room, to allow day-by-day operation of the SwissFEL user facility in a reliable and reproducible way.
- Provide input to a set of beam-based feedback loops, which will automatically stabilize the electron, and therefore also the photon, beam over longer time periods.

In addition, the designs of the diagnostics systems have to be robust and reliable, to enable 24h/7d operation of the final SwissFEL user facility. Wide ranges of parameters – starting with the commissioning phase and extending to user operation modes – have to be incorporated in the designs, and full integration in the control system is a prerequisite for efficient support of machine operation. High data acquisition bandwidths, low-latency data processing and data transfer (over high-speed fibre links) have to be incorporated in all of the feedback-ready monitors (e.g. beam position monitors (BPM) or synchrotron radiation monitors (SRM)). All dedicated diagnostics sections will be designed to be an integral part of the standard SwissFEL beam optics, to allow the measurement, optimization and control of beam parameters with standard accelerator settings.

Although some of the stability requirements are still preliminary at this stage of the project, the two standard SwissFEL beam optics – the so called “200 pC” and the “low charge 10 pC” modes – provide the baseline parameter set for the design of the diagnostics systems. The design approaches not only account for the SASE operation of the hard X-ray (1 \AA) Aramis beamline in the 1st phase of the SwissFEL project, but also include, from the beginning, the seeded operation of the soft X-ray Athos beamline, which will follow during the 2nd SwissFEL project phase, starting in 2018.

3.6.1 Dedicated electron beam diagnostics sections

The SwissFEL accelerator will be equipped with two dedicated diagnostics sections: one located behind the 1st bunch compressor (BC-1) (see Fig. 2.3.2.2), and the second after final bunch compression in the electron beam transport line towards the soft X-ray Athos undulator (see Fig. 2.4.1.1). Both sections are an integral part of the SwissFEL accelerator optics and will allow the measurement of electron beam parameters, which are most relevant for SASE operation – namely projected and “sliced” transverse emittances, bunch length, peak current, and “sliced” and projected energy distributions of the beam.

3.6.1.1 Low-energy diagnostics section

The first diagnostics section is located between BC-1 and Linac 1 at a beam energy of 350 MeV. Its layout follows the design approach of the SwissFEL Injector Test Facility diagnostics line [61], aiming to verify and optimize the beam parameters from the injector for matching into Linac 1. Two transverse deflecting cavities (TDC), which will be operated in the vertical direction, will shear the electron beam to provide high-resolution bunch length information. A multi-quadrupole scanning technique will be used after the TDC for measurement of the horizontal “sliced” emittance, while keeping the vertical phase advance $\Delta\psi_{\text{vert}} = 90^\circ$.

Several high resolution profile monitors (most likely combined OTR and YAG:Ce-type screen monitors) are placed 10 m downstream of the TDC to measure the transverse beam profiles, providing sufficient phase space information for reconstruction of the (horizontal) “sliced” and projected (both planes) emittances utilizing the same beam optics, when switching the TDC off. A spectrometer magnet 8 m downstream of the TDC allows the measurement of the “sliced” and projected energy distributions of the electron beam, with a resolution of the order of 10^{-4} . Table 3.6.1 summarizes the parameters for the SwissFEL low-energy diagnostics section, assuming the same β -functions and TDC performance as implemented in the SwissFEL Injector Test Facility. Further improvement of the time and “sliced” emittance resolutions will be achieved by using two TDC cavities to provide much higher deflecting voltages.

Table 3.6.1: Parameters for “sliced” horizontal emittance and electron bunch length measurements in the SwissFEL low-energy diagnostics section, using the 5-cell SW S-band TDC as in the SwissFEL Injector Test Facility.

Parameter	Symbol	Value	Unit
TDC-1 frequency	f_{TDC-1}	2.998	GHz
TDC-1 shunt impedance	R_S	2.5	M Ω
TDC-1 voltage	V_{TDC-1}	4.5	MV
TDC-1 peak input power	P_{TDC-1}	4.1	MW
TDC-1 phase (crest at 90°)	Φ	0	deg
Beam energy (at TDC-1 and screens)	E_{beam}	355	MeV
RMS bunch length (200 pC)	τ_{200pC}	409	fs
RMS bunch length (10 pC)	τ_{10pC}	200	fs
β -function at TDC-1	β_{TDC-1}	25	m
β -function at screens	β_{SCM}	5	m
Betatron phase advance TDC-1 – screen	$\Delta\Psi$	90	deg
Normalized rms core sliced emittance (200 pC)	ϵ_{200pC}	0.4	$\mu\text{m rad}$
Normalized rms core sliced emittance (10 pC)	ϵ_{10pC}	0.18	$\mu\text{m rad}$
Nominal rms beam size at screens (200 pC)	$\epsilon_{SCM-200pC}$	50	μm
Nominal rms beam size at screens (10 pC)	$\epsilon_{SCM-10pC}$	33	μm
Beam sizes at screens with TDC-1 on (200 pC)	$\sigma_{SCM-200pC}$	376 – 435	μm
Beam sizes at screens with TDC-1 on (10 pC)	$\sigma_{SCM-10pC}$	73 – 85	μm
Number of slices (200 pC)	$n_{slice-200pC}$	7 – 8	
Number of slices (10 pC)	$n_{slice-10pC}$	> 2	
Bunch length resolution (200 pC)	$\tau_{res-200pC}$	21	fs
Bunch length resolution (10 pC)	$\tau_{res-10pC}$	14	fs

3.6.1.2 High-energy diagnostics section

The high-energy diagnostics section is located in the beam transport line to the soft X-ray Athos undulator and can be operated at beam energies of 2.6 / 3.4 GeV. Similar to the low-energy diagnostics section, it will include two TDCs (most probably two C-band structures, following the SCSS design), which deflect the beam in the vertical direction, and a series of quadrupoles with profile monitors, to allow multi-quad scan for measurements of the horizontal “sliced” emittance as well as the bunch length, for peak current of the electron beam after final bunch compression in BC-2.

Table 3.6.2: Parameters for “sliced” horizontal emittance and bunch length measurements in the SwissFEL high-energy diagnostics section using a C-band, TW TDC as currently developed by SCSS [69].

Parameter	Symbol	Value	Unit
TDC-2 frequency	f_{TDC-2}	5.712	GHz
Length of TDC-2	L_{TDC-2}	1.9	m
TDC-2 shunt impedance	R_S	13.9	M Ω
TDC-2 voltage (per deflecting structure)	V_{TDC-2}	140	MV
TDC-2 peak input power	P_{TDC-2}	50	MW
TDC-2 phase (crest at 90°)	Φ	0	deg
Beam energy (at TDC-2 and screens)	E_{beam}	2.4 / 3.1	GeV
RMS bunch length (200 pC)	τ_{200pC}	46	fs
RMS bunch length (10 pC)	τ_{10pC}	2 – 5	fs
β -function at TDC-2	β_{TDC-2}	60	m
β -function at screens	β_{SCM}	10	m
Betatron phase advance TDC-2 – screens	$\Delta\Psi$	90	deg
Normalized rms core sliced emittance (200 pC)	ϵ_{200pC}	0.4	$\mu\text{m rad}$
Normalized rms core sliced emittance (10 pC)	ϵ_{10pC}	0.18	$\mu\text{m rad}$
Nominal rms beam size at screens (200 pC)	$\epsilon_{SCM-200pC}$	29 / 25	μm
Nominal rms beam size at screens (10 pC)	$\epsilon_{SCM-10pC}$	19 / 17	μm
Beam sizes at screens with TDC-2 on (200 pC)	$\sigma_{SCM-200pC}$	730	μm
Beam sizes at screens with TDC-2 on (10 pC)	$\sigma_{SCM-10pC}$	80	μm
Number of slices (200 pC)	$n_{slice-200pC}$	24 – 21 21 – 18	
Number of slices (10 pC)	$n_{slice-10pC}$	–	
Bunch length resolution (200 pC)	$\tau_{res-200pC}$	2 / 2.1	fs
Bunch length resolution (10 pC)	$\tau_{res-10pC}$	/	fs

A spectrometer magnet will permit the determination of the “sliced” and projected energy distributions of the electron beam. The beam dynamics layout of the high-energy diagnostics section still needs to be optimized and completed, but as for the low-energy diagnostics section, it is foreseen that both the (horizontal) “sliced” and the projected (both planes) emittances should be measurable without changing the nominal beam transfer optics to the Athos undulator. By using the fast beam distribution kicker to the Athos beamline already during the first SwissFEL operation phase, the TDC measurements in the high-energy diagnostics section could be

operated in a “pulse stealing mode”, providing continuous information about the “sliced” electron beam parameters even during Aramis user runs.

3.6.1.3 Aramis and Athos beam dump spectrometers

The Beam Dump spectrometers are important diagnostics for an FEL because one can measure the energy lost by the electrons to produce FEL light and thus deduce the FEL photon pulse energy. In addition, the determination of the mean electron beam energy as well as the energy spread will be performed in the beam dump spectrometer.

Table 3.6.3: Beam Dump spectrometers parameters from [70].

	ARAMIS Beam Dump	ATHOS Beam Dump
BEAM		
Nominal Electron Energy [MeV]	5800	3400
Nominal Charge per bunch [pC]	200	200
Repetition rate [Hz]	100	100
Maximum number of bunch per RF pulse	1	1
Nominal energy deposition per bunch [J]	1.16	0.68
Minimum Electron bunch length rms [fs]	20	20
Nominal Average Beam Power [W]	116	68
Minimum Beam diameter rms [μm]	10	10
Expected Energy loss due to lasing, rms [MeV]	0.5	0.5
Beam Momentum spread, rms [keV]	350 – 15000	350 – 10000
Relative Energy Spread [%]	0.006	0.006 – 0.34
MAGNET		
Bending angle [degree]	8	8
Dipole Magnet effective length [m]	2	1.5
DIAGNOSTIC		
Distance Magnet End – Screen / BPM [m]	19	19.5
Min. Momentum Spread Resolution [keV]	90	90
Min. Mean Momentum Resolution [keV] (~ 10 μm BPM resolution)	20	20

The relative energy spread to be measured varies from 6.10^{-5} rms to 0.03 FWHM for the large bandwidth mode. In addition we should be able to measure beam energy losses due to the lasing process on the order of 300 keV to 3 MeV per electron. Fig. 3.6.1.3.1 and Fig. 3.6.1.3.2 show the proposed beam optics to cover this wide range of beam momentum spread: two quadrupoles are included between the beam dump dipole and the spectrometer screens.

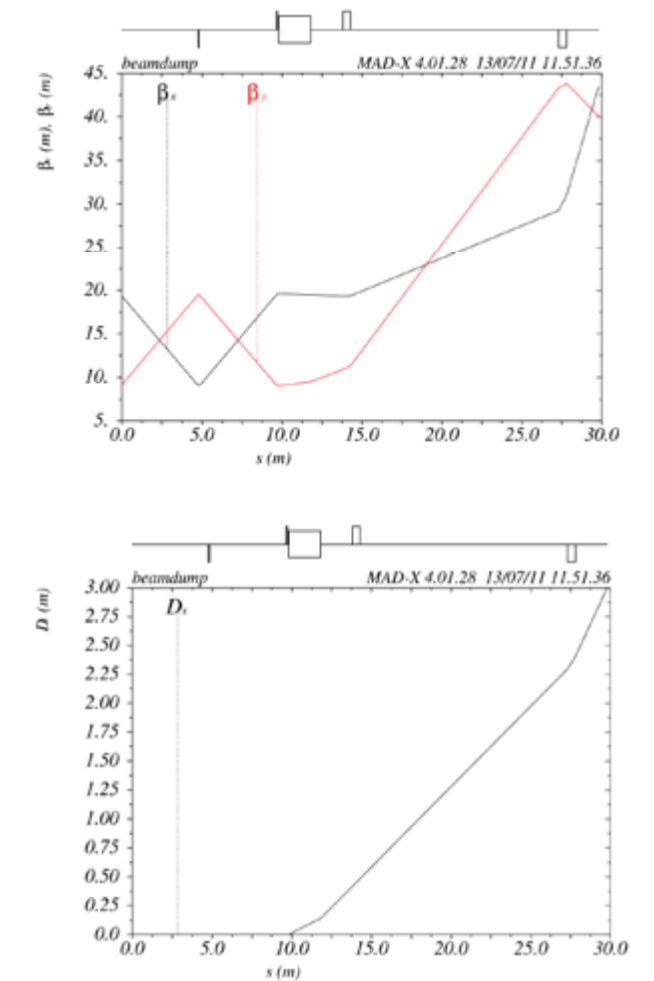


Fig. 3.6.1.3.1: Nominal mode at 200 pC: maximum vertical beam size is 200 μm rms and 40 μm horizontally at beam dump end.

Due to the large distance from dipole to screen and because of the large energy spread of the Large Bandwidth mode of operation, quadrupole magnets are required to reduce the dispersion and avoid excessive beam sizes (see Table 3.6.4). The schematic layout of the Aramis spectrometer is shown in Fig. 3.6.1.3.3, a similar layout is used for the Athos spectrometer.

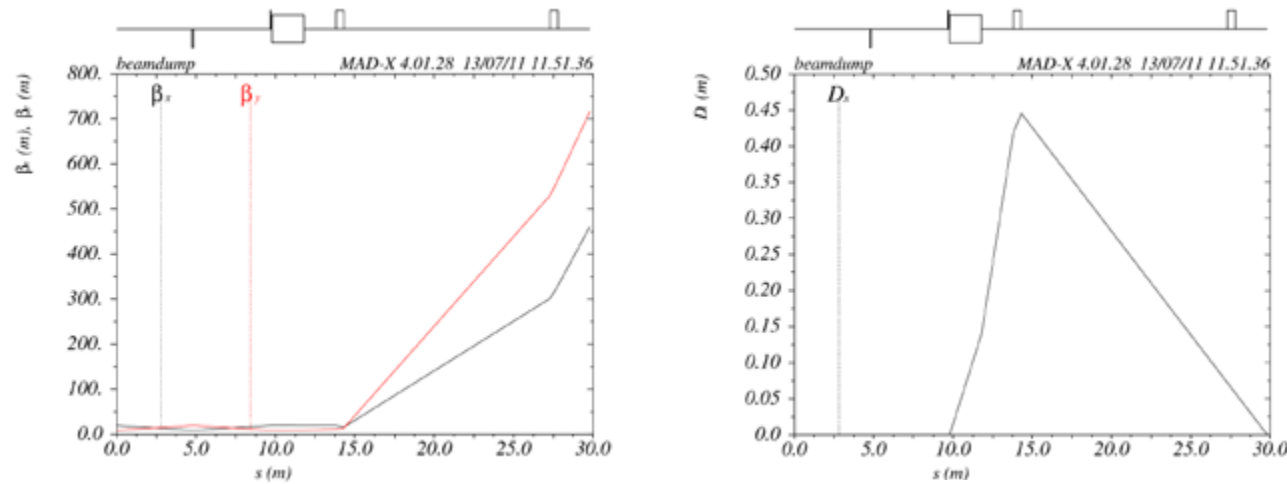


Fig. 3.6.1.3.2: Large Bandwidth mode at 200 pC: Maximum vertical beam size (at 1st quadrupole location) is 13.5 mm FWHM and <20 mm Full Width (beam is flat top shape). The maximum vertical beam size is 200 μm at beam dump end.

Table 3.6.4: Beam size evolution in the Aramis Beam Dump spectrometer for the different operation mode.

Mode	Beam Size at Aramis Dipole Exit	Beam Size at 1 st Quad Location	Beam Size at Last Screen Location
10 pC Mode	$\sigma_{x,y} = 13 \mu\text{m rms}$	$\sigma_x = 13 \mu\text{m}; \sigma_y = 15 \mu\text{m rms}$	$\sigma_x = 25 \mu\text{m}; \sigma_y = 120 \mu\text{m rms}$
200 pC Mode	$\sigma_x=20 \mu\text{m} \sigma_y = 28 \mu\text{m rms}$	$\sigma_x = 20 \mu\text{m}; \sigma_y = 40 \mu\text{m rms}$	$\sigma_x = 40 \mu\text{m}; \sigma_y = 200 \mu\text{m rms}$
200 pC Large bandwidth mode	$\sigma_x=20 \mu\text{m} \sigma_y = 750 \mu\text{m rms}$	$\sigma_x = 20 \mu\text{m}; \sigma_y = 2500 \mu\text{m rms}$	$\sigma_x = 170 \mu\text{m}; \sigma_y = 200 \mu\text{m rms}$

Beam size evolves almost linearly between the 3 z positions shown in the table.

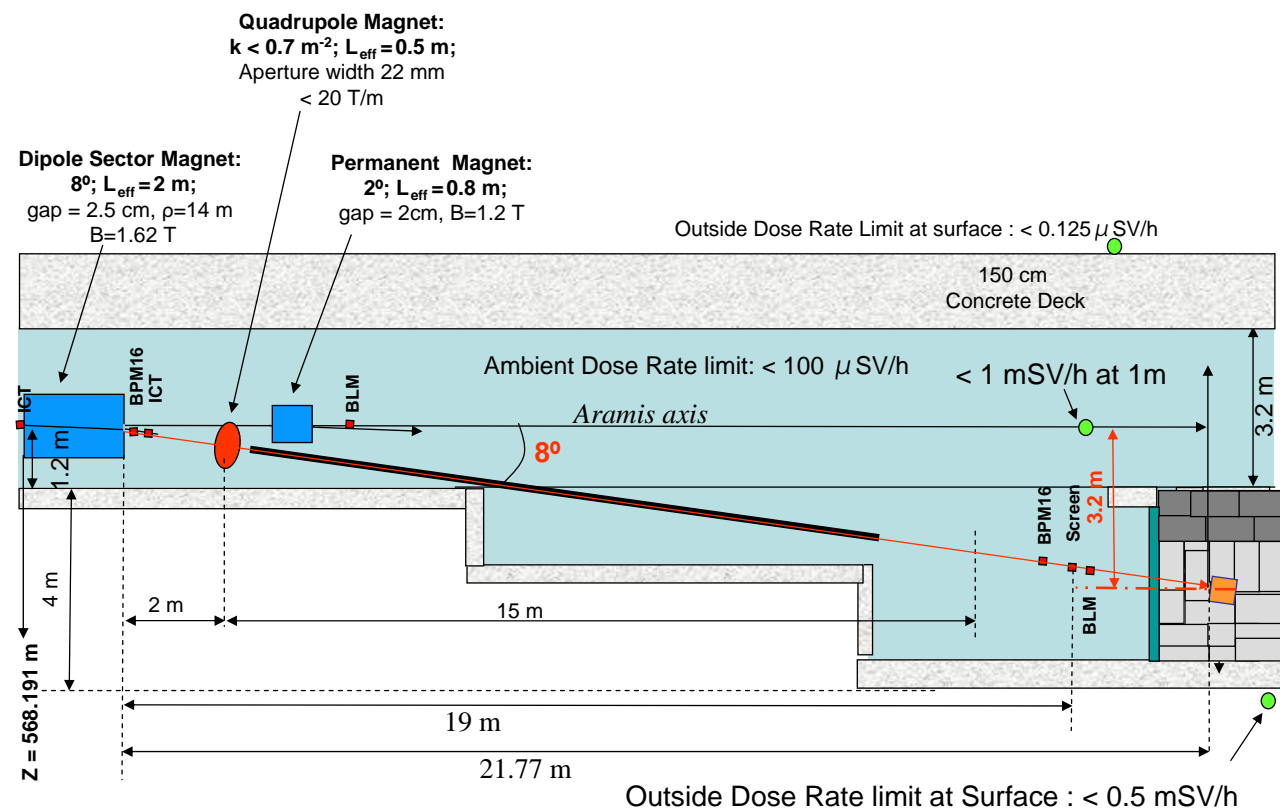


Fig. 3.6.1.3.3: Schematic layout of the Aramis beam dump spectrometer (side view).

3.6.2 Transverse beam profile measurements

Most of the beam properties which will be measured along the SwissFEL accelerator (see transverse profile measurement locations below) are related to emittance and peak brightness, and can be obtained by the determination of transverse profiles. Since, in reality, the bunch structure is often not of Gaussian shape, but contains important information in its tails, the transverse profile monitors require high resolution and a high dynamic range simultaneously. Depending on the location and the transverse beam size to be measured, the profile monitors typically consist of a combination of YAG:Ce crystals (cerium-doped yttrium aluminum garnet of 20 μm and 200 μm thicknesses) for beam finding at low beam energies and for low-charge operation and OTR (optical transition radiation) screens. They will be equipped with two types of imaging optics, providing projected pixel sizes of the order of 25 μm for an “overview path” (with up to 15 mm field of view), and <10 μm for the “high resolution path” (~2 mm field of view). Imaging will normally be performed by CCD sensors. Special CMOS sensors can image bunches separated by 70 ns, but due to rather high investment costs, these cameras will only be placed at selected locations. The screens can be inserted in the electron beam path by means of motorized linear UHV feed-throughs and absolute linear encoders (100 nm resolution) for position control. In case SwissFEL – like LCLS – also suffers from coherent OTR, all profile monitors can be equipped with wire scanners [71]. Experience with the high-brightness beam from the SwissFEL Injector Test Facility may already indicate at the start of SwissFEL commissioning if and where wire scanners will be needed.

3.6.2.1 Locations of transverse beam profile measurements

Apart from the dedicated diagnostics sections which have been described in the previous paragraphs (Sections 3.6.1.1 and 3.6.1.2), a number of additional locations for specific electron beam parameter measurements will be available along the SwissFEL accelerator. At every half FODO period of Linac 1, 2 and 3, a vacuum cube (see Fig. 3.6.2.1) will be installed beside the quadrupole. Not all of those cubes will be equipped with beam transverse profile monitors but modification of the location will still be possible in a later stage.

Directly behind the RF gun, at an electron beam energy of ~7 MeV, the projected transverse emittances as well as beam matching conditions in the injector can be determined with gun solenoid and quadrupole scans. In the case of cathode exchanges or examination (and use) of improved cathode materials, RF photo-gun performance can be optimized by means of horizontal and vertical slit scans. The slits will be installed directly in front of the S-band injector, using the distance of ~4.5 m to a profile monitor behind the 1st S-band structure as a drift space, with the accelerator structure switched off. For complete characterization of the phase space, a dipole spectrometer magnet also permits the measurement of the electron beam energy distribution from the RF gun.

Transverse beam emittances, Twiss parameters and matching conditions into the bunch compressors can be determined in front of BC-1 and BC-2 by application of quadrupole scans. The corresponding profile monitors – OTR/YAG:Ce screens, or in the case of coherent OTR,

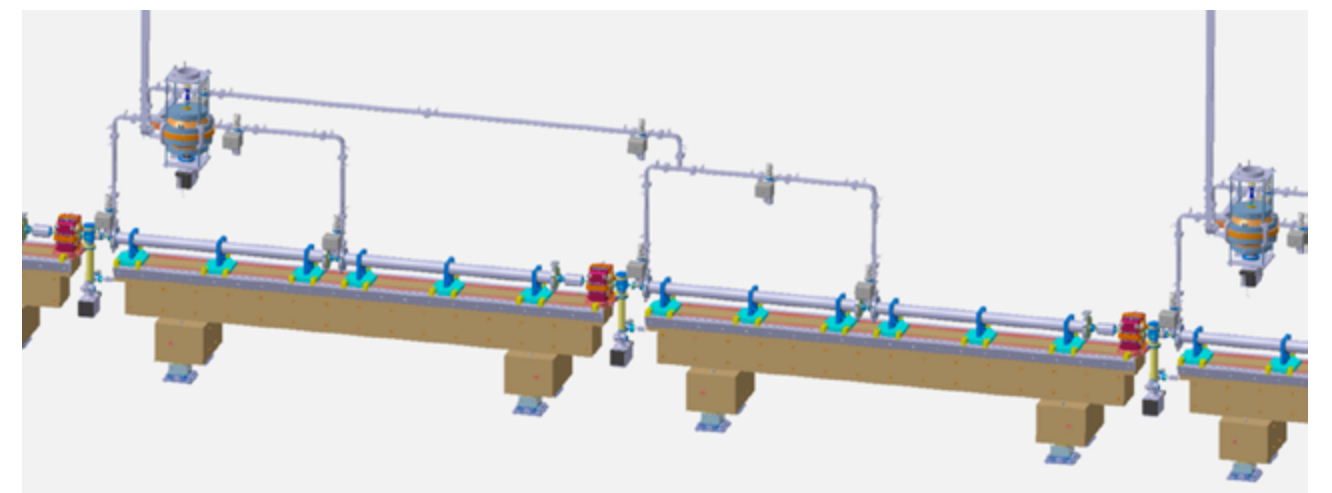


Fig. 3.6.2.1: 3D Layout of a FODO period of Linac 1. At each half FODO period a vacuum cube will offer the possibility to install a beam profile monitors.

wire scanners – will be equipped with high-resolution optics and camera systems to automatically perform these measurements during accelerator set-up and tuning.

Matching into Linacs 1, 2 and 3, as well as into the Aramis and Athos undulators, will be controlled by a number of transverse profile monitors (OTR/YAG:Ce screen or wire scanner) located within the matching sections, and at locations of adequate betatron phase advance along the linacs to identify beta-beating in case of unmatched beam optics (see Fig. 2.3.2.2; Fig. 2.3.2.5 and Fig. 2.4.1.1 for the currently planned location of screens).

The energy distribution of the electron beam after passing the Aramis and Athos undulators will be monitored in spectrometer arms using transverse profile monitors (OTR/YAG:Ce screens or wire scanners), which will be located in the corresponding beam-dump lines. In addition to the beam energy distribution during commissioning, this may also allow the monitoring of the energy transfer from the electron beam to the SASE radiation field during SwissFEL user operation.

3.6.3 Bunch compressor and longitudinal diagnostics

Accurate measurement of the electron beam position in the bunch compressor permits the implementation of energy feedback for stabilization of the previous accelerator sections. Two high-resolution cavity BPMs ($< 5 \mu\text{m}$ single-shot), with a large diameter of 40 mm, will thus be installed in the round vacuum chamber sections between the 1st and 2nd and the 3rd and 4th dipole magnets of BC 1 and BC 2, respectively. Although the dispersion in the bunch compressor arcs is only about half of the value in the BC centre (between the 2nd and 3rd dipole magnet), the excellent position resolution of cavity BPMs – especially in low-charge (10 pC) operation mode – will provide sufficient energy resolution of $\sim 5 \cdot 10^{-5}$ to stabilize the beam energy in the SwissFEL injector (BC-1 feedback) and in Linac 1 (BC-2 feedback).

Synchrotron radiation monitors will be installed behind the 3rd dipole magnets of BC-1 and BC-2, allowing continuous observation of the beam energy distribution at the location of maximum dispersion in the bunch compressors. With an imaging resolution of the order of $10 \mu\text{m}$ and the application of fast, real-time (100 Hz) image processing for determination of beam centre of

mass and energy distribution, as well as high-speed image data transfer, the implementation of a feedback loop for linearization of the energy chirp (e.g.: X-band cavity in front of BC-1) might be possible. The realization of such a feedback loop will be tested at the SwissFEL Injector Test Facility. For BC-1 and BC-2, additional transverse profile (screen) monitors will be installed between the 2nd and 3rd dipole magnets, at the locations of maximum dispersion.

Bunch compression and relative electron bunch length will be monitored with coherent synchrotron (or edge) radiation from the 4th dipole magnet of the bunch compressors. While complete reconstruction of the longitudinal bunch configuration can only be obtained by the determination of the coherent radiation spectrum with scanning [72], [73] (or single-shot [74], [75]) interferometers, a so-called bunching or compression monitor (BCM) will measure the integral intensity of a selected range of wavelengths which are larger than $2\pi\sigma_z$, where σ_z is the rms electron bunch length behind BC-1 and BC-2. A set of suitable transmission filters will thus be inserted in front of the far infra-red, and THz detectors of the BCMs for the 200 pC and 10 pC SwissFEL operation modes. Cross-calibration of the BCM signals with TDC bunch length measurements will allow the implementation of “peak current” (compression ratio) feedback. In the case of BC-1, the phase of the last four – operated off-crest – injector S-band RF structures can be regulated, while RF phases of selected C-band structures from Linac 1 can be adjusted with the BCM signal from BC-2.

In addition to TDC-based bunch length measurements, the non-destructive, online monitoring of the longitudinal current profile in the 200 pC SwissFEL operation mode will be provided by compact and robust electro-optical bunch length monitors applying the method of spectral decoding [76].

Two of these monitors are planned to be installed around BC-1. An in-house developed amplified Ytterbium fiber laser operating at a wavelength of 1050 nm, with a spectral bandwidth of about 100 nm [77], will be used in combination with a 2 mm-thick GaP crystal to observe the rectangular bunch current profile of 10 ps in front of BC-1. The use of a 500 μm -thick GaP crystal behind BC-1 will provide sufficient temporal resolution (~ 150 fs) to permit online monitoring of the compressed bunches in the control room. The EO bunch length monitors should continuously run in the background, in order to permit longitudinal feedback loops on timing, laser pulse shape and RF parameters. For non-destructive monitoring of the longitudinal bunch current profile (~ 45 fs rms) after the final SwissFEL compression stage (BC-2), the method of temporal decoding with a high-bandwidth Ti:Sa laser [78] and the use of broad bandwidth EO materials such as DAST (4-N,N-dimethylamino-4'-N' methyl stilbazolium tosylate) are presently under consideration. Tests with over-compressed bunches in the 200 pC operation mode at the SwissFEL Injector Test Facility are planned, in order to develop such a non-destructive longitudinal (bunch length) diagnostic.

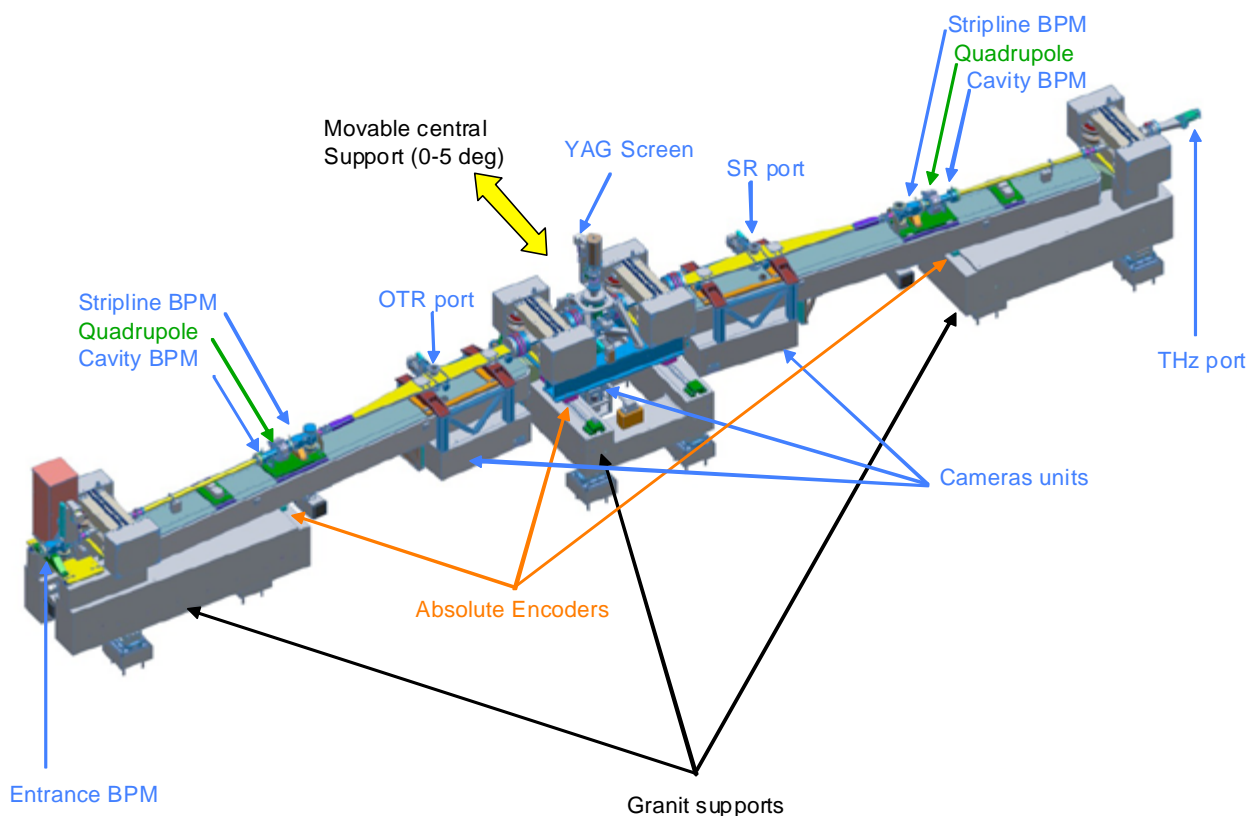


Fig. 3.6.3.1: Layout of the bunch compressor 1 as installed in the SwissFEL Injector Test Facility.

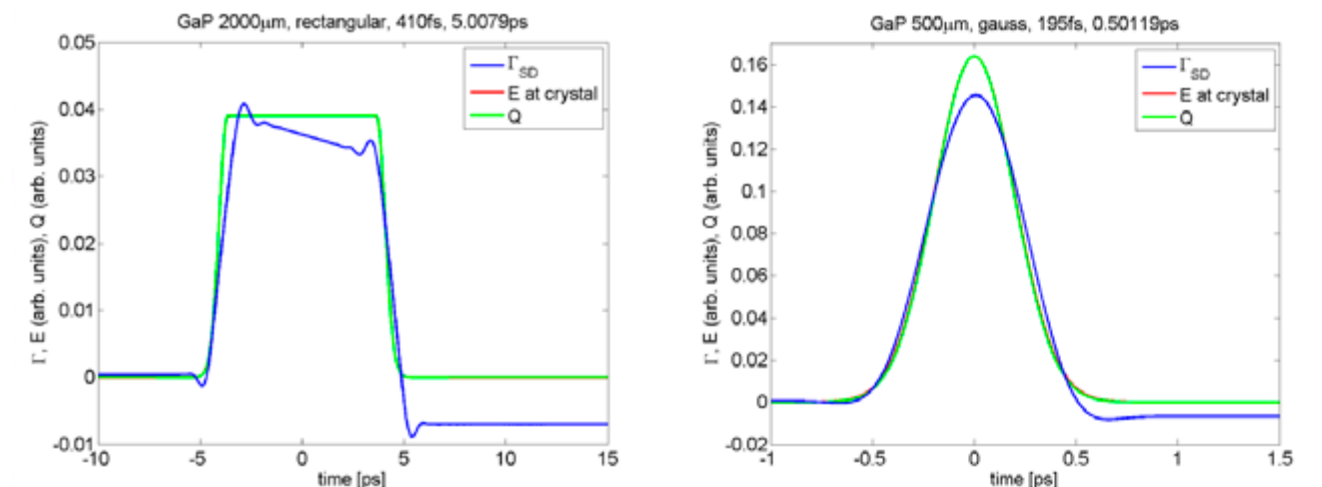


Fig. 3.6.2: Simulation of bunch length measurements applying the method of EO spectral decoding for SwissFEL longitudinal bunch distributions in front of and behind the 1st bunch compressor (simulation parameters are given in the text)

Since non-destructive single-shot bunch length measurements at very low charges (< 100 pC) and below 50 fs pose a challenge which is presently not yet solved, it is so far foreseen for SwissFEL to direct the coherent THz radiation from the 4th dipole magnets of BC-1 and BC-2 to a Martin-Puplett interferometer (scanning polarization interferometer), for determination of the bunch form factor (proportional to the square of the longitudinal charge distribution) by Fourier transform spectroscopy. Single-shot spectrometers (e.g.: [74], [75], [79]) are also under consideration and will be tested at the SwissFEL Injector Test Facility.

Measurement of the electron bunch arrival time in relation to a highly stable optical reference (optical master oscillator), with anticipated time resolution in the order of 5 fs, will be performed with an electro-optical bunch arrival-time monitor (BAM) [80]. The principle of electro-optical BAM operation is illustrated in Figure 3.6.3. The reference laser pulses from the optical master oscillator (~ 100 fs-long pulses at 1550 nm wavelength and with 214 MHz repetition rate) pass through an electro-optical modulator (EOM), which modulates their amplitude according to the applied fast transient RF signal from a high bandwidth beam pick-up, which is sensitive to the bunch transverse Coulomb field. The acquisition is performed at the zero-crossing of the pick-up signal. Any deviation due to bunch arrival time jitter will cause an offset to the reference laser pulse, which will lead to its amplitude modulation. By the use of a delay line with a high-accuracy absolute position encoder, the amplitude modulation can be calibrated with time.

Beam arrival-time resolutions of < 6 fs (rms) short term (10 min), and < 20 fs (rms) long term (10 h), have been demonstrated at FLASH [80]. The intrinsic resolution of the FLASH system was 20 fs/% amplitude modulation at 0.3% laser amplitude stability and 2 μm positioning accuracy of the encoder [81]. For SwissFEL, it is planned to improve the time resolution by the use of higher

bandwidth beam pick-ups, higher accuracy position encoders and improved amplitude stability of the reference laser. The pick-up design can be tailored to the specific needs, e.g. long-bunch, high-charge/short-bunch, or low-charge operation modes. Two pick-up designs will be tested at the SwissFEL Injector Test Facility: a button pick-up with 60 GHz bandwidth, which according to simulations has sensitivity of 1 fs/mV at 1 nC, and a waveguide pick-up with 20 GHz bandwidth and expected sensitivity of 0.7 fs/mV at 200 pC. The bandwidth can be dynamically adjusted by the use of appropriate filters to generate pick-up slopes with different steepness. In this way, both high sensitivity and large dynamic range can be secured to compensate for possible drifts over several tens of ps. High-precision position encoders (< 10 nm) are available on the market, which should also contribute towards improving BAM accuracy. Such improved BAM time resolution will be a helpful diagnostic to support stable operation of the low-charge (10 pC), short-pulse (< 10 fs) SwissFEL operation mode.

3.6.4 SwissFEL beam position monitor system

Although SwissFEL will only have one undulator in the first operation phase, for the generation of hard X-rays the machine is designed to support the future installation of up to two additional undulators for soft X-rays. SwissFEL will have bunch trains of 1–2 bunches at 50 ns spacing and 100 Hz bunch train repetition rate, with a fast kicker that distributes each bunch in the train to a different undulator. The injector and main linac BPMs will be able to measure the position of each bunch in the train individually. The fast fiber-optic links of each BPM electronics and a latency below 1ms allow the integration of the BPMs into fast transverse trajectory or longitudinal feedbacks (using dispersive BPMs, e.g. in bunch compressors) that operate at bunch train repeti-

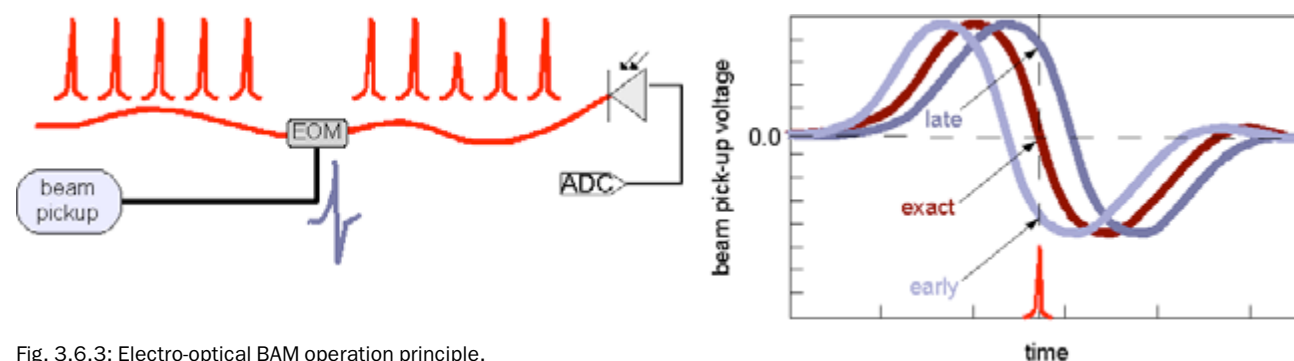


Fig. 3.6.3: Electro-optical BAM operation principle.

tion rates up to 100 Hz (see Section 3.11). The SwissFEL BPM electronics will allow remote-controlled selection of the beam charge/beam position range. For the commissioning of the SwissFEL with 1st beam and large orbit excursions, a ± 5 mm range, or more (depending on the beam charge), are possible. During standard user operation, when the beam positions are usually quite close to the BPM centre, a smaller measurement range of ± 1 mm can be used for lowest (nominal) noise and drift (both scale with the range for the chosen cavity BPM type). If necessary, it is even possible to tune the range of each BPM individually, e.g. for BPMs in special locations, such as the bunch compressor or beam dump, simply by attaching an additional attenuator to the output of the position cavity resonator (see Section 3.6.4.2 and following). The number and locations of BPM are schematically indicated in Fig. 2.3.2.2; Fig. 2.3.2.5 and Fig. 2.4.1.1.

3.6.4.1 Undulator BPM system requirements

The main challenges for the SwissFEL BPM system are the planned operation with beam charges from 200 pC down to 10 pC, and a comparatively small transverse beam dimension down to $\sigma \sim 10$ μm in the U15 undulator. The noise and drift requirements for the undulator BPMs are mainly driven by the beam-based trajectory alignment, e.g. by the dispersion-free steering (DFS) method [82] as well as by the transverse trajectory feedback system. The BPM noise and drift-per-hour requirements for the DFS method are typically of the order of $\sim \sigma/10 \cdot \Delta E/E$ [83], [84], where $\Delta E/E$ is the maximum relative energy change that can be applied during the DFS procedure. For $\Delta E/E=50\%$, this corresponds to 0.5 μm BPM position noise and drift. Assuming the noise can be improved by a factor of two using low pass filters for the BPM readings (where the improvement factor is limited by systematic effects such as differential nonlinearity of the electronics), a single bunch resolution of ~ 1 μm at 200 pC is assumed to be sufficient for the DFS method, that will be performed at the maximum beam charge for optimal resolution. The noise and drift requirements for the transverse feedback (see Section 3.11.2) are also of the order of $\sigma/10$ (~ 1 μm), but over the whole beam charge range of 10 to 200 pC. If necessary, the amount of uncorrectable high-frequency trajectory jitter and BPM noise that is modulated onto the beam by the feedback, e.g. for machine studies below 10 pC, can be reduced

by using low-pass filters or by reducing feedback loop controller gains, at the expense of a lower feedback loop bandwidth.

3.6.4.2 Undulator BPM pick-up

In order to fulfil the requirements described above, the SwissFEL undulators will be equipped with choke-mode cavity BPM pick-ups pioneered by T. Shintake et al. at SCSS/Spring8 [85]. They consist of a monopole (reference) and dipole (position) cavity that both have the same frequency for the relevant TM^{01} (monopole) and TM^{11} (dipole) modes, with the reference cavity signal being proportional to the bunch charge and the position cavity signal (with two ports per plane) being proportional to the product of charge and position. The mode-selective couplers in the position cavity suppress its undesired monopole (“common”) mode that usually limits the resolution and drift of other pick-up types. Using the same frequency for both the reference and position cavity allows the use of the same electronics design for reference and position channels. This symmetry minimizes the temperature-induced position drift that is caused by frequency-dependent drift effects of electronics components in the RF input stage, since the dipole cavity signal is normalized to the monopole cavity signal and a common-gain drift of both channels is thus averaged out.

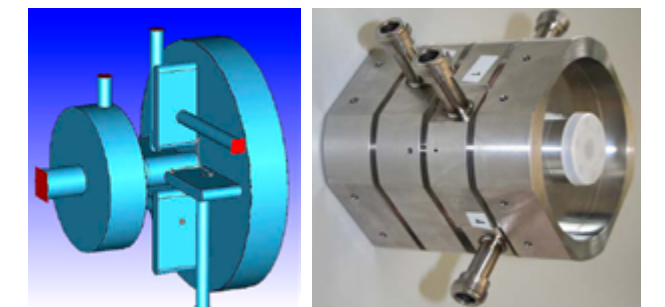


Fig. 3.6.6: E-XFEL choke-mode cavity pick-up [86]. Left: Vacuum and couplers of the reference cavity (1 port) and dipole cavity (4 ports, with mode-selective couplers). Right: 3.3GHz prototype for the E-XFEL undulators (based on an SCSS/Spring8 design by T. Shintake et al.) that will be adapted for the SwissFEL. The E-XFEL undulator pick-up has 100 mm overall length and 10 mm inner beam pipe diameter.

The pick-up and electronics will be based on a design for the European XFEL BPM (E-XFEL) that is presently being developed by a PSI-DESY collaboration within the Swiss E-XFEL in-kind contribution framework. Due to the very similar undulator BPM requirements of both ma-

chines, only a moderate adaptation of the E-XFEL system to the SwissFEL will be required in order to reach the desired performance for the 10x lower bunch charge and 4x shorter bunch spacing of the SwissFEL. First lab tests of 3.3 GHz E-XFEL prototype BPM electronics developed by PSI showed sub-micron intrinsic electronics noise at 300 pC, although the performance of the final system with beam in a real (usually more noisy) accelerator environment still has to be investigated. The theoretical thermal noise limit of 110 nm RMS at 10 pC for a 3.3 GHz cavity should, in principle, allow the required SwissFEL performance to be achieved with this pick-up frequency. However, the noise of cost-efficient, real-world electronics is typically several times higher than the theoretical limit, due to electronics and interference noise, losses in cables and analogue input stage of the electronics, etc. An increase of the frequency would reduce the theoretical thermal noise limit and should thus allow higher resolution, at the expense of higher frequency-related drift effects. Therefore the choice of the optimal frequency (which has a very small impact on the electronics design), which is expected to be in the range of 3–6 GHz, will be made after beam-based noise and drift measurements of cavity pick-up and electronics prototypes at the SwissFEL Injector Test

Facility, based on an overall optimization of criteria such as thermal noise, interference noise, drift, manpower, and hardware costs.

3.6.4.3 Undulator BPM electronics

The SwissFEL BPM electronics will use an RF front-end (RFFE) with IQ down-conversion of one reference and two (x/y) position pick-up signals to baseband. The RFFE IQ output signals for reference and position channels will be digitized by fast (~160 Msps) 16-bit ADCs and then post-processed by an FPGA carrier board that serves as control, timing and feedback system interface. The digitally programmable and tunable local oscillator (LO) in the RFFE, as well as the ADC clocks, will be locked to an external machine RF reference clock. Suitable design and digital processing techniques of the present prototype electronics allow the elimination of the impact of IQ phase and amplitude imbalance on position noise and drift. The electronics will also allow the suppression of an undesired dipole cavity signal component that is proportional to the beam angle (dominated by the cavity angle alignment error), thus reducing the required

angle alignment tolerance to a level that can be reached with common survey-based alignment techniques. A modular cost-efficient electronics design approach, consisting of an FPGA carrier board with two ADC mezzanine modules, two RFFE cards, and a common housing with power supply and fans, minimizes the effort needed to adapt the E-XFEL system to the SwissFEL, while enabling synergies with the planned SLS BPM upgrade that will use the same FPGA carrier board and similar ADC mezzanines.

and software. For the injector, the cavity frequency will be in the range of 3.3–4 GHz, in order to stay sufficiently below the beam-pipe cut-off but above the interference noise of the 3 GHz S-band linac RF, with the possibility to use a somewhat higher common frequency for main linac and/or undulator BPMs (with 16 mm and ~8 mm inner pipe diameter), in order to improve their theoretical thermal noise limit.

3.6.4.5 BPM pick-up supports and alignment

The SwissFEL undulators consist of a periodic sequence of ~4 m-long undulator segments mounted on individual girders, with a motorized 5D mover system. In between two undulator segments, a BPM and quadrupole are mounted on a separate girder (see Section 3.5.3) in order to minimize the impact of undulator gap movements on the quadrupole and BPM positions. Two additional, smaller quadrupoles per undulator are mounted on the same girder as the undulator, at its upstream and downstream ends, to allow beam-based alignment of the undulator axis, as an alternative to beam finder wires that are used, for example, at LCLS. The nominal (electric/magnetic) centres of all components on each girder will be aligned relative to each other within ~30 μm , using non-beam-based survey and field measurement techniques. Then the positions of these girders/supports (and thus of the BPMs, quadrupoles and undulator axis) will be corrected via remotely controlled movers, using beam-based alignment techniques (see Section 3.11). Since these techniques require only relative BPM position measurements and allow the BPM pick-up offset to be determined relative to the golden orbit, a dedicated non-beam-based system for the alignment of the BPM pick-ups, e.g. via laser, is not required.

As described in Section 5.4.3, the non-undulator BPM pick-ups have relaxed drift and alignment requirements. Their supports will only allow manual transverse position adjustment, with an initial survey-based alignment and an optional beam-based post-alignment by dispersion-free steering (energy variation) and quadrupole strength variation techniques that permit reduction of pick-up and trajectory alignment errors, and restrict emittance growth to the desired level. Section 5.4.3 contains further details about BPM and magnet alignment concepts and requirements.

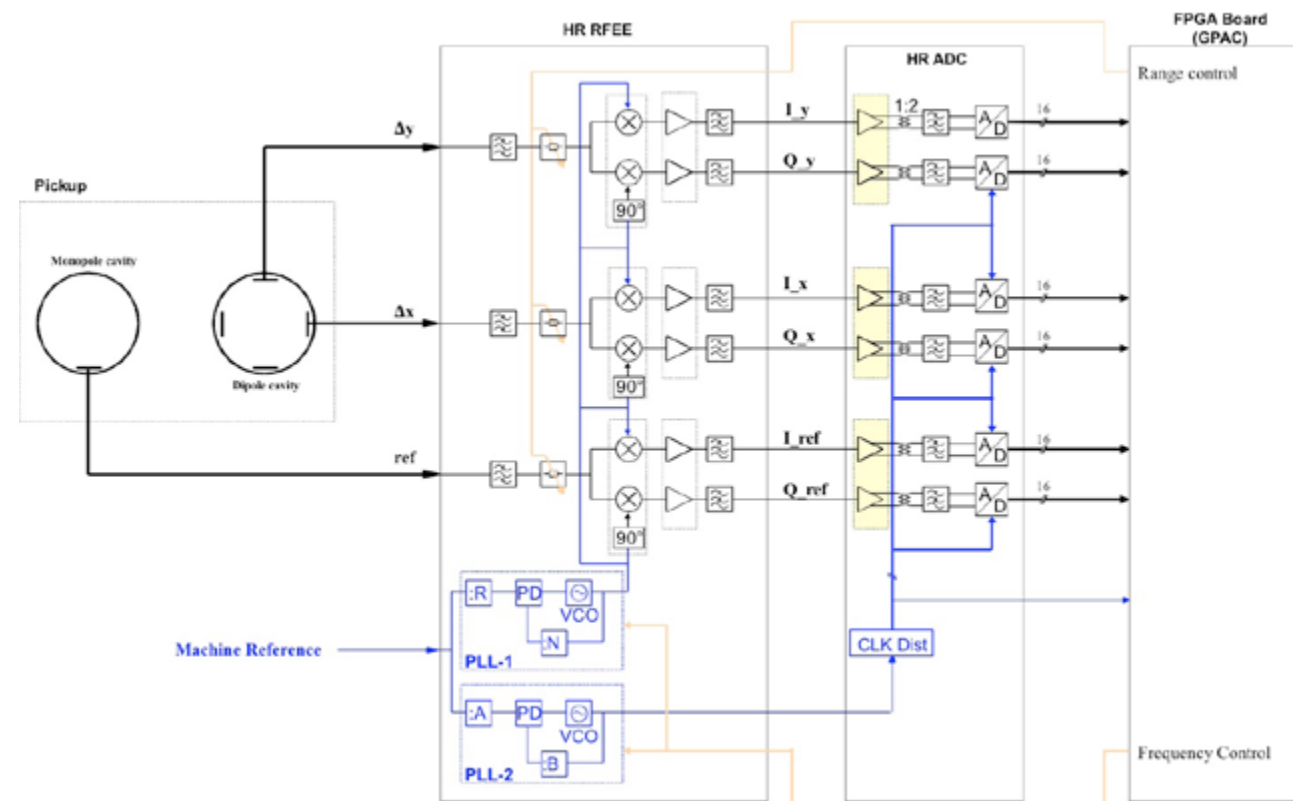


Fig. 3.6.7: Simplified cavity BPM system concept for SwissFEL and E-XFEL, consisting of cavity pick-up, RF front-end electronics, ADC and digital back-end signal processing FPGA board.

3.6.4.4 Main linac and injector BPM system

The SwissFEL main linac and injector will be equipped with the same kind of cavity BPM as the undulators (adapted to the different inner beam pipe diameter of 16 mm for the linac and 38 mm for the injector), although the electronics noise and drift may be higher (up to 3 μm at 10 pC), due to higher RFFE output filter bandwidth (for low intra-train bunch-to-bunch crosstalk), higher RF cable attenuation, and a less-sensitive pick-up design with larger pipe diameter. The highly cost-efficient design and fabrication techniques of the chosen cavity BPM design still allows much better noise and drift to be attained than alternative pick-ups, such as matched or resonant striplines, at comparable or even lower costs. While the orbit trajectory alignment requirements in the main linac are relaxed compared to those of the undulators (see Section 3.11), and thus would allow the use of suitable stripline BPMs, the higher performance of cavity BPMs still has a number of advantages. These allow precise (a few 10^{-5}) energy measurements at dispersive locations in the bunch compressors, as well as the localization of possible transverse perturbations sources that cannot be suppressed by a transverse feedback system, and thus might need to be identified and eliminated in order to achieve stable FEL operation. The low thermal noise limit also allows the exploration of machine operation modes at bunch charges below 10 pC (albeit not with nominal performance), where other BPM types could no longer achieve acceptable performance. Moreover, cavity BPMs allow the precise reconstruction of the centre-of-charge at the location of wire scanners for transverse profile measurements, even at very low beam charges, and the BPM reference cavity can serve as beam current and transmission monitor. Finally, having the same cost-efficient, high-resolution BPM type throughout SwissFEL minimizes the overall development, production and maintenance effort for pick-ups, electronics, firmware

3.7 Vacuum concept

3.7.1 Main accelerator

The detailed list of vacuum components (positions, lengths, ...) which constitute the skeleton of SwissFEL can be found in a PSI note: FEL-SL88-027 [87]. The standard inner vacuum tube diameter in the three SwissFEL Linacs will be 16 mm, with the corresponding flange size of CF 16 mm. Stainless steel will be used for the vacuum tubes and copper for the RF accelerating structures.

The C-band cavities will be connected with RF shielded bellows. The space between the cavities is limited. To achieve a short and compact bellows design, the flange size will be CF 40 mm, while the inner bellows diameter is 16 mm. CuBe will be used for the RF shield in the bellows, which also allows a smooth transition between different tube sizes.

A schematic layout for the Linac 1 standard cell is seen in Figure 3.7.1 and for Linac 2 and 3 in Figure 3.7.2. The common characteristic of all vacuum systems for the SwissFEL accelerator is the strong conductance limitation over the full length of the machine. In the three linear accelerators Linacs 1, 2, and 3, the vacuum pumps can only be installed in the wave guides of the C-band cavities. Due to conductance limitations, the effective pumping speed will be reduced to only a few percent of the nominal pumping speed.

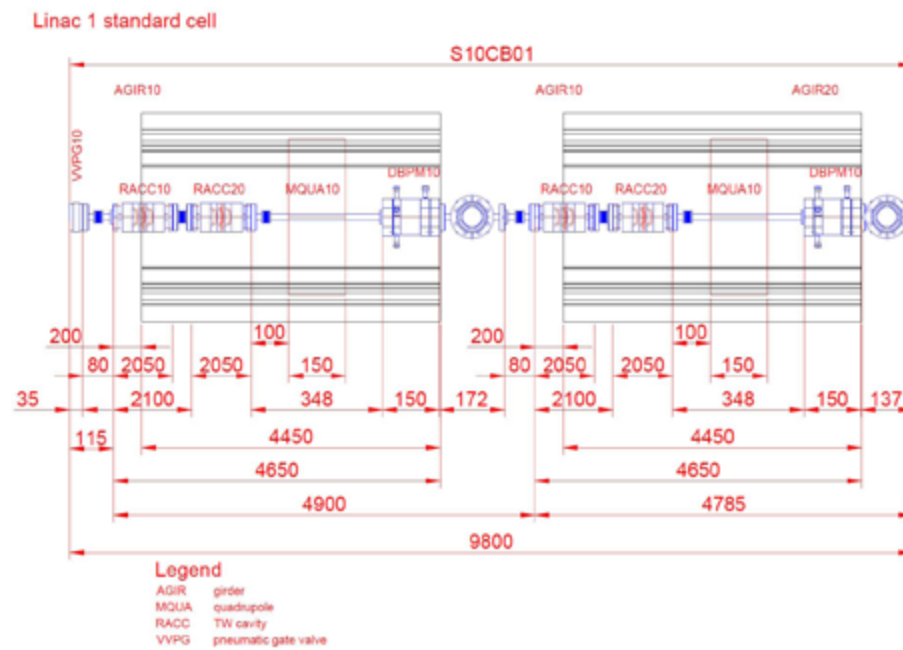


Fig. 3.7.1: Schematic layout of Linac 1 double cell (the length of the C-band cavities is compressed in this sketch) – FEL-SL88-034_0.

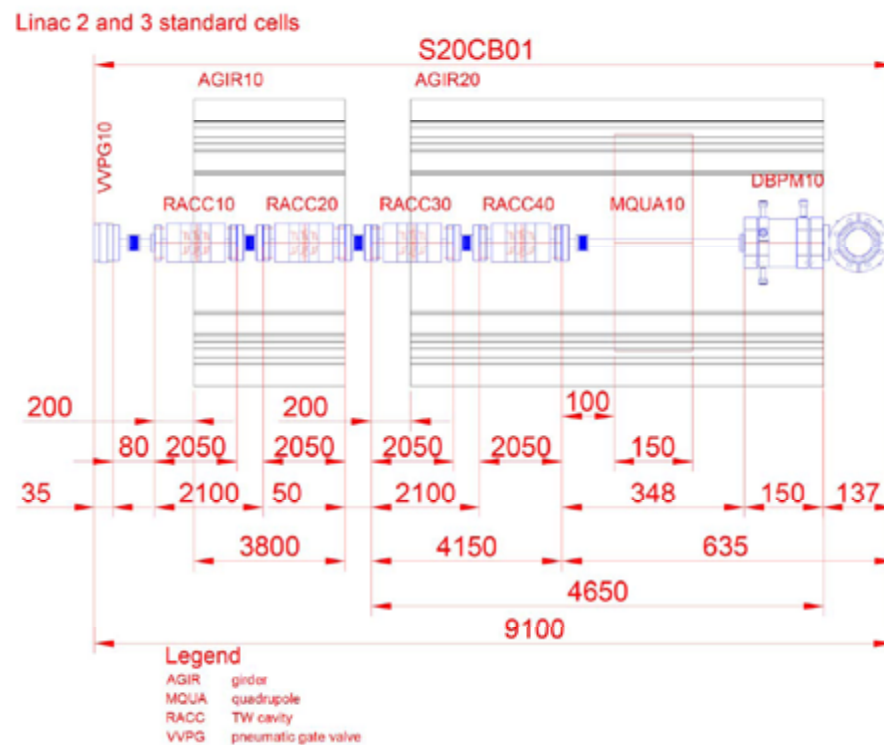


Fig. 3.7.2: Schematic layout of Linac 2 and Linac 3 cells (the length of the C-band cavities is compressed in this sketch) – FEL-SL88-035_0.

For operation of the linacs, average pressure values in the 10^{-7} mbar range are sufficient and 10^{-8} mbar are expected after baking. These pressure requirements might be relaxed, but due to conductance limitations, strict adherence to UHV standards will be essential. Therefore, in-situ bake out to remove water partial pressure will also be beneficial. Figure 3.7.3 shows the pressure distribution in Linac 1 and Figure 3.7.4 that in Linac 2. The general layout of the standard cells is equal in Linac 2 and Linac 3. A similar distribution of vacuum pressure in Linac 3 would also be expected. For pressure calculations, out-gassing rates used were 10^{-12} mbar l/s*cm² for stainless steel and 10^{-11} mbar l/s *cm² [88] for copper at 45 °C operating temperature and RF power on. It can be expected that, after a long time running with RF on, the out-gassing rate for Cu can be reduced to values of 10^{-12} mbar l/s*cm² [89].

The pressure profiles were calculated with the program VACLIN [90], which uses a matrix method to solve the linear system of equations. However, the results have to be confirmed by using a program which uses a Monte Carlo simulation [88].

The vacuum scheme for a Linac 1 double cell is shown in Figure 3.7.5, and for Linac 2 and 3 standard cells in Figure 3.7.6. No RF windows are installed in the RF waveguides, so that they are also part of the accelerator vacuum system. The cavities are pumped on each input and output coupler with a 20 l/s sputter ion pump, connected to a pump T. The pump T also allows the installation of vacuum gauges and all metal cross-angle valves which are used for roughing and venting. To save costs, all 16 sputter ion pumps which will be installed in the waveguides are connected to one pump controller.

For the separation of vacuum sections, rf-shielded all-metal gate valves are foreseen. For a cost optimized

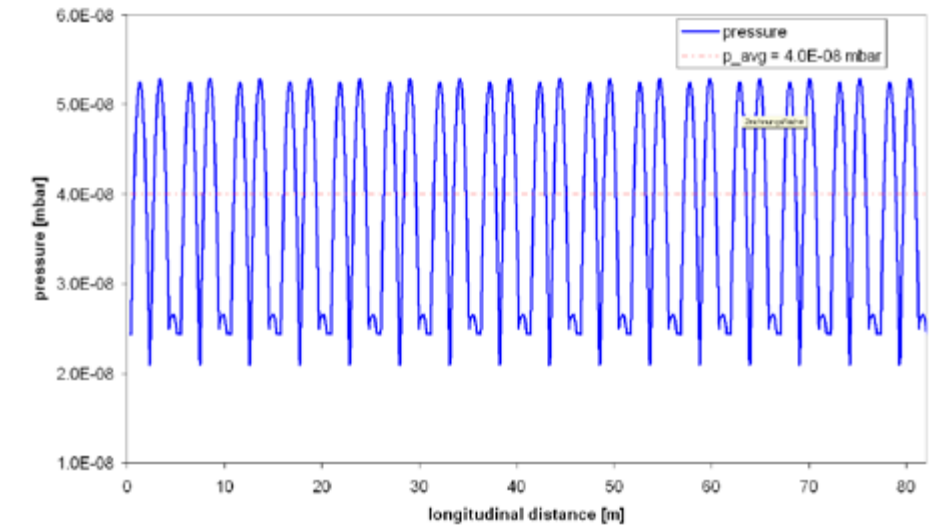


Fig. 3.7.3: Pressure distribution in Linac 1.

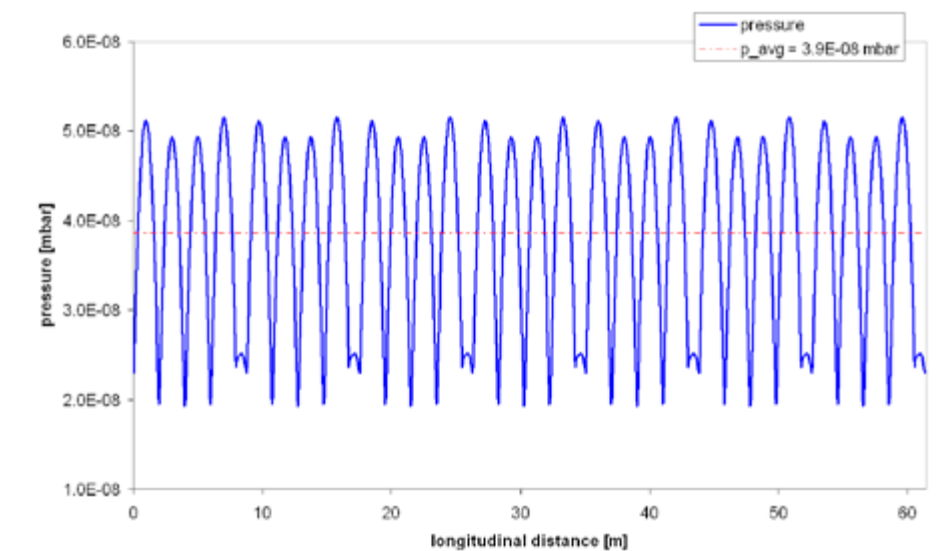


Fig. 3.7.4: Pressure distribution in Linac 2.

design, eight RF accelerating structures with two klystrons will be used for one vacuum section. The gate valve which is being considered at the present design stage has a flange size of 35 mm, but is based on a design for a DN 65 mm all-metal gate valve. It is a very large and heavy valve, which requires large installation space and high investment costs. However, the requirements for a gate valve for the SwissFEL are a little relaxed compared to those of an electron storage ring, and therefore the development of a smaller and more cost-effective gate valve has been started, based on a Viton-sealed gate valve with a simpler RF shield. For the handling and maintenance of the vacuum sections, it would be preferable to have only four cavities and one klystron in each vacuum section.

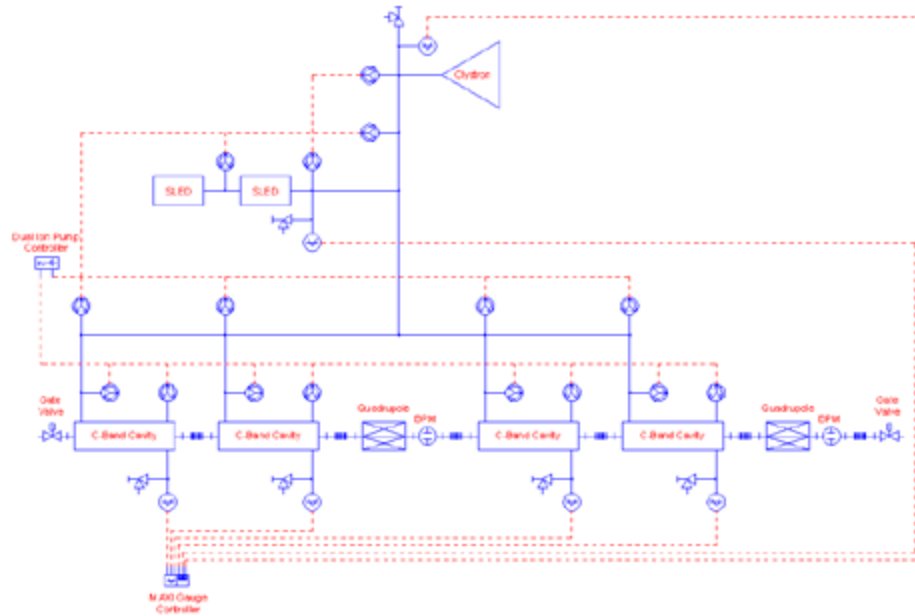


Fig. 3.7.5: Vacuum scheme of the Linac 1 double cell (The 2 SLED system is actually replaced by a BOC cavity – see Section 3.2).

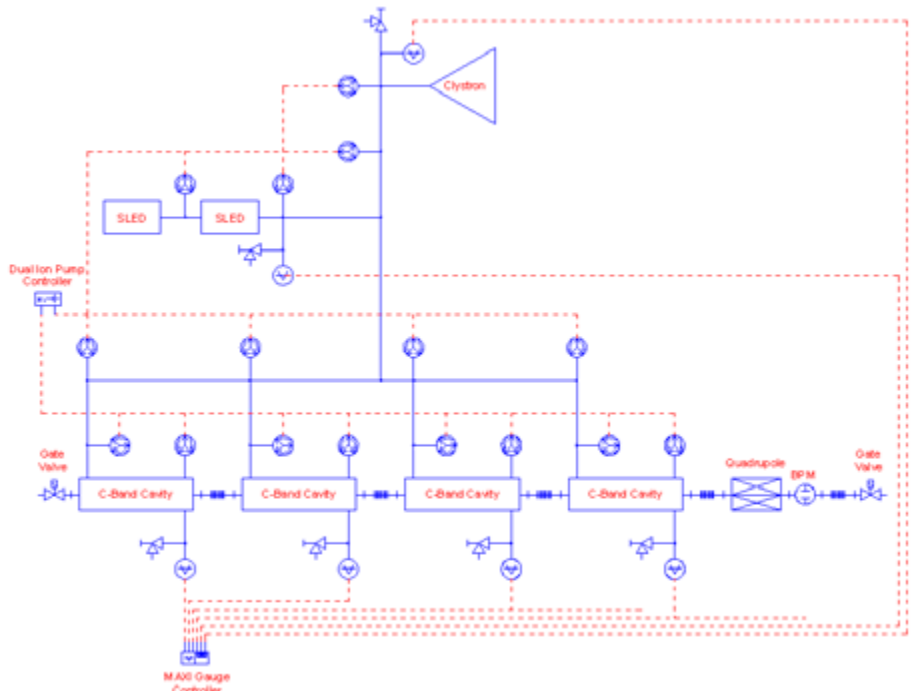


Fig. 3.7.6: Vacuum scheme of the Linac 2 and Linac 3 standard cell (The 2 SLED system is actually replaced by a BOC cavity – see Section 3.2).

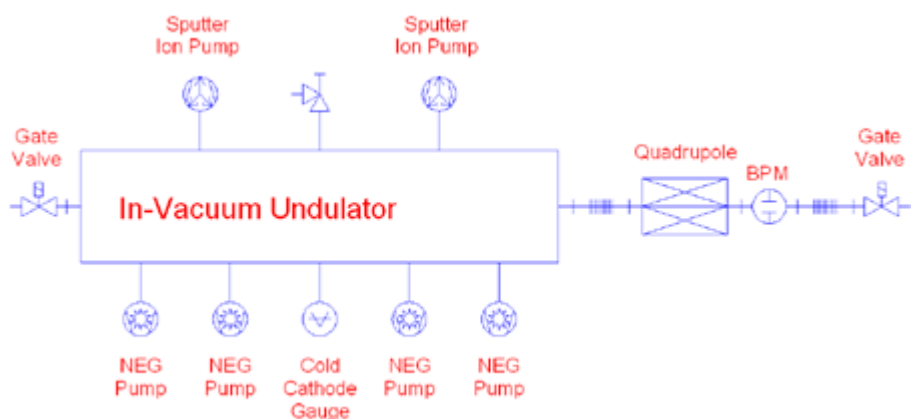


Fig. 3.7.7: Vacuum scheme of the in-vacuum undulator cell.

For the monitoring of vacuum pressures and for the vacuum interlock, cold-cathode gauges will be installed on one pump T in each cavity and on some locations in the RF wave guides.

Dry turbo molecular pumps will be used for roughing and during bake-out. These pumps are installed in pump carts, which also have dry and oil-free diaphragm pumps, a vacuum control, and a venting system. The pump carts are mobile and can be connected via flexible hoses to the several cross-angle valves which are installed in each vacuum section.

3.7.2 Undulator vacuum system (Aramis)

For operation of SwissFEL, average pressure values in the 10^{-7} mbar range are sufficient and expected in Aramis undulators. No baking of the Aramis vacuum chamber will be possible.

The design of the in-vacuum undulators for Aramis strictly follows the design of SLS in-vacuum undulators. With Ni-electroplating or TiN-ionplating of the permanent magnets, UHV-compatible desorption rates can be achieved [91]. The vacuum chamber for the undulator magnets is made of stainless steel and will be equipped with two 150 l/s sputter ion pumps and four NEG pumps delivering 1300 l/s (for hydrogen) (see Figure 3.7.7).

Conductance limitations are not a problem for the in-vacuum undulators. The small magnet gap is open in the horizontal direction, giving good conductance to the undulator vessel.

Between each undulator is a short beam-tube with focusing quadrupole, BPM and rf-shielded bellows. The inner tube diameter is between 8 and 10 mm. The flange size will also be CF 16 mm.

For maintenance reasons, it would be preferable if all in-vacuum undulators could be separated by gate valves. For this, a compact Viton-sealed valve with RF shield would also be preferred.

For the monitoring of vacuum pressures and for the vacuum interlock, cold cathode gauges will also be installed on the undulator vessel.

3.7.3 Undulator vacuum system (Athos)

For the APPLE undulator Athos, a fixed-gap undulator vacuum chamber with an inner beam-clear aperture of 10 mm in the horizontal, and 4 mm in the vertical, direction is required. Depending on the small aperture dimensions, a small wall thickness is required for chamber rigidity. To guarantee small undulator magnet gaps, chamber wall thickness between 0.2 and 0.4 mm is desirable. Low electrical resistance material is necessary for the beam channel, at least for the inner surface, to obtain low resistive wall impedance. OFHC and aluminum alloy are suitable materials for the undulator chamber.

A smooth surface, with roughness values less than 300 nm, for the inner chamber wall is required to avoid a negative influence on beam performance due to wall wakefields.

OFHC is proposed as the chamber material for the Athos undulators [92]. Chamber fabrication will be based on a galvanization method, with the following steps: In the horizontal direction, a machined and polished OFHC support plate will form the inner chamber wall on one or both sides. A smooth aluminum tube with elliptical cross-section is glued to the support plate and to the end flanges. The outer cross-section of the aluminum tube is identical with the resulting inner chamber cross-section. The thin chamber wall is then galvanized to the aluminum tube and also to the support plate and end flanges. Finally, the aluminum tube will be removed by an etching process.

A series of static structural analyses has shown that, in a chamber with two side supports, a wall thickness of 0.2 mm can be achieved, with maximum deformation of $4.3 \mu\text{m}$ and maximum stress of 33 MPa (see Fig. 3.7.8).

An average pressure of less than 10^{-7} mbar is necessary for the undulator line. The overall length of each vacuum chamber is about 4.7 m, while each undulator itself will have a length of 4 m. At the junction between undulator segments will be focusing and steering magnets, beam position monitors, bellows and pumps.

The very small chamber aperture is extremely limited in conductance. Pumps can be installed only at the junction between the undulator segments. To achieve the pressure of 10^{-7} mbar, an in-situ bake-out will be required to reach desorption rates of less than 10^{-11} mbar l/s cm^2 .

The first design work for this new vacuum chamber type has started, and the next step is the fabrication of the first prototypes. Further investigations have to be made to calculate the photon-stimulated desorption rates and the resulting dynamic pressure. Also, the deposited radiation power over the full length has to be investigated. The first designs will be without cooling channels. If synchrotron radiation power calculations indicate large heating, active cooling has to be implemented in the design.

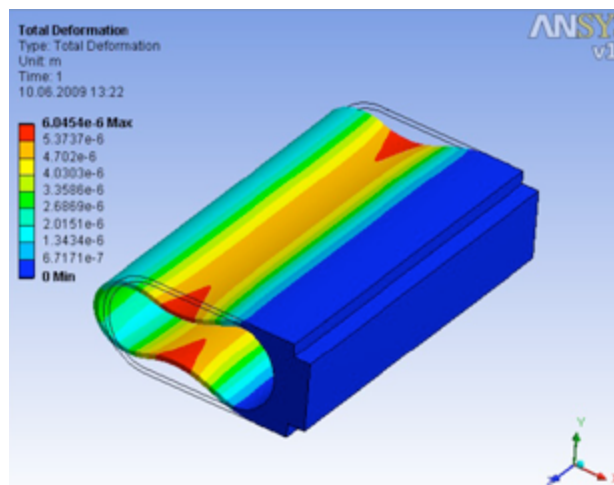
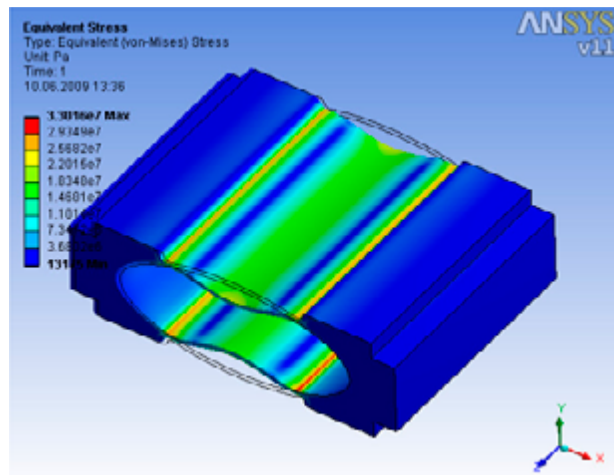


Fig. 3.7.8: Chamber deformation and stress for two-side support (left) and one-side support (right).

Table 3.7.1: Summary inner beam pipe size and vacuum level during operation.

SwissFEL section	Inner diameter vacuum pipe mm	Vacuum level mbar
Injector [z = 0 to z = 81 m]	35 mm	$< 10^{-8}$
Linac 1, 2 and 3 [z = 81 to z = 475 m]	16 mm	10^{-8}
Aramis inter undulator sections [z = 475 m to z = 570 m]	8 mm	10^{-7}
Aramis Beam Dump Spectrometer (vertical/ horizontal)	100 mm / 4 mm	
Athos Undulator Chamber vertical	4 mm	10^{-7}
Athos Undulator Chamber horizontal	10 mm	10^{-7}

3.8 Mechanical support systems

The mechanical support system concept is based on having pre-assembled units for the Linac and Undulator modules. For small components (e.g. single magnets, diagnostic elements, etc) individual supports are foreseen. The design concept combines optimized mechanical properties with an “easy to manufacture” design.

3.8.1 Girder concept

Inspired by the SLS girder system, the SwissFEL girder design is conceived as an “optical table” which allows several components to be aligned with respect to one reference. The girder has a high-precision reference surface for direct vertical and horizontal positioning of components. The girder itself is then positioned on manually adjustable jacks. Each jack is mounted on a steel plate which is cemented to the floor.

The modular supports for components are mounted on the girder's reference surfaces and can be individually aligned.

Design principles for the SwissFEL linac girder and support system:

- Girder as an “optical table”, with high-precision vertical and horizontal reference surfaces for individual alignment of components
- Minimization of tolerance chain by use of fewer parts
- Kinematic “clean” solutions (preferably 3-point) for bearing arrangement of girder and component supports, to avoid “over-constraints” and to simplify alignment
- Bearings must allow free axial movement of the RF structure, to allow free thermal expansion without internal deflection during bakeout and operation
- Adjustable jacks for girder alignment with 6 degrees of freedom
- Adjustable supports for components
- Good mechanical behaviour regarding static and dynamic stabilities

- High damping properties to avoid amplification of potential vibrational excitations
- The use of non-corrosive and non-magnetic materials
- Minimization of effort for alignment procedures
- Minimization of cost for manufacturing in series
- The jacks will allow vertical adjustment (to compensate settlement for example) of – 4 mm to +6 mm.

To achieve the requirements for beam stability and considering the environmental conditions, design criteria are specified, and the criteria for the linac girder and support system are shown in Table 3.8.1.

Figures 3.8.1 and 3.8.2 show the girder as installed in the SwissFEL Injector Test Facility and optimized for the SwissFEL linac. Because of the smaller mass of the foreseen C-band cavity (no solenoid magnets required) in comparison with the S-band cavity (with solenoids), the SwissFEL linac girder can be optimized regarding shape and bearing configuration.

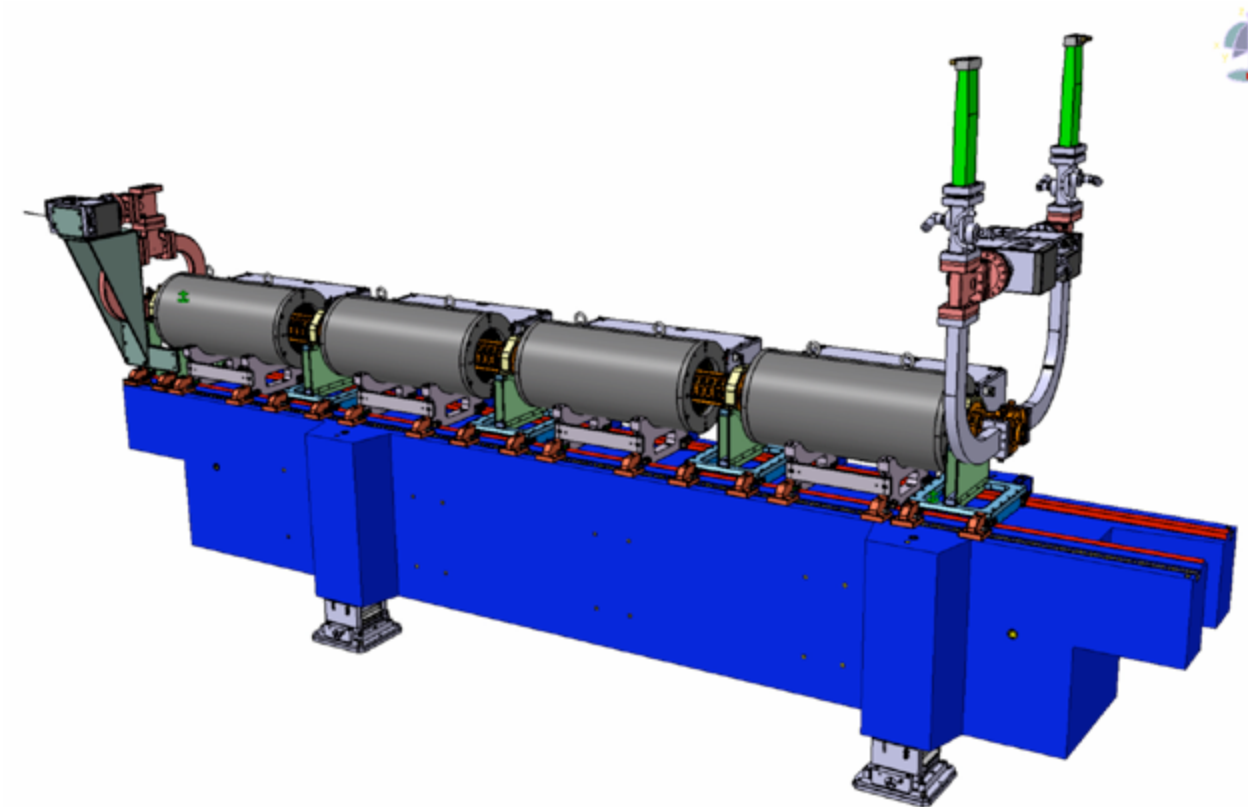


Fig. 3.8.1: S-Band Linac Girder Module of the SwissFEL Injector Test Facility.

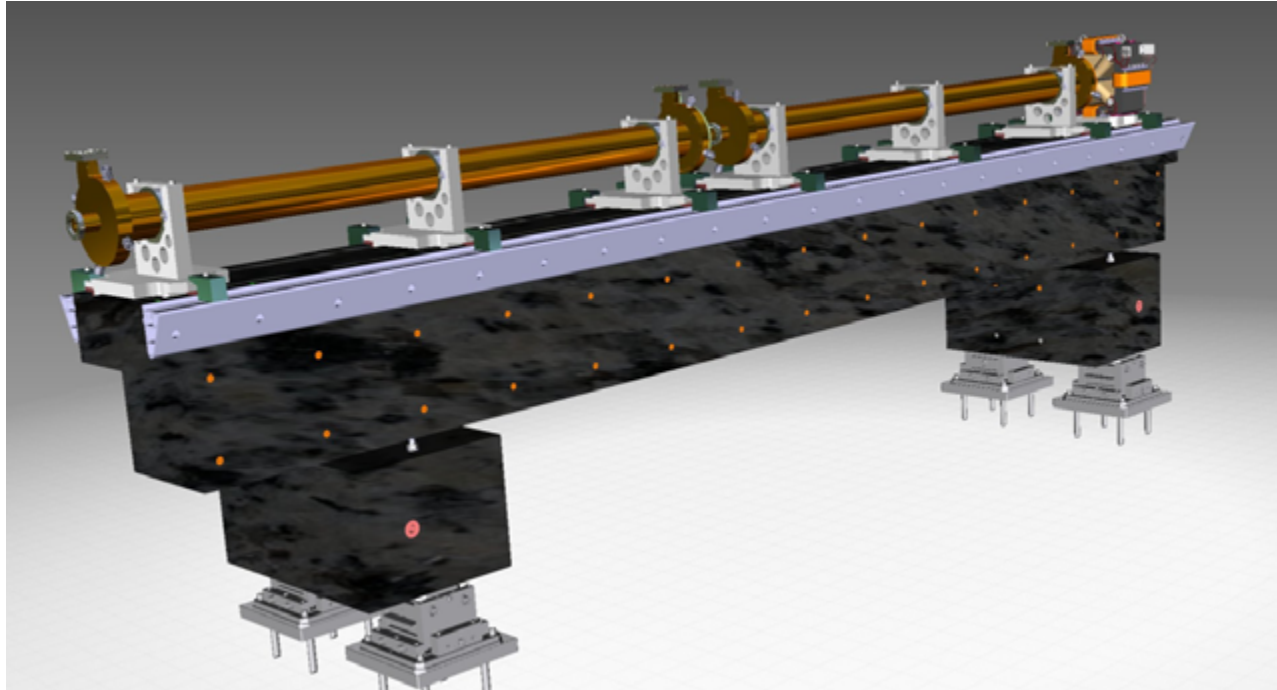


Fig. 3.8.2: Design study of C-Band Linac Girder Module for the SwissFEL Facility.

Table 3.8.1: Design criteria for the SwissFEL Linac girder and support system.

Beam stability	
Maximum allowable orbit deviation from theoretical beam axis	$\Delta x, y_{\text{transversal}} < 0.5 \mu\text{m}$
Static stability	
Maximum deformation at load (weight + thermal load ¹)	$\Delta u_{\text{vertical}} < 10 \mu\text{m}$ $\Delta u_{\text{axial, th.}} < \dots \mu\text{m}$
Maximum allowable stress values ²	$S, S_m = 0.67 R_{p0.2(T0)}$ $S, S_m = 0.3 R_{m(T0)}$
Dynamic stability (derived from beam stability criteria)	
Eigenfrequencies (EF)	1. EF > 50 Hz
Maximum elongation of geometric beam axis from theoretical beam axis due to dynamic excitation (vibration, shock)	$\Delta u_{\text{transversal}} < 0.5 \mu\text{m}$ $\Delta u_{\text{axial}} < 0.5 \mu\text{m}$
Internal damping ratio	c > 4 %
Manufacturing (girder + supports)	
Tolerances (Manufacturing) global length dimensions flatness over total length parallelism (reference surfaces) inclination (reference surfaces)	$t_{\text{length}} < 100 \mu\text{m}$ $t_{\text{flatness}} < 50 \mu\text{m}$ $t_{\text{parallelism}} < 50 \mu\text{m}$ $t_{\text{inclination}} < 0.5^\circ$
Alignment	
Tolerances (Alignment) pre alignment final alignment beam-based alignment (BBA)	$\sigma_{\text{transversal}} \pm 1 \text{ mm}$ $\sigma_{\text{longitudinal}} \pm 1 \text{ mm}$ $\sigma_{\text{transversal}} \pm 100 \mu\text{m}$ $\sigma_{\text{longitudinal}} \pm 100 \mu\text{m}$ $\sigma_{\text{transversal}} \pm 10 \mu\text{m}$

¹ Maximum thermal load occurs during bakeout procedure with $T_{\text{bakeout}} = 150^\circ$ ² Derived from ASME BPV, Section III, Subsection NF (supports); $R_{p0.2(T0), 316LN} = 205 \text{ MPa}$, $R_{m(T0), Granit} > 50 \text{ MPa}$

Besides the girder required for supporting accelerating structures, there are some special components requiring complex and stable girder support. The bunch compressors are quite complex support systems in SwissFEL (Fig. 3.8.3) because the bond angle of the 4 dipole magnetic chicane must be adjustable remotely. This means that the two central dipoles are movable in the horizontal direction orthogonal to the beam axis to allow an adjustment of chicane angle between 0 and 5 degrees. Bunch compressor 2 will be based on the same concept.

As presented in section 3.5, the quadrupole magnets between undulator segments need careful positioning in order to allow an electron beam straightness within $1 \mu\text{m rms}$. Those quadrupole magnets together with a BPM (Beam Position Monitor) will be supported on individual motorized table (Fig. 3.8.4). The requirements in precision and stability of those supports are summarized in table 3.8.2.

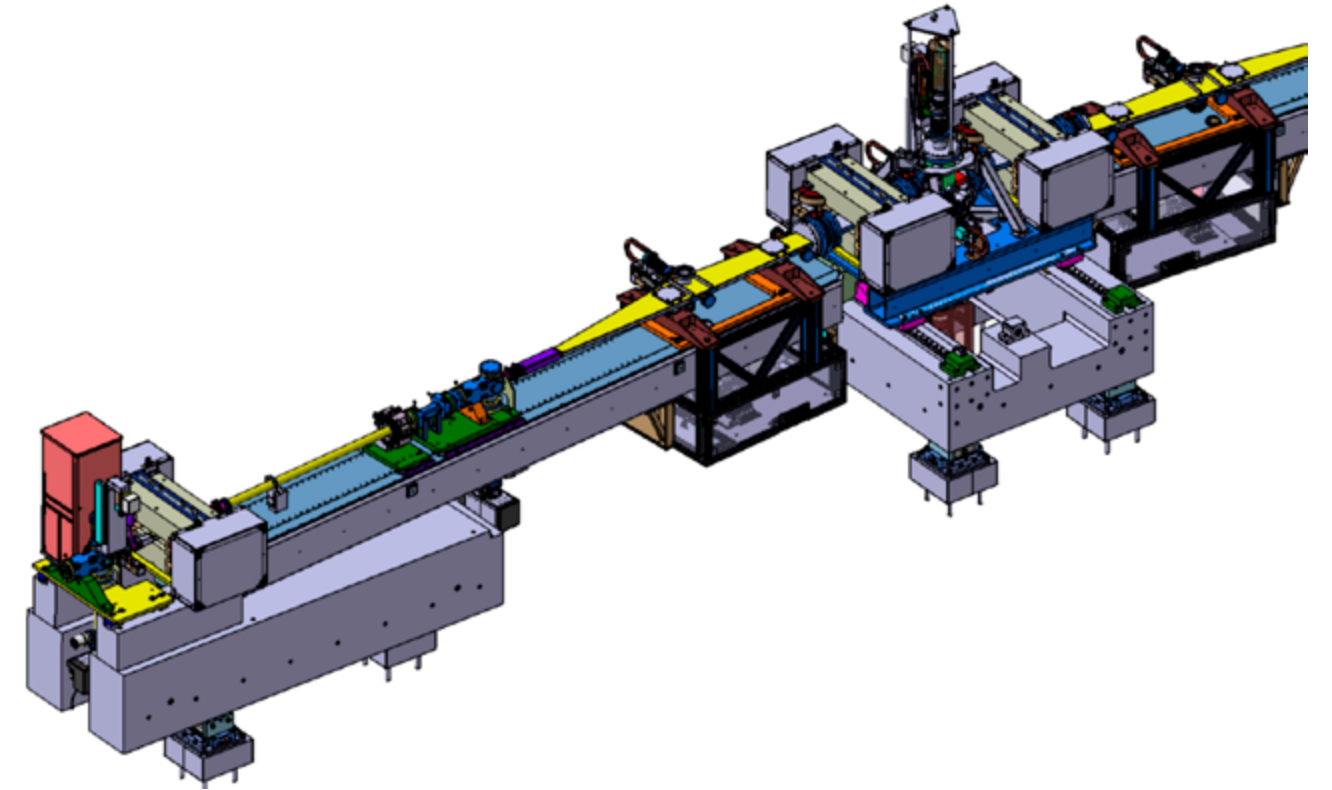


Fig. 3.8.3: Mechanical Design of Bunch Compressor 1 as installed in the SwissFEL Injector Test Facility (Bunch compressor length: 12 m; height: 1.3 m; Width: 1.2 m (with maximum angle)).

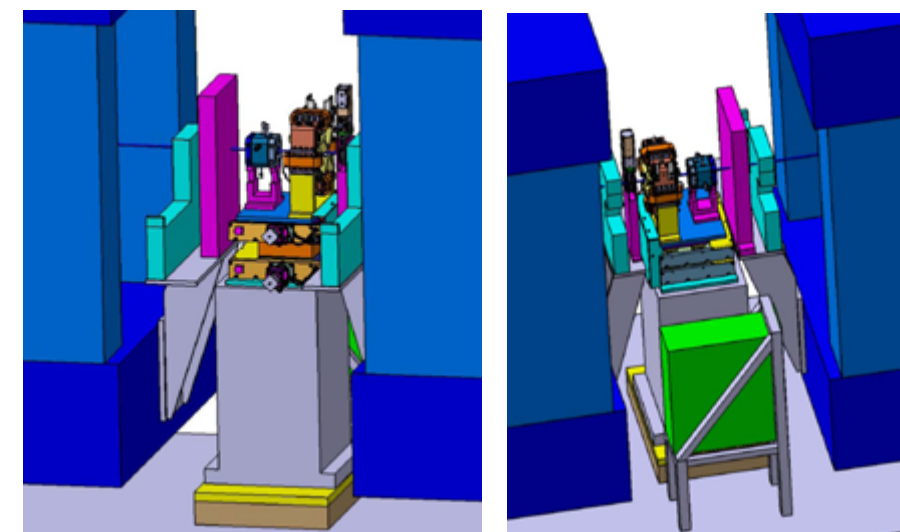


Figure 3.8.4: Design study for the inter-segment quadrupole motorized support based on wedge system.

Table 3.8.2: Design criteria for the SwissFEL Undulator inter segment girder and support system.

Quadrupole / BPM Alignment Tolerances	
Precision in quad magnetic axis pre-alignment in tunnel (rms)	60 μm
Precision in BPM axis alignment on quad magnetic axis (rms)	60 μm
Quad Xquad & Yquad positioning tolerances over 5 m after BBA (rms)	2 μm
BPM Cavity resolution – 8 mm Inner Diameter (rms)	1 μm
Quad mover minimum displacement steps (X and Y)	< 1 μm
Quad (or support table) travel range (X and Y)	± 1 mm
Linear Encoder X and Y of moving table relative to granite block resolution	100 nm
Quad X/Y mechanical center stability for $f > 1$ Hz (rms) (Gives 1 μm orbit fluctuations)	100nm
Quad X/Y magnetic center stability for $f < 1$ Hz (rms) over 24H with feedbacks	0.3 μm
Quad X/Y mechanical center stability for $f < 1$ Hz over 24 H without feedback in respect to all other QFF quads of the same undulator (thermal drift issue)	1 μm
BPM axis Stability for $f < 1$ Hz over 24 H in respect to the other BPMs (thermal drift issue)	1 μm
Support table X/Y stability for $f < 1$ Hz over 24 H in respect to all other support tables of the same undulator (thermal drift issue)	~ 1 μm
Number of Quad / BPM support required for SwissFEL 2016	19

3.8.2 Simulation and tests

Several numerical simulations and tests will be performed to evaluate the mechanical behaviour of the system and to optimize the design.

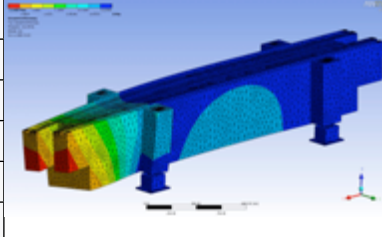
Simulations and tests (planned)

- FEA-based numerical simulation to predict the mechanical behaviour of the girder and supports regarding static, dynamic and thermal loads
- Manufacturing of prototypes, incl. quality checks in preparation for series production
- Girder test set-up (“SwissFEL Linac girder test stand”)
- Functionality tests for single components and assembly

- Experimental modal analysis to verify numerical simulations and to evaluate the dynamic response at the beam axis due to external excitations
- Thermal heat loading tests
- Alignment and pre-assembly tests

For the girder design of the SwissFEL Injector Test Facility, FEA-based numerical simulations and experimental modal analysis have already been performed.

Table 3.8.3: FEA simulation results – Girder for SwissFEL Injector Test Facility.

Mode Shape	Frequency [Hz]	Figure: Mode shape visualization of the 1 st mode shape
1	116.9	
2	125.2	
3	147.5	
4	179.6	
5	212.2	
6	231.6	

To validate the results of the numerical simulations and the design, a number of eigenfrequency measurements have been performed, including set-ups with 3 and 4 feet and several jack set-ups.

The results of the tests confirm the simulation and show first rigid-body motion frequencies above 50 Hz, with amplitudes below 20 nm (see Figure 3.8.4 for details of the test set-up and Figure 3.8.5 for the results).

As shown in section 3.4, the quadrupole magnets in Linac (QFD) and in undulator lines (QFF) are air cooled. In consequence, the question of thermal movement (due to dilatation) when changing magnet current arises.



Fig. 3.8.4: Girder during eigenfrequency measurements: the arrows indicate the location of the accelerometers; test location at the SLS facility.

Thermal analysis of quadrupole magnet supports (air cooled) has been performed. It takes about 10 hours for a quadrupole magnet (QFF type) to reach its steady state temperature (around 50 degrees C at 10 A, 44 W). In the extreme case of going from 0 to maximum current (10 A) and with steel support the magnetic axis would rise in the vertical direction by 25 μm (see Fig. 3.8.6).

During a change of user operation conditions (change of electron beam energy), the current flowing in the undulator quadrupole magnet will vary at maximum between 2 and 6 A so that displacement of magnet axis will be around 5 μm . Finally, low thermal expansion material will be used to limit the displacement to 1–2 micrometers which will be corrected by the orbit feedback system using the steering magnets.

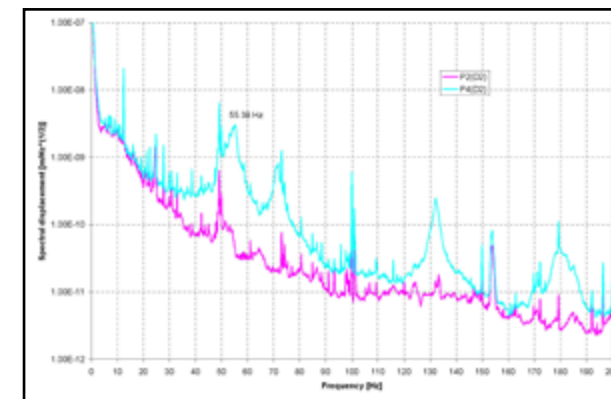


Fig. 3.8.5: Comparison between measured ground motion spectra and response spectra at the girder reference surfaces.

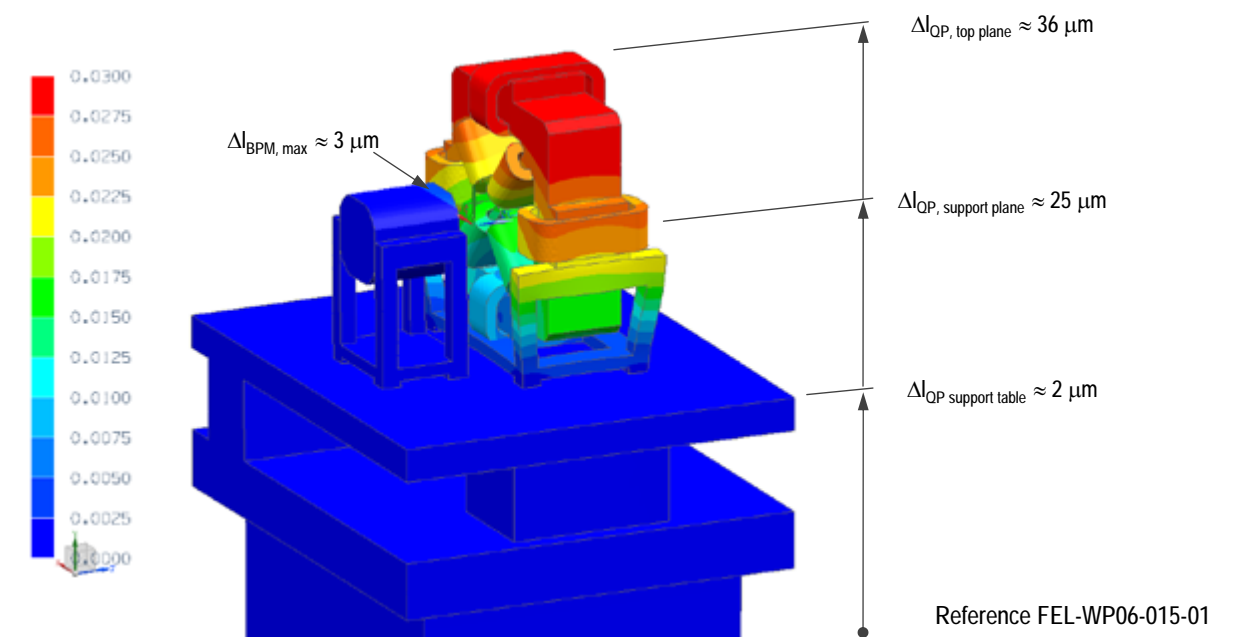


Fig. 3.8.6: Thermal dilatation of the QFF quadrupole / BPM assembly assuming 44 W continuous heat up (10 A current) and steel material support (air cooling losses of 10 W/m².K).

3.8.3 Girder feet adjustment system

The relative position of the girder will be controlled by using jacks. The design of the jack should be consistent with the high eigenfrequencies of the girder; therefore the jack design relies on large surface contact. Screws or spindles in the structure that would generate a weak point for vibrations will be avoided. The design uses commercial driving wedges for vertical adjustment and screws for horizontal adjustment.

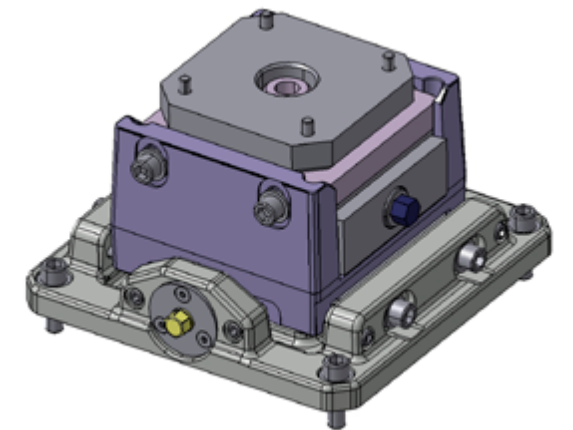


Fig. 3.8.7: The girder jack based on a standard wedge located in a transverse positioning system.

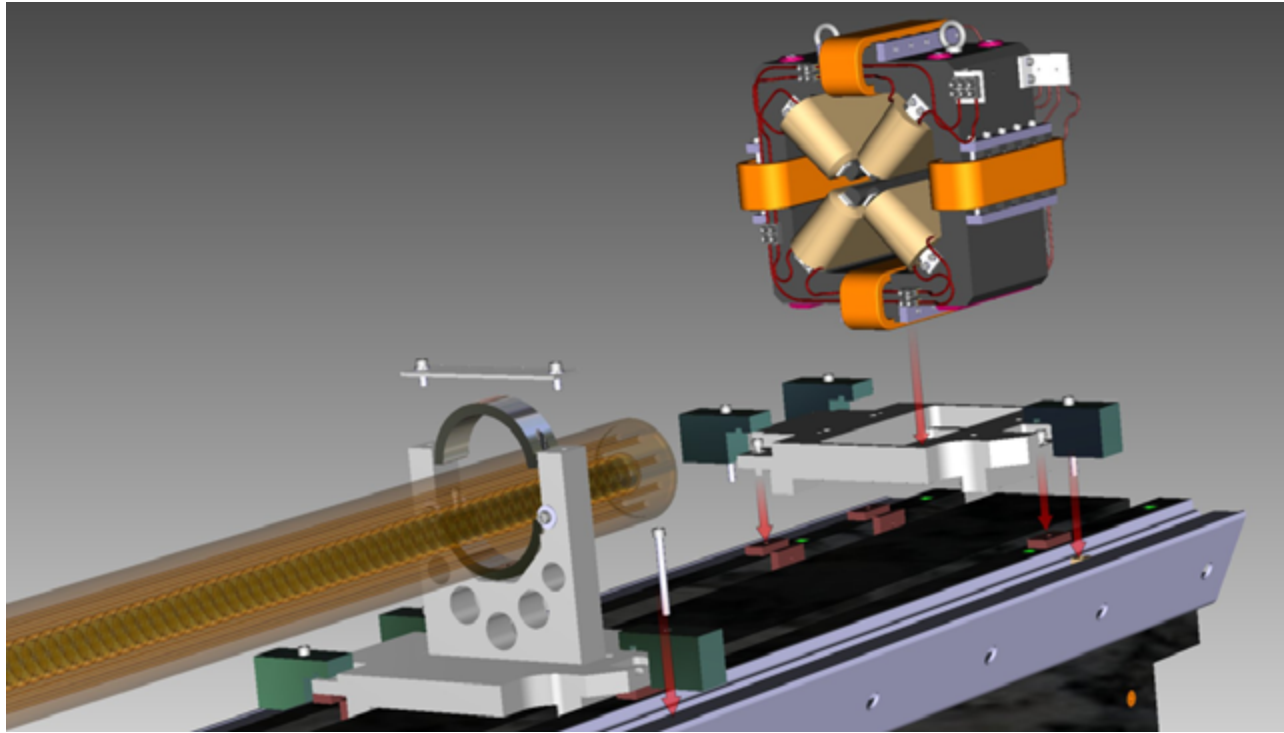


Fig. 3.8.8: Design study of local supports for SwissFEL Linac Girder Module.

3.8.4 Local support system

For the alignment of components, single adjustable supports will be used. These supports can be placed directly on the horizontal and vertical reference surfaces of the girder. Fine adjustment of each support will be performed using shimming techniques.

3.9 Control system

The control system is a central part of all large facilities. Its main task is to integrate the distributed subsystems of the facility into one coherent infrastructure. The control system provides the connection between hardware and the operators, it creates the environment that allows physicists to carry out their measurements, and it archives data to allow retrospective comparison with simulations. Guidelines for the design of the control system are reliability, ease of use, and expandability. Beyond its pure functionality, the maintainability of the whole system and the portability for new developments in computer science are basic requirements.

The hardware and software platforms, boot and archive services, configuration management and logistics developed for the other PSI accelerators will be used, as far as possible, to ensure cost efficiency and maintainability. The control system for SwissFEL will benefit from existing control systems equipment standards and know-how of the other PSI accelerators, whenever possible; in particular, the established close cooperation of the IT department and the controls section will be useful for the design and operation of the complex control system of SwissFEL. Many applications can be based on experience gained with the SwissFEL Injector Test Facility.

Developments which are required for SwissFEL have to meet the project schedule, the budget, and performance specifications, with consideration for knowledge transfer (internally and to the wider accelerator community).

3.9.1 Network infrastructure

The design basics for the network infrastructure of SwissFEL are the experience made by the IT department (AIT) at the Swiss Light Source (SLS) and the SwissFEL Injector Test Facility. Using PSI standard MPLS-VPN technology, it is possible to isolate networks while they share the common PSI network infrastructure and meet the ethernet design rules set up by AIT.

In the machine control network, the number of network ports needed is too high to fit into one Class C subnet, which is standard at PSI. Therefore, results from tests at the SwissFEL Injector Test Facility will be used to connect different subnets along the accelerator.

As in the SLS beamlines and SLS machine network today, the networks of the SwissFEL will be logically separated and use different address ranges. Separation is made using VLAN technology and virtual firewalls under the control of AIT. By using this standard network design, it will be possible to employ the existing centralized PSI network management method FCAPS (FCAPS is an ISO framework for network management) to monitor and maintain the SwissFEL network efficiently. It also provides connections to existing network services, such as DNS, DHCP and NTP.

The SwissFEL network will be set up in such a way that the same technology and infrastructure can be used for all of the following systems:

- SwissFEL machine networks
- SwissFEL experiment networks
- SwissFEL fire-alarm system (Brandmeldeleitsystem)
- Office networks (contains all printers, SIZ, SU network)
- Voice over IP (telephony services)

In addition, the system will be flexible and extensible, to meet new requirements from scientists or to adapt to new technologies.

3.9.2 EPICS environment

The control system will use the EPICS (**E**xperimental **P**hysics and **I**ndustrial **C**ontrol **S**ystem) toolkit. EPICS has been successfully applied at PSI in the SLS and in several similar large projects around the world (for example, LCLS at SLAC). Due to its collaborative nature, using EPICS enables us to take advantage of work done

at other laboratories. Using a standard software toolkit will allow us to make the best use of in-house know-how and to consolidate technical support services.

The basic structure of EPICS is a network-based client-server model implementing Channel Access as network protocol. At PSI, the EPICS servers are mainly IOCs (**I**nput **O**utput **C**ontroller) that can run on various hardware platforms, such as VME boards, Linux PCs, or embedded systems.

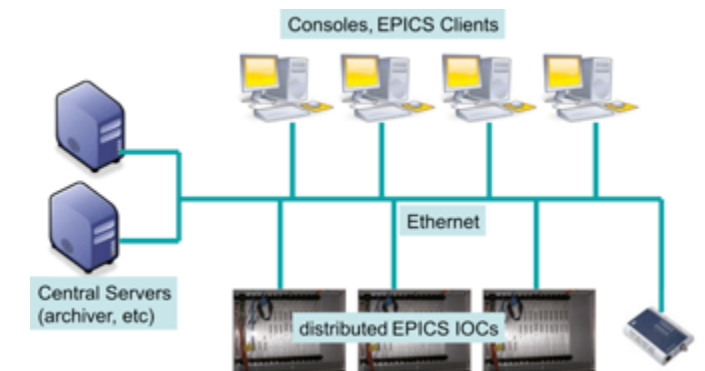


Fig. 3.10.1: Control system architecture.

The IOC is configured at boot time by loading a set of configuration files, start-up scripts and drivers. The IOC may also run a sequencer process which implements a finite-state machine or customized programs.

EPICS client programs run mainly on the control room consoles and can be divided into three categories:

- System expert applications that enable experts to commission and maintain hardware systems
- Operator programs that provide control for routine machine operation
- Data acquisition programs that are used by scientists to perform and analyze experiments (on the accelerator or the experiment)

Requirements (e.g. programming language support) for the last group of programs are especially difficult to predict. Therefore, the control system will provide the flexibility and extensibility to include new developments at a later stage (during commissioning, or even later) of machine operation.

EPICS provides various interfaces to programming languages such as Java, Python, Tcl/Tk and others. To ensure maintainability of the programs and the interface itself, the controls section, in cooperation with the IT

department, provides structures such as versioning systems and installation mechanisms.

An integral part of the control system is the timing system, which is covered in detail in Chapter 3.3. The timing system provides the synchronization of all time-dependent subsystems with the electron bunch.

To connect EPICS clients and servers between the different networks (see Section 3.10.1, on Network Infrastructure), the channel access gateway application will be used. Preliminary tests of performance are organized in the SwissFEL Injector Test Facility, especially considering camera data and high measurement frequencies.

3.9.3 Software maintenance and distribution

Software development is not finished once a program works, but has to be maintained and looked after to provide reliable service. Therefore, the control system not only has to include a development environment that allows easy design and distribution of software, but maintenance and upgrade as well.

SwissFEL will be a challenge in terms of the number of controls components needed. Due to the geographical distance of the components and the installation of some systems into the beam tunnel (to minimize cable length), easy physical access to components and systems can not be expected. Therefore, automation in software distribution, installation and maintenance should be introduced wherever possible.

The general way of software distribution and installation has already been established at the SLS and will be used in the same way at SwissFEL. Further development might be needed to improve flexibility, in order to integrate new hard and software. Experience from the SwissFEL Injector Test Facility will be included the concept.

The basic information needed for automated software installation is stored in relational databases. To make best use of in-house knowledge, the environment provided by the IT department, namely Oracle databases, will be used.

All software needed for machine and experiment operation will be stored using a versioning system, to ensure accessibility and flexibility. General guidelines and support will be provided to make it easy for scientists and operators to include their programs into the control system structure.

As the control system is one of the central parts of the SwissFEL, a fault there will most probably prohibit machine operation or experiments. Therefore, control system reliability should reach 98% of the machine's operation time (the number is a little lower than the achievements of the SLS control system, to take the challenges of the SwissFEL into account). This implies similar reliability for most sub systems, such as file servers, data bases, etc.

A system can only be stable and reliable as long as malicious mischief (e.g. software viruses) is prevented. Therefore, the control system of the SwissFEL will establish close access control to the machine and the experiment networks. The security concept will be based upon the experiences and established rules at the SLS. Further developments, such as remote control of experiments, will be tested at the SLS beamlines and implemented according to the results of these tests by AIT, in co-operation with the controls section.

3.9.4 Control hardware

As far as reasonably possible, hardware used at other PSI accelerators should be preferred, to take advantage of existing expertise and cheaper stock keeping. If new hardware is used, development time and the cost for integration into EPICS (for example, for driver development) has to be taken into account and planned beforehand.

For network components, file servers and PCs, SwissFEL will use hardware based on PSI standards defined by AIT. EPICS IOC's will be the base for standard hardware control, such as analogue and digital signals and motor control (see Figure 3.10.2). A wide variety of hardware is already supported and can be adapted and extended to new developments.

Special requirements may be met by using embedded controllers (for example, FPGA-based systems or micro-controllers). Examples of such systems may include

geographically isolated devices, systems that need the computing speed of a dedicated CPU, or entirely new hardware components which are not yet supported by any PSI standard hardware. However, the embedded controllers will be integrated into the EPICS framework and the software maintenance and distribution processes.

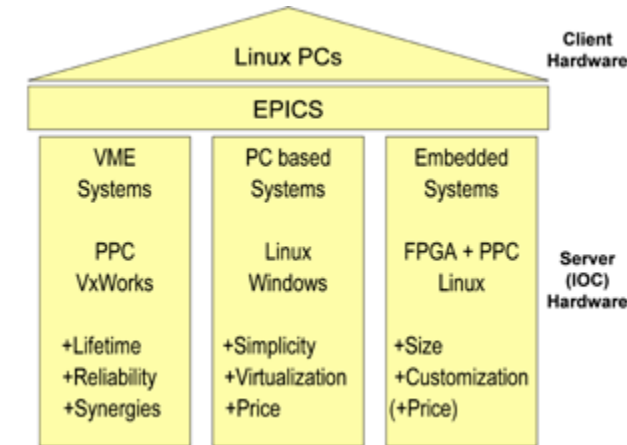


Fig. 3.10.2: The three pillars of the SwissFEL control system.

With the start of experiments at SwissFEL, a large amount of data will need to be stored. At present, a volume of twenty to thirty times the data volume currently used at SLS is expected. Therefore, a server room for data storage and compute nodes for data analysis has to be planned, and the projected infrastructure provided.

3.9.5 Machine interlock concept

The interlock system can be divided into three main parts, which differ in their speed requirements, complexity and protection goal:

1. Beam Loss Interlock System for radiation protection, based on experiences from a similar system at the SwissFEL Injector Test Facility.
2. Beam Permit System for equipment protection, based on the Run Permit System used at the High-Intensity Proton Accelerator (HIPA) at PSI. A test system will be installed at the SwissFEL Injector Test Facility, to verify an upgraded design.
3. Beam Quality Verification System as part of the EPICS environment, which will be designed and realized in the course of the first experience derived from the

SwissFEL Injector Test Facility. Detailed specifications will be based on the installed feedback systems and the requirements of the experiments. This system has to be flexible and easy to adapt to new conclusions derived from measurements.

Only the first two systems described are safety relevant. They are independent of the EPICS environment, in the sense that they could react reliably to situation changes without EPICS working. EPICS will be used in these systems to visualize the situation and archive the data.

In addition (but not described here) there is the vacuum system with a dedicated interlock system that disables the electron gun in the case of bad vacuum, the personal safety system (PSA), which is part of the radiation protection concept, and local routines that supervise single components, such as RF structures.

4 Photon beam components

This chapter describes the main components situated downstream from the last undulator of the Athos and Aramis lines. The photon transport can be split into the following main areas (see Fig. 4.1):

- the Front End Enclosure
- the photon switch-yard
- the Experimental Hall

The purposes of the Front End Enclosure are to diagnose (arrival time, position, intensity, spectrum, ...) and control (attenuate, collimate, ...) the photon beam. The photon switchyard is used to distribute the photon pulses towards one of the three possible experimental hutches. The Front End Enclosure is separated from the Experimental Hall by a 2 m thick shielding wall. The last optical components of the beamline are usually located nearby the experimental station in the Experimental hall.

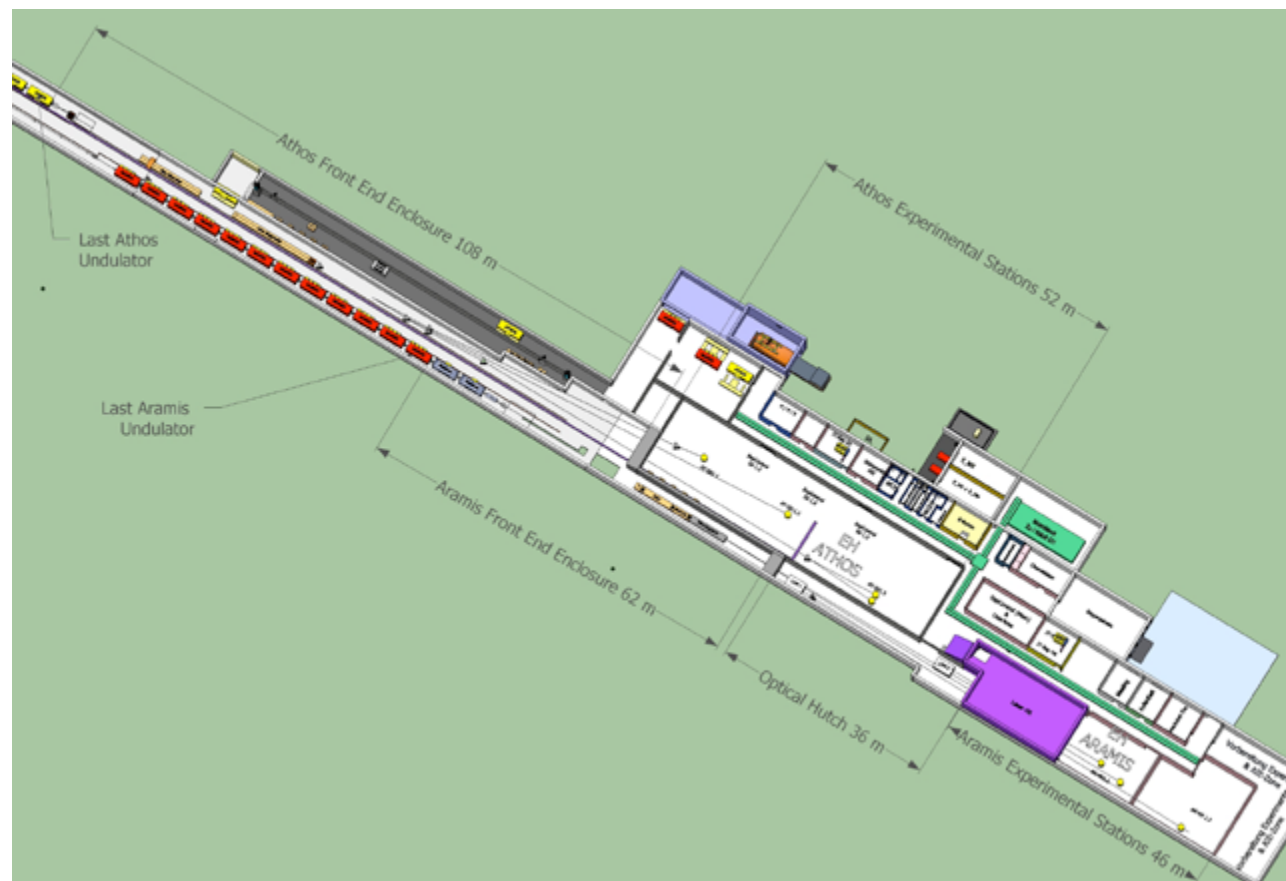


Fig. 4.1: Overview of the front-end, optics and experimental sections for the Aramis (hard x-ray) and Athos (soft x-ray) beamlines.

4.1 Front end enclosure layout (Athos and Aramis)

The Front End Enclosure layouts for Athos and Aramis are given in Figures 4.1.1 and 4.1.2, respectively. The Front End starts at the last undulator and extends up to the 1st mirror. For safety reasons the Photon Switch-yard (from the 1st mirror to the photon beam stopper) is located in the same shielded area as the Front End. The other optical components (downstream of Mirror 2) of the Aramis beamline are situated outside of the Front End Enclosure behind the shielding wall.

Schematic views of the Front Ends components are given in Figure 4.1.3 (for Athos) and Fig. 4.1.4 (for Aramis). The first upstream component is the fixed diaphragm, followed by an x-ray double slit system which is adjustable, from an aperture of 3 x 30 mm to completely closed. The role of these components is to limit the angular acceptance of the beamline to the angular distribution of the FEL radiation and to stop in this way the large angle spontaneous radiation. In general, the opening of the x-ray double slits will be set to 4-6 sigma of the FEL central cone. Each jaw of the x-ray double slits covered by a 10 mm thick B₄C plate bonded onto a 50 mm tungsten alloy block. The B₄C, a low atomic number and high melting temperature material, has been identified as a good candidate to absorb the FEL radiation without beam damage [93].

The Front End includes several diagnostic tools, which are located upstream and downstream from the gas and solid attenuators. A brief description of the attenuators and diagnostic tools is given in chapter 4.2.

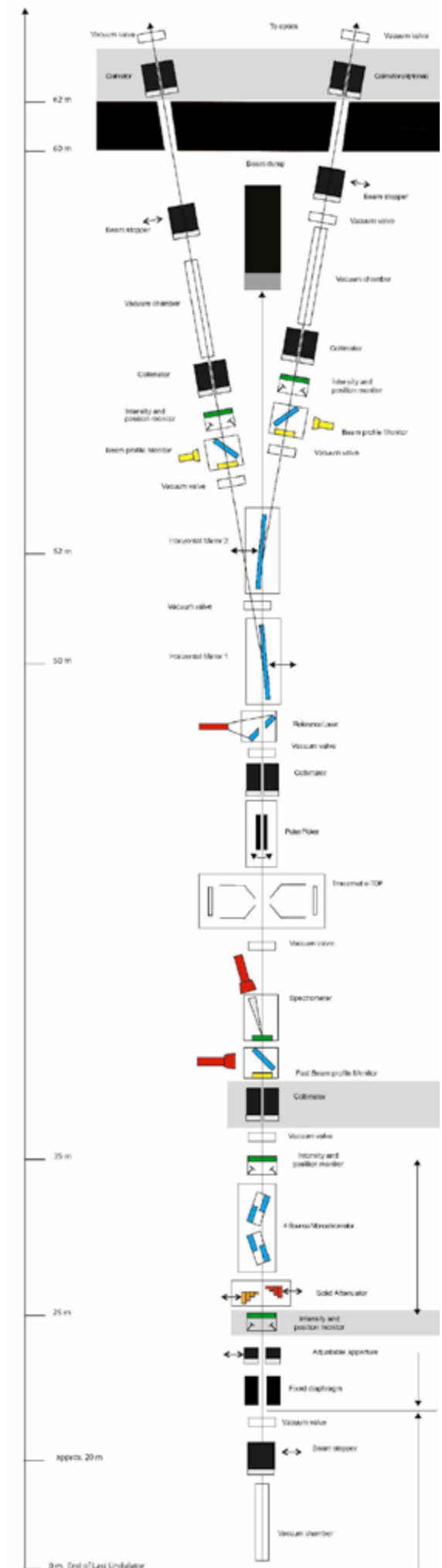


Fig. 4.1.4: Front End enclosure layout of the Aramis Line (from the end of the last Undulator to the Undulator hall shielding wall).

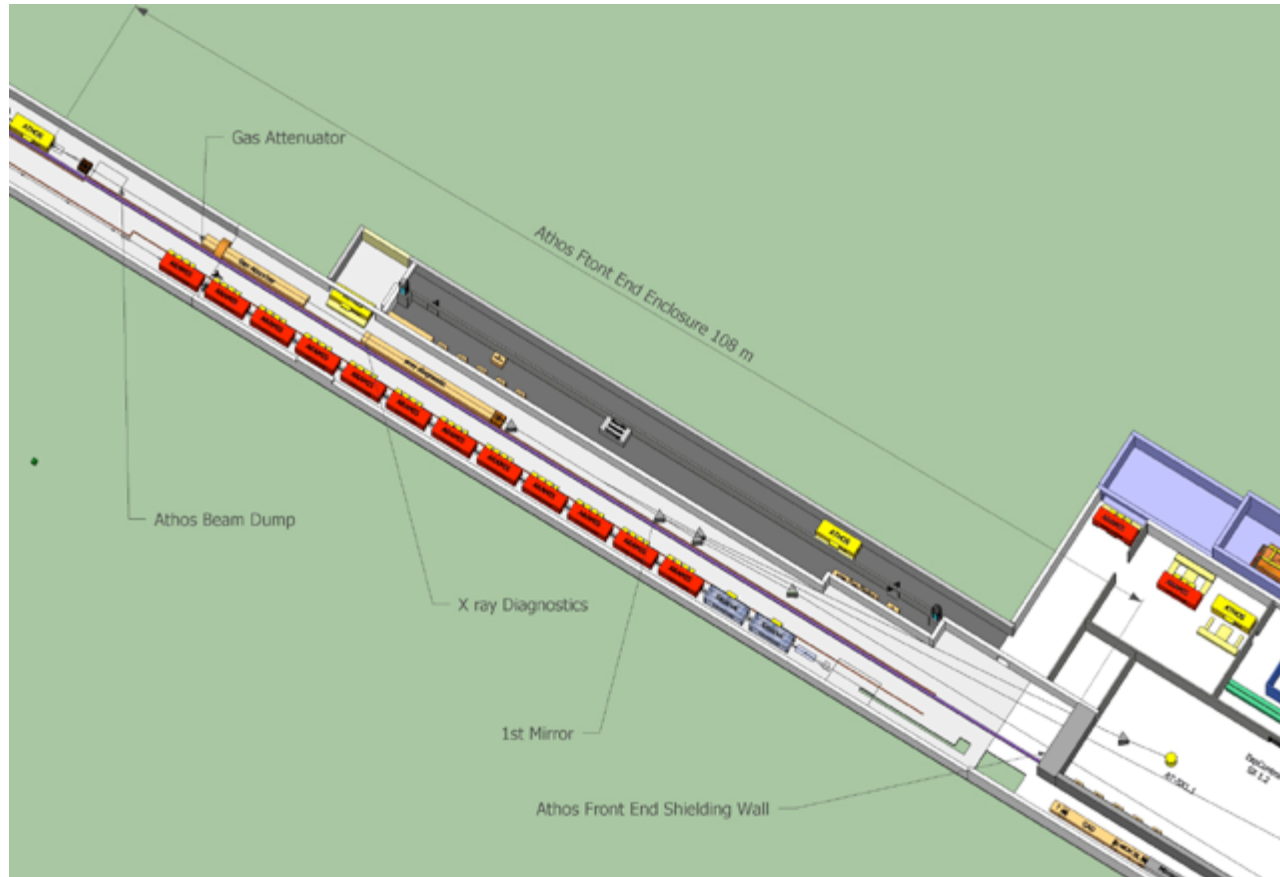


Fig. 4.1.1: Layout of the Athos Front End and Photon switchyard section, behind a 2 m thick shielding wall.



Fig 4.1.2: Layout of the Aramis Front End section and Photon Switch Yard section, behind the shielding wall.

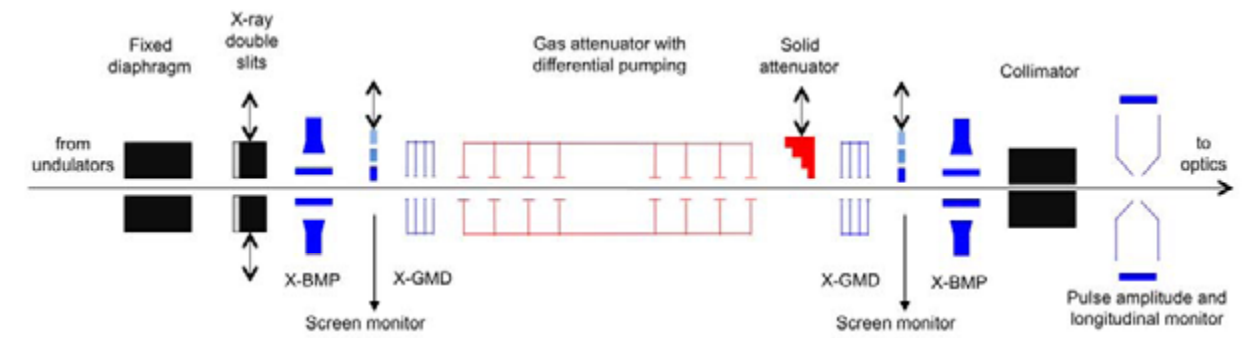


Fig. 4.1.3 Schematic view of the Front End for the Athos beamlines.

Table 4.2.1: Overview of photon diagnostics currently foreseen for SwissFEL.

Photon beam parameters	Performance goal	Possible technique
Photon Intensity	<10% absolute accuracy, <1% relative accuracy	X-ray gas monitor detector
Photon beam position	Profile and position measurement with 25 μm (or better) resolution	Split diode
Pulse Arrival Time and Pulse Length	5 fs or better resolution of arrival time and pulse length for the standard 30 fs pulse	THz streak camera
Photon Wavelength	Measurement of the photon wavelength to a level better than the bandwidth of the FEL	Bent Bragg Crystal, Zone Plate or e-TOF spectrometer
Attenuation (Gas and Solid)	A factor of 1,000 gas attenuation, 10,000 of gas + solid attenuation for all wavelengths	Gas Attenuation
Solid attenuation	A suite of tools for all measurements that would stop the beam – used by the operators	Screens
In-Beam Detectors	A suite of tools for all measurements that would stop the beam – used by the operators	Screens

4.2 Photon beam diagnostics

4.2.1 Introduction

Photon diagnostics are very important tools for the users to monitor their experiment but also for the accelerator operators to align and tune the FEL. Table 4.2.1 summarizes the main type of X-ray photon diagnostics foreseen in the front end enclosure of both Athos and Aramis lines.

4.2.2 Gas and solid attenuators

The attenuation of the FEL beam is something that future users have expressed interest in, and has already been implemented in existing FELs, like FLASH and LCLS. To be able to meet the user expectations for beam attenuation, the SwissFEL is currently planning on building both solid and gas attenuators. For the hard X ray line Aramis,

only solid attenuators will be used, and for the Athos line, both gas and solid attenuators are planned.

The gas attenuation is necessary to ensure that the users can reduce the FEL beam's intensity without significantly distorting the wavefront of the photon pulse, and the solid attenuators will be used to reach a level of attenuation that could not be easily achieved with gas alone. The goal is to ensure that the users can obtain a factor of 1000 attenuation with just the gas over the whole range of the FEL (up to 14,000 eV), and a factor of 10,000 with a combination of the gas and solid attenuators.

To this end, we are planning a long gas attenuator in the front end between the beam dump and the first beamline mirror, followed by a solid attenuator stage (see Figure 4.1.3). Due to the high gas loads that will be used with the gas attenuator, we will need to construct an elaborate and extremely efficient differential pumping stage system, as well as a way to recycle the gases by sucking them out and re-compressing them for future use. A brief explanation of the concepts involved in the construction,

and the expected pressures, gases, foils, and foil thicknesses is given below.

The basic formula for the transmission of light in a material is simply:

$$R = \exp(-n\sigma d) \quad (1)$$

Where R is the transmission, n is the density of the material in atoms per unit volume, σ is the atomic cross section, and d is the thickness of the material.

In a gas, to calculate the pressure P required for some transmission R , one needs to use the ideal gas law to derive the equation:

$$P = -\frac{kT}{\sigma d} \ln(R) \quad (2)$$

Where k is the Boltzmann's constant, and T is the temperature of the gas. The length of the gas attenuator, and the choice of the gas (and its cross section) heavily influence the amount of pressure we will need to achieve the desired attenuation. Cross sections of gases generally decrease as the photon energy of the incident light increases, and for a photon energy of 14,000 eV, the best cross section of a gas that is reasonable to use is that of Xe, at around 12.4 kilobarns [94]. For such a setup (8 m attenuator, Xe gas, 14,000 eV), the pressure would need to be about 28 mbar to achieve an attenuation factor of 1000. Since this pressure is too high for differential pumping, the hard X ray line Aramis will not be equipped with a gas attenuator setup. For lower photon energies (see Fig. 4.2.2.1), the pressure drops sharply as the cross section exponentially increases, and higher attenuation factors with just the gas will be achievable, as shown in Figure 1.

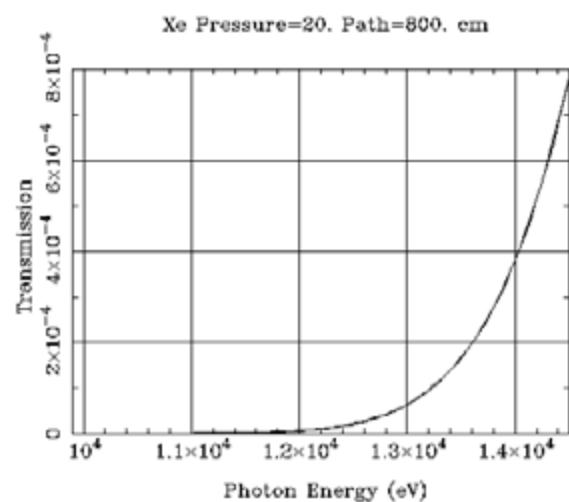


Fig. 4.2.2.1: The transmission of Xe through an 8 m attenuator at a pressure of 20 Torr (27 mbar) between 10 keV and 14 keV photon energy [95].

For a solid, formula (1) lends itself easily to determine the transmission efficiency, simply being modified to:

$$d = \frac{-\ln(R)}{n\sigma} \quad (3)$$

In this case, the problem devolves to finding a non-toxic material with a high density and a large cross section in the hard x-ray region. The best materials to choose seem to be tantalum and tungsten, both of which are highly stable and used in filter production. We will build a stage with three identical sets of filters, with each set having several filters of different thicknesses. By combining the three sets together, one will be able to achieve various levels of solid attenuation, with the 'fine adjustment' being handled by the gas attenuator. Figure 4.2.2.2 shows the expected transmission for a sample filter.

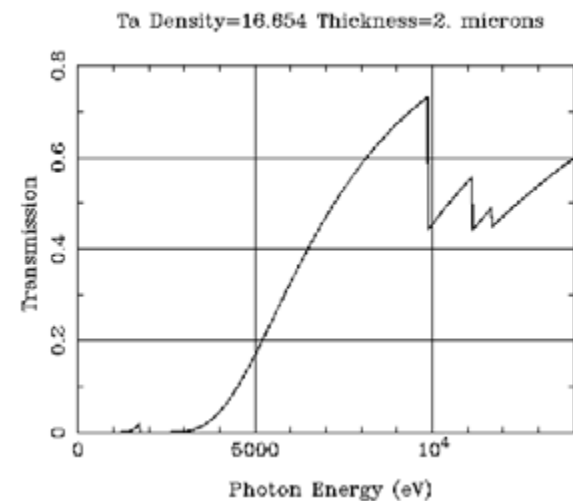


Fig. 4.2.2.2: The transmission for a 2 μ m tantalum filter between 1 keV and 14 keV photon energy [95].

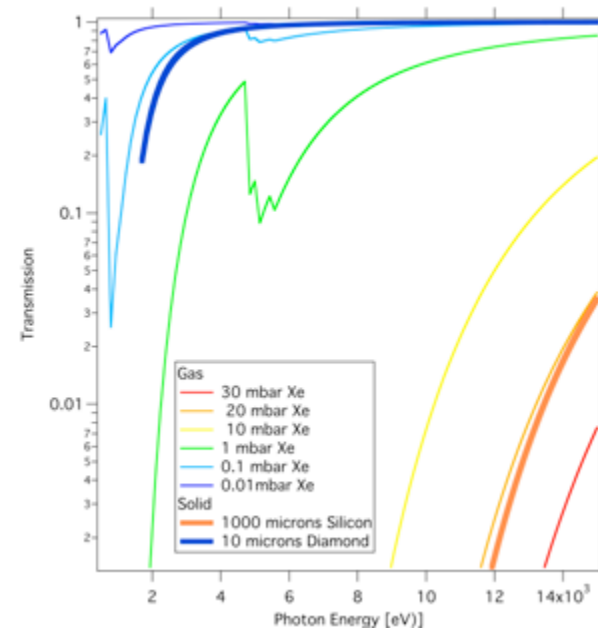


Fig. 4.2.2.3: Transmission coefficient comparison between gas and solid attenuators.

Silicon or diamond crystals are also possible candidates for beam attenuation. Fig. 4.2.2.3 shows that a 1 mm Si crystal provide almost the same attenuation of Hard X ray photons as a long gas tube filled with 20 mbar.

4.2.3 X-ray beam position monitor (X-BMP)

A key component needed for aligning the optical components as well as for the experiments is the possibility of measuring the intensity of the x-ray beam at various locations in a non invasive way. This can be readily achieved using thin scattering foils and x-ray diodes looking at (back-)scattering. The design of the LCLS intensity/position monitors provides a good starting point. This uses silicon nitride (Si_3N_4) of various thickness to optimize the amount of scattered radiation collected by 1 cm^2 diodes, located few cm upstream. Amorphous silicon nitride is used because it has been shown to minimally perturb the transmitted x-ray wavefront. Moreover, it can easily be obtained in various thicknesses. Calculations show that with $\sim 3.6 \cdot 10^{10}$ ph/pulse and a 500 nm thick membrane, about $5 \cdot 10^4$ ph/pulse are expected to arrive at 1 cm^2 diodes, placed 10 cm upstream. State of the art intensity monitors have diodes that start to show saturation at about 10^6 ph/pulse. To optimally match the dynamic range of the diodes/electronics, scattering foils have to be mounted on a motorized translation stage that can support 4–6 of them and allow an "all foils out" position. To make sure to achieve the best possible performances, limited by photon statistic, the S/N of the diode/readout electronics must be better than 10^4 for a single reading. For small (\sim mm) changes of the beam position, the normalized differences (UP-DOWN and LEFT-RIGHT) are proportional to the beam displacement.

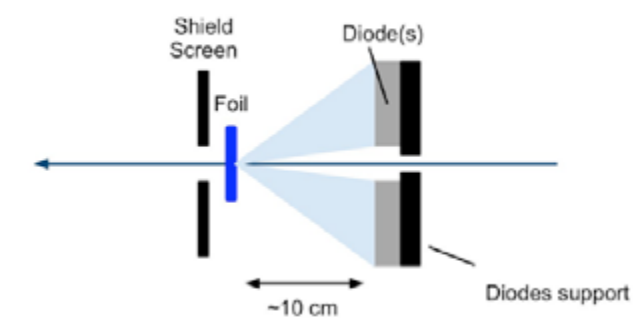


Fig. 4.2.3: Principle of diode based X-BPM as used at LCLS: light going through the thin foil (blue) back-scatters radiation onto the diodes.

At 8 keV, a 10 μ m displacement corresponds to 0.2 % change. Especially when using very thin scattering foils, parasitic scattering from downstream components might be detrimental. A shielding screen has proven to be useful at LCLS.

4.2.4 X-ray gas monitor detector (XGMD)

One of the most important measurements for both the machine operators and the experimenters at the future SwissFEL will be the photon beam intensity. Such a measurement is not only necessary for the operators to determine the effectiveness of their machine setup and the level of SASE they are producing, but is also important for the users at the beamlines to normalize the effects they are seeing in their experiments.

The best option for such an on-line monitoring tool would be a gas-based detector that would measure the ionization rate of a gas through which the beam passes, and allow one to back-calculate the intensity of the light from the known cross sections and average ion charge states. The fact that the detector would be gas-based would mean that the beam would not be significantly disturbed in such a device. Other FELs, like FLASH, have already implemented such measurement methods at their facilities [96], though the intensity measurements have, thus far, been confined to a region below several thousand eV photon energy. The basic principle of such a detector is best summarized in equation 1 below:

$$\Phi = \frac{N}{\sigma_z \eta n a} \quad (1)$$

where Φ is the number of photons, N is the detected number of ions, corrected by the expected average charge of the ions, σ is the cross section of the atom, z the detector acceptance length, η is the detection efficiency, n the atomic gas density, and a is the detector amplification factor. Due to the many parameters involved in using such a device to derive Φ , careful calibration and measurements need to be made in collaboration with a metrology laboratory or institute (like the PTB in Germany) to ensure the best accuracy of the device. Furthermore, although such a device exists for the soft x-ray region of the FEL spectrum, a hard x-ray gas detector still needs to be developed.

The FLASH photon diagnostics group is currently developing an X-ray Gas Monitor Detector (XGMD) for the future

European XFEL, and PSI may benefit from this development. The specifications for the XGMD call for an absolute measurement accuracy of about 10% over the photon energy range of the FEL, with a relative measurement accuracy that is on the level of 1–2%. The intensity will be measured and recorded on a shot-to-shot basis, giving users and operators pulse-resolved information.

4.2.5 Destructive Beam Profile monitor:

A simple technique to study the pulse-to-pulse beam shape fluctuations consists of inserting a screen into the beam path and observing the resulting fluorescence (in the case of a YAG screen) with a camera. Linear feedthroughs with various types of screens (see Fig. 4.2.5.1) could be mounted in the front end to help initial alignment of the Front End components. Such beam profile monitors are already in use to characterize electron beam profiles.

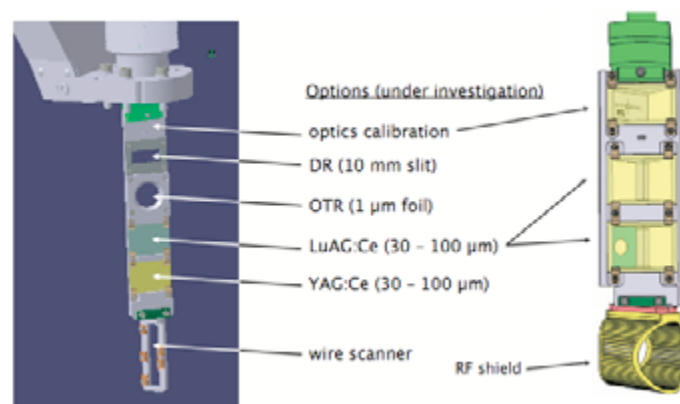


Fig. 4.2.5.1: In vacuum linear feed through, where several kinds of screens are successively inserted (example of an electron beam profile monitor).

4.2.6 Photon beam arrival time and bunch length monitor

The most promising technique for providing the required time resolution of <10 fs for both photon beam pulse length and arrival time measurements at SwissFEL is the so-called “THz streak camera” [97], which is similar to phase-sensitive cross-correlation measurements between coherent, undulator-generated terahertz pulses and optical laser pulses [98]. In this set-up, a THz field, which has been generated by the electron beam in a dedicated THz undulator or in a bending magnet follow-

ing the SASE radiators (e.g. from the electron beam dump line), is cross-correlated with the SASE VUV photon pulse in a gas cell (e.g. Kr gas). The generated photoelectrons are “streaked” by the THz field, leading to a broadening of the photo-electron spectrum, while being synchronized to the zero-crossing of the THz field. The width of the photo-electron spectrum, which can be measured by time-of-flight (TOF) spectrometers, is directly related to the photon beam pulse duration. The application of this method in the recently commissioned FLASH THz beam line has resulted in photon beam pulse length measurements in the VUV spectral range with ~10 fs time resolution and in arrival time information of the same order. The principle of such a light field (laser electric field) driven streak camera is well known from the metrology of attosecond pulses [99].

This gas-based measurement method has already yielded a doctoral thesis and a publication in Nature Photonics [97]. The low interaction level between the FEL beam and the gas preserves the wavelength, intensity, wavefront, and pulse length of the beam, thus non destructively yielding pulse-resolved information. The user is able to see the properties of the beam as he is taking measurements at the focus of the FEL, while the operators can adjust the settings in real time in response to any shifts they see in the beam behavior. This is ideal for on-line measurements, and the Pulse Arrival and Length Monitor (PALM) will be a great asset to the SwissFEL diagnostics suite once it is tested and integrated.

The PALM will be a magnetic and electric-field free vacuum chamber that will house several electron time-of-flight (TOF) spectrometers, a gas jet, pumps, and ports for the THz beam and the X-ray beam. The two beams will pass the densest part of the pulsed gas jet that will be let into the chamber, ionizing the gas and creating an oscillating electrical field in the interaction region. The electron TOFs will be precisely aligned to the interaction point of these three beams (THz, Gas, and X-ray) to measure the kinetic energies of electrons as they leave the focus. Since the electric field applied by the THz beam affects differently electrons travelling in opposite directions in its polarization plane (adding or subtracting kinetic energy), the final kinetic energies measured by the electron TOFs will differ as well. The difference in these energies will then be used to evaluate the strength of the electric field in the interaction region, from which one can evaluate exactly when during the THz pulse the X-ray pulse ionized the gas jet. The measurement will also be able to evaluate the length of the FEL pulse by

the method used by Frühling et al. [100], by including an electron TOF perpendicular to the polarization vector of the FEL and THz pulses, and comparing the electron kinetic energies between it and the two electron TOFs that lie in the polarization plane.

The final goal of these efforts for SwissFEL is to generate the Terahertz pulses by the Ti:Sa experimental pump laser, while the X-ray pulse originates in the undulator. In addition to measuring pulse length, the device can thus be used to determine the relative arrival time between the FEL and the pump laser pulses, and to verify the effectiveness of the fiber optical synchronization system.

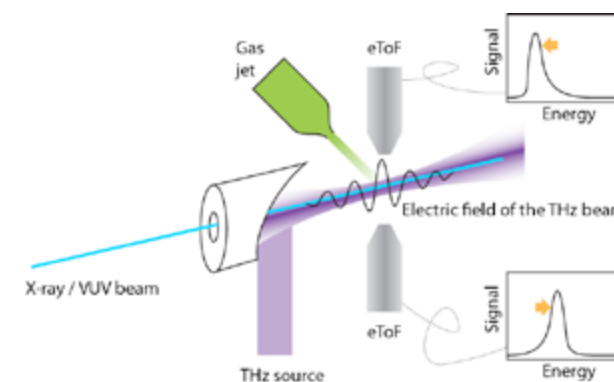


Fig. 4.2.6.1: schematic setup of the photon arrival time monitor. The energy of the photoelectrons is streaked by the externally applied Terahertz field. A third electron TOF could be installed to measure the X-ray pulse length.

The SwissFEL laser group started the development of a THz source in late 2010. The group’s interest has been the development of a powerful compact, laser-driven half/single-cycle THz source which is synchronized to a femtosecond X-ray or IR laser, in order to perform pump-probe experiments. The anticipated electric and magnetic field strengths exceed MV/cm and Tesla, respectively.

The group is currently setting up and commissioning a THz generation scheme based on optical rectification in organic crystalline salts such as DAST (4-N,N-dimethyl-amino-4'-N'-methyl stilbaxolium tosylate), driven by a powerful mid-infrared laser source. Preliminary results show the great potential of this approach. Up to now electric field strengths exceeding 2 MV/cm could be produced at a central frequency around 2 THz, which is about 5 times higher than what was demonstrated by lasers in the past in this THz range [101]. This approach of laser-based THz production in organic crystals already provides record-high field strengths and appears to be

a promising route towards a powerful THz source for high-field THz applications at PSI and at the future SwissFEL facility.

4.3 Photon switchyard (Athos, Aramis)

The photon beamline transports the X-rays from the undulators to the experimental stations. The position of the first mirror is the key parameter for defining the space requirements for the optics and the experiment positions.

The mirror acts as a filter to remove unwanted radiation, such as higher harmonics, Bremsstrahlung, etc., from the X-ray free electron laser pulse and selects which experiments will be illuminated. The mirror must not be damaged by the intense laser pulses, and so the deposited energy has to stay well below the ablation threshold. To define space requirements for the Aramis undulator beamline, we have considered separate scenarios: (a) a double-crystal-monochromator beamline for high resolution, (b) a high-flux beamline which maintains the time structure of the XFEL, and (c) a nano-focusing beamline.

4.3.1 Ablation and single-shot damage

A central problem at storage rings such as the Swiss Light Source (SLS) is the high heat load density, typically 1 W/mm². In contrast to this, the heat load problem at the SwissFEL is negligible (<1 mW/mm²), but ablation is a major concern. To approach the problem, we take into account results from single-shot and multiple-shot damage experiments at FLASH, make reasonable assumptions for boundary conditions and compare the results with known quantities, to judge the feasibility. We assume 50 m distance between the end of the undulator and the first mirror. This length is at the lower limit of other comparable XFEL projects and should be reserved anyway, to put in additional equipment, such as gas filters, diagnostics, etc. . . . We assume typical grazing angles of 2 to 3.5 mrad for hard X-rays and 10 to 20 mrad for soft X-rays, as a consequence of the X-ray reflectivity. To avoid ablation, the radiation dose must be significantly less than the dose for melting, which is of the order ≈ 1 eV/atom. With candidate mate-

rials such as C, SiC or B₄C for the coating of the first optical elements and the grazing angles given above, we estimate a corresponding damage threshold for the fluence on the order of 1 mJ/mm². It is important to note that the obvious approach to reduce the fluence by reducing the grazing angle (to spread the energy over a bigger area) does not necessarily reduce the energy density per atom, i.e. per volume, since the penetration depth for X-rays decreases for small grazing angles. This is the reason for preferring light elements, with larger penetration depth, as coating material. Table 4.3.1 summarizes the relevant machine parameters and X-ray Optics Layout and the resulting thresholds for the SwissFEL in comparison with other XFEL projects. The maximum fluence in normal incidence F has been estimated with the following formulas:

$$F = \frac{W}{2\pi\sigma^2} \quad \text{or} \quad F = \frac{W}{2\pi(\sigma_R^2 + (s\sigma_\theta)^2)}$$

with the pulse energy W , the rms radius of the footprint σ (at a certain position) or alternatively the beam size σ_R , the distance s and the beam divergence σ_θ .

We emphasize the maximum fluence in normal incidence as the important value for the comparison. This value has to be multiplied by the grazing angle, 2–3.5 mrad, to obtain the fluence at the optical surface (1). The grazing angles are similar at all FELs. In conclusion, all FEL's keep the maximum fluence at the optical surface $\ll 1$ mJ/mm², which means a 50 m distance between undulator and optics is reasonable and gives some security margin.

(1) To calculate the fluence (F_A) at the surface of the optics for the Aramis undulator with a grazing angle of 2 mrad: $F_A = 1.85 \text{ mJ/mm}^2 \times 2 \cdot 10^{-3} = 3.7 \cdot 10^{-3} \text{ mJ/mm}^2$.

Table 4.3.1: Damage affecting parameters of the four hard X-ray FELs.

FEL		Aramisa	SASE2 ^b	LCLS ^c	SACLA ^d
Wavelength	(Å)	1	1	1.24	1.24
Pulse energy	(mJ)	0.15 (1.0)	2	2.1	0.78
Beam size	(μm rms)	26.1	36	30	33
Beam divergence	(μrad rms)	1.9	0.35	0.42	0.73
Position in first mirror	(m)	50	290	100	85
Max. fluence @ 1 st mirror	(mJ / mm ²)	2.5 (16)	27	125	25

(a) Table 2.4.1.1, maximum values in parenthesis

(b) XFEL TDR 2007 and draft X-ray optics CDR 2011

4.3.2 Conceptual beamline layout

The conceptual beamline layout defines the space requirements and gives a feasible layout for the optical system and the experiment. The key input parameters are the positions of the first two mirrors, M1 and M2 and the possible grazing angles from the previous section. As an option, we assume a 1:1 focusing with an additional third mirror, M3, located about 70 m from the Aramis undulator. This gives a beamline length of 150 m. Each undulator shall serve 3 experiments in separate hutches, to allow access for installation and maintenance etc., while another experiment receives beam. For each experimental hutch, we reserve an area of about 100 m² $\sim 7 \text{ m} \times 15 \text{ m}$. The achievable transverse separation with mirrors is small, due to the possible grazing angles, in particular for hard X-rays. Therefore, the experiments have to be arranged more or less in a row. A more detailed description of the optical layout of the Aramis undulator beamline is given in the following sections.

4.3.2.1 X-ray optics layout

An optical design of a beamline is strongly dependent on its operational energy range and the scientific case. The main purpose of the X-ray optics is to redirect and shape the X-ray beam according to the users and experimental needs. The choice of optical components has to be done very carefully, since they influence or determine important beam properties like spectral characteristics (brilliance, harmonics), polarization, beam geometry, pulse structure and wavefront preservation. The Aramis undulator (selected parameters in Table 4.3.2) serves a hard X-ray beamline, operated over the energy range of 1.77 keV to 12.4 keV, with a potential upgrade up to 13 keV to reach the selenium edge (12.66 keV).

(c) LCLS CDR 2002

(d) XFEL/Spring-8 Beamline TDR, Ver. 2.0 Feb, 2010

Table 4.3.2: SwissFEL variable parameters of the Aramis undulator, copied from Table 2.4.1.1.

Wavelength	1 Å (12.4 keV)	7 Å (1.77 keV)
Electron beam energy	5.8 GeV	2.2 GeV
Bandwidth	0.05 %	0.2 %
Eff. Peak power	2.8 GW	5.5 GW
Beam size	26 μm	78 μm
Beam divergence (rms)	1.9 μrad	7.4 μrad
Pulse energy	0.15 mJ (1 mJ)*	0.2 mJ

(*) after optimization

Compared to a third generation synchrotron source, the optical components of the XFELs have to cope with several new problems. One of these problems is beam separation. This represents a problem of how to separate physically the beam from its geometrical path to create enough space for experimental end-stations. This problem is partially solved with reflecting mirrors. But the separation with mirrors alone is rather small, because the grazing angles in the hard X-ray region are small, in the order of milliradians (tenths of degrees). Therefore

the concept of the so-called Large Offset Monochromator (LOM) is considered. The LOM is a double crystal monochromator (DCM) with a large offset reaching up to several tens of centimeters.

The second problem is the damage of the optics due to the high spatial energy densities of the FEL pulse structure, see section 4.3.1. To offer the beamline users several types of spot sizes, we investigated various types of focusing optics. In general we can deliver a free-propagating beam (the beam interacts only with M1), a 1 μm spot size possibility and a 1:1 focusing scheme delivering a 100 μm (FWHM) spot size. The preliminary optical layout of the Aramis undulator beamline is shown in Fig. 4.3.2.1. The Aramis undulator beamline is divided into areas. First is the so-called pre-experimental hutch area, where most of the optics is situated, followed by three experimental hutches.

The pre-experimental hall area is the space between the Aramis undulator and the wall of the first experimental hall. In this area, the first two deflecting mirrors (M1 and M2) are situated. Mirrors M1 and M2 are two flat mirrors placed at 50 m and 52 m, respectively, after the Aramis

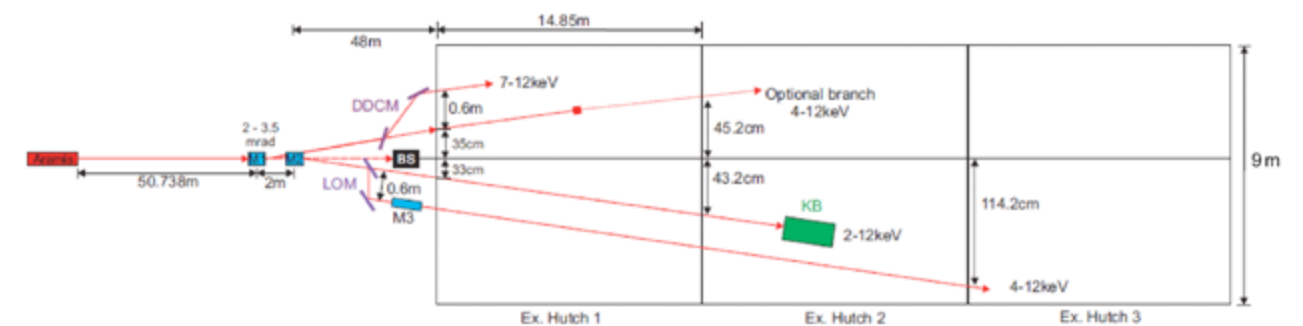


Fig. 4.3.2.1: Aramis undulator optics layout. The beam separation distances shown are valid for a grazing angle of 3.5 mrad (0.2°).

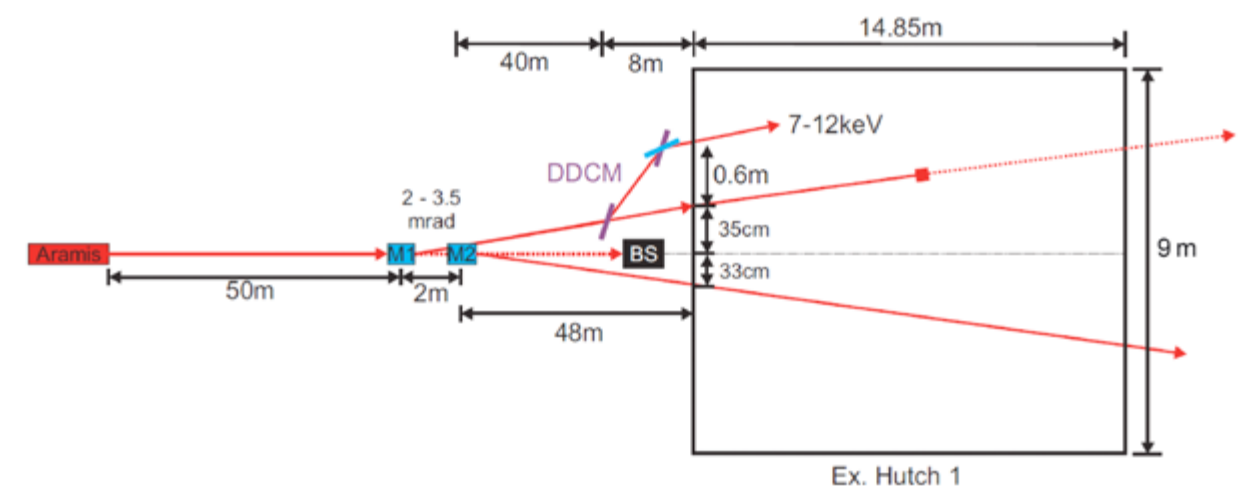


Fig. 4.3.2.2: Optics layout of the experimental hutch 1. The beam separation distances shown are valid for a grazing angle of 3.5 mrad (0.2°).

undulator. The first two mirrors are located inside a tunnel, together with the beam diagnostics and the gas absorber. The tunnel is closed with a 1.8 m thick wall located 11 m behind mirror M1 and 61 m behind the Aramis undulator. After the two mirrors, a beam stop (BS) is situated. The outer wall of the first experimental hut is situated 48 m behind mirror M2. To ensure the switching between the left and right beam branch, either mirror M1 or both mirrors have to be movable in the direction perpendicular to the beam. Because of the low beam total deviation angle, the reflected beam from mirror M1 will propagate through the chamber of mirror M2. Therefore, most probably both vacuum chambers will be connected and share one vacuum unit. The combination of a small source size, small source divergence and a relatively short undulator-mirror distance allows us to accept the whole FEL footprint.

The first experimental hut is situated 100 m behind the Aramis undulator and 48 m after mirror M2. The dimensions are 15×9 m (l \times w). The first experimental hut will use the left beam branch deflected by mirror M1. As an optical system a **Double Diamond Crystal Monochromator** (DDCM) is proposed. The DDCM is a large offset monochromator system placed 42 m behind mirror M1 and 8 m before the wall of the first experimental hut. The schematic layout of experimental hut 1

is shown in Fig. 4.3.2.2. The given beam separation distances in Fig. 4.3.2.2 are valid for a grazing angle of 3.5 mrad (0.2°). The right beam branch deflected from mirror M2 propagates 33 cm from the center of the experimental hut. Thanks to the large offset (0.6 m), the DDCM allows a large separation of the diffracted beam from the right beam branch and makes space for a potential experimental end-station. Diamond crystals are very transparent, which offers a possibility to split the left beam branch into two beams. One will be diffracted within the DDCM and used as the operation beam in the first experimental hut. A detailed description of the DDCM is given in section 4.3.3.3.

The second experimental hut is situated about 63 m from the second mirror M2 and 115 m from the Aramis undulator. The second experimental hut will use the right beam branch reflected from mirror M2, Fig. 4.4.1.3. As mentioned in the previous section, there is also the possibility to use a second beam: the forward-diffracted beam from the first diamond crystal from the DDCM. This beam would cover an energy between 4 – 12 keV and would enter the hut 45.2 cm from the central point of the second experimental hut (to the left). The operational beam reflected from mirror M2 is 43.2 cm from the central point of the experimental hut (to the right). The primary beam reflected from the second mirror M2

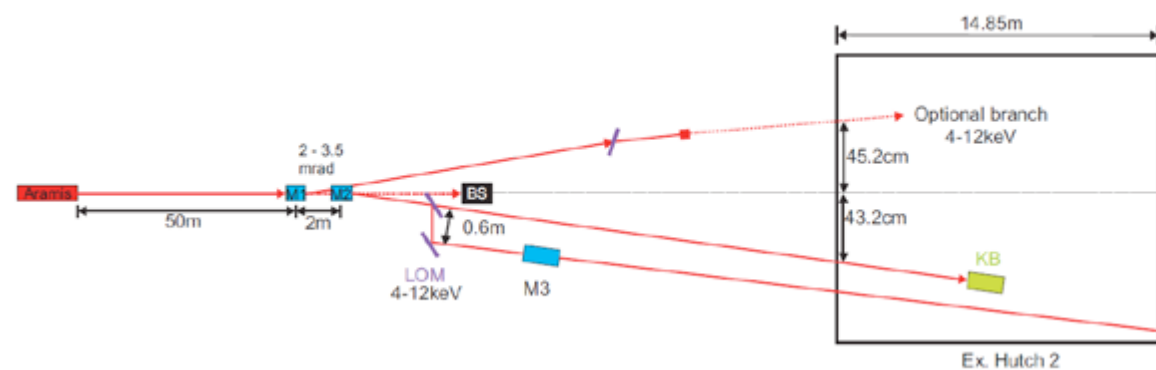


Fig. 4.3.2.3: Optics layout of the experimental hut 2, variant b. The beam separation distances shown are valid for a grazing angle of 3.5 mrad (0.2°).



Fig. 4.3.2.4: Optics layout of the experimental hut 3. The beam separation distances shown are valid for a grazing angle of 3.5 mrad (0.2°).

will propagate through the **Large Offset Monochromator** (LOM) situated between the second mirror M2 and the first experimental hut. The LOM will be placed 2 m behind the 1.8 m thick wall and 12.7 m behind mirror M2. By making the mechanical design of the first crystal movable in the direction perpendicular to the impinging beam, we allow the beam to propagate to the second experimental hut. The second experimental hut would accept the raw FEL beam from the Aramis undulator, exploiting its unique properties. The only optical element interfering with the FEL beam would be for security reasons mirror M2. An additional focusing system could be installed in the second experimental hut. One can think either of a Kirkpatrick-Baez (KB) mirror system, Fresnel zone plates (FZP) or compound refractive lenses (CRL). Because of the strong demagnification, i.e. high ratio between source and image distance ($\sim 125:1$), these optical systems could be used for nanometer focal spot sizes.

The third experimental hut is situated about 78 m behind the second mirror M2 and 130 m behind the Aramis undulator. The operational beam will be the right beam branch reflected from mirror M2, Fig. 4.4.1.4. The main optical system for the third experimental hut will be a LOM, situated between mirror M2 and the first experimental hut. The LOM will be placed 13 m behind mirror M2. The LOM, similar to the DDCM, is a monochromator system where the distance between the two crystals (offset) is large. We assume an offset value of 0.6 m, as at the LCLS. The crystals used in the LOM will be silicon (Si(111)) crystals. By shifting the beam by 0.6 m, we create additional space for the experimental end-station. The working beam will be 114 cm from the middle point of the third experimental hut (to the right). Because of the fixed lattice constant of silicon crystal, the usable energy range is limited to >4 keV. If we place the toroidal mirror 18.2 m behind M2 (29 m before experimental hut 1 and 1.5 m behind the LOM), we will reach a 1.15:1 demagnification. The source to image distance will be 71:62 (m). The toroidal mirror can deflect the beam either vertically or horizontally. By using a horizontal deflection, we will reach even a higher beam separation and gain more space in the second experimental hut. The focus size in the third experimental hut is $95 \times 97 \mu\text{m}$ (FWHM).

Options in discussion

In the current design, only one mirror is foreseen to decouple the X-rays from the Bremsstrahlung, M1 or M2. It is still under discussion if one mirror is sufficient in

radiation safety terms. If not, a two mirror layout has to be implemented, where the first mirror could then be vertically deflecting. In that case the first two deflecting mirrors would be bendable. This concept would have the following, advantages:

- correction of possible astigmatism
 - slope error correction
- and disadvantages:
- vertical deflection
 - additional optical element
 - additional bending mechanism adds to overall complexity

4.3.3 X-ray optics components

4.3.3.1 Mirrors

The choice of a coating material in the case of the SwissFEL for the hard X-ray branch will be either carbon (C) or silicon carbide (SiC). The grazing angle should be chosen such, that over the whole energy range, the reflectivity is $>90\%$. To fulfill this requirement, one has to use very shallow grazing angles. In Fig. 4.3.3.1 and 4.3.3.2 are the reflectivity plots versus grazing angle for a SiC and a C coated mirror. As one can see from the plots, to cover the energy range up to 15 keV with a $>90\%$ reflectivity, one has to use a 3 mrad (0.17°) grazing angle for the SiC coating and a 2.4 mrad (0.14°) grazing angle for the C coated mirror. The grazing angle is not set yet. In the previous section, the beam separation distances in Fig. 4.3.2.2 to 4.4.1.4 are for a grazing angle of 3.5 mrad (0.2°).

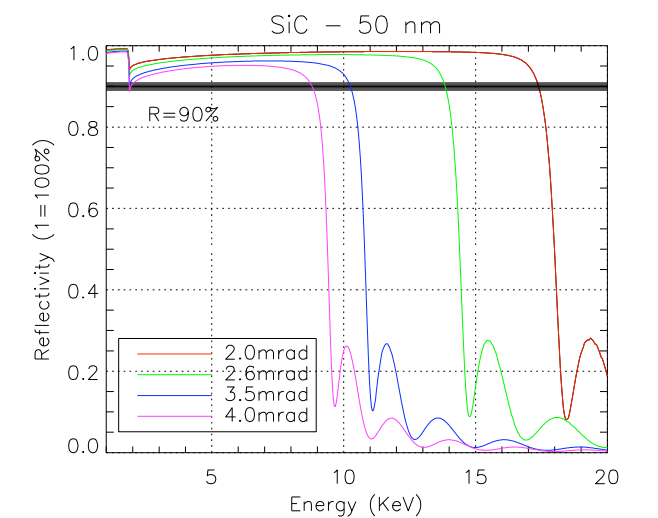


Fig. 4.3.3.1: Reflectivity plot of a SiC coated Si mirror substrate, for various grazing angles.

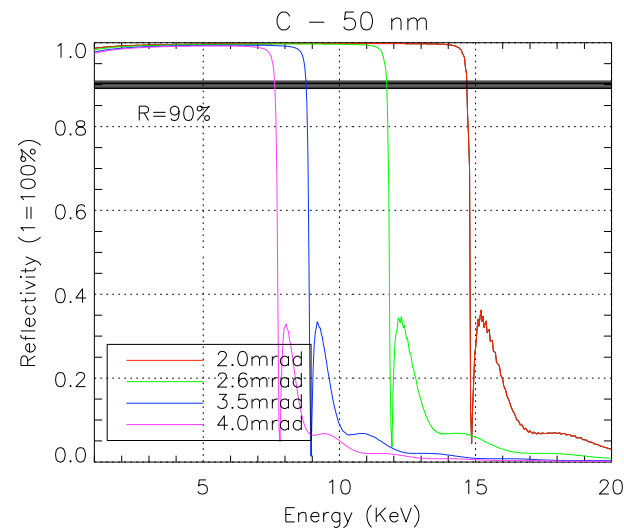


Fig. 4.3.3.2: Reflectivity plot of a C coated Si mirror substrate, for various grazing angles.

The reflectivity requirement has a direct impact on the mirror length. The lower the grazing angle, the higher is the reflectivity we obtain and the longer the mirror will become. Fig. 4.3.3.3 shows the dependence of the mirror length on the grazing angle. The vertical black line in Fig. 4.3.3.3 indicates a mirror length of 800 mm. This length has been identified by the European XFEL as a feasibility limit for mirror manufacturers to deliver high quality mirrors.

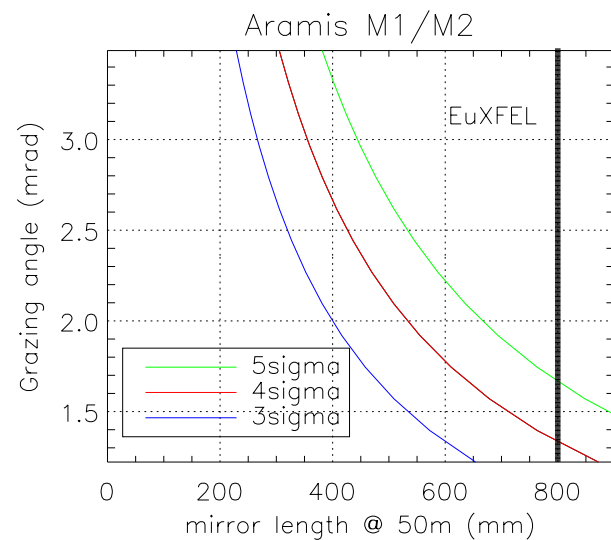


Fig. 4.3.3.3: Grazing angle vs. mirror length at 1.7 keV (5.32 μ rad divergence), for a mirror placed 50 m behind the Aramis undulator, for different σ acceptances.

The Aramis undulator beamline layout has a total of three mirrors. The first two mirrors, M1 and M2 are plane mirrors and act as filter for the spontaneous radiation and as beam deflectors. The parameters of M1 and M2 are tabulated in Table 4.3.3.1.

Table 4.3.3.1: Mirror M1 and M2 parameters.

Parameter	M1	M2
Shape	Plane	Plane
Position (m)	50	53
Bulk Material	Si	Si
Coating	SiC/C	SiC/C
Coating Thickness (nm)	50 nm	50 nm
Grazing angle ($^{\circ}$)	0.12 – 0.2	0.12 – 0.2
Grazing angle (mrad)	2 – 3.5	2 – 3.5
Direction of reference	left	right

Table 4.3.3.2: Mirror M3 parameters.

Parameter	M3
Shape	Toroidal
Position (m)	71
Bulk Material	Si
Coating	Au/Pt/Rh/Si/C/SiC
Coating Thickness (nm)	50
Grazing angle ($^{\circ}$)	0.15 – 0.23
Grazing angle (mrad)	2.6 – 4.0
Direction of reference	right
R radius (km)	18.92 @ 0.2 $^{\circ}$
P radius (mm)	230 @ 0.2 $^{\circ}$

The third mirror, M3 is a toroidal mirror reflecting the beam into the experimental hut 3. Its parameters are tabulated in Table 4.3.3.2. Possible coating materials for mirror M3 are gold (Au), platinum (Pt), rhodium (Rh), polished Si surface, carbon (C) or SiC.

4.3.3.2 Nanometer focusing

The second experimental hut could be used for nanometer focusing. The long distance to the source and the short image distances created by the proposed focusing optics (FZP, CRL, KB) make the optical layout of the second experimental hut a perfect candidate for nanometer focusing. It should be emphasized that only KB mirrors can provide achromatic focusing over the full energy range. FZP or CRL are complementary for applications with a restricted photon energy range. To estimate the performance and required specifications, in particular for KB mirrors, there are several approaches.

(a) Slope error approach. The slope error is a critical issue for present nanometer focusing devices. If we assume a mirror with a slope error (τ_s) of 0.1 μ rad and a focusing distance (f) of 1 m, then the slope error con-

tributions to the focal spot size (FWHM) can be estimated as follows (assuming uncorrelated slope errors):

$$\delta y = 2 \times 2.35 \times f \times \sigma_s \quad (1)$$

From equation (1), the slope error contributions to the focal spot are 500 nm for a focusing distance of 1 m.

(b) Magnification approach: The source is 125 m away from the wall of the second experimental hut, which gives us a demagnification of 125:1, for a 1 m focusing distance. The source size is 43 μ m (rms) @ 7 \AA (1.77 keV), which corresponds to a spot of 101 μ m FWHM. For a demagnification factor of 125:1 this gives us 0.8 μ m FWHM.

(c) Mirror length approach. It has been demonstrated that KB mirror systems are able to reach nm-focus spot sizes. The critical point in using a KB mirror system is its length. The KB system will be located at least at a distance of 125 m from the Aramis undulator. In Fig. 4.3.3.3 is plotted mirror length vs. incidence angle for the lowest energy (with the highest beam divergence (5.32 μ rad)). One can see from the plot, that the mirrors with a 4 sigma acceptance will be up to 1 m in length at that position. For comparison, one can see the mirror length vs. incident angle for the highest energy (with the lowest beam divergence (1.5 μ rad)), in Fig 4.3.3.4. It will be extremely difficult to polish such a long mirror to the desired slope error mentioned above. Therefore we are considering a KB system with variable grazing angle, with the additional benefit able to suppress higher harmonics, which are a concern, particularly at low photon energies. The working range of the KB system would be

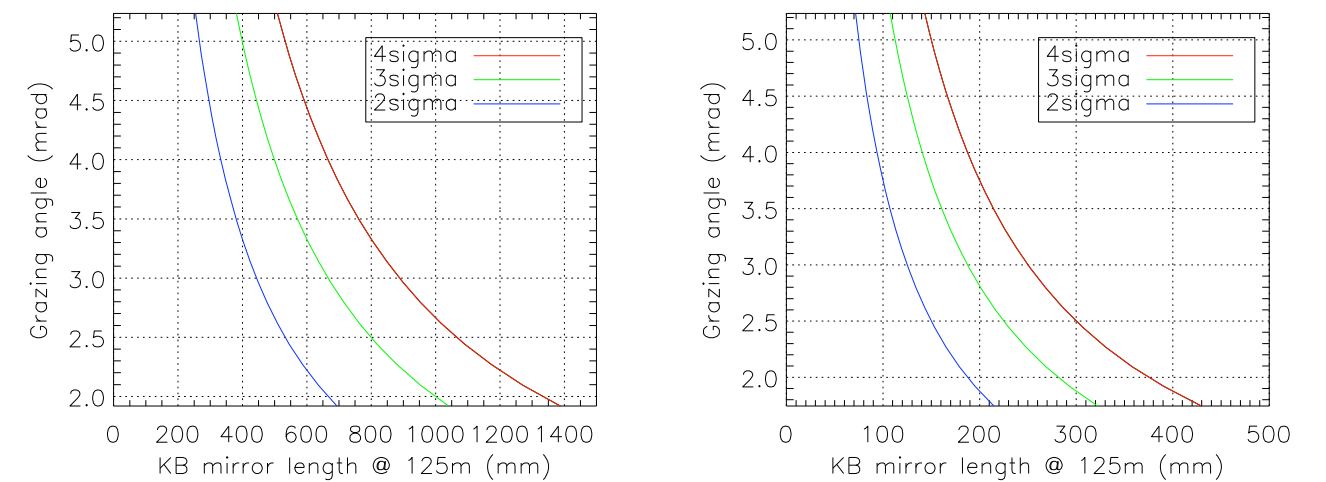


Fig. 4.3.3.4: KB length vs. incidence angle for three different sigma acceptances at 1.7 keV (5.32 μ rad divergence) on the left graph and at 12.4 keV (1.5 μ rad divergence) on the right graph.

divided according to the mirror length. We consider two KB mirror lengths:

(a) 400 mm:

The working range of the 400 mm KB system would be divided into five ranges. Each range would be used for a specific energy range under a certain grazing angle. The approach of defining fixed grazing angles for a specific energy range, is only illustrative. It should demonstrate that by applying a variable grazing angle, the acceptance of the KB system can be $>4\sigma$ for the whole photon energy range. In practice, one can set the KB system to any angle between 2 mrad and 6 mrad. The KB system will have five operational grazing angles. Each angle will cover an energy range of 3 – 4 keV, with an acceptance of $>4\sigma$. For each angle and energy, the KB system reflectivity will be $>90\%$. The working ranges are tabulated in Table 4.4.2.3 and illustrated in Fig. 4.3.3.5. The energy ranges are overlapping, and the grazing angles have been chosen such that the cut-off energy of the reflecting coating (SiC) is 1 keV higher than the working energy. The cut-off energy is the energy at which the reflectivity of the SiC coating steeply drops down from 90%. For example, if we compare the second (4 keV–6 keV) and third (6 keV–9 keV) ranges (Table 4.4.2.3), their cut-off energies are 7 keV and 10 keV, respectively. The third energy range, working with a grazing angle of 3.5 mrad (0.2 $^{\circ}$) is optimized for 6 keV–9 keV with acceptances of 3σ – 3.8σ , respectively. If one needs a higher acceptance for 6 keV (3σ in the third range), the KB system will be switched into the second energy range (4 keV–6 keV), working with a grazing angle of 4.9 mrad (0.28 $^{\circ}$), at which the acceptance for 6 keV is 4.1σ .

(b) 500 mm:

The working range of the 500 mm KB system would be divided into three ranges. The KB system will have three operational grazing angles. Each angle will cover a small energy range of 4–5 keV, with an acceptance of 4σ . For each angle and energy, the KB system reflectivity will be $>90\%$. The working ranges are tabulated in Table 4.3.3.4 and illustrated in Fig. 4.3.3.5. The energy ranges are overlapping, and the grazing angles have been chosen such that the cut-off energy of the reflecting coating (SiC) is 1 keV higher than the working energy.

Using a KB mirror system, one deflects the focal spot both in the vertical and horizontal directions. For each energy range, corresponding to a certain grazing angle, this shift in xy-direction is different: the larger the grazing angle, the bigger the shift. Fig. 4.3.3.6 shows the horizontal and vertical shift of the focal spot for vertical and horizontal focusing distances of 1500 mm and 1000 mm, respectively.

Table 4.3.3.3: KB mirror parameters. Mirror length is fixed to 400 mm and the coating is SiC.

Range	Grazing angle (mrad)	Grazing angle (°)	Cut-off energy (keV)	Energy (keV)	Beam Size Acceptance (unit σ)
1	6	0.34	5	1.7	3.6
				2	3.8
				3	4.0
				4	4.2
2	4.9	0.28	7	2	3.0
				4	3.5
				5	3.9
				6	4.
3	3.5	0.2	10	2	2.2
				6	3.0
				7	3.4
				8	3.6
				9	4.1
4	2.8	0.16	13	2	1.8
				9	3.3
				12.4	6.0
5	2	0.12	17	2	1.2
				9	3.5
				12.4	4.1
				14	7.0

Table 4.3.3.4: KB mirror parameters. Mirror length is fixed to 500 mm and the coating is SiC.

Range	Grazing angle (mrad)	Grazing angle (°)	Cut-off energy (keV)	Energy (keV)	Beam Size Acceptance (unit σ)
1	5.5	0.31	6	1.7	4
				2	4.1
				3	4.6
				4	5.0
				5	5.2
2	3.8	0.22	9	2	2.9
				5	3.8
				6	4.0
				7	4.5
				8	4.7
3	2.0	0.12	17	2	1.6
				9	2.9
				10	3.4
				11	4.0
				12.4	5.3
14	9.0				

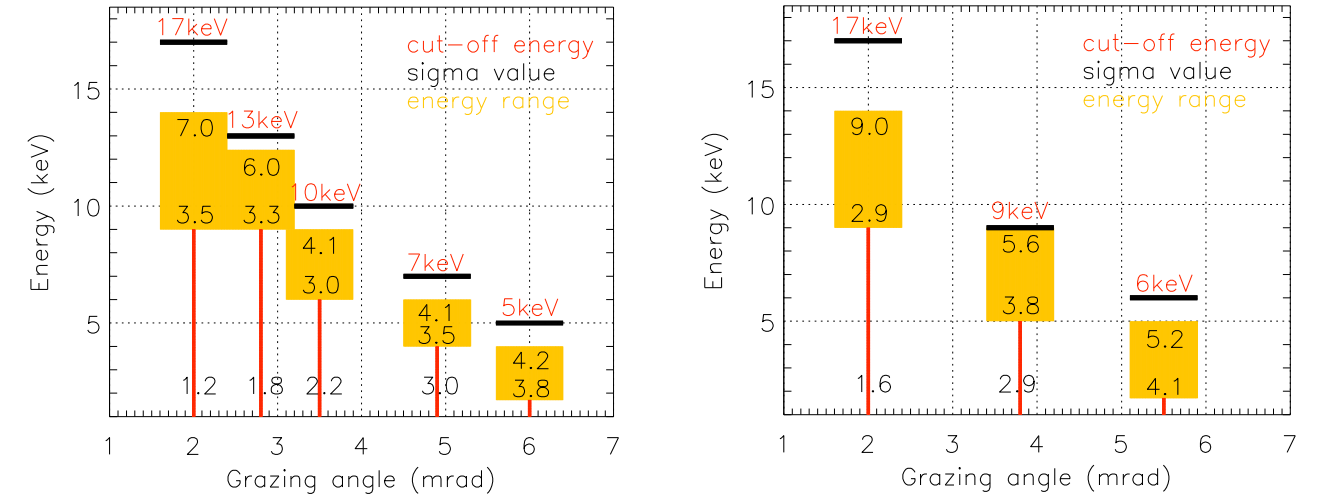


Fig. 4.3.3.5: KB system acceptances. Yellow squares represent the working energy ranges, under a certain grazing angle (red vertical line). The values in the yellow energy ranges represent the σ acceptances at the border energies of the ranges. The cut-off energies (red) are shown as horizontal lines. The mirror length is fixed to 400 mm (left graph) and 500 mm (right graph), with SiC coating.

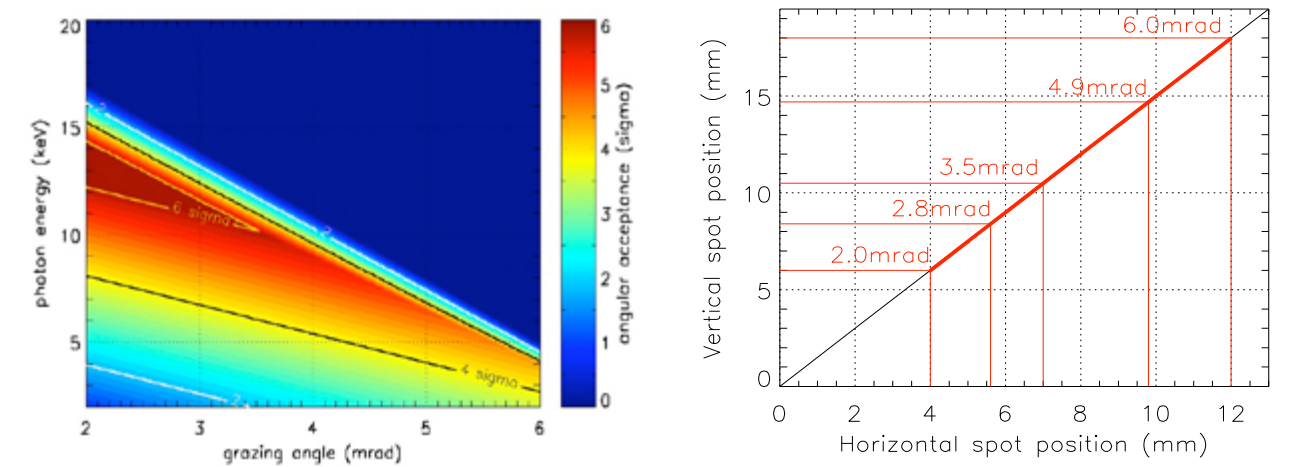


Fig. 4.3.3.6: left: Working range of a 400 mm long KB system as contour plot. right: The dependence of the focal spot position vs. grazing angle. This plot represents the following case: two mirrors separated by 500 mm, vertical focusing distance: 1500 mm, horizontal focusing distance: 1000 mm.

4.3.3.3 Monochromators

Two monochromators are proposed for the Aramis undulator beamline. The monochromator system is special, due to its large offset. The proposed offset of the Large Offset Monochromator (LOM) is 0.6 m. One LOM will be equipped with diamond crystals as working crystals: the Diamond Double Crystal Monochromator (DDCM). The second LOM will use silicon crystals as working crystals, Si(111). The DDCM can be operated either in the Laue or in the Bragg diffraction regime. One can even use a combination of Laue and Bragg diffraction, Fig. 4.3.3.7. Because of the similar lattice spacing (only a difference of 2.95%) between diamond and germanium, one can

also use a germanium crystal in combination with a diamond crystal, forming a DCM. This way one can use the broader acceptance of the germanium crystal. Thanks to a high thermal conductivity and a low expansion coefficient, the diamond crystal does not suffer from lattice distortion. Diamond crystals are also very transparent, which offers a possibility to split the left beam branch into two beams. The usable energy range of a DDCM begins at 7 keV. This range is restricted due to the low transmission of diamond at lower energies and the low diffraction efficiency below 7 keV. In Fig. 4.3.3.8 is plotted absorption vs. energy plot for diamond crystals of four different thicknesses (50 μm , 100 μm , 150 μm and 200 μm).

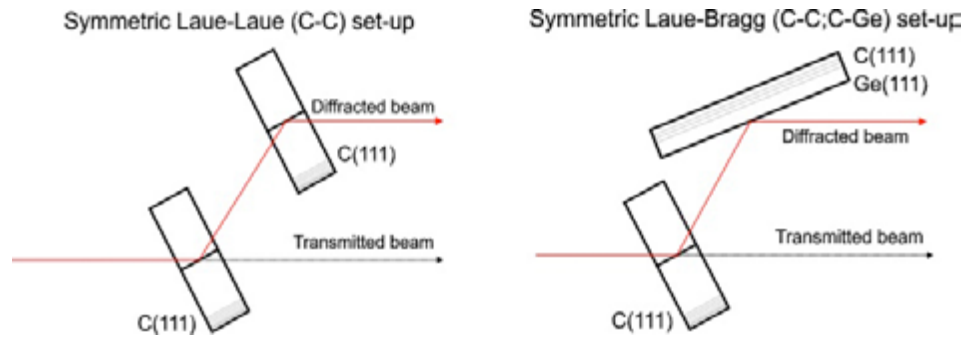


Fig. 4.3.3.7: Possible diffraction schemes of DDCM.

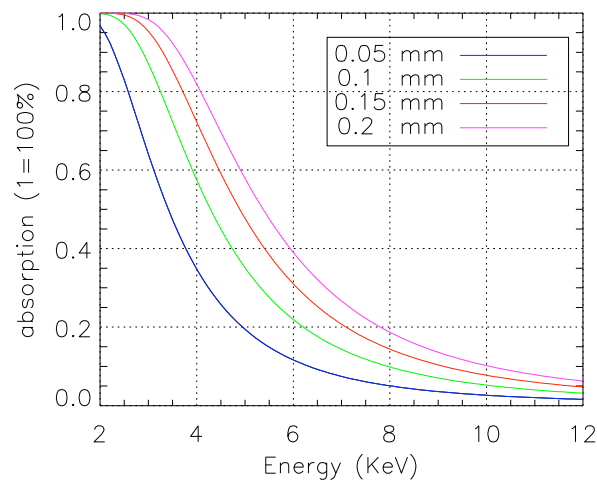


Fig. 4.3.3.8: Absorption vs. photon energy of diamond crystals with various thicknesses.

4.4 Experimental hall

4.4.1 General layout

A top view of the experimental area is presented in Fig. 4.4.1.1. This part of the building consists in the Aramis experimental hall (hard X-rays), the Athos Experimental hall (soft X-rays) and the various auxiliary facilities which include control rooms, laser hutches, preparation laboratories, technical infrastructure, and so on. The main pump laser room located on the first floor (Fig. 4.4.1.2). Simultaneous operation at 100 Hz of one Aramis and one Athos endstation is foreseen.

4.4.2 Aramis experimental hall

The Aramis experimental area is divided into three consecutive hutches of about 9×14 m size each (Fig. 4.4.1.1). The separation will allow activity (preparation of experiments, maintenance,...) in two hutches while measurements take place in the third one.

4.4.3 Aramis experimental stations

At the present stage of planning, the concept of three experimental stations which called ES-A, ES-B and ES-C (Fig. 4.4.2.1), has been developed to a certain extent, although their definitive positioning in one of the hutches has not been fixed yet. The concepts include in par-

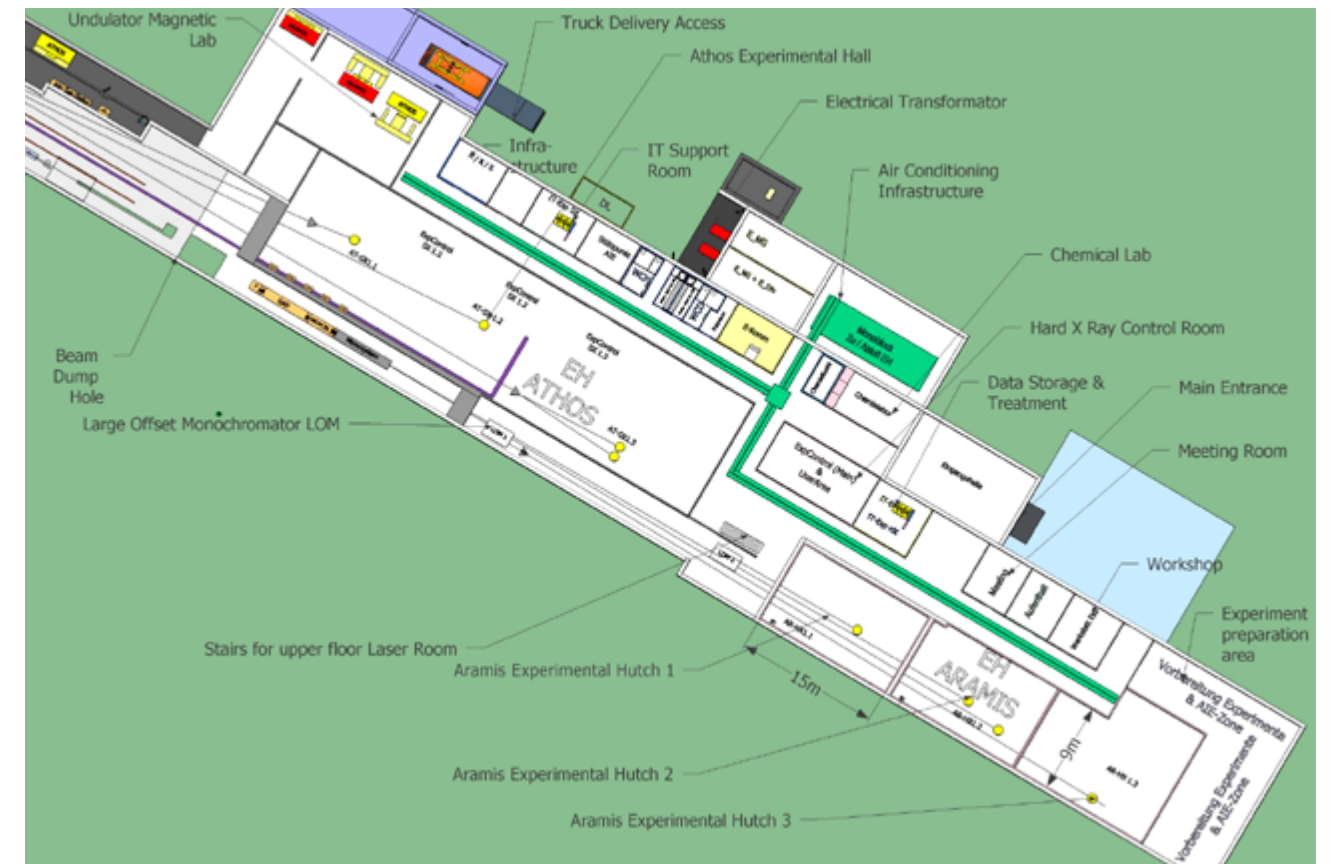


Fig. 4.4.1.1: Layout of the experimental hall (status – Sep. 2011).

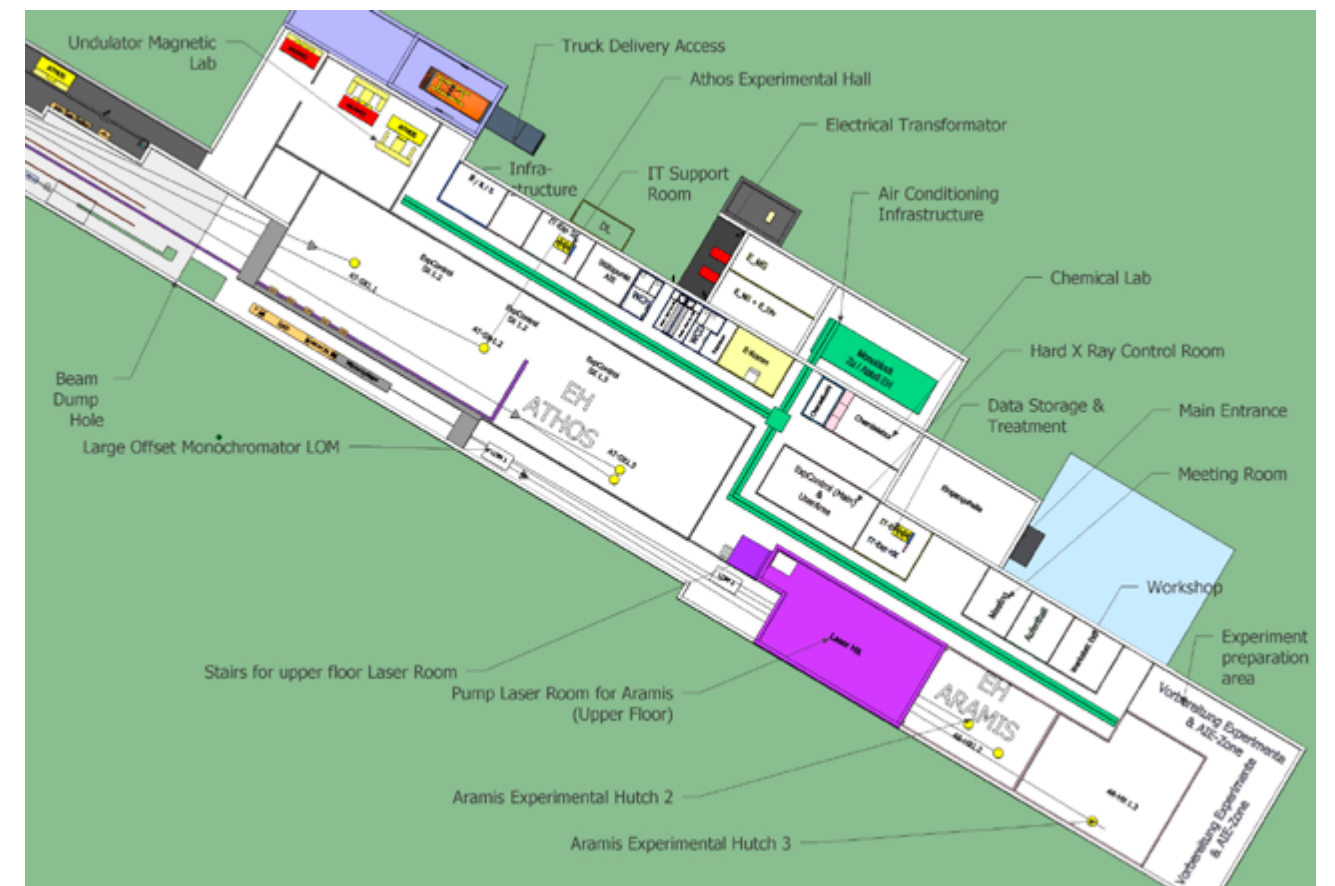


Fig. 4.4.1.2: Layout of the experimental hall showing the laser hutche (second floor) for the pump lasers (status – Sep. 2011).

ticular the permanent instrumental setup dedicated to the experiments foreseen at a specific experimental station. Place for other experiments, which for the moment go under the collective name ES-O, is reserved.

4.4.3.1 Experimental station A (ES-A): multi-purpose, pump-probe

Typical experiments to be conducted at ES-A have been identified to be serial nanocrystallography and time-resolved spectroscopy in solution.

For an earlier experiment [102], nanocrystals of size smaller than 1 μm are serially driven by a liquid jet which is intercepted by the X-ray beam to produce crystal diffraction images (Fig. 4.4.2.2). Since the main problem is the low crystal hit rate, which causes an enormous waste of sample material, the SwissFEL plans the so called “time-vernier” mode, which bases on the detection of the nanocrystals in the jet and subsequent synchronization of the accelerator clock (± 5 μs) to increase the chance of interaction between the nanocrystal and the femtosecond X-ray pulse.

For time-resolved spectroscopy, the key instrumental elements are a single shot X-ray spectrometer (see for example the single shot spectroscopy technique used at FLASH [103] and illustrated in Fig. 4.4.2.3) and a suitable pump source. SwissFEL is focusing on the capability to produce high-field THz pulses (see section 4.5.2.1) to initiate catalytic reactions to be followed at the fs-ps timescale.

In view of the aforementioned experiments, a preliminary list of necessary components has been devised as follows:

- Liquid jet
- Near and far 2D detectors
- Limited cryogenic (LN2, 77 K) goniometer and translation stage
- XAS and XES single shot spectrometer
- Pump-laser (including conversion to THz)

2016	2016	2017	201X
ES-A Multi-purpose Pump-Probe	ES-B Pump-Probe Crystallography	ES-C Coherent diffraction imaging	ES-O “Others”
<ul style="list-style-type: none"> • liquid jet • near and far 2D detectors • limited cryogenic (LN₂, 77 K) goniometer and translation stage • XAS and XES single-shot spectrometers • pump laser • (compact microwave sample cell) 	<ul style="list-style-type: none"> • movable 2D detector • LHe cryostat • single-crystal goniometer • pump laser • (high-temperature, high-pressure, ...) 	<ul style="list-style-type: none"> • near and far 2D detector • LN2 cryo-stage, cryo-transfer of samples • nanofocus • (pump laser) • (360° tomographic axis rotation) 	<ul style="list-style-type: none"> • XPCS • NLXO • Mössbauer spectroscopy • Pulsed TEM • Ion implantation • (Extreme conditions T,p,ρ) • (STXM)

Fig. 4.4.3.1: Overview of the three currently delineated Aramis hard X-ray experimental stations. The indicated year corresponds to the foreseen start of user operation.

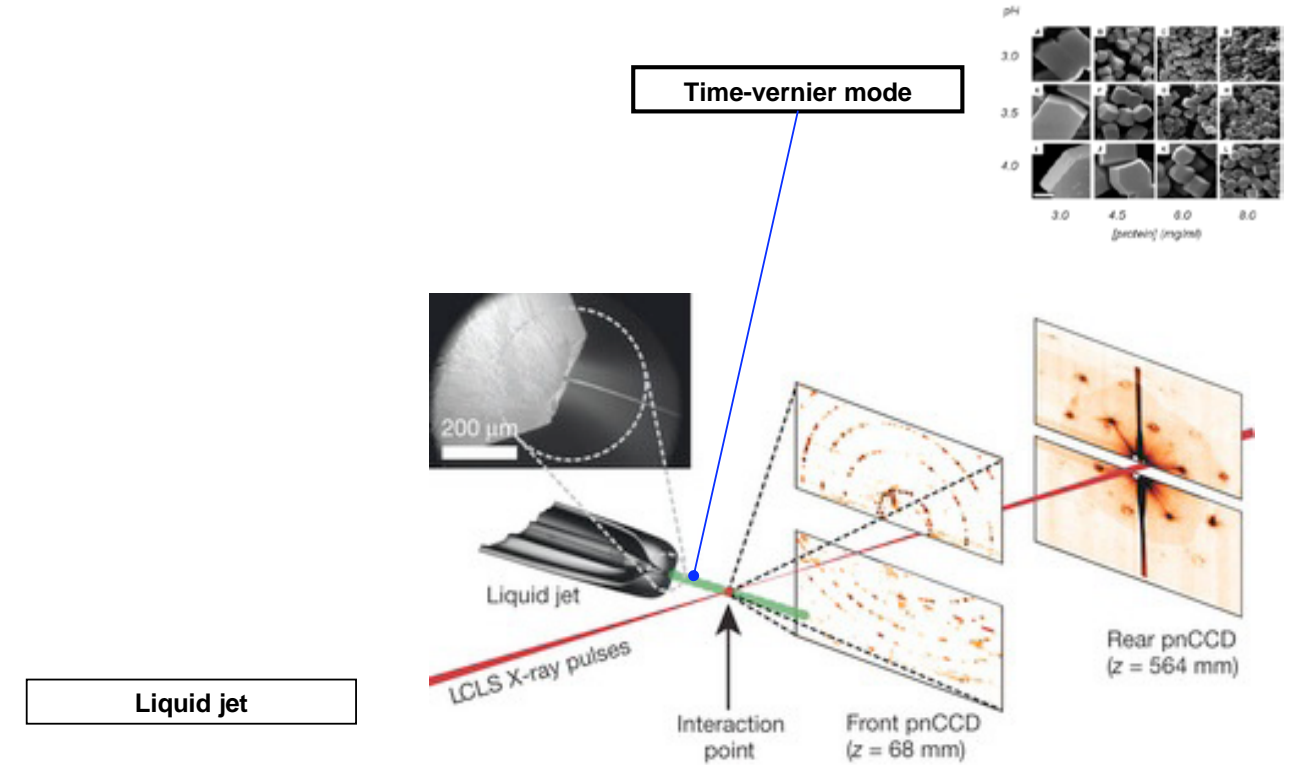


Fig. 4.4.2.2: Illustration of nanocrystallography experiments done at LCLS, in which X ray pulses are intercepting a liquid jet containing nanocrystals.

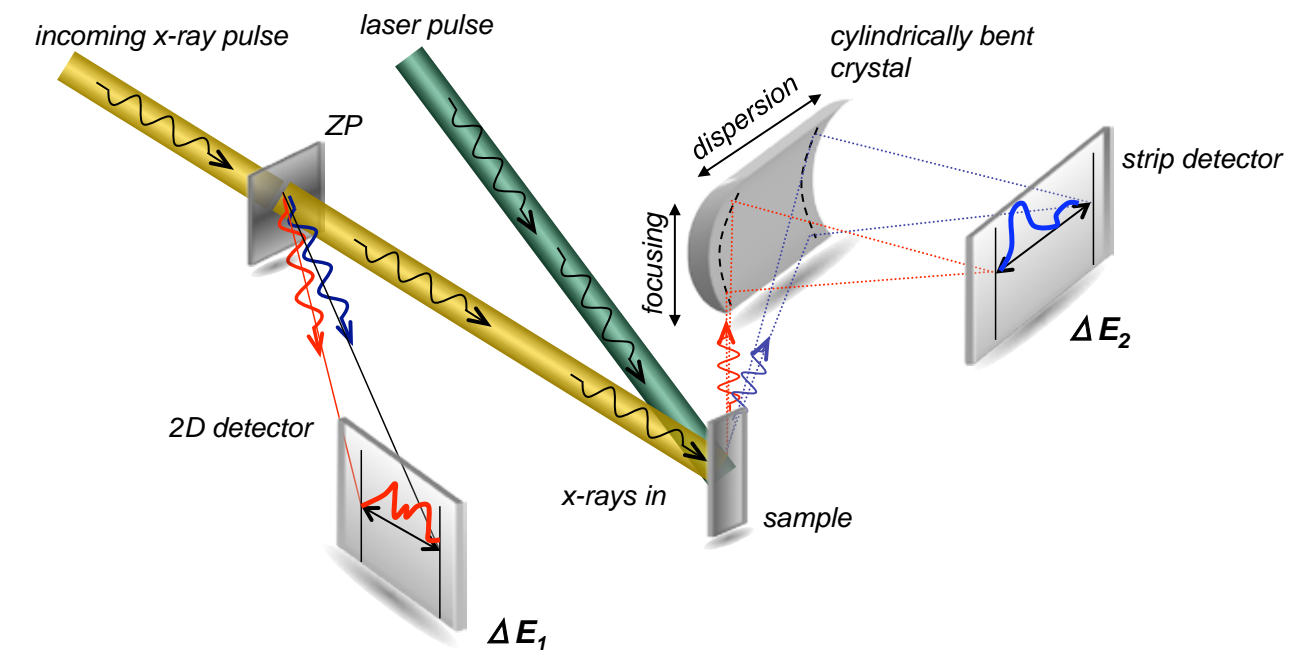


Fig. 4.4.2.3: Illustration of a single shot spectrometer to be employed at SwissFEL (courtesy of J. Szlachetko and J. Cl. Dousse).

4.4.3.2 Experimental station B (ES-B): pump-probe crystallography

ES-B will be mainly dedicated to time-resolved diffraction experiments on macroscopic crystals, to be conducted at various external conditions. This requires an experimental chamber of the kind shown in Fig. 4.4.2.4, furnished with a goniometer to orient the crystal. A large range of pump frequencies are desirable, whereby the THz range is of special interest for driving phonon excitations. A preliminary instrumentation list looks as follows:

- Movable 2D detector
- Cryo-chamber with liquid He cryostat
- Single-crystal goniometer
- Pump-laser, THz source
- (High-temperature and high-pressure setup)

4.4.3.3 Experimental Station C (ES-C): coherent diffraction

ES-C, will be devoted to coherent diffraction experiments, the targets being mainly biological specimen bio-crystals and 2D membrane proteins crystals (see setup shown in Fig. 4.4.2.5). The key feature of ES-C is the possibility to achieve focusing at submicrometer size. The preliminary list of instrumentation is as follows:

- Near and far 2D detector
- Tilttable LN2 cry-stage, cryo-transfer of samples
- Nanofocus
- (Pump-laser)
- (360° tomographic stage)

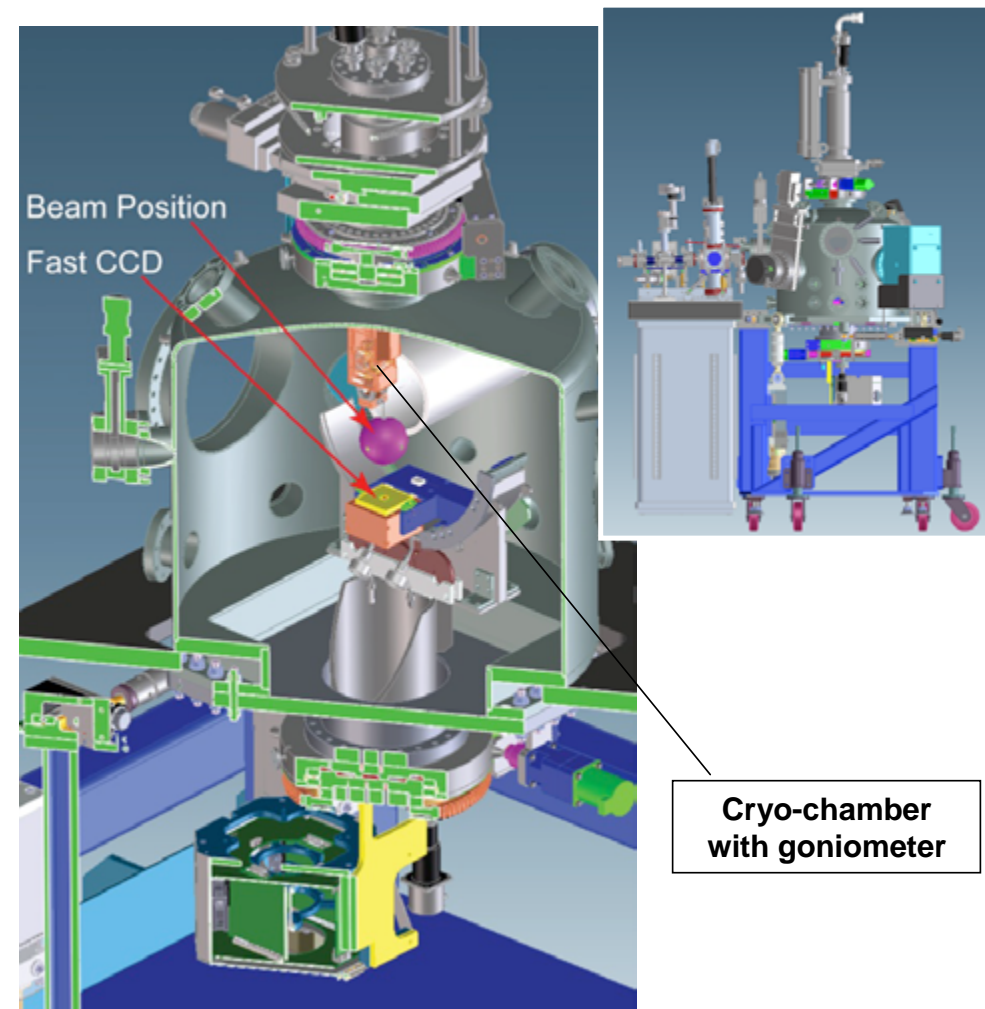


Fig. 4.4.2.4: Example of an experimental chamber for time-resolved diffraction used at the LCLS[104]. The crystal sample can be cooled and its orientation set precisely by means of a cryo-goniometer.

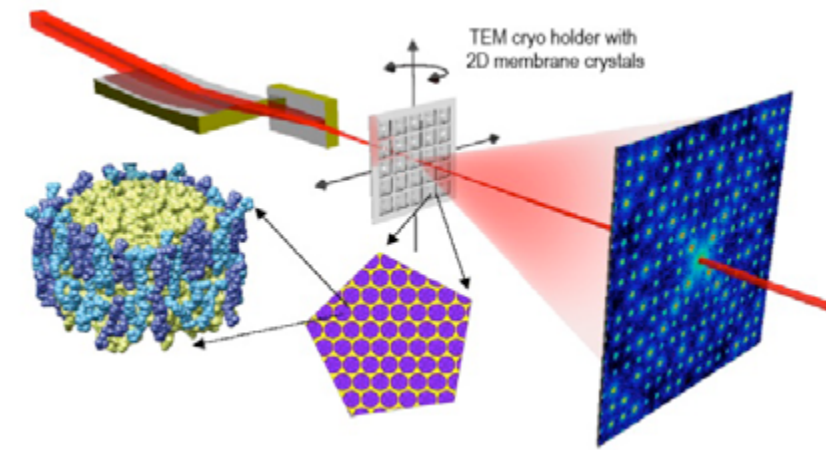


Fig. 4.4.2.5: Illustration of an X-ray diffraction experiment on a 2D membrane protein crystal.

4.4.4 Athos experimental hall

In contrast to Aramis, the Athos experimental hall will not be divided into hutches by fixed walls (Fig. 4.4.1.1), but eventual subdivisions will be achieved by movable shields.

4.4.5 Athos experimental stations

The general plan is to permanently install the standard experimental equipment for the different experimental stations in the Athos experimental hall. Details are not yet defined, because the Athos beamline will come online in a second phase of the project (see Chapter 1). However, the abdication of fixed internal separation walls will guarantee the flexibility to accommodate both permanent instrumentation as well as removable equipment provided by the users.

4.5 Experiment hall special components

4.5.1 Pump lasers

The pump laser for the Aramis stations is located in the laser room, upstairs from Aramis Hutch 1. This regenerative-amplified Ti:sapphire laser system will be connected to three laser transport lines, in order to supply the three hutches. The conversion into THz pulses will be made in the Experimental hutches, very close to the sample, to limit losses. Exact specifications of the pump laser have not yet been defined.

4.5.2 Laser experimental THz source

As part of the infrastructure, a powerful THz source will be available for pump – probe experiments, using the FEL x-rays as a probe. The THz pulses ($>100 \mu\text{J}$, 0.1 – 10 THz; 100 Hz, 0.1 to 1 ps duration) should fulfill the requirements developed in chapter 2 for various experiments (magnetic switching, vibrational excitation, ...).

In addition, the same THz source should be used for the FEL streak camera described above.

Intense THz pulses can be generated utilizing ultrashort laser pulses. In the Fig. 4.5.2.1, the possible high-energy laser-based sources are summarized. Difference frequency generation and optical rectification are non-linear processes employed for frequency down-conversion of NIR radiation into sub-mm wavelengths.

Ti:Sa pulses of 800 nm can efficiently pump a LiNbO₃ crystal and generate frequencies below 1 THz. The velocity mismatching in the crystal between the pump and the THz waves is compensated by wave front tilting the optical pulse. This requires a complex optical setup, and the resulting beam will be affected by astigmatism. The maximum reported field by optical rectification in LiNbO₃ is 1 MV/cm [105].

THz radiation is also emitted in a laser-induced plasma. One proven scheme consists of focusing the laser fundamental and second harmonic in noble gas. The process can be described in the framework of a multi-

photon process: the THz wave is derived from the frequency difference between the input frequencies. The maximum reported THz field from a plasma is less than 400 kV/cm [106] with spectral components up to 8 THz.

Two laser pulses with slightly different central wavelengths can be mixed in GaSe or AgGaSe crystals to produce a difference frequency. These crystals, pumped by ultrashort pulses, produce radiation between 20 and 100 THz. The relatively high frequency permits a smaller focus and consequently higher electric field. Adopting this scheme, generation of up to 100 MV/cm has been demonstrated [107]. Frequency difference generation in the above mentioned crystals is not applicable in the THz gap between 0.1 to 10 THz.

Due to their high non-linear optical coefficient and low losses, organic crystals are good candidates for efficient and compact THz generation via optical rectification. Among these crystals, DAST provides very large nonlin-

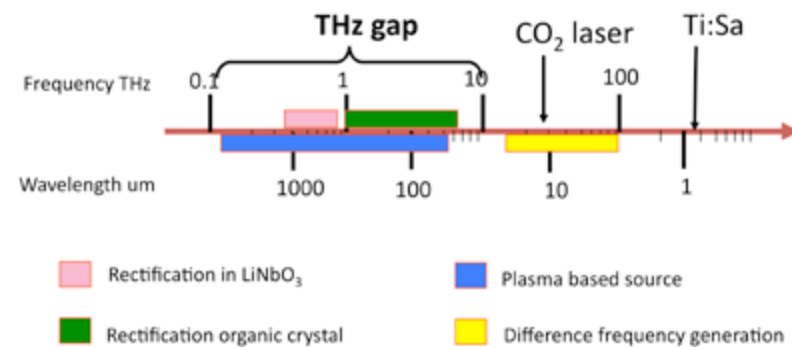


Fig. 4.5.2.1: Spectral range accessible with different laser-based THz sources. For reference, the CO₂ and Ti:Sa spectral lines are also indicated.

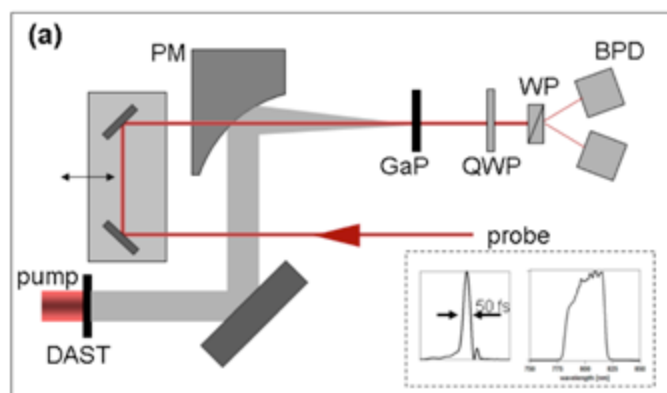


Fig. 4.5.2.2: Experimental setup [4] for the generation and the detection of THz pulses in the organic crystal DAST. In the insert, the resulting temporal profile and spectrum are shown. In this setup, the polarization of the probe pulse is rotated in GaP by the THz electric field and detected by a quarter wave plate (QWP), a polarizer beam splitter (WP) and a balanced photodetector (BPD).

ear optical susceptibility for optical rectification and low absorption for both the THz and the pump laser. This crystal requires intense pumping at wavelength between 1.2 and 1.5 microns, for phase velocity matching between the optical and the THz radiation.

At the SwissFEL laser laboratory, a strong pulsed THz field was obtained from 0.5 mm thick, 8 mm diameter DAST crystal. In Fig. 4.5.2.2, the experimental setup is sketched. Femtosecond optical parametric amplifiers (OPA) were used to pump the organic crystal. The OPA delivered 68 fs FWHM pulses with energy up to 3 mJ at 100 Hz in the wavelength range relevant for pumping the DAST. For THz generation, the collimated infrared pump beam was sent through the crystal at normal incidence. The temporal and spectral THz pulse characteristics were reconstructed by multishot electro-optical sampling in a GaP crystal.

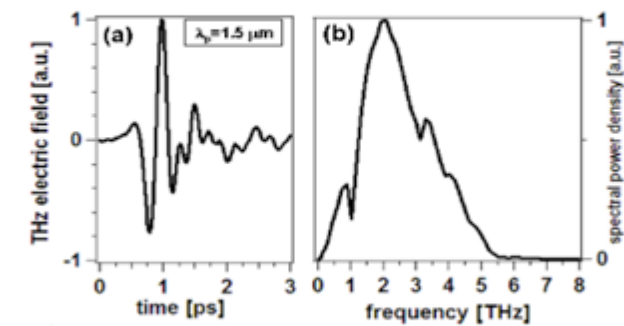


Fig. 4.5.2.3 a) The pulsed THz electric field, reconstructed with multishot electro-optical sampling and b) the resulting spectrum [108]. For the measurement, a pump wavelength of 1.5 μm was used.

In Fig. 4.5.2.3, the THz electric field (Fig. 4.5.2.3a) and the calculated spectrum (Fig. 4.5.2.3b) are shown. The temporal electric field is close to a single-cycle transient. The spectrum is peaked at 2.1 THz and shows the DAST phonon resonances at 1.1 and 3.3 THz. Field strengths of up to 2MV/cm, corresponding to magnetic transient of 0.6T, have been achieved. The energy per pulse measured by calibrated Golay cells is 45 μJ with remarkable energy stability of 1% rms. Another interesting feature of optical rectification sources is that the THz electric exhibits a stable carrier envelope phase, helpful for coherent multishot THz applications. Moreover, the emitted radiation has a low divergence and can be focused to a sub-mm spot. No evidence of saturation has been observed in the output energy. Therefore the THz source holds promise of transients with even higher field strength by scaling up both the pump laser energy and the DAST crystal size.

5 Assembly and commissioning

5.1 Machine installation

5.1.1 Assembly plan

Main steps of SwissFEL time plan is shown in Fig. 5.1.1 for the period 2012 – 2018. The three main components, in terms of cost (hardware and manpower) are the building construction, the undulator modules and the RF acceleration modules.

The key milestones can be summarized as follow:

- 1st of January 2015: Building delivery; components installation start
- 1st of July 2016: Machine Assembly completed and components functionality is tested (without beam); Tunnel is closed to start RF cavities conditioning.
- 1st of November 2016: Hardware Commissioning finished; First electron beam
- 1st of April 2017: First Lasing
- 1st of July 2017: Aramis Nominal Parameters achieved; First Experiments with Photons

In consequence there are 18 months from January 2015 to June 2016 for the installation of all SwissFEL components (Aramis line). A preliminary time plan for the installation of components in SwissFEL is shown in Fig. 5.1.2. This time plan has to take following constraints into account:

- only two access points to the building tunnel (Fig. 5.1.3)
- delivery constraints of measured undulators (1 U15/ month)

- delivery constraints of accelerating structures
- maximization of injector test facility operation time.

This last point comes from the fact that the components currently installed in the SwissFEL Injector Test Facility will be moved to the SwissFEL injector limiting the available time for tests. Indeed, the injector is at one extremity of the building tunnel and would require to be installed at first. Operation at the injector test facility should ideally be stopped around October 2014.

Before the installation of the undulators and RF modules, large components like the beam dumps (Aramis and Athos) and beam stoppers will be installed at their final location.

The installation of undulators will start effectively in april 2015 since the first 3 months of 2015 will be required for the magnet lab commissioning and the tuning and measurements of the first undulator. Then the delivery of undulators will be at a rate of one undulator (tuned and measured) per month. The twelve undulators should then be installed by april 2016. The inter-undulator girders will be installed before the undulators.

The RF C band structures will be pre-assembled on girder with all beamline components in the vacuum hutch of the FormBeton Hall.

SwissFEL Schedule December 2011

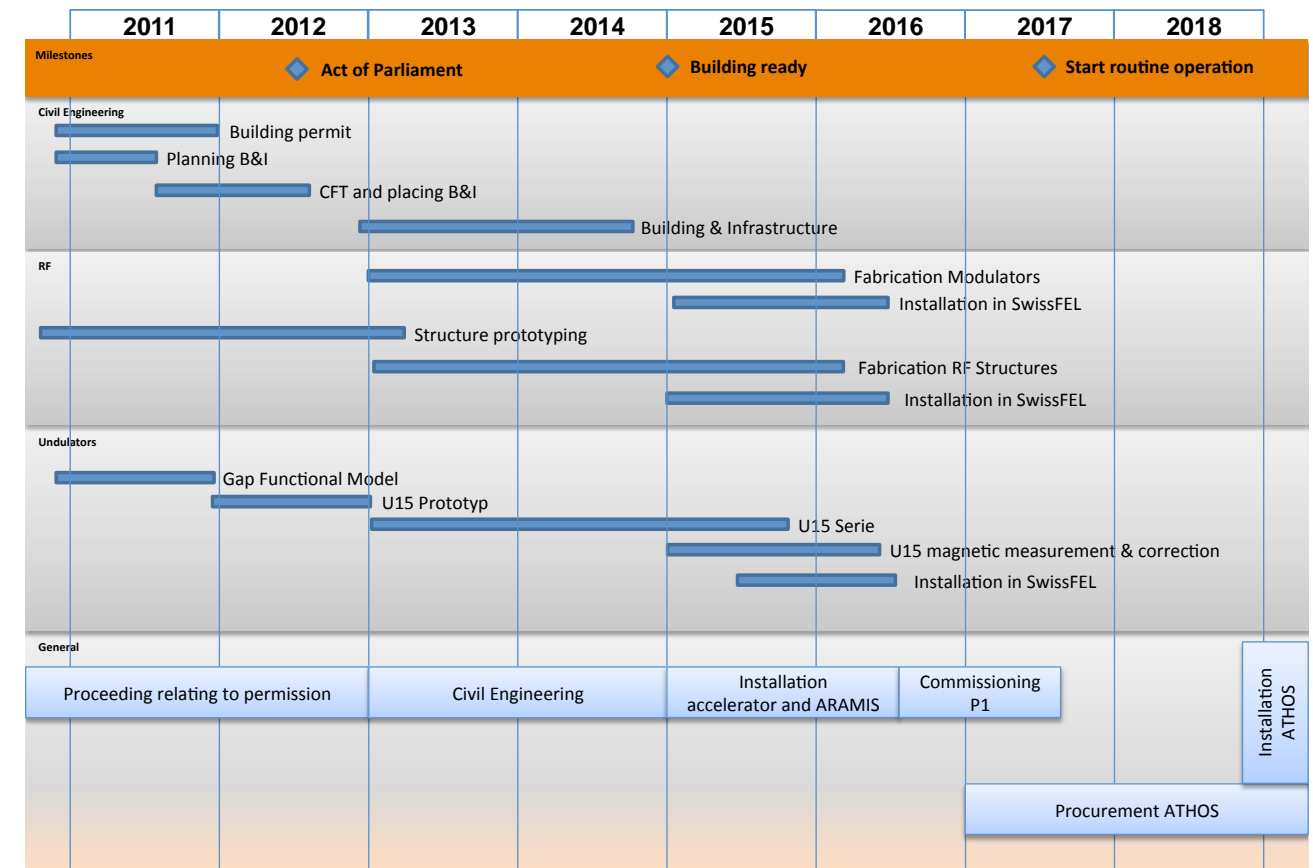


Fig. 5.1.1: SwissFEL main milestones and activity steps.

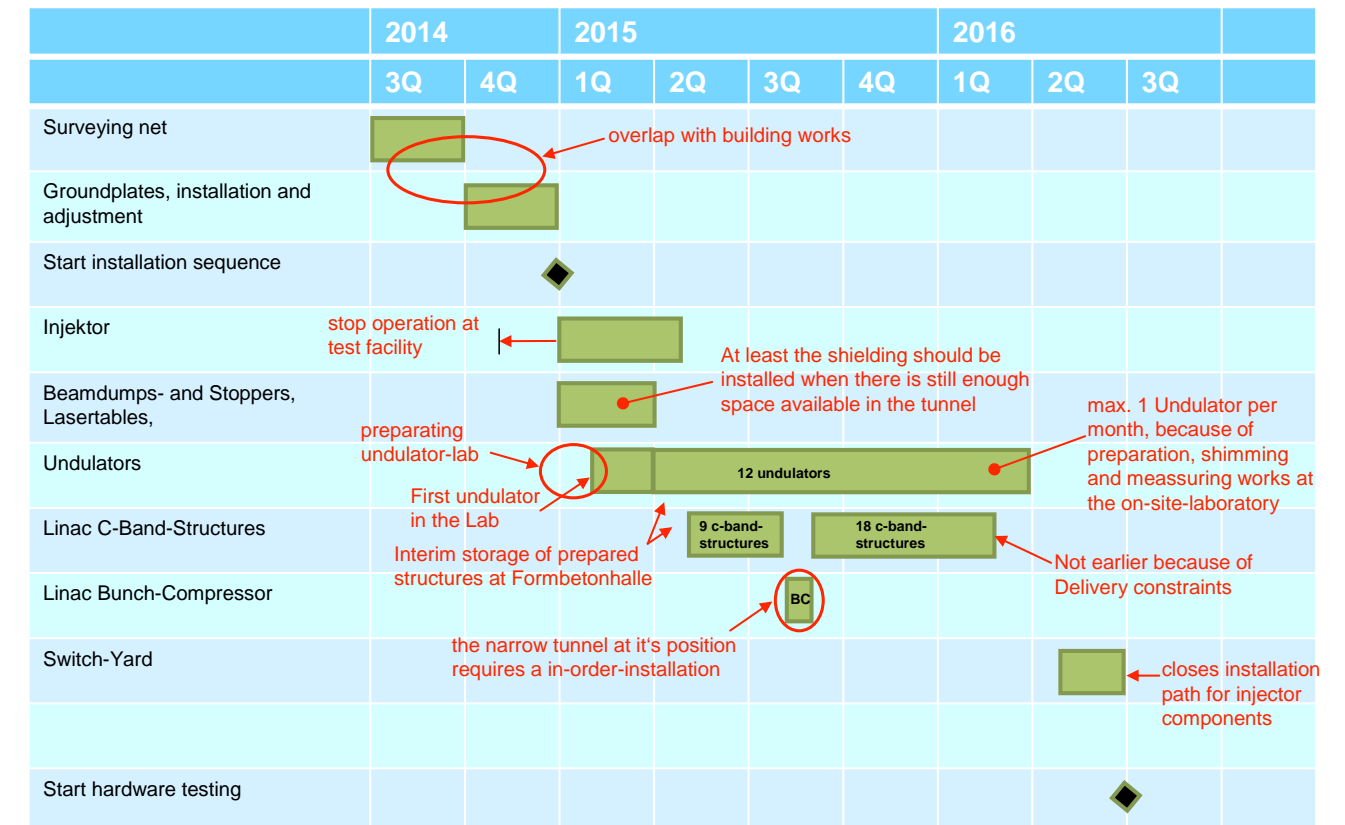


Fig. 5.1.2: Assembly time plan of the SwissFEL beamline components in tunnel.

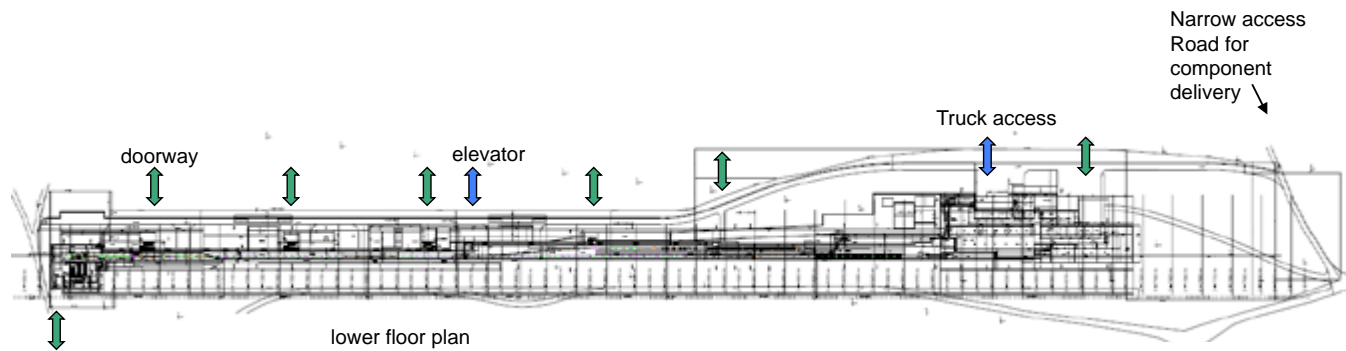


Fig. 5.1.3: Access points to the building beam tunnel: in green the person access points with stairs and in blue the material access points.

5.1.2 Components assembly concept

Installation of SwissFEL is foreseen in a timeline of about three years, starting with the infrastructure and ending with the large machine components. For the large machine components, an installation time of about 18 months is foreseen. Pre-assembly and testing of linac and Undulator modules in advance is very important in order to stay on schedule, this will require dedicated areas at PSI or nearby. Moreover, successful machine installation requires dedicated manpower resources for planning, pre-assembly, installation, alignment and coordination.

Before handover of the tunnel, a first measurement campaign is required to define the alignment network. Therefore, all survey marks will be supported by the general contractor, and this network measurement campaign should start about 4 months before tunnel delivery for installation (summer 2014). The measurements needed are well-established, classical surveying methods, using high-accuracy theodolite Total Station, Laser Tracker, and leveling instruments. Since the environmental conditions at that time will not be suitable for high-accuracy measurements, the measurement campaign has to be repeated prior to the alignment of the machine components.

Based on this alignment network, some reference points for the theoretical beam axis and beam height will be marked at the tunnel wall and floor, to facilitate correct positioning of the infrastructure components, such as cabling and piping.

The position of component fixation points in the tunnel floor and beamline will be marked in the tunnel. Once the markings are available, drilling and other minor civil engineering adaption can take place. In the final stage, before component installation, the jacks and component supports will be installed and aligned at their definitive positions, where they will be cemented locally using a cast around the base.

Then will begin the installation of all large components into the tunnel, such as, for example, the linac girder modules, with a mass of up to 6 tons each, and the Undulator modules, with a mass of 20 tons each. Likewise, single quadrupoles with their supports and bunch compressor components, including the dipole magnets, will be installed in this phase. Also the beamdump as a single heavy components need to be installed in this phase. For this purpose a set of transport tools, air cushion based for the Undulators and wheel based for Linac and magnets will be available. An electric-powered tractor will also be required during the installation. Figure 5.1.2.1 shows an example of a transport convoy. Single magnets, such as BC dipoles, are brought in with a trailer and then installed with a local mobile crane in the tunnel. The heaviest single magnets have an estimated weight of 1.5 tons.

Once the main components are in the tunnel, HF, vacuum and other connections can be made. In the next phase, bakeouts of vacuum systems are carried out and several equipment checks are executed. It is quite clear that careful scheduling of the installation tasks is required and parallel working is essential for staying on



Fig. 5.1.2.1: Example of transport convoy during DFB installation at LHC.

the installation time schedule. Once more, pre-assembly and prior testing of components is indispensable, as well as having all components available on time during the installation.

In the technical buildings, infrastructure work will progress at the same time as in the tunnel. Electrical racks will arrive before the foreseen double floor is built, and in the final stages the modulator and klystron modules will be installed.

5.1.3 Components transport

The SwissFEL tunnel is foreseen to have two entrance points for large components, one main entrance at one end of the building which is on the same floor level than the main beam tunnel and one entrance above linac 2 (via a lift) (see Fig. 5.1.3). Figure 5.1.3.1 shows a preliminary proposal for the northern main entrance.

The main entrance in the north of the building is the arrival hall, 10 m deep and 5.5 m wide. The hall has a crane with a capacity of at least 35 tons and a hook height at 6.5 m. This entrance is foreseen to be used for the arrival of Undulators that are first brought to the Undulator measurement laboratory. Then, after some fine tuning, they are installed in the tunnel. The longest travelling distance for undulators is 200 m. They are transported on an air cushion vehicle and can only be installed via this entrance because of their size and mass. The specification document FEL-W088-028-3 gives

more details on the requirements for the Undulator installation tool. In Figure 5.1.3.2 details of the final stage of the Undulator installation are shown. During the installation phase, this entrance shall also be used for both injector- and linac Girders.

The central entrance above Linac 2 (L2) has an outdoor unloading area equipped with a 7.5 tons crane, from this area wheel based systems have to be used to enter the technical building. Next to the entrance inside the technical building, one level above the tunnel, a 6.3 tons elevator is located with cabin inner dimension 6 m x 2 m. The elevator offers a direct connection to the tunnel bellow, it has doors in both ends of the cabin to allow exit down- or upstream of the tunnel beamline. This secondary entrance point allows the installation of Girders, although a larger effort is required due to the many steps with crane/wheel/lift and the relatively limited area for maneuvering. Next to the lift, a staircase for personnel is foreseen as an access between the levels.

The Linac girders are foreseen to be transported and installed on wheel based tooling. This will allow longitudinal transport and final transversal move into the beamline. In the first phase of the machine installation as the girders are brought in from the northern main entrance the distance to travel on wheel based transport will be up to 700 m. In addition to the Girders and the Undulators that need to be installed in the tunnel, many other components also have to be installed among them a number of quadrupole and dipole magnets and the beamdump, see Table 5.1.3.1 below for a transport parameters summary.

The technical building (top floor) also has a number of large components that need to be installed, the largest being the Injector and Linac Modulators. They will enter the technical building mainly via the central entrance point and via a number of smaller access points available between the central entrance and the southern end

of the building. The modulators have to enter the technical building on wheel based transport, once they are close to their final position they can be lifted with a local crane available next to the modulator final position, note that this crane has a limited travel, due to other infrastructure installation in the roof.

Table 5.1.3.1: List of large components in the first Phase of Construction.

Component	Dimension	Mass	Amount	Mass T
Injector Girder	L 4.7 m x W 1.1 m x H 2.4 m	6500 kg	12	70 tons
Linac Module	L 4.7 m x W 0.7 m x H 1.3 m	3000 kg	~50	500 tons
Undulator Module	L 4.1 m x W 1.7m x H 2.1m	25'000 kg	~12	440 tons
BC 1 Dipole	L 1 m x W 0.5m x H 0.5m	500 kg	~4	2 tons
BC 2 Dipole	L 1 m x W 0.5m x H 0.5m	1000 kg	~4	4 tons
Quadrupoles	L 15–20 cm	70 kg	~120	8,5 tons
Beam dumps	L 2.7 m x W 2.9 m x H 3.4 m	200'000 kg	2	400 tons
Beam Stoppers	L 2.25 m x W 1.7 m x H 3 m	80'000 kg	2	160 tons
Injector Modulators	L 2.8m x W 1,7m x H 2.1m	3 tons	4	~12 tons
Linac Modulators	L 2.8m x W 1,5m x H 2.1m	1 tons	~25	~25 tons

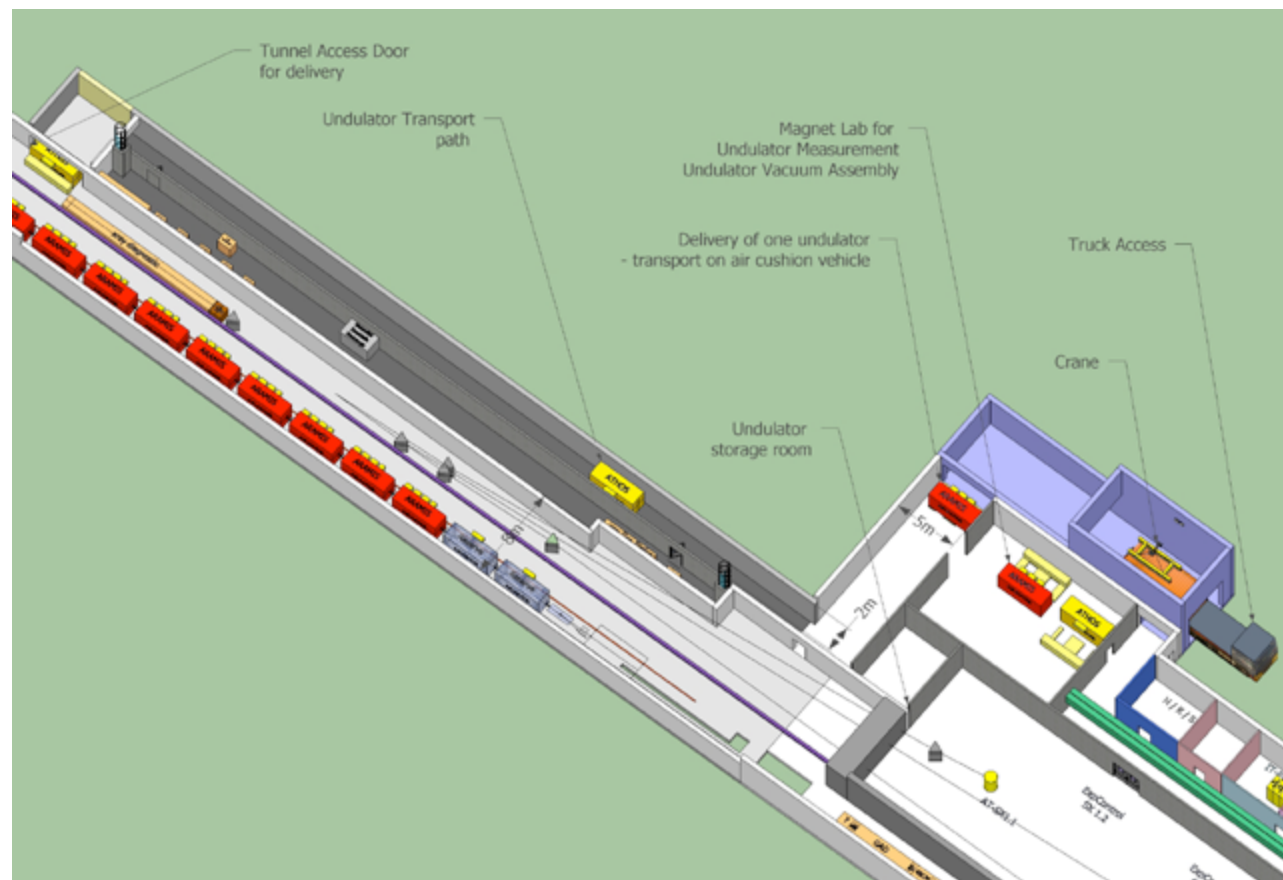


Fig. 5.1.3.1: The loading-zone building above the tunnel, with the arrival area and shaft.

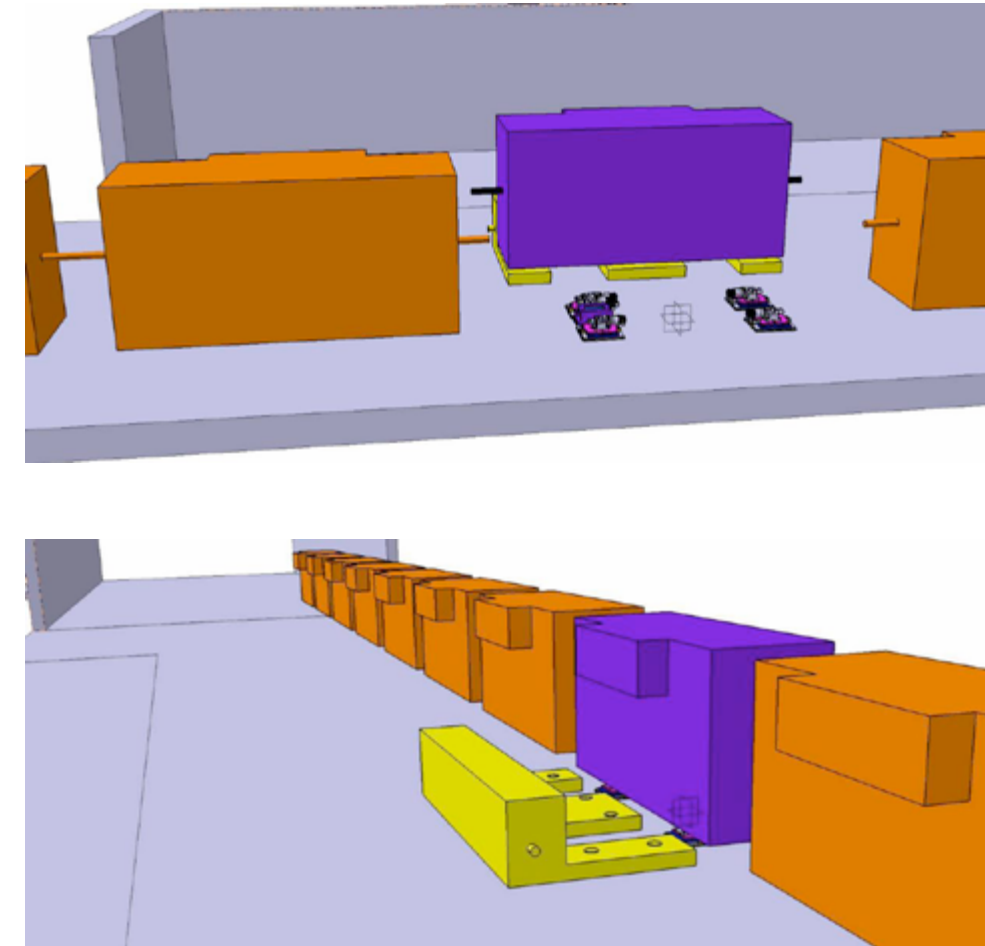


Fig. 5.1.3.2: Last stage of Undulator installation with Air cushion vehicle.

5.1.4 Assembly alignment concept

5.1.4.1 Reference coordinate system

The official Coordinate System LV03 (Landeskoordinaten CH1903) and the official height reference system LN02 (Gebrauchshöhen) or LHN95 (Landeshöhenetz) are not accurate enough and thus not suitable for SwissFEL alignment or survey tasks. These coordinate systems are **not planar, not rectangular** and the scale is **not exactly metric** (varies with the height). For instance the deviations for a 800 m long structure reaches up to 50 mm for vertical (not planar due to curvature of earth), 15 mm for the straightness (not rectangular coordinate grid) and up to 10 mm in scale (height 340 m above reference sea level).

Therefore a local coordinate system [109] has been defined to ensure the data administration and data exchange of the coordinate sets. This coordinate frame is a local metric 3-dimensional and right handed coordinate system which has been determined according to the machine axis (MCS i.e. machine coordinate system). This coordinate-system is the basic working coordinate frame for construction and alignment tasks. All necessary transformations between official external global coordinate-systems (as LV03, LN02, etc.) and the local coordinate-system will be done by the alignment group only.

The alignment group refers of the official computation service REFRAME provided by swisstopo (Bundesamt für Landestopografie).

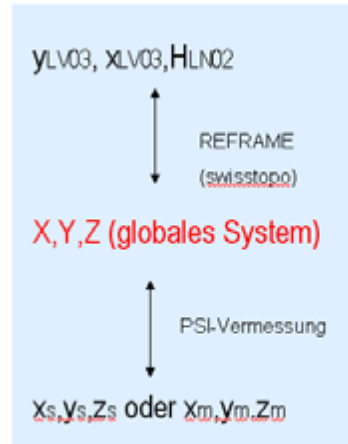


Fig. 5.1.4.1.1: Coordinate and height Transformations between global systems (LV03, LN02) and local coordinate system (MCS).

The fundamental point and the geodetic datum of the local coordinate-system have been defined according to the machine axis definitions of the preliminary planning. To minimize the geometric distortions, the fundamental point was set to the center of the facility.

5.1.4.2 Alignment steps

All beamline components will be pre-assembled and pre-aligned onto girders and support frames. The main instrument for the alignment procedure is a Laser Tracker. The expected accuracy for the internal geometrical alignment of components sitting on one girder

assembly ($L \approx 5$ m) is better than 0.05 mm (σ_x, σ_y) the accuracy for longitudinal position will be about $\sigma_z < 0.5$ mm.

It is necessary that each component is equipped with at least 3 or better 4 visible and well distributed reference cones capable to hold the 0.5" CCR alignment reflector.

It is important, that the relation (distances) of the reference mark coordinates in respect to the physical center is completely known. The task of fiducialisation has to be done well in advance before alignment. This should be generally done by the manufacturer or alternatively by the responsible PSI section.

The pre-assembled girder units will be positioned in the machine tunnel, based on the 3D survey and alignment network using the Laser Tracker. The local accuracy for component alignment in a typical measurement set-up in the machine tunnel (in a measurement range of ± 10 m) is about $\sigma_x, \sigma_y < 0.1$ mm and $\sigma_z < 0.5$ mm. Curvature-of-earth compensation will be included in the reference point coordinates.

Using beam-based alignment methods (BBA) during commissioning, the position of each component could be optimized up to a relative accuracy of about 0.01 mm (rule of thumb – including limits of mechanical movements and measurement tolerances).

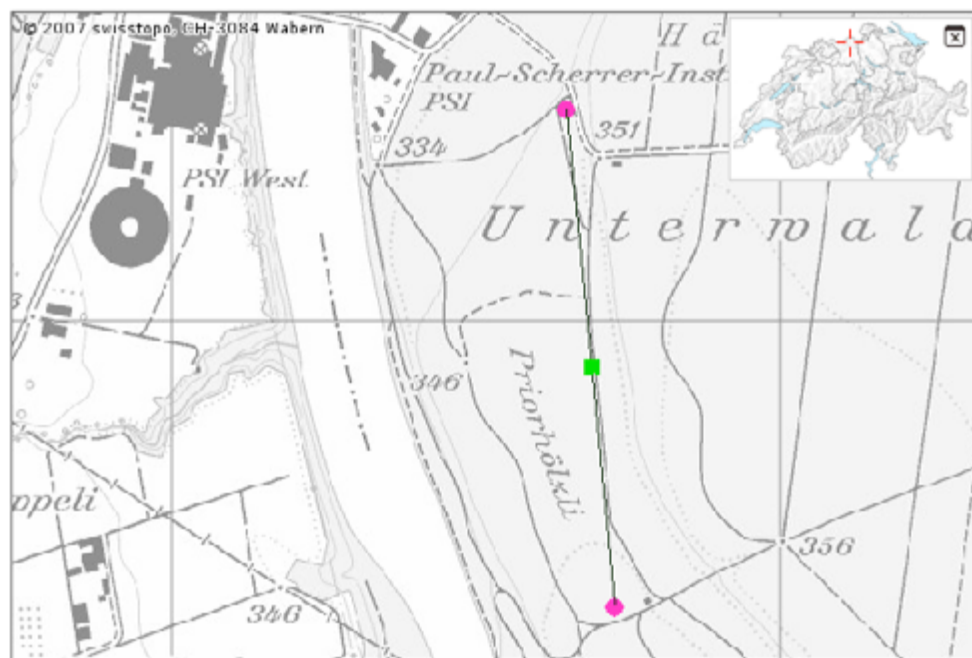


Fig. 5.1.4.1.2: Position of fundamental point (green square).

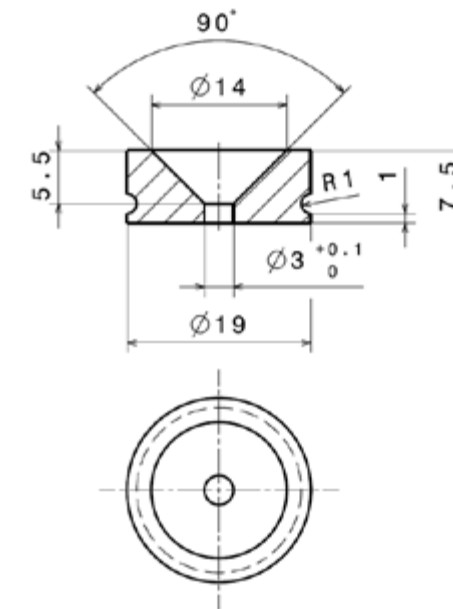


Fig. 5.1.4.2.1: Sample of conic reference mark, according to PSI drawing 4-50021.031.

5.2 Components to infrastructure interface

Installation of the components consists in following steps:

- Pre-assembly, local fiducialisation, measurements/characterisation
- Transport, positioning (fiducialisation) and installation
- Connection to infrastructure mains and/or neighbour components
- Commissioning or Functionality test with control interface

The pre-assembly will be done in a vacuum hutch at the Form-Beton Hall which is also the hall used for storage of components. Some components will be measured and characterized in PSI laboratories (e.g. magnets, power supplies, diagnostics, ...) or at external companies places (undulators, RF structures).

The transport follows as described in section 5.1.3 and 5.1.4.

The connection to infrastructure mains are of three types: the electrical connections; the water pipes for cooling and the air pressure pipes (for pneumatic motion). All the mains are distributed on trays attached to the ceiling (Chapter 6).

The test of the control interface is an important part of the installation process all functionalities should be tested as far as it is possible before the tunnel closes. Some function can only be tested with beam but then the identification of possible problems is also much more difficult.

5.3 Machine commissioning plan

We outline the basic steps of commissioning the SwissFEL accelerator and undulator lines. A more detailed commissioning schedule will be elaborated at a later stage.

5.3.1 Hardware commissioning without beam

5.3.1.1 RF systems commissioning plan

The installation of the 5 S band RF Modules; 1 X band Module and 27 C band RF modules (Section 3.2.4) will be the largest task of the entire SwissFEL installation. The installation will start in January 2015 until 1st of April 2016. As soon as the first C band module will be completed a high power RF test will be performed before to install the full series. If test is successful then all the RF plant will be mounted and the high power tests will start afterwards. The RF conditioning of all the accelerating structure is planned between the 1st of July 2016 and the 1st of November 2016.

5.3.1.2 Undulator commissioning

The undulators will be pre-assembled outside of PSI by an external company and partially stored there. The undulator laboratory in SwissFEL building (Fig. 5.3.1.1) is designed with two measurement station (stations A) and two vacuum assembly stations (stations B), that is to say a maximum capacity of 4 undulators. The preparation of the laboratory will be made in January 2015. A first serie of 4 undulators will be shipped to SwissFEL around february 2015 and each undulator will see the following sequence:

- magnetic measurements and keeper height adjustment (station A)

- removal of magnet array, vacuum chamber installation; re-installation of magnet array (station B)
- re-magnetic measurements and columns height adjustment (station A)
- final vacuum assembly, pumping chamber, leak test (station B)

Undulators are then transported to their final places in Aramis line and positioned with survey methods (Section 5.1.4). The final alignment is done with beam.

5.3.1.3 Magnets commissioning

All the magnets are measured and characterized outside SwissFEL building in the PSI magnet lab. After characterization they will be either stored individually in the Form-beton Hall (large dipole magnets) or pre-assembled on girder (linac quadrupole magnets).

- Check of external interlock signals
- Isolation measurements of DC cables and load magnets
- Load measurements (resistance and inductance)

- Check of correct cabling (current flow in the correct magnet with the correct polarity)
- Final adjustment and tuning of all controller parameters including the closed loop parameters
- Measurement of load current stability (short term)
- For corrector magnets in the BPM closed loop: Measuring and optimization of current step responses

Check of remote access from the EPICS control system.

5.3.2 Beam commissioning plan

Following the experience at the SwissFEL injector test facility the commissioning of each accelerator section will proceed in five main steps:

- *Component commissioning* (see section 5.2): Components must be installed at their final positions, mechanically aligned, connected and initially verified by system's engineer. For RF cavities this step includes the conditioning.
- *Pre-beam hardware and software checkout*: once the components of a section are verified by system's

expert, a global hardware check is still very useful, since interference between the individual commissioning of components can give rise to new inconsistencies. Thus the commissioning team should verify independently all relevant beamline components again for existence and position, electrical and water connections, remote-control capability. The pre-beam checkout further includes in-situ verification of all magnet polarities and thorough checkout of controls and associated software for all components.

- *Beam-based hardware and software checkout*: establish beam transport throughout the section to be commissioned and connected dispersive arms. Test of machine protection system with beam. Basic RF setup. Beam-based check of magnet polarities. Verification of all diagnostics systems (screens, wires, BPM).
- *First-order beam development*: establish orbit correction (beam-based alignment of quadrupoles), initial optics matching (beta-function, dispersion). Setup and commissioning of transverse and longitudinal feedback systems.
- *Full beam characterization*: measurement of key parameters and distributions (projected and slice emittance, energy spread). Assessment of beam sensitivities and stability. Optimization of tuning, beam experiments.

This basic sequence will be repeated for each accelerator section: injector with gun, linac 1, linac 2, linac 3 and undulator line.

5.3.2.1 First injector electron beam commissioning

Commissioning of the injector section will follow the five steps outlined above. *The first-order beam development* will comprise the following tasks:

- Characterization of dark current emitted by the gun
- Laser alignment on cathode
- Determination of the optimal gun phase (laser launch phase)
- Beam transport throughout the section, BPMs, energy measurement
- RF setup (phases)
- First orbit correction
- First-order beam optics:
 - establish matching procedure, initial matching (beta, dispersion)
 - establish emittance measurement

- Establish longitudinal measurements (bunch length, energy spread)
- Feedback setup and commissioning (see section 5.4)
- Commissioning of bunch compressor and harmonic cavities
- Commissioning of laser heater

After these tasks, the injector beam will be fully characterized and optimized.

5.3.2.2 First linac electron beam commissioning

The five principal commissioning steps outlined above will be carried out separately for each of the three linac sections. For one linac section, the *first order beam development* will consist of the following activities:

- Beam transport throughout the section, BPMs, energy measurement
- RF setup (phases)
- First orbit correction
- First-order beam optics
 - Oestablish matching procedure, initial matching (beta, dispersion)
 - establish emittance measurement
- Establish longitudinal measurements (bunch length, energy spread)
- Feedback setup and commissioning
- Linac 1: Commissioning of bunch compressor (linac 1 only)

These tasks will be followed by a final characterization of the linac beam (after bunch compression in the case of linac 1). Once the linac beam has been established, a linac energy management (LEM) system will be put in operation and tested.

5.3.2.3 First photon beam commissioning

The strict requirement for radiation protection of the undulators calls for a particularly careful planning of the commissioning sequence of the undulator section. After the usual component commissioning and pre-beam checkout, the commissioning of the electron beam will first be carried with *open undulators* and in *single-shot mode*. A single low-charge bunch will be sent into the undulator section. After collecting and evaluating as much as possible diagnostics information along the undulators, possible beam losses are identified and



Fig. 5.3.1.1: Undulator Magnetic measurements lab and assembly hutch.

eliminated as far as possible, before more bunches are sent into the undulator section. This procedure is then iterated until a safe orbit is established. A first beam-based alignment can then be performed, followed by initial optics matching, still with open undulators.

Commissioning of electron beam with undulators only starts once the electron beam orbit and optics have been established. Undulator segments are first inserted (gap closed) one at a time only, such that orbit changes due to the undulator can be measured and corrected for individually.

The alignment of the undulator segment axis on the electron beam golden orbit (as found with BBA and gap open) is done thanks to alignment quadrupoles Q_{AI} attached to the undulators (at each extremity). The Q_{AI} axes are already aligned with the undulator axis (pre-alignment done in the undulator magnet lab). The undulator segment is then moved until the steering free position of Q_{AI} is found (ie. the position for which electron beam energy variation gives no steering) which is actually Q_{AI} axis. First the upstream Q_{AI} axis is aligned with the beam and then the downstream quadrupole, so that at the end the undulator axis is aligned on the electron beam golden orbit (see section 5.4.2).

Once all undulator segments have been checked with beam, multiple undulator segments can be tested with beam, before eventually the entire undulator sequence is inserted.

The next steps are then the commissioning of the X-ray diagnostics using spontaneous undulator radiation, the characterization of the undulator radiation, and, finally, the generation and characterization of FEL radiation.

5.4 Feedback systems and electron beam-based alignment

5.4.1 Beam-based magnet and trajectory alignment in linac

The goals for the alignment and correction of the beam trajectory in SwissFEL are:

- 1) The establishment of a “golden orbit” through beam-based alignment and steering, where the orbit deviations and spurious dispersion are minimized, such that the slice emittance stays less than $0.43/0.38 \mu\text{m}\cdot\text{rad}$ for the nominal mode (200 pC, compression factor 127/75) and $0.18 \mu\text{m}\cdot\text{rad}$ for the short-pulse mode (10 pC) (see Section 2). The growth of the projected emittance should also be kept reasonably small, in order to not deteriorate the beam envelope matching into the undulator.
- 2) The establishment of an orbit in the undulators that provides sufficient transverse overlap and relatively small microbunching phase error of electron and photon beams.
- 3) The minimization of transverse fluctuations around the golden orbit to a level that allows stable FEL operation, where the tolerances for a single perturbation are $14 \mu\text{m}$ and $1 \mu\text{rad}$ for beam position and angle at the undulator entrance (see Section 2). It is desirable to achieve smaller fluctuations, in order to allow more error budget for other sources.

Concerning the first point, a simulation study using ELEGANT (as shown in Figure 5.4.1.1) indicates that the maximum orbit perturbation should be less than a few $100 \mu\text{m}$ for 200 pC operation. This corresponds to a few millimeters dispersion.

The trajectory alignment for linac and undulators is discussed separately in the following, since the requirements are largely different. In the following, a BPM resolution of $3 \mu\text{m}$ in the linac and $1 \mu\text{m}$ in the undulator is assumed.

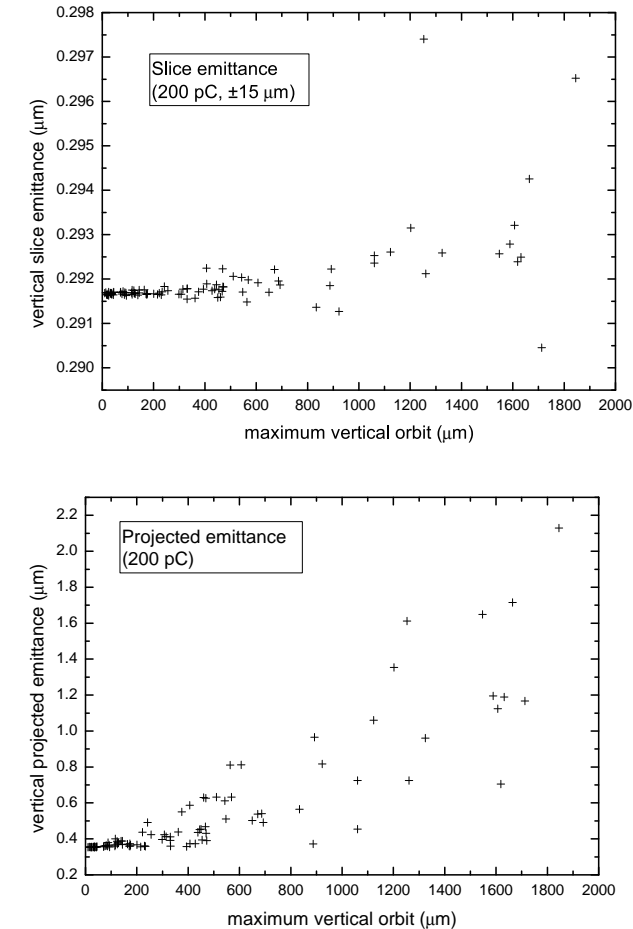


Fig. 5.4.1.1: Slice and projected emittance versus beam orbit. Best-case simulation for 200 pC operation.

As described in Section 5.1.4 (Assembly alignment concept and expected precision), the accelerator components will be aligned with about $50 \mu\text{m}$ rms short-range precision. Based on beam measurements, relatively large short-range alignment errors, of the order of $50\text{--}100 \mu\text{m}$ or more, will be detected and realigned in the early stage of commissioning.

Afterwards, the beam will be steered to minimize the orbit and dispersion. Dispersion-Free Steering (DFS) [110] is generally used, and also Ballistic Alignment (BA) [111] is applicable to the relatively short SwissFEL linac. It will be helpful to compare the results from different algorithms for a better understanding of the machine. For the early stage of commissioning, “quick-steering”, in which the beam is steered to go through the BPMs centres, will be useful for establishing a beam orbit quickly. Typical results of beam steering are shown in Figure 5.4.1.2 (b), (c) and (d), together with the initial orbit and dispersion in (a).

The beam steering results in Figure 5.4.1.2 were obtained from simulations using a MADX optics model, where the linac RF cavity is modelled with an arbitrary transfer matrix, with the determinant not equal to unity in order to simulate the orbit damping due to acceleration. The Earth’s magnetic field, as well as external stray fields and misalignment of accelerating structures, were assumed to be negligible. An initial quadrupole alignment error of $25 \mu\text{m}$ rms and an orbit measurement error of $3 \mu\text{m}$ rms were assumed. In BA, the trajectory is confined to the ballistic orbit with $3 \mu\text{m}$ rms precision. The pivot BPMs are placed every $\sim 30 \text{ m}$. In DFS, a dispersion measurement error of $15 \mu\text{m}$ rms is assumed for 20% momentum shift. The corrector strengths are found by SVD-based fit with an eigenvalue cut-off at 0.001 (rejecting 22 small Eigen values out of 111), where the full weighting factor for the dispersion is assumed. The residual orbit and dispersion can be exchanged by tuning the weighting factor.

In addition to these beam steering algorithms, residual dispersion up to $\sim 100 \mu\text{m}$ can be corrected without disturbing the orbit. When a local orbit bump is closed, the dispersion function is also closed, while this is not true if there is a quadrupole magnet inside. Thus it is possible to control dispersion using an orbit bump at the location of quadrupole (a similar technique using an orbit bump over a linac cell is described in [112]). In conclusion, the orbit and dispersion in the linac will stay much larger than the BPMs’ resolution of $\sim 3 \mu\text{m}$.

The entire linac is not necessarily aligned to a straight line; that is, a distortion of a few mm in $\sim 500 \text{ m}$ machine length is acceptable. The orbit is then steered to be a straight line over a short range, but slightly bent over a long range. Additional bending components to follow the distortion result in dispersion of $\sim 100 \mu\text{m}$, which is an acceptable level and even correctable by the orbit bump.

It is worth mentioning that the Earth’s magnetic field has a large impact on the beam orbit, especially for the low energy part, and that BA is disturbed because the straightness of the ballistic orbit is then violated. Also, the beam-based alignment for the elements with relatively large initial alignment position errors becomes difficult, because of the trajectory curvatures with unknown local field intensity. Spurious dispersion due to the Earth’s magnetic field is estimated to be a few hundreds of micrometers in the horizontal plane, without shielding, which could be corrected either by the orbit bump or at the expense of a comparable orbit excitation.

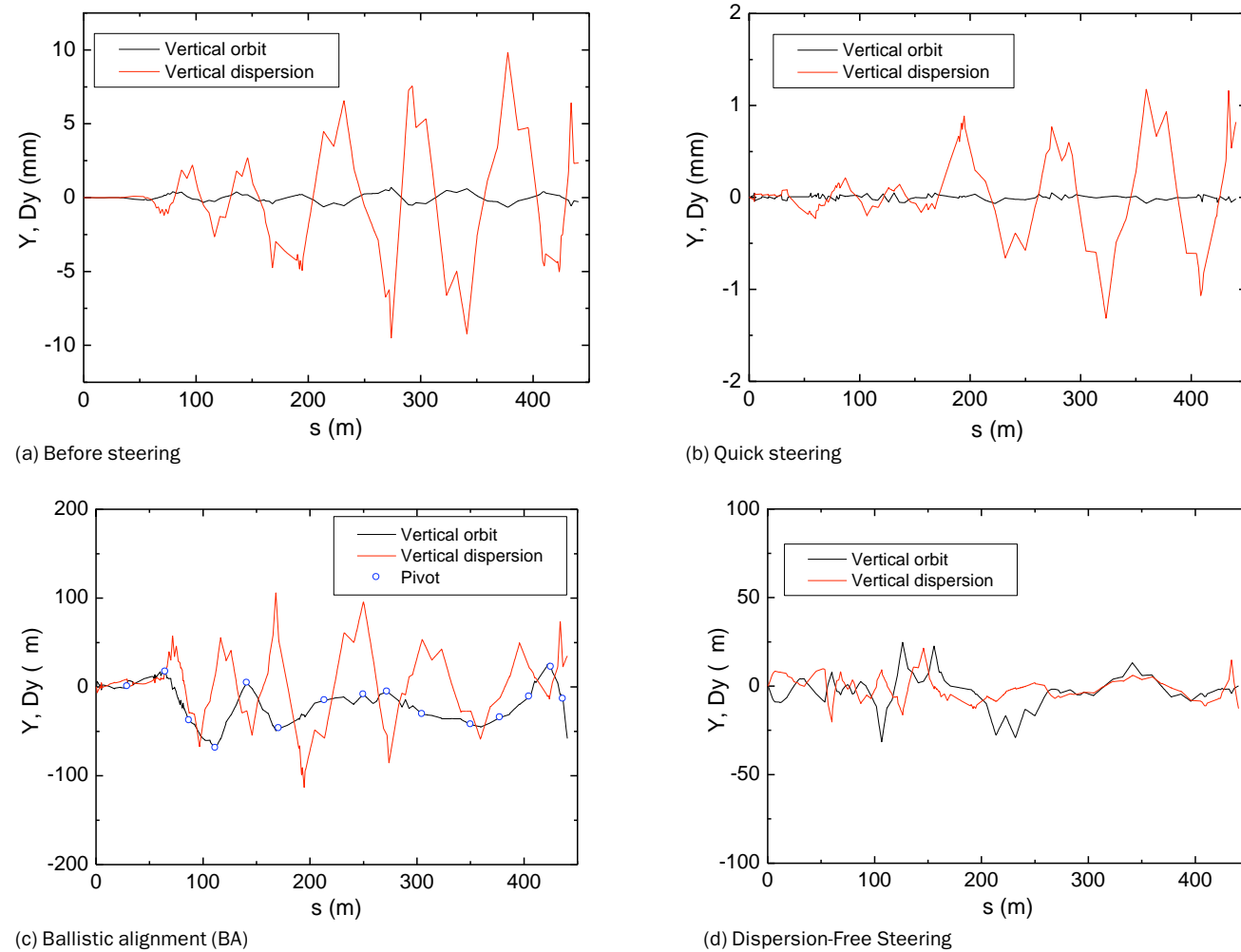


Fig. 5.4.1.2: Typical results for beam steering. Alignment error is introduced by random displacement of quadrupole magnets by 25 μm rms.

Unwanted transverse coupling will be introduced due to the horizontal force component due to the Earth's field, since the machine will be located approximately in a North-South direction. The impact of the coupling to the beam, however, may be not as significant for the case of a nearly cylindrical beam. The tunnel will be shielded by an iron mesh structure and the Earth's field would be attenuated by a factor of ~ 3 . Future studies in the SwissFEL Injector Test Facility will allow specification of the requirements for the shielding.

5.4.2 Beam-based alignment in undulator line

The undulator alignment is a rather delicate part of the beam commissioning, where the goal is to achieve an orbit straightness of a few μm . It cannot be realized with survey alignment, and we need an elaborate beam based alignment procedure.

The LCLS has established an undulator beam based alignment method, in which the beam energy is varied to detect the quadrupole and BPM offsets, respectively [113, 114]. The fundamental basis is that the beam trajectory is independent from the BPM offset while the dipole errors (the dipole component of a misaligned quadrupole) and the first integral of an undulator, deviates the beam trajectory depending on the beam mo-

mentum. A matrix inversion is used to find these errors from the measured beam trajectory.

The procedure practically consists in the pre-alignment (with beam) of the quadrupole firmly attached to an undulator on the same girder. The alignment is performed by moving the entire girder, first one undulator extremity is aligned and the other extremity. Finally the correctors integrated into the quadrupoles are used to align the beam trajectory as precisely as required.

We basically apply the LCLS procedure to our undulator beam based alignment. The FODO quadrupoles are, however, to be situated in separate girder due to the fact that their position, if on the same girder to the undulator, would be shifted by up to 5 μm when the undulator gap is varied. In consequence we will employ on "alignment quadrupole" firmly attached to the undulator girder at each extremity (see Sec. 3.5 Undulators). Those alignment quadrupoles should provide similar resolution as the beam finder wire.

The detailed procedure will be as follow:

- 1) FODO Quadrupole and BPM alignment (Goal: a few μm)
 - Open all the undulator gaps
 - Acquire trajectory data for various beam momenta
 - Analyze the BPM and quadrupole offsets (and the first integral for open gap)
 - Adjust quadrupole offsets and BPM references (movers for offsets $> 10 \mu\text{m}$ and steerers for fine adjustment)
 - Iteration until the orbit straightness of a few μm is obtained
- 2) Undulator alignment (Goal: $\sim 10 \mu\text{m}$)
 - Close the gap of an undulator with the alignment quadrupoles off
 - Turn on the alignment quadrupoles and find the undulator offset
 - Align the undulator
 - Repeat above for all the undulators
- 3) Fine tuning
 - K tapering
 - Phase matching
 - Slight electron beam steering as maximizing the FEL power

The FEL gain length is relatively insensitive to the undulator misalignment since the undulator field is basically alternating dipole. Thus realignment would not be required often while the quadrupole and BPM alignment may need to be performed every one or two weeks.

The specifications relevant to the undulator alignment are summarized in Table 5.4.2.1. They must be sufficient to be compatible with the procedure and to achieve the orbit straightness of a few μm .

Table 5.4.2.1: Relevant specifications to the undulator beam base alignment.

Device/Category	Item	Specification/Resolution
Survey alignment	Long range	$< \pm 1 \text{ mm}$
	Short range	50 μm rms
Undulator	First integral	40 μTm
	Girder mover	$< 10 \mu\text{m}$
Alignment Q		$< 10 \mu\text{m}$
Quadrupole	Mover range	$\pm 1 \text{ mm}$
	Mover resolution	1 μm
	Corrector coil kick	$\sim 1 \text{ nrad}$
BPM	Average	$\sim 0.3 \mu\text{m}$ rms

5.4.3 Transverse trajectory feedback

5.4.3.1 System layout

SwissFEL will have a beam-based transverse trajectory feedback system that allows the implementation of real-time feedback algorithms which calculate the set values for each dipole corrector magnet in the machine, using the position data of all BPMs. Feedback will be based mainly on the BPM and digital signal processing hardware, firmware and embedded software that is being developed by PSI as Swiss in-kind contribution to the European XFEL (E-XFEL) BPM and transverse feedback systems [115]. In contrast to the very long E-XFEL bunch trains of up to ~ 3000 bunches with 200 ns bunch spacing, that allow ultra-fast intra-train corrections with MHz correction rates and sub-microsecond latency, the transverse feedback of the SwissFEL, with its extremely short bunch spacing and train length, will only perform corrections at the bunch train repetition rate of up to 100 Hz, with a corresponding feedback loop latency below 10 ms. The data of all BPMs will be distributed via fast multi-gigabit links to a smaller number of interconnected digital signal processing (DSP) boards that calculate the corrector magnet set values and write them to digitally regulated corrector magnet power supplies. These power supplies will be the successor to the PSI in-house

design used at the SLS [116], with digital current regulation, negligible noise, and several kHz small-signal bandwidth. Laminated iron magnets with a sufficiently thin (~2 mm) stainless steel beam pipe will ensure sufficient corrector bandwidth with negligible eddy current effects.

5.4.3.2 Global real-time feedback network

The multi-gigabit links of the transverse trajectory feedback system components allow their integration into a global beam-based feedback network, together with sensors and actuators of other subsystems like LLRF, lasers, longitudinal diagnostics, photon diagnostics etc. This enables the application of real-time feedback and feed-forward algorithms where one or several signal processing boards combine data from different kinds of sensors to calculate and apply actuator set values at rates up to 100 Hz and latencies down to 10 ms in order to stabilize and optimize electron and FEL X-ray beam properties like beam position, arrival time, charge, intensity, bunch length, energy, etc.

5.4.3.3 Bandwidth considerations

In contrast to storage rings such as the SLS, where fast trajectory feedback allows the correction of random perturbations up to typical cut-off frequencies f_c up to 200 Hz or more, by measuring and correcting the trajectory at rates of many kHz, the SwissFEL BPMs can sample trajectory perturbations only at the bunch train repetition frequency f_{BT} of up to 100 Hz. Therefore the feedback can only damp random perturbations effectively if their frequency is significantly below the cut-off frequency $f_c \sim 0.1 \cdot f_{BT}$. Perturbations above f_c may even be amplified by the feedback loop, which can be prevented by low-pass filters or feedback loop gain reduction. In general, all relevant SwissFEL subsystems, such as girders, magnet power supplies, pumps, beam distribution kickers, etc, should be designed in a way that reduces all such high-frequency perturbations to a level where they do not affect the stability of the lasing process. It should be noted that high-frequency perturbations are downsampled, and therefore the feedback will also be able to damp perturbations that are sufficiently close to an integer multiple N of f_{BT} , e.g. a girder vibration, where the girder eigenmode is $N \cdot f_{BT} + \Delta f$, with $|\Delta f| \ll f_c$.

The stability of the RF system is also vital for transverse beam stability, since, for example, bunch length jitter due to RF phase jitter causes transverse trajectory jitter due to kicks of the last bunch compressor dipole, where the energy loss due to CSR, and thus the bending angle, depends on the bunch length. These kicks tend to dominate the transverse perturbation spectrum in the respective plane for low-charge, short-bunch operation modes [117, 118]. Furthermore, a stable higher-harmonic RF system that creates a symmetric transverse charge distribution within each bunch is also vital for trajectory feedback, in order to guarantee that the part of the bunches with the highest density that lases has no significant offset to the centre of charge of the bunch that is measured by the BPMs, and thus used for transverse trajectory feedback in the undulators.

The signal processing system for the transverse trajectory correction will not only allow the implementation of feedback, but (if necessary) also the additional implementation of harmonic suppressor algorithms that can damp a narrow-band trajectory perturbation with reproducible frequency above f_c , if the perturbation amplitude is constant or varying sufficiently slow (e.g. 50 Hz mains noise), for example by using a narrowband filter that cuts out the relevant frequency component from the BPM data and feeds it back to the corrector power supplies with a suitably adjusted phase delay.

5.4.3.4 Algorithm

The feedback will calculate the corrector magnet settings from the BPM data using the singular value decomposition (SVD) method, with the required corrector current change being fed into a controller (e.g. PID) with adjustable gains. The required beam response matrix will be obtained from an optics model that will be optimized by fitting to measured response matrices and optics data. The matrix and its SVD-inverse will be re-calculated and the feedback system reconfigured when required, e.g. when a new optics is loaded or the energy is changed significantly without changing the quadrupole magnet currents in the undulator intersections.

The number of BPMs and correctors to be used by the algorithm can be selected using a high-level application. For initial trajectory correction, when the machine is commissioned with 1st beam or switched on after a shutdown, the feedback can include all BPMs and cor-

rectors in order to get the beam through the machine. For standard user operation, the number of BPMs and correctors, as well as the feedback bandwidth, can be adapted to the observed perturbation sources and frequencies, as required for maximal stability of the lasing process. The feedback will also support the multiplication of small SVD eigenvalues with weighting factors, before performing the SVD pseudo-inversion (Tikhonov regularization [118, 119]), which allows running a global feedback with different bandwidths for different perturbation patterns (i.e. eigenvectors). By reducing the bandwidth for perturbation patterns where small BPM readings cause large corrector magnet changes while using a larger bandwidth for other patterns, the impact of BPM noise and optics model imperfections on the trajectory, and thus on the lasing process and photon beam pointing stability, is minimized. The positions of BPMs, correctors and quadrupole magnets will be chosen in a way that minimizes the SVD conditioning number (i.e. the quotient between largest and smallest eigenvalues), maximizes the number of large SVD eigenvalues of the beam response matrix, and results in a mainly tri-diagonal structure of the SVD-inverted response matrix, with minimal off-diagonal values and a resulting maximal robustness of the algorithm with respect to beam optics and energy variations.

6 Building and infrastructure

6.1 Building layout

The building design and locations presented below correspond to the status as of October 2011, and is subject to modifications until it fulfils all necessary authorizations and machine requirements. With a total length of 719 m and a width ranging from 6 m to 45 m, the SwissFEL facility will be located a few hundred meters south-east of PSI-East (see Figure 6.1.1). This location presents the advantage of having a continuous area (with possibility of future extensions) and homogeneous ground to contain the SwissFEL installation, in contrast to the PSI-West area, which would be cut by a small river and limited in size. The east side of PSI has also shown the lowest level of ground vibration [120].

The foreseen location is situated in the forest, near the east entrance of the PSI. The building will follow an existing valley in order to have an optimal integration into the environment. Figure 6.1.1 (top) shows, in blue/green, the buildings half-covered by earth, and in gray the buildings under the natural ground level, as planned for 2016. The area coloured yellow/orange corresponds to the new access road and loading zone which need to be built.

Access to the facility is ensured via a road alongside the building. The Beam Tunnel and the Undulator area situated under the natural ground level are accessible through escape stairs and via a loading zone equipped with a crane for large equipment installation (Figure 6.1.1). The electron beam is flowing from south to north.

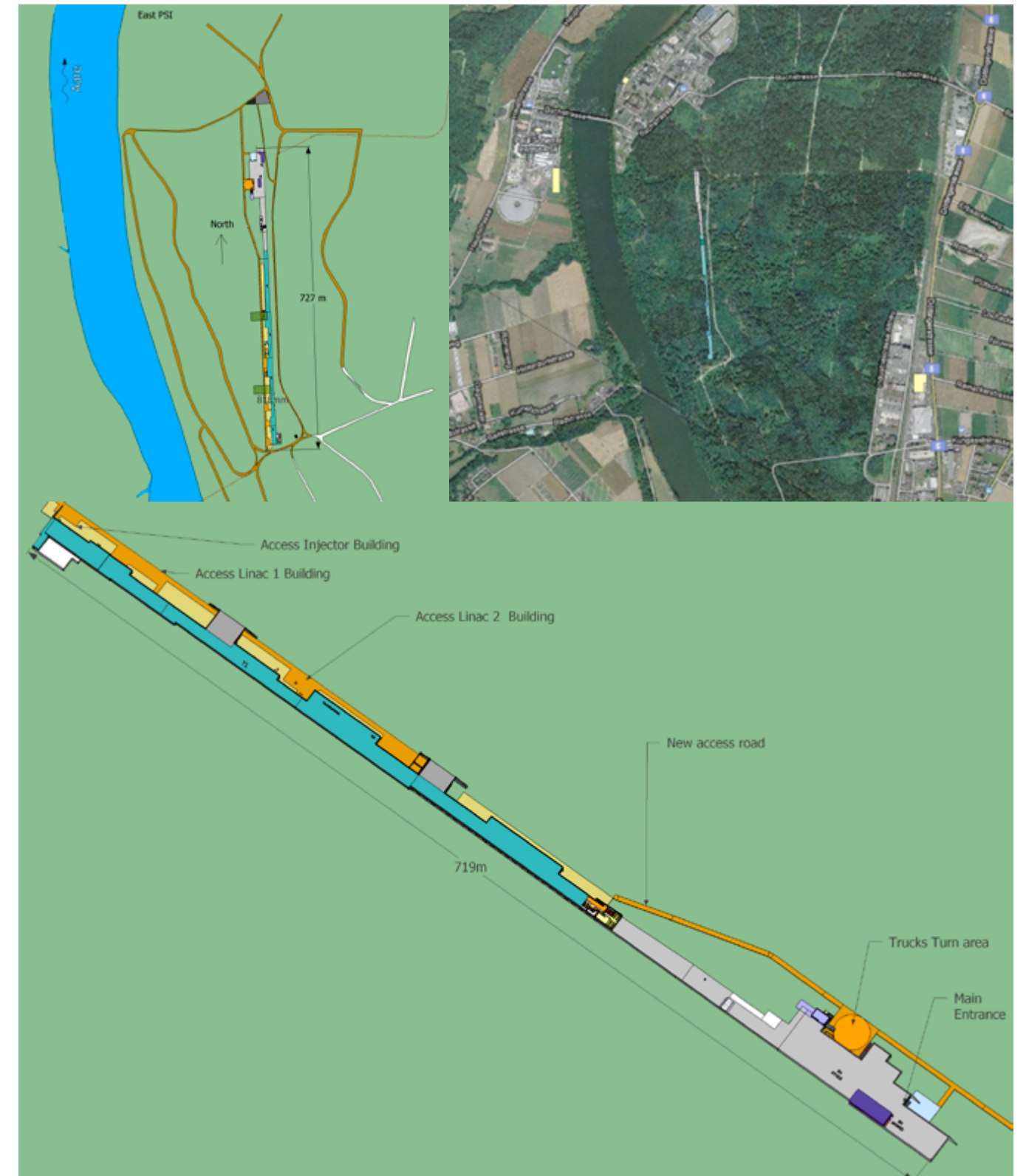


Fig. 6.1.1: Foreseen location for SwissFEL (Top: map; Bottom: aerial view with main access points).

Figure 6.1.2 (bottom) shows a 3D view of the building in its natural surroundings, with the lower floor completely under the natural level of the soil. The upper floor is completely covered with soil on one side, to minimize its visual impact on the environment. Two sections of the building are entirely covered with soil, to allow animals to cross the building. The SwissFEL building is cut longitudinally in sections or sub-buildings having almost independent infrastructures. The names of the different building sections correspond to specific parts of the electron beam line and are depicted in Figure 6.1.2 (top).

Underground:

- Beam Tunnel SK (only electrons): where the electron accelerator is effectively installed (Fig. 6.1.3 to 6.1.6)
- Undulator Hall UH (electrons and photons): where FEL light is produced (Fig. 6.1.7 and 6.1.8)
- Experimental Hall EH (only photons): where all the different experimental stations are installed (Fig. 6.1.9)

Above Ground (but covered with earth)

- Injector IN (Technical building for the Injector): details in Fig. 6.1.3
- Linac 1 L1 (Technical building for Linac 1) : details in Fig. 6.1.4
- Linac 2 L2 (Technical Building Linac 2): details in Fig. 6.1.5
- Linac 3 L3 (Technical Building Linac 3): details in Fig. 6.1.6

The electron beam accelerator sections (Injector to Linac 3) have double-deck architecture (Figure 6.1.2 – top) with the RF accelerating structures being in the lower floor with an as short as possible connection to the RF power plant situated just above in the top floor. Downstream of Linac 3, only the lower floor remains and contains the Aramis undulator section and the two experimental areas (Athos and Aramis experimental halls).

The electrical infrastructure, cooling stations and air conditioning units are distributed in the Infrastructure Gallery and within UH and EH.

More details on the dimensions of the different SwissFEL sections are depicted in Figure 6.1.2 (Top) and in the appendix 6.2. The injector starts at the electron gun and finishes downstream of Bunch Compressor BC1. Linacs 1, 2 and 3 represent the total length of the C-band accelerator sections. The spaces between the linacs are filled with diagnostics, BC2 and matching optics. The space between Linac 3 and the Aramis undulator is also foreseen for the collimator and electron beam matching optics. Details of the length of the different accelerator components can be found in chapters 2 and 3.

Table 6.1.1 summarized the outer surface, volume and height of the different building areas. The facility has been optimized for minimum volume and has a total surface of 15,932 m² on two levels, with a total volume of 77,000 m³.

Table 6.1.1: Outside dimensions of the main sections in the SwissFEL building. A represents the outer surface and V the outer volume. The height corresponds to the outside height of the different building sections (status October 2011).

Level	Location Name	Location Description	A [m ²]	Height [m]	Vi [m ³]
Upper	IN	Injector upper level	1133	5.5	5573
	L1	Linac 1 – upper level	951	4.5	4281
	South Pass	South Animals Pass	333	4.9	1631
	L2	Linac 2 – upper level	1244	7.15	5928
	North Pass	North Animals Pass	266	4.9	1305
	L3	Linac 3 – upper level	1557	4.5	7006
	TBU	Undulator Upper Level	293	4.5	1224
Lower	SK	Beam Tunnel	2301	5.1	10905
	UH	Undulator hall	3853	5.1	19408
	Exp Hall	Experimental hall	4000	5.1	19789
	Total		15932		77051

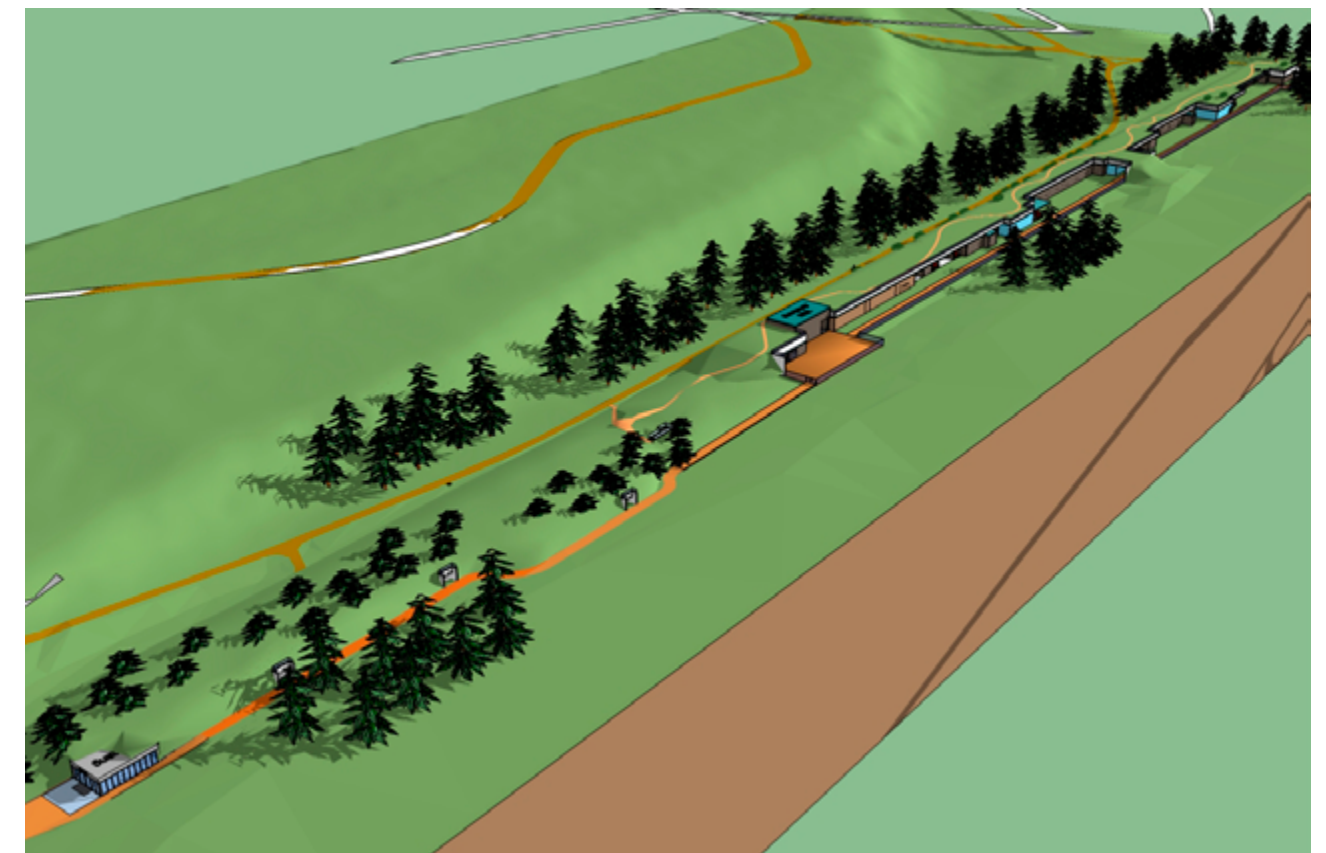
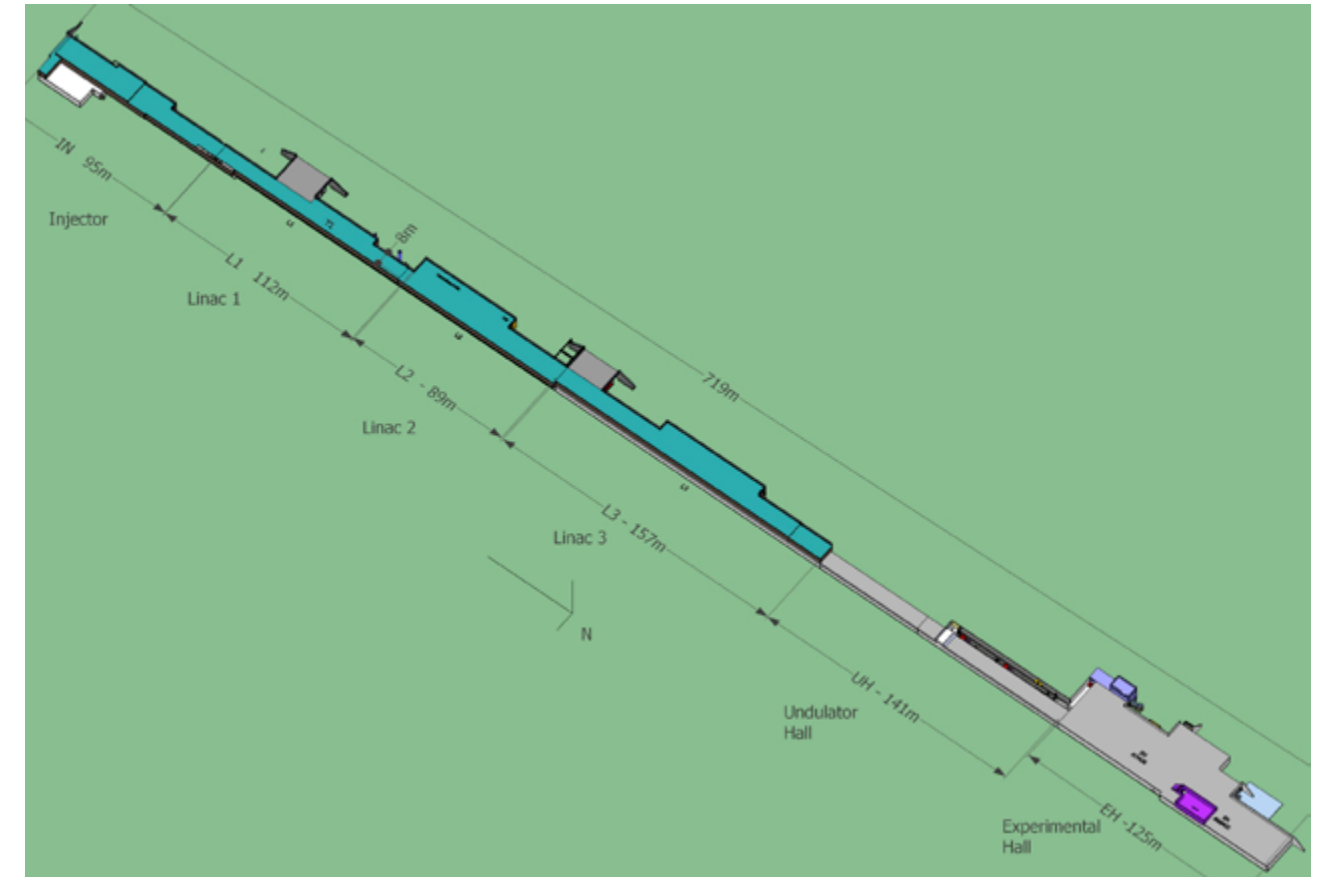


Fig. 6.1.2: SwissFEL building seen from the experimental area entrance, without (top) and with the natural surrounding land.

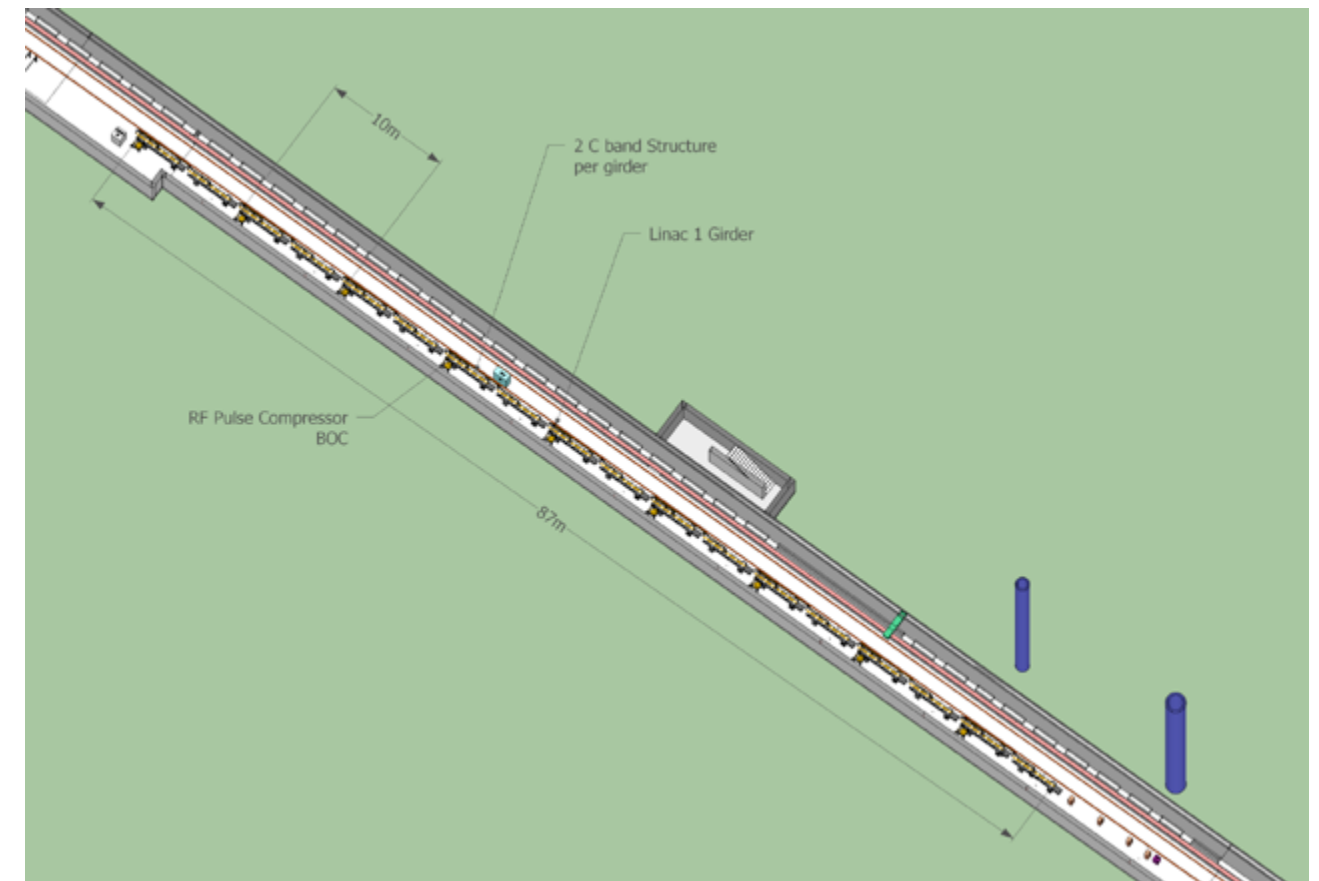
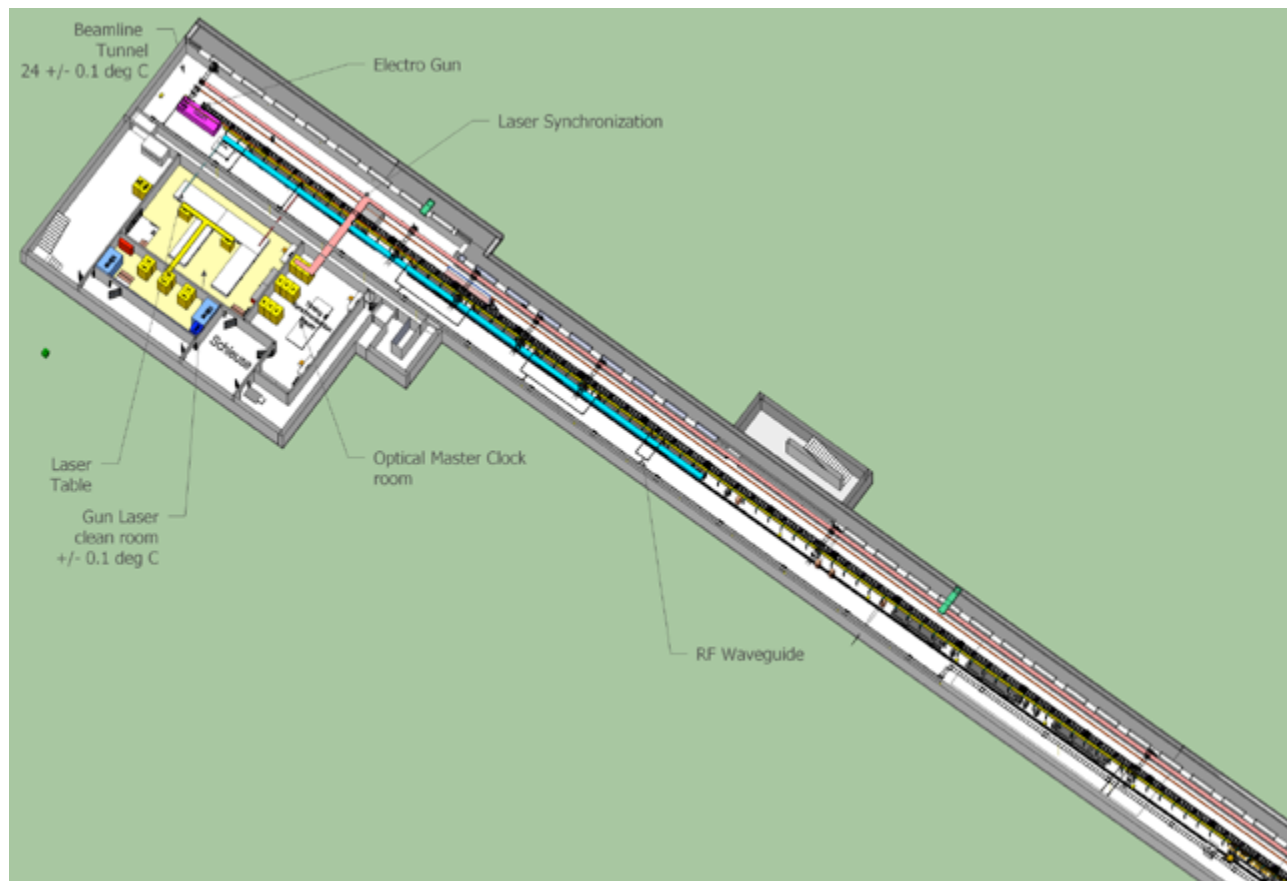
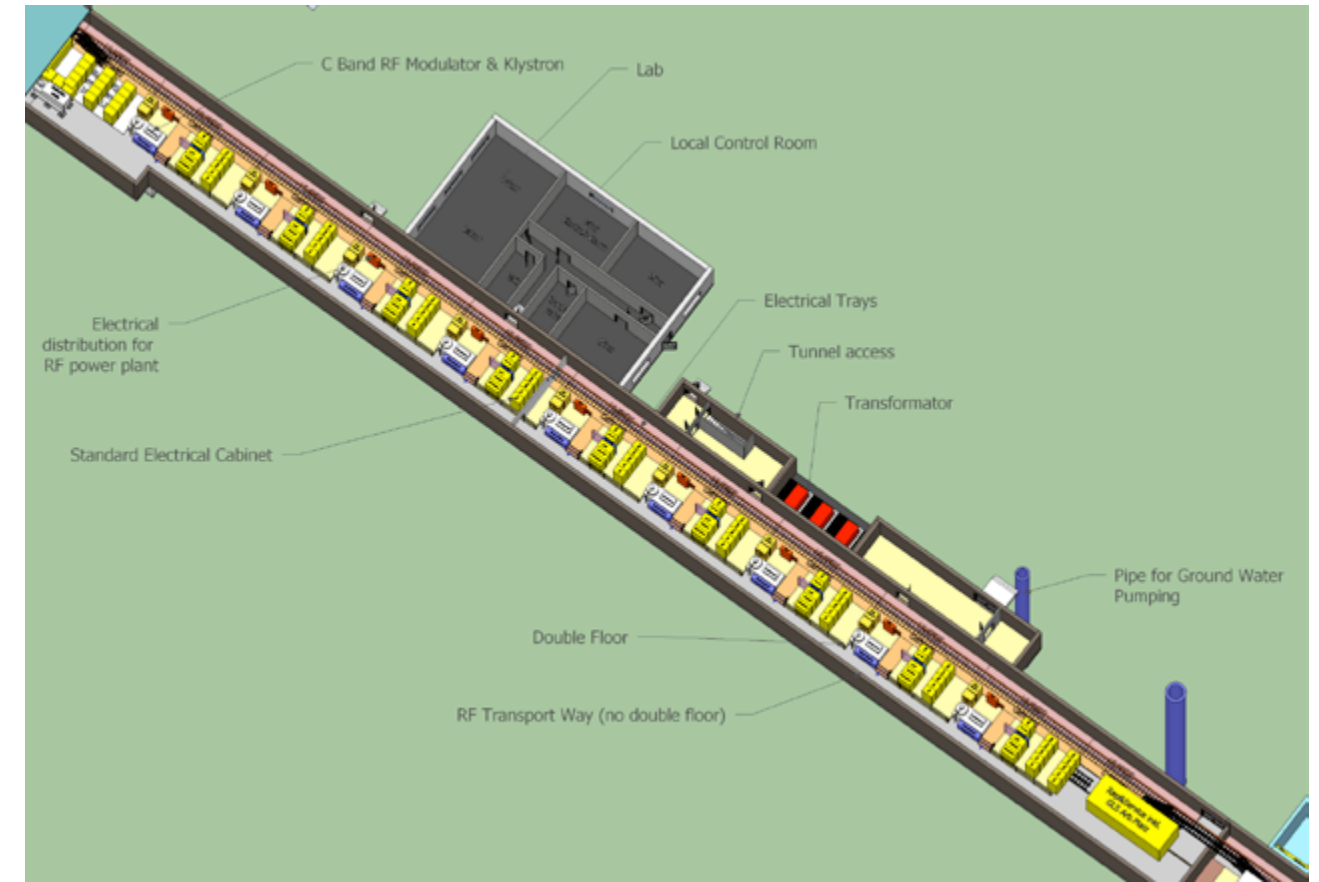
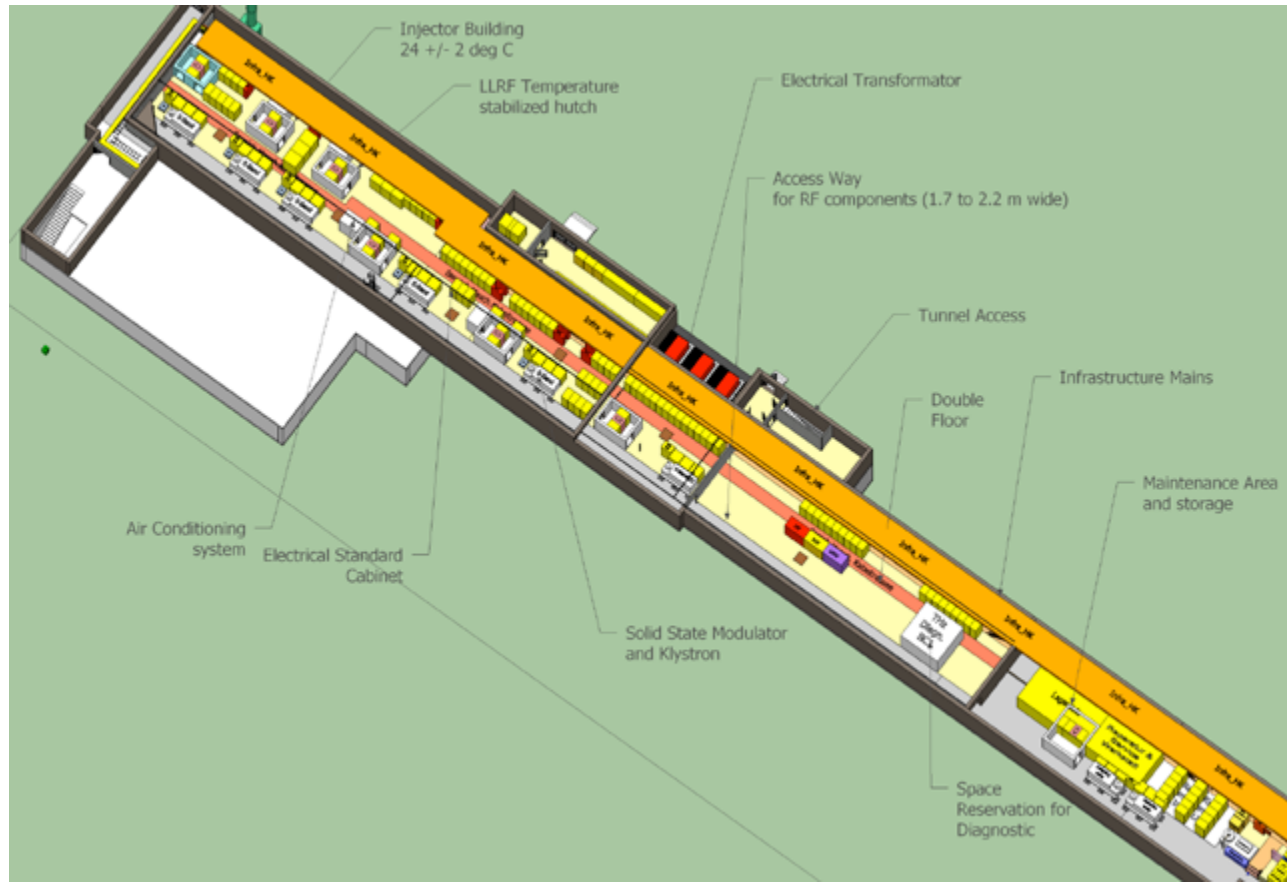


Fig. 6.1.3: Two views of the injector section; the infrastructure gallery in the upper floor (Top), the beam tunnel with the electron gun (bottom).

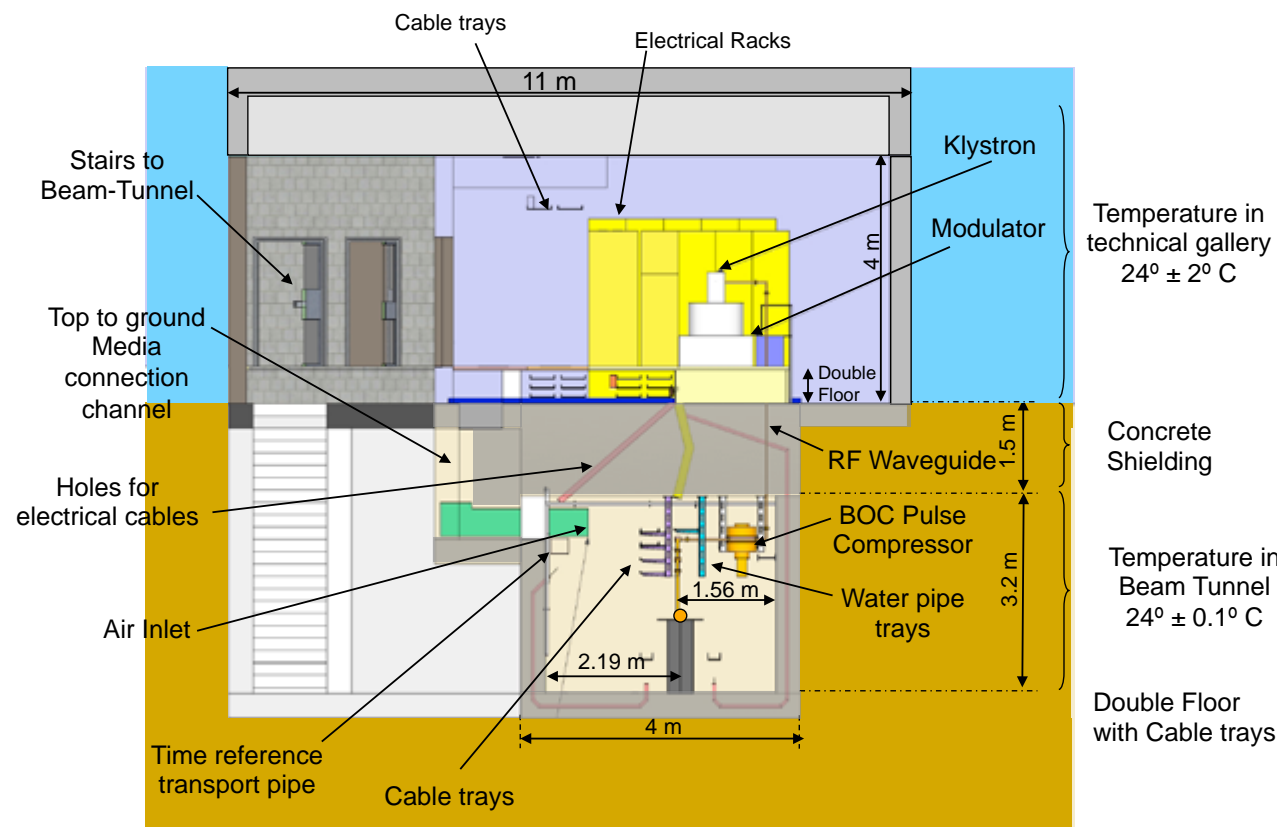


Fig 6.1.4: L1 (Technical Building – Linac 1) showing the infrastructure gallery (Top) and the ground floor with the electron beamline components (middle) and a cut view of the building at $z = 150 \text{ m}$.

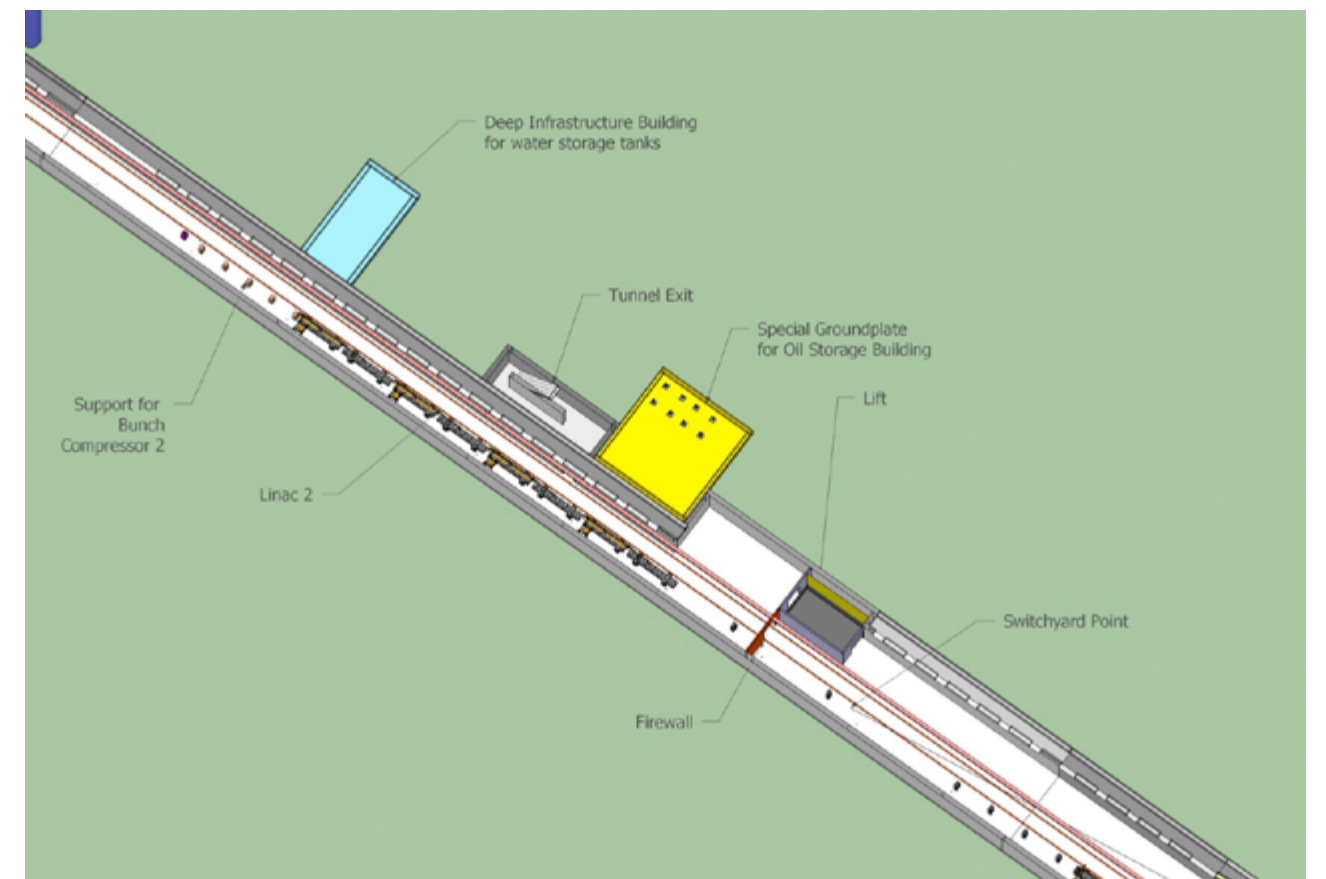
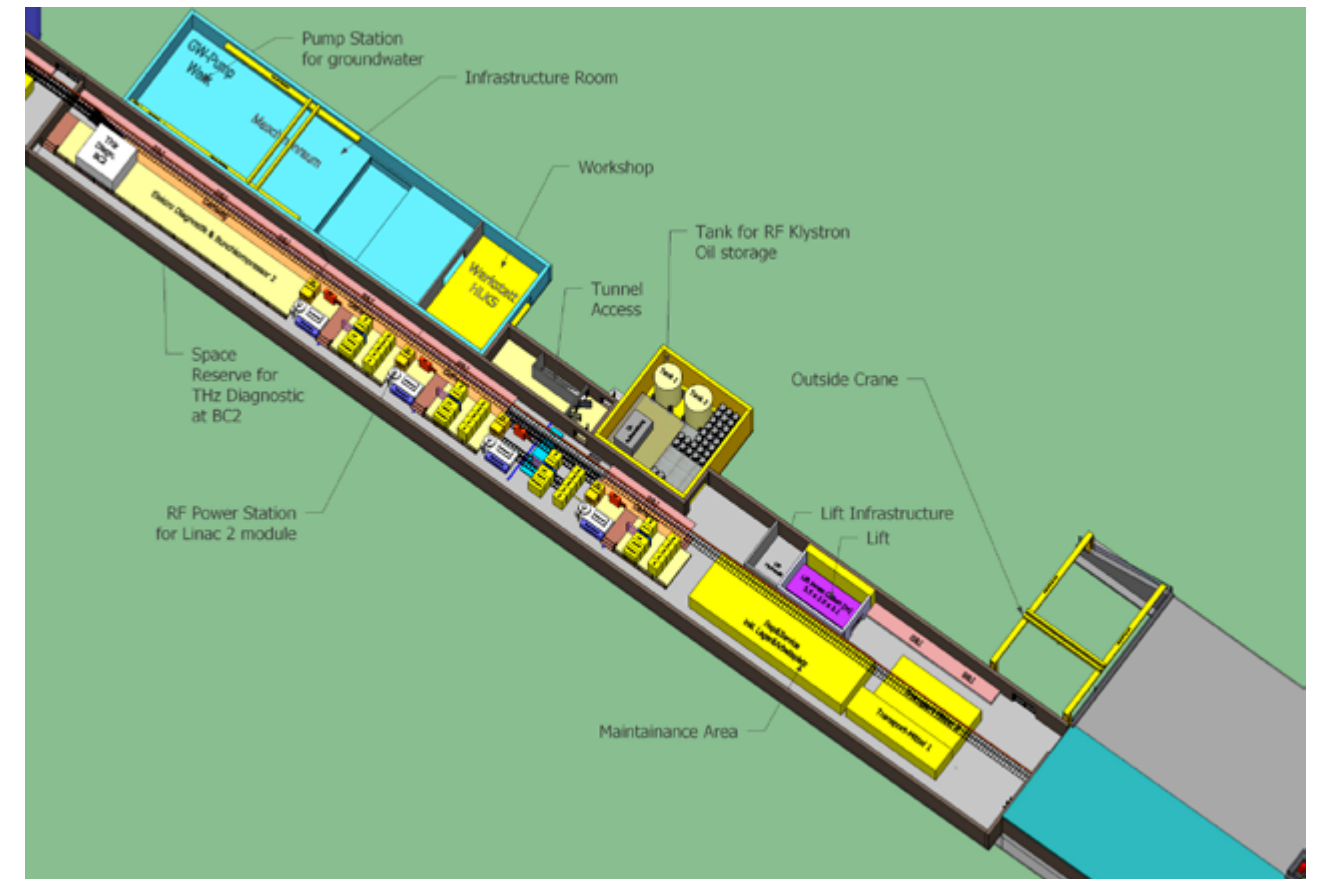
The beam axis is at 1.56 m from the east wall side (Fig. 6.1.4). The beam tunnel has an inside width of 3.75 m and an inside height of 3.2 m. The inner width of the tunnel is however not constant along the entire accelerator, annex 6.2 gives more details on the tunnel width (status October 2011). The electron beam axis height is constant and equal to 1.2 m.

Most of the necessary connections (power, control, water) to beamline component are coming from cable/water trays attached to the roof. The time reference signal, because of his sensitivity, is on a separate support attached to the wall. The RF power plants are sitting upstairs in the upper floor above the accelerating structures to minimize waveguide length.

In the top floor, a 2 m wide transport way (without double floor) is reserved along the east wall for transport of large RF components. On the opposite wall (west wall), a 1.2 m wide corridor is reserved for building infrastructure components installation. The electrical racks (about

400 in total) are installed between these two reserved corridors, they are all sitting on a 55 cm high double floor filled with cable trays to connect racks to machine components (magnets, diagnostics, ...). The electrical connection from top floor to tunnel is insured via holes in the concrete shielding (no direct vertical drilling). In addition, wide access channels for all infrastructure connections are situated (Top to ground media connection – 0.8 m wide) along the west wall.

The linac 1 and the bunch compressor 2 are installed in the beam tunnel under L1 (Fig 6.1.4). SwissFEL linacs consist in a succession of RF modules of 10 m length (4 C-band structures sitting on 2 girders) and connected to one Klystron/Modulator unit. One stairs access to the beam tunnel is located on the side of L1. The Beam Tunnel (Figures 6.1.4) is shielded by a 1.5 m thick concrete roof. This thick roof shielding allows full access to the Infrastructure Gallery during operation time. The thickness of the Beam Tunnel walls and ground plate will be 40 cm.



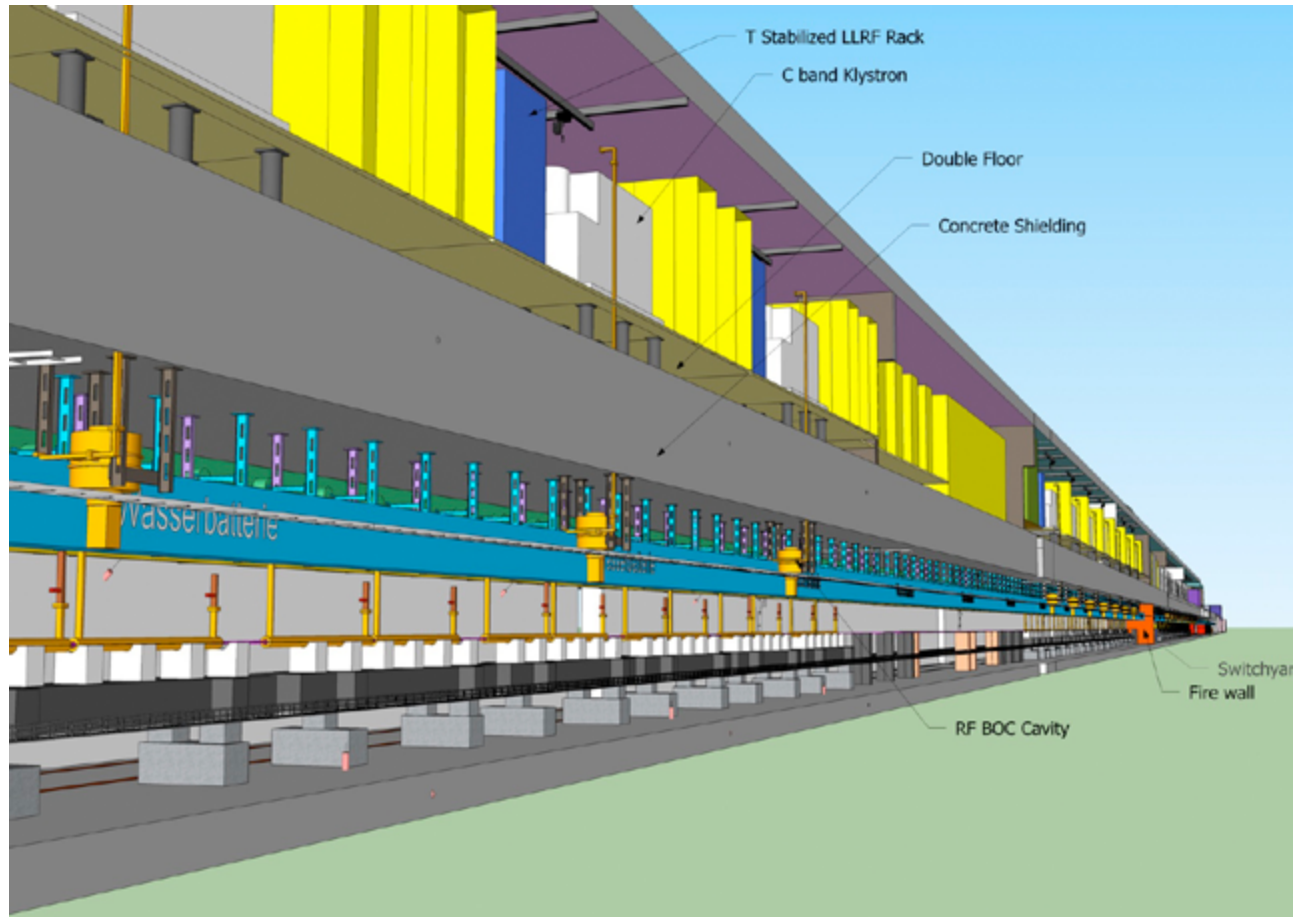


Fig. 6.1.5: Top: L2 (Linac 2) which includes a lift and stairs access to the tunnel. Middle: Lower level L2 with beam components; Bottom: Vertical cut view along the building.

On the side of the RF Infrastructure Gallery of L2, an annex building (blue coloured in Fig. 6.1.5) will contain the main water pump station which will provide cooling water to the entire building. The water is pumped in the ground and rejected in the Aare river after having cooled the electron beam components. A connection to the water circuit of PSI, allows the possibility of re-using, the warm water (up to 80 deg C) for heating purposes at PSI.

Downstream L2, the beam tunnel becomes wider (from 3.75 m to 6.9 m inside width) since the beamline is splitted into two lines (Athos and Aramis) which are 4 m apart.

Emergency exit doors are present every 100 m in the sections IN to L3 buildings.

Downstream L3 ($z > 453$ m), there are no more RF acceleration structures so that the undulator hall (UH) and

the experimental hall (EH) are single floor buildings (under the natural ground level). EH has however a laser room on a second floor (Pump Laser rooms), see Chapter 4 for details.

The Athos beam dump is installed below the undulator hall floor. The Athos Front End (from Athos last undulator until the shielding wall of the Experimental Hall (EH)) is about 100 m long. In the front end, switching mirrors are installed which distribute photons to the 3 possible Athos experimental stations.

The 12 undulators of Aramis (red coloured in Fig. 6.1.7) cover a total length of 58 m, parallel to the Athos front end. The Aramis Front End Enclosure (see Chapter 4) is then about 60 m long. The EH (Experimental Hall) building is separated from the UH building by a 2 m thick shielding wall to protect users from electron induced radiations.

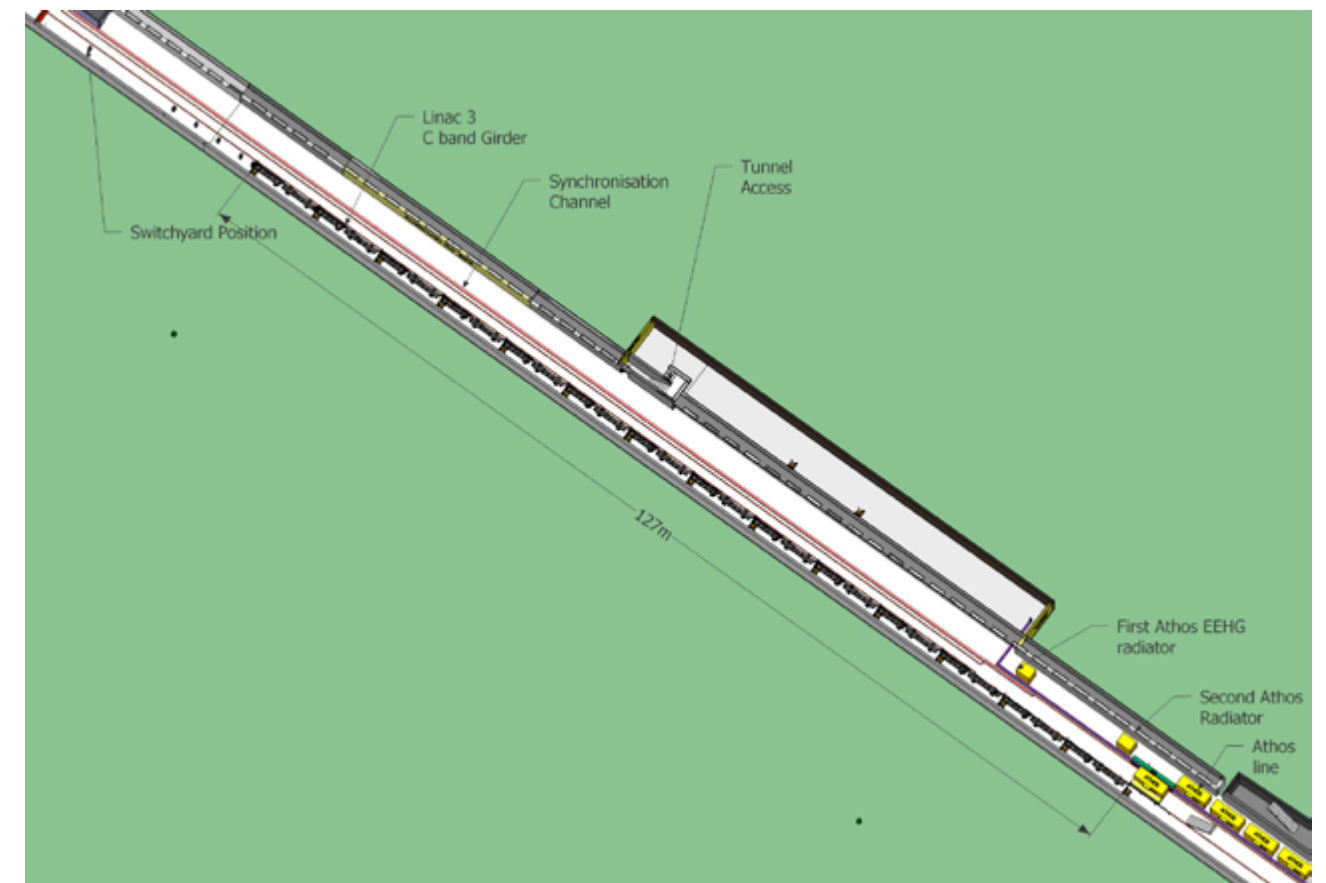
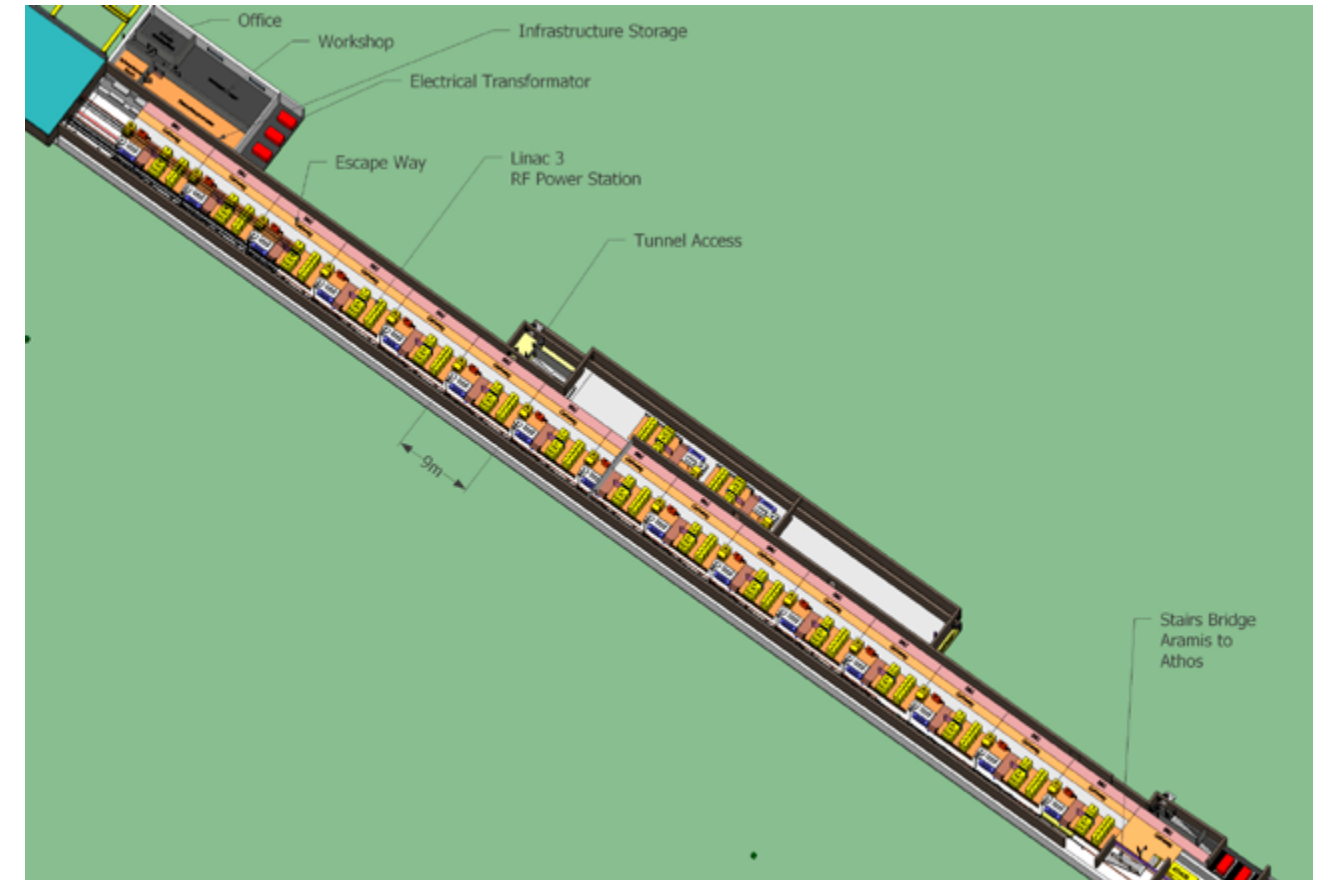


Fig. 6.1.6: Top: L3 (Technical Building Linac 3): Linac 3 towards Aramis and Switchyard towards Athos beamline. Bottom: Lower level L3.

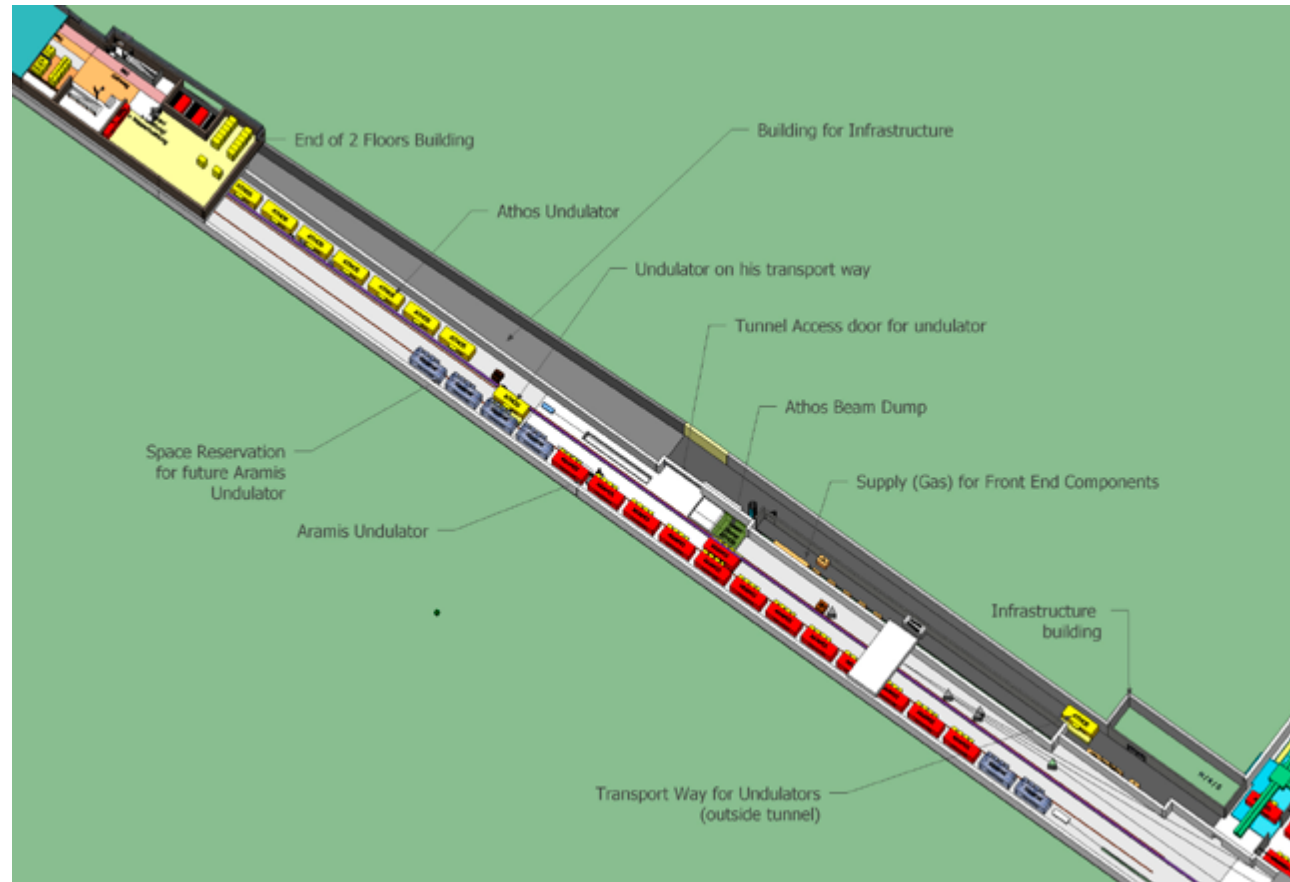


Fig. 6.1.7: Undulator Hall UH with the Athos undulators in yellow and the Aramis undulators in red (Top). The Aramis Undulator line and part of the experimental hall (EH) is shown in the bottom picture.

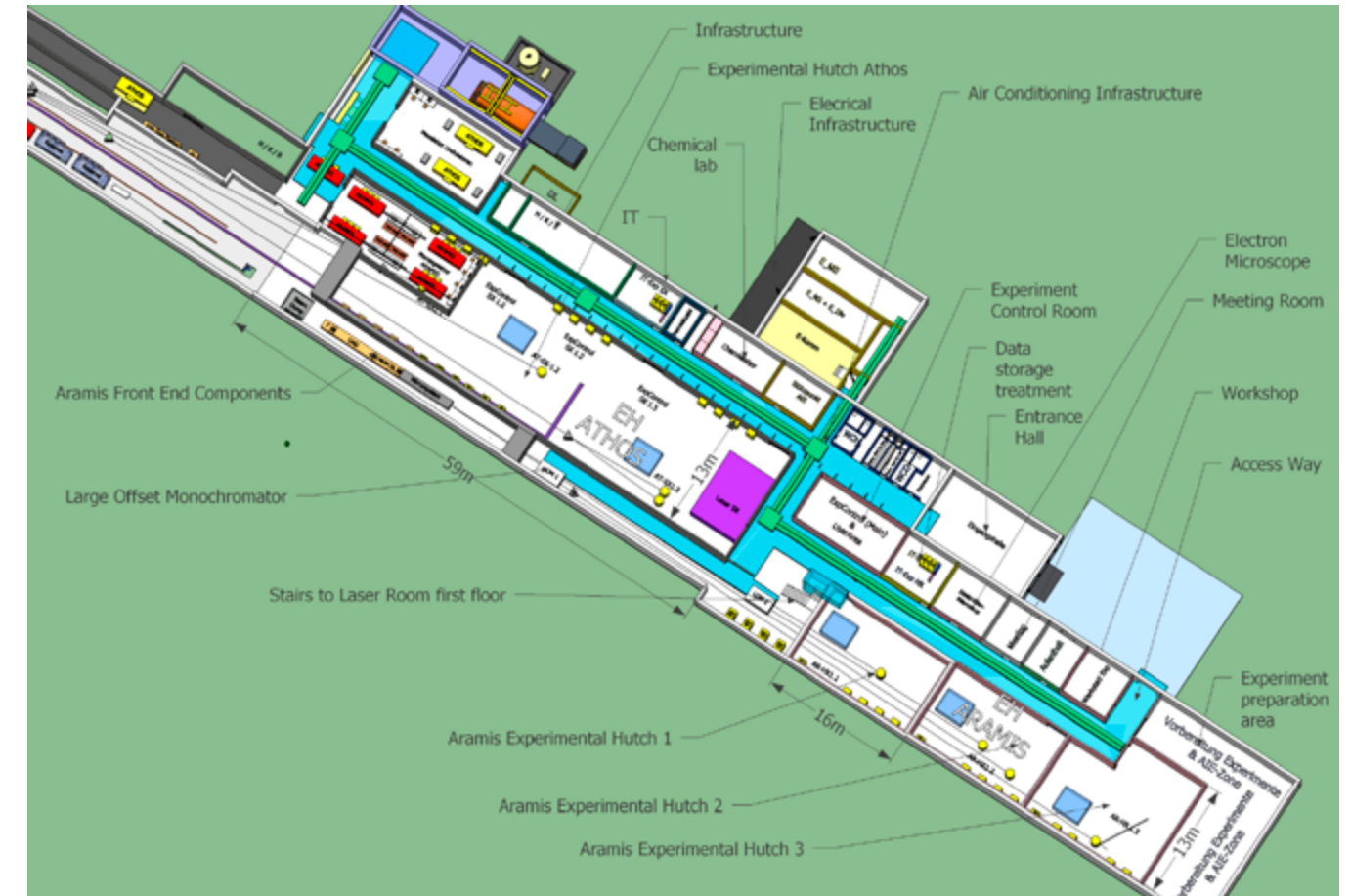


Fig. 6.1.8: Experimental Hall (EH) building layout (Status October 2011).

Transport of the Aramis undulators (20 Tonnes) will start from the Experimental Hall loading zone on air cushion vehicle until their final destination in UH (Fig. 6.1.7).

The building has a simple architecture, with priority given to the functionality and respect to the environment (Figures 6.1.2). The maximum electrical consumption of the accelerator, undulator and experimental areas is estimated to be about 5.2 MW (4.6 MW for SwissFEL components and 0.6 MW for infrastructure components). The electrical energy will be transported at high voltage from PSI West to local transformers (see red boxes in Fig. 6.1.4), which will distribute electricity to sub-dividers and then to the different devices (RF modules, magnets power supplies, etc). About 400 standard electrical cabinets (racks) are foreseen, to contain all the necessary devices for low-level rf, magnets power supplies, vacuum, diagnostics and control devices. These racks will cover a large part of the infrastructure gallery surface, the rest of the space being used for rf-modulator/

klystron assembly and for transport. The required cooling capacity will be of the same magnitude as the electrical consumption and will to 80–90 % be covered by water cooling. Ground water will be used for cooling through local heat exchangers. The rest of the heat will be dissipated to the atmosphere through an air conditioning system, which should maintain the temperature in the Beam Tunnel to within $24 \pm 0.1^\circ\text{C}$, and within 21 to $26 \pm 2^\circ\text{C}$ in the other buildings. During shutdown, temperature stability will be ensured via connection to the distributed heating system REFUNA. Heat-up of PSI site with excess heat from the SwissFEL components will be tested. A detailed functional layout schematic of the SwissFEL infrastructure can be found in Appendix 6.1.

The foreseen safety rules for personnel and the environment will fulfil the strict Swiss regulations and are described in the following section.

6.2 Safety issues

6.2.1 Radiation protection

6.2.1.1 Radiation protection

The operation of the SwissFEL facility is subject to Swiss legislation, in particular to the radiation protection law (Strahlenschutzgesetz, SR 814.50) and related paragraphs. Also relevant are legal guidelines (among others, the "Richtlinie für den überwachten Bereich der Kernanlagen und des Paul Scherrer Institutes", HSK-R-07/d), as well as PSI internal directives. In this section will be summarized the preliminary radiological studies performed according to the present design phase of the SwissFEL facility and the beam tunnel, as well as the preliminary classification of the building and other supervised regions. For references and detailed descriptions, refer to PSI note FEL-FU96-008. Table 6.2.1.1 shows the limits for ambient dose rate for different type of zone classification, whereas table 6.2.1.2 shows the zone definitions for the different areas of SwissFEL.

Table 6.2.1.1: PSI Requirements for ambient dose rate for different type of zone classification.

Type	Value	Area Type / Location Description
Inside controlled zone	< 1 $\mu\text{Sv/h}$	Local control room, permanent workplace
	< 10 $\mu\text{Sv/h}$	Area Type V, experimental area (such as SLS beamlines)
	< 25 $\mu\text{Sv/h}$	Gallery, areaway, temporary workplace (within Type W, without beam)
	< 100 $\mu\text{Sv/h}$	Temporary workplace at beam conditioning (within Type W, without beam)
	<ul style="list-style-type: none"> > 1 mSv/h < 10 mSv/h > 10 mSv/h 	Area Type Y Area Types X and Y both prohibited during operation, secured by personal safety system (PSYS)
Outside controlled zone	< 0.12 $\mu\text{Sv/h}$, (20 $\mu\text{Sv/w}$)	Permanent workplace, office, laser laboratory
	< 0.6 $\mu\text{Sv/h}$, (100 $\mu\text{Sv/w}$)	Outside building, non-permanent stay

Direct radiation outside the fenced of SwissFEL above ground:

According to the present design phase, the SwissFEL above ground building is half covered with at least 1 m of earth. This building and the forecourts have to be fenced against unauthorized access, independent of an Aare sinister or dexter realization. The limitations for the controlled emission of radioactivity (by the air- and water path) as well as the surveillance of radioactivity and direct radiation in the PSI-environment are defined in the "REGLEMENT" BAG 5.07.01-4, HSK 2/370 Rev.1 (2007).

The direct radiation outside the fenced area, should not lead to an individual dose above 0.1 mSv/year. Thereby the duration of stay has to be accounted for and furthermore Art. 102 StSV has to be considered. It can reasonably be assumed, that during a year no one may rest near the fence for more than 10 % of the time. Thus the tolerated annual ambient dose equivalent is 1 mSv. The monitoring will be done by PSI with the commonly used "Arealdosimeters" which will be adequately positioned.

Prevention, contingency

If an overstepping of the limits is happening due to some unexpected reasons several actions can be considered:

- Reduction of operation time (occupancy factor)
- Installation of additional local shielding
- Reduction of beam intensity

Table 6.2.1.2: Zone definitions for the different areas of SwissFEL.

Building name	Zone Type	Area Type	Dose Limit	Remark
Infrastructure Gallery in Upper level (IN to L3)	0	W	< 100 $\mu\text{Sv/h}$	Passages in RF gallery: restricted abidance according to operation regulation. Duration of stay has to be controlled
		V	< 10 $\mu\text{Sv/h}$	(1) Workplace inside controlled area, attention of ALARA principle
Gun Laser Room	0	V	< 10 $\mu\text{Sv/h}$	Experimental Area – Compliance to Class IV Laser Area (Badge, Signs, Glasses), see (1)
Beam Tunnel (SK)	1	Prohibited Area during Operation secured by PSA (Remote Personal Safety System)		
UH – Undulator Hall Lower level	1	Prohibited Area during Operation secured by PSA (Remote Personal Safety System)		
EH (not in hutches)	0	V	< 10 $\mu\text{Sv/h}$	See (1)
EH – Hutches without radioactive probes	0	V	< 10 $\mu\text{Sv/h}$	Limited Access by LAC (Local Access Control), see (1)
EH – Hutches with radioactive probes	1	V	< 10 $\mu\text{Sv/h}$	Limited Access by LAC (Local Access Control), see (1)
Outside on the West side within fence	No	–	< 0.1 mSv/week	PSI domain outside controlled area, non permanent stay
Roof and East side of building	No	–	< 1 mSv/year	Outside PSI domain, public access possible. Maximum of 10 % abidance assumed.

PSI basic rule (StSG, art. 6) (StSG, art. 5): Radiation shielding design should result in a dose rate not exceeding 10 % of the limits valid for the controlled areas.

6.2.1.2 Incidents

The SwissFEL beamline will be equipped with a machine protection system (MPS). Besides machine-relevant parameters, the radiation background at the critical points will also be monitored by the MPS. In this way, a possible technical problem will lead to immediate shutdown of the electron beam by the MPS (closing laser shutter to switch off the electron beam or powering off some RF components to switch off dark current for example). It cannot be excluded that the beam may be deflected towards the shielding for a certain MPS delay time. Nevertheless, the resulting temporary ambient equivalent dose rate outside the shielding has to remain within legal limits (see Table 6.2.1.1).

6.2.1.3 SwissFEL shielding

The operation of the SwissFEL accelerator inevitably gives rise of unwanted radiation fields: unwanted beam misalignment, beam cleaning by collimators, beam monitoring with screens or finally the dumping of the electron beam. This results in beam loss and in the

generation of potentially harmful secondary radiation. The beam tunnel will not be accessible during operation unlike the technical galleries or user laboratories for example. The installation of shielding is a necessity to ensure safe operation, according to the Switzerland radiation protection legislation.

The cascade-like process, initiated by the interaction of an incoming electron with matter, results into various secondary particles. The five major electron radiation loss components are:

- Giant-Resonance-Neutrons (GRN): Those neutrons with energy range between 0.1 MeV and 20 MeV are photo-produced in the core of the shower. The emitted spectrum shows a peak at about 1 MeV with an average of about 2 MeV. The production threshold energy is about 4 MeV for heavy nuclide and about 12 MeV for the light one.
- High-Energy-Neutrons (HEN): Neutrons with energy above 100 MeV are initiated by high energy photons in the hadronic cascade. The production angle is in the forward direction. This radiation component dominates shielding calculations.
- Mid-Energy-Neutrons (MID): Neutrons having energies between GRN and HEN, being produced by quasi-deuteron reactions at energies above 25 MeV. The neutron energy lies between 20 MeV and 100 MeV, peaked in forward direction.

- Direct Bremsstrahlung: Photons leaving the core target material with energies between 0.1 MeV and 20 MeV. In the presence of a nuclear field, these photons may go on to produce electron – positron pairs driving on an electromagnetic shower. The distribution is a slow decreasing function from 0° to 180°, superimposed to a more intense forward core between 0° and 5°.
- Indirect Gamma: Photons and directly ionizing particles created during slowing down of the HEN. The dose rate contribution is about 25 % of the one from neutrons.

For the design phase, the use of analytical methods to get a first estimate is a quite good and reasonable first step approach. The shielding analyses described here have been performed with the SHIELD 11 code [121]. It has been developed at Stanford Linear Accelerator Centre (SLAC) to perform shielding analyses in the vicinity of a high energy electron accelerator. It uses analytical expressions for the production and attenuation of neutrons and photons from electron beam loss at “thick targets” such as beam dumps or collimators.

Having calculated the overall shielding dimensions and identified the critical points, detailed studies can be started. For this purpose, general purpose Monte Carlo codes like FLUKA [122] have proven to be well suited and commonly used in other labs. More detailed predictions on the activation of components, secondary particle fluxes and hot spots based on a detailed geometric description can be made. This information is then used to optimize the shielding design, as well as to prepare decommissioning plans, with possible financial gain.

The losses due to missteering or manipulation mistake are non permanent and would last less than one second depending on the delay time of the machine protection system. The thickness of the building walls are calculated for a permanent beam loss of 0.1 W. A full beam has a power of 560 W (800 pC; 7 GeV; 100 Hz) so that the tunnel shielding can accept full beam losses during a maximum of 0.6 s (or 48 nC at 7 GeV) every hour. The dark current and the beam halo are permanent beam losses of charge Q_{loss} at 100 Hz. These electrons are then not lost uniformly along the entire tunnel but rather at some specific location as described in the next section. The measurements for the evaluation of the dark current generated in the S-, respectively C-band accelerator structures of the SwissFEL Teststand are still in progress.

The preliminary shielding calculations are based on the nominal acceleration field of 30 MV/m for the electron bunches.

6.2.1.4 Dose rate estimates at main beam losses positions

The dose rate estimations (Table 6.2.1.3) are based on a shielding thickness of 0.4 m for the ground plate and side walls of the Beam Tunnel, and 1.5 m for the Beam Tunnel ceiling. In addition, 1 m of soil covers the top of the Infrastructure Building. The area above the SwissFEL building is planned to be a non-controlled zone. The electron beam loss is assumed to have a charge Q_{loss} at 100 Hz and with an energy E_e which depends on the location along the tunnel. Q_{loss} is an estimation based on dark current values measured in other labs. The beamloss location is usually at dipoles (dark current has usually a weaker energy than the beam is over-deflected at dipoles, or at collimators which intercepts electrons too far from the axis (like beam halo). More precise simulations will be carried out at a later stage.

The ambient dose equivalent has been calculated for 3 transverse positions (see Figure 6.2.1.1), at seven different sections of the Beam Tunnel with following average electron beam loss power:

- BC1 ($E_e=0.45$ GeV, $Q_{\text{loss}}=10$ pC; 100 Hz; beam loss: 0.45 W)
- BC2 ($E_e=0.45 - 2.1$ GeV, $Q_{\text{loss}}=10$ pC; 100 Hz; beam loss: 1.65 W)
- switchyard (ejection ATHOS, $E_e=3.0$ GeV, $Q_{\text{loss}}=5$ pC; 100 Hz; beam loss: 1.3 W)
- Collimator Transfer Line ($E_e=4$ GeV; $Q_{\text{loss}}=50$ pC; 100 Hz; beam loss: 20 W)
- Collimator Linac 3 ($E_e=6.88$ GeV; $Q_{\text{loss}}=50$ pC; 100 Hz; beam loss: 36.9 W)
- Collimator ARAMIS ($E_e=6.88$ GeV; $Q_{\text{loss}}=5$ pC; 100Hz; beam loss: 3.5 W)
- hypothetical beam loss at Collimator Linac 3 ($E_e=6.88$ GeV with $Q_{\text{loss}}=100$ pC; 100 Hz; beam loss: 70 W).

Table 6.2.1.3: Ambient dose equivalent (ade) rate in $\mu\text{Sv/h}$ at specified loss points. In red, are the positions requiring local shielding.

Position	$dH \cdot 10 / dt$	Area Type / Location Description
BC1_A	0.3	POSITION A: Above beam tunnel in technical gallery technical gallery, zone type 0: area type V, ademax: 10 $\mu\text{Sv/h}$ within area type W, gallery, temporary workplace, ademax: 25 $\mu\text{Sv/h}$ generally W: abidance is restricted, by direction of authorized body according to operation regulation
BC2_A	3.4	
Switchyard_A	2.7	
Coil-ATHOS_A	41	
Coil-ARAMIS_A	7.2	
Coil-LINAC3_A	3.7	
Coil-LINAC3_A	7.3	POSITION B: Above technical gallery in public zone outside works premises, public access, non permanent stay, ademax: 0.125 $\mu\text{Sv/h}$ Local shielding is required near the collimators
BC1_B	< 1E-2	
BC2_B	3E-2	
Switch yard_B	2.6E-2	
Coil-ATHOS_B	0.4	
Coil-ARAMIS_B	7E-2	
Coil-LINAC3_B	7E-2	POSITION C: West side of the building inside fence. outside building inside works premises, non permanent stay, ademax: 0.6 $\mu\text{Sv/h}$ Local Shielding might be required near compressors and switch yard dipoles
Coil-LINAC3_B	0.14	
BC1_C	1.4	
BC2_C	8.1	
Switch yard_C	6.4	
Coil-ATHOS_C	6.3	
Coil-ARAMIS_C	< 1E-2	
Coil-LINAC3_C	< 1E-2	
Coil-LINAC3_C	< 1E-2	

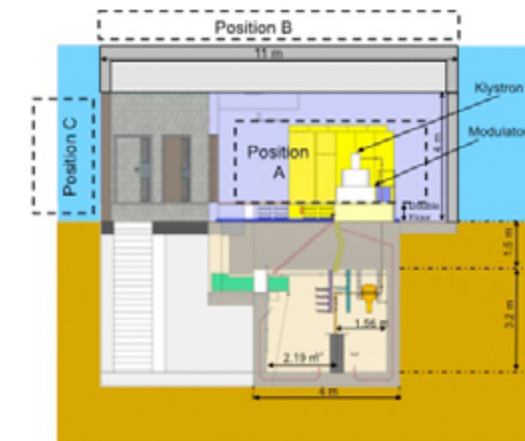


Fig. 6.2.1.1: Transverse positions around the building where the equivalent dose rate has been estimated. Those positions are marked A (gallery), B (top) and C (west side). The east side of the building is actually covered by soil and thus not accessible.

Since the outside of the buildings is, in the current design phase, not declared as a radioactive controlled zone, the legal limits for non-permanent stay is 0.6 $\mu\text{Sv/h}$

(even 0.125 $\mu\text{Sv/h}$ for the roof which is public access). Positions B and C (Figure 6.2.1.1) show dose rate estimates above the legal limit so that local shielding around loss position has to be considered (if dark current assumption is confirmed). For position B, the dose rate is 3 times higher than the legal limit at ATHOS collimator, so that local shielding has to be added. For position C, the legal limit is exceeded by a factor of 10 (at BC2 for example), leading to the same conclusion as for position B. Position A, which is in the infrastructure gallery can fulfil legislation if the area is declared as a radioactive controlled zone. For the public area outside the security fence, the dose should not exceed the legal limit of 0.125 $\mu\text{Sv/h}$. This is the case above the undulator hall and with 1 m of earth coverage, up to 5 W of local beam loss in UH could be tolerated (Fig. 6.2.1.2).

The estimation of dark current levels is crucial to obtain realistic dose rate. Measurements of those levels in SwissFEL Injector Test Facility will help to refine those estimations.

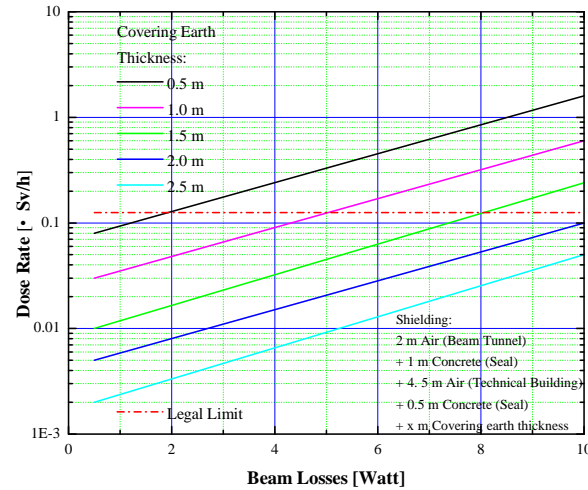


Fig. 6.2.1.2: Dose rate on the top (outside) of the SwissFEL Utility Tunnel as a function of beam losses and thickness of the earth covering the building.

6.2.1.5 Gas bremsstrahlung

High energy electron accelerator facilities like SwissFEL generate energetic gas bremsstrahlung (GB) photons by the interaction of the beam with residual gas molecules inside the beam pipe. The GB is strongly forward peaked so that it accumulates along straight sections of the beam pipe. On the other hand, any curves or chicane in the vacuum chamber is an efficient attenuation of the “0-angle” GB cone. Such chicanes in the vacuum chamber are present for example at bunch compressors BC1 and BC2, collimators where a transversal displacement of about 1 m is realized. Actually the GB will first be scattered on the beam pipe wall at the first pipe curvature, thereby generating an electromagnetic cascade and further multiple scattering effects in the magnet yoke.

The undulator sections of ATHOS and ARAMIS are the most important GB source for the subsequent experimental areas. Indeed the vacuum chamber follows a long straight line until the first optical X-ray mirror. This means an accumulation of GB over more than 120 m for ARAMIS with a divergence of 0.07 mrad at $E=6.88$ GeV.

In order to get an estimate of the GB generated dose rate, semi-empirical equations are useful. Assuming 60 m of GB accumulation in ARAMIS (10^{-7} mbar) and 60 m drift in the Front End section, it should result in a dose rate of 30 $\mu\text{Sv/h}$ in front of the Experimental Hall (EH) shielding wall. Because of the GB divergence (15 mm diameter after 120 m), a good part of the GB

should be scattered by the beam pipe (beam pipe diameter is only 8 mm) before the EH.

Nevertheless to attenuate 30 $\mu\text{Sv/h}$ to a legal value of 1 $\mu\text{Sv/h}$ in the EH, a shielding of 65 cm of normal concrete (or 7 cm of lead) would be sufficient. Since the first X-ray mirror is followed by a 2 m thick concrete wall, the GB will stay contained within the tunnel walls. Such shielding element should also be placed after each experimental vacuum chamber of ARAMIS beamlines.

In fact, the GB cone will be scattered on the walls of the beam pipe at shorter distances as assumed for the GB calculations, generating also high energy, forward directed neutrons and muons. The attenuation length for high energy neutrons (HEN) is about 51.1 cm in concrete and 17.6 cm in lead respectively. Assuming the 25 $\mu\text{Sv/h}$ would be generated by the HEN, 1.65 m of concrete or 57 cm of lead would be required. Regarding the muons energy loss rate, a value of 29 GeV/m for lead and 7.8 GeV/m can be assumed. The resulting attenuation mean free paths for 6.88 GeV muons are 0.88 m and 0.23 m for concrete and lead respectively. Furthermore remembering the strongly reduced muons production cross section compared to that for the pair-production, the muons generated dose rate contribution is not of concern in case of GB for the given situation.

In order to get in-depth information of the local situation and better accuracy, Monte Carlo codes such as FLUKA or EGS5 have to be used.

6.2.1.6 Dose rate estimates at special locations

Emergency exits:

The beam tunnel is equipped with emergency exits approximately every 100 m. Each exit consists in a staircase on the side of the tunnel. Those staircases do not have a roof shielding of 1.5 m thickness and thus can present a potential weakening in the overall shielding.

Calculation of the potential dose rate leaking in the top floor of the stair case (FEL-FU96-009-2) showed a maximum dose rate of 1.9 $\mu\text{Sv}/(\text{h}\cdot\text{Watt})$. Considering the beam losses presented in Table 6.2.1.3, only the Athos Collimator loss point (20 W) might exceed the PSI limit of 25 $\mu\text{Sv/h}$. However the longitudinal distance from Athos Collimator to the escape stairs has not been taken into account and should further reduce the dose rate.

Lift:

The lift well also represents a weakening in the roof shielding of the beam tunnel. An ambient equivalent dose rate of 2.6 $\mu\text{Sv/h}$ at the ground floor of the lift entrance has been calculated (FEL-FU96-011) for a lost power of 1.3 W at the switchyard. This is below the limit of 25 $\mu\text{Sv/h}$ for galleries, areaways and temporary workplaces in controlled areas.

Dose Rate Limit for Electronics before damage:

Devices with sensitive electronics, like for example electronic sensors (CCD cameras), will be positioned all along the SwissFEL beamline. At the location where one can expect electron beam losses (BC1, BC2, ATHOS collimator, etc.) those electronic devices will be irradiated by high energetic photons and neutrons. This causes damages which with time might destroy the electronic device. The easiest solution is to shield locally the sensitive electronics close to beam loss points. Maximum acceptable doses depend on the type of electronic device and it is thus difficult to have an absolute tolerance limit. Tests on a cell phone, showed that it can still work properly after an accumulated dose of 3 Sv of photons and 66 Sv of neutrons (FEL-FU96-014-2).

For comparison at SwissFEL, radiation dose rates near BC2 for example (where profile monitor electronics will be installed) are expected to be in the order of about 14 mSv/h for photons, respectively about 20 mSv/h for the GRN at 140° with respect to the beam direction and a distance of 1 m with respect to the beam loss point. Irradiation test results so far published in the last years indicate an onset for electronic radiation damage around 10 Sv in case of γ -radiation and of 4.2 Sv for n-radiation (2 MeV) respectively. Thus a safe limit of ambient equivalent dose rate limit of about 100 $\mu\text{Sv/h}$ (sum of $n + \gamma$) can be introduced assuming a 15 year operation time at 8000 h/y.

A shielding sandwich consisting of 7.5 cm of lead and 30 cm of polyethylene (distance 2 m from a loss point of 2 W) results in dose rates of about 30 $\mu\text{Sv/h}$ and 3 $\mu\text{Sv/h}$ for the photons and the GRN, for example.

Demagnetization of undulator permanent magnets due to fast neutrons is another possible concern, preliminary measurements at the SLS – PSI, showed that undulators installed at SLS (and which do not suffer from demagnetization) see a dose of 2.5 mSv/h. A safe limit for SwissFEL undulators is then set to 1 mSv/h.

More tests are required to estimate the exact tolerance limit of specific electronic devices, however one can state that local shielding together with longer distance would reduce significantly the risk of damages.

6.2.1.7 Beam stopping devices

It is planned to install five types of stopping devices suitable for the beam properties summarized in table 6.2.1.4 (see also [123]). The beam dump near the gun has a negligible radiological impact on the environment and is therewith not included in Table 6.2.1.4. The remaining devices can be distinguished in permanent (beam dumps) and temporary (beam stopper) operating devices and are designed to achieve dose rates inside the accelerator tunnel and in the soil surrounding the device below 1 mSv/h. The dose rate of the area above the roof (which is accessible by the public) is however limited to 0.125 $\mu\text{Sv/h}$ (see table 6.2.1.1).

Table 6.2.1.4: Machine parameter constrains for the beam stopping devices.

	Injec-tor	Athos		Aramis	
Max. electron Energy [GeV]	0.355	3.8	3.8	7.0	7.0
Max. charge per RF pulse [pC]	250	800	250	800	250
Max. repetition rate [Hz]	10	100	10	100	10
Mode of operation	temporary	perma-nent	temporary	perma-nent	temporary

For the design of those stoppers, simulations have been carried out with the multi purpose Monte Carlo code FLUKA [122] using a realistic model of the device including the tunnel with surrounding walls. The dose rates were estimated in a distance of 30 cm to the nearest wall surface through folding the expected spectral neutron distribution averaged over a sphere with a diameter of 10 cm with the fluence-to-ambient-dose equivalent conversion factors $H^*(10)$ published by [124]. Since parameters like dimension, shielding material and placement in the tunnel of these devices are not finalized, only a preliminary version of the devices with the highest radiological impact meeting the dose rate constrains defined above are described.

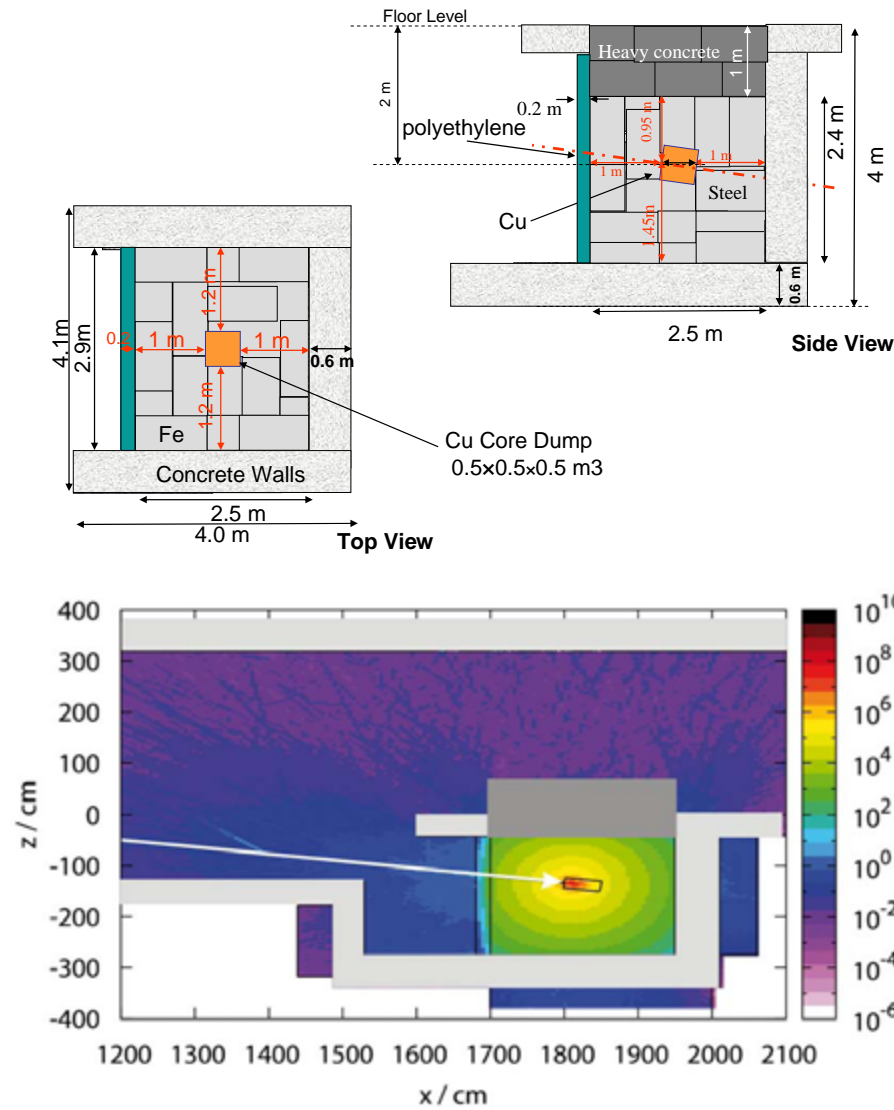


Fig. 6.2.1.7.1: Top: Aramis Beam Dump with copper core (orange) and additional shielding in steel (gray), heavy concrete (dark gray) and polyethylene (green). The device is surrounded by concrete walls of 60 cm thickness. Bottom: FLUKA simulation of the dose rate in mSv/h for a beam of 800 pC; 7 GeV; 100 Hz, 560 W. (Status September 2011)

Aramis beam dump

At the end of each undulator line, a permanent beam dump will be installed. The beam will be deflected vertically by 8 degrees (towards ground) and stopped in a copper block. To shield against secondarily produced radiation, the core block is surrounded by layers of iron and heavy concrete (figure 6.2.1.7.1). This results in the dose rates summarized in table 6.2.1.5.

Table 6.2.1.5: Maximum expected dose rates next to the beam dump in $\mu\text{Sv/h}$.

	Dose rate ($\mu\text{Sv/h}$)
Outside Tunnel	
Above the roof	0.05
Under	430
Lateral	375
Behind	512
Front	20
Inside Tunnel	31
Above the dump	1200
Front	

Aramis beam stopper

During machine tuning, damage to the undulators through a mis-aligned beam has to be prevented by deflecting the beam to a temporary beam stopper in front of the undulator section. Taking constructional aspects of the facility into account, the dimensions of the beam stopper with shielding are limited to a total length of 3 m, a total height of 3.2 m and a lateral width (measured from the beam line) of 1 m.

The core part consists of a copper cube with a length and width of 20 cm, surrounded by an additional layer of Tungsten (thickness 5 cm). This is followed by layers of iron, polyethylene and concrete (figure 6.2.1.7.2).

Irradiating the device with electrons (Beam power 17.5 W) results in the expected dose rate of 0.05 $\mu\text{Sv/h}$ above the roof and of 200 $\mu\text{Sv/h}$ lateral (inside tunnel) to the device.

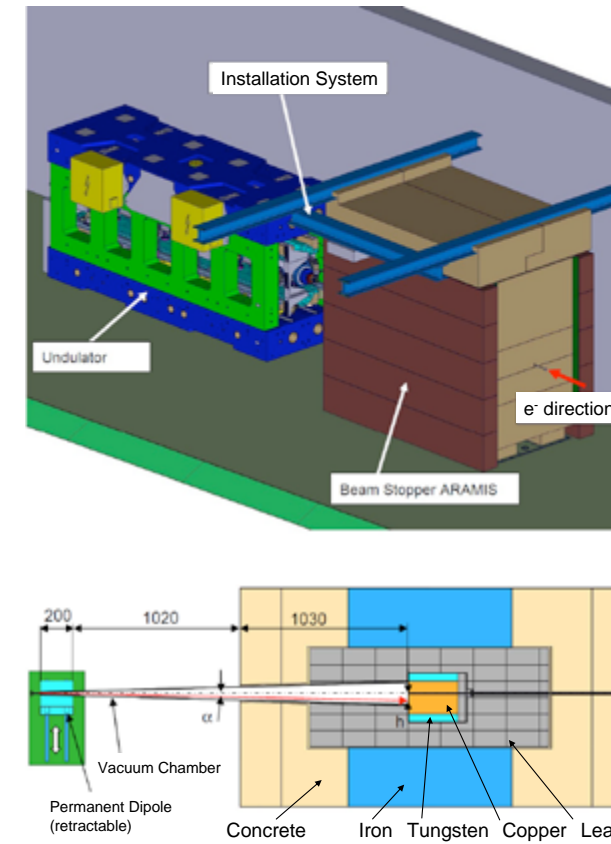


Fig. 6.2.1.7.2: Aramis Beam stopper in front of the first undulator (Top) A dipole magnet is inserted in the beam to deflect the electrons on a copper target surrounded by shielding materials (bottom).

6.2.2 Activation

6.2.2.1 Introduction on material activation with electron beam

Radioactivity is induced in components that are directly hit by an electron beam and in materials surrounding such beam loss points in the close vicinity. It is dependent on the electron energy, the beam power and the material composition. Components such as beam dumps, magnets and collimators absorb most of the bremsstrahlung and will therefore be the most activated. However, high-energy secondary particles can also activate surrounding materials and shielding. A prediction of the expected activation is important for the planning of radiation protection measures, for the estimation of radioactive waste production and for waste disposal. In addition, activation plays a role in the radiation damage of undulator magnets (de-magnetization).

When an electron strikes material, many bremsstrahlung photons are created in the electric field of the nuclei. Most of the highly energetic photons undergo pair production, i.e., a positron and an electron are created, which can in turn produce more bremsstrahlung photons. The spatial extent of this electromagnetic shower is much smaller than that of a hadronic shower produced, for example, by protons. The maximum number of particles is developed at a distance from the first impact of the electron which can be expressed as:

$$t_{\max} = X_0 \ln \frac{E}{E_c} - 0.5$$

In iron, for example, with a radiation length X_0 of 1.7 cm and a critical energy E_c of 22 MeV (above E_c , the emission of bremsstrahlung outweighs the ionization process), the shower maximum for a 6 GeV electron appears at about 9 cm depth. The shower dies out at about three times the shower maximum. The diameter of the shower is even smaller, for iron it is of the order of the radiation length. In this small volume most of the energy of the primary electron is deposited and radioactive isotopes are created by photonuclear reactions. Secondary particles produced in these interactions (mostly neutrons) also contribute to the activation. A small proportion of them has high energies and can thus initiate a hadronic cascade, thereby extending the activation region. The relevant photonuclear reactions are:

- The Giant Dipole Resonance (GDR) interactions ((γ, n) -reactions) between threshold (5–10 MeV) and about 30 MeV: GDR interactions produce neutrons with a Maxwellian energy spectrum ($0.5 \text{ MeV} < \text{kinetic energy} < 1.5 \text{ MeV}$) and an isotropic distribution. These neutrons can in turn interact with nuclei and contribute to induced radioactivity. Their mean attenuation path is of the order of 10 cm in concrete, so that the activity induced by them is roughly contained in the same region as that due to the primary photons. While the neutron fluence is much lower than for photons, their cross-sections are larger, so that they also contribute substantially to the activation.
- The quasi-deuteron effect takes place at energies between 30 and a few hundred MeV. In this process a photon is absorbed by a proton-neutron pair in the nucleus, with the possible subsequent emission of a neutron. The cross-section is small compared to the GDR interaction and thus contributes less to the direct activation. However, the neutrons produced have higher energies (depending on the photon energy) and their activating effect can extend over a wider region of space.

c) Photoproduction of pions: at energies between 200 MeV and a few GeV (nucleon resonances), pion production sets in. Most of the pions are produced in the first resonance (ρ -resonance), whose maximum lies at 300 MeV. The cross-section is of the order of one half of the GDR. But, since photons in the high-energy range are much fewer, the contribution to total activation is comparably small – it may dominate, however, in thin targets, where the electromagnetic shower is not fully developed. Some of the secondary pions and neutrons can have sufficient energy to initiate a hadronic cascade which extends well beyond the GDR activation region.

Direct GDR activation can only lead to a small number of different radioactive nuclides, since only a few nucleons are removed in the interaction. Activation induced by higher-energy photons or secondary particles can yield practically all radioactive nuclides with lower mass number, through spallation or evaporation reactions. While the flux of thermal neutrons is generally small, they can produce large activities in nuclides with very high capture cross-sections, which may be present only as impurities. Because neutrons extend far beyond the region of the electromagnetic shower, the activation is spread over a larger region. With increasing energy of the electron beam, more high-energy neutrons are produced, which are strongly forward peaked. Since the cross-section for inelastic processes of neutrons is almost constant above 200 MeV, their interaction length no longer increases above that energy; for example, the attenuation length for neutrons above 200 MeV in concrete is about 50 cm.

In general, the total induced radioactivity at electron accelerators is less than at proton accelerators of comparable beam power, by typically two orders of magnitude. The number of neutrons and pions produced is, to a good approximation, proportional to the energy of the primary electrons. This can be used as a rough estimate if one compares with the calculations performed for the SwissFEL Injector Test Facility. For a detailed prediction of the induced radioactivity, it is necessary to use Monte Carlo transport codes with photonuclear capabilities and the possibility to score residual nuclei. At PSI, three codes are available for this purpose, each with specific advantages and disadvantages: FLUKA, MCNPX (coupled to a buildup/decay code) and MARS. They will all be evaluated for their suitability and benchmarked against each other.

In the following three paragraphs, a preliminary study of the ground, air and beam dump activation is presented.

6.2.2.2 Estimations of materials activation at SwissFEL facility

a. Activation of soil

Bremsstrahlung, the major part of the electromagnetic emission, is mainly emitted in the forward direction and will thus preferably be absorbed by beam guiding elements such as magnets, slits or similar. The characteristic of emission is isotropic in the lateral direction, where, in general, massive concrete shielding walls are positioned. Nevertheless, high-energy neutrons may be able to survive this barrier and activate the neighboring soil layer. The produced isotopes may diffuse to the ground water due to washout.

The base plate of the SwissFEL building complex has to be well dimensioned, to ensure that there are no operation-correlated soil activations measurable above the StSV exemption levels, expressed in units of LE after decommissioning. One LE is the legal limit for one type of isotope.

In the framework of the SINQ approval procedure, extensive bores have been performed in the region of the former SIN, down to the Jura rock (a depth of 25 m). The subsoil of the western side of the Aare river is known to consist of a homogeneous distributed layer of brash down to the ground water level, at a depth of about 20 m, and conditions on the eastern side of the river are assumed to be the same. The mixture of flint and coarse gravel that is embedded in alternating sparse to fatly sand layers can be compared to normal concrete, with respect to its chemical composition.

In order to estimate the degree of soil activation around the SwissFEL beam tunnel, the following assumptions have been made:

- tunnel ground plate and wall thicknesses of 40 cm
- the soil composition described above
- 30 years of operation of SwissFEL (see beam loss assumptions above)

It is well known that the activation tends to go into saturation depending on the decay constant of the isotope considered and the overall irradiation time. With respect to the SwissFEL facility a useful lifespan of

30×8000 h is assumed. The aim is to estimate the maximum allowed beamloss in order to fulfill the limit given by the equation $\text{total-LE} = \sum(\text{nuclide-activity}) / \sum(\text{nuclide-LE})$, where total-LE must not exceed 1. The evaluation is based on an initial electron energy of 7 GeV, whereas iron is assumed to be the target material. Table 6.2.2.1 summarized of the results in terms of maximum allowed electron loss power (at 7 GeV) and the corresponding neutron fluency rates (condition total-LE \leq 1). The appertaining specific activation in the soil is about 6.8 Bq/g.

Table 6.2.2.1: Maximum allowed electron beam loss power and corresponding critical fluency rates of the middle energy neutrons (MID)- respectively high energy neutrons (HEN) at a distance of 1 m from the loss point.

Loss	MID	HEN
[W]	[cm ² s ⁻¹]	
1.9	1.5E+4	2.3E+3

Also of interest are the corresponding neutron fluency correlated ambient dose equivalent rates in the first soil layer after the shielding. The ambient equivalent dose rates, resulting from the neutron fluency of table 6.2.2.1 are **33 mSv/h and 2.4 mSv/h for the MID and for the HEN respectively**. Such dose rates will not be able to generate earth activation above LE.

In fact, assuming a beam line height at 1.2 m above the floor and a basement thickness of 0.4 m, a permanent local loss of about 25 W would be needed to get a soil activation above 1 LE. Large beam loss can only happen as isolated events, which would immediately trigger the MPS (machine protection system).

b. Contamination of ground water

Contamination of groundwater may occur due to:

- direct activation of the groundwater
- migration of soil activity through the soil layer

In general is the direct water activation mainly guided by spallation processes in oxygen leading to β^+ emitters like ¹¹C, ¹³N or ¹⁵O, having rather short lifetimes compared to the also produced ³H. The height level of the groundwater level is about 325 m above sea level, whereas the height level of the baseplate bottom side is about 340 m, giving a distance of 15 m to the ground water level. The radiation attenuation length of soil ($\rho = 1.6$ g/cm³) is about 56.3 cm for high energy neutrons > 100 MeV. Thus the resulting attenuation factor of the

soil layer is in the order of 10^{12} . Therefore the produced ³H concentration will be negligible compared to radiation protection relevant values.

The activity transport is connected to a liquid phase. Independently from the strong attenuation, such a condition can be neglected during operation of the facility. The building itself will prevent the migration of rain under the basement. Only after the deconstruction of the facility such a migration can be thought about theoretically. Anyway the existing ground water streaming volume of about 10^5 m³/day would result in an enormous dilution. Ground water activation is not a question at all if the limit value of the high energy neutron fluency is respected.

c. Activation of air

In the range of electron accelerators, air activation is mainly induced by photo-activation (γ, n) due to bremsstrahlung, generated during the interaction of electrons with air nuclei above a production threshold of about 10.6 MeV.

An other source for air activation are spallation reactions like ¹⁴N(n,2n)¹³N, ¹⁶O(n,2n)¹⁵O or ¹⁴N(n,3H)¹²C and ¹⁶O(n,3H)¹⁴N for the production of ³H due to HEN.

Above a threshold energy of 4 MeV for heavy targets and about 12 MeV for the light ones, Giant Resonant Neutrons (GRN) are generated due to photon interaction with the core of the nucleus. The energy spectrum follows a Maxwellian distribution with a mean energy around 2 MeV followed by a strongly decreasing tail up to about 20 MeV. The GRN may be interacting with the internal surface of the accelerator concrete wall, thereby generating thermal neutrons that may be backscattered into the accelerator bunker. The thermal neutron fluency rate ϕ_{th} is proportional to the yield of GRN and the inverse of the internal surface. The capture of thermal neutrons is leading to ⁴¹Ar.

Concerning the exposure of the environment the most important isotopes are ³H, ⁷Be, ¹¹C, ¹³N, ¹⁵O and ⁴¹Ar. With the exception of ³H and ⁴¹Ar the halftimes of the isotopes considered are short compared to the normal operation periods.

The SwissFEL air conditioning system operates such, that fresh air (T stabilized) enters the beam line tunnel at the downstream end of the undulator hall (UH) building. It flows then in the opposite direction than the electron beam: from the undulator hall to the injector

part of the tunnel. The air is finally sucked by an outlet channel near the gun and ejected in the atmosphere after being diluted with fresh air. There is then a slow flow rate of the fresh air along the tunnel of about 8000 m³/h (or 0.1 m/s), therefore the passage time of an unit volume through the whole accelerator and undulator tunnel is about 92 min. In addition to this longitudinal air flow, there are 17 transversal air circulation flows (but not with fresh air) where air is sucked at one point and then heated or cooled and re-injected in the tunnel. This system allows a separation between the accelerator and the undulator region with a fire protection wall, located at the position $z = 264$ m, between L2 and L3. Table 6.2.2.2 summarizes the resulting isotope specific and air flow rate dependent air activity concentration and total emitted activity per week, based on the losses given in table 6.2.1.3.

Table 6.2.2.2: Isotope specific and air flow rate dependent air activity concentration and total emitted activity per week.

Isotope:	8000 m ³ /h		
	CA	Bq/m ³	Bq/w
H3	1.73E-07	3.46E-02	4.64E+04
Be7	2.15E-05	2.15E+00	2.89E+06
C11	1.30E-02	9.13E+02	1.23E+09
N13	4.39E-01	3.07E+04	4.13E+10
O15	3.19E-03	2.23E+02	3.00E+08
N16	< 1E-9	–	–
Cl38	1.59E-03	6.37E+01	8.56E+07
Cl39	2.08E-03	4.16E+02	5.59E+08
Ar41	3.68E-04	1.84E+01	2.48E+07

The limitations for the controlled emission of radioactivity (by the air- and water path) as well as the surveillance of radioactivity and direct radiation in the PSI-environment are defined in the “REGLEMENT” BAG 5.07.01-4, HSK 2/370 Rev.1 (2007). The resulting source related dose guideline values are: 0.2 mSv per event or week (short time emission) for each individual balanced emission point (stack) and 0.15 mSv per year (long time emission) for the PSI as a whole. In order to proof compliance the emissions have to be balanced and the isotope specific emitted activities have to be converted to dose. It is distinguished between short time “UDAK-“ and long time “UDAL-“ conversion coefficients.

To get an estimate of the emission related dose the UDAK-values for the SwissFEL operation relevant iso-

topes (see table 6.2.2.2) the emission in a cylinder shaped air section has been calculated. For the 8000 m³/h case with the following cylinder parameters: height = 2 m, diameter = 0.52 m, air exhaust speed = 10 m/s. The resulting UDAK values and the dose for the given activities are presented in table 6.2.2.3. Compared to the short time limit, an utilization of 0.42 % and 0.09 % can be calculated for the two 8000 m³/h cases.

Table 6.2.2.3: calculated environmental dose for the two different air flow rates considered.

Isotope	Saturation activity [Bq/Watt]	LE* [Bq/l]
O-15	330E+6	4E+5
O-14	3.7E+6	4E+5
N-13	3.7E+6	4E+5
C-11	15E+6	4E+5
C-10	3.7E+6	4E+5
Be-7	1.5E+6	4E+5
H-3	7.4E+6	6E+5

*C-11 is used to represent β^+ -emitters, activity in solution are normalized to a mass of 1 kg.

Hence, beside the build-up inside the beam line components, the recirculation causes a decay of the activity inside the coolant fluid, such that the overall activity averaged over the volume is reduced. In reality, the irradiation does not occur simultaneously, as the cooling of any specific component is controlled by volume over bypasses. Table 6.2.2.5 gives a listing of the calculated isotope specific activity after an operation time of 15 years in terms of the exemption level LE and also the resulting specific activation after an additional cooling time of $t_{dec} = 10$ min.

Table 6.2.2.5: isotope specific activation with respect to LE after $t_{irr} = 15$ years of operation and an additional decay time $t_{dec} = 15$ min.

Isotope	Specific activity after t_{irr} [LE]	Specific activity after $t_{irr} + t_{dec}$ [LE]
¹⁵ O	0.1	3.2E-3
¹⁴ O	1.4E-3	3.9E-6
¹³ N	7.1E-4	3.5E-4
¹¹ C	2.7E-3	1.9E-3
¹⁰ C	3.3E-3	–
⁷ Be	2.6E-4	2.6E-4
³ H	4.7E-4	4.7E-4
sum	0.101	6.2E-3

About 90 % of the accumulated activity is contributed by the short-lived 15O isotope ($T_{1/2} = 2.03$ min). Therefore, the activity decays within 10 min after operation to less than 10 % of the saturation level. Isotopes such as ⁷Be (induced by spallation) or activated metals (due to abrasion of the inner cooling pipes) are efficiently absorbed in ion-exchangers. According to current knowledge of the cooling system design and the values shown in table 6.2.2.5, it is not necessary to implement an active monitoring of cooling circuit. Coolant measurements points are foreseen in the design of the cooling circuits.

e. Activation of the beam dump and beam stopper

According to the SwissFEL operation modes, the full electron beam will be dumped in two beam dumps. During the beam tuning a smaller fraction of the beam is stopped in the beam stopper to protect the undulator magnets. There will be also one stopper for each beam line. To have a conservative estimate of the residual activation the beam energy was set to 7 GeV and beam power to 560 W for the beam dump and 14 W for the beam stopper (Aramis line case). Like at SLS a 30 % downtime of the facility is assumed, which is used as the downtime for the beam dump. Since the beam stopper is only needed for tune-up, 90 % downtime is estimated. Of course, in the commissioning phase the beam stopper will be used more heavily, but since the residual activation is accumulated over the whole operation time of 45 years, the effect will be averaged out.

The calculation of the residual dose rates were done with FLUKA using a preliminary design of a beam dump and a beam stopper. The layout used for the beam dump consisted of a cylindrical carbon core surrounded by iron. The outer layer consists of normal concrete. In the very front a small layer of PE suppresses low energetic neu-

trons to protect electronic devices for diagnostics. As one can see from Figure 6.2.2.6 the dose rates after 1 day on the outer sides of the beam dump are of the order of a few μ Sv/h and therefore acceptable for a controlled zone. On the right side of Figure 6.2.2.6 a study of the residual dose rate after 1 h on the beam stopper is shown. The beam stopper has a core of 20 cm copper followed by 10 cm tungsten which can be moved in and out of the beam. It is surrounded by steel and finally normal concrete of about half a meter on each side. The residual dose rates are already low after 1 h of beam-off.

For the final design the nuclide inventory will be calculated for every material block to decide if it has to be disposed as radioactive waste after shutdown of the operation. There will be also considerations about the time to wait before dismantling the beam dump and beam stopper. The residual activation and resulting dose rates are moderate, as far as safety requirements during deconstruction are concerned.

6.2.3 Personal Security System (PSYS: PSA; LAC)

The aim of a Personal Security System (PSYS) is to ensure that no access to a specific area is possible when beam operation might occur, while disabling beam operation in the area when access is allowed. Differentiation is made between systems controlled remotely (“Personensicherheitsanlagen”, PSA) or locally (Local Access Control, LAC) on the basis of the risk associated with the maximum ambient dose rate caused by beam operation, i.e., the zone type as defined in the

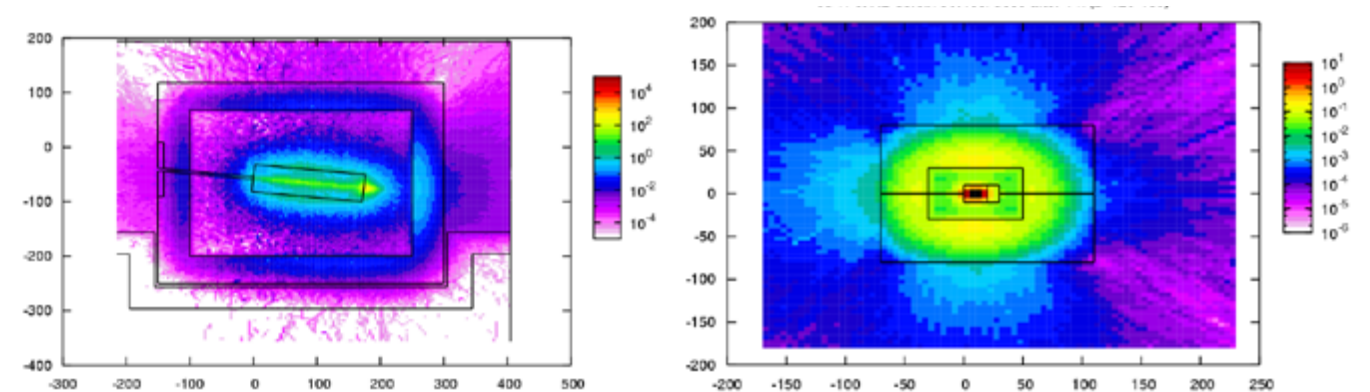


Fig. 6.2.2.6: Left: Residual dose rate in mSv/h for the beam dump at the height of the beam after 1 day cooling. Right: Residual dose rate in mSv/h on the beam stopper at the height of the beam after 1 h cooling.

ENSI directive HSK-R-07. For SwissFEL, a similar concept to that implemented at the Swiss Light Source (SLS) is foreseen: PSA-controlled access to the accelerator parts (zone types Y or Z) and LAC systems for accessing the beamline areas (zone Type W).

As a fundamental rule, the PSYS has priority over all other control or monitoring systems. Any mistake or alarm signal withdraws the beam-enabling signal to the beam components, resulting in an ALARM status. This status can only be changed when the cause has been identified and resolved.

6.2.3.1 Remote access control systems (PSA)

The access to the beam tunnel is controlled by the PSA systems. The accelerator side (without experimental halls) can be subdivided into three separate areas: from the accelerator up to BC2, Linac 2 to Linac 3, and the area with the undulators. Access to each area is controlled through a fully autonomous PSA, with its own power supply, specific hardware and logics. A specific control panel is installed in the control room, through which the operators on shift duty remotely control access to the areas.

Access to an area is disabled for as long as the ionizing beam, RF or laser beam supply to the area is not securely disabled. Signal-enabling beam operation is distributed to the safety components only when the area is in the LOCKED status. Safety components can include machine components such as the laser shutter, the RF-supply to the gun and the RF-supply to the linac, as well as beamline devices such as dipole magnets and beam shutters.

An appropriate dose-rate instrument is connected to the PSA system, and should the measured radiation signal exceed an alarm threshold, this system will prevent access to the affected area.

6.2.3.2 Local access control systems (LAC)

Access to optical and experimental areas of the beamlines is controlled locally by an LAC. Every beamline has its own, independent LAC system, taking into account the specificities of the respective optic and experimental

hutches. Access to each separate hutch is controlled through a fully autonomous LAC, with its own power supply, specific hardware and logics. A control panel is installed locally and operated by the user.

The LAC system prevents access to an area for as long as the beam transport to that area is not securely disabled. Signal-enabling beam operation is distributed to the safety components only when the optics or experimental hutches are in the LOCKED status.

Operation of any LAC is independent of the SwissFEL accelerator status. Alarm signals from an LAC are not forwarded, except with a failure signal from a beam shutter, resulting eventually in the withdrawal of the beam-enabling signal to the accelerator components.

6.2.4 General safety

Introduction

Concerning industrial safety and health protection of staff, the Swiss Labour Law (Arbeitsgesetz) and all pertinent regulations will be followed.

At PSI, responsibility and training concerning industrial safety are regulated in the so-called “SGU instructions” (AW-01-07-02). These regulations also hold for the entire SwissFEL project.

According to the Swiss accident statistics, the highest risk for injuries has to be expected during the time limited forest clearing and construction work periods for SwissFEL. However, the corresponding considerations and measures are beyond the scope of this chapter, which focuses on general safety aspects during operation of the SwissFEL facility.

Regarding general safety it is important to note that following the construction period no permanent working places will be located directly within the SwissFEL facility. The beam will be controlled by the crew already available in PSI’s main accelerator control room in the WBGB building (PSI Western area). Access to the beam tunnel will only be necessary for maintenance and repair work; the same holds for the technical buildings. In the experimental hall and its areas, mainly scientific guests will occupy a small amount of non-permanent working places.

Facility protection

Since SwissFEL will be located outside of PSI’s fenced areas, a door control system including a video surveillance system will be installed.

Ground water protection

For cooling purposes, various power transformers and the modulators of the SwissFEL accelerator have to be filled with isolating oil. For modulator oil refreshment and replacement, a tank room will be necessary. In total, approximately 50 m³ of insulating oil will be always on site. With its flash point of about 144 °C, the flammability of the oil is a minor issue.

However, in order to prevent the environment from the consequences of a potential oil leakage, several constructional and technical measures are planned, e.g.

- transformers and modulators will be placed within an adequate tray,
- the tank room will be equipped with sump and leak detector,
- a so-called SPS system will permanently survey the filling status and ongoing filling processes,
- all valves will be automatically closed in case of missing electricity.

Escape routes

In the technical buildings and in the experimental hall, the width and length of the escape routes will follow Swiss regulations, i.e., normally 1.2 m width and 35 m length if two different escape routes are available from any point in a room. A special situation is given by the beam tunnel, where no general rule is available. Here, the length of the escape routes will be of the order of 100 m–150 m. This length is acceptable since no permanent working places will be located in these areas, where the fire load will anyway be minimized.

Emergency light

SwissFEL will be equipped with an emergency light system, which allows a safe leaving of the facility in case of electrical power outage.

Moving equipment

SwissFEL will be equipped with different types of moving equipment, e.g. the bunch compressors which will be positioned in the beam line of the accelerator. Their moving mass reaches several tons which induces the risk of serious injury. Therefore several measures will be taken in order to reduce such risks, such as

- a speed limitation of these movements,
- an appropriate signalization of the moving equipment and its movement ranges,
- the installation of emergency switches.

Laser safety

For the operation of SwissFEL several Laser systems have to be used. These Lasers will be classified as class 4 Lasers. This means, that their Laser light is very dangerous for the eye and also dangerous for the skin. Such intense Laser light is also an issue for fire safety.

The PSI directive for Laser handling [125] has to be strictly adhered to.

Gases

For SwissFEL, the use of several non-toxic gases (e.g., He, N₂, SF₆) is necessary for different purposes. Depending on the room size, the ventilation and the amounts to be used, certain rooms have to be equipped with oxygen detectors for safety reasons.

6.2.5 Fire safety

Regarding fire safety, the buildings and installations of SwissFEL will be equipped with full monitoring. The fire alarm system will correspond to the VKF guidelines, with control units placed at those entrances which are most relevant for the fire-brigade. Portable extinguishers, filled with the suitable fire extinguishing agent, will be placed in the necessary locations.

Fire compartments and protection distances will be provided in accordance with the VKF guidelines. Escape routes will be provided in accordance with the VKF guidelines and the “Verordnung 4 zum Arbeitsgesetz” (ArGV 4). Emergency vehicles can access the facility from the west side road all along the building. Hydrants will be positioned at suitable positions.

6.3 Supply installations (Status as of October 2011)

6.3.1 Electrical supply and consumption

The electrical distribution comes from PSI site and is distributed from the main divider situated in the Experimental hall to the different building. The middle voltage is converted to low voltage by transformers situated in the different technical building. There are two networks foreseen: one for the machine components and one for the infrastructure components. A similar network is foreseen to transfer data to/from PSI site.

Total electrical consumption is a key parameter for defining the required building infrastructure in terms of electrical supply as well as cooling capacity. Table 6.3.1 depicts the electrical consumption in the different SwissFEL buildings (see Figure 6.1.2 for building names

location). The table is based on 100 Hz operation repetition rate and shows an estimation of the nominal electrical consumption once Athos and Aramis line will be completed. In fact, most of the consumption is for the RF power plants and those power plants will be operated at about 80–90 % of their maximum.

The nominal electrical power consumption for Aramis and Athos lines is about 5.2 MW, of which 3.9 MW are used for beam accelerator components and 1.35 MW for infrastructure components (water pumps, air conditioning, etc). The power going to accelerator components (RF modulator; magnets; etc) is completely dissipated in heat losses (the average FEL light power is only about 100 mW). The main consumption is for the RF power plants units (up to 3.5 MW). Most of the heat (4.2 MW) is dissipated by direct water cooling (magnets or RF modulators) pumped in the ground. The water is then either re-direct to PSI site for heating up other buildings or discharged into the Aare river (Figure 6.3.1). The rest of the heat (1 MW) is dissipated in the air, mainly in the RF gallery and the infrastructure rooms.

Table 6.3.1: Estimation of the nominal Electrical power consumption of SwissFEL building for operation at 100 Hz (status october 2011).

Building name	Device	Nominal Electrical Power Consumption/item [kW]	Number of Devices	Nominal Electrical Power Consumption [kW]	Water cooled power [kW]	Air cooled Power [kW]
IN	RF Power Plants					
	RF Gun Modulator Unit	101	1	101	90.9	10.1
	S Band Modulators Units	120	4	480	432	48
	X Band Modulators Units	80.4	1	80.4	72.36	8.04
	Magnets Power Supplies					
	Dipole Power Supply (LH & BC1)	9	1	9	8.1	0.9
	Quadrupoles Power Supply	0.1	27	2.7	2.43	0.27
	Solenoid Power Supply	27	1	27	24.3	2.7
	BPM MBU Unit	0.3	12	3.6		3.6
	Control (VME, PC, motors, ...)	0.3	14	4.2		4.2
	Laser					
	Laser Diode Pumps	5	1	5	3	2
	VME, PCs, Displays	0.3	40	12		12

L1	RF Power Plants					
	C Band Modulators Units	103.8	9	934.2	840.78	93.42
	Magnets Power Supplies					
	Dipole Power Supply (BC2)	13	1	13	11.7	1.3
	Quadrupole QFD Power Supply	0.15	25	3.75		3.75
	Corrector Power Supply	0.1	28	2.8		2.8
L2	BPM MBU Unit	0.3	11	3.3		3.3
	Control (VME, PC, motors ...)	0.3	40	12		12
	RF Power Plants					
	C Band Modulators Units	103.8	4	415.2	373.68	41.52
	Magnets Power Supplies					
	Quadrupole Power Supply	0.15	16	2.4		2.4
L3	BPM MBU Unit	0.3	6	1.8		1.8
	Control (VME, PC, motors...)	0.3	40	12		12
	Stepper Motor Driver Rack	0.6	4	2.4		2.4
	RF Power Plants					
	C Band Modulators Units	103.8	13	1349.4	1214.46	134.94
	Magnets Power Supplies					
UH	Quadrupole Power Supply	0.15	20	3		3
	Seed Laser	5	1	5	3	2
	BPM MBU Unit	0.3	9	2.7		2.7
	Control (VME, PC, motors...)	0.3	40	12		12
	Undulator					
	Undulator Positioning Motors	0.3	24	7.2	0	7.2
	Magnets Power Supplies					
	Quadrupoles Aramis Line	18	1	18	9	9
	Quadrupole TL & Athos Line	0.15	67	10.05		10.05
	Dipoles Aramis Line (Coll., dump)	53	1	53	47.7	5.3
Dipole Athos Line (Echo, Collimators)	71	1	71	63.9	7.1	
EH	RF Power Plants	103.8	2	207.6	186.84	20.76
	BPM MBU Unit	0.3	41	12.3		12.3
	Control (VME, PC, ...)	0.3	8	2.4		2.4
	Front End Components	10	2	20	18	2
	Infrastructure/People/Reserve	1065	1	1065	500	565
Total				5266.4	4202.15	1064.25

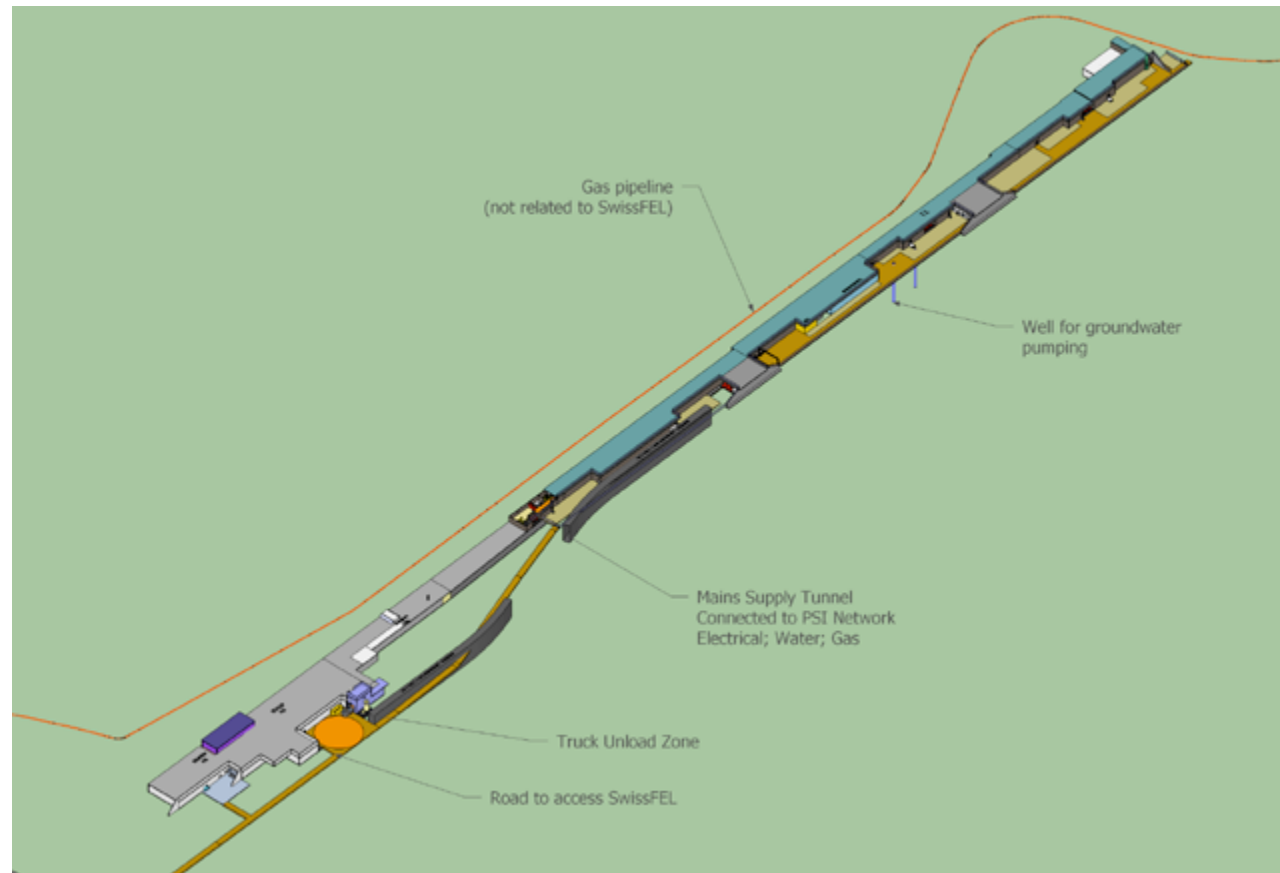


Fig. 6.3.1: SwissFEL building located near the eastern area of PSI. Ground water (25 m deep) is pumped and used for cooling the installation.

• High-Voltage installation

There are two 16 kV middle voltage connection to the existing PSI-East and PSI-West infrastructures. Those two middle-voltage lines will be provided to the SwissFEL location via a mains supply tunnel, underground, which follows the access road (see Fig. 6.3.1 – Mains Supply Tunnel). This tunnel (~3 m high and 3.8 m wide) will be connected to PSI site on one end and to SwissFEL middle voltage divider and related transformers on the other end. After the middle voltage divider, two separate networks will be installed. One network will supply the infrastructure while the other will feed the machine components.

By using the most up-to-date techniques at the intermediate voltage divider (segmented separation) and transformers (fully isolated), the highest possible electrical availability will be provided.

• Main distribution

The main distribution is a modular design and is divided into infrastructure and machine. The concept is based on certificated MNS systems, Model 3b. Lines >100 A will have power switches, lines <100 A will have fuse

techniques or power protection switches. The installation is based on a TN-S grid system. Overall, the electrical distribution systems will be provided with excess voltage protection switches. The MNS systems are foreseen with the so-called insertion technique and devices can be changed under power. The large power switches will be controlled by a GLS system and an alarm system is foreseen in the case of a failure.

• Overall emergency power supply

It is not foreseen to install any grid back-up facilities, (no emergency diesel engines) or connection to the PSI emergency power supply. Local UPS installation will insure for a certain period power supply to critical components.

• Emergency lighting

The design follows the official regulations (VKF / GVA). All buildings, such as the experimental hall, injector building or utility buildings, will have stand-alone emergency lighting installations with individual batteries. All these lights are connected by a LAN system. In the case of an electrical network failure, this emergency system takes over the feeding of the emergency signs and

safety lighting for a specified time frame (generally 60 minutes). All building units, technical stations and the beam channel will have separate circuit installations with function-conserving FE180 cables and separated luminous sources. To provide minimum maintenance effort and energy consumption, these light sources will be LED-based.

• UPS facilities

For each building, an Uninterrupted Power Supply (UPS) system of 30 kVA is foreseen. In case of a power failure, these systems will be used to supply the safety units (controls, data storage), such as: GLS, UKV components, ZUKO and door surveillance, and video for 15 minutes maximum. The centralized facilities are foreseen to be located in separated rooms with the transformer stations.

• Development after the transformer units

Due to voltage loss or break down currents with long cables, the supply grid will be constructed as encapsulated energy lines. Their layout and dimensioning will be made according to the consumption needs and installation regulations. The installation will be placed in the infrastructure tunnel, which leads to the main distribution centre in each technical building.

• Earthing and lightning protection

All earthing and potential equalising installations will insure that voltage errors will not exceed 50 V and the noise current at 50 Hz should not exceed 50 mA. Steel reinforcement within the concrete foundation is defined as part of the potential equalising. In the region of the beam tunnel, every 10 m the core wires will be welded to each other, thereby creating a Faraday cage. From the foundation earthing point onwards, every 10 m earthing points will be made for the connection set V65. All electrical facilities will be connected to the earthing network. All metallic building structures and building services will be connected to each other and to the potential equalising by a link to the earthing system. For the connection of building services and operation facilities, a copper band 20x3 mm will be installed in parallel to the cable trays.

The lightning protection system follows the regulations of SEV 4022 and consists mainly of tin-coated copper conductor, 8 mm in diameter. The mesh size of the catching system will be 100 m² at its maximum. All natural and artificial conductors will be connected at their deepest level with the earthing system.

• Supplies to sub-distributions, cable trays and energy rails

The supplies to sub-distributions for the infrastructure and machine components come, in general, with FEO cables, starting from the main distribution units inside the building units. Large-consumption devices will be connected by encapsulated energy rails, to prevent voltage losses and to limit break-down currents. For the horizontal and vertical development, metallic and perforated cable trays will be used. These will be sorted according to voltage and high and low current. Within the beam tunnel and the utility tunnel, the multi-layer technique will be used for the cable trays. The same technique will also be used for the technical buildings, whenever possible.

• Supply to heating, air, cooling, sanitation

The electrical supply to the cooling station is carried via an earthed cable tray directly from the main transformer. In the cooling station, an electrical cabinet will distribute power to the different components, such as:

- Sensor and control devices (valves, levels, etc)
- Power devices (pumps, compressors, ...)
- Fire controllers

• Installation electrical plugs, CCE 63A

All electrical plugs will be compatible with UKV Plugs Type RJ45.

Such plugs are foreseen in every part of the building, as follow:

- every 15 m in the beam tunnel
- every 15 m in the beam tunnel ,CEE Plug 63 A
- every 30 m in the technical buildings
- every 15 m in gun building, experimental hall and cooling stations
- one plug in every air conditioning room.

• Illumination, lighting delivery

Illumination systems with reflectors and a large angle of diffusion will be hung in the cooling stations, air conditioning rooms, etc. In the beam tunnel and supply tunnel, lighting with high resistance will be installed. The surroundings outside the buildings (along the access path) will have, every 25 m, a lamp at a height of 1 metre. The illumination fluxes foreseen per building area are:

- 500 Lx in the experimental hall, gun building and cooling station
- 200 Lx in the beam tunnel
- 150 Lx in the supply tunnel

- **Phone and wireless hubs**

The wireless phone system will be connected to the PSI phone network, with 60 cover hubs distributed throughout the building. In the communication room (in the gun building), a main VS83 distributor for CU connection is foreseen.

- **Data transfer and communication**

Data transfer between SwissFEL and PSI will be ensured by monomode optic fibers. Between SwissFEL buildings, monomode and multimode optic fibers will be installed.

- **MSRL**

Connection to the MSRL distribution board is ensured by a bus structure, and can be transferred via the LAN to the intervention stations of PSI-East and PSI-West.

- **Interlock, video surveillance and door surveillance**

For each building, and at every entrance a video camera for facial recognition will be installed. In addition, a motorized dome camera for large-area surveillance will also be installed. Data are then transferred through the LAN network to the general surveillance centre at PSI-East. In the beam tunnel, a card reader at the entrance is foreseen. The beam tunnel doors are also connected to the general PSA system (see Section 4.2).

- **Fire detector system and emergency calling points**

A modular microprocessor-controlled fire-detector system is also foreseen. The installation of the fire detectors will follow the VKF and GVA rules. The main fire detector centre will be located in the experimental hall. This main fire detector will be connected by a communication interface to the GLS system. Connection to the PSI-East area is then ensured via a LAN. An emergency call and NFO system is integrated into the fire detection system.

- **Interim electrical supply during construction**

Interim low-power plugs will be available during the construction period. An interim lighting system for general illumination (not working illumination) is foreseen at special locations, such as the staircases, the tunnels, etc. Escape paths will be illuminated with emergency lights, as requested by the VKF regulations.

6.3.2 Heating, cooling, air conditioning and water supplies

6.3.2.1 Summary

The concept of the heating, cooling and air conditioning infrastructure is characterized by a combination of common, cost-effective techniques with low electrical consumption. The challenging requirements regarding temperature stability (± 0.1 K) inside the beam tunnel, as well as the large amount of heat dissipation, can be handled by a proven combination of direct cooling of the magnets, using ground water as sink and a simple forced-air cooling system over the whole tunnel length. The required air conditioning within the experimental hall is ensured by laminar air flow, generated by so-called displacement air outlets. The technical gallery above the beam tunnel will be similar to server rooms, conditioned by local forced-air cooling systems.

The chosen concept will be applied throughout the whole year, without additional cooling. The cooling comes from existing ground water right at the facility location. The variation of the ground water temperature is extremely small, which helps greatly in meeting the high requirements on temperature stability. In addition, it allows the use of simple cooling techniques, and it is at the same time very ecological and economical. Further temperature stabilizing measures typically needed in chiller systems are not necessary.

6.3.2.2 Heating / Cooling facilities

The ground water is pumped from the pump station near Linac 2 (see Figure 6.3.2.1) and will be distributed to several infrastructure rooms along the building. The maximum flux of water which is allowed to be pumped is 95 l/s. The groundwater has a maximum temperature of 15 °C and the maximum temperature of the water rejected to the Aare river is 30 °C.

Three cooling circuits are foreseen for all components between the gun and the last undulator:

- normal water cooling circuit 17/23 °C (In/Out temperature)
- demineralised water circuit 30/36 °C
- demineralised water circuit 60/80 °C

Those cooling circuit are installed in parallel along the entire building on the ceiling of the UH and infrastructure gallery. The experimental hall has an independent cooling circuit of demineralised water 20/26 °C.

The water pipes are attached to the ceiling thanks to supply trays (see Fig 6.1.4). This will allow easy connection to the machine sub-systems, as they are distributed in the infrastructure gallery along the trays. It is foreseen to have all necessary supplies on these trays, such as heating, cooling, special gas lines, electrical power and communication. This main process media distribution system will be connected at its northern end to the PSI infrastructure via the Mains Supply Tunnel (Fig. 6.3.2.1). Inside the beam tunnel, the mains trays will also run along the ceiling, just above the beam components. The trays will contain the following supplies:

- Cooling water in/out
- Pressurized air
- Nitrogen
- Exhaust gas from vacuum pumps.

At the switchyard, the supply tray is going one floor up from the UH ceiling to the infrastructure gallery ceiling. In general, for the water cooling the main water pipes will be connected to local distribution batteries (in the beam tunnel), to which the magnets (or other components) can be connected. The incoming flow will be controlled by irises included in the magnet connection screws. The flow will also be controllable at the distribution batteries.

Pressurized air connection points will be installed every 25 m along the beam tunnel. Nitrogen (N₂) and exhaust gas circuits will be installed in the experimental hall. There will be connection points for all the above-mentioned supply lines on the outer wall of the experimental hall.

The water cooling of SwissFEL components will dissipate 3900 kW which will be partially used for heating the SwissFEL site as well as the PSI site. The RF klystrons alone are already producing about 1700 kW which are converted in warm water at 80 °C. This warm water will

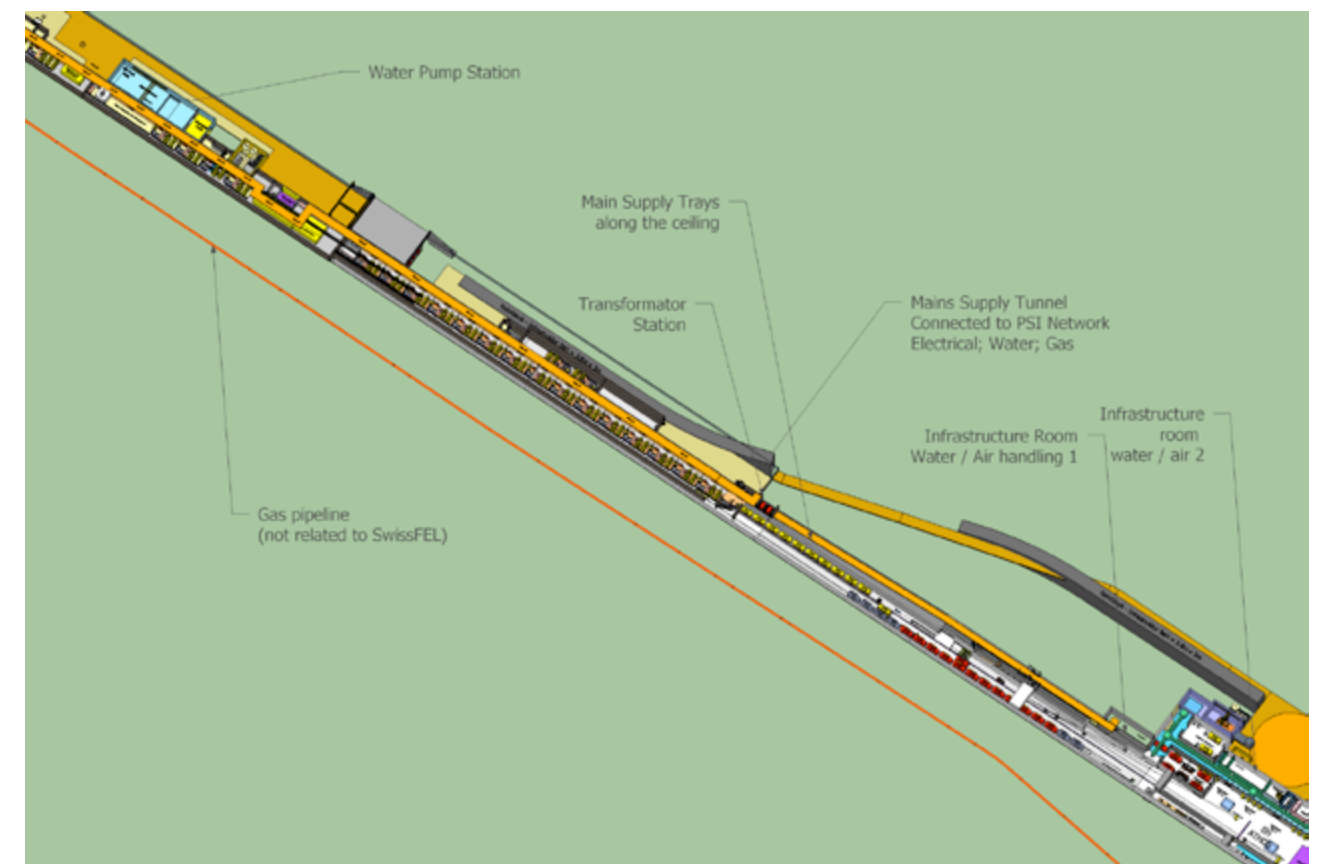


Fig. 6.3.2.1: Overview of the SwissFEL facility showing the different infrastructure buildings.

then be distributed to the local air conditioning units of SwissFEL. In addition, a connection to the Refuna heating network at PSI-East will be led over the mains trays to the Infrastructure room 1 and then to the Main Supply Tunnel (Figure 6.3.2.1). Fine stabilization of the air temperature will be ensured by the local air conditioning units (monoblocks).

6.3.2.3 Air conditioning units

Table 6.3.2.1 summarizes the requirements in terms of temperature and temperature stability. The stability of ± 0.1 K in the undulator hall, for example is insured over a length of 5 m and over 5 hours. The temperature of the undulator hall should never (also during shutdown) change by more than 2°C (ie. $24 \pm 1^\circ\text{C}$) or it could irreversibly affect the position of the magnets in the undulator. The operating temperature of the beam tunnel still needs some optimisation (between 26°C and 22°C , depending on the operating temperature of the RF accelerating structures, which is currently set to 40°C). A separate heating group is foreseen for heating the offices, restrooms and labs.

Table 6.3.2.1: Air Temperature requirements in SwissFEL.

Room	Temperature	Humidity
Beam Tunnel, Undulator Hall, Front End and X ray Switch Yard	$24^\circ\text{C} \pm 0.5$ K (absolute) and ± 0.1 K (over 5 hours)	30–65 %
Infrastructure Gallery and Rooms	$21\text{--}26^\circ\text{C} \pm 1$ K over 24 hours	25–65 %
Undulator Lab	$24^\circ\text{C} \pm 0.3$ K	30–60 %
Experimental Hall	$24^\circ\text{C} \pm 0.5$ K	30–60 %
Laser Rooms (Class 10000)	$24^\circ\text{C} \pm 0.2$ K	$50\% \pm 5\%$

The beam tunnel will be equipped with approximately 12 air circulation cooling units, to control the temperature within approximately $\Delta t = \pm 0.1$ K at a specific point in the tunnel. The temperature difference between different locations in the tunnel, however, will be higher. Each unit has a cooling capacity of about 12 kW and air exchange capacity of $6000\text{ m}^3/\text{h}$. They will all sit on vibration dumpers and are distributed inside the infrastructure gallery. Fresh air will be introduced near the undulator hall side of the tunnel and exhausted at the gun end. In the beam tunnel, air will circulate towards the gun with a speed of 0.1 m/s; the temperature of the tunnel can be measured (and recorded) every 10 m in the tunnel

and locally adjusted if necessary. The functional concept is similar to that which has been installed at the SLS.

The utility tunnel will be controlled within a temperature range of ± 2 K via air circulation cooling units. Each supply building will be equipped with an air handling system, to supply filtered fresh air.

The experimental halls will have two air conditioning units, each having a capacity of $20,000\text{ m}^3/\text{h}$ and a cooling capacity of 40 kW.

6.3.2.4 Sanitation facilities

Wet units

Standard wet units are planned at the injector building and in the experimental hall. At the technical buildings it is foreseen to install a cold and a warm water supply to each sink.

Cold water

Cold water will be taken from PSI-East and brought to SwissFEL through the new Mains Supply Tunnel which will follow the old “reactor road”.

Hot water

Hot water will be produced at each technical cooling station, and at the experimental hall, using a hydro extractor boiler which also includes a reservoir.

Fire-hose cabinet

Fire-hose cabinets will be installed in all buildings, connected to the cold water supply.

Wastewater

All waste water will be collected by a waste-water pipe which runs underground along the SwissFEL facility. Due to the length of the tunnel and the low downhill gradient, pumping stations will be installed every 150 m.

Surface water

The whole drainage of the roof areas will take place through on-site seepage.

Compressed air

Compressed air will be taken from the connection point at the PSI-East site and join the common tunnel supply along the old “Reactor road”. A pipe system will supply all technical buildings including the beam tunnel, with 2 connection points every 4 m in the beam Tunnel.

In the Undulator Hall a connection is foreseen every 20 m for the Air Cushion vehicle.

A ring main is foreseen within the experimental hall.

Nitrogen

A reservoir (25 m^3) for liquid nitrogen will be placed outside the experimental hall. In addition to that, a vaporizer with a pipe system is foreseen for providing the SwissFEL experimental hall (quality 5.0 and at -70°C), with connection points every 25 m.

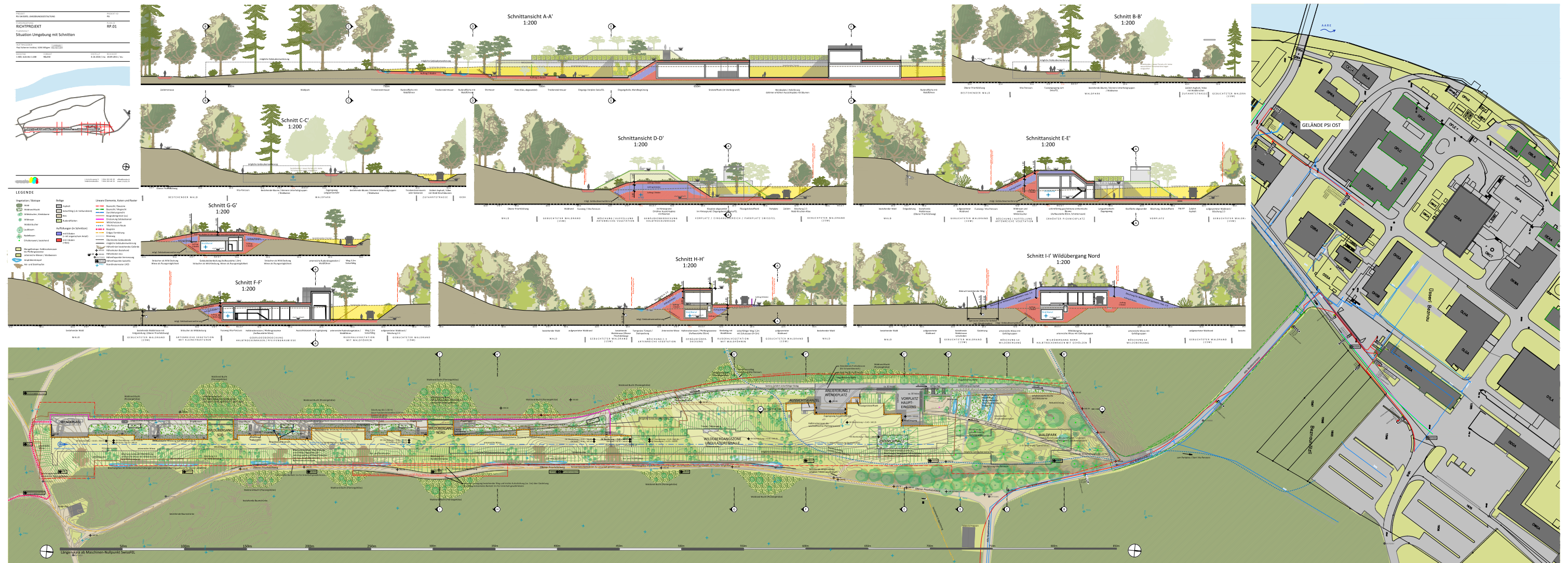
Helium recuperation system

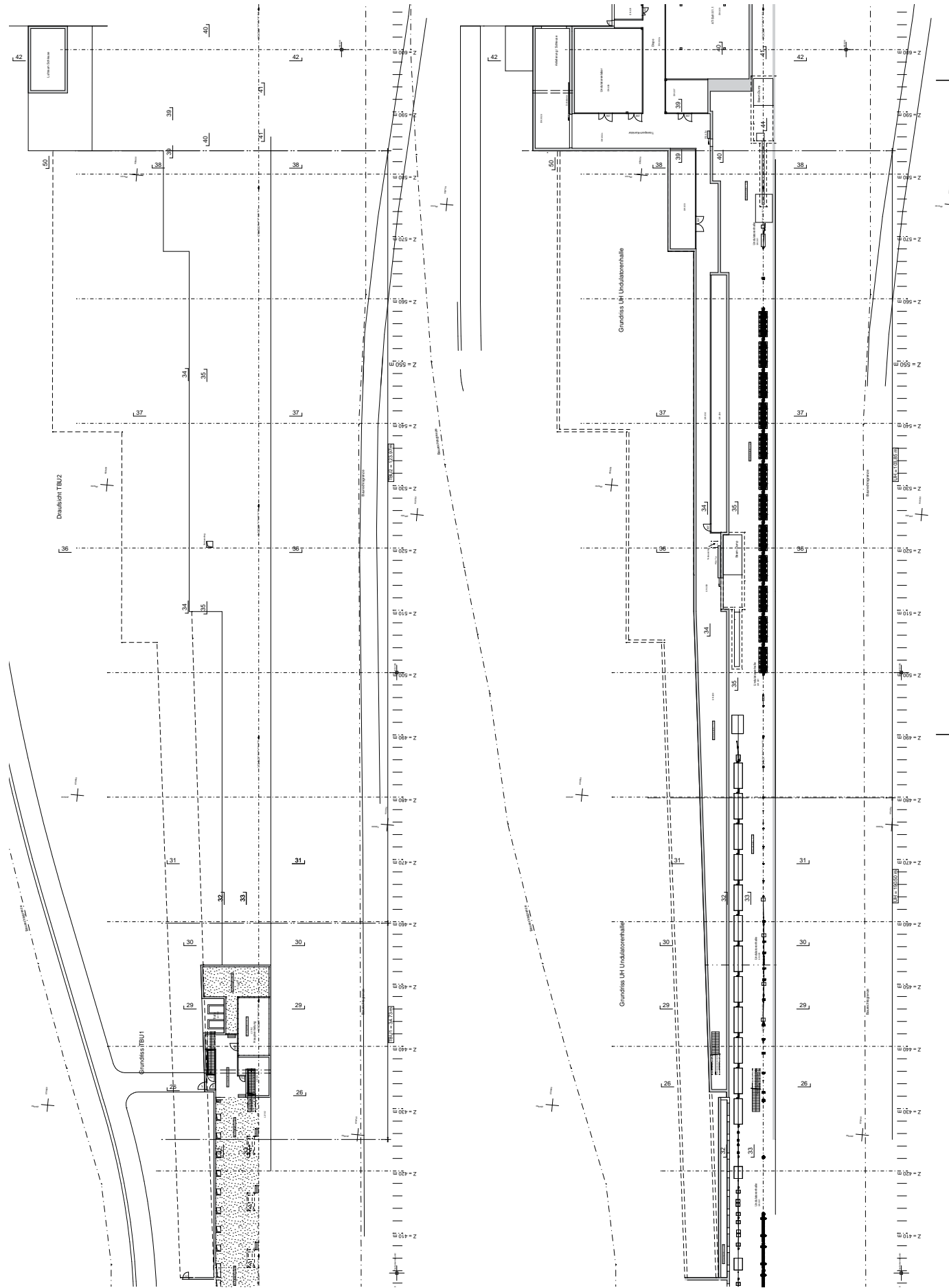
Recuperation of helium gas in the experimental hall will be take place through a collection pipe which will run along the complete beam tunnel. This collection pipe will be connected through the media tunnel with the PSI-East site, where a new helium conditioning plant will be installed.

Building and energy management system (MSR)

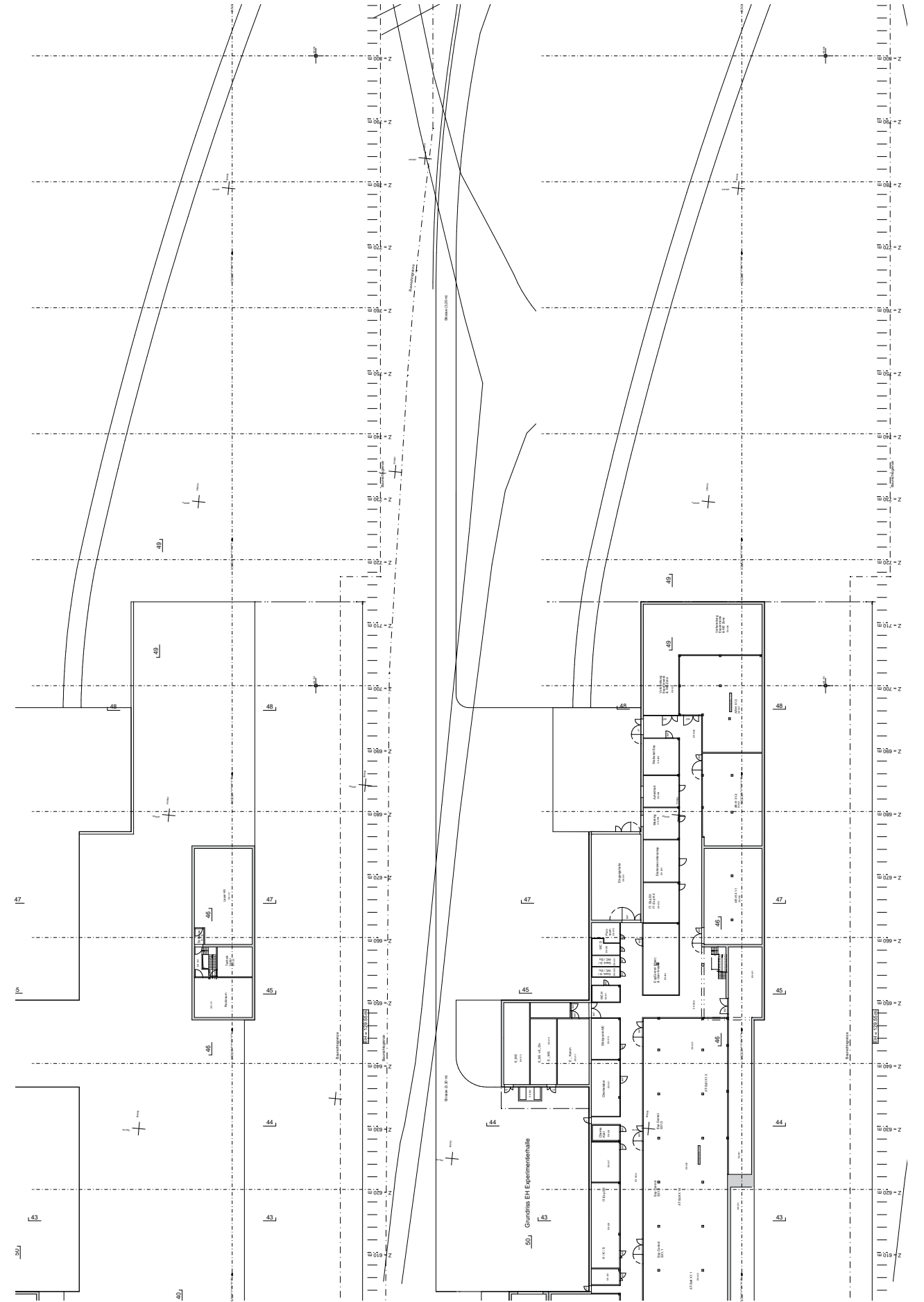
The SwissFEL MSR facility will be connected to the PSI MSR installation.

6.4 Appendix A: Drawing SwissFEL Building (Status October 2011)





Undulator Hall (Left: Top Floor; Right: Bottom Floor)



Experimental Hall (Left: Top Floor; Right Bottom Floor)

6.5 Appendix B: Version modifications SwissFEL CDR

Version Number	Date	Description of modifications since last version
V1	10.04.16	First Printed Version of CDR for the FLAC Meeting of 19th – 20th April 2010
V2	10.04.19	With summary tables on Experiments with Athos and Aramis
V3	10.04.20	Cosmetic Changes
V4	10.05.19	
V5	10.05.20	Cosmetic Changes
V6	10.05.27	Version sent to PSI Direction for ETH Rat Meeting With section on RF modulator concept With RF phase stability measurement from solid state modulator
V7	10.06.15	With the new RF frequencies 2.9988, 5.712, 11.9952 GHz
	10.06.15	With the new RF frequencies 2.9988, 5.712, 11.9952 GHz
V8	10.06.17	Cosmetic changes
V9	10.06.18	Cosmetic changes
V10	10.06.22	With Building Half covered with earth. With improved section 3.3 on synchronization First Version sent to Irma Herzog for Layout preparation
V11	10.07.04	With new Kicker Magnet design With new Undulator Girder Design (undulator quads on stand alone posts) undulator tolerance. With latest RF gun drawing With new inside dimension of Technical Buildings (4 m).
V13	10.07.08	Corrections from Trevor Dury (English Corrections) Removal of Appendix on Radiation Protection
V14	10.07.12	With new Tolerances from Bolko Beutner in Chapter 2 With new Mechanical Support concept from Peter Wiegand With English Corrections of those new sections
V15	10.07.12	Same as V14 but the Word file is splitted in 4 chapters to handle it more easily (large memory size due to the numerous Track changes)
V16	10.07.19	With new Switchyard and Collimator Design from Natalia Milas Removal of Fig 1.2.3 (SwissFEL layout too many times in manuscript).
V17	10.07.22	With Versioning Tables With RF structures key parameters table (filling time, ...) Minor format corrections; Numerous Typos
V18	10.08.19	Version in pdf only and which has the Layout prepared by Irma Herzog for the Inauguration Day of WLHA Version Printed in Large Series for Test Injector Facility inauguration

V19	11.01.19	<p>Chapter 1: Update figs, numbers, add correction M. Pedrozzi: 31.01.11 New SwissFEL overall schedule + Text: 03.03.11</p> <p>Chapter 2: New Fig 2.1.1 with new BC scheme from Bolko Beutner presented at FLAC april 2010 New Tolerances according to new BC scheme (from FLAC Nov. 2010) New Astra Simulation Results from A. Fallone (17.12.10) Some RF precisions (dual coupler) from J-Y. Raguin (18.12.10)</p> <p>Chapter 3: 3.2: RF: modifications from J-Y. Raguin, X band power consumption, r/Q for C band structure (18.12.10); C band power paragraph from Juergen Alex (01.02.11) . Update on magnets, (S. Sanfilippo 22.11.10) +drawings (Romain Ganter Jan 11) and PS parameters (R. Kuenzi – 20.12.10) Undulator: new parameter table (Romain Ganter) Diagnostics: New Layouts from Rasmus Ischebeck (Jan. 2011) Vac: new figs and summary table vac level</p> <p>Chapter 4: New Sketch up images from 13.01.11 New summary of the FLUTE THz source (Romain Ganter); One example of Athos experiment; With slides from Bill Pedrini on CuO exp.</p> <p>Chapter 5: Reference Coordinate system description (K. Dreyer 20.12.10); New transport concept (Johann Wickstrom 31.01.11) Magnet PS commissioning steps (R. Kuenzi) 20.12.10</p> <p>Chapter 6: Exchange of all building figures with New Sketch up V29 images from 07.01.11 Links and summary to Fuchs's latest SU documents; New Zonung Table (01.02.11) 20.01.11: Add corrections from P. Ming With new Electrical Consumption Table – R. Ganter (19.01.11) With W. Roser Corrections (20.01.11) 16.02.11: Implementation of various feedback from Authors. Opal simulations, distance aramis-athos.</p>
V20	11.11.03	<p>Introduction: Update milestones; Include SwissFEL Operation Mode Scenario</p> <p>Design Strategy and Parameter Choice: Removal of Injector Diagnostic FODO section: BC1 closer to L1 Independent Athos and Aramis Operation – Fixed extraction at 3 GeV – Athos Linac Semi-Analytical Compression Scheme Optimization New Switch Yard Design; New Athos EEHG Scheme Start to End FEL simulation with Flat Top Profile: > 600 μJ at 1 Å Update Tolerance Study: 0.018 deg Phase in S band No more Linac THz Source</p> <p>Electron Components: – RF: Final C band Structure design; Wakefield Study; C band module full layout – Magnets: All Magnets Parameters (200 Quads; 44 Dipoles; ...); – Overview PS Layout; 3 fast kickers and 1 septum – Undulator final Design: single column line; Undulator Error sources; measurement & tuning description – Diagnostic: Spectrometer Layout – Linac girder final layout; jack design; bunch compressor design; dilatation analysis</p> <p>Photon Components: – Front End Layout – X ray switchyard layout and Optics Parameters – Experimental Hall Layout: Experimental Stations Specificity and Equipments</p> <p>Assembly and Commissioning: Milestones and Assembly Plan – First assembly plan – Preliminary Commissioning Plan; Undulator Measurement Laboratory – Beam based alignment undulator line – Trajectory feedback</p> <p>Building and infrastructure: – New Experimental Hall; Beam Dump Underground; Undulator Lab and delivery – Temperature is 24 deg C – 2 D drawings in Annex – Infrastructure Data</p>

7 References

- [1] R. Bakker *et al.*, PSI, “X-FEL concept based on a low emittance gun,” Report No. Volume VI (2004).
- [2] R. J. Bakker *et al.*, in *Ultra High Brightness Accelerator Design, FEL06*, Berlin, Germany, 2006.
- [3] B. D. Patterson, Paul Scherrer Institut, “(Editor), SwissFEL Science Case – Ultrafast Phenomena at the Nanoscale: Science opportunities at the SwissFEL X-ray Laser,” Report No. 09–10 (2009).
- [4] P. Emma *et al.*, in *First lasing of the LCLS X-ray FEL at 1.5 Angstrom*, PAC2009, Vancouver, Canada, 2009.
- [5] P. Schmueser *et al.*, *Ultraviolet and Soft X-Ray Free-Electron-Lasers: Introduction to Physical Principles, Experimental Results, Technological Challenges*, Springer Tracts in Modern Physics (2008).
- [6] C. Hauri *et al.*, Intrinsic Emittance reduction of an Electron Beam from Metal Photocathodes, *Phys. Rev. Lett.* **104**, 234802 (2010).
- [7] A. Bolzmann, Investigation of the longitudinal charge distribution of electron bunches at the VUV-FEL using the transverse deflecting cavity LOLA, Master Thesis, Bayerische Julius-Maximilians Universitaet, Wurzburg, 2005.
- [8] S. Reiche, Paul Scherrer Institute (PSI), “Layout and Optics for SwissFEL” Report No. FEL-RV84-002 (2010).
- [9] K. Floettmann; ASTRA – A Space Charge Tracking Algorithm; <http://www.desy.de/~mpyflo/>
- [10] M. Ferrario *et al.*, *Particle Accelerators*, Vol. 52 (I) (1996).
- [11] M. Borland, APS, “Elegant: A flexible SDDS-Compliant Code for Accelerator Simulation,” Report No. APS LS-287 (2000).
- [12] W. Herr *et al.*, CERN, “A Mad-X Primer,” Report No. CERN-AB-2004-027-ABP.
- [13] K. L. F. Bane *et al.*, “LiTrack: A Fast, Longitudinal Phase Space Tracking Code with Graphical User Interface,” Report No. SLAC-PUB-11035.
- [14] S. Reiche, *Nucl. Inst. and Meth. A* **429**, 243 (1999).
- [15] M. Xie, in *PAC05*, 2005.
- [16] A. Adelman *et al.*, in *The Object Oriented Parallel Accelerator Library (OPAL)*, PAC2009, Vancouver (Canada), 2009.
- [17] A. Adelman *et al.*, A fast parallel Poisson solver on irregular domains applied to beam dynamics simulations *J. Comp. Phys.* **229**, 4554-4566 (2010).
- [18] Y. Kim, Future RF Gun for the SwissFEL Project, Presentation at the Project Meeting on July 1st, 2009 Report (2009) (Unpublished Work).
- [19] J. Arthur *et al.*, SLAC, “LCLS Conceptual Design Report,” Report No. SLAC-R-593 (UC-414) (2002).
- [20] R. Roux *et al.*, LAL-Orsay, “PHIN - Design of RF Photogun,” Report No. CARE Note-2004-034-PHIN (2004).
- [21] C.-X. Wang *et al.*, Criteria for emittance compensation in high-brightness photoinjectors *Phys. Rev. ST Accel. Beams* **10**, 104201 (2007).
- [22] L. Serafini *et al.*, *Phys. Rev. E* **55**, 7565 (1997).
- [23] Y. Kim, Personal Communication
- [24] Y. Ding *et al.*, Measurements and Simulations of Ultralow Emittance and Ultrashort Electron beams in the Linac Coherent Light Source, *PRL* **102**, 254801 (2009).
- [25] R. Ganter *et al.*, in *Commissioning of a diode / RF photogun combination*, FEL09, Liverpool, UK, 2009.
- [26] R. Ganter, B. Beutner *et al.*, Electron beam characterization of a combined diode – rf electron gun, *Phys. Rev. ST Accel. Beams* **13** (2010).
- [27] Y. Kim, Linac Beam Dynamics for the PSI XFEL, Presentation at the FLAC Meeting on April 21, 2009 Report (2009) (Unpublished Work).
- [28] I. Zagorodnov *et al.*, Semianalytical modeling of multistage bunch compression with collective effects, *PhysRevSTAB* **14**, 014403 (2011).
- [29] K. L. F. Bane *et al.*, Report No. SLAC-PUB-10707 (2004).
- [30] G. Stupakov *et al.*, *Phys. Rev. ST Accel. Beams* **12**, 030702 (2009).
- [31] D. Xiang, “First demonstration of the echo-enabled harmonic generation technique for short wavelength seeded free electron lasers,” Report No. SLAC-PUB-14199 (2010).
- [32] Z. Zhao, in *Seeding experiments at the SDUV-FEL, FEL*, Shanghai, China, 2011.
- [33] M. Ferray *et al.*, *Journal of Physics B: Atomic Molecular and Optical Physics* **21** (1988).
- [34] J. Feldhaus *et al.*, *Opt. Commun.* **140**, 341 (1997).
- [35] L. Yu *et al.*, *Nucl. Inst. and Meth. A* **393**, 96 (1997).
- [36] S. Reiche *et al.*, in *Seeding option for the soft X-ray beamline of SwissFEL, FEL09*, Liverpool, UK, 2009.
- [37] E. Prat *et al.*, in *EEHG Seeding Design for SwissFEL FEL*, Shanghai, China, 2011.
- [38] B. Beutner, PSI, “Bunch Compression Scheme and Longitudinal Tolerance in SwissFEL” Report No. FEL-BB84-001 (2010).
- [39] www.fastlite.com
- [40] B. J. Claessens *et al.*, Ultracold Electron Source, *Phys. Rev. Letters* **95**, 164801 (2005).
- [41] M. Dehler *et al.*, *Phys. Rev. ST Accel. Beams* **12** (2009).
- [42] H. Ego *et al.*, in *TRANSVERSE C-BAND DEFLECTING STRUCTURE FOR LONGITUDINAL PHASE SPACE DIAGNOSTICS IN THE XFEL/SPRING-8 “SACLA”*, IPAC, San Sebastian, Spain, 2011, p. 1221.
- [43] T. Sakurai *et al.*, in *High-Power RF test on the mass-produced C-band rf components for XFEL / Spring-8*, IPAC, Kyoto, Japan, 2010.
- [44] L. Doolittle *et al.*, in *Digital Low-Level RF Control Using Non-IQ Sampling*, LINAC’06, Knoxville, Tennessee, USA, 2006, p. 568.
- [45] S. Hunziker *et al.*, in *TOWARDS AN ULTRA-STABLE REFERENCE DISTRIBUTION FOR THE NEW PSI 250 MeV INJECTOR*, DIPAC, Basel, Switzerland, 2009, p. 266.
- [46] J. Kim *et al.*, in *Large scale timing distribution and RF-synchronisation for FEL facilities, FEL*, Trieste, Italy, 2004.
- [47] J. Kim *et al.*, Drift-free femtosecond timing synchronisation of remote optical and microwave sources, *Nature Photonics* **2**, 733–736 (2008).
- [48] S. Schulz *et al.*, in *Progress Towards a Permanent Optical Synchronisation Infrastructure at FLASH, FEL*, Liverpool, UK, 2009.
- [49] S. Schulz, in *Progress of the laser – based Synchronization System at FLASH, 48th ICFA Advanced Beam Dynamics Workshop on Future Light Sources*, Stanford, California USA, 2010.
- [50] O. Origami 15; www.onefive.com
- [51] T. Schibli *et al.*, *Opt. Lett.* **28**, 947 (2003).
- [52] J. Kim, *Opt. Lett.* **32**, 1044–1046 (2007).
- [53] S. Schulz *et al.*, in *Precision Synchronisation of the FLASH Photoinjector Laser*, IPAC, Kyoto, Japan, 2010.
- [54] F. Loehl *et al.*, in *PAC*, Albuquerque, USA, 2007, p. 3804–3806.
- [55] Corning; SMF-28 ULL Low PMD optical fiber; http://www.corning.com/opticalfiber/products/SMF-28_ULL_fiber.aspx
- [56] R. B. Wilcox *et al.*, in *A 20 fs synchronization system for lasers and cavities in accelerators and FELs*, SPIE, 2010, p. 7581.
- [57] F. Mueller *et al.*, in *Ytterbium fiber laser for electro-optical pulse length measurements at the SwissFEL*, DIPAC, Basel, Switzerland, 2009.
- [58] M. Felber *et al.*, in *Long-term femtosecond-stable rf signal generation from optical pulse trains*, PAC, Vancouver, Canada, 2009.
- [59] J. Taylor *et al.*, in *Characterization of noise properties in photodetectors: a step toward ultra-low phase noise microwaves*, *Precise Time and Time Interval PTTI*, Santa Ana pueblo, USA, 2009.
- [60] S. Hunziker *et al.*, in *Ultra-stable synchronization system development for FEL-sources: overview, status and perspectives* IRUVX Doellnsee-Schorfheide, Germany, 2010.

- [61] M. Pedrozzi *et al.*, PSI - Switzerland, "250 MeV SwissFEL Test Injector – Conceptual Design Report," Report No. FEL-PM06-089-18-Injector_conceptual_report.doc (2010).
- [62] J. Welch *et al.*, in *LCLS COMPRESSOR DIPOLE FIELD QUALITY AND BEAM MEASUREMENTS, FEL2008*, Korea, 2008.
- [63] M. Negrazus *et al.*, in *Magnet Design and Measurements Results of the Solenoids and Bunch Compressor Bending Magnets of the SwissFEL Test Facility, Conference on Magnet Technology*, Marseille, France, 2011.
- [64] F. Jenni *et al.*, in *A novel Control Concept for Highest Precision Accelerator Power Supplies, EPM-PEMC Cavtat & Dubrovnik*, 2002.
- [65] L. Tanner *et al.*, in *Digital Control for Highest Precision Accelerator Power Supplies, PAC*, Chicago USA, 2001.
- [66] F. Jenni *et al.*, in *Five years of operational experience with digitally controlled Power Supplies for beam control at the Paul Scherrer Institute (PSI), European Power Electronics Conference*, Dresden Germany, 2005.
- [67] M. Emmenegger *et al.*, in *A New Generation of Digital Power Supply Controllers, IPAC Conference*, Kyoto Japan, 2010.
- [68] T. Tanaka, in *In-situ undulator field measurement with the SAFFALI system, FEL 2007*, Novosibirsk, Russia, 2007.
- [69] H. Ego *et al.*, in *Design of the Transverse C-band RF Deflecting Structure for Measurement of Bunch Length in X-FEL, EPAC'08*, Genoa, Italy, 2008.
- [70] R. Ganter *et al.*, PSI Villigen, "SwissFEL Beam Dumps and Beam Stopper Specifications," Report No. FEL-GR06-123-11 (2011).
- [71] R. Ischebeck *et al.*, in *Screen monitor Design for the SwissFEL, DIPAC'09*, Basel, Switzerland, 2009.
- [72] P. Kung *et al.*, Generation and measurements of 50-fs (rms) Electron Pulses, *Phys. Rev. Lett.* **73**, 967 (1994).
- [73] J. Menzel, THz Spektroskopie zur Bunch-Laengemessung an der TESLA-Testanlage TTFThesis, University Hamburg – DESY, 2005.
- [74] D. Suetterlin, Single-Shot Electron Bunch Length Measurement with a Spatial Electro-Optical-Auto Correlation Interferometer using Coherent Transition Radiation at the 100 MeV SLS Pre-Injector LINAC Thesis, Institute of Technology Zurich ETH-Z, 2006.
- [75] G. Andonian *et al.*, in *A Single Shot Bunch Length Diagnostic Using Coherent Terahertz Radiation Interferometry, PAC'09*, Vancouver, Canada, 2009.
- [76] B. Steffen *et al.*, in *A Compact Single Shot Electro-Optical Bunch Length Monitor for the SwissFEL, DIPAC'09*, Basel, Switzerland, 2009.
- [77] F. Mueller *et al.*, in *Ytterbium Fiber Laser for Electro-Optical Pulse Length Measurements at the SwissFEL, DIPAC'09*, Basel, Switzerland, 2009.
- [78] B. Steffen, Electro-Optics Methods for Bunch Length Diagnostics at FLASHThesis, University Hamburg DESY, 2007.
- [79] B. Schmidt *et al.*, in *Longitudinal Structure of Electron Bunches at the Micrometer Scale from Spectroscopy of Coherent Transition Radiation, EPAC'08*, Genoa, Italy, 2008.
- [80] F. Loehl, Optical Synchronization of a Free Electron Laser with Femto-Second PrecisionThesis, University of Hamburg – DESY, 2009.
- [81] M. Bock *et al.*, in *Beam Arrival Time Monitors Used in a Time-Of-Flight Beam Energy Measurement, FEL'09*, Liverpool, UK, 2009.
- [82] T. O. Raubenheimer, SLAC, "A dispersion free trajectory correction technique for linear colliders," Report No. SLAC-PUB-5222 (1990).
- [83] H.-D. Nuhn, in *Electron Beam Alignment Strategy in the LCLS Undulators, FEL'06*, Berlin, Germany, 2006.
- [84] W. Decking, Personal Communication
- [85] H. Maseaka *et al.*, in *Beam Position Monitor at the SCSS Prototype Accelerator, APAC'07*, Indore, India, 2007.
- [86] D. Lipka *et al.*, in *Orthogonal Coupling in Cavity BPM With Slots, DIPAC'09*, Basel, Switzerland, 2009.
- [87] L. Schulz, PSI, "Heilige List Haupt Komponenten," Report No. FEL-SL88-027 (2010).
- [88] G. B. Bowden, in *RF Accelerator Pressure Profile by Monte Carlo, Linear Collider Collaboration Tech Notes LCC-0078*, 2002.
- [89] R. B. Neal *et al.*, SLAC, "The Stanford Two Miles Accelerator."
- [90] M. Seidel, Personal Communication
- [91] H. Kitamura, Spring-8/Riken, "In-Vacuum ID Technology, Spring-8/ Riken."
- [92] L. Yin *et al.*, "Preliminary Design of the Undulator Chamber for PSI XFEL," (2009).
- [93] S. Moeller, Presentation to SLAC Radiation Safety Committee Report (2009) (Unpublished Work).
- [94] B. L. Henke *et al.*, X-ray interactions: photoabsorption, scattering, transmission, and reflection at E=50-30000eV, Z=1-92, *Atomic Data and Nuclear Data Tables* **54**, 181–342 (1993).
- [95] CXRO website; http://henke.lbl.gov/optical_constants/
- [96] K. Tiedtke *et al.*, The soft x-ray free electron laser FLASH at DESY: beamlines, diagnostics, and end-stations, *New Journal of Physics* **11**, 023029 (2009).

- [97] U. Fruehling *et al.*, Single-shot Terahertz-Field-Driven X ray Streak Camera, *Nature Photonics* **3**, 523 (2009).
- [98] F. Tavella *et al.*, Few-Femtosecond Timing at Fourth Generation Light Sources, *Nature Photonics* **5**, 162 (2011).
- [99] E. Gouliemakis *et al.*, Direct Measurement of Light Waves, *Science* **305**, 1267 (2004).
- [100] S. P. Jamison *et al.*, in *Limitations of Electro-Optic Measurements of Electron Bunch longitudinal Profile, EPAC 2008*, Genoa, Italy, 2008, p. 1149.
- [101] T. Bartels *et al.*, Generation of single-cycle THz transients with high electric-field amplitudes, *Opt. Lett.* **30**, 2805 (2005).
- [102] H. N. Chapman *et al.*, *Nature* **470**, 73–77 (2010).
- [103] D. P. Bernstein, *Appl. Phys. Lett.* **95**, 134102 (2009).
- [104] D. Doering, *REVIEW OF SCIENTIFIC INSTRUMENTS* **82**, 073303 (2011).
- [105] H. Hirori *et al.*, Single-cycle terahertz pulses with amplitudes exceeding 1 MV/cm generated by optical rectification in LiNbO3 *Appl. Phys. Lett.* **98**, 091106 (2011).
- [106] T. Bartels *et al.*, Generation of single-cycle THz transients with high electric-field amplitudes, *Opt. Lett.* **30**, 2805 (2005).
- [107] A. Sell *et al.*, Phase-locked generation and field-resolved detection of widely tunable terahertz pulses with amplitudes exceeding 100 MV/cm *Opt. Lett.* **33**, 2767 (2008).
- [108] C. P. Hauri *et al.*, Strong-field single-cycle THz pulse generated in organic crystal, *Appl. Phys. Lett.* **99** (2011).
- [109] P. Ming, "Project Reference Rules," Report No. FEL-ME88-018 (2006).
- [110] T. O. Raubenheimer *et al.*, *NIM A* **302**, 191–208 (1991).
- [111] D. Schulte *et al.*, in *PAC'93*, 1993.
- [112] P. Tenenbaum, SLAC, Report No. SLAC-TN-03-058.
- [113] P. Emma *et al.*, *NIM – A* **429**, 407–413 (1999).
- [114] H.-D. Nuhn *et al.*, in *FEL'09*, Liverpool, UK, 2009, p. 714.
- [115] B. Keil *et al.*, in *Design of an Intra-Bunch-Train Feedback System for the European X-FEL, DIPAC'07*, Chicago, USA, 2007.
- [116] L. Tanner *et al.*, in *Digital Control For Highest Precision Accelerator Power Supplies, PAC'01*, Chicago, USA, 2001.
- [117] Y. Kim *et al.*, in *FEL'09, FEL'09*, Liverpool, UK, 2009.
- [118] M. T. Heron *et al.*, in *Performance and Future Developments of the Diamond Fast Orbit Feedback System, EPAC'08*, Genoa, Italy, 2008.
- [119] A. Neumaier, Solving Ill-Conditioned and Singular Linear Systems: A Tutorial on Regularization, *SIAM Review* **40**, 636–666 (1998).
- [120] A. Ziegler, "Langzeitmessungen der Bodenerschuetterungen fur die Varianten "Wald" und "Aare"," Report No. Ziegler Consultants #1666 (2010).
- [121] W. R. Nelson *et al.*, SLAC – USA, "The SHIELD11 Computer Code," Report No. SLAC-R-737, UC-414.
- [122] A. Fasso *et al.*, "Fluka: A multi-particle transport code," Report No. CERN-2005-010, INFN/TC 05/11, SLAC R-773 (2005).
- [123] R. Ganter *et al.*, PSI SwissFEL, "SwissFEL Beam Dumps and Beam Stoppers Specifications," Report No. FEL-GR06-123 (2011).
- [124] Conversion coefficients for use in radiological protection against external radiation, International Commission on Radiological Protection (ICRP) (1997).
- [125] T. Lippert *et al.*, "Allgemeine Weisung fur den Umgang mit Laser am PSI," Report No. AW-96-08-20.

Published by
Paul Scherrer Institut

Coordination
Romain Ganter

Design and Layout
Irma Herzog

Photographs
© Paul Scherrer Institut

Printing
Paul Scherrer Institut

Available from
Paul Scherrer Institut
Communications Services
5232 Villigen PSI, Switzerland
Phone +41 56 310 21 11
www.psi.ch

PSI public relations
pubrel@psi.ch

Copying is welcomed, provided
the source is acknowledged
and an archive copy sent to PSI.

Paul Scherrer Institut
April 2012

PAUL SCHERRER INSTITUT



Paul Scherrer Institut, 5232 Villigen PSI, Switzerland

Tel. +41 56 310 21 11, Fax +41 56 310 21 99

www.psi.ch